Available online at www.sciencedirect.com
SCIENCE DIRECT®
Nuclear Physics A 768 (2006) 61–79
NUCLEAR PHYSICS A

Mixed representation RPA calculation for octupole excitations on superdeformed states in the ^{40}Ca and neutron-rich sulfur regions

T. Inakura [a], H. Imagawa [b], Y. Hashimoto [b], S. Mizutori [c], M. Yamagami [d], K. Matsuyanagi [e,*]

[a] *Graduate School of Science and Technology, Niigata University, Niigata 950-2181, Japan*
[b] *Institute of Physics, University of Tsukuba, Ibaraki 305-8571, Japan*
[c] *Department of Human Science, Kansai Women's College, Osaka 582-0026, Japan*
[d] *Radioactive Isotope Physics Laboratory, RIKEN, Saitama 351-0198, Japan*
[e] *Department of Physics, Graduate School of Science, Kyoto University, Kyoto 606-8502, Japan*

Received 16 December 2005; accepted 13 January 2006

Available online 26 January 2006

Abstract

By means of the mixed representation RPA based on the Skyrme–Hartree–Fock mean field, we investigate low-frequency octupole excitations built on the superdeformed (SD) states in the $N = Z$ nuclei around ^{40}Ca and the neutron-rich sulfur isotopes. The RPA calculation is carried out fully self-consistently on the three-dimensional Cartesian mesh in a box, and yields a number of low-frequency octupole vibrations built on the SD states in ^{32}S, ^{36}Ar, ^{40}Ca and ^{44}Ti. In particular, a strongly collective $K^\pi = 1^-$ octupole vibration is suggested to appear on top of the SD state in ^{40}Ca. For ^{48,50}S close to the neutron drip line, we find that the low-lying state created by the excitation of a single neutron from a loosely bound low Ω level to a high Ω resonance level acquires an extremely strong octupole transition strength due to the spatially very extended structure of the particle–hole wave functions.

PACS: 21.60.-n; 21.60.Jz; 27.30.+t; 27.40.+z

Keywords: Skyrme–Hartree–Fock method; Mixed representation RPA; Superdeformation; Collective octupole vibration; $N = Z$ nuclei in the ^{40}Ca region; Neutron-rich sulfur isotopes; Neutron drip line

* Corresponding author.
E-mail address: ken@ruby.scphys.kyoto-u.ac.jp (K. Matsuyanagi).

0375-9474/$ – see front matter
doi:10.1016/j.nuclphysa.2006.01.008

1. Introduction

Nowadays, more than two hundreds superdeformed (SD) bands are identified in various mass ($A = 60, 80, 130, 150, 190$) regions [1–6]. Every SD regions have their own characteristics so that we can significantly enlarge and deepen our understanding of nuclear structure by systematically investigating similarities and differences among the SD bands in different mass region. The SD shell structure is significantly different from that of normal deformation. Namely, each major shell at the SD shape consists of about equal numbers of positive- and negative-parity levels. This is a favorable situation for the appearance of negative-parity collective modes. In fact, various mean-field calculations [7–9] and quasiparticle random phase approximation (RPA) [10,11] on the basis of the rotating mean field (cranked shell model) indicated that SD nuclei are very soft against both the axial and non-axial octupole deformations. Thus, low-frequency octupole vibrations have been predicted to appear near the SD yrast lines [12], and recently discovered in experiments for heavy SD nuclei in the Hg–Pb region [13], and also in ^{152}Dy [14].

In recent years, the SD bands have been discovered also in the ^{40}Ca region: in ^{36}Ar the SD band has been identified up to its termination at $I^\pi = 16^+$ [15–17]. The SD band in the spherical doubly magic nucleus ^{40}Ca is built on the 8p–8h excited 0^+ state at 5.213 MeV [18,19]. The SD shell gap at $N = 20$ ($Z = 20$) is associated with the neutron (proton) 4p–4h excitation from below the $N = 20$ ($Z = 20$) spherical closed shell to the $f_{7/2}$ shell. The rotational band built on the excited 0^+ state at 1.905 MeV in ^{44}Ti may also be regarded as belonging to a family of the SD band [20]. The fact that rotational bands built on excited 0^+ states are systematically observed is a unique feature of the SD bands in the ^{40}Ca region, considering that the low angular momentum portions of the SD bands in heavy nuclei are unknown in almost all cases (except the fission isomers). We have confirmed that the symmetry-unrestricted Skyrme–Hartree–Fock (SHF) calculation indeed yields the SD local minima corresponding to these experimental data [21]. It should be stressed that, in spite of the remarkable progress in experiment, the doubly magic SD band in ^{32}S associated with the SD magic number $N = Z = 16$, which has been anticipated quite a long time [22–31], has not yet been observed and remains as a great challenge.

If we believe that $Z = 16$ is a good SD magic number, the existence of the SD shell gap at $N = 20$, revealed by the discovery of the SD band in ^{40}Ca [18], suggests that another SD band would appear in the neutron-rich nucleus ^{36}S. Furthermore, combining with the fact that the SD bands have been observed in ^{60,62}Zn [32,33], we can expect that Sulfur isotopes around ^{48}S, which are situated close to the neutron drip line [34,35], constitute a new SD region associated with the SD shell gaps at $Z = 16$ and $N \simeq 32$. In fact, the symmetry-unrestricted SHF calculation [36] yields the SD local minima for ^{48,50}S as well as ^{32}S.

The investigation of low-frequency octupole vibrations built on the SD states in the $A = 30$–50 region possesses some new features that are absent in the study of heavy SD nuclei. For the $N = Z$ nuclei in the ^{40}Ca region, it may be possible to observe in experiment such collective modes built on the known SD 0^+ states. Moreover, because the proton and neutron shell structures are essentially the same, we can expect that strong coherence takes place between the proton and neutron excitations and brings about an enhanced collectivity of these modes. Concerning the anticipated new SD region around ^{48}S, we will encounter an essentially new situation: because these nuclei are situated close to the neutron drip line, there is almost no bound state above the Fermi surface and nucleons may excite into the continuum states even in the lowest excited states.

The study of soft collective modes unique to unstable nuclei close to the neutron drip line is one of the current major subjects in nuclear structure physics. For this purpose, the continuum RPA [37,38] based on the Green's function method correctly treating the continuum boundary

condition has been widely used (see, e.g., [39,40]). Recently, this method has been extended [41–43] to include the pairing correlations on the basis of the Hartree–Fock–Bogoliubov theory. It is called the continuum quasiparticle-RPA (QRPA). Furthermore, a new technique of solving the QRPA equations using the canonical basis has been developed [44]. The canonical basis has also been used in the QRPA calculation based on the relativistic mean field scheme [45,46]. A serious limitation of these works is that, because the construction of the Green's function for deformed mean fields is difficult, they are restricted to spherical nuclei. Quite recently, however, this limitation has been overcome by Nakatsukasa and Yabana [47]; they have proposed an iterative method of constructing the response functions for deformed systems with the proper boundary condition in the three-dimensional (3D) coordinate space. They have also proposed a feasible method of treating the continuum boundary condition by means of the real-space time-dependent HF approach with the absorbing boundary condition.

In this paper, we investigate low-frequency octupole excitations built on the SD states in neutron rich Sulfur isotopes as well as those in the ^{40}Ca region. For this purpose, we employ the mixed representation RPA [48–50] based on the SHF mean field. In this RPA scheme, the *particles* above the Fermi surface are described in the coordinate representation, while the *holes* are represented in the HF single-particle basis. The RPA calculation is carried out fully self-consistently on the 3D Cartesian mesh in a box. The major advantage of this approach is that it is a fully self-consistent scheme in the sense that the same effective interaction is used in both the mean field and the RPA calculations; i.e., all terms of the Skyrme interaction contributing to the RPA equations of motion are taken into account. It should be stressed here that such a fully self-consistent calculation using the Skyrme-type interaction is difficult in the Green's function approach, so that, usually, the residual particle–hole interactions associated with the spin–orbit and Coulomb interactions, as well as those associated with the time-odd components (related to the spin and current densities) of the mean field, are ignored in the continuum RPA based on the SHF mean field. Another important merit of our approach is that, thanks to the use of the 3D Cartesian mesh representation, we can treat strongly deformed nuclei on the same footing as spherical nuclei. Furthermore, because the *particles* are described in the coordinate representation, we do not need to introduce an upper cut off for their energies. Quite recently, Imagawa and Hashimoto constructed a new computer code that carries out the fully self-consistent RPA calculation in the mixed representation on the basis of the SHF mean field, and they carefully tested its numerical accuracy [51–53]. The numerical calculations of this paper were carried out using a refined version this code.

This paper is organized as follows. In Section 2, a brief account of the self-consistent RPA calculation using the mixed representation is given. In Section 3, we present and discuss the results of numerical calculation for low-frequency octupole vibrations built on the SD states in $N = Z$ nuclei, ^{32}S, ^{36}Ar, ^{40}Ca, and ^{44}Ti. In Section 4, the results for neutron-rich sulfur isotopes, ^{36}S, ^{48}S, and ^{50}S, are presented and discussed. The main results of this paper are summarized in Section 5.

A preliminary version of this work was reported in Refs. [54,55].

2. RPA calculation using the mixed representation

2.1. Basic formulae

The RPA equations in the mixed representation are easily derived either by means of the linearized equations of motion approach [48] or the small-amplitude approximation of the time-

dependent HF theory [49]. Here, we recapitulate the basic formula following the former approach.

The creation and annihilation operators of nucleon, $\psi^\dagger(x)$ and $\psi(x)$, are divided into those for the bound states and those for the continuum states:

$$\psi^\dagger(x) = \sum_\alpha \varphi_\alpha^*(x) c_\alpha^\dagger + \int_0^\infty \mathrm{d}\varepsilon\, \varphi_\varepsilon^*(x) c_\varepsilon^\dagger, \tag{1}$$

$$\psi(x) = \sum_\alpha \varphi_\alpha(x) c_\alpha + \int_0^\infty \mathrm{d}\varepsilon\, \varphi_\varepsilon(x) c_\varepsilon, \tag{2}$$

where x denotes a set of space, spin and isospin coordinates, i.e., $x = \{\boldsymbol{r}, \sigma, \tau\}$. The symbol α denotes the HF bound states with wave functions $\varphi_\alpha(x)$, while the energy ε specifies the continuum states with wave functions $\varphi_\varepsilon(x)$. With the use of the *particle* and *hole* concepts, we then divide the nucleon operators according to the occupation number θ_α in the HF ground state ($\theta_\alpha = 0$ for unoccupied states, $\theta_\alpha = 1$ for occupied states). We consider even–even nuclei and assume that the single-particle states α and their time reversed states are doubly degenerated. Obviously, the continuum states belong to the particle space. On the other hand, for the bound states, the operators $(c_\alpha^\dagger, c_\alpha)$ are divided into the particle operators $(a_m^\dagger, a_m)$ and the hole operators $(b_i^\dagger, b_i)$,

$$c_\alpha^\dagger = (1-\theta_\alpha) a_m^\dagger + \theta_\alpha b_i, \tag{3}$$

$$c_\alpha = (1-\theta_\alpha) a_m + \theta_\alpha b_i^\dagger, \tag{4}$$

where the indices m and i are used in place of α to distinguish the particle and hole states. Thus, the particle creation and annihilation operators, $a^\dagger(x)$ and $a(x)$, at the coordinate x are written in terms of the above $(a_m^\dagger, a_m)$ and the integration with respect to the positive energy ε specifying the continuum states:

$$a^\dagger(x) = \sum_m \varphi_m^*(x) a_m^\dagger + \int \mathrm{d}\varepsilon\, \varphi_\varepsilon^*(x) a_\varepsilon^\dagger, \tag{5}$$

$$a(x) = \sum_m \varphi_m(x) a_m + \int \mathrm{d}\varepsilon\, \varphi_\varepsilon(x) a_\varepsilon. \tag{6}$$

In the mixed representation, the coordinate representation is used for particles, while the HF basis specified by the discrete index i are used for holes. Thus, the following expressions of the nucleon operators are convenient:

$$\psi^\dagger(x) = a^\dagger(x) + \sum_i \varphi_i^*(x) b_i, \tag{7}$$

$$\psi(x) = a(x) + \sum_i \varphi_i(x) b_i^\dagger. \tag{8}$$

Note that

$$\left\{a(x), a^\dagger(x')\right\} = P(x,x') = \delta(x,x') - Q(x,x') \equiv \delta(x,x') - \sum_i \varphi_i(x)\varphi_i^*(x'), \tag{9}$$

where $P(x,x')$ and $Q(x,x')$ are the projectors onto the particle and hole spaces, respectively.

Using an abbreviation, $\sum_x \equiv \sum_{\sigma\tau} \int \mathrm{d}\boldsymbol{r}$, the RPA phonon creation operators in the mixed representation are written as

$$O_\lambda^\dagger = \sum_i \sum_x \left\{ X_i^\lambda(x) a^\dagger(x) b_i^\dagger - Y_i^\lambda(x) b_i a(x) \right\}. \tag{10}$$

Then, the RPA eigenvalue equations determining the eigenenergies, $\hbar\omega_\lambda$, and the forward and backward amplitudes, $X_i^\lambda(x)$ and $Y_i^\lambda(x)$ are given in the following form:

$$\sum_j \sum_{x'} \left[A_{ij}(x,x') X_j^\lambda(x') + B_{ij}(x,x') Y_j^\lambda(x') \right] = \hbar\omega_\lambda X_i^\lambda(x), \tag{11}$$

$$\sum_j \sum_{x'} \left[B_{ij}^*(x,x') X_j^\lambda(x') + A_{ij}^*(x,x') Y_j^\lambda(x') \right] = -\hbar\omega_\lambda Y_i^\lambda(x), \tag{12}$$

where

$$A_{ij}(x,x') = \sum_{x'',x'''} P(x,x'') \tilde{A}_{ij}(x'',x''') P(x''',x'), \tag{13}$$

$$B_{ij}(x,x') = \sum_{x'',x'''} P(x,x'') \tilde{B}_{ij}(x'',x''') Q(x''',x'), \tag{14}$$

and

$$\tilde{A}_{ij}(x,x') = \left[h_{\mathrm{HF}}(x,x') - e_i \delta(x,x') \right] \delta_{ij} + \sum_{x''x'''} \varphi_i(x'') \varphi_j^*(x''') \frac{\partial^2 E[\rho]}{\partial\rho(x'',x)\partial\rho(x',x''')}, \tag{15}$$

$$\tilde{B}_{ij}(x,x') = \sum_{x''x'''} \varphi_i(x'') \varphi_j(x''') \frac{\partial^2 E[\rho]}{\partial\rho(x'',x)\partial\rho(x''',x')}. \tag{16}$$

The above RPA equations can be recast into the following form for the linear combinations, $\phi_i^{(\pm)\lambda}(x) = X_i^\lambda(x) \pm Y_i^{\lambda *}(x)$:

$$\sum_{x'} \left[h_{\mathrm{HF}}(x,x') - e_i \delta(x,x') \right] \phi_i^{(+)\lambda}(x') + \sum_{x'x''} P(x,x') h_{\mathrm{RPA}}^{(+)\lambda}(x',x'') \varphi_i(x'') = \hbar\omega_\lambda \phi_i^{(-)\lambda}(x), \tag{17}$$

$$\sum_{x'} \left[h_{\mathrm{HF}}(x,x') - e_i \delta(x,x') \right] \phi_i^{(-)\lambda}(x') + \sum_{x'x''} P(x,x') h_{\mathrm{RPA}}^{(-)\lambda}(x',x'') \varphi_i(x'') = \hbar\omega_\lambda \phi_i^{(+)\lambda}(x). \tag{18}$$

Here, the RPA Hamiltonian is given by

$$h_{\mathrm{RPA}}^{(\pm)\lambda}(x,x') = \sum_{x'',x'''} \rho^{(\pm)\lambda}(x'',x''') \frac{\delta h_{\mathrm{HF}}(x,x')}{\delta\rho(x'',x''')}, \tag{19}$$

where

$$\rho^{(\pm)\lambda}(x,x') = \sum_i \left[\varphi_i^*(x') \phi_i^{(\pm)\lambda}(x) \pm \phi_i^{(\pm)\lambda *}(x') \varphi_i(x) \right] \tag{20}$$

represents the transition density. The above equations are obtained also by making the small-amplitude approximation for the equations of motion of the time-dependent HF mean field [49].

The explicit expression of $h^{(\pm)\lambda}_{\rm RPA}(x,x')$ is given in Appendix A. The transition matrix elements for the octupole operators Q_{3K} are given by

$$\langle 0|Q_{3K}|\lambda\rangle = \sum_x Q_{3K}(\boldsymbol{r}) \sum_i \left[X_i^\lambda(x)\varphi_i^*(x) + \varphi_i(x)Y_i^\lambda(x)\right].$$

2.2. Details of numerical calculation

We solve the SHF equation on the 3D Cartesian mesh assuming the reflection symmetry about the (x,y)-, (y,z)-, and (z,x)-planes. The derivative operators are treated by means of the Lagrange mesh method [56], except for the derivative of the Coulomb potential for which the finite difference method with the 9 points formula is used. Based on the numerical test explained below, we adopt the mesh spacing $\Delta x = 0.6$ fm. Because we treat the superdeformed nuclei, we use the rectangular box with 15 and 25 mesh points in the positive directions of the minor and major axes, respectively, i.e., we take the mesh points at $x = 0.3, 0.9, \ldots, 8.7$ fm, $y = 0.3, 0.9, \ldots, 8.7$ fm and $z = 0.3, 0.9, \ldots, 14.7$ fm (the major axis is called the z-axis). Considering the reflection symmetries, the total size of the box is thus $17.4 \times 17.4 \times 29.4$ fm^3. For the effective interaction, the standard versions of the Skyrme interaction, SIII [57], SkM* [58] and SLy4 [59], are used.

We then solve the RPA equations, (17) and (18), using the SHF solutions obtained above. With the mesh discretization, Eqs. (17) and (18) become the matrix eigenvalue problem with the $2 \times N_h \times N_p$ dimension, where N_h and N_p denote the numbers of the hole states and the mesh points, respectively. Because we assume the reflection symmetry about the three planes, the RPA eigenvalue equations are separated into four blocks specified by the parity quantum numbers. It is easily ascertained that the negative parity operators are classified into the four groups, $(-,+,+)$, $(+,-,+)$, $(+,+,-)$, and $(-,-,-)$, where the first, the second, and the third signs indicate the parity with respect to the reflection about the (y,z)-, (z,x)-, and (x,y)-planes, respectively. For instance, the octupole operator $Q_{30} = r^3 Y_{30}$ belongs to the $(+,+,-)$ sector. On the other hand, the octupole operators with $K \neq 0$, $Q^{(\pm)}_{3K} = r^3\left(Y_{3K} \pm Y_{3,-K}\right)/\sqrt{2}$, are classified according to the parity quantum numbers as shown in Table 1. We calculate the eigenvalues and eigenvectors of the RPA matrix by means of the conjugate gradient method in a version developed in Refs. [51–53].

It should be noted here that the translational symmetry is broken in the coordinate mesh representation so that the eigenvalues of the RPA corresponding to the spurious center of mass motion do not necessarily become zero. It is possible that the eigenvalue $\hbar\omega_\lambda$ corresponding to the spurious mode become pure imaginary. Moreover, in deformed nuclei, except for the $(-,-,-)$ sector, these spurious modes can mix with the octupole modes having the same symmetry properties (see Table 1 for the classification of the dipole operators corresponding to the center of mass motion). It is therefore very important to carefully check the accuracy of numerical calculation whether or not the spurious center of motions are decoupled from the physical excitations in a good approximation. In the numerical calculation, we manipulate this problem with the following procedure. Combining Eqs. (11) and (12), the RPA eigenvalue problem is transformed into the following form:

$$\sum_{jk}\sum_{x',x''}\left[A_{ij}(x,x')A_{jk}(x',x'') - A_{ij}(x,x')B_{jk}(x',x'') + B_{ij}(x,x')A_{jk}(x',x'') - B_{ij}(x,x')B_{jk}(x',x'')\right]\phi_k^{(-)\lambda}(x'') = (\hbar\omega_\lambda)^2\phi_i^{(-)\lambda}(x). \quad (21)$$

Table 1
Classification of octupole and dipole operators according to the parity quantum numbers with respect to reflections about the (y,z)-, (z,x)- and (x,y)-planes

Symmetry	Octupole	Dipole
$(-,+,+)$	$Q_{31}^{(+)}$, $Q_{33}^{(+)}$	x
$(+,-,+)$	$Q_{31}^{(+)}$, $Q_{33}^{(+)}$	y
$(+,+,-)$	Q_{30}, $Q_{32}^{(+)}$	z
$(-,-,-)$	$Q_{32}^{(-)}$	none

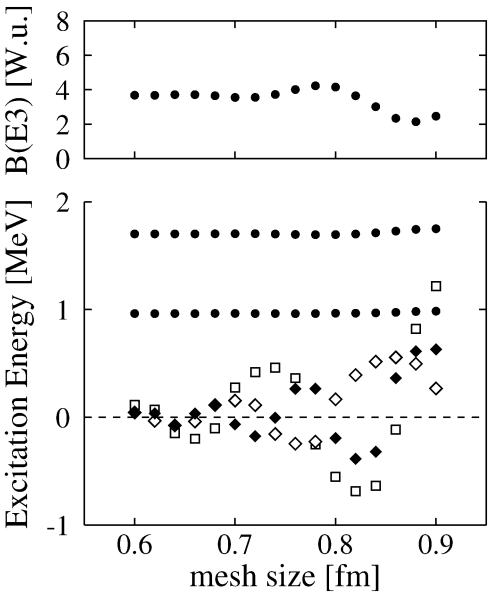

Fig. 1. Low-energy solutions of the RPA for negative-parity excitations on the SD ground state in ^{40}Ca, plotted as functions of the mesh spacing used in the SHF + RPA calculation with the SIII interaction. Lower part: energies of the spurious center of mass modes belonging to the $(-,+,+)$, $(+,-,+)$ and $(+,+,-)$ sectors are plotted with open diamonds, filled diamonds, and open squares, respectively. When their excitation energies, $\hbar\omega_\lambda$, take imaginary values, the $-|\omega_\lambda|$ values are plotted for convenience of presentation. The filled circles at about 1.0 and 1.7 MeV indicate the lowest physical excitations in the $(-,+,+)$ and $(+,-,+)$ sectors, respectively. Upper part: transition strengths for the lowest physical excitation at about 1.7 MeV in the $(+,-,+)$ sector, plotted as a function of mesh spacing.

This form is convenient for applying the conjugate gradient method which is valid only for real eigenvalues, because, when the eigenvalue $\hbar\omega_\lambda$ of the spurious mode take an imaginary value, we can easily identify it as a negative $(\hbar\omega_\lambda)^2$ solution of this equation. The result of such an accuracy test of numerical calculation is presented in Fig. 1. In this figure, low-energy solutions of the above RPA equation for negative-parity excitations on the SD ground state in ^{40}Ca are plotted as functions of the mesh spacing Δx used in the SHF–RPA calculation with the SIII interaction. We see that a good convergence is attained at about $\Delta x = 0.6$ fm, although excitation energies of the spurious center of mass modes fluctuate in the region of $\Delta x > 0.7$ fm. It should be noted that the excitation energies of the physi-

cal excitation modes and their transition strengths almost converge for $\Delta x < 0.7$ fm. Thus, we adopt $\Delta x = 0.6$ fm in the numerical calculations presented below. We note that the use of this mesh spacing corresponds the introduction of an effective energy cut-off $E_{\text{cut-off}} = (\hbar^2/2m)(\pi/\Delta x)^2 \sim 500$ MeV. This value is sufficiently large. Accordingly, it may be allowed to say that our calculation is, in practice, cut-off free. Certainly, it is desirable to use a smaller Δx and a larger box for better numerical accuracy, but it is difficult to do so with the available computing power at the present time. This limitation will be overcome in the near future.

In presenting the results of the SHF–RPA calculation in the subsequent sections, we label the SHF single-particle levels in terms of the asymptotic quantum numbers $[N_{\text{osc}}, n_z, \Lambda, \Omega]$ for the modified oscillator potential. It should be noted that this labeling is used solely for convenience of presentation, and do not always mean that they are good quantum numbers. The labeling of the SHF single-particle states is done by examining their properties, like reflection symmetries and expectation values of the angular momentum, and by comparison with the single-particle level scheme obtained in Ref. [60], where the deformed Woods–Saxon potential simulating the SHF potential was constructed and properties of both the bound states and the discretized continuum states for this potential are analyzed in detail. In this reference, the RPA calculations were also carried out for the octupole excitations on the SD states under consideration, using the conventional matrix formulation with these single-particle levels in a truncated model space and a density dependent contact interaction. The results of this simple RPA calculation qualitatively agree with the results of the mixed representation RPA calculation presented below. Thus, we have used the correspondence between the two calculations for checking the numerical calculation. As we shall discuss later, this comparison was especially useful for the purpose of distinguishing the resonant levels from the non-resonant discretized continuum levels.

3. Results of calculation for the ^{40}Ca region

Fig. 2 displays the transition strength distributions obtained by the SHF–RPA calculation with the SIII interaction for low-frequency octupole excitations built on the SD states in ^{32}S, ^{36}Ar, and ^{40}Ca. The RPA transition strengths $B(Q^{\text{IS}}3)$ are here defined as the squared matrix elements of the isoscalar octupole operators between the SD excited state $|\lambda\rangle$ and the SD ground state $|0\rangle$, $B(Q^{\text{IS}}3) = |\langle 0|Q^{\pi}_{3K} + Q^{\nu}_{3K}|\lambda\rangle|^2$. In this figure, the RPA transition strengths for the electric octupole operators, $B(\text{E3}) = |\langle 0|Q^{\pi}_{3K}|\lambda\rangle|^2$, are also indicated for levels possessing strong collectivity. Here, Q^{π}_{3K} and Q^{ν}_{3K} denote the proton and neutron octupole operators. It should be noted that these quantities represent the intrinsic matrix elements squared. Accordingly, in order to evaluate the reduced transition probabilities in the laboratory frame, appropriate Clebsch–Gordan (CG) coefficients squared and other kinematical factors should be multiplied to them [61]. Specifically, for the transition from the 3^- member of the $K = 0$ ($K \neq 0$) band to the SD 0^+ band head, the CG coefficient is unity and the kinematical factor is $1/7$ $(2/7)$. The SHF calculation for ^{40}Ca in fact yields a SD mean field with small triaxially of $\gamma = 7°$, while the SD solutions for ^{32}S and ^{36}Ar are axially symmetric. Nevertheless, for simplicity, we here present the result of the RPA calculation on the basis of the SHF mean field obtained under the constraint $\gamma = 0°$. The effect of the small triaxial deformation on these excitation modes will be discussed in the end of this section.

For ^{32}S, we obtain a low-frequency collective $K^{\pi} = 2^-$ mode at 2.6 MeV above the SD band head. It possesses a large isoscalar octupole transition strength of 30 W.u. (1 W.u. $\simeq$ 61 fm^6 for ^{32}S). The unperturbed strengths in the 3.5 MeV region, seen in Fig. 2, are associated

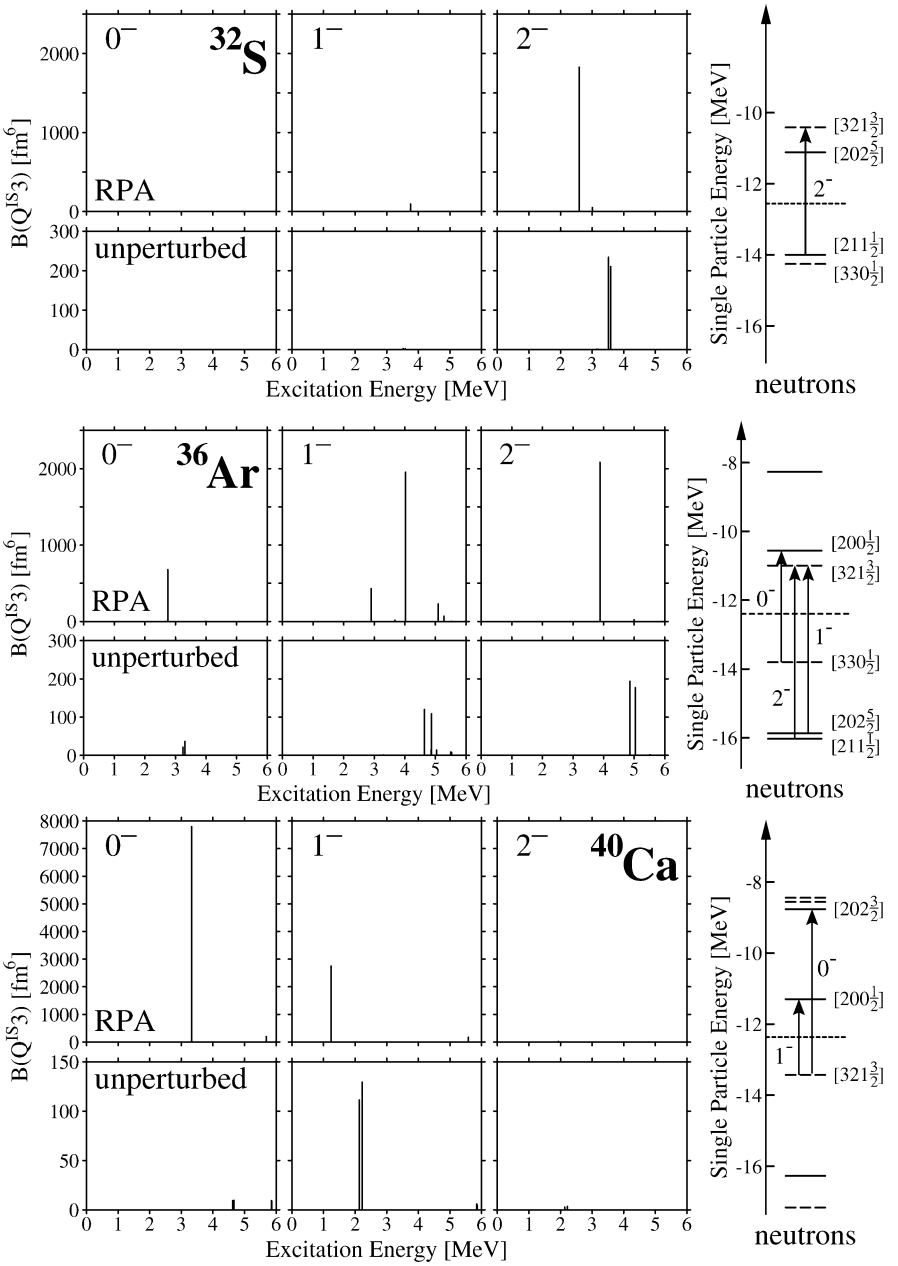

Fig. 2. Isoscalar octupole transition strengths for $K^\pi = 0^-$, 1^- and 2^- excitations on the SD states in (a) ^{32}S, (b) ^{36}Ar, and (c) ^{40}Ca, obtained by the SHF–RPA calculation with the SIII interaction. The unit is fm^6. For comparison with the RPA strengths, unperturbed particle–hole strengths are also shown in the lower panels for each nucleus. There are no significant strengths for $K^\pi = 3^-$ excitations values in this low-energy region, so that they are not shown. Some particle–hole excitations of neutrons near the Fermi surface are drawn by arrows with their K^π values in the rightmost part for each nucleus. We have similar excitations also for protons. The solid, dashed, and dotted lines indicate positive-parity levels, negative-parity levels, and the Fermi surface, respectively. The asymptotic quantum numbers $[Nn_z\Lambda\Omega]$ are indicated for pertinent levels.

with the proton and neutron excitations from the $[211\frac{1}{2}]$ level to the $[321\frac{3}{2}]$ level. The RPA transition strength is greatly enhanced in comparison with the unperturbed strengths and the RPA eigenenergy is significantly shifted down from the unperturbed particle–hole excitation energies, so that this $K^\pi = 2^-$ mode can be regarded as a collective octupole vibration.

For ^{36}Ar, we obtain two strongly collective modes; a $K^\pi = 2^-$ mode at 3.9 MeV and a $K^\pi = 1^-$ mode at 4.0 MeV. They possess large isoscalar octupole transition strengths of 27 and 25 W.u., respectively (1 W.u. $\simeq$ 77 fm^6 for ^{36}Ar). This 2^- mode is similar to that in ^{32}S discussed above, except for the following difference: because the quadrupole deformation of the SD state in ^{36}Ar is smaller ($\beta_2 = 0.51$) than that in ^{32}S ($\beta_2 = 0.72$), the unperturbed particle–hole excitation energies (4.9–5.0 MeV) of protons and neutrons from the up-sloping $[211\frac{1}{2}]$ level to the down-sloping $[321\frac{3}{2}]$ level are larger in ^{36}Ar than in ^{32}S. Accordingly, the RPA excitation energy of the 2^- mode in ^{36}Ar is higher than that in ^{32}S. Concerning the 1^- mode, its excitation energy is considerably shifted down from the particle–hole excitation energies (4.6–4.9 MeV) of protons and neutrons from the $[202\frac{5}{2}]$ level to the $[321\frac{3}{2}]$ level. Considering this together with the enhanced transition strength, this 1^- mode can also be regarded as a mode possessing strongly collectivity. In addition to the 2^- and 1^- modes mentioned above, we also obtain a 0^- mode and another 1^- mode in the 2.8–2.9 MeV region, which are moderately collective.

For ^{40}Ca, we obtain a low-frequency collective $K^\pi = 1^-$ mode at about 1.2 MeV. It possesses a large isoscalar octupole transition strengths of 29 W.u. (1 W.u. $\simeq$ 95 fm^6 for ^{40}Ca). The unperturbed particle–hole strengths in the 2.2 MeV region are associated with the proton and neutron excitations from the $[321\frac{3}{2}]$ level to the $[200\frac{1}{2}]$ level. The fact that the RPA transition strength is significantly enhanced in comparison with the unperturbed strength and the RPA eigenenergy is shifted down from the unperturbed particle–hole excitation energies indicates that this $K^\pi = 1^-$ mode possesses a strong collectivity. We also obtained a strongly collective $K^\pi = 0^-$ mode possessing quite large strength (82 W.u.) at about 3.3 MeV. For this $K^\pi = 0^-$ transitions, although small unperturbed strengths (about 0.1 W.u.) associated with the particle–hole excitations of protons and neutrons from the $[321\frac{3}{2}]$ level to the $[202\frac{3}{2}]$ level are seen at about 4.6 MeV, their strengths are small mainly because they strongly violate the asymptotic selection rule for low-energy octupole transitions in the SD harmonic-oscillator potential [11]. Thus, this collective $K^\pi = 0^-$ mode is generated mainly from many particle–hole configurations lying in the energy region higher than that shown in this figure. We mention that these collective modes in ^{40}Ca were previously reported by one of authors (H.I.) in Ref. [51].

For all the RPA eigenmodes presented in Fig. 2, we can say the followings:

(1) The approximate relation, $B(Q^{\mathrm{IS}}3) \approx 4B(\mathrm{E3})$, holds, indicating that they are collective modes generated by coherent superposition of proton and neutron excitations.
(2) The RPA strengths are greatly enhanced from the unperturbed strengths of individual particle–hole excitations. This indicates that these RPA eigenmodes are generated by collective contributions of quite a number of particle–hole excitations.

The role of coherence between the neutron and proton excitations in building up these collective enhancements can also be seen by comparing these RPA transition strengths for the $N = Z$ nuclei, ^{32}S and ^{40}Ca, with those for the $N \neq Z$ nucleus ^{36}S presented in the succeeding section.

We also carried out the same kind of calculation using the SkM* [58] and the SLy4 [59] interactions. The results for strongly collective excitations of these SHF–RPA calculations with different versions of the Skyrme interaction are compared in Fig. 3. Note that the calculations for ^{40}Ca were done with the constraint $\gamma = 0^\circ$ for the mean fields, although the SHF calculations

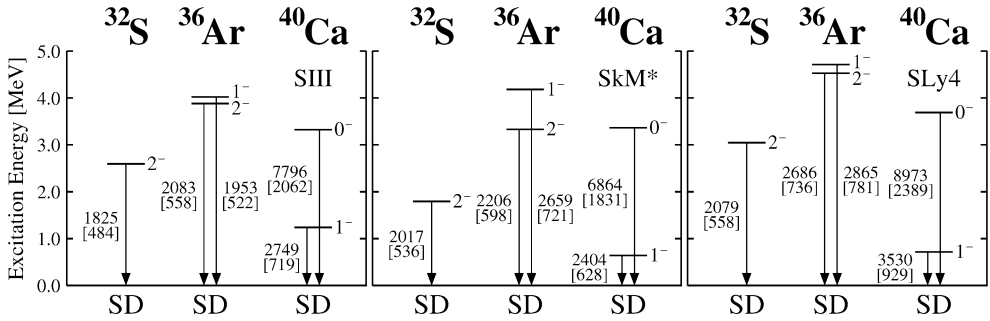

Fig. 3. Comparison of the SHF–RPA calculations with the SIII, SkM* and SLy4 interactions for collective octupole excitations on the SD states in ^{32}S, ^{36}Ar, and ^{40}Ca. Only collective excitations having $B(Q^{\mathrm{IS}}3)$ greater than 10 W.u. are displayed here (see Fig. 2 for other excitations having smaller strengths). The numbers on the right-hand sides of individual levels indicate the K quantum numbers. The numbers beside the arrows indicate the intrinsic transition matrix elements squared of the isoscalar octupole operator, $B(Q^{\mathrm{IS}}3)$, in units of fm^6. Those for the electric octupole operator, B(E3), are also given in brackets in units of e^2 fm^6.

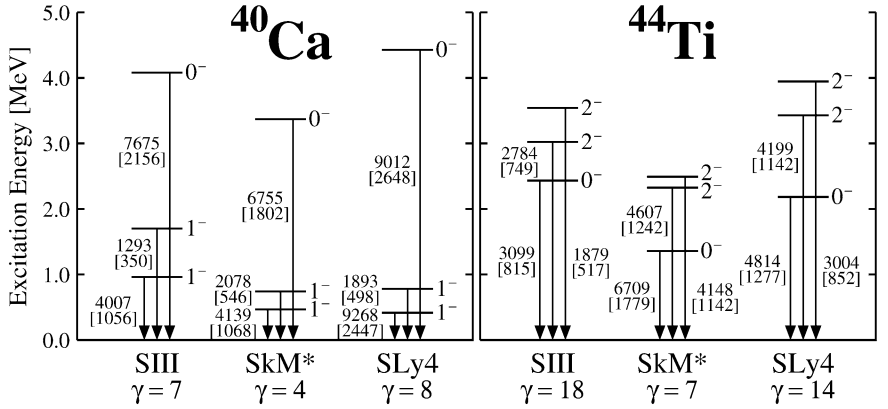

Fig. 4. Low-frequency collective octupole excitations on the SD states in ^{40}Ca and ^{44}Ti, obtained by the SHF–RPA calculation taking into account the triaxial deformation of the mean field. Only collective excitations having $B(Q^{\mathrm{IS}}3)$ greater than 10 W.u. are displayed here. The numbers on the right-hand sides of individual levels indicate the approximate K quantum numbers, The numbers beside the arrows indicate the intrinsic transition matrix elements squared of the isoscalar octupole operator, $B(Q^{\mathrm{IS}}3)$, in units of fm^6. Those for the electric octupole operator, B(E3), are also given in brackets in units of e^2 fm^6. The Skyrme interaction used and the triaxial deformation γ of the mean field are indicated at the bottom.

yield small triaxial deformations; 4° and 8° with the SkM* and SLy4 interactions, respectively. For all excitation modes discussed above, we obtained the results qualitatively similar to those with the SIII interaction. Namely, our prediction about the existence of these collective modes is rather robust, depending little on the choice of the Skyrme interaction.

Next, let us examine the effects of the triaxial deformations of the SD mean field on the RPA eigenmodes discussed above. Fig. 4 shows the strongly collective excitations in ^{40}Ca and ^{44}Ti, obtained by the RPA calculation taking into account the triaxiality of the SD mean fields. Because K is not a good quantum number due to the K mixing, the K values denoted on the right-hand sides of individual levels indicate the maximum components, and the transition strengths for these K values are indicated beside the arrows in this figure. A clear consequence of the triaxi-

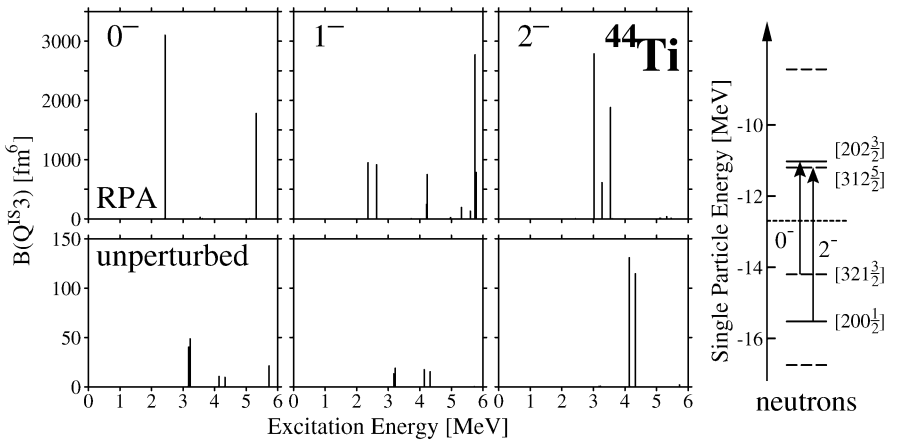

Fig. 5. The same as Fig. 2, but for octupole excitations on the triaxial SD state in ^{44}Ti. Note that, due to the triaxial deformation, K is not a good number for single-particle levels. The asymptotic quantum numbers $[Nn_z\Lambda\Omega]$ beside the pertinent levels in the rightmost figure merely indicate their main components.

ality is that the $K \neq 0$ modes split into doublets. This qualitative feature is common to the RPA calculations with the SIII, SkM* and SLy4 interactions. Concerning the ^{40}Ca case, however, the small triaxiality ($\gamma < 10°$) in the HF mean field might be easily diminished by, e.g., the zero-point fluctuation in the γ direction and/or pairing correlations. Therefore, it is not clear whether this splitting of the 1^- mode is important or not. On the other hand, the triaxial deformations for ^{44}Ti, obtained in the SHF calculations with the SIII and SLy4 interactions, are significantly larger than those for ^{40}Ca (see the γ values indicated at the bottom of Fig. 4). In such cases, it may be interesting to examine the theoretical calculation against possible experimental signatures of the triaxiality. For instance, the calculation with the SIII interaction yields a "$K^\pi = 0^-$" collective mode at 2.4 MeV and a "$K^\pi = 2^-$" doublet at 3.0 and 3.5 MeV, which possess large isoscalar octupole transition strengths of 27, 24 and 16 W.u., respectively (1 W.u. $\simeq$ 115 fm^6 for ^{44}Ti). In addition, we also obtain another 0^- mode at 5.3 MeV, two 1^- doublets at 2.5 and 4.2 MeV, and another 2^- doublet at 3.2 MeV, which are moderately collective (not shown in Fig. 4 but displayed in Fig. 5).

The RPA transition strengths are compared with the unperturbed particle–hole strengths in Fig. 5. For the $K = 0$ transitions, small unperturbed strengths (about 0.15 W.u.) associated with the particle–hole excitations of protons and neutrons from the $[321\frac{3}{2}]$ level to the $[202\frac{3}{2}]$ level are seen at about 3.2 MeV. For the $K = 2$ transitions, the peaks in the 4.1–4.3 MeV region in the unperturbed strengths are associated with the particle–hole excitations of protons and neutrons from the $[200\frac{1}{2}]$ level to the $[312\frac{5}{2}]$ level. These "$K^\pi = 0^-$" and "$K^\pi = 2^-$" RPA modes are generated by collective superpositions of not only these relatively low-lying configurations but also many particle–hole configurations lying in the higher energy region. Thus, the present RPA calculation suggests that the appearance of the 2^- doublet may serve as a good indicator of the triaxial nature of the SD state of ^{44}Ti. Experimental search for such a doublet on top of the SD band head seems very interesting.

4. Results of calculation for the neutron-rich sulfur region

Fig. 6 displays the transition strength distributions obtained by the SHF–RPA calculation with the SIII interaction for low-frequency octupole excitations built on the SD states in ^{36,48,50}S. Let

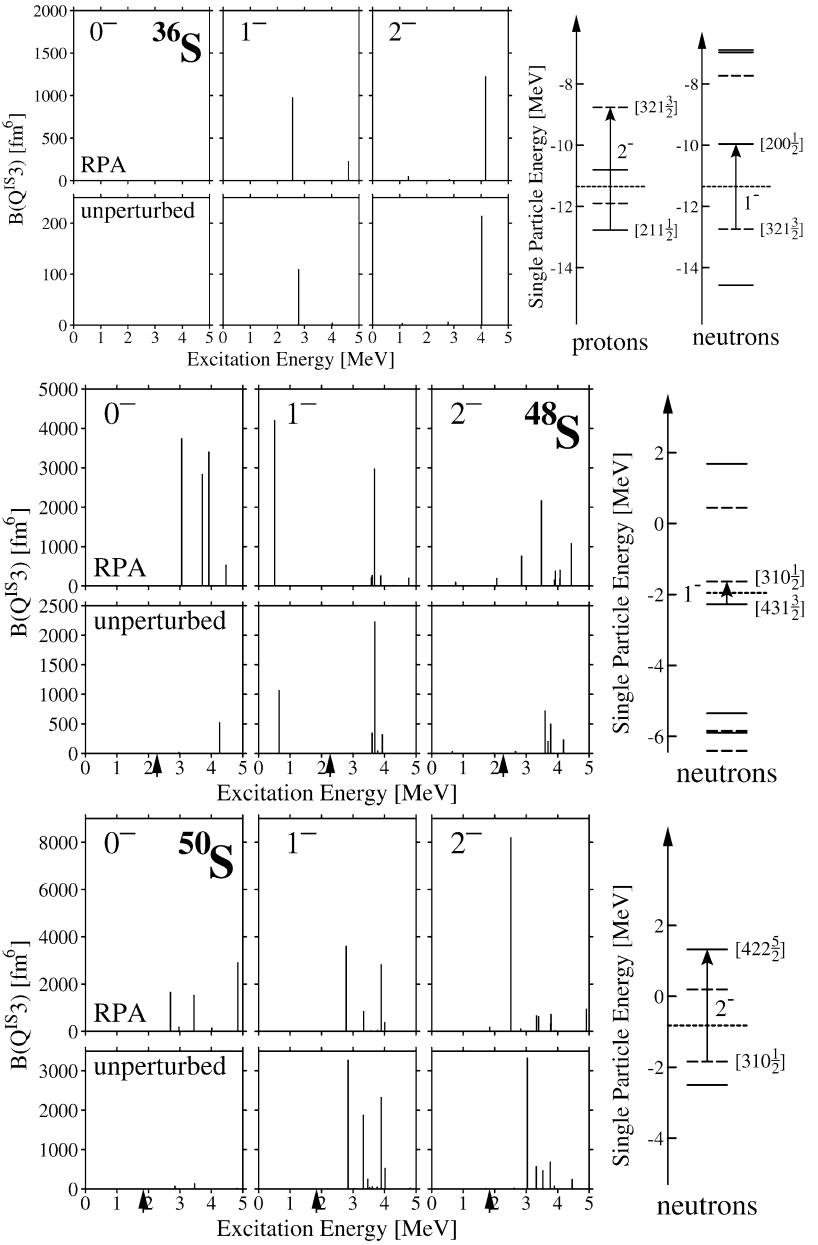

Fig. 6. Isoscalar octupole transition strengths for $K^\pi = 0^-, 1^-$ and 2^- excitations on the SD states in (a) ^{36}S, (b) ^{48}S, and (c) ^{50}S, obtained by the SHF–RPA calculation with the SIII interaction. The unit is fm^6. For comparison with the RPA strengths, unperturbed particle–hole strengths are also shown in the lower panels for each nucleus. The arrows indicate the threshold energies for neutron emission. There are no significant strengths for $K^\pi = 3^-$ excitations in this low-energy region, so that they are not shown. Some particle–hole excitations near the Fermi surface are drawn by arrows with their K^π values in the rightmost part for each nucleus. The solid, dashed, and dotted lines indicate the positive-parity levels, negative-parity levels, and the Fermi surface, respectively. The asymptotic quantum numbers $[Nn_z\Lambda\Omega]$ are indicated for pertinent levels. For the positive energy region, only the discretized continuum levels possessing resonance character are drawn.

us first discuss the result of calculation for the neutron-rich ^{36}S. For this nucleus, we obtain a $K^\pi = 1^-$ mode at 2.6 MeV and a $K^\pi = 2^-$ mode at 4.2 MeV. As they possess the isoscalar octupole transition strengths of 13 W.u. and 16 W.u., respectively, they are moderately collective (1 W.u. $\simeq$ 77 fm^6 for ^{36}S). It is interesting to compare this result with those for ^{32}S and ^{40}Ca discussed in the previous section. The 1^- mode in this nucleus is similar to the 1^- mode in ^{40}Ca, but its transition strength is less than half of the latter. This reduction of the collectivity is understood in terms of the weakening of the coherence between the proton and neutron excitations when one goes from the $N = Z$ nucleus to the $N \neq Z$ nucleus. Looking into the microscopic details, we find that, for example, the particle–hole excitations of protons and neutrons from the $[321\frac{3}{2}]$ level to the $[200\frac{1}{2}]$ level act coherently to produce the $K^\pi = 1^-$ collective mode in ^{40}Ca, but this proton excitation is absent in the case of ^{36}S because the $[321\frac{3}{2}]$ level is unoccupied. Analogous argument also applies to the $K^\pi = 2^-$ mode. This mode is similar to the 2^- mode in ^{32}S, but, its transition strength is about half of the latter. This is understood again in terms of the weakening of the coherence between the proton and neutron excitations. For instance, the particle–hole excitations of protons and neutrons from the $[211\frac{1}{2}]$ level to the $[321\frac{3}{2}]$ level act coherently to produce the $K^\pi = 2^-$ collective mode in ^{32}S, but this neutron excitation is absent in the case of ^{36}S because the $[321\frac{3}{2}]$ level is already occupied.

Next, let us discuss the result of calculation for ^{48}S and ^{50}S close to the neutron drip line. For ^{48}S, we obtain a $K^\pi = 1^-$ mode at very low excitation energy, 0.51 MeV. This mode possesses a large octupole transition strength of 31 W.u. (1 W.u. $\simeq$ 137 fm^6 for ^{48}S). The RPA eigenenergy is shifted down only slightly (0.14 MeV) from the unperturbed energy (0.65 MeV) of the neutron excitation from the $[431\frac{1}{2}]$ level to the $[310\frac{1}{2}]$ level. The unperturbed transition strength for this single-particle excitation is extremely large, i.e., $B(Q^{\mathrm{IS}}3) = 7.7$ W.u. The major cause of this remarkable strength is understood as follows: both the $[431\frac{1}{2}]$ and $[310\frac{1}{2}]$ levels are loosely bound with binding energy about 2 MeV. Because, as is well known, wave functions of the loosely bound states are significantly extended outside of the half-density radius, the matrix element of the octupole operator between these configurations acquires a large contribution from the region outside of the nuclear surface. Thus, such a transition strength can become very large in nuclei close to the neutron drip. Although the increase of the RPA transition strength from the unperturbed strength indicates the presence of collective effects, it may be appropriate to consider that the major character of this mode is of single-particle type. In contrast to the low energy peak at 0.51 MeV discussed above, the peaks above the neutron-emission threshold (indicated by arrows in Fig. 6) are considered to be associated with the excitations to discretized non-resonant continuum states. We examined that these peaks in the continuum indeed moves when we increase the box size in the numerical calculation. Therefore, we cannot give definite physical meanings to these peaks.

For ^{50}S, we obtain a $K^\pi = 2^-$ mode at 2.5 MeV. Like the $K^\pi = 1^-$ mode in ^{48}S, it is essentially a single-particle-type excitation, although it has extremely large octupole transition strength, 55 W.u. (1 W.u. $\simeq$ 149 fm^6 for ^{50}S). Namely, it is created mainly by the neutron excitation from the loosely bound $[310\frac{1}{2}]$ level to the resonance $[422\frac{5}{2}]$ level. The RPA eigenenergy of this mode is shifted down only slightly (0.5 MeV) from the unperturbed excitation energy (3.0 MeV) of this particle–hole configuration. Because the resonance $[422\frac{5}{2}]$ level is situated near the centrifugal barrier top, its wave function is significantly extended far out side of the half-density radius of this nucleus. Thus, the unperturbed octupole transition strength for this particle–hole excitation takes an extremely large value, $B(Q^{\mathrm{IS}}3) = 22$ W.u. This resonance interpretation of the $[422\frac{5}{2}]$ level is largely based on the analysis made in Ref. [60] where the deformed Woods–

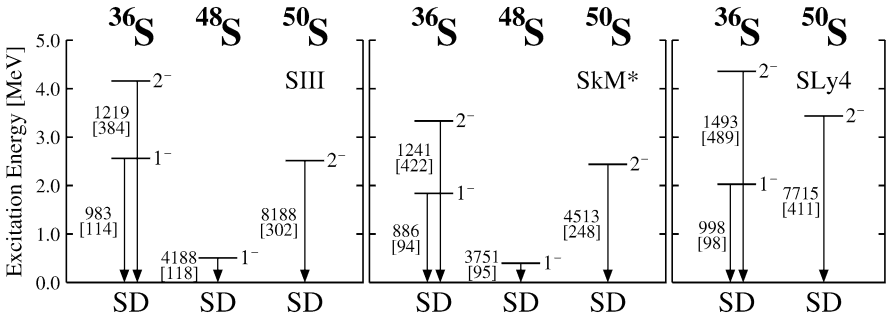

Fig. 7. Comparison of the SHF–RPA calculations with the SIII, SkM* and SLy4 interactions for low-frequency $K^\pi = 1^-$ and 2^- excitations on the SD states in ^{36,48,50}S. For SLy4, the SD local minimum does not appear in ^{48}S. Only excitations having $B(Q^{\mathrm{IS}}3)$ greater than 10 W.u. are displayed here (see Fig. 6 for other excitations having smaller strengths). The numbers on the right-hand sides of individual levels indicate the K quantum numbers. The numbers beside the arrows indicate the intrinsic transition matrix elements squared of the isoscalar octupole operator, $B(Q^{\mathrm{IS}}3)$, in units of fm^6. Those for the electric octupole operator, B(E3), are also given in brackets in units of e^2 fm^6.

Saxon potential simulating our SHF potential was constructed and properties of the discretized continuum states for this potential are analyzed in detail. It was then found that the energy and the root-mean-square radius of this level were stable against the variation of the box size. In the same paper, this conclusion was confirmed also by carrying out the eigenphase analysis for this level. The appearance of this resonance level is easily understood as due to the rather high centrifugal barrier for the relatively large value of the symmetry axis component of the angular momentum, $\Omega = 5/2$. We confirmed that this 2^- peak at 2.5 MeV does not move but the other peaks moves when we increase the box size in the numerical calculation. Thus, like in ^{48}S, except for the 2^- peak, the peaks above the neutron-emission threshold are considered to be associated with the excitations to discretized non-resonant continuum states.

We also carried out the same kind of calculation using the SkM* [58] and the SLy4 [59] interactions. The results of calculations with different versions of the Skyrme interaction are compared in Fig. 7. For the SLy4 interaction, the SD local minimum does not appear in ^{48}S, so that the RPA calculation was not done for this nucleus. Except for this, these Skyrme interactions yield qualitatively similar results for the $K^\pi = 1^-$ and $K^\pi = 2^-$ modes.

To accurately describe the spatially extended wave functions, like the loosely bound levels and resonance levels in ^{48}S and ^{50}S discussed above, it is certainly desirable to use a bigger box in the numerical calculation. Although it is difficult to significantly enlarge the box size under the present situation of computing power, we plan to manipulate this problem by incorporating the adaptive coordinate method into our scheme of numerical calculation. We believe, however, that the qualitative features of the present RPA calculation will remain valid. We have not obtained well-developed collective octupole modes for ^{48}S and ^{50}S. In such unstable nuclei close to the neutron drip line, there is almost no bound state above the Fermi surface and neutrons are excited to the continuum states. It seems difficult to develop collective correlations among different particle–hole configurations under such situations. Quite recently, however, one of the authors (M.Y.) pointed out that the pairing correlations play an important role for the emergence of low-frequency collective modes in such drip-line nuclei [62]. For studying such pairing effects for collective excitations, it will be interesting to extend the mixed representation RPA based on the SHF mean field to that based on the SHF-Bogoliubov mean field.

5. Conclusions

By means of the mixed representation RPA based on the SHF mean field, we have investigated low-frequency octupole excitations on the SD states in the $N = Z$ nuclei around ^{40}Ca and the neutron-rich sulfur isotopes. The RPA calculation has been carried out on the 3D Cartesian mesh in a box, and yielded a number of low-frequency octupole vibrations built on the SD states in ^{32}S, ^{36}Ar, ^{40}Ca and ^{44}Ti. In particular, a strongly collective $K^\pi = 1^-$ octupole vibration has been suggested to appear on top of the SD state in ^{40}Ca. For ^{48,50}S close to the neutron drip line, we have found that the low-lying state created by the excitation of a single neutron from a loosely bound low Ω level to a high Ω resonance level acquires an extremely strong octupole transition strength due to the spatially very extended structure of the particle–hole wave functions.

Acknowledgements

This work was done as a part of the Japan–US Cooperative Science Program "Mean-Field Approach to Collective Excitations in Unstable Medium-Mass and Heavy Nuclei" during the academic years 2003–2004, and we greatly appreciate useful discussions with the members of this project. This work was supported by the Grant-in-Aid for Scientific Research (No. 16540249) from the Japan Society for the Promotion of Science. We also thank the Yukawa Institute for Theoretical Physics at Kyoto University: Discussions during the YITP workshop YITP-W-05-01 on "New Developments in Nuclear Self-Consistent Mean-Field Theories" were useful to complete this work. The numerical calculations were performed on the NEC SX-5 supercomputers at RCNP, Osaka University, and at Yukawa Institute for Theoretical Physics, Kyoto University.

Appendix A. Explicit expressions of the RPA Hamiltonian

Here, using the notations of Ref. [63], we recapitulate the quantities appearing in the RPA Hamiltonian (19). More detailed expressions are given in Ref. [51].

The RPA Hamiltonian $h^{(\pm)\lambda}_{\mathrm{RPA}}$ is written

$$h^{(\pm)\lambda}_{\mathrm{RPA}}(\boldsymbol{r}\sigma\tau,\boldsymbol{r}\sigma'\tau') = \left[F^{(\pm)\lambda}_{00}(\boldsymbol{r})\delta_{\tau\tau'} + \sum_{t_3} F^{(\pm)\lambda}_{1t_3}(\boldsymbol{r})\tau^{t_3}_{\tau\tau'}\right]\delta_{\sigma\sigma'} + \left[\boldsymbol{G}^{(\pm)\lambda}_{00}(\boldsymbol{r})\delta_{\tau\tau'} + \sum_{t_3} \boldsymbol{G}^{(\pm)\lambda}_{1t_3}(\boldsymbol{r})\tau^{t_3}_{\tau\tau'}\right]\cdot\boldsymbol{\sigma}_{\sigma\sigma'}, \tag{A.1}$$

$$F^{(\pm)\lambda}_{tt_3} = -\nabla\cdot\left[M^{(\pm)\lambda}_{tt_3}\nabla\right] + U^{(\pm)\lambda}_{tt_3} - \frac{i}{2}\left[\nabla\cdot\boldsymbol{I}^{(\pm)\lambda}_{tt_3} + \boldsymbol{I}^{(\pm)\lambda}_{tt_3}\cdot\nabla\right] + U^{(\pm)\lambda}_{\mathrm{Coul},tt_3}\delta_{\pi\tau}, \tag{A.2}$$

$$\boldsymbol{G}^{(\pm)\lambda}_{tt_3} = -\sum_{\mu}\nabla_\mu\cdot\left[\boldsymbol{C}^{(\pm)\lambda}_{tt_3}\nabla_\mu\right] + \boldsymbol{\Sigma}^{(\pm)\lambda}_{tt_3} - \frac{i}{2}\sum_{\mu\nu}\left[\nabla_\mu B^{(\pm)\lambda}_{tt_3,\mu\nu} + B^{(\pm)\lambda}_{tt_3,\mu\nu}\nabla_\mu\right]\boldsymbol{e}_\nu. \tag{A.3}$$

The quantities, $M^{(\pm)\lambda}_{tt_3}$, $U^{(\pm)\lambda}_{tt_3}$, etc. appearing in the above expressions are obtained by the second derivative of the time-even and time-odd energy functionals, $\mathcal{E}^{\mathrm{even}}$ and $\mathcal{E}^{\mathrm{odd}}$, with respect to the local densities:

$$M^{(\pm)\lambda}_{tt_3} = \frac{\partial^2\mathcal{E}^{\mathrm{even}}_t}{\partial\tau_{tt_3}\partial\rho_{tt_3}}\rho^{(\pm)\lambda}_{tt_3}\ , \tag{A.4}$$

$$U_{00}^{(\pm)\lambda} = \frac{\partial}{\partial\rho_{00}}\left[\sum_{tt_3}\left(\frac{\partial\mathcal{E}_{\rm Sk}}{\partial\rho_{tt_3}}\rho_{tt_3}^{(\pm)\lambda} + \frac{\partial\mathcal{E}_t^{\rm odd}}{\partial\boldsymbol{s}_{tt_3}}\cdot\boldsymbol{s}_{tt_3}^{(\pm)\lambda}\right) + \frac{\partial\mathcal{E}_0^{\rm even}}{\partial\tau_{00}}\tau_{00}^{(\pm)\lambda} + \frac{\partial\mathcal{E}_0^{\rm even}}{\partial\boldsymbol{J}_{00}}\cdot\boldsymbol{J}_{00}^{(\pm)\lambda}\right], \tag{A.5}$$

$$U_{1t_3}^{(\pm)\lambda} = \frac{\partial}{\partial\rho_{1t_3}}\left[\frac{\partial\mathcal{E}_1^{\rm even}}{\partial\rho_{1t_3}}\rho_{1t_3}^{(\pm)\lambda} + \frac{\partial\mathcal{E}_1^{\rm even}}{\partial\tau_{1t_3}}\tau_{1t_3}^{(\pm)\lambda} + \frac{\partial\mathcal{E}_1^{\rm even}}{\partial\boldsymbol{J}_{1t_3}}\cdot\boldsymbol{J}_{1t_3}^{(\pm)\lambda} + \frac{\partial\mathcal{E}_1^{\rm even}}{\partial\rho_{00}}\rho_{00}^{(\pm)\lambda}\right], \tag{A.6}$$

$$B_{tt_3,\mu\nu}^{(\pm)\lambda} = \frac{\partial}{\partial J_{tt_3,\mu\nu}}\left[\frac{\partial\mathcal{E}_t^{\rm even}}{\partial J_{tt_3,\mu\nu}}J_{tt_3,\mu\nu}^{(\pm)\lambda} + \frac{\partial\mathcal{E}_t^{\rm even}}{\partial\rho_{tt_3}}\rho_{tt_3}^{(\pm)\lambda}\right], \tag{A.7}$$

$$\boldsymbol{C}_{tt_3}^{(\pm)\lambda} = \frac{\partial^2\mathcal{E}_t^{\rm odd}}{\partial\boldsymbol{T}_{tt_3}\partial\boldsymbol{s}_{tt_3}}\cdot\boldsymbol{s}_{tt_3}^{(\pm)\lambda}, \tag{A.8}$$

$$\boldsymbol{\Sigma}_{tt_3}^{(\pm)\lambda} = \frac{\partial}{\partial\boldsymbol{s}_{tt_3}}\left[\frac{\partial\mathcal{E}_t^{\rm odd}}{\partial\boldsymbol{s}_{tt_3}}\cdot\boldsymbol{s}_{tt_3}^{(\pm)\lambda} + \frac{\partial\mathcal{E}_t^{\rm odd}}{\partial\boldsymbol{T}_{tt_3}}\cdot\boldsymbol{T}_{tt_3}^{(\pm)\lambda} + \frac{\partial\mathcal{E}_t^{\rm odd}}{\partial\boldsymbol{j}_{tt_3}}\cdot\boldsymbol{j}_{tt_3}^{(\pm)\lambda} + \frac{\partial\mathcal{E}_t^{\rm odd}}{\partial\rho_{00}}\rho_{00}^{(\pm)\lambda}\right], \tag{A.9}$$

$$\boldsymbol{I}_{tt_3}^{(\pm)\lambda} = \frac{\partial}{\partial\boldsymbol{j}_{tt_3}}\left[\frac{\partial\mathcal{E}_t^{\rm odd}}{\partial\boldsymbol{j}_{tt_3}}\cdot\boldsymbol{j}_{tt_3}^{(\pm)\lambda} + \frac{\partial\mathcal{E}_t^{\rm odd}}{\partial\boldsymbol{s}_{tt_3}}\cdot\boldsymbol{s}_{tt_3}^{(\pm)\lambda}\right], \tag{A.10}$$

$$U_{{\rm Coul},tt_3}^{(\pm)\lambda} = \frac{\partial}{\partial\rho_{tt_3}}\left[\frac{\partial\mathcal{E}_{\rm Coul}}{\partial\rho_{00}}\rho_{00}^{(\pm)\lambda} + \frac{\partial\mathcal{E}_{\rm Coul}}{\partial\rho_{10}}\rho_{10}^{(\pm)\lambda}\right]. \tag{A.11}$$

The local transition densities $\rho_{tt_3}^{(\pm)\lambda}$, the local transition spin densities $\boldsymbol{s}_{tt_3}^{(\pm)\lambda}$, the local transition kinetic energy densities $\tau_{tt_3}^{(\pm)\lambda}$, the local transition kinetic spin densities $\boldsymbol{T}_{tt_3}^{(\pm)\lambda}$, the local transition current densities $\boldsymbol{j}_{tt_3}^{(\pm)\lambda}$, the local transition spin–orbit current tensors $J_{tt_3,\mu\nu}^{(\pm)\lambda}$ are given by

$$\rho_{tt_3}^{(\pm)\lambda}(\boldsymbol{r}) = \rho_{tt_3}^{(\pm)\lambda}(\boldsymbol{r},\boldsymbol{r}), \tag{A.12}$$

$$\boldsymbol{s}_{tt_3}^{(\pm)\lambda}(\boldsymbol{r}) = \boldsymbol{s}_{tt_3}^{(\pm)\lambda}(\boldsymbol{r},\boldsymbol{r}), \tag{A.13}$$

$$\tau_{tt_3}^{(\pm)\lambda}(\boldsymbol{r}) = \nabla\cdot\nabla'\rho_{tt_3}^{(\pm)\lambda}(\boldsymbol{r},\boldsymbol{r}')\big|_{\boldsymbol{r}=\boldsymbol{r}'}, \tag{A.14}$$

$$\boldsymbol{T}_{tt_3}^{(\pm)\lambda}(\boldsymbol{r}) = \nabla\cdot\nabla'\boldsymbol{s}_{tt_3}^{(\pm)\lambda}(\boldsymbol{r},\boldsymbol{r}')\big|_{\boldsymbol{r}=\boldsymbol{r}'}, \tag{A.15}$$

$$\boldsymbol{j}_{tt_3}^{(\pm)\lambda}(\boldsymbol{r}) = -\frac{i}{2}(\nabla-\nabla')\rho_{tt_3}^{(\pm)\lambda}(\boldsymbol{r},\boldsymbol{r}')\big|_{\boldsymbol{r}=\boldsymbol{r}'}, \tag{A.16}$$

$$J_{tt_3,\mu\nu}^{(\pm)\lambda}(\boldsymbol{r}) = -\frac{i}{2}(\nabla-\nabla')_\mu\boldsymbol{s}_{tt_3,\nu}^{(\pm)\lambda}(\boldsymbol{r},\boldsymbol{r}')\big|_{\boldsymbol{r}=\boldsymbol{r}'}. \tag{A.17}$$

The local transition spin–orbit currents $\boldsymbol{J}_{tt_3}^{(\pm)\lambda}$ are defined by

$$\boldsymbol{J}_{tt_3}^{(\pm)\lambda} = \sum_{\mu\nu\omega}\epsilon_{\mu\nu\omega}J_{tt_3,\mu\nu}^{(\pm)\lambda}\boldsymbol{e}_\omega, \tag{A.18}$$

where $\epsilon_{\mu\nu\omega}$ is the Levi-Civita symbol and $\boldsymbol{e}_\omega$ is the unit vector in the ω-direction. The scalar transition densities $\rho_{tt_3}^{(\pm)\lambda}(\boldsymbol{r},\boldsymbol{r}')$ and the vector transition densities $\boldsymbol{s}_{tt_3}^{(\pm)\lambda}(\boldsymbol{r},\boldsymbol{r}')$ appearing in the above equations are defined by decomposing the transition density matrix $\rho^{(\pm)\lambda}(x,x') = \rho^{(\pm)\lambda}(\boldsymbol{r}\sigma\tau,\boldsymbol{r}'\sigma'\tau')$ into the spin–isospin channels:

$$\rho^{(\pm)\lambda}(\boldsymbol{r}\sigma\tau,\boldsymbol{r}'\sigma'\tau') = \frac{1}{4}\Bigg[\rho_{00}^{(\pm)\lambda}(\boldsymbol{r},\boldsymbol{r}')\delta_{\sigma\sigma'}\delta_{\tau\tau'} + \boldsymbol{s}_{00}^{(\pm)\lambda}(\boldsymbol{r},\boldsymbol{r}')\cdot\boldsymbol{\sigma}_{\sigma\sigma'}\delta_{\tau\tau'} + \delta_{\sigma\sigma'}\sum_{t_3=-1}^{1}\rho_{1t_3}^{(\pm)\lambda}(\boldsymbol{r},\boldsymbol{r}')\tau_{\tau\tau'}^{t_3} + \sum_{t_3=-1}^{1}\boldsymbol{s}_{1t_3}^{(\pm)\lambda}(\boldsymbol{r},\boldsymbol{r}')\cdot\boldsymbol{\sigma}_{\sigma\sigma'}\tau_{\tau\tau'}^{t_3}\Bigg]. \tag{A.19}$$

In the above expressions, the charge-exchange $t_3 = \pm 1$ components are included for completeness, although they do not contribute to the excitation modes considered in this paper.

References

[1] P.J. Nolan, P.J. Twin, Annu. Rev. Nucl. Part. Sci. 38 (1988) 533.
[2] S. Åberg, H. Flocard, W. Nazarewicz, Annu. Rev. Nucl. Part. Sci. 40 (1990) 439.
[3] R.V.F. Janssens, T.L. Khoo, Annu. Rev. Nucl. Part. Sci. 41 (1991) 321.
[4] C. Baktash, B. Haas, W. Nazaerewicz, Annu. Rev. Nucl. Part. Sci. 45 (1995) 485.
[5] C. Baktash, Prog. Part. Nucl. Phys. 38 (1997) 291.
[6] J. Dobaczewski, in: C. Baktash (Ed.), Proceedings of the International Conference on Nuclear Structure '98, in: AIP Conference Proceedings, vol. 481, American Institute of Physics, New York, 1999, p. 315.
[7] J. Dudek, T.R. Werner, Z. Szymanski, Phys. Lett. B 248 (1990) 235.
[8] J. Skalski, Phys. Lett. B 274 (1992) 1.
[9] P.A. Butler, W. Nazarewicz, Rev. Mod. Phys. 68 (1996) 349.
[10] S. Mizutori, Y.R. Shimizu, K. Matsuyanagi, Prog. Theor. Phys. 85 (1991) 559;
S. Mizutori, Y.R. Shimizu, K. Matsuyanagi, Prog. Theor. Phys. 86 (1991) 131.
[11] S. Mizutori, T. Nakatsukasa, K. Arita, Y.R. Shimizu, K. Matsuyanagi, Nucl. Phys. A 557 (1993) 125.
[12] T. Nakatsukasa, K. Matsuyanagi, S. Mizutori, Y.R. Shimizu, Phys. Rev. C 53 (1996) 2213.
[13] A. Korichi, et al., Phys. Rev. Lett. 86 (2001) 2746;
D. Rossbach, et al., Phys. Lett. B 513 (2001) 9.
[14] T. Lauritsen, et al., Phys. Rev. Lett. 89 (2002) 282501.
[15] C.E. Svensson, et al., Phys. Rev. Lett. 85 (2000) 2693.
[16] C.E. Svensson, et al., Phys. Rev. C 63 (2001) 061301(R) .
[17] C.E. Svensson, et al., Nucl. Phys. A 682 (2001) 1.
[18] E. Ideguchi, et al., Phys. Rev. Lett. 87 (2001) 222501.
[19] C.J. Chiara, et al., Phys. Rev. C 67 (2003) 041303.
[20] C.D. O'Leary, M.A. Bentley, B.A. Brown, D.E. Appelbe, R.A. Bark, D.M. Cullen, S. Ertürk, A. Maj, A.C. Merchant, Phys. Rev. C 61 (2000) 064314.
[21] T. Inakura, S. Mizutori, M. Yamagami, K. Matsuyanagi, Nucl. Phys. A 710 (2002) 261.
[22] R.K. Sheline, I. Ragnarsson, S.G. Nilsson, Phys. Lett. B 41 (1972) 115.
[23] G. Leander, S.E. Larsson, Nucl. Phys. A 239 (1975) 93.
[24] I. Ragnarsson, S.G. Nilsson, R.K. Sheline, Phys. Rep. 45 (1978) 1.
[25] T. Bengtsson, M.E. Faber, G. Leander, P. Möller, M. Ploszajczak, I. Ragnarsson, S. Åberg, Phys. Scr. 24 (1981) 200.
[26] M. Girod, B. Grammaticos, Phys. Rev. C 27 (1983) 2317.
[27] M. Yamagami, K. Matsuyanagi, Nucl. Phys. A 672 (2000) 123.
[28] H. Molique, J. Dobaczewski, J. Dudek, Phys. Rev. C 61 (2000) 044304.
[29] R.R. Rodriguez-Guzmán, J.L. Egido, L.M. Robeldo, Phys. Rev. C 62 (2000) 054308.
[30] T. Tanaka, R.G. Nazmitdinov, K. Iwasawa, Phys. Rev. C 63 (2001) 034309.
[31] A.V. Afanasjev, P. Ring, I. Ragnarsson, in: D. Rudolph, M. Hellström (Eds.), Proceedings of International Workshop on Selected Topics on $N = Z$ Nuclei (PINGST 2000), Lund, Sweden, 6–10 June 2000, Bloms i Lund, 2000, p. 183.
[32] C.E. Svensson, et al., Phys. Rev. Lett. 82 (1999) 3400.
[33] C.E. Svensson, et al., Phys. Rev. Lett. 79 (1997) 1233.
[34] T.R. Werner, J.A. Sheikh, W. Nazarewicz, M.R. Strayer, A.S. Umar, M. Misu, Phys. Lett. B 333 (1994) 303.
[35] T.R. Werner, J.A. Sheikh, M. Misu, W. Nazarewicz, J. Rikovska, K. Heeger, A.S. Umar, M.R. Strayer, Nucl. Phys. A 597 (1996) 327.

[36] T. Inakura, S. Mizutori, M. Yamagami, K. Matsuyanagi, Nucl. Phys. A 728 (2003) 52.
[37] G.F. Bertsch, S.F. Tsai, Phys. Rep. 18 (1975) 125.
[38] S. Shlomo, G.F. Bertsch, Nucl. Phys. A 243 (1975) 507.
[39] I. Hamamoto, H. Sagawa, X.Z. Zhang, Nucl. Phys. A 648 (1999) 203.
[40] H. Sagawa, Prog. Theor. Phys. Suppl. 142 (2001) 1.
[41] M. Matsuo, Nucl. Phys. A 696 (2001) 371.
[42] E. Khan, N. Sandulescu, M. Grasso, Nguyen Van Giai, Phys. Rev. C 66 (2002) 024309.
[43] M. Yamagami, Nguyen Van Giai, Phys. Rev. C 69 (2004) 034301.
[44] J. Terasaki, J. Engel, M. Bender, J. Dobaczewski, W. Nazarewicz, M. Stoitsov, Phys. Rev. C 71 (2005) 034310.
[45] D. Vretenar, N. Paar, P. Ring, G.A. Lalazissis, Nucl. Phys. A 692 (2001) 496.
[46] N. Paar, T. Niksic, D. Vretenar, P. Ring, Phys. Lett. B 606 (2005) 288.
[47] T. Nakatsukasa, K. Yabana, Phys. Rev. C 71 (2005) 024301.
[48] R.H. Lemmer, M. Vénéroni, Phys. Rev. 170 (1968) 883.
[49] G.F. Bertsch, Prog. Theor. Phys. Suppl. 74/75 (1983) 115.
[50] A. Muta, J.-I. Iwata, Y. Hashimoto, K. Yabana, Prog. Theor. Phys. 108 (2002) 1065.
[51] H. Imagawa, Doctor Thesis, University of Tsukuba, 2003.
[52] H. Imagawa, Y. Hashimoto, Phys. Rev. C 67 (2003) 037302.
[53] H. Imagawa, Y. Hashimoto, in preparation.
[54] T. Inakura, M. Yamagami, K. Matsuyanagi, S. Mizutori, H. Imagawa, Y. Hashimoto, in: Proceedings of the 10th Marie and Pierre Curie Nuclear Physics Workshop, 24–28 September 2003, Kazimierz Dolny, Poland, Int. J. Mod. Phys. E 13 (2004) 157.
[55] T. Inakura, H. Imagawa, Y. Hashimoto, M. Yamagami, S. Mizutori, K. Matsuyanagi, in: Proceedings of the Fourth International Conference on Exotic Nuclei and Atomic Masses, 12–16 September 2004, Pine Mountain, Eur. Phys. J. A 25 (Suppl. 1) (2005) 545.
[56] D. Baye, P.-H. Heenen, J. Phys. A 19 (1986) 2041.
[57] M. Beiner, H. Flocard, Nguyen Van Giai, P. Quentin, Nucl. Phys. A 238 (1975) 29.
[58] J. Bartel, P. Quentin, M. Brack, C. Guet, H.B. Håkansson, Nucl. Phys. A 386 (1982) 79.
[59] E. Chanbanat, P. Bonche, P. Haensel, J. Mayer, R. Schaeffer, Nucl. Phys. A 627 (1997) 710.
[60] K. Yoshida, M. Yamagami, K. Matsuyanagi, Prog. Theor. Phys. 113 (2005) 1251.
[61] A. Bohr, B.R. Mottelson, Nuclear Structure, vol. 2, Benjamin, Reading, MA, 1975.
[62] M. Yamagami, Phys. Rev. C 72 (2005) 064308.
[63] M. Bender, J. Dobaczewski, J. Engel, W. Nazarewicz, Phys. Rev. C 65 (2002) 054322.

Available online at www.sciencedirect.com
ScienceDirect
ELSEVIER
Nuclear Physics A 779 (2006) 99–115
NUCLEAR PHYSICS A

Pairing and continuum effects on low-frequency quadrupole vibrations in deformed Mg isotopes close to the neutron drip line

K. Yoshida [a], M. Yamagami [b], K. Matsuyanagi [a,*]

[a] *Department of Physics, Graduate School of Science, Kyoto University, Kyoto 606-8502, Japan*
[b] *Radioactive Isotope Physics Laboratory, RIKEN, Wako, Saitama 351-0198, Japan*

Received 27 May 2006; received in revised form 6 September 2006; accepted 8 September 2006

Available online 25 September 2006

Abstract

Low-frequency quadrupole vibrational modes in deformed ^{36,38,40}Mg close to the neutron drip line are studied by means of the quasiparticle-random-phase approximation based on the coordinate-space Hartree–Fock–Bogoliubov formalism. Strongly collective $K^\pi = 0^+$ and 2^+ excitation modes carrying 10–20 Weisskopf units in the intrinsic isoscalar quadrupole transition strengths are obtained at about 3 MeV. There are two reasons for the enhancement of the transition strengths. First, the quasiparticle wave functions generating these modes possess spatially very extended structure. The asymptotic selection rules characterizing the β and γ vibrations in stable deformed nuclei are thus strongly violated. Second, the dynamic pairing effects act strongly to enhance the collectivity of these modes. It is suggested that the lowest $K^\pi = 0^+$ collective mode is a particularly sensitive indicator of the nature of pairing correlations in deformed nuclei close to the neutron drip line.

PACS: 21.60.Ev; 21.60.Jz; 21.10.Re

Keywords: Hartree–Fock–Bogoliubov method; Quasiparticle-RPA; Collective excitations; Deformed unstable nuclei; Neutron drip line; Mg isotopes

* Corresponding author.
E-mail address: ken@ruby.scphys.kyoto-u.ac.jp (K. Matsuyanagi).

0375-9474/$ – see front matter
doi:10.1016/j.nuclphysa.2006.09.003

1. Introduction

The physics of drip-line nuclei is one of the current frontiers in nuclear structure physics [1–3]. The number of unstable nuclei experimentally accessible will remarkably increase when the next generation of radioactive ion beam facilities start running. We shall be able to study the properties not only of the ground states but also of low-lying excited states of drip-line nuclei in the medium-mass region. Collective excitation in neutron-rich nuclei is one of the most interesting issues in this field. Because properties of low-frequency collective vibrational modes are quite sensitive to surface effects and details of shell structure, we expect that new kinds of collective excitations emerge under such new situations of nuclear structure. In order to quest for collective modes of excitation unique to unstable nuclei associated with new features such as neutron skins, many attempts have been made using the self-consistent RPA based on the Skyrme–Hartree–Fock (SHF) method [4–6] and the Quasiparticle-RPA (QRPA) including the pairing correlations [7–12]. A number of similar approaches using different mean fields have also been carried out [14–22]. (See Refs. [12,19,23] for extensive lists of references concerning the self-consistent RPA and mean-field calculations.) Most of these calculations, however, are restricted to spherical nuclei.

Quite recently, low-frequency RPA modes in deformed nuclei close to the neutron drip line have been investigated by several authors. The time-dependent Hartree–Fock method formulated in the three-dimensional coordinate space with a complex absorbing boundary condition was applied to low-frequency isovector dipole modes [24]. Possible appearance of low-frequency octupole vibrations built on superdeformed states in neutron drip-line nuclei was discussed in Ref. [25] on the basis of the SHF plus mixed representation RPA [26–28] calculations. In Ref. [29], we investigated properties of octupole excitations built on superdeformed states in neutron-rich sulfur isotopes by means of the RPA based on the deformed Woods–Saxon (WS) potential in the coordinate-space mesh-representation. We found that low-lying states created by excitation of a single neutron from a loosely bound low-Ω state to a high-Ω resonance state (Ω being the z-component of the angular momentum) acquire extremely strong octupole transition strengths due to very extended spatial structure of particle–hole wave functions. All of these calculations, however, did not take into account the pairing correlation. In Refs. [30,31], low-lying Gamow–Teller β-decay strengths were investigated by means of the proton–neutron RPA using the SHF + BCS approximation. Gamma vibrations in ^{38}Mg were studied using the QRPA with the BCS approximation [32] on the basis of the response function formalism. It should be noted that these calculations relied on the BCS approximation, which is inappropriate, because of the unphysical nucleon gas problem [34], for describing continuum coupling effects in drip-line nuclei.

The nature of pairing correlations in neutron drip-line nuclei is one of the most important subjects in the physics of unstable nuclei. One of the unique features of drip-line nuclei is that the pairing correlation takes place not only among bound levels but also including continuum states. To describe this unique character of pairing, the coordinate-space Hartree–Fock–Bogoliubov (HFB) formalism is suitable [33,34] and has been widely used for the study of single-particle motion and shell structure near the continuum [35–38]. Due to the pairing and continuum effects, spatial structure of quasiparticle wave functions near the chemical potential changes significantly, which affects the properties of low-frequency excitation modes [39]. In order to study the effects of pairing on the low-frequency excitation modes in deformed nuclei near the neutron drip line, we have extended the previous work to self-consistently include pairing correlations, and con-

structed a new computer code that carries out the deformed QRPA calculation on the basis of the coordinate-space HFB formalism.

The aim of this paper is to carry out the deformed QRPA calculation for neutron drip-line nuclei and investigate the low-frequency quadrupole vibrational modes with $K^\pi = 0^+$ and 2^+ in ^{36,38,40}Mg close to the neutron drip line. According to the Skyrme–HFB calculations [40,41] and Gogny–HFB calculation [42], these isotopes are well deformed. The shell-model calculation [43] also suggests that the ground state of ^{40}Mg is dominated by the neutron two-particle–two-hole components, which is consistent with the breaking of the $N = 28$ shell closure discussed in [44]. We investigate properties of low-frequency modes of excitation in these Mg isotopes simultaneously taking into account the deformed mean-field effects, the pairing correlations, and excitations into the continuum.

This paper is organized as follows: in the next section, the framework of the mean-field and QRPA calculations is briefly described. In Section 3, results of the QRPA calculation for low-frequency quadrupole vibrations with $K^\pi = 0^+$ and 2^+ in ^{36,38,40}Mg are presented and discussed focusing our attention to the microscopic mechanism of emergence of collective modes in deformed superfluid nuclei close to the neutron drip line. Concluding remarks are given in Section 4.

A preliminary version of this work was previously reported in Ref. [45].

2. Method

2.1. Mean-field calculation

In order to discuss simultaneously effects of nuclear deformation and pairing correlations including the continuum, we solve the HFB equation [33,34,46]

$$\begin{pmatrix} h^\tau(\boldsymbol{r}\sigma) - \lambda^\tau & \tilde{h}^\tau(\boldsymbol{r}\sigma) \\ \tilde{h}^\tau(\boldsymbol{r}\sigma) & -(h^\tau(\boldsymbol{r}\sigma) - \lambda^\tau) \end{pmatrix} \begin{pmatrix} \varphi^\tau_{1,\alpha}(\boldsymbol{r}\sigma) \\ \varphi^\tau_{2,\alpha}(\boldsymbol{r}\sigma) \end{pmatrix} = E_\alpha \begin{pmatrix} \varphi^\tau_{1,\alpha}(\boldsymbol{r}\sigma) \\ \varphi^\tau_{2,\alpha}(\boldsymbol{r}\sigma) \end{pmatrix} \tag{1}$$

directly in the cylindrical coordinate space assuming axial and reflection symmetry. In comparison to the conventional method of using a deformed harmonic oscillator basis, this method is more effective in the treatment of spatially extended wave functions, like loosely bound states, resonant states and continuum states. As is well known, when the quasiparticle energy E is greater than the absolute magnitude $|\lambda|$ of the chemical potential, the upper component $\varphi_1(\boldsymbol{r}\sigma)$ obeys the scattering-wave boundary condition, while the lower component $\varphi_2(\boldsymbol{r}\sigma)$ is always exponentially decaying at infinity.

For the mean-field Hamiltonian h, we employ the deformed Woods–Saxon potential with the parameters used in [29], except the isovector potential strength for which a slightly smaller value, 30 MeV in stead of 33 MeV, is adopted in order to describe ^{40}Mg as a drip-line nucleus in accordance with the Skyrme–HFB [40,41] and Gogny–HFB calculations [42]. The pairing field is treated self-consistently by using the density-dependent contact interaction [47,48],

$$v_{\rm pp}(\boldsymbol{r}, \boldsymbol{r}') = V_0 \frac{1 - P_\sigma}{2} \left[1 - \eta \left(\frac{\varrho^{\rm IS}(\boldsymbol{r})}{\varrho_0} \right) \right] \delta(\boldsymbol{r} - \boldsymbol{r}'), \tag{2}$$

with $V_0 = -450$ MeV fm^3 and $\varrho_0 = 0.16$ fm^{-3}, where $\varrho^{\rm IS}(\boldsymbol{r})$ denotes the isoscalar density and P_σ is the spin exchange operator. The pairing force strength V_0 is chosen such that the average pairing gap roughly agrees with the systematics (see Table 1). For the parameter η, which repre-

Table 1
Ground state properties of ^{36,38,40}Mg obtained by the deformed WS–HFB calculation with $\beta_2 = 0.28$. Chemical potentials, average pairing gaps, and root-mean-square radii for protons and neutrons are listed

Nucleus	λ_π (MeV)	$\langle\Delta_\pi\rangle$ (MeV)	$\sqrt{\langle r^2\rangle_\pi}$ (fm)	λ_ν (MeV)	$\langle\Delta_\nu\rangle$ (MeV)	$\sqrt{\langle r^2\rangle_\nu}$ (fm)
^{36}Mg	−20.0	0.0	3.06	−2.09	1.93	3.74
^{38}Mg	−23.0	0.0	3.08	−1.15	2.05	3.86
^{40}Mg	−25.1	0.0	3.10	−0.41	2.15	3.99

sents density dependence, we use $\eta = 1.0$ (surface type). Sensitivity of calculated results to the parameter η will be examined in Section 3.4. The pairing Hamiltonian is then given by

$$\tilde{h}^\tau(\boldsymbol{r}) = \frac{V_0}{2}\left[1 - \eta\left(\frac{\varrho^{\mathrm{IS}}(\boldsymbol{r})}{\varrho_0}\right)\right]\tilde{\varrho}^\tau(\boldsymbol{r}). \tag{3}$$

The normal (particle) and abnormal (pairing) densities are given by

$$\varrho^\tau(\rho, z) = \sum_\alpha \sum_{\sigma=\pm 1/2} \left|\varphi^\tau_{2,\alpha}(\rho, z, \sigma)\right|^2, \tag{4}$$

$$\tilde{\varrho}^\tau(\rho, z) = -\sum_\alpha \sum_{\sigma=\pm 1/2} \varphi^\tau_{1,\alpha}(\rho, z, \sigma)\varphi^\tau_{2,\alpha}(\rho, z, \sigma) \tag{5}$$

and the mean-square radii of protons and neutrons are calculated as

$$\langle r^2\rangle_\tau = \frac{\int \rho\,\mathrm{d}\rho\,\mathrm{d}z\, r^2\varrho^\tau(\rho, z)}{\int \rho\,\mathrm{d}\rho\,\mathrm{d}z\,\varrho^\tau(\rho, z)}, \tag{6}$$

where $\boldsymbol{r} = (\rho, z)$, $r = \sqrt{\rho^2 + z^2}$ and $\tau{=}\pi$ or ν; $\varrho^\pi(\rho, z)$ and $\varrho^\nu(\rho, z)$ being the proton and neutron densities. The average gaps are defined by [49–52]

$$\langle\Delta_\tau\rangle = -\int \mathrm{d}\boldsymbol{r}\,\tilde{\varrho}^\tau(\boldsymbol{r})\tilde{h}^\tau(\boldsymbol{r}) \Big/ \int \mathrm{d}\boldsymbol{r}\,\tilde{\varrho}^\tau(\boldsymbol{r}). \tag{7}$$

We construct the discretized Hamiltonian matrix by use of the finite difference method for derivatives and then diagonalize the matrix to obtain the quasiparticle wave functions on the two-dimensional lattice consisting of the cylindrical coordinates ρ and z. The kinetic energy term and the spin-orbit potential are evaluated using the 9-point formula. Because the time-reversal symmetry and the reflection symmetry with respect to the x–y plane are assumed, we have only to solve for positive Ω and positive z. We use the lattice mesh size $\Delta\rho = \Delta z = 0.8$ fm and the box boundary condition at $\rho_{\max} = 10.0$ fm and $z_{\max} = 12.8$ fm. The quasiparticle energy is cut off at 50 MeV and the quasiparticle states up to $\Omega^\pi = 13/2^\pm$ are included. This model space is larger than that used in Ref. [45]. It is certainly desirable to use a larger box for a better evaluation of matrix elements involving spatially very extended quasiparticle wave functions. This improvement remains as a future task, however.

We impose the condition on the convergence of the pairing energy as $|(E^{(i)}_{\mathrm{pair}} - E^{(i-1)}_{\mathrm{pair}})/E^{(i)}_{\mathrm{pair}}| < 10^{-5}$, where i denotes the iteration number and the pairing energy is defined by [37]

$$E_{\mathrm{pair}} = \frac{1}{2}\sum_{\tau=\pi,\nu}\int \mathrm{d}\boldsymbol{r}\,\tilde{\varrho}^\tau(\boldsymbol{r})\tilde{h}^\tau(\boldsymbol{r}). \tag{8}$$

We use the same deformation parameter $\beta_2 = 0.28$ in the Woods–Saxon potential for both neutrons and protons. This parameter is chosen to approximately reproduce the Q-moments calculated in Ref. [40]. We checked that properties of the QRPA modes do not change significantly when the deformation parameter is varied around $\beta_2 \sim 0.3$.

2.2. Quasiparticle-RPA calculation

Using the quasiparticle basis obtained in the previous subsection, we solve the QRPA equation in the standard matrix formulation [53]

$$\sum_{\gamma\delta} \begin{pmatrix} A_{\alpha\beta\gamma\delta} & B_{\alpha\beta\gamma\delta} \\ B_{\alpha\beta\gamma\delta} & A_{\alpha\beta\gamma\delta} \end{pmatrix} \begin{pmatrix} f^{\lambda}_{\gamma\delta} \\ g^{\lambda}_{\gamma\delta} \end{pmatrix} = \hbar\omega_{\lambda} \begin{pmatrix} 1 & 0 \\ 0 & -1 \end{pmatrix} \begin{pmatrix} f^{\lambda}_{\alpha\beta} \\ g^{\lambda}_{\alpha\beta} \end{pmatrix}. \tag{9}$$

This method is convenient to analyze microscopic structures of the QRPA eigenmodes in comparison with other RPA formalisms based on the Greens function method. Namely, individual two-quasiparticle components, $(\alpha\beta)$, $(\gamma\delta)$, etc., constituting the QRPA mode λ are directly represented by the amplitudes $f^{\lambda}_{\gamma\delta}$ and $g^{\lambda}_{\gamma\delta}$, whereas an additional procedure is needed to obtain them in the latter method [54].

The residual interactions in the particle–particle channel appearing in the QRPA matrices A and B are self-consistently treated using the density-dependent contact interaction (2). On the other hand, for residual interactions in the particle–hole channel, we use the Skyrme-type interaction [55]

$$v_{\rm ph}(\boldsymbol{r}, \boldsymbol{r}') = \left[t_0(1 + x_0 P_\sigma) + \frac{t_3}{6}(1 + x_3 P_\sigma)\varrho^{\rm IS}(\boldsymbol{r}) \right] \delta(\boldsymbol{r} - \boldsymbol{r}'), \tag{10}$$

with $t_0 = -1100$ MeV fm^3, $t_3 = 16000$ MeV fm^6, $x_0 = 0.5$, and $x_3 = 1.0$. Because the deformed Wood–Saxon potential is used for the mean-field, we renormalize the residual interaction in the particle–hole channel by multiplying a factor $f_{\rm ph}$ to get the spurious $K^\pi = 1^+$ mode (representing the rotational mode) at zero energy ($v_{\rm ph} \to f_{\rm ph} \cdot v_{\rm ph}$). This factor is found to be 0.380, 0.376 and 0.374 for ^{36}Mg, ^{38}Mg, and ^{40}Mg, respectively. It is desirable to carry out the QRPA calculation by using a model space which is consistent with that adopted in the HFB calculation. It requires, however, excessively demanding computer memory, so that we cut the model space by $E_\alpha + E_\beta \leqslant 30$ MeV. Accordingly, we need another self-consistency factor $f_{\rm pp}$ for the particle–particle channel. We determine this factor such that the spurious $K^\pi = 0^+$ mode associated with the number fluctuation appears at zero energy ($v_{\rm pp} \to f_{\rm pp} \cdot v_{\rm pp}$). This factor is found to be 1.536 for $^{36\text{–}40}$Mg. The dimension of the QRPA matrix is about 3700 for the $K^\pi = 0^+$ modes in ^{40}Mg. We checked accuracy of the numerical calculation by applying our procedure to quadrupole excitations of the spherical nucleus ^{24}O and comparing the result with that of the continuum QRPA calculation by Matsuo [7] which exactly fulfills the energy-weighted sum-rule. It turned out that, although the overall structure of the strength distribution was well reproduced, the energy-weighted sum-rule value was underestimated by 14% due to the truncation of the model space. This shortcoming should be overcome in future by enlarging the QRPA model space.

In terms of the nucleon annihilation and creation operators in the coordinate representation, $\hat{\psi}(\boldsymbol{r}\sigma)$ and $\hat{\psi}^\dagger(\boldsymbol{r}\sigma)$, the quadrupole operator is represented as $\hat{Q}_{2K} = \sum_\sigma \int {\rm d}\boldsymbol{r}\, r^2 Y_{2K}(\hat{r}) \times$

$\hat{\psi}^\dagger(\boldsymbol{r}\sigma)\hat{\psi}(\boldsymbol{r}\sigma)$. The intrinsic matrix elements $\langle\lambda|\hat{Q}_{2K}|0\rangle$ of the quadrupole operator between the excited state $|\lambda\rangle$ and the ground state $|0\rangle$ are given by

$$\langle\lambda|\hat{Q}_{2K}|0\rangle = \sum_{\alpha\beta} Q^{(\mathrm{uv})}_{2K,\alpha\beta}\left(f^{\lambda}_{\alpha\beta} + g^{\lambda}_{\alpha\beta}\right) = \sum_{\alpha\beta} M^{(\mathrm{uv})}_{2K,\alpha\beta}, \tag{11}$$

where

$$Q^{(\mathrm{uv})}_{2K,\alpha\beta} \equiv 2\pi\,\delta_{K,\Omega_\alpha+\Omega_\beta}\int \mathrm{d}\rho\,\mathrm{d}z\; Q^{(\mathrm{uv})}_{2K,\alpha\beta}(\rho,z), \tag{12}$$

with

$$\begin{aligned} Q^{(\mathrm{uv})}_{2K,\alpha\beta}(\rho,z) = \rho\big\{&\varphi_{1,\alpha}(\rho,z,\downarrow)\varphi_{2,\beta}(\rho,z,\uparrow) - \varphi_{1,\alpha}(\rho,z,\uparrow)\varphi_{2,\beta}(\rho,z,\downarrow) \\ &- \varphi_{1,\beta}(\rho,z,\downarrow)\varphi_{2,\alpha}(\rho,z,\uparrow) + \varphi_{1,\beta}(\rho,z,\uparrow)\varphi_{2,\alpha}(\rho,z,\downarrow)\big\}\,Q_{2K}(\rho,z). \end{aligned} \tag{13}$$

Here $Q_{2K}(\rho,z) = Q_{2K}(\boldsymbol{r})e^{-iK\varphi} = r^2 Y_{2K}(\theta,\varphi)e^{-iK\varphi}$.

We calculate the transition strength functions

$$S^{\mathrm{IS}}(\omega) = \sum_{\lambda}\left|\langle\lambda|\hat{Q}^{\mathrm{IS}}_{2K}|0\rangle\right|^2\delta(\hbar\omega-\hbar\omega_\lambda) \tag{14}$$

for isoscalar quadrupole operators $\hat{Q}^{\mathrm{IS}}_{2K} = \hat{Q}^{\pi}_{2K} + \hat{Q}^{\nu}_{2K}$, and use notations $B(Q^\tau 2) = |\langle\lambda|\hat{Q}^{\tau}_{2K}|0\rangle|^2$ for transition strengths and $M_\tau = \langle\lambda|\hat{Q}^{\tau}_{2K}|0\rangle$ for transition matrix elements ($\tau = \pi, \nu$, IS). Note that these quantities are defined in the intrinsic coordinate frame associated with the deformed mean field, so that appropriate Clebsh–Gordan coefficients should be multiplied to obtain transition probabilities in the laboratory frame [56]. For instance, a factor $1/5$ should be multiplied for obtaining the transition strength $B(\mathrm{E2};\,2^+_1 \to 0^+_\beta)$ from the 2^+_1 state to the 0^+_β state, while the factor is unity for obtaining the transition strength $B(\mathrm{E2};\,0^+_{\mathrm{gs}} \to 2^+_\beta)$ from the ground state to the 2^+_β state built on the excited $K^\pi = 0^+$ state. Here, 2^+_1 denotes the 2^+ member of the ground-state rotational band, while 0^+_β and 2^+_β indicate the rotational band members associated with the $K^\pi = 0^+$ intrinsic excitations.

3. Results and discussion

3.1. Some features of calculated results

The single-particle shell structure around the Fermi surface for neutrons in ^{36,38,40}Mg exhibits an interesting feature. Fig. 1 shows the single-particle energy diagram for the WS potential as a function of deformation parameter β_2. As β_2 increases, a level crossing between the up-sloping [303]7/2 level and the down-sloping [310]1/2 level takes place, and a deformed shell gap is formed at $N = 28$ around $\beta_2 = 0.3$. This deformed closed shell approximately corresponds to the $(f_{7/2})^{-2}(p_{3/2})^2$ configuration in the spherical shell model representation. The highest occupied level in this deformed closed shell is situated very near to the continuum threshold, so that there is no bound level above it. However, neutron particle–hole excitations may take place into resonance levels like [303]7/2, [301]1/2 [312]3/2 lying just above the continuum threshold. In fact, as we shall discuss below, these resonance levels participate in the pairing correlations and play an important role in generating low-frequency collective modes of excitation in ^{36,38,40}Mg. Thus, ^{40}Mg and its neighboring isotopes provide an interesting situation to investigate collective

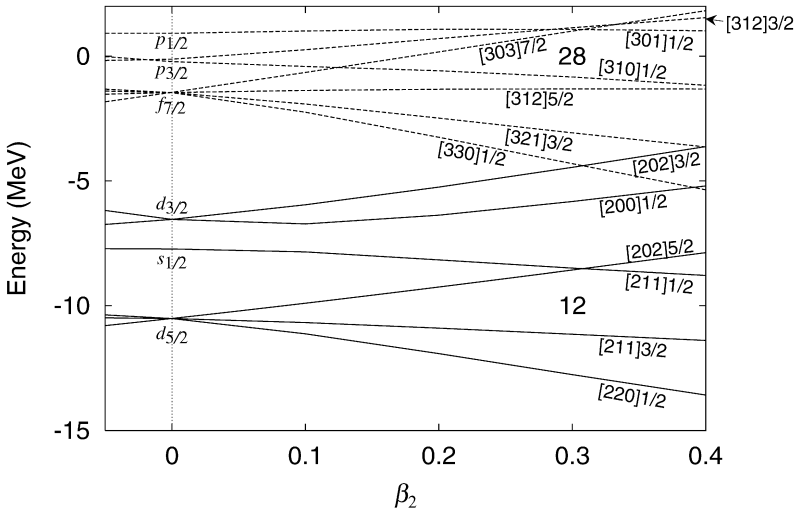

Fig. 1. Single-particle energies in the deformed WS potential for neutrons in ^{40}Mg, plotted as functions of the quadrupole deformation parameter β_2. Solid and dotted lines denote positive- and negative-parity levels, respectively. Single-particle levels are labeled with the asymptotic quantum numbers $[Nn_3\Lambda]\Omega$.

modes unique in unstable nuclei near the neutron drip line. The resonance character of these levels just above the continuum threshold is confirmed by means of the eigenphase-sum method (see Appendix A).

Results of the deformed WS plus HFB calculation for the ground state properties of ^{36,38,40}Mg are listed in Table 1. Calculated values of the average pairing gap for neutrons are rather close to the value estimated in terms of the conventional systematics [57] $\Delta_{\rm syst} \simeq 12/\sqrt{A} \simeq 1.9$ MeV. On the other hand, the average pairing gaps for protons vanish. As shown in this table, the neutron root-mean-square radius increases as approaching the neutron drip line, while the proton root-mean-square radius remains almost constant. This means that the neutron skin structure emerges in these nuclei; the difference between the neutron and proton radii in ^{40}Mg is about 0.9 fm.

Results of the QRPA calculation for quadrupole transition strengths are displayed in Fig. 2. We see prominent peaks at about 3 MeV for both the $K^\pi = 0^+$ and 2^+ excitations. Their strengths are much larger than the single-particle strengths indicating collective character of these excitations. The strength of the lowest $K^\pi = 2^+$ excitation gradually increases as approaching the neutron drip line, while the lowest $K^\pi = 0^+$ excitations in ^{36}Mg and ^{40}Mg seem to be split into two peaks in the case of ^{38}Mg. In the following, we make an extensive analysis on microscopic structure of these low-frequency collective excitations.

3.2. $K^\pi = 0^+$ modes

We first discuss the $K^\pi = 0^+$ excitation modes in ^{40}Mg. The QRPA transition strengths are compared with unperturbed two-quasiparticle strengths in Fig. 3. A prominent peak is seen at about 3.2 MeV in the QRPA strength distribution; it possesses an enhanced strength of about 22 Weisskopf unit (1 W.u. $\simeq 8.1$ fm^4 for ^{40}Mg). From the QRPA amplitudes listed in Table 2, it is clear that this collective mode is generated by coherent superposition of neutron excitations of both particle–hole and particle–particle types. In Fig. 3, the QRPA strengths are also compared with the strengths without the dynamical pairing effects, i.e., the result of QRPA calculation

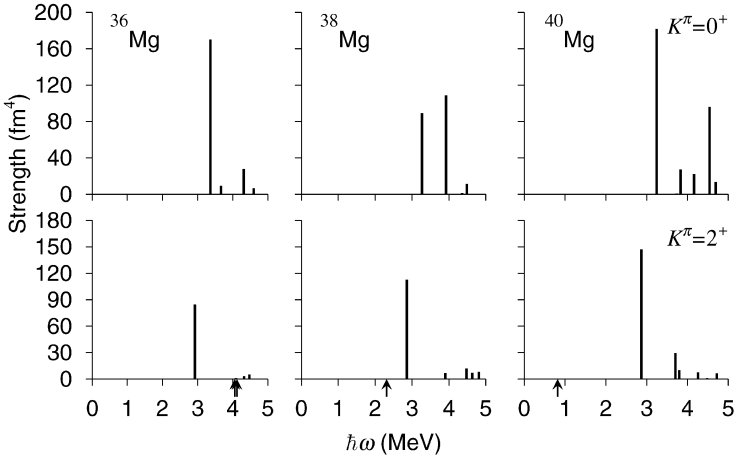

Fig. 2. Isoscalar quadrupole transition strengths $B(Q^{\mathrm{IS}}2)$ for the $K = 0^+$ excitations (upper panel) and the $K = 2^+$ excitations (lower panel) built on the prolately deformed ground states of ^{36,38,40}Mg. The arrows beside the abscissa axes indicate the neutron threshold energies, $E_{\mathrm{th}} = 4.06$ MeV (one-quasiparticle (1qp) continuum; $|\lambda| + \min E_\alpha$), 4.12 MeV (two quasiparticle (2qp) continuum; $2|\lambda|$) for ^{36}Mg, 2.31 MeV (2qp continuum) for ^{38}Mg and 0.82 MeV (2qp continuum) for ^{40}Mg. The QRPA calculations are made by using the surface-type pairing interaction and $\beta_2 = 0.28$ for both protons and neutrons.

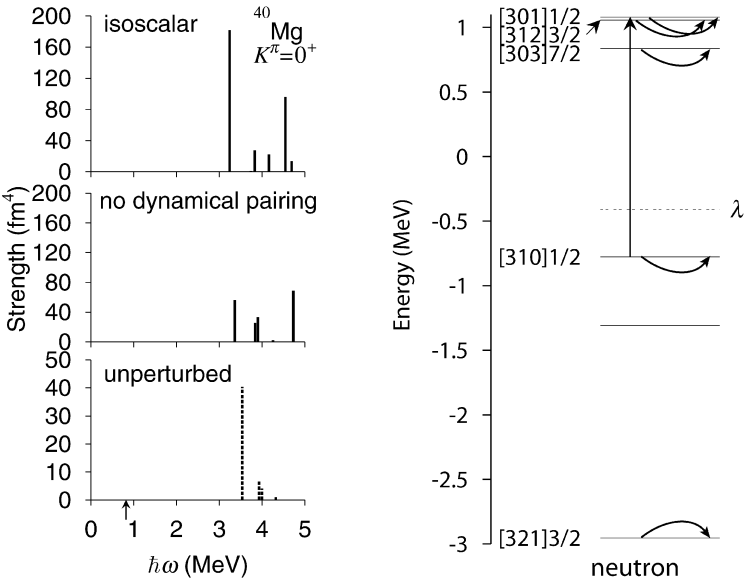

Fig. 3. Left: Isoscalar quadrupole transition strengths $B(Q^{\mathrm{IS}}2)$ for the $K^\pi = 0^+$ excitations in ^{40}Mg. Results of the QRPA calculation with and without including the dynamical pairing effects are plotted in the upper and middle panels, respectively, while unperturbed two-quasiparticle strengths are shown in the lower panel. Notice that different scale is used for the unperturbed strengths. The arrow beside the abscissa axis indicates the neutron threshold energy $2|\lambda| = 0.82$ MeV. Right: Two-quasiparticle excitations generating the lowest $K^\pi = 0^+$ mode at 3.2 MeV. The single-particle levels for the deformed WS potential are labeled with the asymptotic quantum numbers $[Nn_3\Lambda]\Omega$. The chemical potential λ is indicated by the dashed line.

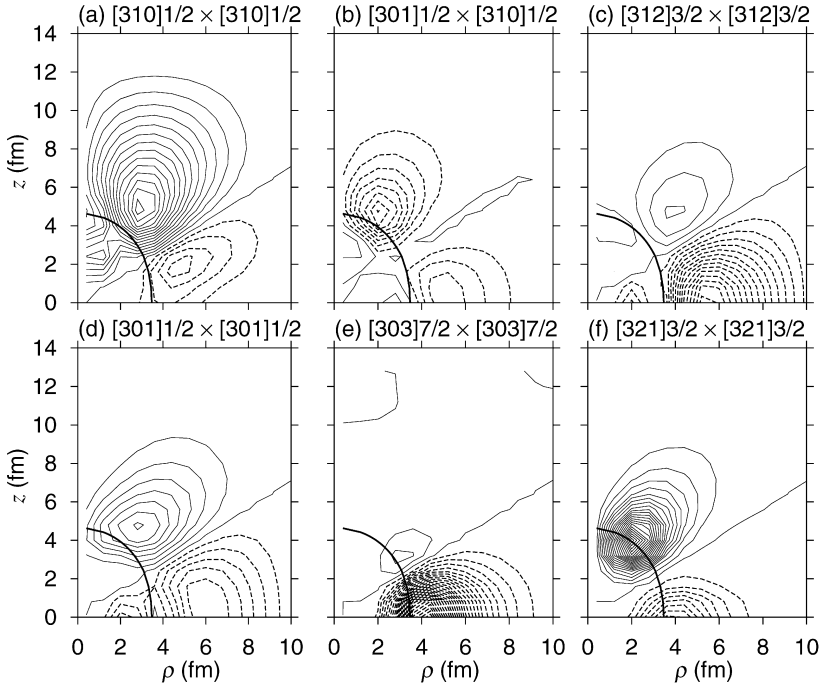

Fig. 4. Spatial distribution functions $Q^{(\mathrm{uv})}_{20,\alpha\beta}(\rho, z)$ for some two-quasiparticle excitations generating the lowest $K^\pi = 0^+$ mode in ^{40}Mg. The contour lines are plotted at intervals of 0.002. The solid and dashed lines represent positive and negative quantities, respectively. The thick solid line indicates the neutron half-density radius; $\varrho_\nu(0)/2 \sim 0.045$ fm^{-3}.

Table 2
QRPA amplitudes of the $K^\pi = 0^+$ mode at 3.2 MeV in ^{40}Mg. This mode has $B(\mathrm{E2}) = 3.4\, e^2\,\mathrm{fm}^4$, $B(Q^\nu 2) = 136\,\mathrm{fm}^4$, and $B(Q^{\mathrm{IS}}2) = 182\,\mathrm{fm}^4$. The single-particle levels are labeled with the asymptotic quantum numbers $[Nn_3\Lambda]\Omega$ of the dominant components of the wave functions. Only components with $|f_{\alpha\beta}|^2 - |g_{\alpha\beta}|^2 > 0.01$ are listed

	α	β	$E_\alpha + E_\beta$ (MeV)	$\lvert f_{\alpha\beta}\rvert^2 - \lvert g_{\alpha\beta}\rvert^2$	$Q^{(\mathrm{uv})}_{20,\alpha\beta}$ (fm^2)	$M^{(\mathrm{uv})}_{20,\alpha\beta}$ (fm^2)
(a)	ν[310]1/2	ν[310]1/2	3.54	0.438	6.36	4.27
(b)	ν[301]1/2	ν[310]1/2	3.93	0.067	−2.57	0.925
(c)	ν[312]3/2	ν[312]3/2	3.99	0.280	−2.03	1.08
(d)	ν[301]1/2	ν[301]1/2	4.32	0.027	0.992	−0.176
(e)	ν[303]7/2	ν[303]7/2	5.76	0.077	−3.39	0.966
(f)	ν[321]3/2	ν[321]3/2	7.15	0.011	3.23	0.396

ignoring the residual pairing interactions. One immediately notice that the transition strength to the lowest excited state is drastically reduced when the dynamical pairing effects are ignored.

Let us discuss the reason why the lowest $K^\pi = 0^+$ mode acquires eminently large transition strength. There are two points to understand this mechanism: (1) existence of unperturbed two-quasiparticle configurations possessing large transition strengths, and (2) effect of residual interactions producing coherence among various two-quasiparticle configurations.

To examine the first point, we plot in Fig. 4 spatial distributions of the quadrupole transition amplitudes for major two-quasiparticle configurations generating the lowest $K^\pi = 0^+$ mode. We see that they are notably extended beyond the half-density radius. This is a situation similar to

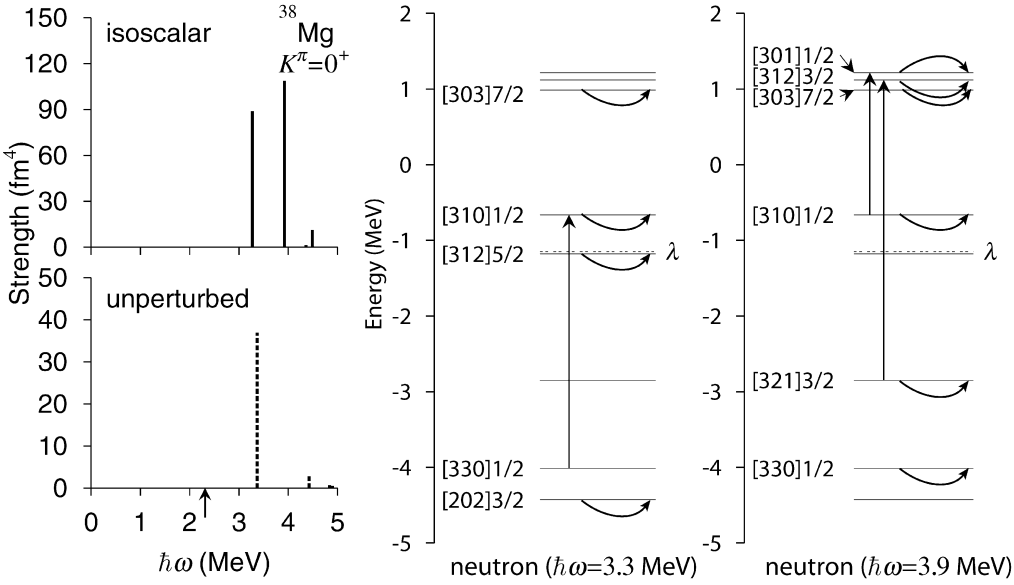

Fig. 5. Left: Isoscalar quadrupole transition strengths $B(Q^{\mathrm{IS}}2)$ for the $K^\pi = 0^+$ excitations in ^{38}Mg are plotted in the upper panel, while unperturbed two-quasiparticle strengths are shown in the lower panel. The arrow beside the abscissa axis indicates the neutron threshold energy $2|\lambda| = 2.31$ MeV. Right: Two-quasiparticle excitations generating the low-lying $K^\pi = 0^+$ modes at 3.3 MeV and 3.9 MeV.

that encountered in Ref. [29], where a neutron excitation from a loosely bound state to a resonance state brings about very large transition strength. We also note that the transition strength associated with the $\nu[301]1/2 \otimes \nu[310]1/2$ configuration is much enhanced although it should be hindered if the selection rule $\Delta N = 2$ for the asymptotic quantum numbers [56] is applied. This selection rule is broken for matrix elements associated with loosely bound states, because their radial wave functions are spatially extended and quite different from those of the harmonic oscillator potential.

Concerning the second point, we have found that the dynamical pairing plays an especially important role. This point is easily seen by comparing the QRPA calculations with and without the dynamical pairing effects, which are shown in Fig. 3. It is apparent that the prominent lowest peak disappears when the dynamical paring effects are ignored. We can say that the coherent superpositions among the particle–hole, particle–particle and hole–hole excitations are indispensable for the emergence of this mode. The importance of the coupling between the (particle–hole type) β vibration and the (particle–particle and hole–hole type) pairing vibration has been well known in stable deformed nuclei [56]. A new feature of the $K^\pi = 0^+$ mode in neutron drip-line nuclei under discussion is that this coupling takes place among two-quasiparticle configurations that are loosely bound or resonances, so that their transition strengths are strikingly enhanced. In addition, as seen in Fig. 4, their spatial structures (peak positions and distribution) are rather similar with each other. This is a favorable situation to generates coherence among them [39]. The importance of dynamical pairing effects in generating soft dipole excitations has been demonstrated by Matsuo et al. [13] for spherical unstable nuclei near the neutron drip line.

Next we discuss the $K^\pi = 0^+$ excitations in ^{38}Mg and ^{36}Mg. The quadrupole transition strengths calculated for ^{38}Mg are presented in Fig. 5, which exhibits two peaks below 4 MeV.

Table 3
QRPA amplitudes of the $K^\pi = 0^+$ mode at 3.3 MeV in ^{38}Mg. This mode has $B(\mathrm{E2}) = 1.67\, e^2\,\mathrm{fm}^4$, $B(Q^\nu 2) = 66.3\,\mathrm{fm}^4$, $B(Q^{\mathrm{IS}}2) = 89.0\,\mathrm{fm}^4$, and $\sum |g_{\alpha\beta}|^2 = 2.32 \times 10^{-2}$. Only components with $|f_{\alpha\beta}|^2 - |g_{\alpha\beta}|^2 > 0.01$ are listed

	α	β	$E_\alpha + E_\beta$ (MeV)	$\lvert f_{\alpha\beta}\rvert^2 - \lvert g_{\alpha\beta}\rvert^2$	$Q^{(\mathrm{uv})}_{20,\alpha\beta}$ (fm^2)	$M^{(\mathrm{uv})}_{20,\alpha\beta}$ (fm^2)
(a)	ν[310]1/2	ν[310]1/2	3.37	0.673	6.08	5.25
(b)	ν[312]5/2	ν[312]5/2	4.84	0.146	0.821	−0.293
(c)	ν[310]1/2	ν[330]1/2	5.35	0.023	−3.59	0.769
(d)	ν[303]7/2	ν[303]7/2	6.35	0.066	−2.64	0.614
(e)	ν[202]3/2	ν[202]3/2	7.82	0.021	−1.29	0.149

Table 4
QRPA amplitudes of the $K^\pi = 0^+$ mode at 3.9 MeV in ^{38}Mg. This mode has $B(\mathrm{E2}) = 4.72\, e^2\,\mathrm{fm}^4$, $B(Q^\nu 2) = 68.1\,\mathrm{fm}^4$, $B(Q^{\mathrm{IS}}2) = 109\,\mathrm{fm}^4$, and $\sum |g_{\alpha\beta}|^2 = 2.71 \times 10^{-2}$. Only components with $|f_{\alpha\beta}|^2 - |g_{\alpha\beta}|^2 > 0.01$ are listed

	α	β	$E_\alpha + E_\beta$ (MeV)	$\lvert f_{\alpha\beta}\rvert^2 - \lvert g_{\alpha\beta}\rvert^2$	$Q^{(\mathrm{uv})}_{20,\alpha\beta}$ (fm^2)	$M^{(\mathrm{uv})}_{20,\alpha\beta}$ (fm^2)
(a)	ν[310]1/2	ν[310]1/2	3.37	0.037	6.08	1.34
(b)	ν[301]1/2	ν[310]1/2	4.42	0.258	1.67	−1.20
(c)	ν[312]3/2	ν[312]3/2	4.90	0.048	0.716	0.169
(d)	ν[312]3/2	ν[321]3/2	5.47	0.250	−3.04	−2.20
(e)	ν[301]1/2	ν[301]1/2	5.47	0.018	0.802	0.131
(f)	ν[321]3/2	ν[321]3/2	6.04	0.058	1.66	−0.411
(g)	ν[303]7/2	ν[303]7/2	6.35	0.084	−2.64	−0.853
(h)	ν[330]1/2	ν[330]1/2	7.33	0.099	4.57	−1.48

The major two-quasiparticle excitations generating these peaks are illustrated in the middle and right panels of this figure. Their QRPA amplitudes are listed in Tables 3 and 4. From these tables, it is seen that the peak at 3.3 MeV is mainly generated by the particle–particle type $\nu[310]1/2 \otimes \nu[310]1/2$ and $\nu[312]5/2 \otimes \nu[312]5/2$ excitations, while the peak at 3.9 MeV is mainly associated with the particle–hole type $\nu[301]1/2 \otimes \nu[310]1/2$ and $\nu[312]3/2 \otimes \nu[321]3/2$ excitations.

The quadrupole transition strengths calculated for ^{36}Mg are displayed in Fig. 6. We notice a prominent peak at about 3.4 MeV below the one-neutron threshold energy (4.1 MeV), which possesses a strongly enhanced transition strength of about 24 W.u. (1 W.u. $\simeq 7.1\,\mathrm{fm}^4$ for ^{36}Mg). This peak exhibits a clear character of collective vibration: as seen from Table 5, this collective mode is created by coherent neutron excitations. Its main components are the particle–hole type $\nu[310]1/2 \otimes \nu[330]1/2$ and $\nu[301]1/2 \otimes \nu[310]1/2$ excitations and the particle–particle type $\nu[312]5/2 \otimes \nu[312]5/2$ and $\nu[321]3/2 \otimes \nu[321]3/2$ excitations. These particle–particle type and particle–hole type excitations are coherently superposed to generate this collective neutron mode.

3.3. $K^\pi = 2^+$ modes

Let us now turn to the $K^\pi = 2^+$ excitation modes. The quadrupole transition strengths calculated for ^{40}Mg are displayed in Fig. 7. We notice a prominent peak at about 2.8 MeV which possesses strongly enhanced transition strength of about 19 W.u. The QRPA amplitudes of this excitation are listed in Table 6. From this table, we see that this peak represents a collective excitation consisting of a coherent superposition of the proton particle–hole excitation from the [211]3/2 level to the [211]1/2 level and a number of neutron two-quasiparticle excitations. Similarly to the $K^\pi = 0^+$ excitation modes discussed in the previous subsection, the asymptotic

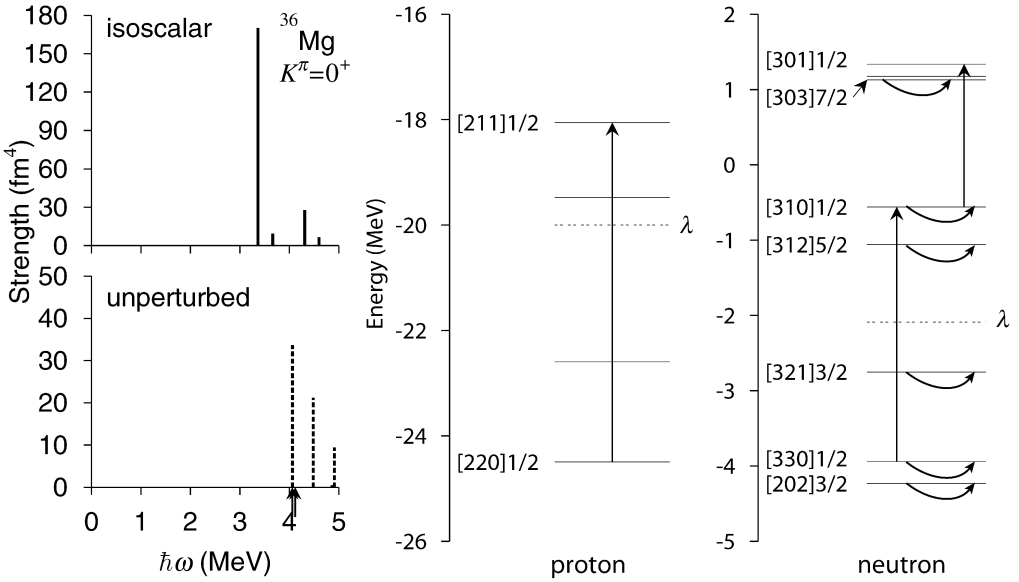

Fig. 6. Left: Isoscalar quadrupole transition strengths $B(Q^{\mathrm{IS}}2)$ for the $K^\pi = 0^+$ excitations in ^{36}Mg are plotted in the upper panel, while unperturbed two-quasiparticle strengths are shown in the lower panel. The arrows beside the abscissa axis indicate the neutron threshold energy $E_{\mathrm{th}} = 4.06$ MeV (1qp continuum) and 4.12 MeV (2qp continuum). Right: Two-quasiparticle excitations generating the lowest $K^\pi = 0^+$ mode at 3.4 MeV in ^{36}Mg.

Table 5
QRPA amplitudes of the $K^\pi = 0^+$ mode at 3.4 MeV in ^{36}Mg. This mode has $B(\mathrm{E2}) = 8.1\ e^2\,\mathrm{fm}^4$, $B(Q^\nu 2) = 104\ \mathrm{fm}^4$, $B(Q^{\mathrm{IS}}2) = 170\ \mathrm{fm}^4$, and $\sum |g_{\alpha\beta}|^2 = 3.91 \times 10^{-2}$. Only components with $|f_{\alpha\beta}|^2 - |g_{\alpha\beta}|^2 > 0.01$ are listed

	α	β	$E_\alpha + E_\beta$ (MeV)	$\lvert f_{\alpha\beta}\rvert^2 - \lvert g_{\alpha\beta}\rvert^2$	$Q^{(\mathrm{uv})}_{20,\alpha\beta}$ (fm^2)	$M^{(\mathrm{uv})}_{20,\alpha\beta}$ (fm^2)
(a)	ν[310]1/2	ν[310]1/2	4.06	0.071	5.80	−1.58
(b)	ν[321]3/2	ν[321]3/2	4.48	0.098	4.60	−1.61
(c)	ν[312]5/2	ν[312]5/2	4.87	0.227	0.714	0.347
(d)	ν[310]1/2	ν[330]1/2	4.91	0.211	−3.08	−2.11
(e)	ν[301]1/2	ν[310]1/2	5.69	0.033	2.02	−0.511
(f)	ν[330]1/2	ν[330]1/2	5.76	0.116	3.98	−1.50
(g)	ν[202]3/2	ν[202]3/2	5.79	0.046	−1.47	−0.271
(h)	ν[303]7/2	ν[303]7/2	7.67	0.049	−1.82	−0.411
(i)	π[211]1/2	π[220]1/2	6.44	0.054	−0.251	−0.599

selection rule ($\Delta N = 0$, $\Delta n_3 = 0$, $\Delta \Lambda = 2$) well known for the γ vibrations [56] is violated for the neutron excitations, because these levels are loosely bound or resonances and their quasiparticle wave functions are significantly extended outside of the nucleus. On the other hand, proton particle–hole excitations satisfy the selection rule because they are deeply bound. We also show in Fig. 7 the result of QRPA calculation where the residual pairing interaction is turned off. Comparing with the full QRPA result, we see that the transition strength is reduced about 30%. Thus, the dynamical pairing effect is important, though its effect is weaker than for the $K^\pi = 0^+$ mode. This is because the $K^\pi = 2^+$ mode consists of both proton and neutron excitations and the pairing is effective only for neutrons.

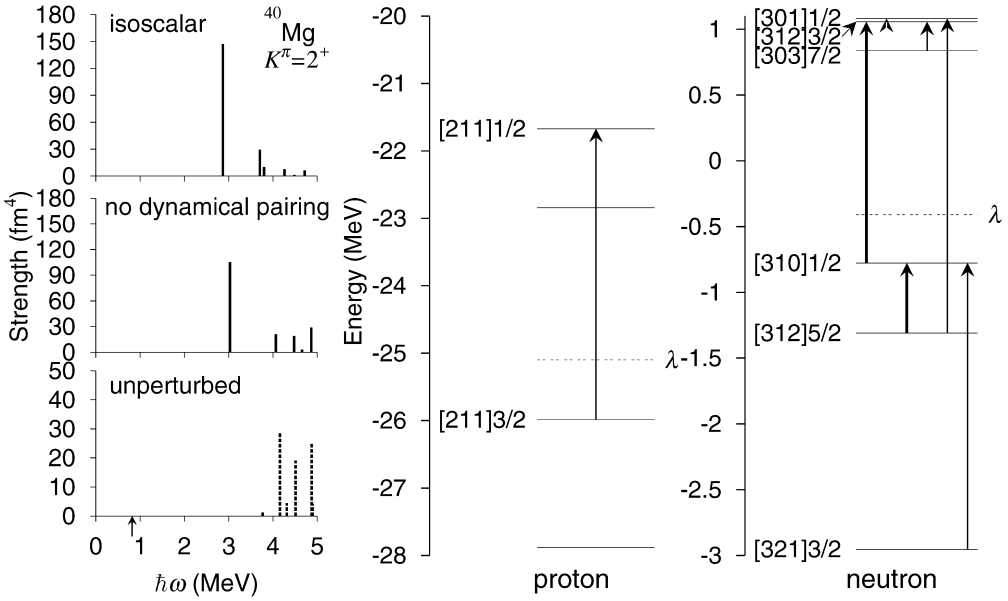

Fig. 7. Left: Isoscalar quadrupole transition strengths $B(Q^{\rm IS}2)$ for the $K^\pi = 2^+$ excitations in ^{40}Mg. Results of the QRPA calculation with and without including the dynamical pairing effects are plotted in the upper and middle panels, respectively, while unperturbed two-quasiparticle strengths are shown in the lower panel. Notice that different scale is used for the unperturbed strengths. The arrow beside the abscissa axis indicates the neutron threshold energy $2|\lambda| = 0.82$ MeV. Right: Two-quasiparticle excitations generating the lowest $K^\pi = 2^+$ mode at 2.9 MeV. Two-quasiparticle excitations satisfying the asymptotic selection rule for the γ vibration ($\Delta N = 0$, $\Delta n_3 = 0$, $\Delta\Lambda = 2$) are drawn by thick arrows.

Table 6
QRPA amplitudes of the $K^\pi = 2^+$ mode at 2.9 MeV in ^{40}Mg. This mode has $B(\mathrm{E2}) = 11.7\, e^2\,\mathrm{fm}^4$, $B(Q^\nu 2) = 75.7\,\mathrm{fm}^4$, $B(Q^{\rm IS}2) = 147\,\mathrm{fm}^4$, and $\sum |g_{\alpha\beta}|^2 = 6.73\times 10^{-2}$. Only components with $|f_{\alpha\beta}|^2 - |g_{\alpha\beta}|^2 > 0.01$ are listed. The label $\nu 1/2^-$ denotes a discretized non-resonant continuum state

	α	β	$E_\alpha + E_\beta$ (MeV)	$\lvert f_{\alpha\beta}\rvert^2 - \lvert g_{\alpha\beta}\rvert^2$	$Q^{(\mathrm{uv})}_{22,\alpha\beta}$ (fm^2)	$M^{(\mathrm{uv})}_{22,\alpha\beta}$ (fm^2)
(a)	ν[312]3/2	ν[310]1/2	3.77	0.013	1.22	−0.145
(b)	ν[301]1/2	ν[312]3/2	4.16	0.098	−5.37	−1.75
(c)	ν[310]1/2	ν[312]5/2	4.51	0.085	−4.37	−1.34
(d)	ν[312]3/2	ν[303]7/2	4.88	0.011	−5.03	−0.454
(e)	ν[301]1/2	ν[312]5/2	4.90	0.016	−2.07	−0.296
(f)	ν[310]1/2	ν[321]3/2	5.34	0.047	−2.67	−0.663
(g)	$\nu 1/2^-$	ν[312]5/2	6.96	0.015	1.93	−0.298
(h)	$\nu 1/2^-$	ν[321]3/2	7.28	0.018	1.46	−0.265
(i)	π[211]1/2	π[211]3/2	4.32	0.596	−2.11	−2.02

For ^{36,38}Mg, we also obtained a prominent peak at about 2.9 MeV which possesses strongly enhanced transition strength (about 15 W.u. and 12 W.u. for ^{38}Mg and ^{36}Mg, respectively) as shown in Fig. 2. These modes possess essentially the same microscopic structure as the collective $K^\pi = 2^+$ mode in ^{40}Mg discussed above. They also correspond to the γ vibrational mode obtained in the previous QRPA calculation [32] for ^{38}Mg. In our calculation, however, the collec-

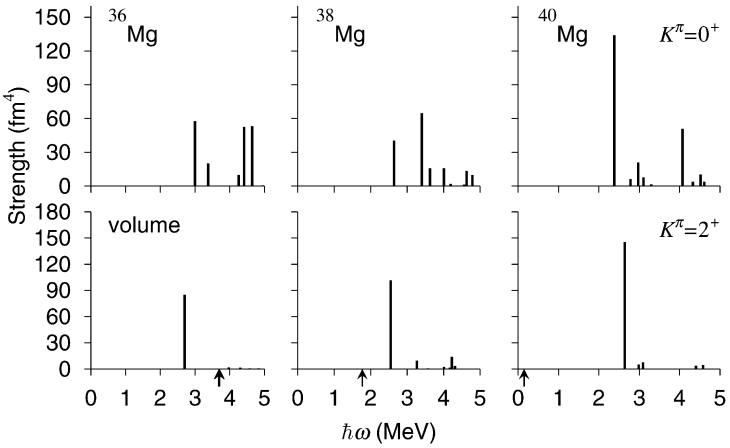

Fig. 8. Isoscalar quadrupole transition strengths $B(Q^{\mathrm{IS}}2)$ for the $K = 0^+$ excitations (upper panel) and the $K = 2^+$ excitations (lower panel) built on the prolately deformed ground states of ^{36,38,40}Mg. The QRPA calculations are made in the same way as in Fig. 2, except that the volume-type pairing interaction is used here. The arrows indicate the neutron threshold energies; 3.69 MeV (1qp continuum) and 3.71 MeV (2qp continuum) for ^{36}Mg, 1.77 MeV (2qp continuum) for ^{38}Mg, and 0.15 MeV (2qp continuum) for ^{40}Mg.

tivity of these modes remains almost the same even if we use different deformations for protons and neutrons, differently from Ref. [32].

3.4. Dependence on pairing interaction

In this subsection, we examine sensitivity of the low-frequency $K^\pi = 0^+$ and 2^+ modes on the density dependence of the pairing interaction. For this purpose, we repeated the HFB and QRPA calculations using pairing interactions with density dependence different from the surface type ($\eta = 1.0$ in Eq. (2)); i.e., the mixed type ($\eta = 0.5$) and the volume type ($\eta = 0.0$). Since the result for the mixed-type pairing is intermediate between those for the surface-type and the volume-type, we show in Fig. 8 only the quadrupole transition strengths obtained using the volume-type pairing interaction. In this calculation, the pairing interaction strength $V_0 = -215.0$ MeV fm^3 is chosen to yield approximately the same average pairing gaps as those for the surface type. Comparing with the results obtained using the surface-type pairing, shown in Fig. 2, we see that the transition strengths for the $K^\pi = 0^+$ collective modes are appreciably reduced, while those for the $K^\pi = 2^+$ collective modes are almost the same. We have checked that, although the strengths are reduced, the microscopic structure of these collective modes are basically the same as discussed above on the basis of the results of calculation using the surface-type pairing interaction. Thus, we can say that the quadrupole transition strengths for the low-frequency $K^\pi = 0^+$ collective modes are especially sensitive to the density dependence of the pairing interaction. Such a sensitivity has been stressed also in Refs. [7,10,13] in their continuum QRPA calculations for E1 and E2 strength functions in neutron rich spherical nuclei.

4. Concluding remarks

We have carried out the QRPA calculations on the basis of the deformed WS plus HFB mean field in the coordinate representation, and obtained the low-frequency $K^\pi = 0^+$ and 2^+ collec-

tive modes in deformed ^{36,38,40}Mg close to the neutron drip line. It has been shown that these modes possess very strong isoscalar quadrupole transition strengths. One of the reasons of this enhancement is that the quasiparticle wave functions participating in these collective excitations have spatially extended structure. The other reason is that the residual pairing interactions, in addition to the particle–hole type residual interactions, enhance the collectivity of these modes. The result of the present calculation suggests that the low-frequency $K^\pi = 0^+$ collective mode is a particularly sensitive indicator of the nature of pairing correlations in nuclei close to the neutron drip line.

This paper should be regarded as an exploratory work toward understanding low-frequency collective modes of excitation in unstable nuclei close to the neutron drip line. It is certainly desirable to improve the treatment of the continuum at least in the following points. First, one may try to use a smaller mesh size and a larger box by implementing an adaptive coordinate method [24]. Second, one may try to take into account the width of resonance by employing Gamow states as basis of the QRPA calculation [62]. The result of the present work indicates that calculations using such an improved framework will be very interesting and worthwhile. We plan to attack this subject in future.

Acknowledgements

This work was done as a part of the Japan–US Cooperative Science Program "Mean-Field Approach to Collective Excitations in Unstable Medium-Mass and Heavy Nuclei" during the academic year 2003–2004, and we acknowledge useful discussions with the member of this project. This work was also supported by the JSPS Core-to-Core Program "International Research Network for Exotic Femto Systems". One of the authors (M.Y.) is grateful for the financial assistance from the Special Postdoctoral Researcher Program of RIKEN. The numerical calculations were performed on the NEC SX-8 and SX-5 supercomputers at Yukawa Institute for Theoretical Physics, Kyoto University and NEC SX-5 supercomputer at Research Center for Nuclear Physics, Osaka University.

Appendix A. Eigenphase sum for single-particle resonance states

We examine properties of three single-particle states in the continuum, which play a key role in generating the low-lying excitations modes in ^{36,38,40}Mg. The resonance energy and width in a deformed potential can be estimated using the eigenphase sum $\Delta(E)$. It is defined in terms of the eigenvalues of the scattering matrix (S-matrix) as

$$\left(U^\dagger S U\right)_{aa'} = e^{2i\delta_a(E)}\delta_{aa'}, \qquad \Delta(E) = \sum_a \delta_a(E). \tag{A.1}$$

We evaluate the eigenphase sum for three states following the procedure of Ref. [58]. The resonance energy and width are identified with the peak energy of $\frac{1}{\pi}\mathrm{d}\Delta(E)/\mathrm{d}E$ and its FWHM, respectively [59,60]. This evaluation is in good correspondence with another definition of the resonance; the Gamow state in a deformed potential [61] which represents the pole of the S-matrix in the complex momentum plane.

The result of this calculation, presented in Fig. 9, indicates that the [301]1/2 and [312]3/2 states can be regarded as resonances with rather large widths; their energies are $0.53 - i0.46$ (MeV) and $0.42 - i0.33$ (MeV), respectively. On the other hand, the [303]7/2 state is evaluated as a narrow resonance with energy $0.44 - i0.0005$ (MeV). Obviously, the small width is due to its high centrifugal barrier.

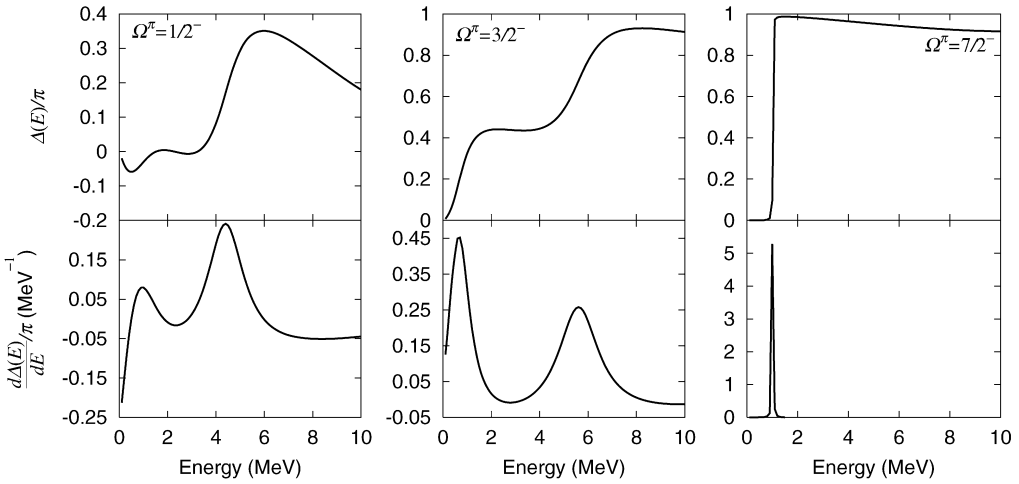

Fig. 9. The eigenphase sum (upper panel) and its derivative (lower panel) for the $\Omega^\pi = 1/2^-, 3/2^-$ and $7/2^-$ states in ^{40}Mg are plotted as functions of energy.

References

[1] I. Tanihata (Ed.), Nucl. Phys. A 693 (1–2) (2001).
[2] H. Horiuchi, T. Otsuka, Y. Suzuki (Eds.), Prog. Theor. Phys. Suppl. 142 (2001).
[3] K. Hagino, H. Horiuchi, M. Matsuo, I. Tanihata (Eds.), Prog. Theor. Phys. Suppl. 146 (2002).
[4] I. Hamamoto, H. Sagawa, X.Z. Zhang, Phys. Rev. C 53 (1996) 765;
I. Hamamoto, H. Sagawa, X.Z. Zhang, Phys. Rev. C 64 (2001) 024313.
[5] I. Hamamoto, H. Sagawa, Phys. Rev. C 60 (1999) 064314;
I. Hamamoto, H. Sagawa, Phys. Rev. C 66 (2002) 044315.
[6] S. Shlomo, B. Agrawal, Nucl. Phys. A 722 (2003) 98c.
[7] M. Matsuo, Nucl. Phys. A 696 (2001) 371.
[8] K. Hagino, H. Sagawa, Nucl. Phys. A 695 (2001) 82.
[9] M. Bender, J. Dobaczewski, J. Engel, W. Nazarewicz, Phys. Rev. C 65 (2002) 054322.
[10] E. Khan, N. Sandulescu, M. Grasso, N. Van Giai, Phys. Rev. C 66 (2002) 024309.
[11] M. Yamagami, N. Van Giai, Phys. Rev. C 69 (2004) 034301.
[12] J. Terasaki, J. Engel, M. Bender, J. Dobaczewski, W. Nazarewicz, M. Stoitsov, Phys. Rev. C 71 (2005) 034310.
[13] M. Matsuo, K. Mizuyama, Y. Serizawa, Phys. Rev. C 71 (2005) 064326.
[14] D. Vretenar, N. Paar, P. Ring, G.A. Lalazissis, Nucl. Phys. A 692 (2001) 496.
[15] N. Paar, P. Ring, T. Nikšić, D. Vretenar, Phys. Rev. C 67 (2003) 034312.
[16] N. Paar, T. Nikšić, D. Vretenar, P. Ring, Phys. Rev. C 69 (2004) 054303.
[17] N. Paar, T. Nikšić, D. Vretenar, P. Ring, Phys. Lett. B 606 (2005) 288.
[18] L.G. Cao, Z.Y. Ma, Phys. Rev. C 71 (2005) 034305.
[19] D. Vretenar, A.V. Afanasjev, G.A. Lalazissis, P. Ring, Phys. Rep. 409 (2005) 101.
[20] G. Giambrone, S. Scheit, F. Barranco, P.F. Bortignon, G. Colò, D. Sarchi, E. Vigezzi, Nucl. Phys. A 726 (2003) 3.
[21] S. Péru, J.F. Berger, P.F. Bortignon, Eur. Phys. J. A 26 (2005) 25.
[22] D. Sarchi, P.F. Bortignon, G. Coló, Phys. Lett. B 601 (2004) 27.
[23] M. Bender, P.-H. Heenen, P.-G. Reinhard, Rev. Mod. Phys. 75 (2003) 121.
[24] T. Nakatsukasa, K. Yabana, Phys. Rev. C 71 (2005) 024301.
[25] T. Inakura, H. Imagawa, Y. Hashimoto, S. Mizutori, M. Yamagami, K. Matsuyanagi, Nucl. Phys. A 768 (2006) 61.
[26] R.H. Lemmer, M. Vénéroni, Phys. Rev. 170 (1968) 883.
[27] A. Muta, J.-I. Iwata, Y. Hashimoto, K. Yabana, Prog. Theor. Phys. 108 (2002) 1065.
[28] H. Imagawa, Y. Hashimoto, Phys. Rev. C 67 (2003) 037302.
[29] K. Yoshida, M. Yamagami, K. Matsuyanagi, Prog. Theor. Phys. 113 (2005) 1251.
[30] P. Urkedal, X.Z. Zhang, I. Hamamoto, Phys. Rev. C 64 (2001) 054304.

[31] R. Álvarez-Rodríguez, P. Sarriguren, E. Moya de Guerra, L. Pacearescu, A. Faessler, F. Šimkovic, Phys. Rev. C 70 (2004) 064309, and references therein.
[32] K. Hagino, N. Van Giai, H. Sagawa, Nucl. Phys. A 731 (2004) 264.
[33] A. Bulgac, Preprint No. FT-194-1980, Institute of Atomic Physics, Bucharest, 1980, nucl-th/9907088.
[34] J. Dobaczewski, H. Flocard, J. Treiner, Nucl. Phys. A 422 (1984) 103.
[35] R. Smolańczuk, J. Dobaczewski, Phys. Rev. C 48 (1993) R2166.
[36] J. Dobaczewski, I. Hamamoto, W. Nazarewicz, J.A. Sheikh, Phys. Rev. Lett. 72 (1994) 981.
[37] J. Dobaczewski, W. Nazarewicz, T.R. Werner, J.F. Berger, C.R. Chinn, J. Dechargé, Phys. Rev. C 53 (1996) 2809.
[38] K. Bennacuer, J. Dobaczewski, M. Płoszajczak, Phys. Rev. C 60 (1999) 034308.
[39] M. Yamagami, Phys. Rev. C 72 (2005) 064308.
[40] J. Terasaki, H. Flocard, P.-H. Heenen, P. Bonche, Nucl. Phys. A 621 (1997) 706.
[41] M.V. Stoitsov, J. Dobaczewski, W. Nazarewicz, S. Pittel, D.J. Dean, Phys. Rev. C 68 (2003) 054312.
[42] R. Rodoríguez-Guzmán, J.L. Egido, L.M. Robledo, Nucl. Phys. A 709 (2002) 201.
[43] E. Caurier, F. Nowacki, A. Poves, Nucl. Phys. A 742 (2004) 14.
[44] P.-G. Reinhard, D.J. Dean, W. Nazarewicz, J. Dobaczewski, J.A. Maruhn, M.R. Strayer, Phys. Rev. C 60 (1999) 014316, and references therein.
[45] K. Yoshida, M. Yamagami, K. Matsuyanagi, Proceedings of the International Conference on Finite Fermionic Systems–Nilsson Model 50 Years, Lund, Sweden, 14–18 June 2005, Phys. Scr. T 125 (2006) 45.
[46] E. Teran, V.E. Oberacker, A.S. Umar, Phys. Rev. C 67 (2003) 064314.
[47] G.F. Bertsch, H. Esbensen, Ann. Phys. 209 (1991) 327.
[48] J. Terasaki, P.-H. Heenen, P. Bonche, J. Dobaczewski, H. Flocard, Nucl. Phys. A 593 (1995) 1.
[49] J. Sauvage-Letessier, P. Quentin, H. Flocard, Nucl. Phys. A 370 (1981) 231.
[50] M. Bender, K. Rutz, P.-G. Reinhard, J.A. Maruhn, Eur. Phys. J. A 8 (2000) 59.
[51] T. Duguet, P. Bonche, P.-H. Heenen, Nucl. Phys. A 679 (2001) 427.
[52] M. Yamagami, K. Matsuyanagi, M. Matsuo, Nucl. Phys. A 693 (2001) 579.
[53] D.J. Rowe, Nuclear Collective Motion, Methuen, London, 1970.
[54] E. Khan, N. Sandulescu, N. Van Giai, Phys. Rev. C 71 (2005) R042801.
[55] S. Shlomo, G.F. Bertsch, Nucl. Phys. A 243 (1975) 507.
[56] A. Bohr, B.R. Motteleson, Nuclear Structure, vol. II, Benjamin, 1975, World Scientific, 1998.
[57] A. Bohr, B.R. Motteleson, Nuclear Structure, vol. I, Benjamin, 1969, World Scientific, 1998.
[58] K. Hagino, N. Van Giai, Nucl. Phys. A 735 (2004) 55.
[59] M. Grasso, N. Sandulescu, N. Van Giai, R.J. Liotta, Phys. Rev. C 64 (2001) 064321.
[60] A. Muta, T. Otsuka, Prog. Theor. Phys. Suppl. 142 (2001) 355.
[61] K. Yoshida, K. Hagino, Phys. Rev. C 72 (2005) 064311.
[62] P. Curutchet, T. Vertse, R.J. Liotta, Phys. Rev. C 39 (1989) 1020.

Progress of Theoretical Physics, Vol. 117, No. 3, March 2007

Gauge-Invariant Formulation of the Adiabatic Self-Consistent Collective Coordinate Method

Nobuo HINOHARA,[1] Takashi NAKATSUKASA,[2] Masayuki MATSUO[3] and Kenichi MATSUYANAGI[1]

[1]*Department of Physics, Graduate School of Science, Kyoto University, Kyoto 606-8502, Japan*
[2]*Institute of Physics and Center for Computational Sciences, University of Tsukuba, Tsukuba 305-8571, Japan*
[3]*Department of Physics, Faculty of Science, Niigata University, Niigata 950-2181, Japan*

(Received December 27, 2006)

The adiabatic self-consistent collective coordinate (ASCC) method is a practical microscopic theory of large-amplitude collective motion in nuclei with superfluidity. We show that its basic equations are invariant under transformations involving the gauge angle in particle-number space. By virtue of this invariance, a clean separation of the large-amplitude collective motion and the pairing rotational motion can be made, and this allows us to restore the particle-number symmetry broken by the Hartree-Fock-Bogoliubov (HFB) approximation. We formulate the ASCC method explicitly in a gauge-invariant form. In solving the ASCC equations, it is necessary to fix the gauge. Applying this new formulation to the multi-$O(4)$ model, we compare different gauge-fixing procedures and demonstrate that calculations using different gauges indeed yield the same results for gauge-invariant quantities, such as the collective path and quantum spectra. We propose a gauge-fixing prescription that seems most convenient in realistic calculations.

§1. Introduction

The construction of a microscopic theory of large-amplitude collective motion is a long-standing and fundamental problem in the study of nuclear many-body systems.[1)–35)] As is well known, pairing correlations play crucial roles in low-lying states of medium and heavy nuclei, and they are taken into account in the Hartree-Fock-Bogoliubov (HFB) mean-field theory by violating the particle number conservation.[36)–38)] The broken particle-number symmetry can be restored, however, by making the self-consistent quasiparticle random-phase approximation (QRPA), on top of the HFB mean field.[36)–38)] It is an advantage of the QRPA that number-conserving collective modes, such as shape-vibrational modes, are exactly decoupled from number-fluctuation modes. The latter modes are associated with the nucleon-number degrees of freedom and are called the 'pairing rotational modes'. It is a unique feature of nuclei as finite quantum systems that such rotational motion in gauge space is actually observed in quantum spectra.[39)] Because the applicability of the QRPA is limited to small-amplitude collective motion, it is highly desirable to extend the QRPA to a general theory which has its decoupling feature. Such a theory should be capable of describing the interplay between large-amplitude collective motion and the pairing rotational modes.

The self-consistent collective coordinate (SCC) method[7] is a microscopic theory of large-amplitude collective motion based on the time-dependent Hartree-Fock (TDHF) method. This method enables us to extract the collective submanifold in a fully self-consistent manner. The SCC method was originally formulated[7] for systems without pairing correlations, and then extended[18] to systems with superfluidity. To extract the collective submanifold embedded in the time-dependent Hartree-Fock-Bogoliubov (TDHFB) phase space, number and angle variables describing the pairing rotational motion are explicitly introduced,[18] in addition to the collective variables describing the large-amplitude collective motion. This extended version of the SCC method has been applied successfully to various kinds of anharmonic vibration and high-spin rotational motion.[40–51] However, obtaining solutions with this method requires use of a technique employing expansion with respect to the collective coordinates and momenta around the HFB states. Thus it is difficult to describe large-amplitude collective motion using this expansion. Recently, the adiabatic SCC (the ASCC) method has been proposed to overcome this difficulty.[52] The ASCC method is an alternative way to solve the SCC basic equations in the case that the large-amplitude collective motion of interest is slow (adiabatic). Under this assumption, the basic equations of the SCC method are expanded up to second order in the collective momentum, but no expansion is carried out with respect to the collective coordinate. This method has been applied[53] to the study of shape-coexistence phenomena[54–56] in which there is large-amplitude collective motion that appears as the transition between the oblate and prolate HFB equilibrium shapes. However, the calculation to determine the collective degrees of freedom often involves a numerical instability, caused by the existence of a redundant degree of freedom in the ASCC equations. This problem has been treated by imposing an additional condition by hand.[57] However we now understand the origin of this redundancy: It is due to the gauge invariance of the ASCC equations.

The main purpose of this paper is to formulate the ASCC method in a manner that makes manifest the invariance under transformations with respect to the angle variable in the gauge space. This invariance is necessary to realize a clean separation of the large-amplitude collective motion and the pairing rotational motion, and to restore the particle-number symmetry broken by the HFB approximation. This new formulation of the ASCC method also provides justification of the prescription adopted in our previous work.[57] In the present work, we apply this method to the multi-$O(4)$ model[57–62] with several choices of the gauge and test the internal consistency of the proposed scheme by carrying out a detailed numerical calculation.

This paper is organized as follows. In §2 the basic equations of the ASCC method are presented. In §3 a gauge-invariant formulation of the ASCC method is given. This formulation is applied to the multi-$O(4)$ model in §4, and the results of numerical calculations testing its validity are reported in §5. Concluding remarks are given in §6.

§2. Basic equations of the ASCC method

2.1. *Basic ideas*

The time evolution of large-amplitude collective motion is described by the time-dependent variational principle expressed as

$$\delta \langle \phi(t)| \, i\frac{\partial}{\partial t} - \hat{H} \, |\phi(t)\rangle = 0, \tag{2·1}$$

where $|\phi(t)\rangle$ is the time-dependent HFB state vector. Assuming that the time-dependence of the collective motion is governed by the collective coordinate q and the momentum p, we parameterize the time-dependent HFB state vector as

$$|\phi(t)\rangle = |\phi(q, p, \varphi, n)\rangle \, . \tag{2·2}$$

Here, φ represents the gauge angle conjugate to the particle number $n \equiv N - N_0$. We measure the particle number from a reference value N_0 specified below and assume, for simplicity, that there is one collective coordinate. We define the intrinsic state vector $|\phi(q, p, n)\rangle$ in the particle-number (gauge) space by

$$|\phi(q, p, \varphi, n)\rangle = e^{-i\varphi\tilde{N}} \, |\phi(q, p, n)\rangle \, , \tag{2·3}$$

where $\tilde{N} \equiv \hat{N} - N_0$. Two sets of collective variables, (q, p) and (φ, n), are determined such that the canonical variable conditions

$$\begin{aligned} \langle \phi(q,p,n)| \, i\frac{\partial}{\partial q} \, |\phi(q,p,n)\rangle &= p + \frac{\partial S}{\partial q}, \quad \langle \phi(q,p,n)| \, \frac{\partial}{i\partial p} \, |\phi(q,p,n)\rangle = -\frac{\partial S}{\partial p}, \\ \langle \phi(q,p,n)| \, \tilde{N} \, |\phi(q,p,n)\rangle &= n + \frac{\partial S}{\partial \varphi}, \quad \langle \phi(q,p,n)| \, \frac{\partial}{i\partial n} \, |\phi(q,p,n)\rangle = -\frac{\partial S}{\partial n} \end{aligned} \tag{2·4}$$

are satisfied. Here, the generating function S is an arbitrary function of q, p, φ, and n. We choose $S = 0$, because it is appropriate for the adiabatic approximation.[15),16),20)] The collective Hamiltonian is defined by

$$\mathcal{H}(q, p, n) = \langle \phi(q, p, \varphi, n)| \, \hat{H} \, |\phi(q, p, \varphi, n)\rangle = \langle \phi(q, p, n)| \, \hat{H} \, |\phi(q, p, n)\rangle \, . \tag{2·5}$$

Note that this collective Hamiltonian is independent of the gauge angle φ, because the original Hamiltonian commutes with the particle number operator $\hat{N}$.

The equation of collective path is obtained by replacing the time derivative term in Eq. (2·1) with derivatives with respect to the four collective variables:

$$\delta \langle \phi(q, p, n)| \, \hat{H} - i \left(\frac{\partial \mathcal{H}}{\partial p}\frac{\partial}{\partial q} - \frac{\partial \mathcal{H}}{\partial q}\frac{\partial}{\partial p} + \frac{1}{i}\frac{\partial \mathcal{H}}{\partial n}\tilde{N} \right) |\phi(q, p, n)\rangle = 0. \tag{2·6}$$

Here, the canonical equations of motion for the collective variables (q, p) and (φ, n) are used in order to eliminate the time derivative of the collective variables. Equations (2·4), (2·5) and (2·6) constitute the basic equations of the SCC method.[7),18)]

2.2. *Basic equations of the ASCC method*

Assuming that the large-amplitude collective motion is slow, i.e., that p is small, let us write the TDHFB state vector $|\phi(q,p,n)\rangle$ in the following form:

$$|\phi(q,p,n)\rangle = e^{ip\hat{Q}(q)+in\hat{\Theta}(q)}\,|\phi(q)\rangle\,. \tag{2·7}$$

Here $\hat{Q}(q)$ and $\hat{\Theta}(q)$ are Hermitian one-body operators, which may be written as

$$\hat{Q}(q) = \sum_{\alpha\beta}\left(Q_{\alpha\beta}(q)a^\dagger_\alpha a^\dagger_\beta + Q_{\alpha\beta}(q)^* a_\beta a_\alpha\right), \tag{2·8}$$

$$\hat{\Theta}(q) = i\sum_{\alpha\beta}\left(\Theta_{\alpha\beta}(q)a^\dagger_\alpha a^\dagger_\beta - \Theta_{\alpha\beta}(q)^* a_\beta a_\alpha\right), \tag{2·9}$$

where $a^\dagger_\alpha$ and a_α are the quasiparticle creation and annihilation operators associated with the time-even state vector $|\phi(q)\rangle$, which satisfy $a_\alpha\,|\phi(q)\rangle = 0$, and $n = N - N_0$, N_0 being the expectation value of the particle number with respect to $|\phi(q)\rangle$. In §3, we show that it is also possible to adopt a slightly different representation for $\hat{Q}(q)$.

Substituting (2·7) into (2·4) and comparing the coefficients of zeroth-order and first-order terms in p and n, we obtain the canonical variable conditions in the adiabatic limit:

$$\langle\phi(q)|\,\hat{P}(q)\,|\phi(q)\rangle = 0, \tag{2·10}$$

$$\langle\phi(q)|\,\hat{Q}(q)\,|\phi(q)\rangle = 0, \tag{2·11}$$

$$\langle\phi(q)|\,\tilde{N}\,|\phi(q)\rangle = 0, \tag{2·12}$$

$$\langle\phi(q)|\,\hat{\Theta}(q)\,|\phi(q)\rangle = 0, \tag{2·13}$$

$$\langle\phi(q)|\,[\hat{\Theta}(q),\tilde{N}]\,|\phi(q)\rangle = i, \tag{2·14}$$

$$\langle\phi(q)|\,[\hat{Q}(q),\hat{\Theta}(q)]\,|\phi(q)\rangle = 0, \tag{2·15}$$

$$\langle\phi(q)|\,\frac{\partial\hat{Q}}{\partial q}\,|\phi(q)\rangle = -1, \tag{2·16}$$

where $\hat{P}(q)$ is the local shift operator defined by

$$\hat{P}(q)\,|\phi(q)\rangle = i\frac{\partial}{\partial q}\,|\phi(q)\rangle\,. \tag{2·17}$$

Differentiating (2·11) and (2·12) with respect to q and using (2·16), we obtain

$$\langle\phi(q)|\,[\hat{Q}(q),\hat{P}(q)]\,|\phi(q)\rangle = i, \tag{2·18}$$

$$\langle\phi(q)|\,[\tilde{N},\hat{P}(q)]\,|\phi(q)\rangle = 0. \tag{2·19}$$

The collective Hamiltonian (2·5) is also expanded up to second order in p and first order in n, and we write

$$\mathcal{H}(q,p,n) = V(q) + \frac{1}{2}B(q)p^2 + \lambda(q)n, \tag{2·20}$$

where the collective potential $V(q)$, the inverse mass parameter $B(q)$, and the chemical potential $\lambda(q)$ are defined by

$$V(q) = \mathcal{H}(q,p,n)\Big|_{p=n=0} = \langle\phi(q)|\,\hat{H}\,|\phi(q)\rangle\,, \tag{2·21}$$

$$B(q) = \frac{1}{2}\frac{\partial^2\mathcal{H}}{\partial p^2}\Big|_{p=n=0} = \langle\phi(q)|\,[[\hat{H}, i\hat{Q}(q)], i\hat{Q}(q)]\,|\phi(q)\rangle\,, \tag{2·22}$$

$$\lambda(q) = \frac{\partial\mathcal{H}}{\partial n}\Big|_{p=n=0} = \langle\phi(q)|\,[\hat{H}, i\hat{\Theta}(q)]\,|\phi(q)\rangle\,. \tag{2·23}$$

We obtain the ASCC equations by expanding the equation of collective path (2·6) with respect to p and n, and requiring that the variations vanish at each order in p and n. At zeroth order, we obtain the moving-frame HFB equation

$$\delta\,\langle\phi(q)|\,\hat{H}_M(q)\,|\phi(q)\rangle = 0, \tag{2·24}$$

where

$$\hat{H}_M(q) = \hat{H} - \lambda(q)\tilde{N} - \frac{\partial V}{\partial q}\hat{Q}(q) \tag{2·25}$$

is the moving-frame Hamiltonian. At first and second orders, we obtain the moving-frame QRPA equations (also called the local harmonic equations),

$$\delta\,\langle\phi(q)|\,[\hat{H}_M(q), i\hat{Q}(q)] - B(q)\hat{P}(q)\,|\phi(q)\rangle = 0, \tag{2·26}$$

$$\begin{aligned}\delta\,\langle\phi(q)|\,[\hat{H}_M(q), \hat{P}(q)] - iC(q)\hat{Q}(q)\\ - \frac{1}{2B(q)}\Big[\Big[\hat{H}_M(q), \frac{\partial V}{\partial q}\hat{Q}(q)\Big], i\hat{Q}(q)\Big] - i\frac{\partial\lambda}{\partial q}\tilde{N}\,|\phi(q)\rangle = 0,\end{aligned} \tag{2·27}$$

where

$$C(q) = \frac{\partial^2 V}{\partial q^2} + \frac{1}{2B(q)}\frac{\partial B}{\partial q}\frac{\partial V}{\partial q}. \tag{2·28}$$

Note that in Ref. 52) the curvature term $1/2B(q)[[\hat{H}_M(q), \partial V/\partial q\hat{Q}(q)], i\hat{Q}(q)]$ is linearized with respect to $\hat{Q}(q)$ using the relation

$$(\hat{H} - \lambda(q)\hat{N})^A = \frac{\partial V}{\partial q}\hat{Q}(q), \tag{2·29}$$

where the superscript A in Eq. (2·29) denotes the two-quasiparticle creation ($a^\dagger a^\dagger$) and annihilation (aa) part of the operator in the parentheses. Hereafter, we call this part the "A-part" and the $a^\dagger a$ terms the "B-part". The collective variables (q,p) and the collective Hamiltonian $\mathcal{H}(q,p,n)$ are determined by solving the ASCC equations, (2·24), (2·26), and (2·27), under the canonical variable conditions. Note that we can carry out a scale transformation of the collective coordinate q such that $B(q) = 1$. We adopt this choice. Then, $C(q)$ represents the curvature of the collective potential:

$$C(q) = \frac{\partial^2 V(q)}{\partial q^2}. \tag{2·30}$$

§3. Gauge invariance of the ASCC equations with respect to the pairing rotational degree of freedom

3.1. *Gauge invariance at the HFB equilibrium point*

As mentioned in the preceding section, the first step to solve the ASCC equations is to find a solution at one of the HFB equilibrium points, denoted $q = q_0$, which corresponds to the local minimum of the collective potential $V(q)$, satisfying $\partial V/\partial q = 0$. The moving-frame HFB equation reduces to the conventional HFB equation at the equilibrium point:

$$\delta \langle \phi(q_0)| \hat{H} - \lambda(q_0)\tilde{N} |\phi(q_0)\rangle = 0. \tag{3·1}$$

The moving-frame QRPA equations at the equilibrium point are given by

$$\delta \langle \phi(q_0)| [\hat{H} - \lambda(q_0)\tilde{N}, i\hat{Q}(q_0)] - B(q_0)\hat{P}(q_0) |\phi(q_0)\rangle = 0, \tag{3·2}$$

$$\delta \langle \phi(q_0)| [\hat{H} - \lambda(q_0)\tilde{N}, \hat{P}(q_0)] - iC(q_0)\hat{Q}(q_0) - i\frac{\partial \lambda}{\partial q}\tilde{N} |\phi(q_0)\rangle = 0. \tag{3·3}$$

These equations reduce to the QRPA equations if the quantity $\partial\lambda/\partial q$ vanishes. In other words, the QRPA solution corresponds to the special solution of the moving-frame QRPA equations with $\partial\lambda/\partial q = 0$.

Let us consider the following transformations:

$$\hat{Q}(q_0) \to \hat{Q}(q_0) + \alpha \hat{N}^A(q_0), \tag{3·4a}$$

$$\hat{\Theta}(q_0) \to \hat{\Theta}(q_0) + \alpha \hat{P}(q_0), \tag{3·4b}$$

$$\frac{\partial \lambda}{\partial q}(q_0) \to \frac{\partial \lambda}{\partial q}(q_0) - \alpha C(q_0). \tag{3·4c}$$

Here, α is an arbitrary number and $\hat{N}^A$ denotes the A-part of the number operator $\hat{N}$. This is a kind of gauge transformation with respect to the pairing rotational degree of freedom. We can easily confirm that the moving-frame QRPA equations at the HFB equilibrium point, (3·2)–(3·3), and the canonical variable conditions, (2·10)–(2·15) and (2·18)–(2·19), are invariant under this transformation. Due to this invariance, the solution of the moving-frame QRPA equations is not uniquely determined at the HFB equilibrium point. If we choose a value of α such that the relation $\partial\lambda/\partial q = 0$ holds, the moving-frame QRPA equations coincide with the conventional QRPA equations. We can choose other values of α, however, if they are more convenient.

3.2. *Gauge invariance at non-equilibrium points*

At non-equilibrium points, $\partial V/\partial q$ is non-zero, and the moving-frame Hamiltonian (2·25) depends on the collective coordinate operator $\hat{Q}(q)$. However, we can generalize the above considerations applying to the HFB equilibrium point to a general non-equilibrium point q on the collective path. Indeed, it is straightforward to confirm that all the basic equations of the ASCC method [i.e., the collective Hamiltonian $\mathcal{H}(q, p, n)$, (2·20), the inverse mass parameter $B(q)$, (2·22), the moving-frame

HFB equation, (2·24), the moving-frame QRPA equations, (2·26)–(2·27), and the canonical variable conditions, (2·10)–(2·15) and (2·18)–(2·19)] are invariant under the transformations with respect to the pairing rotational degree of freedom

$$\hat{Q}(q) \to \hat{Q}(q) + \alpha\tilde{N}, \tag{3·5a}$$

$$\hat{\Theta}(q) \to \hat{\Theta}(q) + \alpha\hat{P}(q), \tag{3·5b}$$

$$\lambda(q) \to \lambda(q) - \alpha\frac{\partial V}{\partial q}(q), \tag{3·5c}$$

$$\frac{\partial\lambda}{\partial q}(q) \to \frac{\partial\lambda}{\partial q}(q) - \alpha C(q) \tag{3·5d}$$

if the collective coordinate operator $\hat{Q}(q)$ is constructed such that it exactly commutes with the number operator $\hat{N}$, i.e.

$$[\hat{Q}(q), \hat{N}] = 0. \tag{3·6}$$

In association with the above transformations of $\hat{Q}(q)$ and $\hat{\Theta}(q)$, the original TDHFB state vector,

$$|\phi(q,p,\varphi,n)\rangle = e^{-i\varphi\tilde{N}}e^{ip\hat{Q}(q)}e^{in\hat{\Theta}(q)}\,|\phi(q)\rangle\,, \tag{3·7}$$

is transformed as

$$\begin{aligned}|\phi(q,p,\varphi,n)\rangle \to& e^{-i\varphi\tilde{N}}e^{ip(\hat{Q}(q)+\alpha\tilde{N})}e^{in(\hat{\Theta}(q)+\alpha\hat{P}(q))}\,|\phi(q)\rangle \\ =& e^{-i(\varphi-\alpha p)\tilde{N}}e^{ip\hat{Q}(q)}e^{in\hat{\Theta}(q)}\,|\phi(q-\alpha n)\rangle\,.\end{aligned} \tag{3·8}$$

Here, the relation

$$|\phi(q+\delta q)\rangle = e^{-i\delta q\hat{P}(q)}\,|\phi(q)\rangle \tag{3·9}$$

is used, and it is assumed that the operators $\hat{\Theta}(q)$ and $\hat{P}(q)$ commute under the adiabatic approximation. We also note that the expression (3·7) is slightly different from (2·7). However, the difference between $e^{ip\hat{Q}(q)+in\hat{\Theta}(q)}$ and $e^{ip\hat{Q}(q)}e^{in\hat{\Theta}(q)}$ gives rise to only higher-order contributions, which are ignored in the adiabatic approximation under consideration. We see that the gauge angle φ changes to $\varphi - \alpha p$ under the transformation (3·5). Thus, hereafter, we refer to the transformations (3·5) as "gauge transformations", the lack of dependence on the choice of α as "gauge invariance", and the choice of the value of α as "gauge fixing".

The commutation relation (3·6) implies that $\hat{Q}(q)$ is a normal one-body operator written in terms of the nucleon creation and annihilation operators $(c^\dagger, c)$ in the following form:

$$\hat{Q}(q) = \sum_{ij} Q_{ij}(q) : c_i^\dagger c_j : \;\equiv \hat{Q}^A(q) + \hat{Q}^B(q). \tag{3·10}$$

Here, the symbol : : denotes the normal product part when $\hat{Q}(q)$ is written in terms of the quasiparticle operators $(a^\dagger, a)$ defined at $|\phi(q)\rangle$, and the coefficients satisfy

the relation $Q_{ij}(q) = Q_{ji}(q)^*$, because $\hat{Q}(q)$ is assumed to be Hermitian. Note that this $\hat{Q}(q)$ operator contains the B-part, $\hat{Q}^B(q) = \sum_{kl} Q^B_{kl} a^\dagger_k a_l$, as well as the A-part, $\hat{Q}^A(q) = \sum_{kl} Q^A_{kl} a^\dagger_k a^\dagger_l + \text{h.c.}$ Accordingly, the relation (2·29) does not hold for this $\hat{Q}(q)$ operator.

In this way, we arrive at a new formulation of the ASCC method in which the gauge invariance (3·5) is manifest. The gauge-invariant ASCC method consists of the basic equations, which are the same as those in the original ASCC method,[52] except for the use of Eq. (2·27), and the $\hat{Q}(q)$ operator given in the form of (3·10).

3.3. *Gauge fixing and the numerical algorithm*

The fact that the ASCC equations are invariant under the gauge transformations (3·5) suggests the necessity of choosing a particular gauge for the numerical computation: If the gauge is not fixed, an instability with respect to the gauge degree of freedom might arise during the course of numerical calculation. Let us outline the procedure for the gauge fixing and the numerical algorithm for solving the gauge invariant ASCC equations. We start the calculation by solving the moving-frame QRPA equations at one of the HFB equilibrium points. A solution of the moving-frame QRPA equations at the HFB equilibrium point can be obtained, as discussed in §3.1, by choosing the gauge $\partial\lambda/\partial q = 0$. Hereafter we call this gauge the "QRPA gauge", because under this gauge, the moving-frame QRPA equations at the HFB equilibrium reduce to the conventional QRPA equations. As we see below, numerical calculations using the QRPA gauge encounters a difficulty at inflection points of the collective potential $V(q)$. It is possible, however, to choose another gauge that is free from this difficulty. With the use of the multi-$O(4)$ model, we explicitly show in §5 how this is done.

Since the moving-frame HFB equation at non-equilibrium points contains $\hat{Q}(q)$ that should be determined by the local harmonic equations, we have to resort to an iterative procedure. We proceed in the direction of the lowest energy solution of the moving-frame QRPA equations and successively derive solutions in the following manner. Suppose that we have already obtained the solution at $q' = q - \delta q$, where δq is the numerical mesh size in the computation. The moving-frame HFB equation at q for the n-th iteration,

$$\delta \left\langle \phi^{(n)}(q) \right| \hat{H}^{(n)}_M(q) \left| \phi^{(n)}(q) \right\rangle = 0, \tag{3·11}$$

$$\hat{H}^{(n)}_M(q) = \hat{H} - \lambda^{(n)}(q)\hat{N} - \frac{\partial V}{\partial q}^{(n)}(q)\hat{Q}^{(n-1)}(q), \tag{3·12}$$

is solved under the constraints

$$\left\langle \phi^{(n)}(q) \right| \hat{N} \left| \phi^{(n)}(q) \right\rangle = N_0, \tag{3·13}$$

$$\left\langle \phi^{(n)}(q) \right| \hat{Q}(q - \delta q) \left| \phi^{(n)}(q) \right\rangle = \delta q, \tag{3·14}$$

which are derived from the canonical variable conditions (2·12) and (2·16), respectively. In starting this iterative procedure at q, the neighboring solution $\hat{Q}(q - \delta q)$

(or a linear combination of the moving-frame QRPA modes at $q - \delta q$) may be used as an initial trial for the operator $\hat{Q}(q)^{(0)}$. The moving-frame QRPA equations for the n-th iteration are written

$$\delta \left\langle \phi^{(n)}(q) \right| [\hat{H}_M^{(n)}(q), i\hat{Q}^{(n)}(q)] - B^{(n)}(q)\hat{P}^{(n)}(q) \left| \phi^{(n)}(q) \right\rangle = 0, \tag{3·15}$$

$$\delta \left\langle \phi^{(n)}(q) \right| [\hat{H}_M^{(n)}(q), \hat{P}^{(n)}(q)] - \frac{1}{2B^{(n)}(q)} \left[\left[\hat{H}_M^{(n)}(q), \frac{\partial V}{\partial q}\hat{Q}(q) \right], i\hat{Q}(q) \right] - iC^{(n)}(q)\hat{Q}^{(n)}(q) - i\frac{\partial \lambda^{(n)}}{\partial q}(q)\hat{N} \left| \phi^{(n)}(q) \right\rangle = 0. \tag{3·16}$$

As the curvature term is nonlinear with respect to $\hat{Q}(q)$, we replace one of the operators $\hat{Q}(q)$ with that of the previous iteration step, $\hat{Q}^{(n-1)}(q)$. This procedure is discussed in detail for the multi-$O(4)$ model in §4.5. Thus, the moving-frame QRPA equations are linearized with respect to $\hat{Q}^{(n)}(q)$ and $\hat{P}^{(n)}(q)$. Its A-part, $\hat{Q}^{A(n)}(q)$, can be determined in a manner similar to that employed in solving the conventional QRPA equations. After obtaining $\hat{Q}^{A(n)}(q)$, its B-part, $\hat{Q}^{B(n)}(q)$, is determined with the requirement Eq. (3·6). This iterative procedure is repeated until we obtain convergence for $\lambda^{(n)}(q), \hat{Q}^{(n)}(q)$, and $\left|\phi^{(n)}(q)\right\rangle$.

§4. Application of the gauge-invariant ASCC method to the multi-$O(4)$ model

In the following sections, we apply the scheme formulated above to the multi-$O(4)$ model and discuss the gauge-fixing conditions suitable for solving the gauge-invariant ASCC equations. We study excitation spectra and transition strengths in systems with definite particle number $N = N_0$, and for this reason, we set $n = 0$ in the following sections.

4.1. *The multi-$O(4)$ model*

The multi-$O(4)$ model Hamiltonian has been used to test the validity of microscopic theories of nuclear collective motion.[57)–62)] In this work, we employ the model Hamiltonian used in Ref. 57). The model is constructed in terms of the generators of the $O(4)$ symmetry,

$$\hat{A}_j^\dagger = \sum_{m>0} c_{jm}^\dagger c_{j-m}^\dagger, \qquad \hat{B}_j^\dagger = \sum_{m>0} \sigma_{jm} c_{jm}^\dagger c_{j-m}^\dagger, \tag{4·1}$$

$$\hat{N}_j = \sum_m c_{jm}^\dagger c_{jm}, \qquad \hat{D}_j = \sum_m \sigma_{jm} c_{jm}^\dagger c_{jm}, \tag{4·2}$$

where the nucleon creation and annihilation operators $(c_{jm}^\dagger, c_{jm})$ are used, and the quantity σ_{jm} is given by

$$\sigma_{jm} = \begin{cases} 1 & |m| < \Omega_j/2, \\ -1 & |m| > \Omega_j/2. \end{cases} \tag{4·3}$$

These four operators represent the monopole pair, the (simplified) quadrupole pair, the particle number, and the (simplified) quadrupole operators for each j-shell, respectively. The model Hamiltonian is written in the form

$$\hat{H} = \hat{h}_0 - \frac{1}{2}G_0(\hat{A}^\dagger\hat{A} + \hat{A}\hat{A}^\dagger) - \frac{1}{2}G_2(\hat{B}^\dagger\hat{B} + \hat{B}\hat{B}^\dagger) - \frac{1}{2}\chi\hat{D}^2, \tag{4·4}$$
$$\hat{h}_0 = \sum_j e_j^0\hat{N}_j,$$

where

$$\hat{A}^\dagger = \sum_j \hat{A}_j^\dagger, \quad \hat{B}^\dagger = \sum_j d_j\hat{B}_j^\dagger, \quad \hat{N} = \sum_j \hat{N}_j, \quad \hat{D} = \sum_j d_j\hat{D}_j, \tag{4·5}$$

and d_j represents the quadrupole matrix element. The first term on the right-hand side of Eq. (4·4) is the single-particle Hamiltonian, giving a spherical single-particle energy e_j^0 for each j-shell, which possesses $(2\Omega_j)$-fold degeneracy ($2\Omega_j = 2j+1$). The other terms represent the residual two-body interactions: the monopole-pairing interaction, the quadrupole-type pairing interaction, and the quadrupole-type particle-hole interaction. Their interaction strengths are denoted G_0, G_2, and χ, respectively. Here, the operators $\hat{A}$ and $\hat{N}$ are the monopole-pair and the number operators, while $\hat{B}$ and $\hat{D}$ represent the simplified quadrupole-pair and quadrupole particle-hole operators, respectively.

The residual interactions of this model are separable, and we can always write such a separable Hamiltonian in the form

$$\hat{H} = \hat{h}_0 - \frac{1}{2}\sum_s \kappa_s\hat{F}_s^{(+)}\hat{F}_s^{(+)} + \frac{1}{2}\sum_s \kappa_s\hat{F}_s^{(-)}\hat{F}_s^{(-)}, \tag{4·6}$$

where

$$\hat{F}_s^{(\pm)} \equiv (\hat{F}_s \pm \hat{F}_s^\dagger)/2 = \pm\hat{F}_s^{(\pm)\dagger}. \tag{4·7}$$

Here, the superscript $(+)$ indicates that the bilinear operator $\hat{F}$ is Hermitian and $(-)$ indicates that it is anti-Hermitian. The multi-$O(4)$ model Hamiltonian under consideration contains three kinds of residual interactions. The subscripts s =1, 2, and 3 on the operators $\hat{F}$ and the interaction strengths κ_s indicate the monopole-pairing, the quadrupole-pairing and the quadrupole particle-hole interactions, respectively: $\hat{F}_{s=1} = A$, $\hat{F}_{s=2} = B$, $\hat{F}_{s=3} = \hat{D}$, $\kappa_1 = 2G_0, \kappa_2 = 2G_2$ and $\kappa_3 = \chi$.

4.2. *Quasiparticle representation*

To solve the ASCC equations, it is convenient to use the quasiparticle basis defined locally with respect to the state $|\phi(q)\rangle$ on the collective path. For the multi-$O(4)$ model, the Bogoliubov transformation to the quasiparticle creation and annihilation operators, $a_i^\dagger(q)$ and $a_i(q)$, satisfying the vacuum condition $a_i(q)\,|\phi(q)\rangle = 0$ is written

$$\begin{pmatrix} a_i^\dagger(q) \\ a_{-i}(q) \end{pmatrix} \equiv \begin{pmatrix} u_i(q) & -v_i(q) \\ v_i(q) & u_i(q) \end{pmatrix} \begin{pmatrix} c_i^\dagger \\ c_{-i} \end{pmatrix}. \tag{4·8}$$

Here, the indices $\pm i$ represent the set of angular momentum quantum numbers $(j, \pm m)$. The Bogoliubov transformation is locally determined on the collective path by the moving-frame HFB equation for a given collective coordinate operator $\hat{Q}(q)$.

Using the quasiparticle bilinear operators

$$\boldsymbol{A}_i^\dagger(q) = a_i^\dagger(q) a_{-i}^\dagger(q), \tag{4·9}$$

$$\boldsymbol{N}_i(q) = a_i^\dagger(q) a_i(q) + a_{-i}^\dagger(q) a_{-i}(q), \tag{4·10}$$

the nucleon bilinear operators $\hat{A}_i^\dagger$ and $\hat{N}_i$ can be rewritten as

$$\hat{A}_i^\dagger = u_i(q)v_i(q) + u_i^2(q)\boldsymbol{A}_i^\dagger(q) - v_i^2(q)\boldsymbol{A}_i(q) - u_i(q)v_i(q)\boldsymbol{N}_i(q), \tag{4·11}$$

$$\hat{N}_i = 2v_i^2(q) + 2u_i(q)v_i(q)(\boldsymbol{A}_i^\dagger(q) + \boldsymbol{A}_i(q)) + (u_i^2(q) - v_i^2(q))\boldsymbol{N}_i(q). \tag{4·12}$$

The quasiparticle bilinear operators $\boldsymbol{A}_i^\dagger(q), \boldsymbol{A}_i(q)$, and $\boldsymbol{N}_i(q)$ satisfy the following commutation relations:

$$\left[\boldsymbol{A}_i(q), \boldsymbol{A}_{i'}^\dagger(q)\right] = \delta_{ii'}(1 - \boldsymbol{N}_i(q)), \tag{4·13}$$

$$\left[\boldsymbol{N}_i(q), \boldsymbol{A}_{i'}^\dagger(q)\right] = 2\delta_{ii'}\boldsymbol{A}_{i'}^\dagger(q). \tag{4·14}$$

The particle number N_0, the quadrupole deformation $D(q)$, the monopole-pairing gap $\Delta_0(q)$, and the quadrupole-pairing gap $\Delta_2(q)$ are given by the expectation values of the corresponding operators with respect to the mean-field state vector $|\phi(q)\rangle$:

$$N_0 = \langle\phi(q)|\,\hat{N}\,|\phi(q)\rangle = 2\sum_{i>0} v_i^2(q), \tag{4·15}$$

$$D(q) = \langle\phi(q)|\,\hat{D}\,|\phi(q)\rangle = 2\sum_{i>0} d_i\sigma_i v_i^2(q), \tag{4·16}$$

$$\Delta_0(q) = G_0\,\langle\phi(q)|\,\hat{A}^\dagger\,|\phi(q)\rangle = G_0\sum_{i>0} u_i(q)v_i(q), \tag{4·17}$$

$$\Delta_2(q) = G_2\,\langle\phi(q)|\,\hat{B}^\dagger\,|\phi(q)\rangle = G_2\sum_{i>0} d_i\sigma_i u_i(q)v_i(q). \tag{4·18}$$

Below, we often omit q as the argument of such functions, for example, writing $\boldsymbol{A}_i(q)$ as $\boldsymbol{A}_i$. It should be kept in mind, however, that these quantities are locally defined with respect to the quasiparticle vacuum $|\phi(q)\rangle$ and depend on q.

4.3. *The ASCC equations for separable interactions*

The ASCC equations for the separable Hamiltonian are given by

$$\delta\,\langle\phi(q)|\,\hat{h}_M(q)\,|\phi(q)\rangle = 0, \tag{4·19}$$

$$\delta\,\langle\phi(q)|\,[\hat{h}_M(q), \hat{Q}(q)] - \sum_s f_{Q,s}^{(-)}\hat{F}_s^{(-)} - \frac{1}{i}B(q)\hat{P}(q)\,|\phi(q)\rangle = 0, \tag{4·20}$$

$$\delta \langle\phi(q)| \left[\hat{h}_M(q), \frac{1}{i}B(q)\hat{P}(q)\right] - \sum_s f^{(+)}_{P,s}(q)\hat{F}^{(+)}_s - B(q)C(q)\hat{Q}(q) - \sum_s f^{(+)}_{R,s}(q)\hat{F}^{(+)}_s - \frac{1}{2}\left[\left[\hat{h}_M(q), \frac{\partial V}{\partial q}\hat{Q}(q)\right], \hat{Q}(q)\right] + \sum_s \left[\hat{F}^{(-)}_s, \frac{\partial V}{\partial q}\hat{Q}(q)\right] f^{(-)}_{Q,s} - f_N(q)\tilde{N}\,|\phi(q)\rangle = 0, \tag{4·21}$$

where $\hat{h}_M(q)$ denotes the self-consistent mean-field Hamiltonian in the moving frame, defined by

$$\hat{h}_M(q) = \hat{h}(q) - \lambda(q)\tilde{N} - \frac{\partial V}{\partial q}\hat{Q}(q), \tag{4·22}$$

with

$$\hat{h}(q) = \hat{h}_0 - \sum_s \kappa_s \hat{F}^{(+)}_s \langle\phi(q)|\, \hat{F}^{(+)}_s\, |\phi(q)\rangle\,. \tag{4·23}$$

We also define the following quantities:

$$f^{(-)}_{Q,s}(q) = -\kappa_s \langle\phi(q)|\, [\hat{F}^{(-)}_s, \hat{Q}(q)]\, |\phi(q)\rangle\,, \tag{4·24}$$

$$f^{(+)}_{P,s}(q) = \kappa_s \langle\phi(q)|\left[\hat{F}^{(+)}_s, \frac{1}{i}B(q)\hat{P}(q)\right]|\phi(q)\rangle\,, \tag{4·25}$$

$$f^{(+)}_{R,s}(q) = -\frac{1}{2}\kappa_s \langle\phi(q)|\left[\left[\hat{F}^{(+)}_s, \frac{\partial V}{\partial q}\hat{Q}(q)\right], \hat{Q}(q)\right]|\phi(q)\rangle\,, \tag{4·26}$$

$$f_N(q) = B(q)\frac{\partial \lambda}{\partial q}. \tag{4·27}$$

Note that all matrix elements are real, and then $\langle\phi(q)|\, \hat{F}^{(-)}_s\, |\phi(q)\rangle = 0$. The fifth term in Eq. (4·21) appears only in the gauge-invariant formulation of the ASCC equations, because there is a contribution from this term only if $\hat{Q}(q)$ contains the B-part.

4.4. *The moving-frame HFB equation*

The moving-frame HFB equation (4·19) at a given q determines the time-even TDHB state vector $|\phi(q)\rangle$. The variation of Eq. (4·19) is taken with respect to two arbitrary quasiparticle states:

$$\delta\,|\phi(q)\rangle = a^\dagger_i(q)a^\dagger_j(q)\,|\phi(q)\rangle\,. \tag{4·28}$$

If we know the operator $\hat{Q}(q)$, we can solve this equation using the gradient method so as to eliminate the two-quasiparticle terms proportional to $\boldsymbol{A}^\dagger_i$ and $\boldsymbol{A}_i$. The quantities $\lambda(q)$ and $\partial V/\partial q$ can be regarded as Lagrange multipliers, which are determined by the following two constraints. The first is the particle number constraint given by (4·15). This constraint specifies the location in particle-number space. The second

constraint is written as (3·14). For the $\hat{Q}$ operator defined by (3·10), this equation yields

$$\langle\phi(q)|\,\hat{Q}(q-\delta q)\,|\phi(q)\rangle = 2\sum_{i>0} Q_i(q-\delta q)(v_i(q)^2 - v_i(q-\delta q)^2) = \delta q. \tag{4·29}$$

4.5. *The moving-frame QRPA equations*

We solve the moving-frame QRPA equations to obtain the operators $\hat{Q}(q)$ and $\hat{P}(q)$. The collective coordinate operator $\hat{Q}(q)$ is written

$$\hat{Q}(q) = \sum_i Q_i(q) : \hat{N}_i := \sum_{i>0} \left\{ Q_i^A(q)(\boldsymbol{A}_i^\dagger + \boldsymbol{A}_i) + Q_i^B(q)\boldsymbol{N}_i \right\}, \tag{4·30}$$

while the collective momentum operator $\hat{P}(q)$ is expressed as

$$\hat{P}(q) = i\sum_{i>0} P_i(q)(\boldsymbol{A}_i^\dagger - \boldsymbol{A}_i). \tag{4·31}$$

As mentioned in the preceding section, the B-part of the operator $\hat{P}(q)$ is unnecessary in second order with respect to the collective momentum p.

We solve the moving-frame QRPA equations in the following way. First, we assume that the solution $\hat{Q}^{(n-1)}(q)$ (obtained in the previous iteration step) of the moving-frame QRPA equations and the solutions, such as $|\phi(q)\rangle$ and $V(q)$, of the moving-frame HFB equation are known. [The superscript n is omitted, except on $\hat{Q}(q)$.] In solving the moving-frame QRPA equations, we note that the moving-frame Hamiltonian $\hat{h}_M(q)$ and the operators $\hat{F}_s^{(\pm)}$ can be expressed in terms of the quasiparticle bilinear operators $\boldsymbol{A}_i^\dagger$, $\boldsymbol{A}_i$, and $\boldsymbol{N}_i$ as

$$\hat{h}_M(q) = V(q) + \sum_{i>0} E_i(q)\boldsymbol{N}_i, \tag{4·32}$$

$$\begin{aligned}\hat{F}_s^{(+)} &= \langle\phi(q)|\,\hat{F}_s^{(+)}\,|\phi(q)\rangle + \hat{F}_{A,s}^{(+)} + \hat{F}_{B,s}^{(+)} \\ &= \langle\phi(q)|\,\hat{F}_s^{(+)}\,|\phi(q)\rangle + \sum_{i>0} F_{A,s}^{(+)}(i)(\boldsymbol{A}_i^\dagger + \boldsymbol{A}_i) + \sum_{i>0} F_{B,s}^{(+)}(i)\boldsymbol{N}_i,\end{aligned} \tag{4·33}$$

$$\hat{F}_s^{(-)} = \sum_{i>0} F_{A,s}^{(-)}(i)(\boldsymbol{A}_i^\dagger - \boldsymbol{A}_i). \tag{4·34}$$

Here, we have

$$F_{A,1}^{(+)}(i) = \frac{1}{2}(u_i^2 - v_i^2), \quad F_{A,2}^{(+)}(i) = \frac{1}{2}d_i\sigma_i(u_i^2 - v_i^2), \quad F_{A,3}^{(+)}(i) = 2d_i\sigma_i u_i v_i, \tag{4·35}$$

$$F_{A,1}^{(-)}(i) = -\frac{1}{2}, \qquad F_{A,2}^{(-)}(i) = -\frac{1}{2}d_i\sigma_i, \qquad F_{A,3}^{(-)}(i) = 0, \tag{4·36}$$

$$F_{B,1}^{(+)}(i) = -u_i v_i, \qquad F_{B,2}^{(+)}(i) = -d_i\sigma_i u_i v_i, \qquad F_{B,3}^{(+)}(i) = d_i\sigma_i(u_i^2 - v_i^2), \tag{4·37}$$

$$\begin{aligned}E_i(q) = (u_i^2 - v_i^2)\left(e_i - \chi d_i\sigma_i D(q) - \lambda(q) - \frac{\partial V}{\partial q}Q_i^{(n-1)}(q)\right) \\ - 2(\Delta_0(q) + d_i\sigma_i\Delta_2(q))u_i v_i.\end{aligned} \tag{4·38}$$

These quantities are determined by solving the moving-frame HFB equation (4·19). For later convenience, we define the following quasiparticle bilinear operators:

$$\hat{R}_s^{(\pm)} \equiv \left[\hat{F}_s^{(\pm)}, \frac{\partial V}{\partial q}\hat{Q}^{(n-1)}(q)\right] = 2\sum_{i>0} R_{A,s}^{(\pm)}(i)(\boldsymbol{A}_i^\dagger \mp \boldsymbol{A}_i), \tag{4·39}$$

with

$$R_{A,s}^{(+)}(i) = \frac{\partial V}{\partial q}\left(F_{B,s}^{(+)}(i)Q_i^{A(n-1)}(q) - F_{A,s}^{(+)}(i)Q_i^{B(n-1)}(q)\right), \tag{4·40}$$

$$R_{A,s}^{(-)}(i) = -\frac{\partial V}{\partial q}F_{A,s}^{(-)}(i)Q_i^{B(n-1)}(q). \tag{4·41}$$

We can express the matrix elements $Q_i^{A(n)}$ and P_i in terms of $f_{Q,s}^{(-)}$, $f_{P,s}^{(+)}$, $f_{R,s}^{(+)}$ and f_N by substituting Eqs. (4·30) and (4·31) into Eqs. (4·20) and (4·21). This yields

$$\begin{aligned} Q_i^{A(n)} =& \frac{1}{(2E_i)^2 - \omega^2 + 2\frac{\partial V}{\partial q}E_iQ_i^{B(n-1)}} \\ & \left\{2E_i\sum_s F_{A,s}^{(-)}(i)f_{Q,s}^{(-)} + \sum_s\left(F_{A,s}^{(+)}(i)f_{PR,s}^{(+)} - 2R_{A,s}^{(-)}(i)f_{Q,s}^{(-)}\right) + N_if_N\right\}, \end{aligned} \tag{4·42}$$

$$\begin{aligned} P_i =& \frac{2E_i}{(2E_i)^2 - \omega^2 + 2\frac{\partial V}{\partial q}E_iQ_i^{B(n-1)}}\left\{\sum_s\left(F_{A,s}^{(+)}(i)f_{PR,s}^{(+)} - 2R_{A,s}^{(-)}(i)f_{Q,s}^{(-)}\right) + N_if_N\right\} \\ & + \frac{\omega^2 - 2\frac{\partial V}{\partial q}E_iQ_i^{B(n-1)}}{(2E_i)^2 - \omega^2 + 2\frac{\partial V}{\partial q}E_iQ_i^{B(n-1)}}\sum_s F_{A,s}^{(-)}(i)f_{Q,s}^{(-)}, \end{aligned} \tag{4·43}$$

where

$$N_i = 2u_i(q)v_i(q), \tag{4·44}$$

$$f_{PR,s}^{(+)} = f_{P,s}^{(+)}(q) + f_{R,s}^{(+)}(q), \tag{4·45}$$

$$\omega = \sqrt{B(q)C(q)}. \tag{4·46}$$

Substituting Eqs. (4·30), (4·31) and (4·39) into Eqs. (4·24), (4·25) and (4·26), we obtain

$$f_{Q,s}^{(-)} = 2\kappa_s\sum_{i>0} F_{A,s}^{(-)}(i)Q_i^{A(n)}, \tag{4·47}$$

$$f_{PR,s}^{(+)} = 2\kappa_s\sum_{i>0}\left\{F_{A,s}^{(+)}(i)P_i + R_{A,s}^{(+)}(i)Q_i^{A(n)}\right\}. \tag{4·48}$$

Note that $f_{Q,3}^{(-)} = 0$. From the canonical variable condition, the orthogonality of the collective and number fluctuation modes is required, i.e.

$$\langle\phi(q)|[\tilde{N}, \hat{P}(q)]|\phi(q)\rangle = 2i\sum_{i>0} N_iP_i = 0. \tag{4·49}$$

Eliminating $Q_i^{A(n)}$ and P_i from Eqs. (4·47), (4·48), and (4·49) with use of Eqs. (4·42) and (4·43), we finally obtain the dispersion equation

$$\boldsymbol{S}(\omega^2)\cdot\boldsymbol{f}=0, \tag{4·50}$$

for the quantity $\boldsymbol{f}=\boldsymbol{f}(q)=\{f^{(-)}_{Q,1},\ f^{(-)}_{Q,2},\ f^{(+)}_{PR,1},\ f^{(+)}_{PR,2},\ f^{(+)}_{PR,3},\ f_N\}$. Here $\boldsymbol{S}=\{S_{ij}\}$ is a 6×6 matrix whose elements are given by

$$S_{11}=2\kappa_1\left\{S^{(1)}(F^{(-)}_{A,1},F^{(-)}_{A,1})-2S^{(2)}(F^{(-)}_{A,1},R^{(-)}_{A,1})\right\}-1, \tag{4·51a}$$

$$S_{12}=2\kappa_1\left\{S^{(1)}(F^{(-)}_{A,1},F^{(-)}_{A,2})-2S^{(2)}(F^{(-)}_{A,1},R^{(-)}_{A,2})\right\}, \tag{4·51b}$$

$$S_{13}=2\kappa_1 S^{(2)}(F^{(-)}_{A,1},F^{(+)}_{A,1}), \tag{4·51c}$$

$$S_{14}=2\kappa_1 S^{(2)}(F^{(-)}_{A,1},F^{(+)}_{A,2}), \tag{4·51d}$$

$$S_{15}=2\kappa_1 S^{(2)}(F^{(-)}_{A,1},F^{(+)}_{A,3}), \tag{4·51e}$$

$$S_{16}=2\kappa_1 S^{(2)}(F^{(-)}_{A,1},N), \tag{4·51f}$$

$$S_{21}=2\kappa_2\left\{S^{(1)}(F^{(-)}_{A,2},F^{(-)}_{A,1})-2S^{(2)}(F^{(-)}_{A,2},R^{(-)}_{A,1})\right\}, \tag{4·52a}$$

$$S_{22}=2\kappa_2\left\{S^{(1)}(F^{(-)}_{A,2},F^{(-)}_{A,2})-2S^{(2)}(F^{(-)}_{A,2},R^{(-)}_{A,2})\right\}-1, \tag{4·52b}$$

$$S_{23}=2\kappa_2 S^{(2)}(F^{(-)}_{A,2},F^{(+)}_{A,1}), \tag{4·52c}$$

$$S_{24}=2\kappa_2 S^{(2)}(F^{(-)}_{A,2},F^{(+)}_{A,2}), \tag{4·52d}$$

$$S_{25}=2\kappa_2 S^{(2)}(F^{(-)}_{A,2},F^{(+)}_{A,3}), \tag{4·52e}$$

$$S_{26}=2\kappa_2 S^{(2)}(F^{(-)}_{A,2},N), \tag{4·52f}$$

$$S_{31}=2\kappa_1\Big\{\omega^2 S^{(2)}(F^{(+)}_{A,1},F^{(-)}_{A,1})-S^{(1)}(F^{(+)}_{A,1},R^{(-)}_{A,1}) +S^{(1)}(R^{(+)}_{A,1},F^{(-)}_{A,1})-2S^{(2)}(R^{(+)}_{A,1},R^{(-)}_{A,1})\Big\}, \tag{4·53a}$$

$$S_{32}=2\kappa_1\Big\{\omega^2 S^{(2)}(F^{(+)}_{A,1},F^{(-)}_{A,2})-S^{(1)}(F^{(+)}_{A,1},R^{(-)}_{A,2}) +S^{(1)}(R^{(+)}_{A,1},F^{(-)}_{A,2})-2S^{(2)}(R^{(+)}_{A,1},R^{(-)}_{A,2})\Big\}, \tag{4·53b}$$

$$S_{33}=2\kappa_1\left\{S^{(1)}(F^{(+)}_{A,1},F^{(+)}_{A,1})+S^{(2)}(R^{(+)}_{A,1},F^{(+)}_{A,1})\right\}-1, \tag{4·53c}$$

$$S_{34}=2\kappa_1\left\{S^{(1)}(F^{(+)}_{A,1},F^{(+)}_{A,2})+S^{(2)}(R^{(+)}_{A,1},F^{(+)}_{A,2})\right\}, \tag{4·53d}$$

$$S_{35}=2\kappa_1\left\{S^{(1)}(F^{(+)}_{A,1},F^{(+)}_{A,3})+S^{(2)}(R^{(+)}_{A,1},F^{(+)}_{A,3})\right\}, \tag{4·53e}$$

$$S_{36}=2\kappa_1\left\{S^{(1)}(F^{(+)}_{A,1},N)+S^{(2)}(R^{(+)}_{A,1},N)\right\}, \tag{4·53f}$$

$$S_{41} = 2\kappa_2 \Big\{ \omega^2 S^{(2)}(F^{(+)}_{A,2}, F^{(-)}_{A,1}) - S^{(1)}(F^{(+)}_{A,2}, R^{(-)}_{A,1}) + S^{(1)}(R^{(+)}_{A,2}, F^{(-)}_{A,1}) - 2S^{(2)}(R^{(+)}_{A,2}, R^{(-)}_{A,1}) \Big\}, \quad (4\cdot54a)$$

$$S_{42} = 2\kappa_2 \Big\{ \omega^2 S^{(2)}(F^{(+)}_{A,2}, F^{(-)}_{A,2}) - S^{(1)}(F^{(+)}_{A,2}, R^{(-)}_{A,2}) + S^{(1)}(R^{(+)}_{A,2}, F^{(-)}_{A,2}) - 2S^{(2)}(R^{(+)}_{A,2}, R^{(-)}_{A,2}) \Big\}, \quad (4\cdot54b)$$

$$S_{43} = 2\kappa_2 \Big\{ S^{(1)}(F^{(+)}_{A,2}, F^{(+)}_{A,1}) + S^{(2)}(R^{(+)}_{A,2}, F^{(+)}_{A,1}) \Big\}, \quad (4\cdot54c)$$

$$S_{44} = 2\kappa_2 \Big\{ S^{(1)}(F^{(+)}_{A,2}, F^{(+)}_{A,2}) + S^{(2)}(R^{(+)}_{A,2}, F^{(+)}_{A,2}) \Big\} - 1, \quad (4\cdot54d)$$

$$S_{45} = 2\kappa_2 \Big\{ S^{(1)}(F^{(+)}_{A,2}, F^{(+)}_{A,3}) + S^{(2)}(R^{(+)}_{A,2}, F^{(+)}_{A,3}) \Big\}, \quad (4\cdot54e)$$

$$S_{46} = 2\kappa_2 \Big\{ S^{(1)}(F^{(+)}_{A,2}, N) + S^{(2)}(R^{(+)}_{A,2}, N) \Big\}, \quad (4\cdot54f)$$

$$S_{51} = 2\kappa_3 \Big\{ \omega^2 S^{(2)}(F^{(+)}_{A,3}, F^{(-)}_{A,1}) - S^{(1)}(F^{(+)}_{A,3}, R^{(-)}_{A,1}) + S^{(1)}(R^{(+)}_{A,3}, F^{(-)}_{A,1}) - 2S^{(2)}(R^{(+)}_{A,3}, R^{(-)}_{A,1}) \Big\}, \quad (4\cdot55a)$$

$$S_{52} = 2\kappa_3 \Big\{ \omega^2 S^{(2)}(F^{(+)}_{A,3}, F^{(-)}_{A,2}) - S^{(1)}(F^{(+)}_{A,3}, R^{(-)}_{A,2}) + S^{(1)}(R^{(+)}_{A,3}, F^{(-)}_{A,2}) - 2S^{(2)}(R^{(+)}_{A,3}, R^{(-)}_{A,2}) \Big\}, \quad (4\cdot55b)$$

$$S_{53} = 2\kappa_3 \Big\{ S^{(1)}(F^{(+)}_{A,3}, F^{(+)}_{A,1}) + S^{(2)}(R^{(+)}_{A,3}, F^{(+)}_{A,1}) \Big\}, \quad (4\cdot55c)$$

$$S_{54} = 2\kappa_3 \Big\{ S^{(1)}(F^{(+)}_{A,3}, F^{(+)}_{A,2}) + S^{(2)}(R^{(+)}_{A,3}, F^{(+)}_{A,2}) \Big\}, \quad (4\cdot55d)$$

$$S_{55} = 2\kappa_3 \Big\{ S^{(1)}(F^{(+)}_{A,3}, F^{(+)}_{A,3}) + S^{(2)}(R^{(+)}_{A,3}, F^{(+)}_{A,3}) \Big\} - 1, \quad (4\cdot55e)$$

$$S_{56} = 2\kappa_3 \Big\{ S^{(1)}(F^{(+)}_{A,3}, N) + S^{(2)}(R^{(+)}_{A,3}, N) \Big\}, \quad (4\cdot55f)$$

$$S_{61} = \omega^2 S^{(2)}(N, F^{(-)}_{A,1}) - S^{(1)}(N, R^{(-)}_{A,1}), \qquad S_{62} = \omega^2 S^{(2)}(N, F^{(-)}_{A,2}) - S^{(1)}(N, R^{(-)}_{A,2}), \quad (4\cdot56a)$$

$$S_{63} = S^{(1)}(N, F^{(+)}_{A,1}), \qquad S_{64} = S^{(1)}(N, F^{(+)}_{A,2}), \quad (4\cdot56b)$$

$$S_{65} = S^{(1)}(N, F^{(+)}_{A,3}), \qquad S_{66} = S^{(1)}(N, N). \quad (4\cdot56c)$$

Here, the quantities $S^{(1)}$ and $S^{(2)}$ are defined by

$$S^{(1)}(X, Y) = \sum_{i>0} \frac{2E_i(q)}{(2E_i(q))^2 - \omega^2(q) + 2\frac{\partial V}{\partial q} E_i Q_i^{(B(n-1))}} X_i Y_i, \quad (4\cdot57)$$

$$S^{(2)}(X, Y) = \sum_{i>0} \frac{1}{(2E_i(q))^2 - \omega^2(q) + 2\frac{\partial V}{\partial q} E_i Q_i^{(B(n-1))}} X_i Y_i. \quad (4\cdot58)$$

The unknown quantities in the dispersion equation (4·50) are $\boldsymbol{f}(q)$ and $\omega^2(q)$. The squared frequency $\omega^2(q)$ can be determined by the condition that the matrix $\boldsymbol{S}(\omega^2(q))$ has no inverse:

$$\det \boldsymbol{S}(\omega^2(q)) = 0. \tag{4·59}$$

In the case that there are many solutions $\omega^2(q)$ satisfying this equation, we choose the smallest of these (including negative values) as the collective mode. Once the value of $\omega^2(q)$ and, consequently, the matrix $\boldsymbol{S}(q)$ is specified, the direction of the vector $\boldsymbol{f}(q)$ is known. Then, its absolute value is fixed by the normalization condition for the collective mode,

$$\langle\phi(q)|\,[\hat{Q}^{(n)}(q), \hat{P}(q)]\,|\phi(q)\rangle = 2i\sum_{i>0} Q_i^{A(n)}(q)P_i(q) = i. \tag{4·60}$$

The choice of the signs of $\hat{Q}^{(n)}(q)$ and $\hat{P}(q)$ are still arbitrary. This choice specifies the "rear" and "front" of the one-dimensional collective path.

The B-part of $\hat{Q}(q)$ is automatically determined in terms of its A-part according to its definition (4·30):

$$Q_i^{B(n)}(q) = \frac{u_i^2 - v_i^2}{2u_iv_i} Q_i^{A(n)}(q). \tag{4·61}$$

4.6. *Gauge fixing*

Under the gauge transformation (3·5), the quantities, $f_{Q,1}^{(-)}(q)$, $f_{Q,2}^{(-)}(q)$, and $f_N(q)$ appearing in the dispersion equation (4·50) transform as

$$f_{Q,1}^{(-)}(q) \to f_{Q,1}^{(-)}(q) - 4\alpha\Delta_0(q), \tag{4·62}$$

$$f_{Q,2}^{(-)}(q) \to f_{Q,2}^{(-)}(q) - 4\alpha\Delta_2(q), \tag{4·63}$$

$$f_N(q) \to f_N(q) - \alpha\omega^2(q). \tag{4·64}$$

These properties clearly indicate that one of the above three quantities can be eliminated: By choosing an appropriate value for α (gauge fixing), we can reduce the dispersion equation (4·50) to a 5×5 matrix equation. In other words, Eq. (4·50) is redundant, and the gauge fixing is equivalent to the reduction of its dimension. The QRPA gauge corresponds to setting $f_N(q) = 0$. In Ref. 57), we set $f_{Q,1}^{(-)}(q) = 0$, which corresponds to another gauge. Because the quantity $f_{Q,1}^{(-)}(q)$ represents the contribution from the time-odd component of the monopole-pairing interaction, let us call this gauge the "ETOP (eliminating time-odd pairing) gauge"

4.7. *Requantization*

The solution of the ASCC equations yields the classical collective Hamiltonian:

$$\mathcal{H}(q,p) = \frac{1}{2}p^2 + V(q). \tag{4·65}$$

We can thus obtain the quantum collective Hamiltonian by carrying out the canonical quantization $\mathcal{H}(q,p) \to \mathcal{H}\left(q, \frac{1}{i}\frac{\partial}{\partial q}\right)$. Note that, in this quantization step, there is no ambiguity associated with the ordering of q and p, because the coordinate scale is chosen such that the inverse mass function is unity, i.e., $B(q) = 1$.

§5. Numerical test of the internal consistency of the proposed scheme

5.1. *Details of numerical calculation*

We numerically solved the gauge-invariant ASCC equations for the multi-$O(4)$ model with the same parameters as in Refs. 57) and 62). The system consists of 28 particles (one kind of fermion). The model space consists of three j-shells, labeled j_1, j_2 and j_3, with the pair degeneracies $\Omega_{j_i} = 14, \Omega_{j_2} = 10$ and $\Omega_{j_3} = 4$, single-particle energies $e_{j_1} = 0, e_{j_2} = 1.0$ and $e_{j_3} = 3.5$, and the single-particle quadrupole moments $d_{j_1} = 2$ and $d_{j_2} = d_{j_3} = 1$. Within this model space, the deformation $D = \langle\phi(q)|\,\hat{D}\,|\phi(q)\rangle$ ranges from $D_{\min} = -42$ to $D_{\max} = 42$. The calculation was done with the quadrupole-interaction strength $\chi = 0.04$ and the monopole-pairing-interaction strengths $G_0 = 0.14, 0.16$ and 0.20. The nature of the system changes from a double-well ($G_0 = 0.14$) to a spherical vibrator ($G_0 = 0.20$) as the value of G_0 is changed. The effect of the quadrupole pairing is studied by comparing the results for $G_2 = 0.00, 0.02$ and 0.04. As pointed out in Ref. 57), the quadrupole pairing has a strong effect on the collective mass. However, it need not be considered for investigation of the gauge-fixing condition. Therefore, we present the results for $G_2 = 0$ in the next subsection and show its effect in the final subsection only. The calculation starts from one of the HFB equilibrium states, labeled by $q = 0$ (see Fig. 2). For the deformed cases ($G_0 = 0.14$ and 0.16), the HFB equilibrium state with positive (prolate) deformation is chosen as the starting point.

5.2. *Comparison of the two gauge fixing conditions*

Let us examine whether or not we can find a gauge independent solution of the ASCC equations. The existence of the collective path that simultaneously satisfies all equations of the ASCC method is not self-evident. The aim of the numerical calculation here is to check the internal consistency of the equations presented in the preceding section. We solve the gauge-invariant ASCC equations with two different gauge fixing conditions: the QRPA gauge [$f_N(q) = 0$] and the ETOP gauge [$f^{(-)}_{Q,1}(q) = 0$]. In the QRPA gauge, the chemical potential $\lambda(q)$ along the collective path is set to a constant, while in the ETOP gauge, the time-odd contribution of the monopole pairing interaction is fully eliminated from the ASCC equations.

Figure 1 displays the collective potential $V(q)$ and the monopole pairing gap $\Delta_0(q)$ as functions of the quadrupole deformation $D(q)$. Figure 2 displays the relation between the collective variables q and the quadrupole deformation D, as well as the squared frequency $\omega^2(q)$ obtained by solving the local-harmonic equations. The collective mass $M(D(q)) = (dq/dD)^2$, which is derived by transforming the collective kinetic energy as a function of the velocity $\dot{D}$ under the condition $B(q) = 1$,[57] is

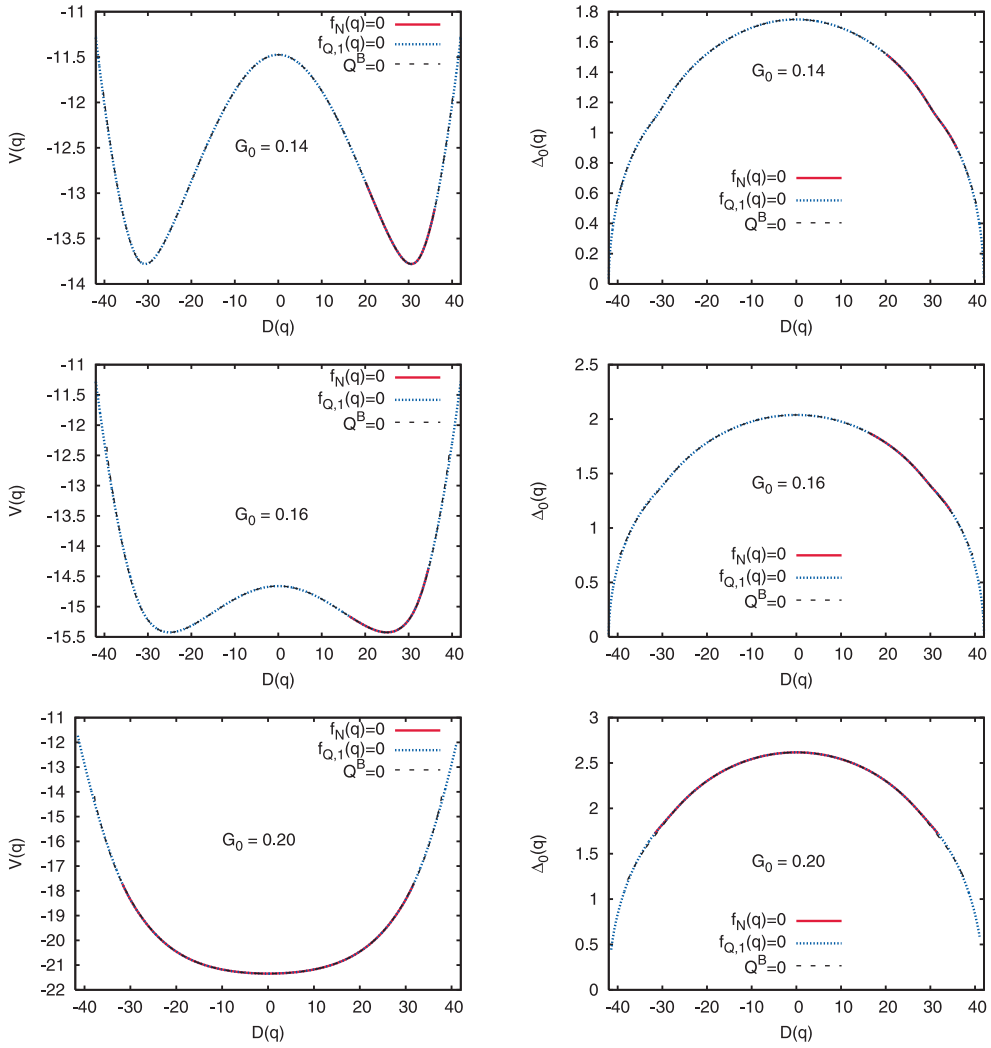

Fig. 1. Collective potentials $V(q)$ and monopole pairing gaps $\Delta_0(q)$ plotted as functions of the quadrupole deformation D. The upper, middle and lower panels display the results for $G_0 = 0.14, 0.16$ and 0.20, respectively. In each graph, results obtained from different calculations are compared. Those obtained using the QRPA gauge $[f_N(q) = 0]$ and the ETOP gauge $[f^{(-)}_{Q,1}(q) = 0]$ are plotted by solid (red) and dotted (blue) curves, respectively, while those obtained ignoring the B-part of $\hat{Q}(q)$ [i.e., setting $Q^B_i(q) = 0$] are plotted by the dashed curves.

plotted as a function of D in Fig. 3. We find that the calculation using the ETOP gauge encounters no difficulties, and the collective path connecting the two local (oblate and prolate) minima with different signs of the deformation are successfully obtained. By contrast, the calculation using the QRPA gauge encounters a point beyond which we cannot proceed. In the region where the solutions have been found for both gauges, they are consistent. This should be the case, because these are gauge invariant quantities. The cause of the difficulty encountered in the QRPA

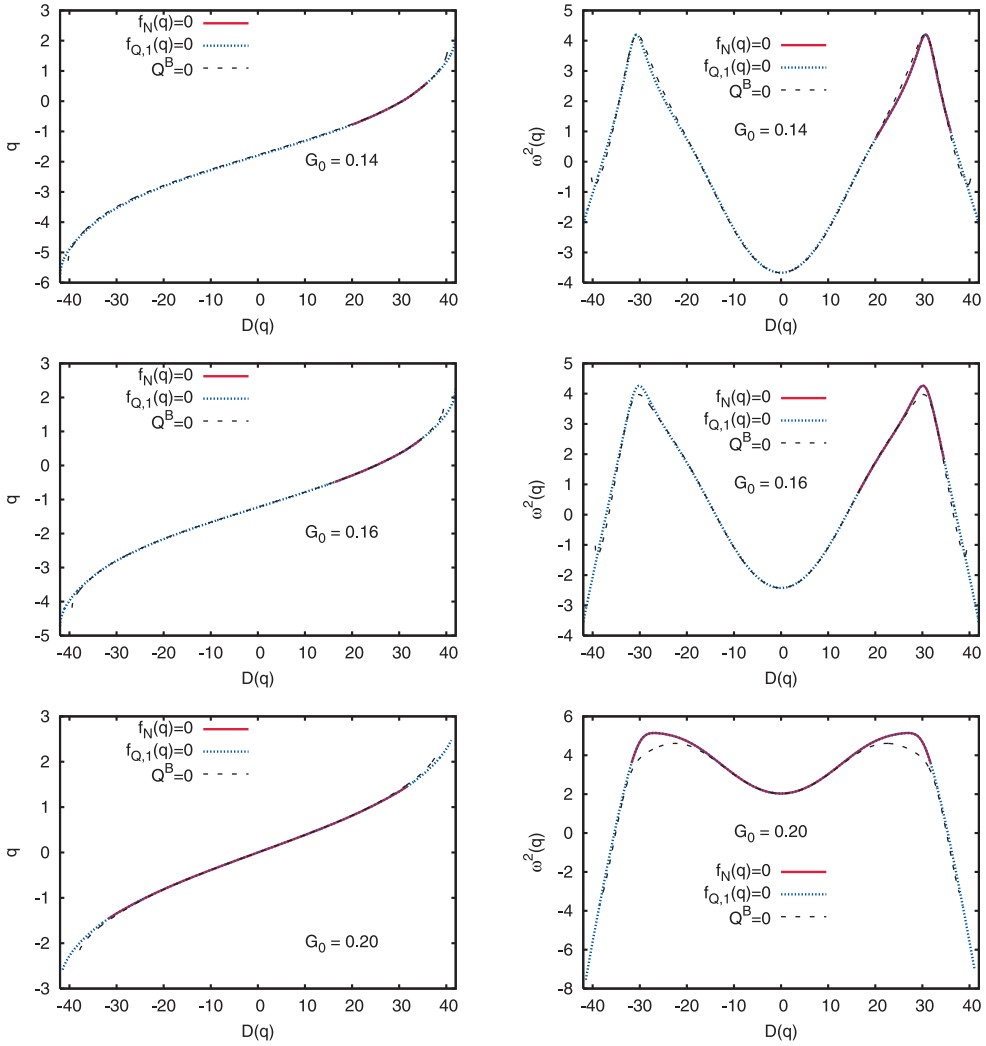

Fig. 2. *Left column*: Relation between the collective coordinate q and the quadrupole deformation $D(q) = \langle\phi(q)|\,\hat{D}\,|\phi(q)\rangle$. The point $q = 0$ corresponds to the HFB equilibrium, which is the starting point of the numerical calculation. *Right column*: Squared frequencies $\omega^2(q)$ of the moving-frame QRPA equations, plotted as functions of D. Note that they are negative; i.e., $\omega(q)$ is purely imaginary in the region where the curvature of the collective potential is negative. The upper, middle and lower rows display the results for $G_0 = 0.14, 0.16$ and 0.20, respectively. (See the caption of Fig. 1.)

gauge can be understood as follows.

Figures 4 and 5 display the chemical potential $\lambda(q)$ and the quantities $f^{(-)}_{Q,1}(q)$ and $f_N(q)$, respectively. Their values depend on the gauge adopted. If the QRPA gauge is used, $\lambda(q)$ should be constant along the path, because of the condition $f_N(q) = B(q)\partial\lambda/\partial q = 0$. We find, however, that $\lambda(q)$ diverges near the inflection point of the collective potential, where $\omega(q)^2 = \partial^2 V/\partial q^2 = 0$. This divergence occurs because the inflection point is a singularity for the gauge transformation

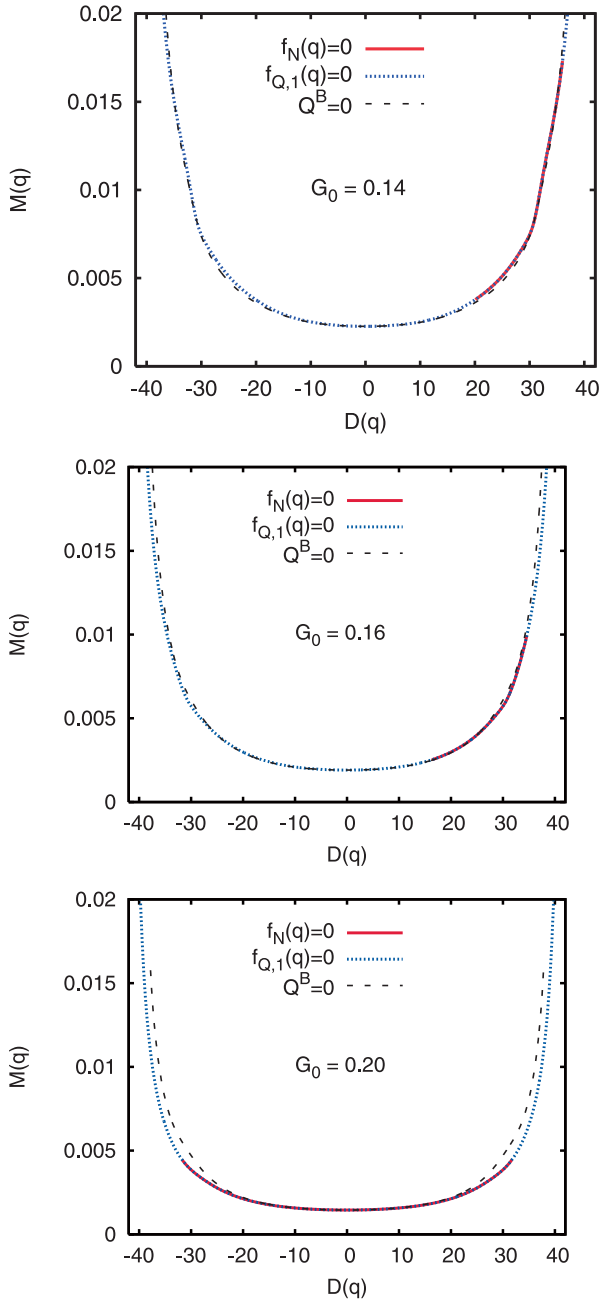

Fig. 3. The ASCC collective mass $M(q(D))$ as functions of the deformation D. The upper, middle and lower rows display the results for $G_0 = 0.14$, 0.16 and 0.20, respectively. (See the caption of Fig. 1.)

(4·64), where an arbitrary α gives the same $f_N(q)$. Thus, the calculation using the QRPA gauge stops at the inflection point. Contrastingly, we can go over the inflection point using the ETOP gauge, because the gauge transformation for $f^{(-)}_{Q,1}(q)$, (4·62), involves only the monopole pairing gap $\Delta_0(q)$, which always takes finite

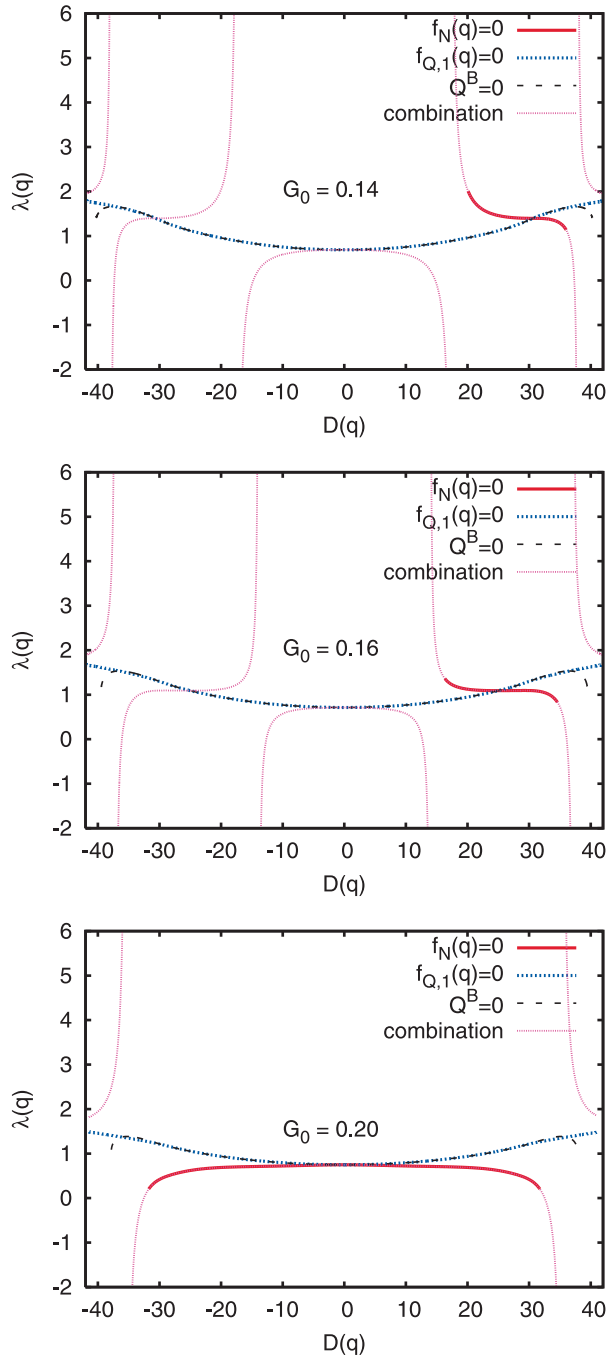

Fig. 4. The chemical potentials $\lambda(q)$ as functions of the deformation D. The upper, middle and lower rows display the results for $G_0 = 0.14$, 0.16 and 0.20, respectively. In each graph, the results obtained from different calculations are compared. The solid (red) and dotted (blue) curves represent the results obtained using the QRPA gauge [$f_N(q) = 0$] and the ETOP gauge [$f^{(-)}_{Q,1}(q) = 0$], respectively, while the dashed curves represent those obtained using the ETOP gauge but ignoring the B-part of $\hat{Q}(q)$ [i.e., setting $Q^B_i(q) = 0$]. The dotted (purple) curves labeled "combination" represent the results calculated by switching to the QRPA gauge after the collective path is determined using the ETOP gauge.

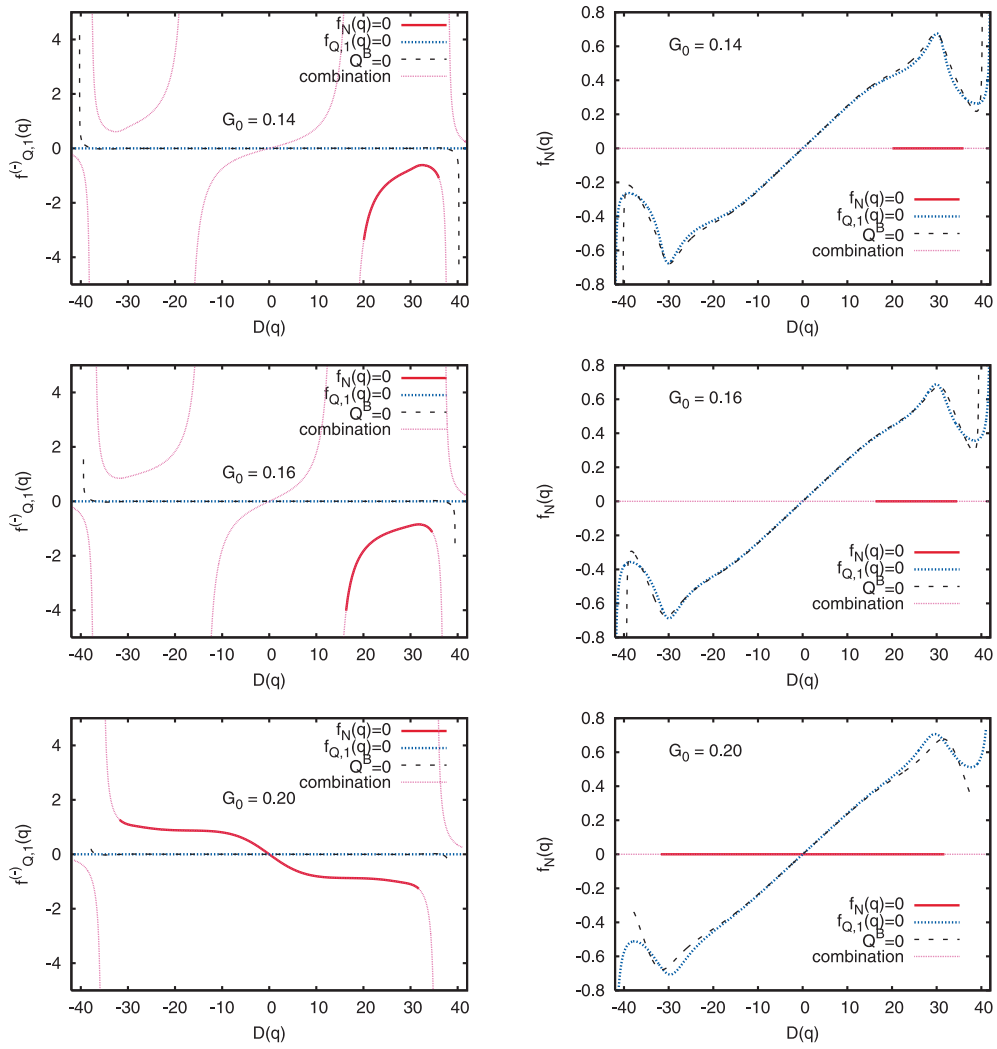

Fig. 5. The gauge dependent quantities $f^{(-)}_{Q,1}(q)$ (*left column*) and $f_N(q)$ (*right column*) plotted as functions of the deformation D. The upper, middle and lower rows display the results for $G_0 = 0.14, 0.16$ and 0.20, respectively. (See the caption of Fig. 4.)

values along the collective path (except at the limit of the model space). In these figures, we also present the results that obtained with the following procedure. After determining the collective paths employing the ETOP gauge, we calculate the gauge-dependent quantities $\lambda(q)$, $f^{(-)}_{Q,1}(q)$ and $f_N(q)$ by switching to the QRPA gauge using the relations

$$f^{(-)}_{Q,1(\mathrm{QRPA})} = -\frac{4f_N(q)_{(\mathrm{ETOP})}\Delta_0(q)}{\omega^2(q)}, \tag{5·1a}$$

$$\lambda(q)_{(\mathrm{QRPA})} = \lambda(q)_{(\mathrm{ETOP})} - \frac{4f_N(q)_{(\mathrm{ETOP})}}{\omega^2(q)}\frac{\partial V}{\partial q}. \tag{5·1b}$$

We see in Figs. 4 and 5 that the results obtained by this procedure are consistent with those calculated using the QRPA gauge [$f_N(q) = 0$] from the beginning [in the region of deformation $D(q)$, where the collective path can be obtained using the QRPA gauge]. This agreement demonstrates that the collective paths determined by using different gauge fixing conditions are the same, as should be the case. Nevertheless, there is a particularly suitable gauge fixing condition for finding solutions of the ASCC equations and constructing the collective path. For the multi-$O(4)$ model with superfluidity, we find that the ETOP gauge is more useful than the QRPA gauge, because the gauge transformation (4·62) is well-defined as long as the pairing gap $\Delta_0(q)$ is non-zero.

5.3. *Comparison with the previous calculation*

In a previous paper,[57] we employed the ETOP gauge condition [$f^{(-)}_{Q,1}(q) = 0$], but the B-part of $\hat{Q}(q)$ was ignored. Let us evaluate the error caused by this approximation. The results of these calculations are also presented in Figs. 1–4 and compared with those of the full calculations. We see that they differ little, which indicates that the approximation made by ignoring the B-part is rather good.

In Fig. 5, we present the quantity

$$f^{(-)}_{Q,1}(q) = -\kappa_1 \langle\phi(q)| [\hat{F}^{(-)}_1, \hat{Q}(q)] |\phi(q)\rangle = -\kappa_1 \sum_{i>0} Q^A_i(q), \tag{5·2}$$

evaluated using the $\hat{Q}(q)$ operator that is obtained by ignoring the B-part in the process of solving the ASCC equations. This quantity should be zero if the $\hat{Q}(q)$ operator determined by the gauge-invariant ASCC equations is used. We see that the deviation from zero is negligible (except near the limit of the model space), again indicating that the approximation is good.

The quantum spectra and transition strengths are displayed in Fig. 6. These were obtained by solving the Schrödinger equation for the quantized collective Hamiltonian. In this figure, the effects of the quadrupole pairing interaction are also shown. We see that the results of the previous calculation [in which the B-part of $\hat{Q}(q)$ is ignored] are quite similar to those of the full calculation (including the B-part), and both results accurately reproduce the trend of the excitation spectra obtained through the exact diagonalization of the microscopic Hamiltonian (Fig. 7). The numerical calculation discussed above thus suggests that the approximation of ignoring the B-part of $\hat{Q}(q)$, adopted in Ref. 57), is valid, and it may serve as an economical way of determining the collective path.

§6. Concluding remarks

We have shown that the basic equations of the ASCC method are invariant under transformations involving the angle in the gauge space conjugate to the particle number. By virtue of this invariance, a clean separation of the large-amplitude collective motion and the pairing rotational motion can be realized. This allows us to restore the particle-number symmetry broken by the HFB approximation. We have formulated the ASCC method explicitly in a gauge-invariant form. Then, we

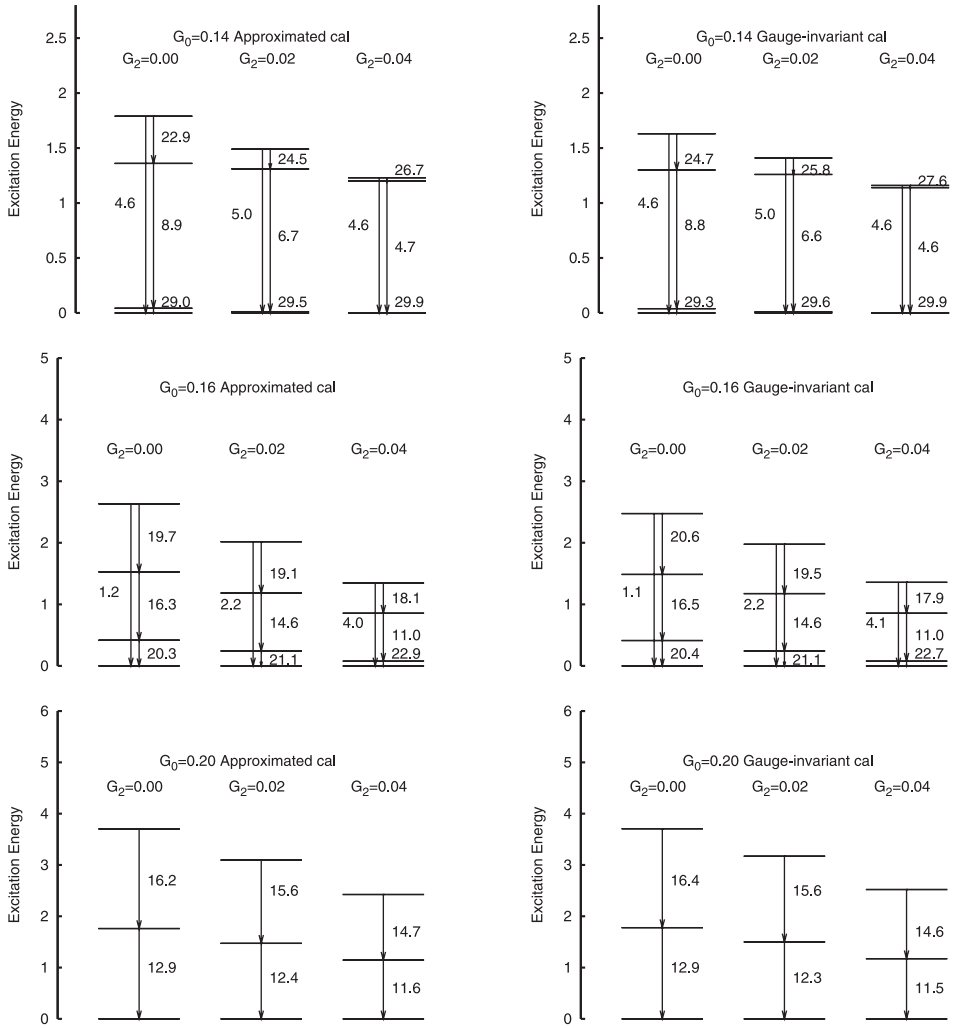

Fig. 6. Excitation spectra and quadrupole transition matrix elements. *Left column*: The result obtained using the ETOP gauge $[f^{(-)}_{Q,1}(q) = 0]$ but ignoring the B-part of the collective coordinate operator $\hat{Q}(q)$. This is the same as that presented in Ref. 57). *Right column*: The result obtained by solving the gauge-invariant ASCC equations using the ETOP gauge. The upper, middle and lower rows display the results for $G_0 = 0.14$, 0.16 and 0.20, respectively. In each row, the results for $G_2 = 0.00, 0.02$ and 0.04 are compared. The numbers adjacent to the vertical lines are the absolute values of the transition matrix elements. The matrix elements between the doublets are indicated beside them.

applied it to the multi-$O(4)$ model using different gauge-fixing procedures. The calculations using different gauges indeed yield the same results for gauge-invariant quantities, such as the collective path, the collective mass parameter, and the spectra obtained by requantizing the collective Hamiltonian. We suggested a gauge-fixing prescription that can be used in realistic calculations.

The explicit gauge invariance requires the B-part ($a^\dagger a$ part) of the collective

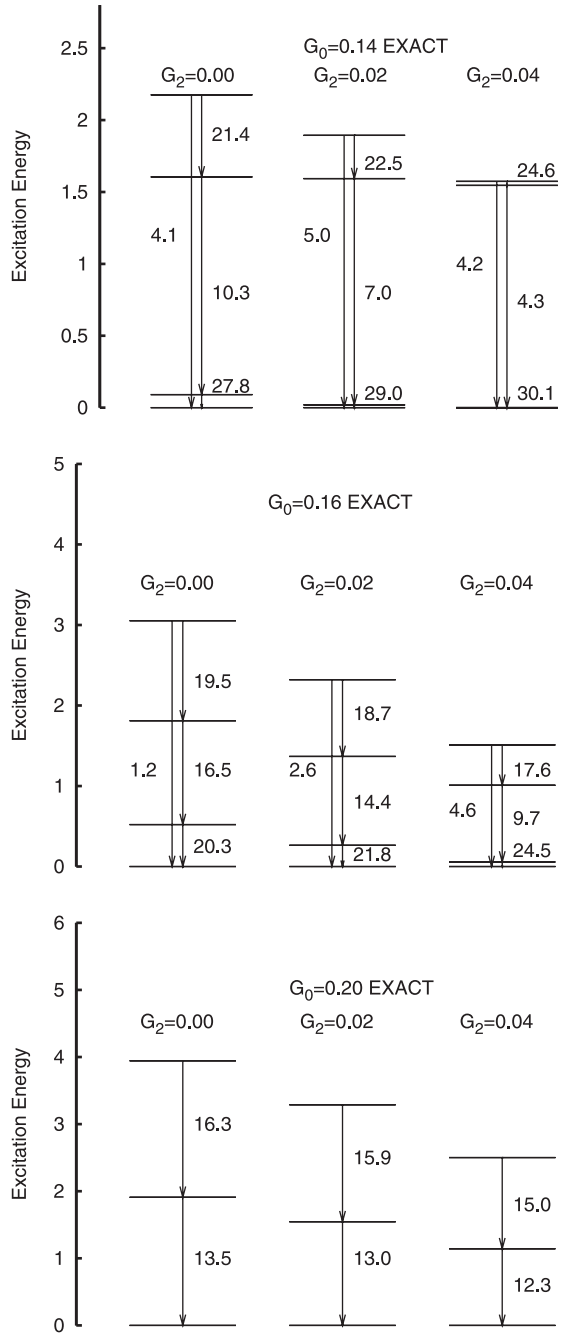

Fig. 7. Excitation spectra calculated with the exact diagonalization of the multi-$O(4)$ model Hamiltonian. The upper, middle and lower rows display the results for $G_0 = 0.14$, 0.16, and 0.20, respectively. In each row, the results for $G_2 = 0.00, 0.02, 0.04$ are compared. The numbers adjacent to vertical lines indicate the transition matrix elements. The matrix elements between the doublets are indicated beside them.

coordinate operator $\hat{Q}(q)$. Actually, it is stated in Ref. 27) that the separation of the Nambu-Goldstone modes in the local harmonic formulation requires higher-order terms in the collective coordinate. This is consistent with the present conclusion in the gauge-invariant formalism. We have also demonstrated that the approximation made by ignoring the B-part leads to results almost identical to those obtained in the full calculation, at least for the multi-$O(4)$ model.

We are presently investigating oblate-prolate shape coexistence phenomena[54)–56)] in nuclei around ^{68}Se with the pairing-plus-quadrupole interactions[63)–65)] using a prescription based on the new formulation of the ASCC method proposed in this paper. The result will be reported in the near future.

Acknowledgements

This work is supported by Grants-in-Aid for Scientific Research (Nos. 18·2670, 16540249, 17540231, and 17540244) from the Japan Society for the Promotion of Science. We thank the members of the Yukawa Institute for Theoretical Physics at Kyoto University for organizing the YITP workshop YITP-W-05-01, "New Developments in Nuclear Self-Consistent Mean-Field Theories". Discussions during this workshop were useful in completing this work. We also thank the members of Institute for Nuclear Theory at the University of Washington for their hospitality and the United States Department of Energy for partial support during the completion of this work.

References

1) D. J. Rowe and R. Bassermann, Can. J. Phys. **54** (1976), 1941.
2) D. M. Brink, M. J. Giannoni and M. Véneroni, Nucl. Phys. A **258** (1976), 237.
3) F. Villars, Nucl. Phys. A **285** (1977), 269.
4) T. Marumori, Prog. Theor. Phys. **57** (1977), 112.
5) M. Baranger and M. Véneroni, Ann. of Phys. **114** (1978), 123.
6) K. Goeke and P.-G. Reinhard, Ann. of Phys. **112** (1978), 328.
7) T. Marumori, T. Maskawa, F. Sakata and A. Kuriyama, Prog. Theor. Phys. **64** (1980), 1294.
8) M. J. Giannoni and P. Quentin, Phys. Rev. C **21** (1980), 2060; Phys. Rev. C **21** (1980), 2076.
9) J. Dobaczewski and J. Skalski, Nucl. Phys. A **369** (1981), 123.
10) K. Goeke, P.-G. Reinhard and D. J. Rowe, Nucl. Phys. A **359** (1981), 408.
11) A. K. Mukherjee and M. K. Pal, Phys. Lett. B **100** (1981), 457; Nucl. Phys. A **373** (1982), 289.
12) D. J. Rowe, Nucl. Phys. A **391** (1982), 307.
13) C. Fiolhais and R. M. Dreizler, Nucl. Phys. A **393** (1983), 205.
14) P.-G. Reinhard, F. Grümmer and K. Goeke, Z. Phys. A **317** (1984), 339.
15) A. Kuriyama and M. Yamamura, Prog. Theor. Phys. **70** (1983), 1675; Prog. Theor. Phys. **71** (1984), 122.
16) M. Yamamura, A. Kuriyama and S. Iida, Prog. Theor. Phys. **71** (1984), 109.
17) M. Matsuo and K. Matsuyanagi, Prog. Theor. Phys. **74** (1985), 288.
18) M. Matsuo, Prog. Theor. Phys. **76** (1986), 372.
19) Y. R. Shimizu and K. Takada, Prog. Theor. Phys. **77** (1987), 1192.
20) M. Yamamura and A. Kuriyama, Prog. Theor. Phys. Suppl. No. 93 (1987), 1.
21) A. Bulgac, A. Klein, N. R. Walet and G. Do Dang, Phys. Rev. C **40** (1989), 945.
22) N. R. Walet, G. Do Dang and A. Klein, Phys. Rev. C **43** (1991), 2254.
23) A. Klein, N. R. Walet and G. Do Dang, Ann. of Phys. **208** (1991), 90.

24) K. Kaneko, Phys. Rev. C **49** (1994), 3014.
25) T. Nakatsukasa and N. R. Walet, Phys. Rev. C **57** (1998), 1192.
26) T. Nakatsukasa and N. R. Walet, Phys. Rev. C **58** (1998), 3397.
27) T. Nakatsukasa, N. R. Walet and G. Do Dang, Phys. Rev. C **61** (1999), 014302.
28) J. Libert, M. Girod and J.-P. Delaroche, Phys. Rev. C **60** (1999), 054301.
29) E. Kh. Yuldashbaeva, J. Libert, P. Quentin and M. Girod, Phys. Lett. B **461** (1999), 1.
30) L. Próchniak, P. Quentin, D. Samsoen and J. Libert, Nucl. Phys. A **730** (2004), 59.
31) D. Almehed and N. R. Walet, Phys. Rev. C **69** (2004), 024302.
32) D. Almehed and N. R. Walet, Phys. Lett. B **604** (2004), 163.
33) A. Klein and E. R. Marshalek, Rev. Mod. Phys. **63** (1991), 375.
34) G. Do Dang, A. Klein and N. R. Walet, Phys. Rep. **335** (2000), 93.
35) A. Kuriyama, K. Matsuyanagi, F. Sakata, K. Takada and M. Yamamura (ed.), Prog. Theor. Phys. Suppl. No. 141 (2001), 1.
36) P. Ring and P. Schuck, *The Nuclear Many-Body Problem* (Springer-Verlag, 1980).
37) J.-P. Blaizot and G. Ripka, *Quantum Theory of Finite Systems* (The MIT press, 1986).
38) A. Abe and T. Suzuki (ed.), Prog. Theor. Phys. Suppl. Nos. 74 & 75 (1983), 1.
39) D. M. Brink and R. A. Broglia, *Nuclear Superfluidity, Pairing in Finite Systems* (Cambridge University Press, 2005).
40) M. Matsuo, Prog. Theor. Phys. **72** (1984), 666.
41) M. Matsuo and K. Matsuyanagi, Prog. Theor. Phys. **74** (1985), 1227; Prog. Theor. Phys. **76** (1986), 93; Prog. Theor. Phys. **78** (1987), 591.
42) M. Matsuo, Y. R. Shimizu and K. Matsuyanagi, *Proceedings of The Niels Bohr Centennial Conf. on Nuclear Structure*, ed. R. Broglia, G. Hagemann and B. Herskind (North-Holland, 1985), p. 161.
43) K. Takada, K. Yamada and H. Tsukuma, Nucl. Phys. A **496** (1989), 224.
44) K. Yamada, K. Takada and H. Tsukuma, Nucl. Phys. A **496** (1989), 239.
45) K. Yamada and K. Takada, Nucl. Phys. A **503** (1989), 53.
46) H. Aiba, Prog. Theor. Phys. **84** (1990), 908.
47) K. Yamada, Prog. Theor. Phys. **85** (1991), 805; Prog. Theor. Phys. **89** (1993), 995.
48) J. Terasaki, T. Marumori and F. Sakata, Prog. Theor. Phys. **85** (1991), 1235.
49) J. Terasaki, Prog. Theor. Phys. **88** (1992), 529; Prog. Theor. Phys. **92** (1994), 535.
50) M. Matsuo, in *New Trends in Nuclear Collective Dynamics*, ed. Y. Abe, H. Horiuchi and K. Matsuyanagi (Springer-Verlag, 1992), p. 219.
51) Y. R. Shimizu and K. Matsuyanagi, Prog. Theor. Phys. Suppl. No. 141 (2001), 285.
52) M. Matsuo, T. Nakatsukasa and K. Matsuyanagi, Prog. Theor. Phys. **103** (2000), 959.
53) M. Kobayasi, T. Nakatsukasa, M. Matsuo and K. Matsuyanagi, Prog. Theor. Phys. **112** (2004), 363; Prog. Theor. Phys. **113** (2005), 129.
54) J. L. Wood, K. Heyde, W. Nazarewicz, M. Huyse and P. van Duppen, Phys. Rep. **215** (1992), 101.
55) S. M. Fischer et al., Phys. Rev. Lett. **84** (2000), 4064; Phys. Rev. C **67** (2003), 064318.
56) E. Bouchez et al., Phys. Rev. Lett. **90** (2003), 082502.
57) N. Hinohara, T. Nakatsukasa, M. Matsuo and K. Matsuyanagi, Prog. Theor. Phys. **115** (2006), 567.
58) K. Matsuyanagi, Prog. Theor. Phys. **67** (1982), 1441; *Proceedings of the Nuclear Physics Workshop*, Trieste, 5-30 Oct. 1981, ed. C. H. Dasso, R. A. Broglia and A. Winther (North-Holland, 1982), p. 29.
59) Y. Mizobuchi, Prog. Theor. Phys. **65** (1981), 1450.
60) T. Suzuki and Y. Mizobuchi, Prog. Theor. Phys. **79** (1988), 480.
61) T. Fukui, M. Matsuo and K. Matsuyanagi, Prog. Theor. Phys. **85** (1991), 281.
62) M. Kobayasi, T. Nakatsukasa, M. Matsuo and K. Matsuyanagi, Prog. Theor. Phys. **110** (2003), 65.
63) M. Baranger and K. Kumar, Nucl. Phys. **62** (1965), 113; Nucl. Phys. A **110** (1968), 529; Nucl. Phys. A **122** (1968), 241; Nucl. Phys. A **122** (1968), 273.
64) M. Baranger and K. Kumar, Nucl. Phys. A **110** (1968), 490.
65) D. R. Bes and R. A. Sorensen, *Advances in Nuclear Physics*, vol. 2 (Prenum Press, 1969), p. 129.

Progress of Theoretical Physics, Vol. 119, No. 1, January 2008

Microscopic Derivation of Collective Hamiltonian by Means of the Adiabatic Self-Consistent Collective Coordinate Method

—— *Shape Mixing in Low-Lying States of* ^{68}*Se and* ^{72}*Kr* ——

Nobuo HINOHARA,[1] Takashi NAKATSUKASA,[2] Masayuki MATSUO[3] and Kenichi MATSUYANAGI[1]

[1]*Department of Physics, Graduate School of Science, Kyoto University, Kyoto 606-8502, Japan*
[2]*Theoretical Nuclear Physics Laboratory, RIKEN Nishina Center, Wako 351-0198, Japan*
[3]*Department of Physics, Faculty of Science, Niigata University, Niigata 950-2181, Japan*

(Received November 2, 2007)

The microscopic dynamics of oblate-prolate shape coexistence/mixing phenomena in ^{68}Se and ^{72}Kr are studied by means of the adiabatic self-consistent collective coordinate (ASCC) method in conjunction with the pairing-plus-quadrupole (P+Q) Hamiltonian, including the quadrupole pairing interaction. A quantum collective Hamiltonian is constructed, and excitation spectra, spectroscopic quadrupole moments and quadrupole transition properties are evaluated. The effect of the time-odd pair field on the collective mass (inertia function) of the large-amplitude vibration and the rotational moments of inertia about three principal axes is evaluated. It is found that the basic properties of the shape coexistence/mixing are qualitatively reproduced. The results of the calculation indicate that the oblate-prolate shape mixing decreases as the angular momentum increases.

§1. Introduction

Obtaining a microscopic understanding of nuclear collective dynamics is one of the goals of nuclear structure theory. The quasiparticle random phase approximation (QRPA), based on the Hartree-Fock-Bogoliubov (HFB) mean field, is a well-known theoretical approach to the collective dynamics, but it is applicable only to small-amplitude collective motion around the local minima of the potential energy surface.[1)–5)] Nuclei exhibit a variety of large-amplitude collective processes such as anharmonic vibrations, shape coexistence, and fission. Though the challenge to construct microscopic theories of large-amplitude collective motion has a long history,[6)–42)] some important problems remain unsolved.

The self-consistent collective coordinate (SCC) method[12),23)] is a microscopic theory of large-amplitude collective motion. This method, with the (η^*, η) expansion technique, enables us to extract the collective variables from the many-dimensional phase space associated with the time-dependent Hartree-Fock-Bogoliubov (TDHFB) state vectors, and to derive the collective Hamiltonian starting from a microscopic Hamiltonian. The SCC method has been successfully applied to various kinds of non-linear phenomena in nuclei, such as anharmonic γ-vibrations,[43)–46)] shape phase

transitions,[47)–50)] two-phonon states[51)] and collective rotations.[52)–54)] The (η^*, η) expansion is not necessarily convenient, however, for large-amplitude collective motion like shape coexistence/mixing phenomena, in which a microscopic description of the many-body tunneling effect between different local minima in the collective potential energy surface becomes the major task.

The adiabatic SCC (ASCC) method[55)] is an alternative way of solving the basic equations of the SCC method, assuming that the large-amplitude collective motion of interest is slow (adiabatic). Under this assumption, the basic equations of the SCC method are expanded up to second order with respect to the collective momentum, but the collective coordinate is treated non-perturbatively. Quite recently, we have given a rigorous formulation of the ASCC method in which the gauge invariance with respect to the particle number fluctuation degrees of freedom is taken into account.[56)]

As is well known, in contrast to the significant progress in the calculation of the collective potential energy, the present status of the microscopic theory is quite unsatisfactory with regard to the evaluation of the collective mass (inertia function) associated with the collective kinetic energy. Although the Inglis-Belyaev cranking mass is widely used, it violates self-consistency by ignoring the effect of the time-odd component of the moving mean field.[1)] The time-odd mean-field effect is taken into account in the collective mass derived with the QRPA, but its application is restricted to small-amplitude collective motion around equilibrium states. Concerning large-amplitude collective motion, though the effect of the time-odd component generated by the residual particle-hole interaction was investigated a few decades ago,[14)] the time-odd effect generated by the residual pairing interaction has not yet been studied. Quite recently, we showed, using the ASCC method in conjunction with the schematic model Hamiltonian,[58)–61)] that the time-odd pair field increases the collective mass.[57)] It remains to be seen, however, how it affects the shape coexistence dynamics discussed below.

Let us consider recent experimental data of interest. The shapes of nuclei along the $N = Z$ line change significantly as the numbers of protons and neutrons change.[62)–66)] The HFB calculation[67)] indicates that various shapes will appear along the $N = Z$ lines: a triaxial ground state for ^{64}Ge, oblate ground states for ^{68}Se and ^{72}Kr, strongly deformed prolate ground states for ^{76}Sr, ^{80}Zr and ^{84}Mo. Furthermore, oblate and prolate states may coexist in these nuclei, other than^{64}Ge. In ^{68}Se and ^{72}Kr, the ground and excited states corresponding to oblate and prolate shapes have been found experimentally.[63)–65)] From the viewpoint of collective dynamics based on the mean-field theory, it is expected that the oblate and prolate shapes are mixed by the many-body tunneling effect through the potential barrier lying between the two local minima in the potential energy landscape. The low-lying states in ^{68}Se and ^{72}Kr have been investigated using various theoretical approaches beyond the mean-field approximation: large-scale shell model calculations for ^{68}Se using the pfg-shells outside the ^{56}Ni core,[68)] shell model Monte Carlo calculations for ^{72}Kr employing the pf-sdg shells,[69)] configuration mixing calculations for $^{72-78}$Kr on the basis of the particle number and angular momentum projected generator coordinate method,[70)] and the EXCITED VAMPIR variational calculation for ^{68}Se and ^{72}Kr.[71)–73)] Quite

recently, Almehed and Walet[36)–39)] discussed collective paths connecting the oblate and prolate minima in ^{68}Se and $^{72-78}$Kr by means of an approach similar to the ASCC method.

The ASCC method was first tested[74)] in a schematic model[58)–61)] and then it was applied[75)] to oblate-prolate shape coexistence phenomena in ^{68}Se and ^{72}Kr with use of the pairing-plus-quadrupole (P+Q) Hamiltonian.[76)–79)] In both nuclei, the one-dimensional collective path connecting the two local minima of the potential is extracted. It was found that the collective path runs approximately along the valley of the potential energy surface lying in the triaxial deformed region. This indicates that the triaxial degree of freedom is essential for the description of large-amplitude shape mixing in ^{68}Se and ^{72}Kr. In Ref. 75), however, requantization of the collective Hamiltonian was not carried out, and excitation spectra, electromagnetic transition probabilities, and shape mixing probabilities in individual eigenstates were not evaluated.

This paper presents the result of the first application of the gauge invariant formulation[56)] of the ASCC method to nuclear structure phenomena. Thus, its major thrust is directed at examining the feasibility of the gauge-invariant ASCC method for describing the shape coexistence/mixing phenomena. Hereafter, we call this new version the "ASCC method", dropping the adjective "gauge-invariant" for simplicity. A more detailed investigation of experimental data and comparison with other approaches are planned for the future. We derive the quantum collective Hamiltonian that describes the coupled collective motion of the large-amplitude vibration responsible for the oblate-prolate shape mixing and the three-dimensional rotation of the triaxial shape. To evaluate the rotational moments of inertia, we extend the well-known QRPA equation for rotational motion, which yields the Thouless-Valatin moment of inertia,[80)] to non-equibrium states that are defined in the moving-frame associated with large-amplitude vibrational motion. To clarify the role of the time-odd pair field in shape mixing dynamics, we investigate, with use of the P+Q Hamiltonian including the quadrupole pairing interaction, its effects on the collective mass of large-amplitude vibration, the rotational moments of inertia, the energy spectra, transition probabilities, and shape mixing probabilities in individual eigenstates.

This paper is organized as follows. The basic equations of the ASCC method are summarized in §2. The quasiparticle representation of the microscopic Hamiltonian is given in §3. The procedure for solving the ASCC equations is presented in §4. The collective Schrödinger equation is derived in §5. Results of numerical calculations for energy spectra, spectroscopic quadrupole moments and quadrupole transition probabilities of low-lying states in ^{68}Se and ^{72}Kr are presented and discussed in §6. Concluding remarks are given in §7.

A preliminary version of this work was previously reported in Ref. 81).

§2. The ASCC method

2.1. *Basic equations of the ASCC method*

We first summarize the basic equations of the ASCC method. The TDHFB state $|\phi(t)\rangle$ is written in terms of the collective variables as

$$|\phi(t)\rangle = |\phi(q,p,\boldsymbol{\varphi},\boldsymbol{n})\rangle = e^{-i\sum_\tau \varphi^{(\tau)}\tilde{N}^{(\tau)}}\,|\phi(q,p,\boldsymbol{n})\rangle\,, \tag{2·1}$$

where q and p represent the one-dimensional collective coordinate and the collective momentum, respectively. The variables $\boldsymbol{\varphi} = (\varphi^{(n)}, \varphi^{(p)})$ and $\boldsymbol{n} = (n^{(n)}, n^{(p)})$ denote the gauge angles in particle number space and number fluctuations, respectively, which correspond to the canonical coordinates and momenta of the pairing rotation restoring the particle number conservation broken by the HFB approximation. The operator $\tilde{N}^{(\tau)} \equiv \hat{N}^{(\tau)} - N_0^{(\tau)}$ represents the particle number measured with respect to the reference value $N_0^{(\tau)}$, which is set to the number of the valence protons ($\tau = p$) and neutrons ($\tau = n$) in the model space.

The intrinsic state with respect to the pairing rotation is written $|\phi(q,p,\boldsymbol{n})\rangle = e^{i\hat{G}(q,p,\boldsymbol{n})}\,|\phi(q)\rangle$, where $|\phi(q)\rangle \equiv |\phi(q,p=0,\boldsymbol{n}=\boldsymbol{0})\rangle$. Assuming that large-amplitude collective motion is adiabatic, that is, the collective momentum p and the number fluctuation $\boldsymbol{n}$ are small, we expand the one-body operator $\hat{G}(q,p,\boldsymbol{n})$ with respect to p and $n^{(\tau)}$ and consider only the first order:

$$|\phi(q,p,\boldsymbol{n})\rangle = e^{ip\hat{Q}(q)+i\sum_\tau n^{(\tau)}\hat{\Theta}^{(\tau)}(q)}\,|\phi(q)\rangle\,. \tag{2·2}$$

Here, $\hat{Q}(q)$ is a time-even one-body operator, while $\hat{\Theta}^{(\tau)}(q)$ is a time-odd one-body operator. Using the quasiparticle creation and annihilation operators, $a^\dagger_\alpha(q)$ and $a_\alpha(q)$, defined with respect to a moving-frame HFB state $|\phi(q)\rangle$, which satisfy the condition $a_\alpha(q)\,|\phi(q)\rangle = 0$, they can be written as

$$\begin{aligned}\hat{Q}(q) &= \hat{Q}^A(q) + \hat{Q}^B(q) \\ &= \sum_{\alpha\beta}\left(Q^A_{\alpha\beta}(q)a^\dagger_\alpha(q)a^\dagger_\beta(q) + Q^{A*}_{\alpha\beta}(q)a_\beta(q)a_\alpha(q) + Q^B_{\alpha\beta}(q)a^\dagger_\alpha(q)a_\beta(q)\right), \end{aligned}\tag{2·3}$$

$$\hat{\Theta}^{(\tau)}(q) = \sum_{\alpha\beta}\left(\Theta^{(\tau)A}_{\alpha\beta}(q)a^\dagger_\alpha(q)a^\dagger_\beta(q) + \Theta^{(\tau)A*}_{\alpha\beta}(q)a_\beta(q)a_\alpha(q)\right). \tag{2·4}$$

Note that the operator $\hat{Q}(q)$ contains the B-part (the third term in the r.h.s.), in addition to the A-part (the first and second terms) in order to satisfy the gauge-invariance of the ASCC equations.[56] In the following, we omit the index q in the quasiparticle operators for simplicity.

The basic equations of the SCC method consist of the canonical variable conditions, the moving-frame HFB equation, and the moving-frame QRPA equations. Below we summarize the lowest-order expressions of these equations with respect to expansion in p and $\boldsymbol{n}$. (See Ref. 56) for their derivations.) The canonical variable conditions are given by

$$\langle\phi(q)|\,\hat{P}(q)\,|\phi(q)\rangle = 0, \tag{2·5}$$

$$\langle\phi(q)|\,\hat{Q}(q)\,|\phi(q)\rangle = 0, \tag{2·6}$$

$$\langle\phi(q)|\,\tilde{N}^{(\tau)}\,|\phi(q)\rangle = 0, \tag{2·7}$$

$$\langle\phi(q)|\,\hat{\Theta}^{(\tau)}(q)\,|\phi(q)\rangle = 0, \tag{2·8}$$

$$\langle\phi(q)|\,[\hat{\Theta}^{(\tau)}(q), \tilde{N}^{(\tau')}]\,|\phi(q)\rangle = i\delta_{\tau\tau'}, \tag{2·9}$$

$$\langle\phi(q)|\,[\hat{Q}(q), \hat{\Theta}^{(\tau)}(q)]\,|\phi(q)\rangle = 0, \tag{2·10}$$

$$\langle\phi(q)|\,\frac{\partial\hat{Q}}{\partial q}\,|\phi(q)\rangle = -1, \tag{2·11}$$

where $\hat{P}(q)$ is the local shift operator, defined by

$$\hat{P}(q)\,|\phi(q)\rangle = i\frac{\partial}{\partial q}\,|\phi(q)\rangle\,. \tag{2·12}$$

Differentiating (2·6) and (2·7) with respect to q and using (2·11) and (2·12), we obtain

$$\langle\phi(q)|\,[\hat{Q}(q), \hat{P}(q)]\,|\phi(q)\rangle = i, \tag{2·13}$$

$$\langle\phi(q)|\,[\tilde{N}^{(\tau)}, \hat{P}(q)]\,|\phi(q)\rangle = 0. \tag{2·14}$$

Equations (2·5), (2·6), (2·7) and (2·8) ensure that the constant terms of those operators are zero in their quasiparticle representations, while Eqs. (2·9), (2·10), (2·13) and (2·14) guarantee orthonormalization of the collective mode and the number fluctuation modes. Equation (2·11) defines the scaling of the collective coordinate.

The moving-frame HFB equation is given by

$$\delta\,\langle\phi(q)|\,\hat{H}_M(q)\,|\phi(q)\rangle = 0, \tag{2·15}$$

where

$$\hat{H}_M(q) = \hat{H} - \sum_\tau \lambda^{(\tau)}(q)\tilde{N}^{(\tau)} - \frac{\partial V}{\partial q}\hat{Q}(q) \tag{2·16}$$

represents the moving-frame Hamiltonian with the chemical potential $\lambda^{(\tau)}(q)$ and the collective potential $V(q)$ defined by

$$\lambda^{(\tau)}(q) = \frac{\partial\mathcal{H}}{\partial n^{(\tau)}}\Big|_{p=0,\boldsymbol{n}=\boldsymbol{0},\vec{I}=\vec{0}} = \langle\phi(q)|\,[\hat{H}, i\hat{\Theta}^{(\tau)}(q)]\,|\phi(q)\rangle\,, \tag{2·17}$$

$$V(q) = \mathcal{H}(q,p,\boldsymbol{n},\vec{I})\,\Big|_{p=0,\boldsymbol{n}=\boldsymbol{0},\vec{I}=\vec{0}} = \langle\phi(q)|\,\hat{H}\,|\phi(q)\rangle\,. \tag{2·18}$$

The moving-frame QRPA equations are given by

$$\delta\,\langle\phi(q)|\,[\hat{H}_M(q), i\hat{Q}(q)] - B(q)\hat{P}(q)\,|\phi(q)\rangle = 0, \tag{2·19}$$

$$\delta\,\langle\phi(q)|\,[\hat{H}_M(q), \hat{P}(q)] - iC(q)\hat{Q}(q) - \frac{1}{2B(q)}\left[\left[\hat{H}_M(q), \frac{\partial V}{\partial q}\hat{Q}(q)\right], i\hat{Q}(q)\right] - i\sum_\tau \frac{\partial\lambda^{(\tau)}}{\partial q}\tilde{N}^{(\tau)}\,|\phi(q)\rangle = 0, \tag{2·20}$$

where $B(q)$ and $C(q)$ represent the inverse collective mass and the local stiffness, respectively. They are defined by

$$B(q) = \frac{\partial^2 \mathcal{H}}{\partial p^2}\Big|_{p=0,\boldsymbol{n}=\boldsymbol{0},\vec{I}=\vec{0}} = \langle\phi(q)|\,[[\hat{H}, i\hat{Q}(q)], i\hat{Q}(q)]\,|\phi(q)\rangle\,, \tag{2·21}$$

$$C(q) = \frac{\partial^2 V}{\partial q^2} + \frac{1}{2B(q)}\frac{\partial B}{\partial q}\frac{\partial V}{\partial q}. \tag{2·22}$$

Note that the ASCC equations, (2·15), (2·19) and (2·20), are invariant under the following transformation:[56)]

$$\begin{aligned} \hat{Q}(q) &\to \hat{Q}(q) + \alpha^{(\tau)}\tilde{N}^{(\tau)}, \\ \lambda^{(\tau)}(q) &\to \lambda^{(\tau)}(q) - \alpha^{(\tau)}\frac{\partial V}{\partial q}(q), \\ \frac{\partial \lambda^{(\tau)}}{\partial q}(q) &\to \frac{\partial \lambda^{(\tau)}}{\partial q}(q) - \alpha^{(\tau)}C(q). \end{aligned} \tag{2·23}$$

Therefore, it is necessary to fix the particle number gauge for neutrons and protons in order to derive the unique solution of the ASCC equations. The algorithm to find simultaneous solutions of Eqs. (2·15), (2·19) and (2·20) satisfying the canonical variable conditions and the gauge-fixing condition is described in §4.

In this paper, we take into account the rotational motion as well as the large-amplitude vibrational motion by considering the collective Hamiltonian defined as follows:

$$\begin{aligned} \mathcal{H}(q,p,\boldsymbol{n},\vec{I}) &= \langle\phi(q,p,\boldsymbol{n})|\,\hat{H}\,|\phi(q,p,\boldsymbol{n})\rangle + \sum_{i=1}^{3}\frac{1}{2\mathcal{J}_i(q)}I_i^2 \\ &= V(q) + \frac{1}{2}B(q)p^2 + \sum_{\tau}\lambda^{(\tau)}(q)n^{(\tau)} + \sum_{i=1}^{3}\frac{1}{2\mathcal{J}_i(q)}I_i^2. \end{aligned} \tag{2·24}$$

The first and the second terms represent the potential and kinetic energies of the large-amplitude collective vibration, respectively, while the third and the fourth terms represent the energies associated with the particle-number fluctuations and the three-dimensional rotation of triaxially deformed mean fields, respectively. The three rotational moments of inertia, $\mathcal{J}_i(q)$, are defined with respect to the principal axes associated with the moving-frame HFB state $|\phi(q)\rangle$ and evaluated as

$$\delta\,\langle\phi(q)|\,[\hat{H}_M(q), \hat{\Psi}_i(q)] - \frac{1}{i}\mathcal{J}_i^{-1}(q)\hat{I}_i\,|\phi(q)\rangle = 0, \tag{2·25}$$

$$\langle\phi(q)|\,[\hat{\Psi}_i(q), \hat{I}_j]\,|\phi(q)\rangle = \delta_{ij}, \tag{2·26}$$

where $\hat{\Psi}_i(q)$ and $\hat{I}_i$ represent the rotational angle and the angular momentum operators, respectively. These equations reduce to the well-known QRPA equations giving the Thouless-Valatin moments of inertia[80)] when $|\phi(q)\rangle$ is an equilibrium state corresponding to a local minimum of the collective potential energy, $V(q)$. We call them

"Thouless-Valatin equations", although they are in fact extensions of the QRPA equations for collective rotation to non-equilibrium HFB states $|\phi(q)\rangle$. Note that $\hat{H}_M(q)$ appears in Eq. (2·25) instead of $\hat{H}$. We remark that Eqs. (2·24)–(2·26) have been introduced intuitively, leaving a full derivation of them as a challenging subject for future.

§3. Hamiltonian

We adopt the following Hamiltonian consisting of the spherical single-particle energy, the monopole and the quadrupole pairing interactions, and the quadrupole particle-hole interaction:

$$\hat{H} = \sum_k \varepsilon_k c_k^\dagger c_k - \sum_\tau \frac{G_0^{(\tau)}}{2} (\hat{A}^{(\tau)\dagger} \hat{A}^{(\tau)} + \hat{A}^{(\tau)} \hat{A}^{(\tau)\dagger}) - \sum_\tau \frac{G_2^{(\tau)}}{2} \sum_{K=-2}^{2} (\hat{B}_{2K}^{(\tau)\dagger} \hat{B}_{2K}^{(\tau)} + \hat{B}_{2K}^{(\tau)} \hat{B}_{2K}^{(\tau)\dagger}) - \frac{\chi}{2} \sum_{K=-2}^{2} \hat{D}_{2K}^\dagger \hat{D}_{2K}. \tag{3·1}$$

Here, the monopole pairing operator $\hat{A}^{(\tau)\dagger}$, the quadrupole pairing operator $\hat{B}_{2K}^{(\tau)\dagger}$, the quadrupole particle-hole operator $\hat{D}_{2K}$ are defined by

$$\hat{A}^{(\tau)\dagger} = \sum_{(k,\tilde{k})\in\tau} c_k^\dagger c_{\tilde{k}}^\dagger, \tag{3·2}$$

$$\hat{B}_{2K}^{(\tau)\dagger} = \sum_{kl\in\tau} D_{2K}^{(\tau)}(kl) c_k^\dagger c_{\tilde{l}}^\dagger, \tag{3·3}$$

$$\hat{D}_{2K} = \sum_{\tau=n,p} \sum_{kl\in\tau} D_{2K}^{(\tau)}(kl) c_k^\dagger c_l, \tag{3·4}$$

where $c_k^\dagger$ is the nucleon creation operator, and k denotes the set of quantum numbers of the single-particle state (N_k, j_k, l_k, m_k). The operator $c_{\tilde{k}}^\dagger$ represents its time-reversal state,

$$c_{\tilde{k}}^\dagger = (-1)^{j_k+m_k} c_{-k}^\dagger, \tag{3·5}$$

where the index $-k$ represents $(N_k, j_k, l_k, -m_k)$. The quadrupole matrix elements are given by

$$D_{2K}^{(\tau)}(kl) = \alpha_\tau^2 \langle k| r^2 Y_{2K} |l\rangle, \quad (kl \in \tau) \tag{3·6}$$

where the factors $\alpha_n^2 = (2N/A)^{2/3}$ and $\alpha_p^2 = (2Z/A)^{2/3}$ are multiplied to yield the same root mean square radius for neutrons and protons. For $N{=}Z$ nuclei, such as ^{68}Se and ^{72}Kr, these factors are unity. Following Baranger and Kumar,[78] we employ a model space consisting of two major oscillator shells (with the total quantum number of the lower shell denoted by N_L and that of the upper shell denoted by $N_L + 1$), and multiply the quadrupole matrix elements $D_{2K}^{(\tau)}(kl)$ of the upper shell by the reduction factor $\zeta = (N_L + 3/2)/(N_L + 5/2)$.

Following the conventional prescription of the P+Q model, we ignore the Fock terms. Accordingly, we use the abbreviation "HB" in place of "HFB" in the following.

We rewrite the Hamiltonian (3·1) into the form

$$\hat{H} = \sum_k \varepsilon_k c_k^\dagger c_k - \frac{1}{2}\sum_s \kappa_s \hat{F}_s^{(+)}\hat{F}_s^{(+)} + \frac{1}{2}\sum_s \kappa_s \hat{F}_s^{(-)}\hat{F}_s^{(-)}, \tag{3·7}$$

where the Hermite operators $\hat{F}_s^{(+)}$ and the anti-Hermite operators $\hat{F}_s^{(-)}$ are defined by

$$\hat{F}_s^{(\pm)} = \frac{1}{2}(\hat{F}_s \pm \hat{F}_s^\dagger), \tag{3·8}$$

$$\begin{aligned}\hat{F}_{s=1-15} = \{&\hat{A}^{(n)}, \hat{A}^{(p)}, \hat{B}^{(n)}_{20(+)}, \hat{B}^{(n)}_{21(+)}, \hat{B}^{(n)}_{21(-)}, \hat{B}^{(n)}_{22(+)}, \hat{B}^{(n)}_{22(-)},\\ &\hat{B}^{(p)}_{20(+)}, \hat{B}^{(p)}_{21(+)}, \hat{B}^{(p)}_{21(-)}, \hat{B}^{(p)}_{22(+)}, \hat{B}^{(p)}_{22(-)}, \hat{D}_{20}, \hat{D}_{21}, \hat{D}_{22}\}.\end{aligned} \tag{3·9}$$

Here we use

$$\hat{B}^{(\tau)\dagger}_{2K(\pm)} \equiv \frac{1}{2}(\hat{B}^{(\tau)\dagger}_{2K} \pm \hat{B}^{(\tau)\dagger}_{2-K}) \quad (K \geq 0) \tag{3·10}$$

in place of $\hat{B}^{(\tau)\dagger}_{2K}$ for the quadrupole pairing operators. The interaction strengths κ_s are given by

$$\begin{aligned}\kappa_{s=1-15} = \{&2G_0^{(n)}, 2G_0^{(p)}, 2G_2^{(n)}, 4G_2^{(n)}, 4G_2^{(n)}, 4G_2^{(n)}, 4G_2^{(n)},\\ &2G_2^{(p)}, 4G_2^{(p)}, 4G_2^{(p)}, 4G_2^{(p)}, 4G_2^{(p)}, \chi, 2\chi, 2\chi\}.\end{aligned} \tag{3·11}$$

This Hamiltonian is invariant under a rotation by π about the x-axis. The quantum number associated with this is called the signature, $r = e^{-i\pi\alpha}$. The single-particle basis with definite signatures is defined by

$$\begin{aligned} d_k &\equiv \frac{1}{\sqrt{2}}(c_k + c_{\tilde{k}}), \quad r = -i \quad \left(\alpha = \frac{1}{2}\right),\\ d_{\bar{k}} &\equiv \frac{1}{\sqrt{2}}(c_{\tilde{k}} - c_k), \quad r = i \quad \left(\alpha = -\frac{1}{2}\right),\end{aligned} \tag{3·12}$$

where k denotes the single-particle basis whose magnetic quantum number satisfies the condition $m_k - 1/2 = [\text{even}]$. The operators $\hat{F}_s^{(\pm)}$ can be classified according to their signatures and K-quantum numbers, as shown in Table I.

The large-amplitude collective vibration responsible for the oblate-prolate shape mixing is associated with the $K = 0$ and 2 components of the interactions in the positive-signature ($r = +1$) sector. Thus, the infinitesimal generator of large-amplitude collective motion, $\hat{Q}(q)$, can be written in terms of the single-particle basis with definite signature as

$$\hat{Q}(q) = \sum_\tau {\sum_{kl\in\tau}}' \left(Q^{(\tau)}_{kl}(q) d_k^\dagger d_l + Q^{(\tau)}_{\bar{k}\bar{l}}(q) d_{\bar{k}}^\dagger d_{\bar{l}}\right), \tag{3·13}$$

Table I. Classification of the one-body operators $\hat{F}_s^{(\pm)}$ in terms of the signature r (or α) and K quantum numbers.

	$r=+1(\alpha=0)$	$r=-1(\alpha=1)$
$K=0$	$\{\hat{A}_n^{(\pm)}, \hat{A}_p^{(\pm)}, \hat{B}_{20(+)}^{(n)(\pm)}, \hat{B}_{20(+)}^{(p)(\pm)}, \hat{D}_{20}^{(+)}\}$	–
$K=1$	$\{\hat{B}_{21(-)}^{(n)(\pm)}, \hat{B}_{21(-)}^{(p)(\pm)}, \hat{D}_{21}^{(-)}\}$	$\{\hat{B}_{21(+)}^{(n)(\pm)}, \hat{B}_{21(+)}^{(p)(\pm)}, \hat{D}_{21}^{(+)}\}$
$K=2$	$\{\hat{B}_{22(+)}^{(n)(\pm)}, \hat{B}_{22(+)}^{(p)(\pm)}, \hat{D}_{22}^{(+)}\}$	$\{\hat{B}_{22(-)}^{(n)(\pm)}, \hat{B}_{22(-)}^{(p)(\pm)}, \hat{D}_{22}^{(-)}\}$

where $\sum'$ represents a sum over the signature pairs $(k, \bar{k})$, and $Q_{kl}^{(\tau)} = Q_{\bar{k}\bar{l}}^{(\tau)}$. The $K=1$ component of the interaction in the $r=+1$ sector and the $K=1$ and 2 components in the $r=-1$ sector contribute to the Thouless-Valatin equations (2·25).

§4. Solution of the ASCC equations for separable interactions

4.1. *The ASCC equations for separable interactions*

For the separable interactions given in (3·7), the ASCC equations are written[55),56)]

$$\delta \langle\phi(q)| \hat{h}_M(q) |\phi(q)\rangle = 0, \tag{4·1}$$

$$\delta \langle\phi(q)| [\hat{h}_M(q), \hat{Q}(q)] - \sum_s f_{Q,s}^{(-)}(q)\hat{F}_s^{(-)} - \frac{1}{i}B(q)\hat{P}(q) |\phi(q)\rangle = 0, \tag{4·2}$$

$$\begin{aligned}\delta \langle\phi(q)| &\left[\hat{h}_M(q), \frac{1}{i}B(q)\hat{P}(q)\right] - \sum_s f_{P,s}^{(+)}(q)\hat{F}_s^{(+)} - \omega^2(q)\hat{Q}(q) \\ &- \sum_s f_{R,s}^{(+)}(q)\hat{F}_s^{(+)} - \frac{1}{2}\left[\left[\hat{h}_M(q), \frac{\partial V}{\partial - q}\hat{Q}(q)\right], \hat{Q}(q)\right] \\ &+ \sum_s \left[\hat{F}_s^{(-)}, \frac{\partial V}{\partial q}\hat{Q}(q)\right] f_{Q,s}^{(-)}(q) - \sum_\tau f_N^{(\tau)}(q)\tilde{N}^{(\tau)} |\phi(q)\rangle = 0,\end{aligned} \tag{4·3}$$

where $\omega^2(q) = B(q)C(q)$ is the moving-frame QRPA frequency squared, and $\hat{h}_M(q)$ denotes the self-consistent mean-field Hamiltonian in the moving frame, defined by

$$\hat{h}_M(q) = \hat{h}(q) - \sum_\tau \lambda^{(\tau)}(q)\tilde{N}^{(\tau)} - \frac{\partial V}{\partial q}\hat{Q}(q), \tag{4·4}$$

with

$$\hat{h}(q) = \hat{h}_0 - \sum_s \kappa_s \hat{F}_s^{(+)} \langle\phi(q)| \hat{F}_s^{(+)} |\phi(q)\rangle . \tag{4·5}$$

In the above equations, the summation over s is restricted to the operators with $K=0$ and 2 in the positive-signature sector. We also define the quantities

$$f_{Q,s}^{(-)}(q) = -\kappa_s \langle\phi(q)| [\hat{F}_s^{(-)}, \hat{Q}(q)] |\phi(q)\rangle , \tag{4·6a}$$

$$f^{(+)}_{P,s}(q) = \kappa_s \langle\phi(q)| [\hat{F}^{(+)}_s, \frac{1}{i}B(q)\hat{P}(q)] |\phi(q)\rangle\,, \tag{4·6b}$$

$$f^{(+)}_{R,s}(q) = -\frac{1}{2}\kappa_s \langle\phi(q)| \left[\left[\hat{F}^{(+)}_s, \frac{\partial V}{\partial q}\hat{Q}(q)\right], \hat{Q}(q)\right] |\phi(q)\rangle\,, \tag{4·6c}$$

$$f^{(\tau)}_N(q) = B(q)\frac{\partial \lambda^{(\tau)}}{\partial q}. \tag{4·6d}$$

Note that all matrix elements are real and $\langle\phi(q)|\,\hat{F}^{(-)}_s\,|\phi(q)\rangle = 0$.

4.2. *Overview of the procedure to solve the ASCC equations*

The infinitesimal generators $\hat{Q}(q)$ and $\hat{P}(q)$, which are represented with respect to the quasiparticle vacuum $|\phi(q)\rangle$, are the solutions of the moving-frame QRPA equations, while the quasiparticle vacuum $|\phi(q)\rangle$, which depends on $\hat{Q}(q)$, is a solution of the moving-frame HB equation. In order to construct the collective path, we have to obtain a self-consistent solution for the quasiparticle vacuum and the infinitesimal generators. This requires a double iterative procedure for each value of q, because the moving-frame HB equation is also solved by iteration.

Step 0: Starting point

The shape coexistence phenomena imply that there exist several solutions of the static HB equation representing different local minima in the potential energy surface. We can choose one of the HB solutions and assume that it is on the collective path. This starting state is denoted by $|\phi(q=0)\rangle$. In the calculation for ^{68}Se and ^{72}Kr presented in this paper, we choose the HB state at the lowest minimum, which possesses an oblate shape. As discussed in Ref. 56), gauge fixing is necessary to solve the moving-frame QRPA equations. We choose the "ETOP" gauge.

Step 1: Initial setting

Assume that the solution of the ASCC equations at $q - \delta q$ is obtained. In order to calculate the solution at q, we start by solving the moving-frame HB equation (4·1). As an infinitesimal generator in the moving-frame Hamiltonian, we use an initial trial generator $\hat{Q}(q)^{(0)}$ constructed from the lowest two solutions of the moving-frame QRPA equations at $q - \delta q$ of the form

$$\hat{Q}(q)^{(0)} = (1-\varepsilon)\hat{Q}_1(q-\delta q) + \varepsilon\hat{Q}_2(q-\delta q), \tag{4·7}$$

where $\hat{Q}_1(q-\delta q)$ and $\hat{Q}_2(q-\delta q)$ denote the lowest and the second-lowest solutions of the moving-frame QRPA equations at $q-\delta q$, respectively. The mixing parameter ε is set to 0.1. This choice is crucial to find a symmetry-breaking solution in the moving-frame QRPA equations when the moving-frame HB state $|\phi(q-\delta q)\rangle$ and the moving-frame QRPA mode $\hat{Q}_1(q-\delta q)$ possess the axial symmetry.[75] [If $\hat{Q}_2(q-\delta q)$ is also axially symmetric, then we choose, for the second mode, the lowest one among the axial symmetry-breaking QRPA modes.] The quantity δq is set to 0.0157 in the present calculations.

Step 2: Solving the moving-frame HB equation

Using the operator $\hat{Q}^{(n-1)}(q)$ $(n \geq 1)$, we solve the moving-frame HB equation at q,

$$\delta \left\langle \phi^{(n)}(q) \right| \hat{H} - \sum_{\tau} (\lambda^{(\tau)}(q))^{(n)} \tilde{N}^{(\tau)} - \frac{\partial V}{\partial q}^{(n)}(q) \hat{Q}^{(n-1)}(q) \left| \phi^{(n)}(q) \right\rangle = 0, \quad (4\cdot8)$$

with three constraints from the canonical variable conditions,

$$\left\langle \phi^{(n)}(q) \right| \tilde{N}^{(\tau)} \left| \phi^{(n)}(q) \right\rangle = 0, \quad (4\cdot9)$$

$$\left\langle \phi^{(n)}(q) \right| \hat{Q}(q - \delta q) \left| \phi^{(n)}(q) \right\rangle = \delta q. \quad (4\cdot10)$$

This step is discussed in §4.3 in detail.

Step 3: Solving the moving-frame QRPA equations

Using the moving-frame HB state $\left|\phi^{(n)}(q)\right\rangle$ and the Lagrange multipliers $(\lambda^{(\tau)}(q))^{(n)}$ and $\partial V/\partial q(q)^{(n)}$ obtained in the previous step, we solve the moving-frame QRPA equations with the gauge-fixing condition used for the HB state in *Step 0*. This determines the infinitesimal generator $\hat{Q}^{(n)}(q)$ as the lowest solution of Eqs. (4·2) and (4·3). Details of this step are described in §4.4 and Appendix B.

Step 4: Realizing self-consistency

Updating the operator $\hat{Q}^{(n)}(q)$, we return to *Step 2*, and repeat *Steps 2* and *3* until all quantities at q converge.

Step 5: Progression

Change q to $q + \delta q$ and return to *Step 1*.

Carrying out *Steps 1-5*, we obtain a collective path starting from the HB minimum in one direction $(q > 0)$. We then change the sign of δq and repeat the above procedure in the opposite direction $(q < 0)$. In this way, we obtain an entire collective path.

After obtaining the solutions of the ASCC equations, we solve the Thouless-Valatin equation, (2·25), at every point on the collective path using the moving-frame HB state $|\phi(q)\rangle$ to evaluate the rotational moments of inertia $\mathcal{J}_i(q)$. Details of this calculation are described in Appendix C.

4.3. *The moving-frame HB equation in the quasiparticle representation*

The quasiparticle operators $a^\dagger_\mu(q)$ and $a_\mu(q)$ associated with the moving-frame HB state $|\phi(q)\rangle$ are written in terms of the nucleon operators, $d^\dagger_k$ and $d_{\bar{k}}$, with definite signature as

$$\begin{pmatrix} a^\dagger_\mu(q) \\ a_{\bar{\mu}}(q) \end{pmatrix} = \sum_k{}' \begin{pmatrix} U_{\mu k}(q) & V_{\mu \bar{k}}(q) \\ V_{\bar{\mu} k}(q) & U_{\bar{\mu}\bar{k}}(q) \end{pmatrix} \begin{pmatrix} d^\dagger_k \\ d_{\bar{k}} \end{pmatrix}. \quad (4\cdot11)$$

Its inverse transformation is

$$\begin{pmatrix} d^\dagger_k \\ d_{\bar{k}} \end{pmatrix} = \sum_\mu{}' \begin{pmatrix} U_{k\mu}(q) & V_{k\bar{\mu}}(q) \\ V_{\bar{k}\mu}(q) & U_{\bar{k}\bar{\mu}}(q) \end{pmatrix} \begin{pmatrix} a^\dagger_\mu(q) \\ a_{\bar{\mu}}(q) \end{pmatrix}. \quad (4\cdot12)$$

The U and V matrices are determined by solving the moving-frame HB equation (4·1). Note that superscripts $\tau\,(=n,p)$ for U, V, and the Fermion operators are omitted for simplicity.

The moving-frame Hamiltonian is written

$$\hat{h}_M(q) = \sum_{\tau} {\sum_{kl\in\tau}}' \left((h_M^{(\tau)})_{kl}(q)(d_k^\dagger d_l + d_{\bar{k}}^\dagger d_{\bar{l}}) - \Delta_{k\bar{l}}^{(\tau)}(q)(d_k^\dagger d_{\bar{l}}^\dagger + d_{\bar{l}} d_k) \right), \tag{4·13}$$

where the particle-hole part and the particle-particle part of the moving-frame Hamiltonian are given by

$$(h_M^{(\tau)})_{ll'}(q) = h_{ll'}^{(\tau)}(q) - \lambda^{(\tau)}(q)\delta_{ll'} - \frac{\partial V}{\partial q}(q) Q_{ll'}^{(\tau)}(q), \tag{4·14}$$

$$h_{ll'}^{(\tau)} = \varepsilon_l^{(\tau)}\delta_{ll'} - \sum_{s\in ph} \kappa_s \langle\phi(q)|\, \hat{F}_s^{(+)}\, |\phi(q)\rangle\, (l|\hat{F}_s^{(+)}|l'), \tag{4·15}$$

$$\Delta_{l\bar{l}'}^{(\tau)} = \sum_{s\in pp,hh} \kappa_s \langle\phi(q)|\, \hat{F}_s^{(+)}\, |\phi(q)\rangle\, (0|\hat{F}_s^{(+)}|l\bar{l}'). \tag{4·16}$$

The matrix elements $(k|\hat{F}_s^{(+)}|l)$ are defined by

$$(l|\hat{F}_s^{(+)}|\bar{l}') = (0|d_l \hat{F}_s^{(+)} d_{\bar{l}}^\dagger|0), \quad (0|\hat{F}_s^{(+)}|l\bar{l}') = (0|\hat{F}_s^{(+)} d_l^\dagger d_{\bar{l}'}^\dagger|0), \tag{4·17}$$

where $|0)$ denotes the vacuum for nucleon operators.

The moving-frame HB equation is thus written

$${\sum_{ll'\in\tau}}' \left((h_M^{(\tau)})_{ll'}(q) U_{l'k}(q) + \Delta_{ll'}^{(\tau)}(q) V_{l'k}(q) \right) = E_k^{(\tau)} U_{lk}(q), \tag{4·18a}$$

$${\sum_{ll'\in\tau}}' \left(\Delta_{ll'}^{(\tau)}(q) U_{l'k}(q) + (h_M^{(\tau)})_{ll'}(q) V_{l'k}(q) \right) = -E_k^{(\tau)} V_{lk}(q), \tag{4·18b}$$

where $E_k^{(\tau)}$ denotes the quasiparticle energy. These equations are solved under the following three constraints:

$$\langle\phi(q)|\, \hat{N}^{(n)}\, |\phi(q)\rangle = N_0^{(n)}, \tag{4·19}$$

$$\langle\phi(q)|\, \hat{N}^{(p)}\, |\phi(q)\rangle = N_0^{(p)}, \tag{4·20}$$

$$\langle\phi(q)|\, \hat{Q}(q-\delta q)\, |\phi(q)\rangle = \delta q. \tag{4·21}$$

The Lagrange multipliers $\lambda^{(n)}(q), \lambda^{(p)}(q)$ and $dV/dq(q)$ are determined such that these constraints are satisfied. The expectation values in the moving-frame Hamiltonian are updated using U_{lk} and V_{lk} thus obtained until self-consistency is realized.

In the quasiparticle representation, the moving-frame Hamiltonian, $\hat{h}_M(q)$, the neutron and proton number operators, $\tilde{N}^{(\tau)}$, and the operators $\hat{F}_s^{(\pm)}$ with $K=0$ and 2 in the $r=1$ sector are written in the following forms:

$$\hat{h}_M(q) = \langle\phi(q)|\, \hat{h}_M(q)\, |\phi(q)\rangle + {\sum_{\mu}}' \left(E_\mu(q) \boldsymbol{B}_{\mu\mu}(q) + E_{\bar{\mu}}(q) \boldsymbol{B}_{\bar{\mu}\bar{\mu}}(q) \right), \tag{4·22}$$

$$\tilde{N}^{(\tau)} = \sum_{\mu\bar{\nu}}{}' N_A^{(\tau)}(\mu\bar{\nu})(\boldsymbol{A}^\dagger_{\mu\bar{\nu}}(q) + \boldsymbol{A}_{\mu\bar{\nu}}(q)) + \sum_{\mu}{}' N_B^{(\tau)}(\mu\mu)(\boldsymbol{B}_{\mu\mu}(q) + \boldsymbol{B}_{\bar{\mu}\bar{\mu}}(q)), \tag{4·23}$$

$$\begin{aligned}\hat{F}_s^{(\pm)} &= \langle\phi(q)|\,\hat{F}_s^{(\pm)}\,|\phi(q)\rangle + \sum_{\mu\bar{\nu}}{}' F_{A,s}^{(\pm)}(\mu\bar{\nu})(\boldsymbol{A}^\dagger_{\mu\bar{\nu}}(q) + \boldsymbol{A}_{\mu\bar{\nu}}(q)) \\ &\quad + \sum_{\mu\nu}{}' F_{B,s}^{(\pm)}(\mu\nu)(\boldsymbol{B}_{\mu\nu}(q) + \boldsymbol{B}_{\bar{\mu}\bar{\nu}}(q)),\end{aligned} \tag{4·24}$$

where

$$\boldsymbol{A}^\dagger_{\mu\bar{\nu}}(q) = a^\dagger_\mu(q)a^\dagger_{\bar{\nu}}(q), \quad \boldsymbol{A}_{\mu\bar{\nu}}(q) = a_{\bar{\nu}}(q)a_\mu(q), \quad \boldsymbol{B}_{\mu\nu}(q) = a^\dagger_\mu(q)a_\nu(q). \tag{4·25}$$

Explicit expressions for the matrix elements $N_A^{(\tau)}, N_B^{(\tau)}, F_{A,s}^{(\pm)}$ and $F_{B,s}^{(\pm)}$ are given in Appendix A.

We define the monopole-pairing gaps $\Delta_0^{(\tau)}(q)$, the quadrupole-pairing gaps $\Delta_{2,K=0,2}^{(\tau)}(q)$, and the quadrupole deformations $D_{2,K=0,2}^{(+)}(q)$ by

$$\Delta_0^{(\tau)}(q) = G_0^{(\tau)}\,\langle\phi(q)|\,\hat{A}^{(\tau)(+)}\,|\phi(q)\rangle\,, \tag{4·26}$$

$$\Delta_{2,K=0,2}^{(\tau)}(q) = G_{2,K=0,2}^{(\tau)}\,\langle\phi(q)|\,\hat{B}_{2,K=0,2(+)}^{(\tau)(+)}\,|\phi(q)\rangle\,, \tag{4·27}$$

$$D_{2,K=0,2}^{(+)}(q) = \langle\phi(q)|\,\hat{D}_{2,K=0,2}^{(+)}\,|\phi(q)\rangle\,. \tag{4·28}$$

4.4. *The moving-frame QRPA equations*

The infinitesimal generators $\hat{Q}(q)$ and $\hat{P}(q)$ are represented in the quasiparticle representation as

$$\begin{aligned}\hat{Q}(q) &= Q^A(q) + Q^B(q) \\ &= \sum_{\mu\bar{\nu}}{}' Q^A_{\mu\bar{\nu}}(q)(\boldsymbol{A}^\dagger_{\mu\bar{\nu}}(q) + \boldsymbol{A}_{\mu\bar{\nu}}(q)) + \sum_{\mu\nu}{}' Q^B_{\mu\nu}(q)(\boldsymbol{B}_{\mu\nu}(q) + \boldsymbol{B}_{\bar{\mu}\bar{\nu}}(q)),\end{aligned} \tag{4·29}$$

$$\hat{P}(q) = i\sum_{\mu\bar{\nu}}{}' P_{\mu\bar{\nu}}(q)(\boldsymbol{A}^\dagger_{\mu\bar{\nu}}(q) - \boldsymbol{A}_{\mu\bar{\nu}}(q)). \tag{4·30}$$

In the following, we discuss the method for obtaining the n-th solution of the moving-frame QRPA equations in *Step 3* assuming that the $(n-1)$-th solution $\hat{Q}^{(n-1)}(q)$ is already known. For later convenience, we introduce the one-body operator

$$\begin{aligned}\hat{R}_s^{(\pm)} &= \left[\hat{F}_s^{(\pm)}, \frac{\partial V}{\partial q}\hat{Q}^{(n-1)}(q)\right] \\ &= \langle\phi(q)|\,\hat{R}_s^{(\pm)}\,|\phi(q)\rangle + \sum_{\mu\bar{\nu}}{}' R_{A,s}^{(\pm)}(\mu\bar{\nu})(\boldsymbol{A}^\dagger_{\mu\bar{\nu}} \mp \boldsymbol{A}_{\mu\bar{\nu}}) + \sum_{\mu\nu}{}' R_{B,s}^{(\pm)}(\mu\nu)(\boldsymbol{B}_{\mu\nu} + \boldsymbol{B}_{\bar{\mu}\bar{\nu}}),\end{aligned} \tag{4·31}$$

with

$$R_{A,s}^{(\pm)}(\mu\bar{\nu}) = \frac{\partial V}{\partial q}\sum_{\rho}{}' \Big(F_{B,s}^{(\pm)}(\mu\rho)(Q^A_{\rho\bar{\nu}})^{(n-1)} \pm (Q^A_{\mu\bar{\rho}})^{(n-1)}F_{B,s}^{(\pm)}(\bar{\rho}\bar{\nu})$$

$$-(Q^B_{\mu\rho})^{(n-1)}F^{(\pm)}_{A,s}(\rho\bar{\nu}) - F^{(\pm)}_{A,s}(\mu\bar{\rho})(Q^B_{\bar{\rho}\bar{\nu}})^{(n-1)}\Big). \tag{4·32}$$

We can express the matrix elements $Q^A_{\mu\bar{\nu}}(q)$ and $P_{\mu\bar{\nu}}(q)$ using Eqs. (4·2) and (4·3) as

$$\begin{aligned}(Q^A_{\mu\bar{\nu}}(q))^{(n)} =& {\sum_{\mu'\bar{\nu}'}}' g_2(\mu\bar{\nu},\mu'\bar{\nu}')\left\{\sum_s\left(F^{(+)}_{A,s}(\mu'\bar{\nu}')f^{(+)}_{PR,s}(q) - R^{(-)}_{A,s}(\mu'\bar{\nu}')f^{(-)}_{Q,s}(q)\right)\right.\\ &\left.+\sum_\tau N^{(\tau)}(\mu'\bar{\nu}')f^{(\tau)}_N(q)\right\} + g_1(\mu\bar{\nu},\mu'\bar{\nu}')\sum_s F^{(-)}_{A,s}(\mu'\bar{\nu}')f^{(-)}_{Q,s}(q), \quad (4·33)\\ P_{\mu\bar{\nu}}(q) =& {\sum_{\mu'\bar{\nu}'}}' g_3(\mu\bar{\nu},\mu'\bar{\nu}')\left\{\sum_s\left(F^{(+)}_{A,s}(\mu'\bar{\nu}')f^{(+)}_{PR,s}(q) - R^{(-)}_{A,s}(\mu'\bar{\nu}')f^{(-)}_{Q,s}(q)\right)\right.\\ &\left.+\sum_\tau N^{(\tau)}(\mu'\bar{\nu}')f^{(\tau)}_N(q)\right\} + g_4(\mu\bar{\nu},\mu'\bar{\nu}')\sum_s F^{(-)}_{A,s}(\mu'\bar{\nu}')f^{(-)}_{Q,s}(q), \quad (4·34)\end{aligned}$$

where $f^{(+)}_{PR,s}(q) \equiv f^{(+)}_{P,s}(q) + f^{(+)}_{R,s}(q)$. The metrics $g_i\,(i = 1-4)$ are defined by

$$\begin{aligned} g_1(\mu\bar{\nu},\mu'\bar{\nu}') &\equiv (\mathcal{M}^{-1}\mathcal{E})_{\mu\bar{\nu},\mu'\bar{\nu}'}, \qquad g_2(\mu\bar{\nu},\mu'\bar{\nu}') \equiv (\mathcal{M}^{-1})_{\mu\bar{\nu},\mu'\bar{\nu}'}, \quad (4·35)\\ g_3(\mu\bar{\nu},\mu'\bar{\nu}') &\equiv (\mathcal{E}\mathcal{M}^{-1})_{\mu\bar{\nu},\mu'\bar{\nu}'}, \qquad g_4(\mu\bar{\nu},\mu'\bar{\nu}') \equiv (\mathcal{E}\mathcal{M}^{-1}\mathcal{E})_{\mu\bar{\nu},\mu'\bar{\nu}'} - \delta_{\mu\mu'}\delta_{\bar{\nu}\bar{\nu}'}, \quad (4·36)\end{aligned}$$

where $\mathcal{M}$ and $\mathcal{E}$ are given by

$$\begin{aligned}\mathcal{M}_{\mu\bar{\nu},\mu'\bar{\nu}'}(\omega^2(q)) =& \{(E_\mu + E_{\bar{\nu}})^2 - \omega^2(q)\}\delta_{\mu\mu'}\delta_{\bar{\nu}\bar{\nu}'}\\ &+ \delta_{\mu\mu'}\left(\frac{1}{2}E_{\mu'} + E_{\nu'} - \frac{1}{2}E_{\bar{\nu}}\right)(Q^B_{\nu'\bar{\nu}})^{(n-1)}\frac{\partial V}{\partial q}(q),\\ &+ (Q^B_{\mu\mu'})^{(n-1)}\left(E_{\mu'} - \frac{1}{2}E_\mu + \frac{1}{2}E_{\bar{\nu}'}\right)\delta_{\bar{\nu}\bar{\nu}'}\frac{\partial V}{\partial q}(q), \quad (4·37)\\ \mathcal{E}_{\mu\bar{\nu},\mu'\bar{\nu}'} =& (E_\mu + E_{\bar{\nu}})\delta_{\mu\mu'}\delta_{\bar{\nu}\bar{\nu}'}. \quad (4·38)\end{aligned}$$

The quantities given in (4·6) and the canonical variable condition (2·14) can be expressed in terms of $(\hat{Q}^A(q))^{(n)}$ and $\hat{P}(q)$ as

$$\begin{aligned} f^{(-)}_{Q,s}(q) =& -\kappa_s\langle\phi(q)|\,[\hat{F}^{(-)}_s, \hat{Q}^{(n)}(q)]\,|\phi(q)\rangle = -2\kappa_s(F^{(-)}_{A,s}, (Q^A(q))^{(n)}), \quad (4·39)\\ f^{(+)}_{PR,s}(q) =& \kappa_s\langle\phi(q)|\,[\hat{F}^{(+)}_s, \frac{1}{i}B(q)\hat{P}(q)]\,|\phi(q)\rangle\\ &-\frac{1}{2}\kappa_s\langle\phi(q)|\left[\left[\hat{F}^{(+)}_s, \frac{\partial V}{\partial q}\hat{Q}^{(n-1)}(q)\right], \hat{Q}^{(n)}(q)\right]|\phi(q)\rangle\\ =& 2\kappa_s(F^{(+)}_{A,s}, P(q)) - \kappa_s(R^{(+)}_{A,s}, (Q^A(q))^{(n)}), \quad (4·40)\end{aligned}$$

$$\langle\phi(q)|\,[\hat{N}^{(\tau)}, \hat{P}(q)]\,|\phi(q)\rangle = -2i(N^{(\tau)}_A, P(q)) = 0, \tag{4·41}$$

where

$$(X,Y) \equiv \sum_{\mu\bar{\nu}}{}' X(\mu\bar{\nu})Y(\mu\bar{\nu}). \tag{4·42}$$

Substituting Eqs. (4·39), (4·40) and (4·41) into Eqs. (4·33) and (4·34), we derive the dispersion equation

$$\boldsymbol{S}\cdot\boldsymbol{f} = \sum_{s'\tau'} \begin{pmatrix} S^{Q,Q}_{ss'} & S^{Q,PR}_{ss'} & S^{Q,N}_{s\tau'} \\ S^{PR,Q}_{ss'} & S^{PR,PR}_{ss'} & S^{PR,N}_{s\tau'} \\ S^{N,Q}_{\tau s'} & S^{N,PR}_{\tau s'} & S^{N,N}_{\tau\tau'} \end{pmatrix} \begin{pmatrix} f^{(-)}_{Q,s'}(q) \\ f^{(+)}_{PR,s'}(q) \\ f^{(\tau')}_{N}(q) \end{pmatrix} = 0, \tag{4·43}$$

where the matrix elements of $\boldsymbol{S}$ are given by

$$\begin{aligned}
S^{Q,Q}_{ss'} &= 2(F^{(-)}_{A,s}, F^{(-)}_{A,s'})_{g_1} - 2(F^{(-)}_{A,s}, R^{(-)}_{A,s'})_{g_2} - \frac{1}{\kappa_s}\delta_{ss'}, && (4·44a)\\
S^{Q,PR}_{ss'} &= 2(F^{(-)}_{A,s}, F^{(+)}_{A,s'})_{g_2}, && (4·44b)\\
S^{Q,N}_{s\tau'} &= 2(F^{(-)}_{A,s}, N^{(\tau')}_{A})_{g_2}, && (4·44c)\\
S^{PR,Q}_{ss'} &= 2(F^{(+)}_{A,s}, F^{(-)}_{A,s'})_{g_4} - 2(F^{(+)}_{A,s}, R^{(-)}_{A,s'})_{g_3} \\
&\quad + (R^{(+)}_{A,s}, F^{(-)}_{A,s'})_{g_1} - (R^{(+)}_{A,s}, R^{(-)}_{A,s'})_{g_2}, && (4·44d)\\
S^{PR,PR}_{ss'} &= 2(F^{(+)}_{A,s}, F^{(+)}_{A,s'})_{g_3} + (R^{(+)}_{A,s}, F^{(+)}_{A,s'})_{g_2} - \frac{1}{\kappa_s}\delta_{ss'}, && (4·44e)\\
S^{PR,N}_{s\tau'} &= 2(F^{(+)}_{A,s}, N^{(\tau')}_{A})_{g_3} + (R^{(+)}_{A,s}, N^{(\tau')}_{A})_{g_2}, && (4·44f)\\
S^{N,Q}_{\tau s'} &= (N^{(\tau)}_{A}, F^{(-)}_{A,s'})_{g_4} - (N^{(\tau)}_{A}, R^{(-)}_{A,s'})_{g_3}, && (4·44g)\\
S^{N,PR}_{\tau s'} &= (N^{(\tau)}_{A}, F^{(+)}_{A,s'})_{g_3}, && (4·44h)\\
S^{N,N}_{\tau\tau'} &= (N^{(\tau)}_{A}, N^{(\tau')}_{A})_{g_3}. && (4·44i)
\end{aligned}$$

The parentheses in the above matrix elements are defined by

$$(X,Y)_{g_i} = \sum_{\mu\bar{\nu}\mu'\bar{\nu'}}{}' X(\mu\bar{\nu})g_i(\mu\bar{\nu}\mu'\bar{\nu'})Y(\mu'\bar{\nu'}). \quad (i=1-4) \tag{4·45}$$

As mentioned above, the ASCC equations are invariant under the gauge transformation associate with number fluctuations. The quantities

$$f^{(-)}_{Q,s=1,2}(q) = -2G_0^{(\tau=n,p)} \langle\phi(q)|\,[\hat{A}^{(\tau=n,p)(-)}, \hat{Q}(q)]\,|\phi(q)\rangle \tag{4·46}$$

and $f^{(\tau)}_N(q)$ are transformed under (2·23) as

$$\begin{aligned}
f^{(-)}_{Q,s=1,2}(q) &\to f^{(-)}_{Q,s=1,2}(q) - 4\alpha^{(\tau=n,p)}\Delta_0^{(\tau=n,p)}(q), && (4·47)\\
f^{(\tau=n,p)}_{N}(q) &\to f^{(\tau=n,p)}_{N}(q) - \alpha^{(\tau=n,p)}\omega^2(q). && (4·48)
\end{aligned}$$

Thus, we have to fix the gauge when solving the dispersion equation (4·43). For both neutrons and protons, we choose the "ETOP" gauge,[56]

$$f^{(-)}_{Q,s=1}(q) = 0, \quad f^{(-)}_{Q,s=2}(q) = 0. \tag{4·49}$$

This gauge-fixing condition reduces the dimension of the dispersion equations. We can then use the submatrix $\boldsymbol{S'}$ of $\boldsymbol{S}$, where terms related to the anti-Hermite part of the monopole pairing operators, $(\hat{F}^{(-)}_{s=1,2})$, are dropped. From Eq. (4·43), the moving-frame QRPA frequency squared, $\omega^2(q)$, is determined by the condition

$$\det \boldsymbol{S'}(\omega^2(q)) = 0. \tag{4·50}$$

The solution with the smallest value of $\omega^2(q)$ (including negative values) is regarded as the most collective mode at q. Note that we consider imaginary $\omega(q)$ solutions as well as real ones. Once $\omega^2(q)$ is determined, $\boldsymbol{f}(q)$, $(Q^A_{\mu\bar{\nu}}(q))^{(n)}$ and $P_{\mu\bar{\nu}}(q)$ can be obtained by use of the normalization condition

$$\langle\phi(q)|\,[(\hat{Q}^A(q))^{(n)}, \hat{P}(q)]\,|\phi(q)\rangle = 2i((Q^A(q))^{(n)}, P(q)) = i. \tag{4·51}$$

§5. Requantization of the collective Hamiltonian

5.1. *Requantization and construction of wave functions in the laboratory frame*

Solving the basic equations of the ASCC method and the Thouless-Valatin equations, we obtain the collective Hamiltonian (2·24); we can set the collective mass $B(q)^{-1}$ to unity without loss of generality, because it merely defines the scale for measuring the length of the collective path. We also set the number fluctuation $\boldsymbol{n}$ to zero. Requantization is carried out simply by replacing the classical variables with the quantum operators:

$$p \to \frac{\hbar}{i}\frac{\partial}{\partial q}, \quad I_i \to \hat{I}_i, \tag{5·1}$$

where $\hat{I}_i$ are three components of the angular momentum operator acting on three Euler angles that define the orientation of the principal axes with respect to the laboratory frame. The Schrödinger equation for the requantized collective Hamiltonian is

$$\left(-\frac{1}{2}\frac{\partial^2}{\partial q^2} + \sum_{i=1}^{3}\frac{\hat{I}_i^2}{2\mathcal{J}_i(q)} + V(q)\right)\Psi_{IMk}(q,\Omega) = E_{I,k}\Psi_{IMk}(q,\Omega). \tag{5·2}$$

The collective wave function in the laboratory frame, $\Psi_{IM,k}(q,\Omega)$, is a function of the collective coordinate q and the three Euler angles Ω, and it is specified by the total angular momentum I, its projection M on the laboratory z-axis, and the index k distinguishing different quantum states having the same I and M. Note that the three components $\hat{I}_i$ of the angular momentum operator are defined with respect to the principal axes $(1,2,3) \equiv (x',y',z')$ associated with the moving-frame HB state $|\phi(q)\rangle$.

Using the rotational wave functions $\mathscr{D}^I_{MK}(\Omega)$, we can write the collective wave functions in the laboratory frame as

$$\Psi_{IMk}(q,\Omega) = \sum_{K=-I}^{I} \Phi'_{IKk}(q)\sqrt{\frac{2I+1}{8\pi^2}}\mathscr{D}^I_{MK}(\Omega) \tag{5·3}$$

$$= \sum_{K=0}^{I} \Phi_{IKk}(q)\,\langle\Omega|IMK\rangle\,. \tag{5·4}$$

Here, Φ'_{IKk} are intrinsic wave functions that represent the large-amplitude collective vibrations responsible for the oblate-prolate shape mixing. They are specified by the projection K of the angular momentum on the intrinsic z'-axis, instead of by M. We assume that the intrinsic states have positive signature. Then, their K and $-K$ components are connected by

$$\Phi'_{IKk}(q) = (-)^I\Phi'_{I-Kk}(q). \tag{5·5}$$

Accordingly, it is convenient to use new rotational wave functions, defined by

$$\langle\Omega|IMK\rangle = \frac{1}{\sqrt{2(1+\delta_{K0})}}\sqrt{\frac{2I+1}{8\pi^2}}\left(\mathscr{D}^I_{MK}(\Omega) + (-)^I\mathscr{D}^I_{M-K}(\Omega)\right), \tag{5·6}$$

and new vibrational wave functions,

$$\Phi_{IKk}(q) = \sqrt{\frac{2}{1+\delta_{K0}}}\Phi'_{IKk}(q) = (-)^I\sqrt{\frac{2}{1+\delta_{K0}}}\Phi'_{I-Kk}(q), \tag{5·7}$$

in place of $\Phi'_{IK,k}$. Because the $\mathscr{D}$ functions are normalized as

$$\int d\Omega\mathscr{D}^{I*}_{MK}(\Omega)\mathscr{D}^{I'}_{M'K'}(\Omega) = \frac{8\pi^2}{2I+1}\delta_{II'}\delta_{MM'}\delta_{KK'}, \tag{5·8}$$

the normalization of the vibrational wave functions is given by

$$\int dq \sum_{K=0}^{I} \Phi^*_{IKk}(q)\Phi_{IKk'}(q) = \delta_{kk'}. \tag{5·9}$$

5.2. *Boundary conditions*

Multiplying the Schrödinger equation (5·2) from the left by a rotational wave function $\langle\Omega|IMK\rangle$ and integrating out the Euler angles Ω, we obtain the collective Schrödinger equation for large-amplitude vibration:

$$\left(-\frac{1}{2}\frac{\partial^2}{\partial q^2} + V(q)\right)\Phi_{IKk}(q) + \sum_{K'=0}^{I}\langle IMK|\,\hat{T}_{\rm rot}\,\big|IMK'\big\rangle\,\Phi_{IK'k}(q) = E_{I,k}\Phi_{IKk}(q), \tag{5·10}$$

where $\hat{T}_{\rm rot} = \sum_i \hat{I}_i^2/(2\mathcal{J}_i(q))$.

The boundary conditions can be specified by projecting the collective path onto the (β, γ) plane and by using the well-known symmetry properties of the Bohr-Mottelson collective Hamiltonian.[5),79)] The deformation parameters β and γ are defined by

$$\beta(q)\cos\gamma(q) = \chi' \langle\phi(q)|\, \hat{D}^{(+)}_{20}\, |\phi(q)\rangle /(\hbar\omega_0 b^2), \tag{5·11}$$

$$\beta(q)\sin\gamma(q) = \sqrt{2}\chi' \langle\phi(q)|\, \hat{D}^{(+)}_{22}\, |\phi(q)\rangle /(\hbar\omega_0 b^2), \tag{5·12}$$

and they measure the magnitude and triaxiality of the quadrupole deformation of the HB mean field in the moving-frame as functions of the collective coordinate q. Here, $\hbar\omega_0$ denotes the frequency of the harmonic-oscillator potential, $\chi' \equiv \chi b^4$, and the harmonic-oscillator length parameter b is related to the radius parameter r_0 by

$$b^2 = \frac{4}{5}\left(\frac{2}{3}\right)^{\frac{1}{3}} r_0^2 A^{\frac{1}{3}}. \tag{5·13}$$

The boundary conditions for the vibrational collective wave functions are specified according to the form of the collective path in the (β, γ) plane. As we discuss in §6.3, the collective path for ^{68}Se passes through the γ-direction (see Fig.1). In this case, the following boundary conditions are employed in the prolate and oblate limits. In the prolate limit, $\gamma(q_{\rm pro}) \to 0^\circ$, the vibrational wave functions must satisfy

$$\Phi_{IKk}(q_{\rm pro} - q) = (-)^{\frac{K}{2}} \Phi_{IKk}(q_{\rm pro} + q), \tag{5·14}$$

which is equivalent to

$$\Phi_{IKk}(q_{\rm pro}) = 0, \quad (K = 2, 6, \cdots) \tag{5·15}$$

$$\left.\frac{d\Phi_{IKk}}{dq}\right|_{q=q_{\rm pro}} = 0. \quad (K = 0, 4, \cdots) \tag{5·16}$$

In the oblate limit, $\gamma(q_{\rm ob}) \to 60^\circ$, the HB mean field is symmetric about the intrinsic y'-axis, and thus the boundary conditions are given by[79)]

$$\Phi_{IKk}(q_{\rm ob} - q) = (-)^{\frac{K}{2}} \sum_{K'} \frac{2}{\sqrt{(1+\delta_{K0})(1+\delta_{K'0})}} \mathscr{D}^I_{KK'}\left(\frac{\pi}{2}, \frac{\pi}{2}, \pi\right) \Phi_{IK'k}(q_{\rm ob} + q). \tag{5·17}$$

In the case of ^{72}Kr, the collective path connecting the oblate and prolate shapes is not periodic with respect to the γ-direction (see Fig. 3). Accordingly, we set the box boundary conditions at the edge of the path:

$$\Phi_{IKk}(q_{\rm min}) = \Phi_{IKk}(q_{\rm max}) = 0. \tag{5·18}$$

The matrix elements $\langle IMK|\, \hat{T}_{\rm rot}\, |IMK'\rangle$ of the rotational kinetic energy operator in Eq. (5·10) can be easily calculated:

$$\langle IMK|\, \hat{T}_{\rm rot}\, |IMK\rangle = a(q)I(I+1) + b(q)K^2, \tag{5·19}$$

$$\begin{aligned}\langle IMK|\, \hat{T}_{\rm rot}\, |IM, K+2\rangle &= \langle IM, K+2|\, \hat{T}_{\rm rot}\, |IMK\rangle \\ &= c(q)\{(I+K+2)(I+K+1)(I-K)(I-K-1)\}^{-\frac{1}{2}},\end{aligned} \tag{5·20}$$

where

$$a(q) = \frac{1}{4}\left(\frac{1}{\mathcal{J}_1(q)} + \frac{1}{\mathcal{J}_2(q)}\right), \tag{5·21}$$

$$b(q) = \frac{1}{4}\left(\frac{2}{\mathcal{J}_3(q)} - \frac{1}{\mathcal{J}_1(q)} - \frac{1}{\mathcal{J}_2(q)}\right), \tag{5·22}$$

$$c(q) = \frac{1}{8}\left(\frac{1}{\mathcal{J}_1(q)} - \frac{1}{\mathcal{J}_2(q)}\right). \tag{5·23}$$

The other matrix elements are zero.

5.3. *Electric quadrupole moments and transitions*

To evaluate the electric quadrupole (E2) moments and transition probabilities, we need to derive expressions for the E2 operator in the collective subspace. This can be easily done by using the procedure we used to derive the quantum collective Hamiltonian. As described below, we first evaluate the expectation values of the E2 operators with respect to the moving-frame HB state $|\phi(q,p)\rangle$ and then apply the canonical quantization procedure.

In accordance with the quadrupole operators (3·4), we define the E2 operators in the model space under consideration as

$$\hat{D}'^{(\mathrm{E2})}_{\mu} = \sum_{\tau} e^{(\tau)}_{\mathrm{eff}} \sum_{kl\in\tau} D^{(\tau)}_{2\mu}(kl) c^{\dagger}_{k} c_{l}, \tag{5·24}$$

$$\hat{D}'^{(\mathrm{E2})}_{\mu+} = \frac{1}{2}(\hat{D}'^{(\mathrm{E2})}_{\mu} + \hat{D}'^{(\mathrm{E2})}_{-\mu}), \tag{5·25}$$

where $e^{(\tau)}_{\mathrm{eff}}$ are the effective charges. Their expectation values in the collective subspace are expanded up to second order in the collective momentum p as

$$\begin{aligned} D'^{(\mathrm{E2})}_{\mu+}(q,p) &= \langle\phi(q,p)|\, \hat{D}'^{(\mathrm{E2})}_{\mu+}\, |\phi(q,p)\rangle \\ &= D'^{(\mathrm{E2})}_{\mu+}(q) + \frac{1}{2} D''^{(\mathrm{E2})}_{\mu+}(q) p^2, \end{aligned} \tag{5·26}$$

where

$$D'^{(\mathrm{E2})}_{\mu+}(q) = \langle\phi(q)|\, \hat{D}'^{(\mathrm{E2})}_{\mu+}\, |\phi(q)\rangle\,, \tag{5·27}$$

$$D''^{(\mathrm{E2})}_{\mu+}(q) = -\,\langle\phi(q)|\, [[\hat{D}'^{(\mathrm{E2})}_{\mu+}, \hat{Q}(q)], \hat{Q}(q)]\, |\phi(q)\rangle\,. \tag{5·28}$$

The quantities $D'^{(\mathrm{E2})}_{\mu+}(q,p)$ are called collective representations of the E2 operators. Note that these are defined in the intrinsic frame associated with the moving-frame HB mean field. We now apply the canonical quantization to them. Then, the collective coordinate q and the collective momentum p become quantum operators acting on the vibrational wave functions $\Phi_{IKk}(q)$. We call the requantized E2 operators "collective E2 operators" and denote them $\hat{D}'^{(\mathrm{E2})}_{\mu+}$. Thus, the E2 matrix elements between two collective vibrational states are evaluated as

$$\langle\Phi_{IKk}|\, \hat{D}'^{(\mathrm{E2})}_{\mu+}\, |\Phi_{IK'k'}\rangle = \int dq\, \Phi^{*}_{IKk}(q) \left(D'^{(\mathrm{E2})}_{\mu+}(q) - \frac{1}{2}\frac{d}{dq} D''^{(\mathrm{E2})}_{\mu+}(q) \frac{d}{dq}\right) \Phi_{IK'k'}(q). \tag{5·29}$$

We need to calculate these integrals only for vibrational states which satisfy the selection rules of the E2 operators. (As shown in §6, the contribution from the second term in the r.h.s. of Eq. (5·29) is negligible, so that the ordering problem in the canonical quantization procedure is not important here.)

The collective E2 operators $\hat{D}'^{(\mathrm{E2})}_{\mu}$ are defined in the intrinsic frame, and those in the laboratory frame $\hat{D}^{(\mathrm{E2})}_{\mu}$ are obtained as

$$\hat{D}^{(\mathrm{E2})}_{\mu} = \sum_{\mu} \mathscr{D}^{2}_{\mu\mu'}(\Omega)\hat{D}'^{(\mathrm{E2})}_{\mu'}. \tag{5·30}$$

As is well known, $B(\mathrm{E2})$ values and spectroscopic quadrupole moments $Q(Ik)$ are given in terms of reduced matrix elements $\langle Ik||\hat{D}^{(\mathrm{E2})}_{+}||Ik\rangle$ as

$$B(\mathrm{E2}; Ik \to I'k') = (2I+1)^{-1}\left|\langle Ik||\hat{D}^{(\mathrm{E2})}||I'k'\rangle\right|^2, \tag{5·31}$$

$$\begin{aligned} Q(Ik) &= \sqrt{\frac{16\pi}{5}}\,\langle I, M=I, k|\,\hat{D}^{(\mathrm{E2})}\,|I, M=I, k\rangle \\ &= \sqrt{\frac{16\pi}{5}}\begin{pmatrix} I & 2 & I \\ -I & 0 & I \end{pmatrix}\langle Ik||\hat{D}^{(\mathrm{E2})}_{\mu}||Ik\rangle. \end{aligned} \tag{5·32}$$

These reduced matrix elements can be evaluated by using the Wigner-Eckart theorem,

$$\langle I, M=I, k|\,\hat{D}^{(\mathrm{E2})}_{0}\,\big|I', M=I, k'\big\rangle = \begin{pmatrix} I & 2 & I' \\ -I & 0 & I \end{pmatrix}\langle I, k||\hat{D}^{(\mathrm{E2})}||I', k'\rangle, \tag{5·33}$$

and calculating the left-hand side as[79]

$$\begin{aligned} &\langle I, M=I, k|\hat{D}^{(\mathrm{E2})}_{0}\,\big|I', M=I, k'\big\rangle \\ &\quad= \frac{\sqrt{(2I+1)(2I'+1)}}{8\pi^2}\sum_{KK'\mu}\left\langle \Phi'_{IKk}\right|\hat{D}'^{(\mathrm{E2})}_{\mu}\left|\Phi'_{I'K'k'}\right\rangle\left\langle \mathscr{D}^{I}_{IK}\right|\mathscr{D}^{2}_{0\mu}\left|\mathscr{D}^{I'}_{IK'}\right\rangle \\ &\quad= \sqrt{(2I+1)(2I'+1)}\sum_{KK'\mu}\left\langle \Phi'_{IKk}\right|\hat{D}'^{(\mathrm{E2})}_{\mu}\left|\Phi'_{I'K'k'}\right\rangle \\ &\qquad (-)^{I-K}\begin{pmatrix} I & 2 & I' \\ -I & 0 & I \end{pmatrix}\begin{pmatrix} I & 2 & I' \\ -K & \mu & K' \end{pmatrix}. \end{aligned} \tag{5·34}$$

In the intrinsic frame, the $\mu = \pm 1$ components of the collective E2 operator vanish, and those for the $\mu = \pm 2$ components are equal. Thus we obtain

$$\begin{aligned} &\langle Ik||\hat{D}^{(\mathrm{E2})}||I'k'\rangle \\ &\quad= \sqrt{(2I+1)(2I'+1)}(-)^{I}\sum_{K\geq 0}\left[\begin{pmatrix} I & 2 & I' \\ -K & 0 & K \end{pmatrix}\langle \Phi_{IKk}|\,\hat{D}'^{(\mathrm{E2})}_{0+}\,|\Phi_{I'K'k'}\rangle\right. \\ &\qquad + \sqrt{1+\delta_{K0}}\left\{\begin{pmatrix} I & 2 & I' \\ -K-2 & 2 & K \end{pmatrix}\langle \Phi_{I,K+2,k}|\,\hat{D}'^{(\mathrm{E2})}_{2+}\,|\Phi_{I'Kk'}\rangle\right. \\ &\qquad \left.\left. + \begin{pmatrix} I & 2 & I' \\ K & 2 & -K-2 \end{pmatrix}(-)^{I+I'}\left\langle \Phi_{IKk}\right|\hat{D}'^{(\mathrm{E2})}_{2+}\left|\Phi_{I',K+2,k'}\right\rangle\right\}\right]. \end{aligned} \tag{5·35}$$

§6. Results of numerical calculation and discussion

6.1. *Details of numerical calculation*

In the numerical calculations, we considered two major shells ($N_{\rm sh} = 3, 4$) for protons and neutrons and used the same values for the single-particle energies, the monopole pairing strength $G_0^{(\tau)}$, and the quadrupole particle-hole interaction strength χ as in Ref. 75). The single-particle energies are listed in Table II. The interaction strengths were adjusted to approximately reproduce the pairing gaps and the quadrupole deformations obtained with the Skyrme-HFB calculation carried out by Yamagami et al.[67] These values are $G_0^{(n)} = G_0^{(p)} = 0.320$ and $\chi' \equiv \chi b^4 = 0.248$ MeV for ^{68}Se and $G_0^{(n)} = 0.299, G_0^{(p)} = 0.309$ and $\chi' = 0.255$ MeV for ^{72}Kr. The oscillator frequency and the radius parameters were set to $\hbar\omega_0 = 41.2A^{1/3}$ MeV and $r_0 = 1.2$ fm. For the quadrupole pairing strength, we used the self-consistent value derived by Sakamoto and Kishimoto,[82]

$$G_{2K}^{(\tau)\rm self} = \left[\sum_{\alpha\beta\in\tau} \frac{1}{4} \left(\frac{1}{E_\alpha} + \frac{1}{E_\beta} \right) |D_{2K}^{(\tau)}(\alpha\beta)|^2 \right]^{-1}, \tag{6·1}$$

where E_α is the quasiparticle energy evaluated using the BCS approximation in the case of spherical shape. Accordingly, we have $G_{20}^{\rm self} = G_{21}^{\rm self} = G_{22}^{\rm self}$.

The effective charges $e_{\rm eff}^{(\tau)}$ are written as $e_{\rm eff}^{(n)} = \delta e_{\rm pol}$ for neutrons and $e_{\rm eff}^{(p)} = e + \delta e_{\rm pol}$ for protons. For simplicity, we use the same polarization charge, $\delta e_{\rm pol} = 0.905e$, for protons and neutrons, which is chosen to reproduce the experimental $B({\rm E2};2_1^+ \to 0_1^+)$ value[66] in ^{72}Kr. Only these data are available for E2 transitions among low-lying states in ^{68}Se and ^{72}Kr. This value of $\delta e_{\rm pol}$ seems slightly too large and needs further investigation. We take into account the momentum-dependent term in the collective representation of the E2 operators, Eq. (5·26), although numerical calculations indicate that it gives only a few percent correction, at most, to the main term.

In the present calculation, we ignored the curvature terms [the fourth, fifth and sixth terms in Eq. (4·3)] in order to reduce the CPU time. We have verified that their contributions are negligible.

In the numerical calculations, careful treatment is necessary in the prolate limit, as the moment of inertia about the symmetry axis, $\mathcal{J}_3(q)$, vanishes there. Actually, this does not cause a problem, because the $K \neq 0$ components of the vibrational wave function also vanish there. To avoid numerical instability, however, we set $\mathcal{J}_3(q) = 10^{-13}\hbar^2$ (MeV)$^{-1}$ in the prolate limit, and we confirmed that this works well without losing numerical accuracy. We applied this recipe also in the oblate limit, where $\mathcal{J}_2(q)$ vanishes. Actually, the y'-axis component of the vibrational wave function also vanishes there, although this is not directly seen from Eq. (5·10), in which the wave functions are decomposed with respect to the K quantum numbers, choosing the z'-axis as the quantization axis.

Table II. Energies in units of MeV of the spherical single-particle levels used in the calculation. These values are taken from Ref. 75).

orbits	$1f_{7/2}$	$2p_{3/2}$	$1f_{5/2}$	$2p_{1/2}$	$1g_{9/2}$	$2d_{5/2}$	$1g_{7/2}$	$3s_{1/2}$	$2d_{3/2}$
neutrons	−9.02	−4.93	−2.66	−2.21	0.00	5.27	6.36	8.34	8.80
protons	−8.77	−4.23	−2.41	−1.50	0.00	6.55	5.90	10.10	9.83

6.2. *Properties of local minima in ^{68}Se and ^{72}Kr*

In Table III we list the results of the calculations for the properties of the HB equilibrium states (local minima in the potential energy surface). For both ^{68}Se and ^{72}Kr, the lowest HB minimum possesses an oblate shape, while the second minimum is prolate. The energy differences between the oblate and prolate minima evaluated using the P+Q Hamiltonian with (without) the quadrupole pairing interaction are 300 keV (196 keV) for ^{68}Se and 827 keV (626 keV) for ^{72}Kr. We thus find no qualitative change in the mean-field properties due to the inclusion of the quadrupole pairing interaction.

The QRPA collective modes at the oblate and prolate minima can be classified in terms of the projections of the angular momenta on the symmetry axis, K_y and $K_z \equiv K$, respectively. Table IV lists the properties of the QRPA collective modes at the oblate and prolate minima. In ^{68}Se, the lowest modes are γ-vibrational (K_y or K_z=2), and the second lowest modes are β-vibrational (K_y or K_z=0), both at the oblate and the prolate minima. It is seen that the quadrupole pairing interaction lowers their excitation energies without changing their ordering. In ^{72}Kr, the lowest QRPA modes at the two minima are both β-vibrational if the quadrupole pairing interaction is ignored. Note, however, that the $K_z = 0$ and 2 modes at the prolate local minimum are close in energy, and their ordering changes when the quadrupole pairing interaction is taken into account, whereas the lowest mode at the lowest oblate minimum is always β-vibrational.

6.3. *Collective path connecting the oblate and prolate minima in ^{68}Se*

We start by solving the basic equations of the ASCC method from the oblate minimum ($q = 0$) and progressively determine the collective path, following the algorithm outlined in §4.2. Figure 1 illustrates the collective path thus obtained by projecting it onto the (β, γ) potential energy surface. The path connects the two local minima passing through a potential valley lying in the triaxial deformed region. The

Table III. The quadrupole deformations and the pairing gaps $\Delta_0^{(\tau)}$ (in MeV) and $\Delta_{2K}^{(\tau)}$ (in MeV fm^2) at the HB local minima in ^{68}Se and ^{72}Kr, calculated using the P+Q Hamiltonian, including the quadrupole pairing interaction.

$(G_2 = G_2^{\rm self})$	β	γ	$\Delta_0^{(n)}$	$\Delta_0^{(p)}$	$\Delta_{20}^{(n)}$	$\Delta_{20}^{(p)}$	$\Delta_{22}^{(n)}$	$\Delta_{22}^{(p)}$
^{68}Se (oblate)	0.30	60°	1.17	1.26	0.08	0.09	0.10	0.11
^{68}Se (prolate)	0.26	0°	1.34	1.40	0.14	0.15	0	0
^{72}Kr (oblate)	0.35	60°	0.92	1.06	0.05	0.06	0.06	0.07
^{72}Kr (prolate)	0.38	0°	1.14	1.27	0.19	0.19	0	0

Table IV. The excitation energies ω (in MeV) and the K quantum numbers of the lowest two QRPA modes at the oblate and prolate minima in ^{68}Se and ^{72}Kr. The results of the calculation with ($G_2 = G_2^{\rm self}$) and without ($G_2 = 0$) the quadrupole pairing interaction are compared. The K quantum numbers here represent K_y or K_z, according to the shape (oblate or prolate).

	$G_2 = 0$				$G_2 = G_2^{\rm self}$			
	ω_1	K_1	ω_2	K_2	ω_1	K_1	ω_2	K_2
^{68}Se (oblate)	1.555	2	2.342	0	1.373	2	2.131	0
^{68}Se (prolate)	1.015	2	1.915	0	0.898	2	1.369	0
^{72}Kr (oblate)	1.150	0	1.909	0	1.239	0	2.010	2
^{72}Kr (prolate)	1.606	0	1.674	2	1.644	2	1.714	0

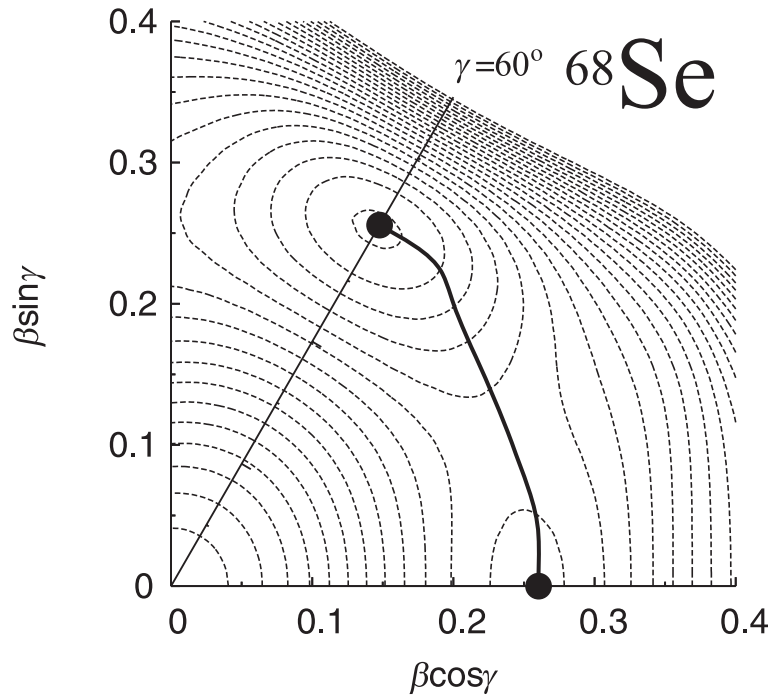

Fig. 1. The collective path for ^{68}Se calculated with the P+Q Hamiltonian including the quadrupole pairing interaction. The path is projected onto the (β, γ) potential energy surface. The dots in the figure indicate the HB local minima. Equipotential lines are drawn every 100 keV.

collective path for ^{68}Se obtained with the P+Q Hamiltonian including the quadrupole pairing interaction is very similar to that obtained in Ref. 75), in which its effect was ignored. As solutions of the ASCC equations, we obtain various quantities: the canonical collective coordinate q, the quadrupole deformations $\beta(q)$ and $\gamma(q)$, the monopole and quadruple pairing gaps $\Delta_0^{(\tau)}(q)$ and $\Delta_{2K}^{(\tau)}(q)$, the collective potential $V(q)$, the collective mass $M(s(q))$, the moving-frame QRPA frequency squared $\omega^2(q)$, and the three rotational moments of inertia $\mathcal{J}_i(q)$. These quantities are plotted in Fig. 2 as functions of $\gamma(q)$. It is seen that the quadrupole deformation $\beta(q)$ is almost constant along the collective path, while the triaxial deformation $\gamma(q)$ varies and

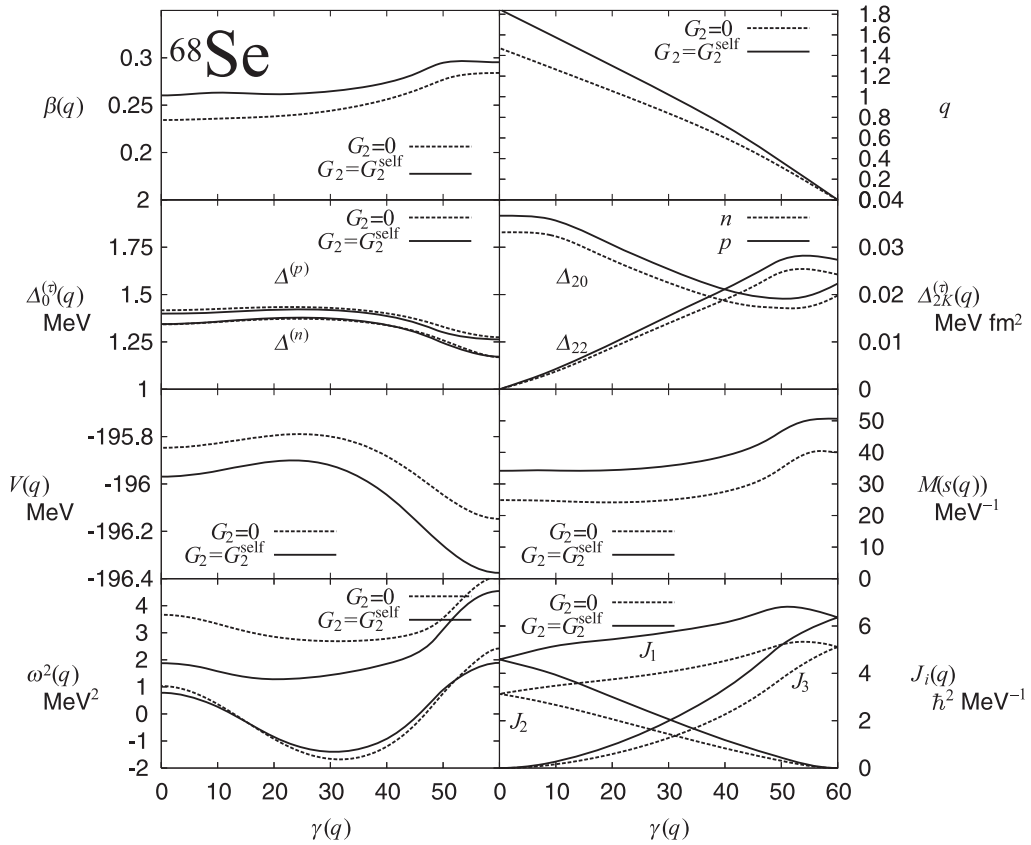

Fig. 2. Results of the calculation for ^{68}Se. The monopole pairing gap $\Delta_0^{(\tau)}(q)$, the quadrupole pairing gaps $\Delta_{20}^{(\tau)}(q)$ and $\Delta_{22}^{(\tau)}(q)$, the collective potential $V(q)$, the collective mass $M(s(q))$, the rotational moments of inertia $\mathcal{J}_i(q)$, the lowest two moving-frame QRPA frequencies squared $\omega^2(q)$, the axial quadrupole deformation $\beta(q)$, and the canonical collective coordinate q are plotted as functions of $\gamma(q)$. The results of the two calculations using the P+Q Hamiltonian with ($G_2 = G_2^{\rm self}$) and without ($G_2 = 0$) the quadrupole pairing interaction are compared.

changes from an oblate shape to a prolate shape. It is seen that the quadrupole pairing interaction slightly increases the values of $\beta(q)$ for all values of $\gamma(q)$.

The collective mass $M(s(q))$ plotted in Fig. 2 is defined as a function of the geometrical length, $ds = \sqrt{d\beta^2 + \beta^2 d\gamma^2}$, in the (β, γ) plane:

$$M(s(q)) = M(q)/\{(d\beta/dq)^2 + \beta^2(d\gamma/dq)^2\}. \tag{6·2}$$

As explained in §5.1, we can set $M(q) = B(q)^{-1} = 1\text{MeV}^{-1}$ here. We have found that the quadrupole pairing interaction increases the collective mass. This enhancement takes place almost independently of $\gamma(q)$, and it is mainly due to the decrease of $d\gamma/dq$ along the collective path.

Because the HB mean field becomes symmetric about the y'- and z'-axes in the oblate and prolate limits, respectively, the rotational moment of inertia about the y' (z')-axis vanishes, and the other two moments take the same values at the oblate (prolate) minimum. Their γ dependence is similar to that of the irrotational

moments of inertia. It is found the rotational moments of inertia increase by about $20-30\%$ through the effect of the quadrupole pairing interaction. This enhancement, as well as that of the inertial functions $M(s(q))$, is due to the time-odd pair field generated by the quadrupole pairing interaction.

6.4. *Collective path connecting the oblate and prolate minima in ^{72}Kr*

We have determined the collective path for ^{72}Kr starting from the oblate minimum. The collective path projected onto the (β, γ) plane is shown in Fig. 3, and various quantities defined along the collective path are plotted in Fig. 4 as functions of q. The collective paths calculated with and without the quadrupole pairing interaction are similar. Because the lowest mode of the moving-frame QRPA equations is β-vibrational around the oblate minimum, the path first goes along the axially symmetric line. Then, around $(\beta, \gamma) = (0.2, 60^\circ)$, the nature of the lowest mode changes to γ-vibrational, and thus the path deviates from the axially symmetric line. When the collective path reaches the $\gamma = 0^\circ$ line, the nature of the lowest mode again changes to β-vibrational. Approaching the prolate minimum, the nature of the lowest mode changes once more to γ-vibrational, and the collective path deviates from the $\gamma = 0^\circ$ line.

We note that the lowest two modes at the prolate local minimum are very close, and their ordering with respect to energy may be sensitive to the interactions used. We examined whether, for example, the lowest mode at the prolate local minimum becomes β-vibrational if the quadrupole pairing interaction is switched off, and in

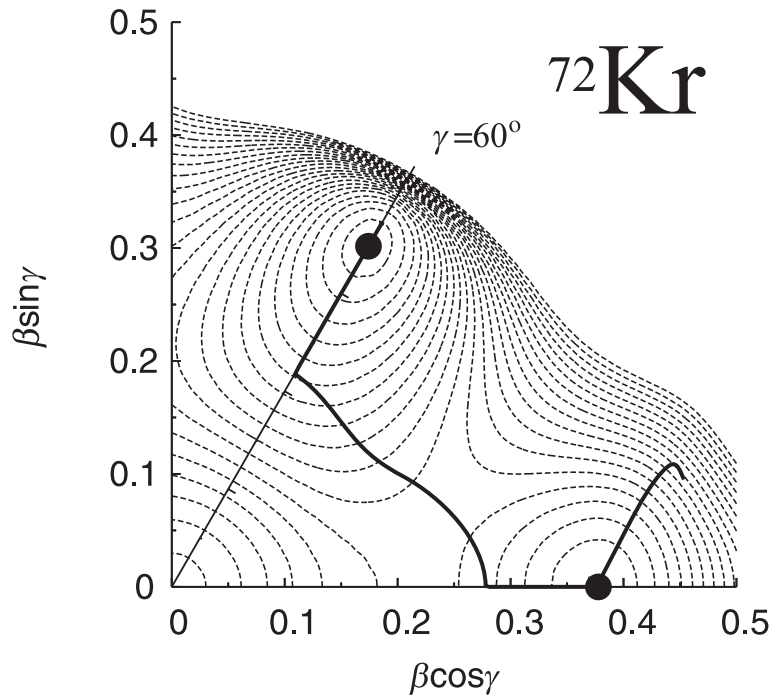

Fig. 3. The same as Fig. 1, but for ^{72}Kr.

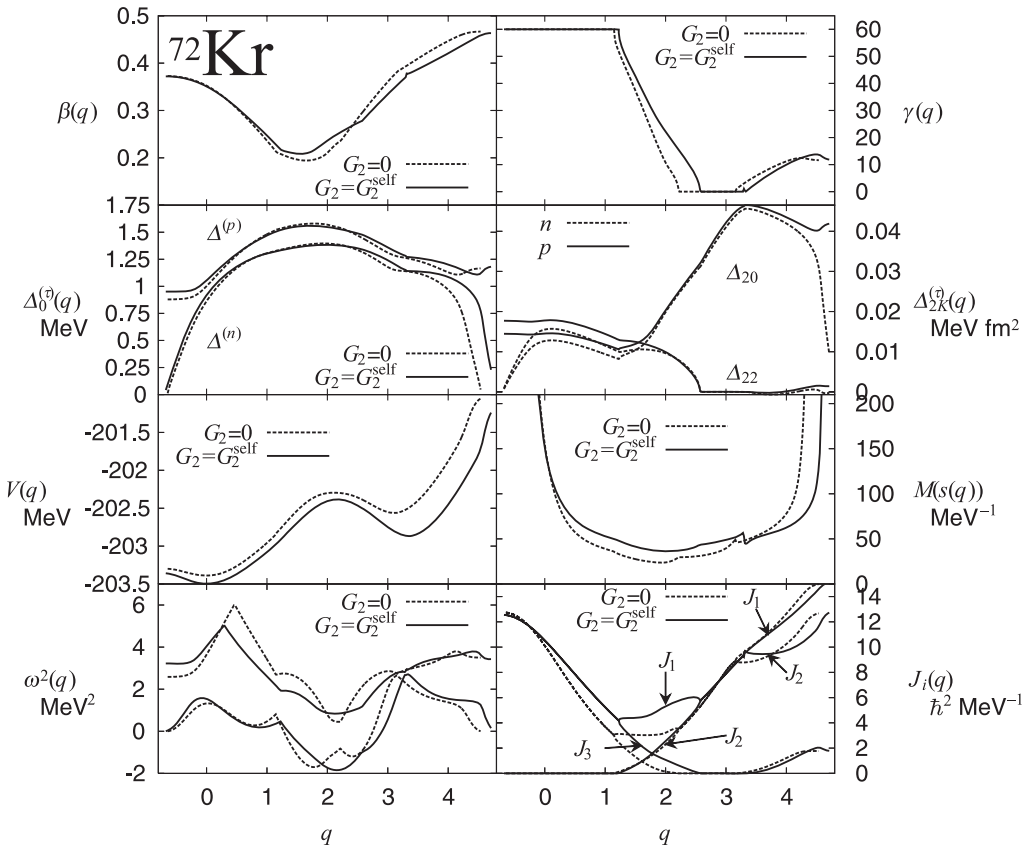

Fig. 4. Results of the calculations for ^{72}Kr. The notation here is the same as in Fig. 2, except that the quantities are plotted as functions of q along the collective path. The point $q = 0$ corresponds to the oblate minimum, while the prolate local minimum is located near $q = 3.3$ ($q = 3.1$) for the calculation using the P+Q Hamiltonian with (without) the quadrupole pairing interaction.

this case the axial symmetry breaking takes place at a larger value of β beyond the prolate local minimum. In such a situation, two collective coordinates may be needed to describe the collective dynamics more effectively. This is an interesting subject for future investigation. It should be emphasized that such a problem arises only locally in a small region in the (β, γ) plane, and the collective path is well-defined globally.

In the region of large β beyond the oblate minimum ($q < 0$) along the $\gamma = 60^\circ$ line, the lowest $K = 0$ mode exhibits a strong mixture of β-vibration (fluctuation of an axially symmetric shape) and neutron pairing vibration (fluctuation of pairing gaps), and the calculation to determine the collective path eventually stops when the neutron monopole pairing collapses.

We have found that the collective mass and the rotational moments of inertia increase also for ^{72}Kr, due to the time-odd pair field generated by the quadrupole pairing interaction. We note that the collective mass $M(s(q))$ diverges for large

deformations. This behavior, found also in previous works,[57),74),75)] is associated with the disappearance of the pairing gaps.

6.5. *Excitation spectra and quadrupole transitions in ^{68}Se*

The collective Schrödinger equation (5·2) was solved with the boundary conditions (5·14) and (5·17) for ^{68}Se to obtain energy spectra, quadrupole moments and transition probabilities. The results of the calculations are displayed in Fig. 5. The calculations yield the excited prolate rotational bands as well as the oblate ground state band. It is seen that the inter-band E2 transitions are weaker than the intra-band E2 transitions, indicating that the oblate-prolate shape coexistence picture is valid. The results of the calculation suggest the existence of an excited 0^+ state which has not yet been found in experiments. The spectroscopic quadrupole moments presented in Fig. 6 are also consistent with the oblate-prolate shape coexistence picture: The yrast states possess positive spectroscopic quadrupole moments, indicating oblate deformation, while the second lowest states for each angular momentum have negative values indicating prolate deformation. In Fig. 5, the excitation spectra calculated with and without the quadrupole pairing interaction are compared. We see that the quadrupole pairing plays an important role in decreas-

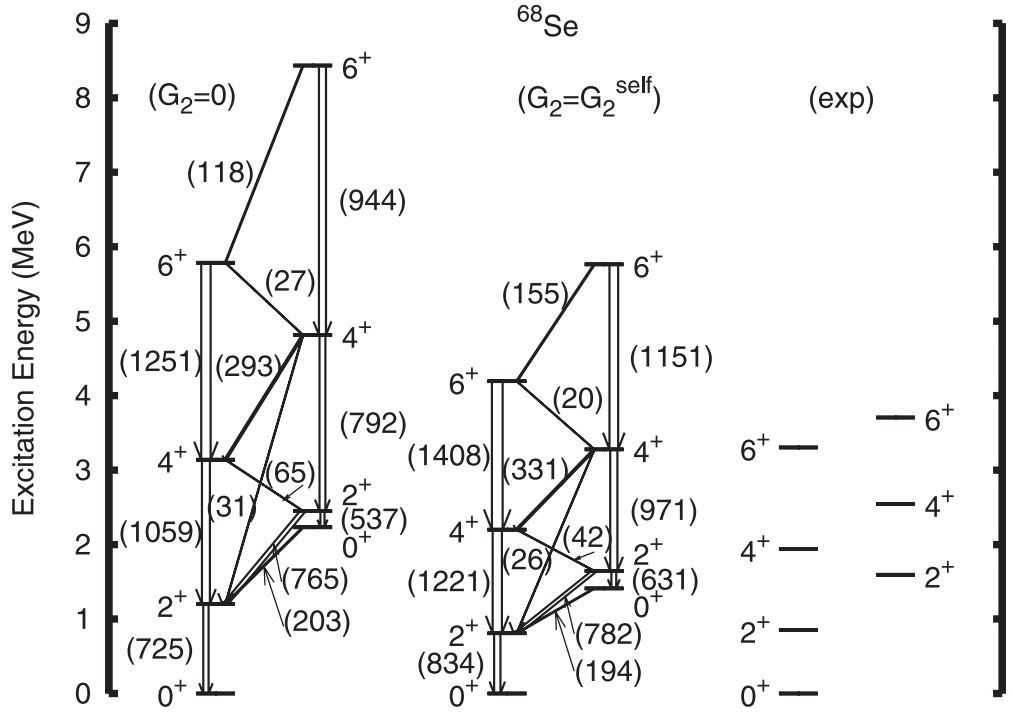

Fig. 5. Excitation spectra and B(E2) values of low-lying states in ^{68}Se calculated with the ASCC method. In the left (middle) panel, the quadrupole pairing is ignored (included) in the microscopic Hamiltonian. Experimental data[63)] are displayed in the right panel. The B(E2) values larger than 1 W.u. are indicated in the parentheses beside the arrows in units of e^2 fm^4.

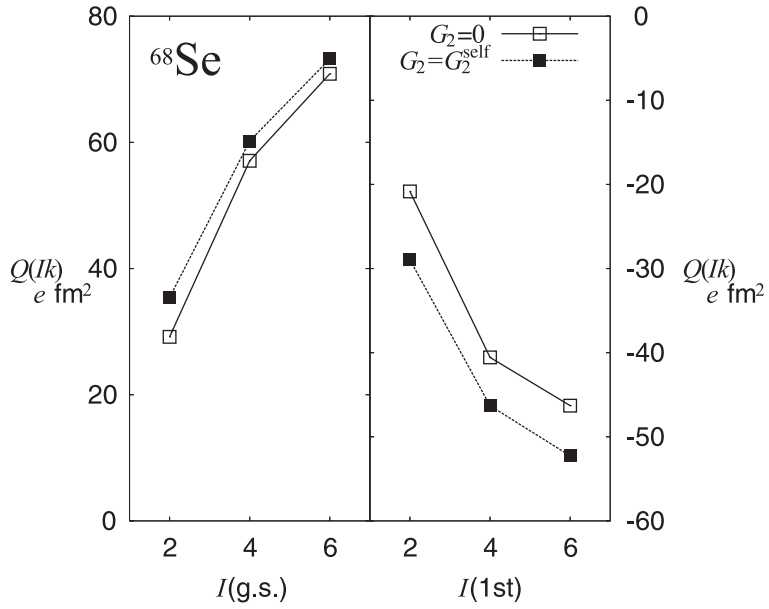

Fig. 6. Spectroscopic quadrupole moments of low-lying states in ^{68}Se. The left and right panels plot the spectroscopic quadrupole moments of the yrast states and of the second lowest states in each angular momentum, respectively. The units for the right panels are indicated beside the right vertical lines. The results of the calculations with (without) the quadrupole pairing interaction are indicated by the filled (open) squares.

ing the excitation energies. This is because the time-odd pair field generated by the quadrupole pairing enhances the collective mass and the rotational moments of inertia.

In Fig. 7, the vibrational wave functions are presented. It is seen that the behavior of the 0^+ states is significantly different from that of the $I \neq 0$ states: The vibrational wave functions of the lowest and the second lowest 0^+ states spread over the entire collective path, indicating that the oblate and prolate shapes are strongly mixed via the triaxial degree of freedom. In contrast to the 0^+ states, the $I \neq 0$ wave functions contain $K \neq 0$ components, which realize their maximum values in the oblate limit. We can see this trend more clearly by plotting the collective wave functions squared. This is done in Fig. 8. The vibrational wave function of the ground 0^+ state spreads over the entire region of γ, while that of the excited 0^+ state exhibits prominent peaks both in the oblate and prolate limits. By contrast, the vibrational wave functions of the $I \neq 0$ yrast states are localized around the oblate shape, while those of the second lowest states (for each angular momentum) are localized around the prolate shape. This localization becomes stronger with increasing angular momentum. In the yrast states, all the $K \neq 0$ components realize the maxima at the oblate shape, while the $K = 0$ component dominates at the prolate shape in the second lowest states.

In order to evaluate the oblate-prolate shape mixing in a more quantitative

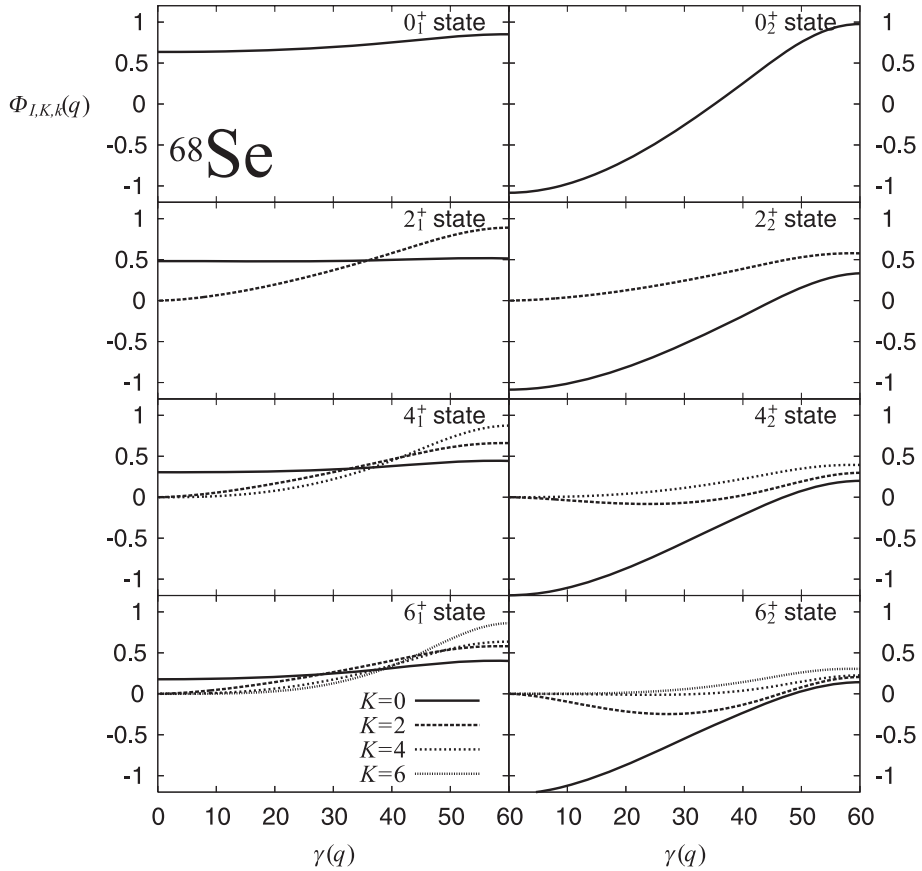

Fig. 7. Vibrational wave functions $\Phi_{IKk}(q)$ of the yrast states (*left*) and the second lowest states for each angular momentum (*right*) in ^{68}Se. In each panel, different K components of the vibrational wave functions are plotted as functions of $\gamma(q)$. The calculation was performed with the P+Q Hamiltonian including the quadrupole pairing interaction.

manner, we define the oblate and prolate probabilities as

$$P_{\rm ob}(I,k) = \int_{q_{\rm min}}^{q_0} dq \sum_{K=0}^{I} |\Phi_{IKk}(q)|^2, \quad P_{\rm pro}(I,k) = \int_{q_0}^{q_{\rm max}} dq \sum_{K=0}^{I} |\Phi_{IKk}(q)|^2, \quad (6{\cdot}3)$$

where we assume $q_{\rm min} \le q_{\rm ob} < q_0 < q_{\rm pro} \le q_{\rm max}$. The "boundary" between the oblate and the prolate regions is set to the top of the potential barrier between the two minima, or at $\gamma = 30^\circ$. Figure 9 displays these probabilities for ^{68}Se. The oblate and prolate states are strongly mixed in the 0^+ states. It is clearly seen that the shape mixing rapidly decreases as the angular momentum increases.

6.6. *Excitation spectra and quadrupole transitions in ^{72}Kr*

For ^{72}Kr, the collective Schrödinger equation is solved under the boundary conditions (5·18). The result of the calculation exhibits two coexisting rotational bands. [See the energy spectra and the B(E2) values displayed in Fig. 10.] The spectroscopic quadrupole moments presented in Fig. 11 indicate that the yrast band is

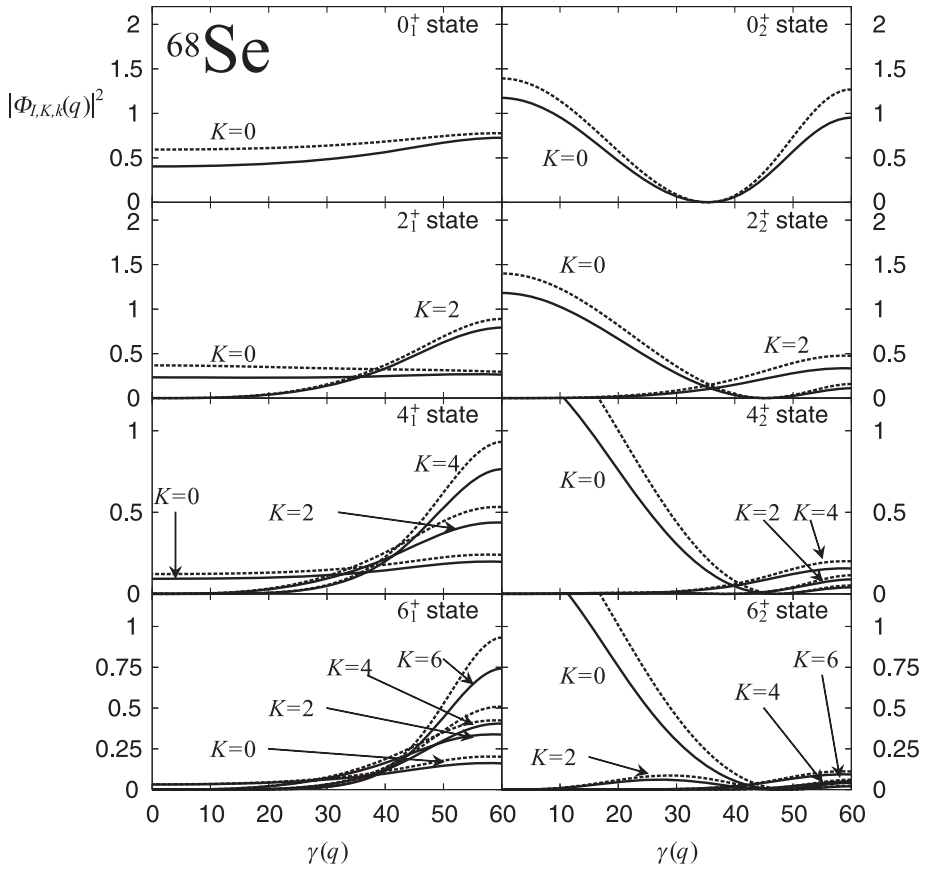

Fig. 8. Vibrational wave functions squared $|\Phi_{IKk}(q)|^2$ the yrast states (*left*), and the second lowest states at each angular momentum (*right*) for ^{68}Se. In each panel, different K components are plotted as functions of $\gamma(q)$. The solid (dashed) lines represent the results of calculations using the P+Q Hamiltonian with (without) the quadrupole pairing interaction. Note that the vibrational wave functions are normalized as in Eq. (5·9) with respect to the collective coordinate q, so that they are multiplied by the factor $d\gamma/dq$ when integrating with respect the triaxial deformation parameter γ. The $d\gamma/dq$ values calculated with the quadrupole pairing interaction are larger than those without it for all values of q.

oblate, while the excited band is prolate. For all states, including the 0^+ states, the inter-band B(E2) values are smaller by about one order of magnitude than the intra-band B(E2) values, and they rapidly decrease as the angular momentum increases. This indicates that the oblate-prolate shape mixing is rather weak in ^{72}Kr.

In Fig. 12, the vibrational wave functions are plotted. It is seen that the wave function of the 0_1^+ state is strongly localized in the oblate region, while that of the 0_2^+ state exhibits a major peak in the prolate region. In the yrast states with $I \neq 0$, localization about the oblate shape further develops for all K-components of the vibrational wave functions. The extent of this localization is larger for higher K. Contrastingly, the collective wave functions of the second lowest states in each angular momentum are essentially composed of the $K = 0$ component, which is

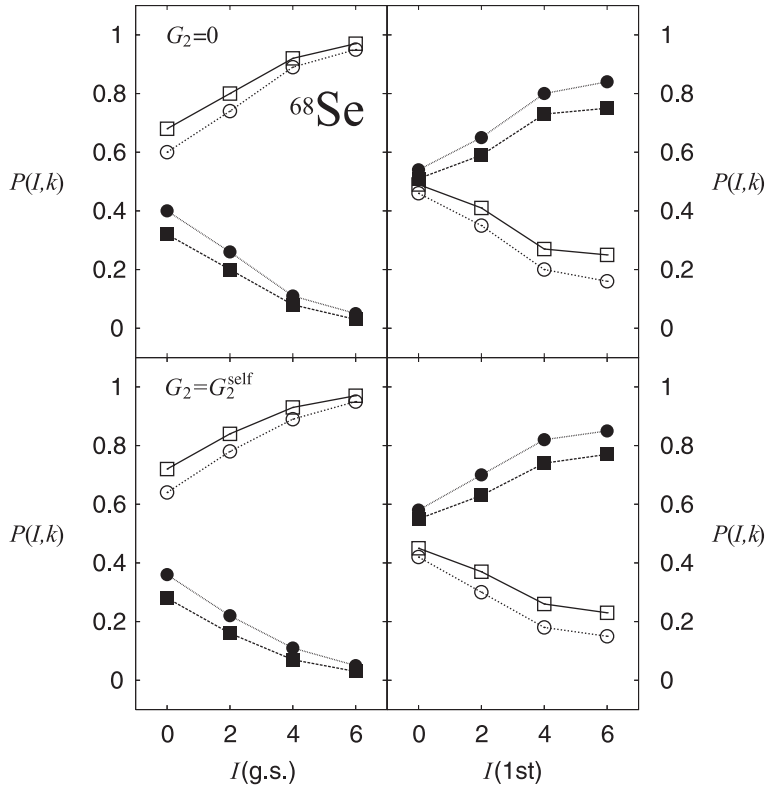

Fig. 9. The oblate and prolate probabilities evaluated for individual eigenstates of ^{68}Se. The upper (lower) panel plots the probabilities calculated using the P+Q Hamiltonian without (with) the quadrupole pairing interaction. The probabilities defined by setting the boundary at the barrier top ($\gamma = 30^\circ$) are indicated by squares (circles).

localized in the prolate region. Figure 13 plots the vibrational wave function squared. Rather weak oblate-prolate shape mixing is seen only for the excited 0^+ state, and other members of the rotational bands possess well-defined oblate or prolate forms. The oblate and prolate probabilities are presented in Fig. 14. It is seen that the shape mixing in the 0^+ states is much weaker than for ^{68}Se, and it almost vanishes at finite angular momentum.

§7. Concluding remarks

Shape coexistence/mixing phenomena in low-lying states of ^{68}Se and ^{72}Kr were investigated using the ASCC method. The excitation spectra, the spectroscopic quadrupole moments and the E2 transition properties of the low-lying states were evaluated for the first time using the ASCC method. We have derived the quantum collective Hamiltonian that describes the coupled collective motion of the large-amplitude vibration responsible for the oblate-prolate shape mixing and the three-dimensional rotation of the triaxial shape. The calculations yielded the excited prolate rotational band as well as the oblate ground-state band. The basic pattern of the

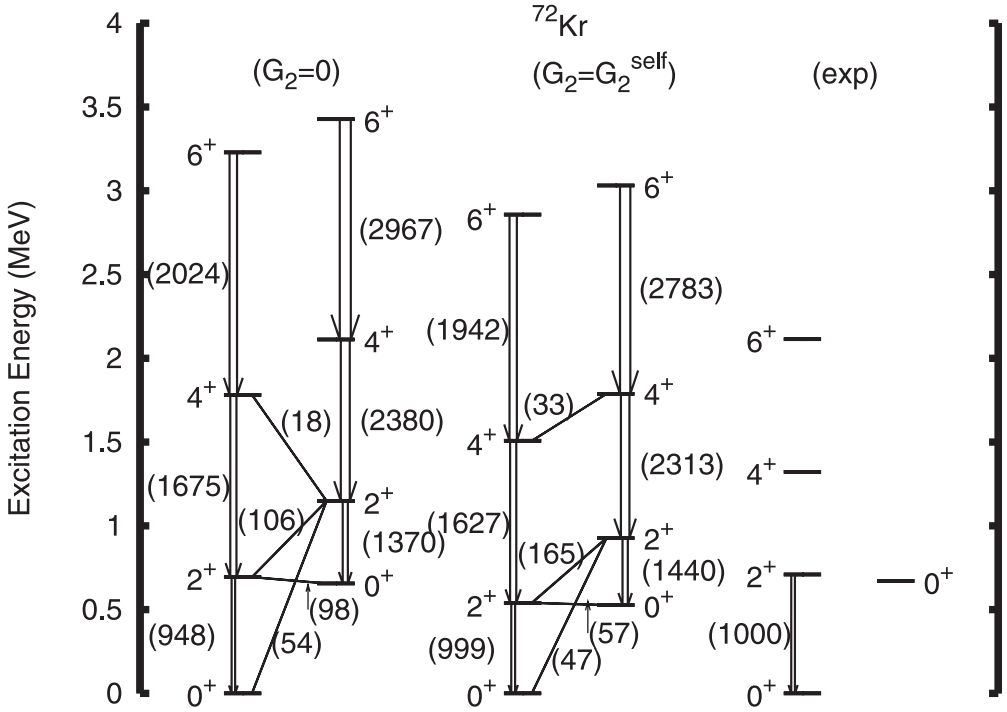

Fig. 10. The same as Fig. 5, but for ^{72}Kr. The experimental data are taken from Refs. 64)–66).

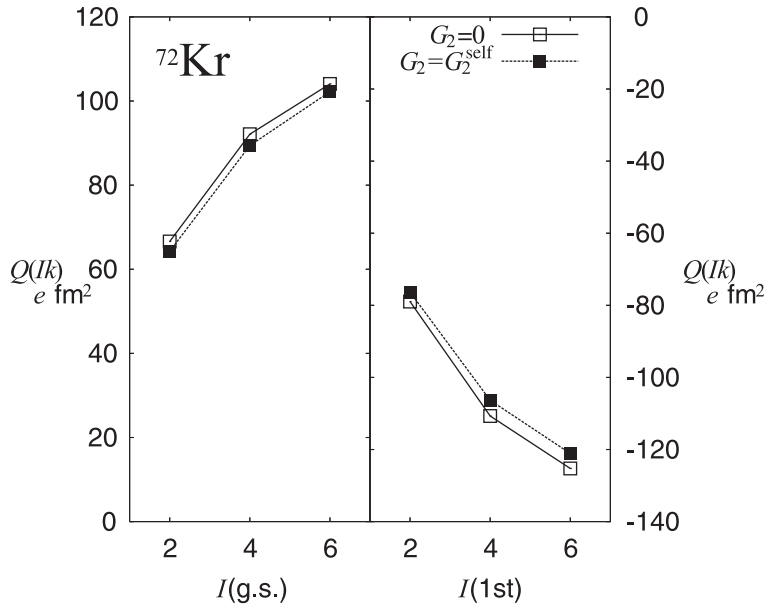

Fig. 11. The same as Fig. 6, but for ^{72}Kr. (See the caption of Fig. 6.)

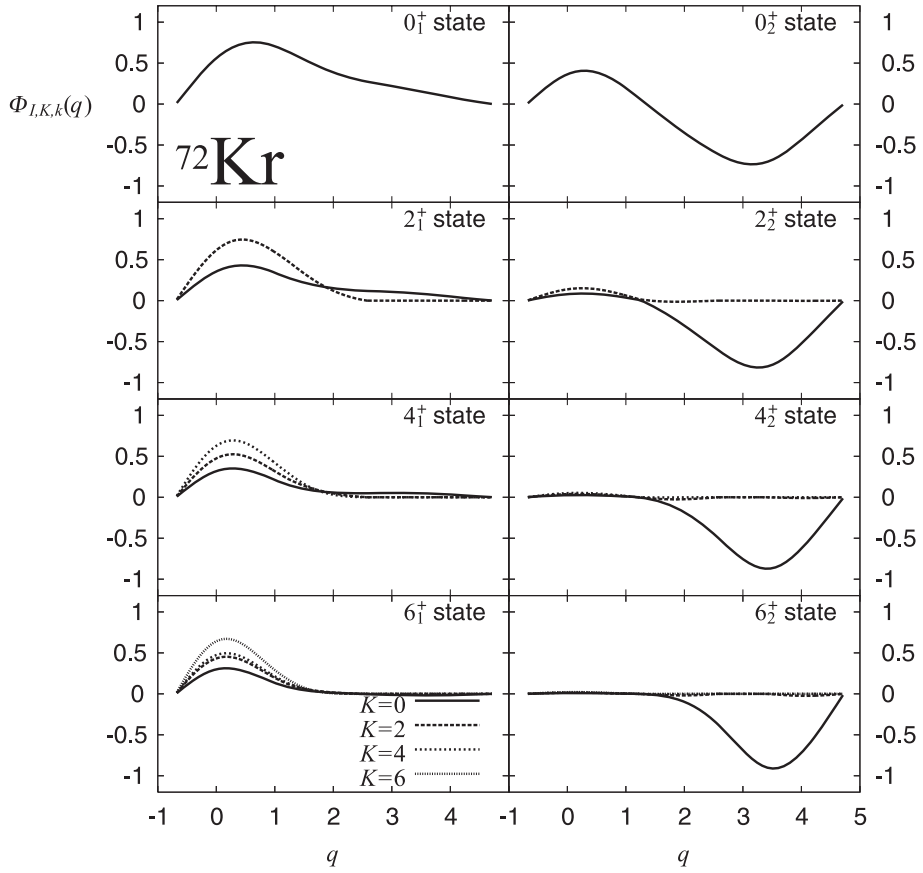

Fig. 12. Vibrational wave functions $\Phi_{IKk}(q)$ of low-lying states for ^{72}Kr plotted as functions of q. (See the caption of Fig. 7.)

shape coexistence/mixing phenomena has been qualitatively reproduced using the one-dimensional collective path in the two-dimensional (β, γ) plane. This collective path was self-consistently extracted from the many-dimensional TDHB manifold. Thus, the result of calculation indicates that the TDHB collective dynamics of the shape coexistence/mixing phenomena in these nuclei is essentially controlled by the single collective coordinate microscopically derived by means of the ASCC method.

We have also shown that the low-lying states can be described significantly more effectively by including the quadrupole pairing interaction. The reason for this is that the time-odd component of the mean field generated by the quadrupole pairing interaction enhances the collective mass of the vibrational motion and the moments of inertia of the rotational motion, and this lowers the energy of the collective excitation.

The present calculations clearly indicate that the oblate-prolate shape mixing decreases as the angular momentum increases. This implies that the rotational dynamics play the important role in realizing the localization of vibrational wave functions around the oblate and prolate minima in the situation that the barrier between these local minima is very low. We shall attempt a more detailed investigation

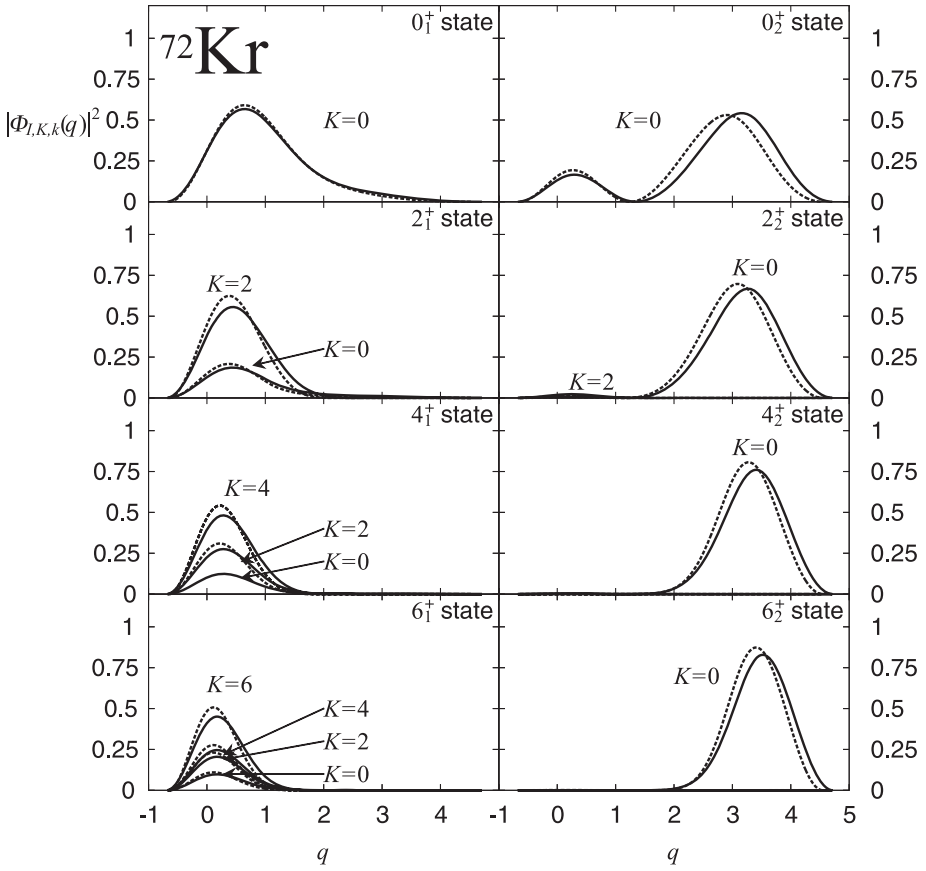

Fig. 13. Vibrational wave functions squared $|\Phi_{IKk}(q)|^2$ of low-lying states for ^{72}Kr plotted as functions of q. (See the caption of Fig. 8.)

of the dynamical reason why the rotational motion hinders the oblate-prolate shape mixing in a separate paper.

Acknowledgements

We thank Professors H. Aiba and S. Mizutori for useful discussions. This work is supported by Grants-in-Aid for Scientific Research (Nos. 18·2670, 16540249, 17540231, and 17540244) from the Japan Society for the Promotion of Science and the JSPS Core-to-Core Program "International Research Network for Exotic Femto Systems". We also thank the referee, whose comments were useful for improving the manuscript.

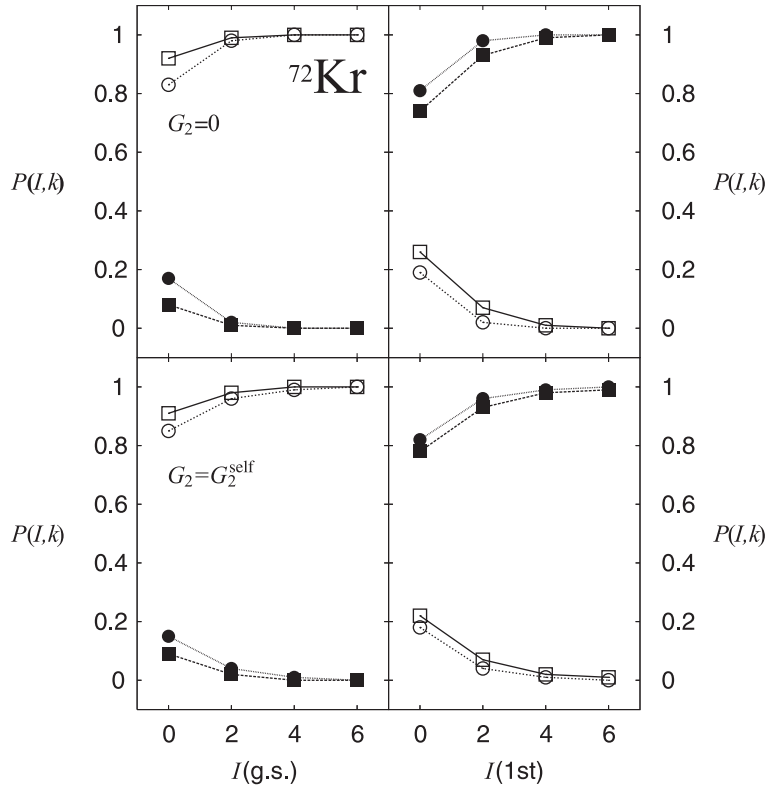

Fig. 14. The same as Fig. 9, but for ^{72}Kr.

Appendix A

Quasiparticle Representation of One-Body Operators

Because the moving mean field $|\phi(q)\rangle$ has positive signature, the conditions

$$U_{k\mu} = U_{\bar{k}\bar{\mu}}, \quad V_{k\bar{\mu}} = -V_{\bar{k}\mu}, \tag{A·1}$$

hold. The matrix elements of the pairing one-body operators $\hat{F}^{(\pm)}_{s=1,2,3,6,8,11}$ with $K = 0$ and 2 and $r = +1$ ($\hat{A}^{(\tau)(\pm)}$, $\hat{B}^{(\tau)(\pm)}_{20(+)}$, and $\hat{B}^{(\tau)(\pm)}_{22(+)}$) given in Eq. (4·24) are

$$\langle\phi(q)|\,\hat{F}^{(+)}_s\,|\phi(q)\rangle = 2{\sum_{\bar{k}l}}'(0|F^{(+)}_s|l\bar{k}){\sum_{\bar{\mu}}}' U_{\bar{k}\bar{\mu}}(q)V_{l\bar{\mu}}(q), \tag{A·2}$$

$$F^{(\pm)}_{A,s}(\mu\bar{\nu}) = {\sum_{k\bar{l}}}'(0|F^{(\pm)}_s|k\bar{l})(V_{k\bar{\nu}}(q)V_{\bar{l}\mu}(q) \pm U_{k\mu}(q)U_{\bar{l}\bar{\nu}}(q)), \tag{A·3}$$

$$F^{(\pm)}_{B,s}(\mu\nu) = {\sum_{k\bar{l}}}'(0|F^{(\pm)}_s|k\bar{l})(V_{\bar{l}\mu}(q)U_{k\nu}(q) \pm U_{k\mu}(q)V_{\bar{l}\nu}(q)). \tag{A·4}$$

The matrix elements of the particle-hole operators with $K = 0$ and 2 and $r = +1$ ($\hat{D}^{(+)}_{20}$ and $\hat{D}^{(+)}_{22}$) appearing in Eq. (4·24) are

$$\langle\phi(q)|\,\hat{F}^{(+)}_{s=13,15}\,|\phi(q)\rangle = 2{\sum_{kl}}'(k|F^{(+)}_{s=13,15}|l){\sum_{\mu}}'V_{k\bar{\mu}}(q)V_{l\bar{\mu}}(q), \tag{A·5}$$

$$F^{(+)}_{A,s=13,15}(\mu\bar{\nu}) = {\sum_{kl}}'(k|F^{(+)}_{s=13,15}|l)(U_{k\mu}(q)V_{l\bar{\nu}}(q) - U_{\bar{k}\bar{\nu}}(q)V_{\bar{l}\mu}(q)), \tag{A·6}$$

$$F^{(+)}_{B,s=13,15}(\mu\nu) = {\sum_{kl}}'(k|F^{(+)}_{s=13,15}|l)(U_{k\mu}(q)U_{l\nu}(q) - V_{\bar{k}\nu}(q)V_{\bar{l}\mu}(q)). \tag{A·7}$$

The matrix elements of the particle number operators given in Eq. (4·23) are

$$N^{(\tau)}(q) = \langle\phi(q)|\,\hat{N}^{(\tau)}\,|\phi(q)\rangle = 2{\sum_{k\in\tau}}'{\sum_{\bar{\mu}}}'V_{k\bar{\mu}}(q)^2, \tag{A·8}$$

$$N^{(\tau)}_A(\mu\bar{\nu}) = {\sum_{k\in\tau}}'(U_{k\mu}(q)V_{k\bar{\nu}}(q) - U_{\bar{k}\bar{\nu}}(q)V_{\bar{k}\mu}(q)), \tag{A·9}$$

$$N^{(\tau)}_B(\mu\nu) = {\sum_{k\in\tau}}'(U_{k\mu}(q)U_{k\nu}(q) - V_{\bar{k}\nu}(q)V_{\bar{k}\mu}(q)). \tag{A·10}$$

The constraint on the $\hat{Q}(q-\delta q)$ operator expressed by (4·21) in the moving-frame HB equation is written

$$\langle\phi(q)|\,\hat{Q}(q-\delta q)\,|\phi(q)\rangle = {\sum_{kl}}'Q_{kl}(q-\delta q){\sum_{\mu}}'V_{k\bar{\mu}}(q)V_{l\bar{\mu}}(q). \tag{A·11}$$

Appendix B
—— *Determination of the B-Part of* $\hat{Q}(q)$ ——

In this appendix, we show that the B-part of the operator ($\hat{Q}(q)$) can be determined through its A-part, ($\hat{Q}^A(q)$), which is obtained by solving the moving-frame QRPA equations. In terms of the quasiparticle operators, $a^\dagger_i$ and a_i, defined by the Bogoliubov transformation

$$\begin{pmatrix} c \\ c^\dagger \end{pmatrix} = \begin{pmatrix} U & V \\ V^* & U^* \end{pmatrix}\begin{pmatrix} a \\ a^\dagger \end{pmatrix}, \tag{B·1}$$

the Hermitian operator $\hat{Q}(q)$ is written

$$\begin{aligned}\hat{Q}(q) &= \sum_{ij} Q_{ij}(q)c^\dagger_i c_j \\ &= \sum_{ij}\left(Q^A_{ij}(q)a^\dagger_i a^\dagger_j + Q^{A*}_{ij}(q)a_j a_i + Q^B_{ij}(q)a^\dagger_i a_j\right),\end{aligned} \tag{B·2}$$

where

$$Q^A = U^\dagger QV, \quad Q^B = U^\dagger QU - V^\dagger QV. \tag{B·3}$$

Thus, the matrices Q and Q^B can be written in terms of Q^A as

$$Q = (U^\dagger)^{-1} Q^A V^{-1}, \tag{B·4}$$

$$Q^B = Q^A V^{-1} U - V^\dagger (U^\dagger)^{-1} Q^A. \tag{B·5}$$

We cannot directly use these relations, however, to determine Q and Q^B, because the matrices Q and Q^B calculated using (B·4) and (B·5) are not Hermitian. For this reason, we have to construct Hermitian matrices Q and Q^B from Q^A. This is done by adding a symmetric matrix S to the solution of the moving-frame QRPA equation, which we here write Q_0^A, as

$$Q^A = Q_0^A + S. \tag{B·6}$$

For this matrix, Q is written

$$Q = (U^\dagger)^{-1}(Q_0^A + S)V^{-1} = Q_0 + (U^\dagger)^{-1} S V^{-1}, \tag{B·7}$$

$$Q^\dagger = (V^\dagger)^{-1}(Q_0^A + S)^\dagger U^{-1} = Q_0^\dagger + (V^\dagger)^{-1} S^\dagger U^{-1}. \tag{B·8}$$

From the Hermicity condition, $Q = Q^\dagger$, we obtain the following equation for S:

$$(V^\dagger)^{-1} S^\dagger U^{-1} - (U^\dagger)^{-1} S V^{-1} = Q_0 - Q_0^\dagger. \tag{B·9}$$

This determines the symmetric matrix S. Explicitly, the above equation is given by

$$\sum_{kl} \{(V^{-1})_{ki}(U^{-1})_{lj} - (U^{-1})_{ki}(V^{-1})_{lj}\} S_{kl} = (Q_0)_{ij} - (Q_0)_{ji}, \tag{B·10}$$

where we assume that all quantities are real. The number of unknown quantities and the number of equations are the same, $N(N+1)/2$, N being the dimension of the matrix. Therefore, it is possible to determine the matrix S by solving this equation.

In the case of the P+Q model, we start from the skew symmetric matrix Q_0^A,

$$(Q_0^A)_{\mu\bar{\nu}}(q) = \frac{1}{2} Q^A_{\mu\bar{\nu}}(q), \quad (Q_0^A)_{\bar{\nu}\mu}(q) = -\frac{1}{2} Q^A_{\mu\bar{\nu}}(q). \tag{B·11}$$

The symmetric matrix $S_{\mu\bar{\nu}} = S_{\bar{\nu}\mu}$ is determined by solving the equations,

$$\sum_{\mu\bar{\nu}}{}' \{(V^{-1})_{\bar{\nu}k}(U^{-1})_{\mu l} - (U^{-1})_{\mu k}(V^{-1})_{\bar{\nu}l}\} S_{\mu\bar{\nu}} = (Q_0)_{kl} - (Q_0)_{lk}, \tag{B·12}$$

$$\sum_{\mu\bar{\nu}}{}' \{(V^{-1})_{\mu\bar{k}}(U^{-1})_{\bar{\nu}\bar{l}} - (U^{-1})_{\bar{\nu}\bar{k}}(V^{-1})_{\mu\bar{l}}\} S_{\mu\bar{\nu}} = (Q_0)_{\bar{k}\bar{l}} - (Q_0)_{\bar{l}\bar{k}}, \tag{B·13}$$

where

$$(Q_0)_{kl}(q) = \sum_{\mu\bar{\nu}}{}' (U^{-1})_{\mu k}(Q_0^A)_{\mu\bar{\nu}}(q)(V^{-1})_{\bar{\nu}l}, \tag{B·14}$$

$$(Q_0)_{\bar{k}\bar{l}}(q) = \sum_{\mu\bar{\nu}}{}' (U^{-1})_{\bar{\nu}\bar{k}}(Q_0^A)_{\bar{\nu}\mu}(q)(V^{-1})_{\mu\bar{l}}. \tag{B·15}$$

As the relation $(Q_0^A)_{\mu\bar{\nu}} = (Q_0^A)_{\nu\bar{\mu}}$ holds, the matrix S satisfies the relation $S_{\mu\bar{\nu}} = -S_{\nu\bar{\mu}}$, and thus, Eqs. (B·12) and (B·13) are written

$$\sum_{\mu\bar{\nu}}{}' \{-(V^{-1})_{\bar{\nu}k}(U^{-1})_{\mu l} - (U^{-1})_{\nu k}(V^{-1})_{\bar{\mu}l}\} S_{\mu\bar{\nu}} = (Q_0)_{kl} - (Q_0)_{lk}. \tag{B·16}$$

Using the transformed matrix $Q^{A'}(q)$,

$$Q^{A'}_{\mu\bar{\nu}}(q) = (Q_0^A)_{\mu\bar{\nu}}(q) + S_{\mu\bar{\nu}}, \tag{B·17}$$

the Hermite matrices $Q(q)$ and $Q^B(q)$ are obtained as follows:

$$Q_{kl}(q) = \sum_{\mu\bar{\nu}}{}' (U^{-1})_{\mu k} Q^{A'}_{\mu\bar{\nu}}(q) (V^{-1})_{\bar{\nu}l}, \tag{B·18}$$

$$Q_{\bar{k}\bar{l}}(q) = \sum_{\bar{\mu}\nu}{}' (U^{-1})_{\bar{\mu}\bar{k}} Q^{A'}_{\bar{\mu}\nu}(q) (V^{-1})_{\nu\bar{l}}, \tag{B·19}$$

$$Q^B_{\mu\nu}(q) = \sum_{kl}{}' U_{k\mu} Q_{kl}(q) U_{l\nu} - V_{\bar{k}\mu} Q_{\bar{k}\bar{l}}(q) V_{\nu\bar{l}}, \tag{B·20}$$

$$Q^B_{\bar{\mu}\bar{\nu}}(q) = \sum_{\bar{k}\bar{l}}{}' U_{\bar{\mu}\bar{k}} Q_{\bar{k}\bar{l}}(q) U_{\bar{l}\bar{\nu}} - V_{k\bar{\mu}} Q_{kl}(q) V_{l\bar{\nu}}. \tag{B·21}$$

Appendix C

—— *Calculation of the Rotational Moments of Inertia* ——

For the separable interactions (3·7), the Thouless-Valatin equations (2·26) determining the three rotational moments of inertia, $\mathcal{J}_i(q)$, about the principal axes in a non-equilibrium state $|\phi(q)\rangle$ can be written in the form

$$\delta \langle\phi(q)| [\hat{h}_M(q), \hat{\Psi}_i(q)] + i \sum_s f^{(+)}_{\Psi_i,s}(q) \hat{F}^{(+)}_s - \sum_s f^{(-)}_{\Psi_i,s}(q) \hat{F}^{(-)}_s - \frac{1}{i} \mathcal{J}_i^{-1}(q) \hat{I}_i |\phi(q)\rangle = 0, \tag{C·1}$$

where

$$f^{(+)}_{\Psi_i,s}(q) = i\kappa_s \langle\phi(q)| [\hat{F}^{(+)}_s, \hat{\Psi}_i(q)] |\phi(q)\rangle , \tag{C·2}$$

$$f^{(-)}_{\Psi_i,s}(q) = -\kappa_s \langle\phi(q)| [\hat{F}^{(-)}_s, \hat{\Psi}_i(q)] |\phi(q)\rangle . \tag{C·3}$$

The quasiparticle representation of the angular momentum operators is expressed as

$$\hat{I}_x = \sum_{\mu\nu}{}' I_{A,x}(\mu\bar{\nu})(\boldsymbol{A}^\dagger_{\mu\bar{\nu}} + \boldsymbol{A}_{\mu\bar{\nu}}) + \sum_{\mu\nu}{}' I_{B,x}(\mu\nu)(\boldsymbol{B}_{\mu\nu} - \boldsymbol{B}_{\bar{\mu}\bar{\nu}}), \tag{C·4}$$

$$i\hat{I}_y = \sum_{\mu\nu}{}' I_{A,y}(\mu\nu)(\boldsymbol{A}^\dagger_{\mu\nu} - \boldsymbol{A}_{\mu\nu}) + I_{A,y}(\bar{\mu}\bar{\nu})(\boldsymbol{A}^\dagger_{\bar{\mu}\bar{\nu}} - \boldsymbol{A}_{\bar{\mu}\bar{\nu}}) + \sum_{\mu\nu}{}' I_{B,y}(\mu\bar{\nu})(\boldsymbol{B}_{\mu\bar{\nu}} - \boldsymbol{B}_{\bar{\mu}\nu}), \tag{C·5}$$

$$\hat{I}_z = \sum_{\mu\nu}{}' I_{A,z}(\mu\nu)(\boldsymbol{A}^\dagger_{\mu\nu} + \boldsymbol{A}_{\mu\nu}) + I_{A,z}(\bar{\mu}\bar{\nu})(\boldsymbol{A}^\dagger_{\bar{\mu}\bar{\nu}} + \boldsymbol{A}_{\bar{\mu}\bar{\nu}}) + \sum_{\mu\nu}{}' I_{B,z}(\mu\bar{\nu})(\boldsymbol{B}_{\mu\bar{\nu}} + \boldsymbol{B}_{\bar{\mu}\nu}), \tag{C·6}$$

where the matrix elements of $I_{A,x}, I_{A,y}$ and $I_{A,z}$ are given by

$$I_{A,x}(\mu\bar{\nu}) = \sum_{kl}{}' (k|I_x|l)(U_{k\mu}(q)V_{l\bar{\nu}}(q) + U_{\bar{k}\bar{\nu}}(q)V_{\bar{l}\mu}(q)), \tag{C·7}$$

$$I_{A,y}(\mu\nu) = I_{A,y}(\bar{\mu}\bar{\nu}) = \sum_{kl}{}' (k|I_y|l)U_{k\mu}(q)V_{\bar{l}\nu}(q), \tag{C·8}$$

$$I_{A,z}(\mu\nu) = -I_{A,z}(\bar{\mu}\bar{\nu}) = -\sum_{k}{}' m_k U_{k\mu}(q)V_{\bar{k}\nu}(q). \tag{C·9}$$

The residual interactions with $(r = +1, K = 1)$, $(r = -1, K = 1)$ and $(r = -1,\ K = 2)$ contribute to rotations about the x, y and z-axis, respectively. The quasiparticle representation of the one-body operators having these quantum numbers is given by

$$\hat{F}^{(\pm)}_s = \sum_{\mu\bar{\nu}}{}' F^{(\pm)}_{A,s}(\mu\bar{\nu})(\boldsymbol{A}^\dagger_{\mu\bar{\nu}} \pm \boldsymbol{A}_{\mu\bar{\nu}}) + \sum_{\mu\nu}{}' F^{(\pm)}_{B,s}(\mu\nu)(\boldsymbol{B}_{\mu\nu} - \boldsymbol{B}_{\bar{\mu}\bar{\nu}}), \quad (r = +1, K = 1) \tag{C·10}$$

$$\hat{F}^{(\pm)}_s = \sum_{\mu\nu}{}' F^{(\pm)}_{A,s}(\mu\nu)(\boldsymbol{A}^\dagger_{\mu\nu} \pm \boldsymbol{A}_{\mu\nu} + \boldsymbol{A}^\dagger_{\bar{\mu}\bar{\nu}} \pm \boldsymbol{A}_{\bar{\mu}\bar{\nu}}) + \sum_{\mu\nu}{}' F^{(\pm)}_{B,s}(\mu\bar{\nu})(\boldsymbol{B}_{\mu\bar{\nu}} - \boldsymbol{B}_{\bar{\mu}\nu}), \quad (r = -1, K = 1) \tag{C·11}$$

$$\hat{F}^{(\pm)}_s = \sum_{\mu\nu}{}' F^{(\pm)}_{A,s}(\mu\nu)\{\boldsymbol{A}^\dagger_{\mu\nu} \pm \boldsymbol{A}_{\mu\nu} - (\boldsymbol{A}^\dagger_{\bar{\mu}\bar{\nu}} \pm \boldsymbol{A}_{\bar{\mu}\bar{\nu}})\} + \sum_{\mu\nu}{}' F^{(\pm)}_{B,s}(\mu\bar{\nu})(\boldsymbol{B}_{\mu\bar{\nu}} + \boldsymbol{B}_{\bar{\mu}\nu}). \quad (r = -1, K = 2) \tag{C·12}$$

The matrix elements of the quadrupole pairing operators are

$$F^{(\pm)}_{A,s=4,9}(\mu\bar{\nu}) = 2\sum_{kl\in\tau}{}' (0|B^{(\tau)(\pm)}_{21(-)}|k\bar{l})(V_{\bar{l}\mu}(q)V_{k\bar{\nu}}(q) \pm U_{k\mu}(q)U_{\bar{l}\bar{\nu}}(q)), \tag{C·13}$$

$$F^{(\pm)}_{A,s=5,10}(\mu\nu) = \sum_{kl\in\tau}{}' (0|B^{(\tau)(\pm)}_{21(+)}|kl)(V_{l\bar{\mu}}(q)V_{k\bar{\nu}}(q) \pm U_{\bar{k}\bar{\mu}}(q)V_{\bar{l}\bar{\nu}}(q)), \tag{C·14}$$

$$F^{(\pm)}_{A,s=7,12}(\mu\nu) = \sum_{kl\in\tau}{}' (0|B^{(\tau)(\pm)}_{22(-)}|kl)(-V_{\bar{l}\mu}(q)V_{\bar{k}\nu}(q) \pm U_{k\mu}(q)U_{l\nu}(q)), \tag{C·15}$$

$$F^{(\pm)}_{A,s=5,10}(\mu\nu) = F^{(\pm)}_{A,s=5,10}(\bar{\mu}\bar{\nu}), \quad F^{(\pm)}_{A,s=7,12}(\mu\nu) = -F^{(\pm)}_{A,a=7,12}(\bar{\mu}\bar{\nu}). \tag{C·16}$$

Note that the quadrupole operators $\hat{D}^{(\pm)}_{21}$ and $\hat{D}^{(-)}_{22}$ do not contribute to the moments of inertia.

The three Thouless-Valatin equations, appearing in (C·1), for a non-equilibrium state can be solved independently. The angle operators $\hat{\Psi}_x(q), \hat{\Psi}_y(q)$ and $\hat{\Psi}_z(q)$ can be written as

$$\hat{\Psi}_x(q) = i{\sum_{\mu\bar{\nu}}}' \Psi_{A,x}(\mu\bar{\nu})(\boldsymbol{A}^\dagger_{\mu\bar{\nu}} - \boldsymbol{A}_{\mu\bar{\nu}}) + (\boldsymbol{B} - \text{part}), \tag{C·17a}$$

$$\hat{\Psi}_y(q) = {\sum_{\mu\nu}}' \Psi_{A,y}(\mu\nu)(\boldsymbol{A}^\dagger_{\mu\nu} + \boldsymbol{A}_{\mu\nu}) + \Psi_{A,y}(\bar{\mu}\bar{\nu})(\boldsymbol{A}^\dagger_{\bar{\mu}\bar{\nu}} + \boldsymbol{A}_{\bar{\mu}\bar{\nu}}) + (\boldsymbol{B}-\text{part}), \tag{C·17b}$$

$$\hat{\Psi}_z(q) = i{\sum_{\mu\nu}}' \Psi_{A,z}(\mu\nu)(\boldsymbol{A}^\dagger_{\mu\nu} - \boldsymbol{A}_{\mu\nu}) + \Psi_{A,z}(\bar{\mu}\bar{\nu})(\boldsymbol{A}^\dagger_{\bar{\mu}\bar{\nu}} - \boldsymbol{A}_{\bar{\mu}\bar{\nu}}) + (\boldsymbol{B}-\text{part}). \tag{C·17c}$$

These matrix elements are easily obtained from Eq. (C·1) as

$$\Psi_{A,x}(\mu\bar{\nu}) = \frac{-1}{E_\mu + E_{\bar{\nu}}} \left(\sum_s f^{(+)}_{\Psi_x,s}(q) F^{(+)}_{A,s}(\mu\bar{\nu}) + \mathcal{J}_x^{-1}(q) I_{A,x}(\mu\bar{\nu}) \right), \tag{C·18a}$$

$$\Psi_{A,y}(\mu\nu) = \frac{1}{E_\mu + E_\nu} \left(\sum_s f^{(-)}_{\Psi_y,s}(q) F^{(-)}_{A,s}(\mu\nu) - \mathcal{J}_y^{-1}(q) I_{A,y}(\mu\nu) \right), \tag{C·18b}$$

$$\Psi_{A,y}(\bar{\mu}\bar{\nu}) = \frac{1}{E_{\bar{\mu}} + E_{\bar{\nu}}} \left(\sum_s f^{(-)}_{\Psi_y,s}(q) F^{(-)}_{A,s}(\bar{\mu}\bar{\nu}) - \mathcal{J}_y^{-1}(q) I_{A,y}(\bar{\mu}\bar{\nu}) \right), \tag{C·18c}$$

$$\Psi_{A,z}(\mu\nu) = \frac{1}{E_\mu + E_\nu} \left(-\sum_s f^{(+)}_{\Psi_z,s}(q) F^{(+)}_{A,s}(\mu\nu) - \mathcal{J}_z^{-1}(q) I_{A,z}(\mu\nu) \right), \tag{C·18d}$$

$$\Psi_{A,z}(\bar{\mu}\bar{\nu}) = \frac{1}{E_{\bar{\mu}} + E_{\bar{\nu}}} \left(-\sum_s f^{(+)}_{\Psi_z,s}(q) F^{(+)}_{A,s}(\bar{\mu}\bar{\nu}) - \mathcal{J}_z^{-1}(q) I_{A,z}(\bar{\mu}\bar{\nu}) \right). \tag{C·18e}$$

It is easy to confirm that $f^{(-)}_{\Psi_x,s}(q) = 0, f^{(+)}_{\Psi_y,s}(q) = 0$ and $f^{(-)}_{\Psi_z,s}(q) = 0$. Substituting (C·18) into the quantities $f^{(+)}_{\Psi_x,s}(q), f^{(-)}_{\Psi_y,s}(q)$ and $f^{(+)}_{\Psi_z,s}(q)$ and the canonical variable condition (2·26), we obtain

$$\begin{aligned} f^{(+)}_{\Psi_x,s}(q) &= i\kappa_s \langle\phi(q)| [\hat{F}^{(+)}_s, \hat{\Psi}_x(q)] |\phi(q)\rangle \\ &= 2\kappa_s \sum_{s'} (F^{(+)}_{A,s}, F^{(+)}_{A,s'})_{E+} f^{(+)}_{\Psi_x,s'}(q) + 2\kappa_s (F^{(+)}_{A,s}, I_{A,x})_{E+} \mathcal{J}_x^{-1}(q), \end{aligned} \tag{C·19a}$$

$$\begin{aligned} f^{(-)}_{\Psi_y,s}(q) =& -\kappa_s \langle\phi(q)| [\hat{F}^{(-)}_s, \hat{\Psi}_y] |\phi(q)\rangle \\ =& 2\kappa_s \sum_{s'} (F^{(-)}_{A,s}, \overline{F^{(-)}_{A,s'}})_{E-} f^{(-)}_{\Psi_y,s'}(q) - 2\kappa_s (F^{(-)}_{A,s}, \overline{I_{A,y}})_{E-} \mathcal{J}_y^{-1}(q), \end{aligned} \tag{C·19b}$$

$$\begin{aligned} f^{(+)}_{\Psi_z,s}(q) =& i\kappa_s \langle\phi(q)| [\hat{F}^{(+)}_s, \hat{\Psi}_z(q)] |\phi(q)\rangle \\ =& 2\kappa_s \sum_{s'} (F^{(+)}_{A,s}, \overline{I_{A,z}})_{E-} f^{(+)}_{\Psi_z,s'}(q) + 2\kappa_s (F^{(+)}_{A,s}, \overline{I_{A,z}})_{E-} \mathcal{J}_z^{-1}(q), \end{aligned} \tag{C·19c}$$

$$\langle\phi(q)| [\hat{\Psi}_x(q), \hat{I}_x] |\phi(q)\rangle / i = -2{\sum_{\mu\bar{\nu}}}' \Psi_{A,x}(\mu,\bar{\nu}) I_{A,x}(\mu\bar{\nu})$$

$$= -2\sum_{s}(F^{(+)}_{A,s}, I_{A,x})_{E+} f^{(+)}_{\Psi_x,s}(q) - 2(I_{A,x}, I_{A,x})_{E+}\mathcal{J}_x^{-1}(q)$$
$$= 1, \tag{C·20a}$$
$$\langle\phi(q)|\,[\hat{\Psi}_y(q), i\hat{I}_y]\,|\phi(q)\rangle = 2{\sum_{\mu\nu}}' \Psi_{A,y}(\mu\nu)\overline{I_{A,y}}(\mu\nu) + 2{\sum_{\bar{\mu}\bar{\nu}}}' \Psi_{A,y}(\bar{\mu}\bar{\nu})\overline{I_{A,y}}(\bar{\mu}\bar{\nu})$$
$$= 2\sum_{s}(F^{(-)}_{A,s}, \overline{I_{A,y}})_{E-} f^{(-)}_{\Psi_y,s}(q) - 2(I_{A,y}, \overline{I_{A,y}})_{E-}\mathcal{J}_y^{-1}(q)$$
$$= -1, \tag{C·20b}$$
$$\langle\phi(q)|\,[\hat{\Psi}_z(q), \hat{I}_z]\,|\phi(q)\rangle\,/i = -2{\sum_{\mu\nu}}' \Psi_{A,z}(\mu\nu)\overline{I_{A,z}}(\mu\nu) - 2{\sum_{\bar{\mu}\bar{\nu}}}' \Psi_{A,z}(\bar{\mu}\bar{\nu})\overline{I_{A,z}}(\bar{\mu}\bar{\nu})$$
$$= 2\sum_{s}(F^{(+)}_{A,s}, \overline{I_{A,z}})_{E-} f^{(+)}_{\Psi_z,s'}(q) + 2(I_{A,z}, \overline{I_{A,z}})_{E-}\mathcal{J}_z^{-1}(q)$$
$$= 1, \tag{C·20c}$$

where

$$(X, Y)_{E+} = {\sum_{\mu\bar{\nu}}}' \frac{X(\mu\bar{\nu})Y(\mu\bar{\nu})}{E_\mu + E_{\bar{\nu}}}, \tag{C·21}$$
$$\overline{X}(\mu\nu) = X(\mu\nu) - X(\nu\mu), \tag{C·22}$$
$$(X, Y)_{E-} = {\sum_{\mu\nu}}' \frac{X(\mu\nu)Y(\mu\nu)}{E_\mu + E_\nu} + {\sum_{\bar{\mu}\bar{\nu}}}' \frac{X(\bar{\mu}\bar{\nu})Y(\bar{\mu}\bar{\nu})}{E_{\bar{\mu}} + E_{\bar{\nu}}}. \tag{C·23}$$

Equations (C·19) and (C·20) are linear equations with respect to $f^{(+)}_{\Psi_i,s}(q)$ and $\mathcal{J}_i^{-1}(q)$, and they can be rewritten as follows:

$$\sum_{s'}\begin{pmatrix} 2\kappa_s(F^{(+)}_{A,s}, F^{(+)}_{A,s'})_{E+} - \delta_{ss'} & 2\kappa_{s'}(F^{(+)}_{A,s}, I_{A,x})_{E+} \\ 2(F^{(+)}_{A,s}, I_{A,x})_{E+} & 2(I_{A,x}, I_{A,x})_{E+}, \end{pmatrix}\begin{pmatrix} f^{(+)}_{\Psi_x,s'}(q) \\ \mathcal{J}_x^{-1}(q) \end{pmatrix} = \begin{pmatrix} 0 \\ 1 \end{pmatrix}, \tag{C·24a}$$

$$\sum_{s'}\begin{pmatrix} 2\kappa_s(F^{(-)}_{A,s}, \overline{F^{(-)}_{A,s'}})_{E-} - \delta_{ss'} & -2\kappa_s(F^{(-)}_{A,s}, \overline{I_{A,y}})_{E-} \\ -2(F^{(-)}_{A,s}, \overline{I_{A,y}})_{E-} & 2(I_{A,y}, \overline{I_{A,y}})_{E-} \end{pmatrix}\begin{pmatrix} f^{(-)}_{\Psi_y,s}(q) \\ \mathcal{J}_y^{-1} \end{pmatrix} = \begin{pmatrix} 0 \\ 1 \end{pmatrix}, \tag{C·24b}$$

$$\sum_{s'}\begin{pmatrix} 2\kappa_s(F^{(+)}_{A,s}, \overline{F^{(+)}_{A,s}})_{E-} - \delta_{ss'} & 2\kappa_s(F^{(+)}_{A,s}, \overline{I_{A,z}})_{E-} \\ 2(F^{(+)}_{A,s'}, \overline{I_{A,z}})_{E-} & 2(I_{A,z}, \overline{I_{A,z}})_{E-} \end{pmatrix}\begin{pmatrix} f^{(+)}_{\Psi_z,s'}(q) \\ \mathcal{J}_z^{-1}(q) \end{pmatrix} = \begin{pmatrix} 0 \\ 1 \end{pmatrix}. \tag{C·24c}$$

References

1) P. Ring and P. Schuck, *The Nuclear Many-Body Problem* (Springer-Verlag, 1980).
2) J.-P. Blaizot and G. Ripka, *Quantum Theory of Finite Systems* (The MIT press, 1986).
3) A. Abe and T. Suzuki (ed.), Prog. Theor. Phys. Suppl. Nos. 74 & 75 (1983), 1.
4) D. M. Brink and R. A. Broglia, *Nuclear Superfluidity, Pairing in Finite Systems* (Cambridge University Press, 2005).

5) A. Bohr and B. R. Mottelson, *Nuclear Structure*, Vol. II (W. A. Benjamin Inc., 1975; World Scientific, 1998).
6) D. J. Rowe and R. Bassermann, Can. J. Phys. **54** (1976), 1941.
7) D. M. Brink, M. J. Giannoni and M. Vénéroni, Nucl. Phys. A **258** (1976), 237.
8) F. Villars, Nucl. Phys. A **285** (1977), 269.
9) T. Marumori, Prog. Theor. Phys. **57** (1977), 112.
10) M. Baranger and M. Veńéroni, Ann. of Phys. **114** (1978), 123.
11) K. Goeke and P.-G. Reinhard, Ann. of Phys. **112** (1978), 328.
12) T. Marumori, T. Maskawa, F. Sakata and A. Kuriyama, Prog. Theor. Phys. **64** (1980), 1294.
13) M. J. Giannoni and P. Quentin, Phys. Rev. C **21** (1980), 2060; Phys. Rev. C **21** (1980), 2076.
14) J. Dobaczewski and J. Skalski, Nucl. Phys. A **369** (1981), 123.
15) K. Goeke, P.-G. Reinhard and D. J. Rowe, Nucl. Phys. A **359** (1981), 408.
16) A. K. Mukherjee and M. K. Pal, Phys. Lett. B **100** (1981), 457; Nucl. Phys. A **373** (1982), 289.
17) D. J. Rowe, Nucl. Phys. A **391** (1982), 307.
18) C. Fiolhais and R. M. Dreizler, Nucl. Phys. A **393** (1983), 205.
19) P.-G. Reinhard, F. Grümmer and K. Goeke, Z. Phys. A **317** (1984), 339.
20) A. Kuriyama and M. Yamamura, Prog. Theor. Phys. **70** (1983), 1675; Prog. Theor. Phys. **71** (1984), 122.
21) M. Yamamura, A. Kuriyama and S. Iida, Prog. Theor. Phys. **71** (1984), 109.
22) M. Matsuo and K. Matsuyanagi, Prog. Theor. Phys. **74** (1985), 288.
23) M. Matsuo, Prog. Theor. Phys. **76** (1986), 372.
24) Y. R. Shimizu and K. Takada, Prog. Theor. Phys. **77** (1987), 1192.
25) M. Yamamura and A. Kuriyama, Prog. Theor. Phys. Suppl. No. 93 (1987), 1.
26) A. Bulgac, A. Klein, N. R. Walet and G. Do Dang, Phys. Rev. C **40** (1989), 945.
27) N. R. Walet, G. Do Dang and A. Klein, Phys. Rev. C **43** (1991), 2254.
28) A. Klein, N. R. Walet and G. Do Dang, Ann. of Phys. **208** (1991), 90.
29) K. Kaneko, Phys. Rev. C **49** (1994), 3014.
30) T. Nakatsukasa and N. R. Walet, Phys. Rev. C **57** (1998), 1192.
31) T. Nakatsukasa and N. R. Walet, Phys. Rev. C **58** (1998), 3397.
32) T. Nakatsukasa, N. R. Walet and G. Do Dang, Phys. Rev. C **61** (1999), 014302.
33) J. Libert, M. Girod and J.-P. Delaroche, Phys. Rev. C **60** (1999), 054301.
34) E. Kh. Yuldashbaeva, J. Libert, P. Quentin and M. Girod, Phys. Lett. B **461** (1999), 1.
35) L. Próchniak, P. Quentin, D. Samsoen and J. Libert, Nucl. Phys. A **730** (2004), 59.
36) D. Almehed and N. R. Walet, Phys. Rev. C **69** (2004), 024302.
37) D. Almehed and N. R. Walet, Phys. Lett. B **604** (2004), 163.
38) D. Almehed and N. R. Walet, J. of Phys. G **31** (2005), S1523.
39) D. Almehed and N. R. Walet, nucl-th/0509079.
40) A. Klein and E. R. Marshalek, Rev. Mod. Phys **63** (1991), 375.
41) G. Do Dang, A. Klein and N. R. Walet, Phys. Rep. **335** (2000), 93.
42) A. Kuriyama, K. Matsuyanagi, F. Sakata, K. Takada and M. Yamamura (Ed.), Prog. Theor. Phys. Suppl. No. 141 (2001), 1.
43) M. Matsuo, Prog. Theor. Phys. **72** (1984), 666.
44) M. Matsuo and K. Matsuyanagi, Prog. Theor. Phys. **74** (1985), 1227; Prog. Theor. Phys. **76** (1986), 93; Prog. Theor. Phys. **78** (1987), 591.
45) M. Matsuo, Y. R. Shimizu and K. Matsuyanagi, *Proceedings of The Niels Bohr Centennial Conf. on Nuclear Structure*, ed. R. Broglia, G. Hagemann and B. Herskind (North-Holland, 1985), p. 161.
46) M. Matsuo, in *New Trends in Nuclear Collective Dynamics*, ed. Y. Abe, H. Horiuchi and K. Matsuyanagi (Springer-Verlag, 1992), p. 219.
47) K. Takada, K. Yamada and H. Tsukuma, Nucl. Phys. A **496** (1989), 224.
48) K. Yamada, K. Takada and H. Tsukuma, Nucl. Phys. A **496** (1989), 239.
49) K. Yamada and K. Takada, Nucl. Phys. A **503** (1989), 53.
50) K. Yamada, Prog. Theor. Phys. **85** (1991), 805; Prog. Theor. Phys. **89** (1993), 995.
51) H. Aiba, Prog. Theor. Phys. **84** (1990), 908.
52) J. Terasaki, T. Marumori and F. Sakata, Prog. Theor. Phys. **85** (1991), 1235.

53) J. Terasaki, Prog. Theor. Phys. **88** (1992), 529; Prog. Theor. Phys. **92** (1994), 535.
54) Y. R. Shimizu and K. Matsuyanagi, Prog. Theor. Phys. Suppl. No. 141 (2001), 285.
55) M. Matsuo, T. Nakatsukasa and K. Matsuyanagi, Prog. Theor. Phys. **103** (2000), 959.
56) N. Hinohara, T. Nakatsukasa, M. Matsuo and K. Matsuyanagi, Prog. Theor. Phys. **117** (2007), 451.
57) N. Hinohara, T. Nakatsukasa, M. Matsuo and K. Matsuyanagi, Prog. Theor. Phys. **115** (2006), 567.
58) K. Matsuyanagi, Prog. Theor. Phys. **67** (1982), 1441; *Proceedings of the Nuclear Physics Workshop*, Trieste, 5-30 Oct. 1981, ed. C. H. Dasso, R. A. Broglia and A. Winther (North-Holland, 1982), p. 29.
59) Y. Mizobuchi, Prog. Theor. Phys. **65** (1981), 1450.
60) T. Suzuki and Y. Mizobuchi, Prog. Theor. Phys. **79** (1988), 480.
61) T. Fukui, M. Matsuo and K. Matsuyanagi, Prog. Theor. Phys. **85** (1991), 281.
62) J. L. Wood, K. Heyde, W. Nazarewicz, M. Huyse and P. van Duppen, Phys. Rep. **215** (1992), 101.
63) S. M. Fischer et al., Phys. Rev. Lett. **84** (2000), 4064.
64) S. M. Fischer et al., Phys. Rev. C **67** (2003), 064318.
65) E. Bouchez et al., Phys. Rev. Lett. **90** (2003), 082502.
66) A. Gade et al., Phys. Rev. Lett. **95** (2005), 022502 [Errata; **96** (2006), 189901].
67) M. Yamagami, K. Matsuyanagi and M. Matsuo, Nucl. Phys. A **693** (2001), 579.
68) K. Kaneko, M. Hasegawa and T. Mizusaki, Phys. Rev. C **70** (2004), 051301.
69) K. Langanke, D. J. Dean and W. Nazarewicz, Nucl. Phys. A **728** (2003), 109.
70) M. Bender, P. Bonche and P.-H. Heenen, Phys. Rev. C **74** (2006), 024312.
71) A. Petrovici, K. W. Schmid and A. Faessler, Nucl. Phys. A **710** (2002), 246.
72) A. Petrovici, K. W. Schmid and A. Faessler, Nucl. Phys. A **605** (1996), 290.
73) A. Petrovici, K. W. Schmid and A. Faessler, Nucl. Phys. A **665** (2000), 333.
74) M. Kobayasi, T. Nakatsukasa, M. Matsuo and K. Matsuyanagi, Prog. Theor. Phys. **110** (2003), 65.
75) M. Kobayasi, T. Nakatsukasa, M. Matsuo and K. Matsuyanagi, Prog. Theor. Phys. **112** (2004), 363; Prog. Theor. Phys. **113** (2005), 129.
76) D. R. Bes and R. A. Sorensen, *Advances in Nuclear Physics* vol. 2 (Prenum Press, 1969), p. 129.
77) M. Baranger and K. Kumar, Nucl. Phys. **62** (1965), 113; Nucl. Phys. A **110** (1968), 529; Nucl. Phys. A **122** (1968), 241; Nucl. Phys. A **122** (1968), 273.
78) M. Baranger and K. Kumar, Nucl. Phys. A **110** (1968), 490.
79) K. Kumar and M. Baranger, Nucl. Phys. A **92** (1967), 608.
80) D. J. Thouless and G. J. Valatin, Nucl. Phys. **31** (1962), 211.
81) N. Hinohara, T. Nakatsuaksa, M. Matsuo and K. Matsuyanagi, to be published in *Proceedings of International Symposium on Physics of Unstable Nuclei (ISPUN07)*, Hoi An, Vietnam, 3-7 July 2007 (World Scientific); arXiv:0709.3897.
82) H. Sakamoto and T. Kishimoto, Phys. Lett. B **245** (1990), 321.

New efficient method for performing Hartree-Fock-Bogoliubov calculations for weakly bound nuclei

M. Stoitsov
Department of Physics, Graduate School of Science, Kyoto University, Kyoto 606-8502, Japan,
Department of Physics and Astronomy, University of Tennessee, Knoxville, Tennessee 37996, USA,
Physics Division, Oak Ridge National Laboratory, P. O. Box 2008, Oak Ridge, Tennessee 37831, USA, and
Institute of Nuclear Research and Nuclear Energy, Bulgarian Academy of Sciences, Sofia-1784, Bulgaria

N. Michel* and K. Matsuyanagi
Department of Physics, Graduate School of Science, Kyoto University, Kyoto 606-8502, Japan
(Received 10 September 2007; published 1 May 2008)

We propose a new method to solve the Hartree-Fock-Bogoliubov equations for weakly bound nuclei, which works for both spherical and axially deformed cases. In this approach, the quasiparticle wave functions are expanded in a complete set of analytical Pöschl-Teller-Ginocchio and Bessel/Coulomb wave functions. Correct asymptotic properties of the quasiparticle wave functions are endowed in the proposed algorithm. Good agreement is obtained with the results of the Hartree-Fock-Bogoliubov calculation using box boundary condition for a set of benchmark spherical and deformed nuclei.

DOI: 10.1103/PhysRevC.77.054301 PACS number(s): 21.60.Jz, 03.65.Ge, 21.10.Dr, 21.10.Gv

I. INTRODUCTION

The study of nuclei far from stability is an increasingly important part of contemporary nuclear physics. This topic is related to newly created radioactive beams facilities, allowing more experiments on nuclei beyond the stability line. The new experimental opportunities on nuclei with extreme isospin ratio and weak binding bring new phenomena which inevitably require a universal theoretical description of nuclear properties for all nuclei. The current approach to the problem is the nuclear density functional theory which implicitly rely on Hartree-Fock-Bogoliubov (HFB) theory, unique in its ability to span the whole nuclear chart.

The HFB equations can be solved in coordinate space using box boundary condition [1,2]. This approach (abbreviated HFB/Box in this paper) has been used as a standard tool in the description of spherical nuclei [3]. Its implementation to systems with deformed equilibrium shapes is much more difficult, however. Different approaches have been developed to deal with this problem, such as the two-basis method [4–6], the canonical-basis framework [7–9], and basis-spline techniques in coordinate-space calculations developed for axially symmetric nuclei [10,11]. These algorithms are precise, but time consuming.

Configuration-space HFB diagonalization is a useful alternative to coordinate-space calculations whereby the HFB solution is expanded in a complete set of single-particle states. In this context, the harmonic oscillator (HO) basis turned out to be particularly useful. Over the years, many configuration-space HFB codes using the HO basis (abbreviated HFB/HO) have been developed, employing either the Skyrme or the Gogny effective interactions [12–17], or using a relativistic Lagrangian [18] in the context of the relativistic Hartree-Bogoliubov theory. In the absence of fast coordinate-space methods to obtain deformed HFB solutions, the configuration-space approach has proved to be a very fast and efficient alternative allowing large-scale calculations [17,19].

Close to drip lines, however, the continuum states start playing an increasingly important role and it becomes necessary to treat the interplay of both continuum and deformation effects in an appropriate manner. Unfortunately, none of the existing configuration-space HFB techniques manage to incorporate continuum effects.

The goal of the present work is to find an efficient numerical scheme to solve HFB equations for spherical and axially deformed nuclei, which properly takes the continuum effects into account. We will denote this problem as continuum HFB (CHFB). Aiming at treating spherical and deformed nuclei on the same footing, we rely on the configuration-space HFB approach.

The HO basis has important numerical advantages; for example, the use of the Gauss-Hermite quadrature allows for a fast evaluation of matrix elements. On the other hand, its Gaussian asymptotics prevents from expanding systems with large spatial extension, such as halo nuclear states. This problem can be successfully fixed by using the transformed HO basis (THO) [20]. The latter transforms the unphysical Gaussian fall-off of HO states into a more physical exponential decay. Neither HO nor THO bases, however, are able to provide proper discretization of the quasiparticle continuum. This has repercussions already at the HFB level, for which the HO and THO bases cannot reproduce simultaneously all asymptotic properties of nuclear densities (see Sec. V). While this shortcoming is obvious for the HO basis, it also arises for the THO basis because the latter can provide only one type of asymptotic form, i.e., the one inserted in the scaling function defining the THO wave functions [17]. Hence, the THO basis fails to reproduce asymptotic properties, as asymptotic behavior is different for respective channels: proton and neutron, normal and pairing densities, different angles for the deformed case. In fact, differences between calculations using the THO

*nicolas-l.michel@cea.fr

and the coordinate-space bases have been noticed in pairing properties of nuclei (see Sec. V and Ref. [21]). This indicates that THO calculations may not always be fully accurate even in the nuclear region and necessitate a careful check of obtained results. For the aim of carrying out quasiparticle random phase approximation (QRPA) calculations with the HFB quasiparticle representation, the HO and THO bases are very likely to be insufficient as they cannot provide accurate quasiparticle wave functions in the continuum region.

Obviously, a more practical basis is needed. The Gamow Hartree-Fock (GHF) basis [22] would be appropriate, as it has been demonstrated that it can provide the correct asymptotic of loosely bound nuclear states. However, it implies the use of complex symmetric matrices. Moreover, the presence of basis states which increase exponentially in modulus leads to numerical divergences, unless the costly two-basis method is employed [23].

As we plan to consider bound HFB ground states only, it is more advantageous numerically to employ Hermitian completeness relations, whose radial wave functions are real. They are either bound, thus integrable, or oscillate with almost constant amplitude, so that we are free from the numerical cancellation problems associated with the Gamow states. It should be stressed that we can generate a Gamow quasiparticle basis using the HFB potentials thus obtained. We can then describe resonant excited states by means of the quasiparticle random phase approximation representing the QRPA matrix elements in terms of the Gamow quasiparticle basis. This serves as an interesting subject for future investigation.

One could expect that the employment of the spherical Hartree-Fock (HF) potential to generate the real continuum HF (CHF) complete basis would solve the problem. Unfortunately, the CHF basis is not numerically stable due to the presence of resonances in the vicinity of the real continuum. The continuum states lying close to a narrow resonance are rapidly changing, so that a very dense continuum discretization around this resonance is necessary to accurately represent this energy region. Important numerical cancellations would occur as continuum wave functions become very large in amplitude close to narrow resonances.

To overcome this difficulty, we adopt a technique based on the exactly solvable Pöschl-Teller-Ginocchio (PTG) potential [24]. The spherical HF potential, seemingly the best candidate to generate a rapidly converging basis expansion, but providing numerically costly GHF bases or unstable CHF bases, is replaced by a PTG potential fitted to the HF potential if the latter give rise to resonant structure. It will be shown that the narrow resonant states of the GHF basis will become bound in the PTG basis, so that its scattering states will have no rapid phase shift change, a necessary condition for numerically stable continuum discretization. As a result, we obtain a very good basis for HFB calculations. We call this approach HFB/PTG.

To test the feasibility of this new method, we have performed numerical calculations for spherical Ni isotopes near the drip line, ^{84}Ni–^{90}Ni, for a strongly deformed nucleus ^{110}Zr, and two HFB solutions for ^{40}Mg with different, prolate and oblate, deformations. Good agreement with THO calculations is obtained.

The paper is organized as it follows. The HFB/PTG algorithm is described in Sec. II, while the method used to generate the PTG basis is formulated in Sec. III. Asymptotic properties of the HFB quasiparticle wave functions are discussed in Sec. IV. Results of numerical calculation are presented in Sec. V. Brief summary and conclusions are given in Sec. VI. Some technical details related to the PTG basis and calculation of matrix elements are collected in the Appendices.

II. THE HFB/PTG APPROACH

Our aim is to develop an efficient method of solving the CHFB equation

$$\int d\mathbf{r}' \sum_{\sigma'} \begin{pmatrix} h(\mathbf{r}\sigma,\mathbf{r}'\sigma') - \lambda & \tilde{h}(\mathbf{r}\sigma,\mathbf{r}'\sigma') \\ \tilde{h}(\mathbf{r}\sigma,\mathbf{r}'\sigma') & -h(\mathbf{r}\sigma,\mathbf{r}'\sigma') + \lambda \end{pmatrix} \times \begin{pmatrix} U(E,\mathbf{r}'\sigma') \\ V(E,\mathbf{r}'\sigma') \end{pmatrix} = E \begin{pmatrix} U(E,\mathbf{r}\sigma) \\ V(E,\mathbf{r}\sigma) \end{pmatrix} \quad (1)$$

for weakly bound nuclei, which equally works both for spherical and axially deformed nuclei. In the above equation, $\mathbf{r}$ and σ are the coordinate of the particle in normal and spin space, $h(\mathbf{r}\sigma,\mathbf{r}'\sigma')$ and $\tilde{h}(\mathbf{r}\sigma,\mathbf{r}'\sigma')$ denote the particle-hole and the particle-particle (hole-hole) components of the single-particle Hamiltonian, respectively, $U(\mathbf{r}\sigma)$ and $V(\mathbf{r}\sigma)$ the upper and the lower components of the single-quasiparticle wave function, and λ is the chemical potential [3]. For simplicity of notation, the isospin index q is omitted in Eq. (1), but, of course, we solve the CHFB equation for coupled systems of protons and neutrons. In this section, we outline the calculational scheme and details will be presented in the succeeding sections.

The proposed method to solve the CHFB equations, abbreviated HFB/PTG, consists of the following steps:

(i) One starts with spherical or deformed HFB calculations in the HO basis (HFB/HO). This provides a good approximate solution for the HF potential and the effective mass.
(ii) One considers a HF potential and an effective mass for each ℓj subspace, and fits the associated shifted PTG potential to them when the HF potential possesses bound or narrow resonant states in this ℓj subspace (see Sec. III A). If no such states appear in the HF ℓj spectrum, a set of Bessel/Coulomb wave functions [25] is selected for the ℓj partial wave basis.
(iii) One diagonalizes the HFB eigenvalue equations in the basis composed of the PTG and Bessel/Coulomb wave functions. This step continues until self-consistency is achieved.

The use of the Bessel/Coulomb wave functions in step (2) occurs for partial waves of high angular momentum, for which the centrifugal part becomes dominant. As no resonant structure can appear therein in the real HF continuum, Bessel/Coulomb wave functions provide a numerically stable set of states for this partial wave. For the generation of Coulomb wave functions, one can use the recently published C++ code [26] or its FORTRAN alternative [27]. A complete

set of wave functions is thus formed, which will be used as a basis to expand the HFB quasiparticle wave functions.

The necessary truncation of the basis in step (3) implies that spurious effects may eventually appear at very large distances, where both the particle density ρ and the pairing density $\tilde{\rho}$ are very small. Consequently, quasiparticle wave functions have to be matched to their exact asymptotics at moderate distances as it is explained further in Sec. IV. In addition, special care must be taken to calculate matrix elements due to the presence of nonintegrable scattering states (see Appendix B).

When the HF mean-field resulting from the HFB/HO calculation in step (1) is deformed, there are several ways to extract the HF potential for each ℓj subspace to be used in step (2). Because it is used just as a generator for the complete PTG basis, its choice will have little effect on the final HFB solution, however. In the present calculation, we therefore adopt a simple procedure; the particle-hole part of the HFB/HO potential and the HFB/HO effective mass are used in step (2) after averaging their angular and spin degrees of freedom. The resulting HF potential is spherical and the same for all ℓj subspaces. In such a case, the effect of the spin-orbit splitting is not taken into account in the stage of constructing the PTG basis but it is of course taken into account in step (3). This implies to consider a basis generated by a spherical potential, which might seem inefficient in the case of large deformation, for which deformed bases are more appropriate, as is done with the HO and THO bases. The deformed nuclei considered in this paper are nevertheless fairly reproduced within this framework (see Sec. V). If necessary, it is possible to generate a deformed basis by diagonalizing the deformed HF potential within the PTG basis, which can then serve as a particle basis for the HFB problem.

III. GENERATION OF BASIS

A. PTG potentials fitting procedure

The PTG potential has four parameters Λ, s, ν, and a, which have to be determined in each ℓj subspace (see Appendix A). For this purpose, we use the spherical HF potential and effective mass in a given ℓj subspace.

The PTG mass parameter a is obtained from the requirement that the PTG and the HF effective masses are the same at the origin. One first adds the centrifugal term $V_{\ell(\ell+1)} \propto \ell(\ell+1)/r^2$ to the nuclear plus Coulomb potential, $V_N + V_C$, and determines the height E_b of the centrifugal (plus Coulomb) barrier. Then, one adds E_b to the PTG potential; the resulting potential may be called the shifted PTG potential. The parameters Λ and ν are fitted in such a way that the χ^2 difference between the shifted PTG potential and the HF potential is minimal. Note that s is directly obtained from Λ and ν values during the fit, as it is determined by way of the property that the PTG potential of parameters Λ, s, ν, and a for $r \to 0$ is equivalent to s^2 times the PTG potential of parameters Λ, $s = 1$, ν, and a. The reason why we use the barrier height E_b in our fitting procedure will become apparent by an illustrative example presented below.

To test the fitting procedure and the quality of the resulting PTG basis we performed GHF calculations in the coordinate space for the spherical nucleus ^{84}Ni. Let us examine the quality

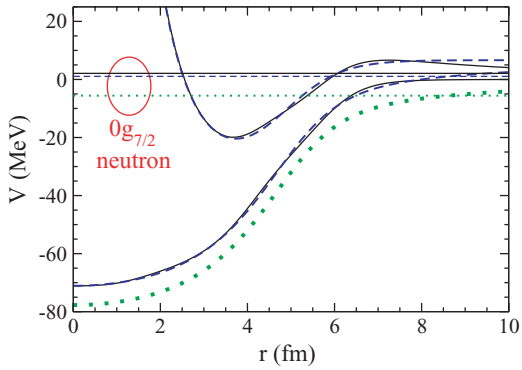

FIG. 1. (Color online) The shifted PTG potential, the HF potential calculated with the SLy4-force, and the unshifted PTG potential for neutrons in ^{84}Ni. HF and shifted PTG potentials to which the centrifugal part is added are provided as well, and the energies of $0g_{7/2}$ levels for each potential are indicated. All data respectively associated to HF, shifted and unshifted PTG potentials are respectively shown in solid, dashed, and dotted lines.

of single-particle energies and wave functions resulting from the shifted PTG potential by comparing them with the GHF energies and wave functions for bound and resonance states.

Figure 1 illustrates the PTG fitting procedure and compare the results with the GHF ones taking the neutron $0g_{7/2}$ level as an example. It is seen that the energy of the bound $0g_{7/2}$ state in the original (unshifted) PTG potential (horizontal dotted line) become positive after being shifted with E_b (horizontal dashed line) and its position agrees in a good approximation with the resonance energy obtained by the GHF calculation (horizontal solid line). This is due to a special feature of the PTG potential, for which the centrifugal potential decreases exponentially and not as r^{-2} for $r \to +\infty$ (see Appendix A). This implies that the centrifugal + shifted PTG potential goes very quickly to the constant value, E_b, for $r \to +\infty$.

In this way, the PTG treatment replaces the GHF resonance with a weakly bound PTG state whose wave function will be very similar in the nuclear region. Approximating resonant states by weakly bound states in our framework resembles the standard two-potential method described in Ref. [28]. Thus, one can expect that the fitted PTG potential provides a rapidly converging basis for solving the HFB equations.

In fact, it is not necessary to find the PTG potential that exactly minimize the χ^2 difference with the HF potential. As the PTG potential is used as a basis generator, slight differences with the exact minimum lead only to slightly different bases states to expand the HFB quasiparticle wave functions, preserving its rapidly converging properties. Thus, one can take rather large steps for the Λ, ν variations and few radii for the χ^2 evaluation to save computer time, keeping the quality of the basis essentially the same.

B. Single-particle energies

Single-particle energies and widths for neutrons in ^{84}Ni obtained by the GHF calculations are compared with the PTG energies in Table I. One can clearly see the following facts.

Firstly, the overall agreement between the GHF and the shifted PTG energies is good, which means that the PTG

TABLE I. Neutron GHF levels in ^{84}Ni calculated with the SLy4 Skyrme-force and the surface-type delta pairing interaction (see Sec. V for the parameters used), which are compared with the PTG estimates. All energies are given in MeV while the width Γ is given in keV.

States	GHF		PTG	
	Γ	e	$e + E_b$	e
$0s_{1/2}$	0	−52.38	−51.89	−51.89
$1s_{1/2}$	0	−24.37	−25.55	−25.55
$2s_{1/2}$	0	−0.72	−0.97	−0.97
$0p_{3/2}$	0	−41.25	−40.67	−41.09
$1p_{3/2}$	0	−12.52	−12.95	−13.36
$0p_{1/2}$	0	−39.44	−38.79	−39.22
$1p_{1/2}$	0	−10.67	−10.73	−11.16
$0d_{5/2}$	0	−29.38	−29.50	−31.02
$1d_{5/2}$	0	−1.90	−1.94	−3.46
$0d_{3/2}$	0	−25.20	−25.53	−27.11
$1d_{3/2}$	10.03	0.18	0.24	−1.34
$0f_{7/2}$	0	−17.56	−17.45	−20.88
$0f_{5/2}$	0	−10.87	−12.40	−16.01
$0g_{9/2}$	0	−6.11	−5.52	−11.74
$0g_{7/2}$	31.62	2.09	1.05	−5.58
$0h_{11/2}$	92.93	4.53	6.18	−3.79

potential is flexible enough to reproduce the main features of the HF potential.

Secondly, all narrow GHF resonances are represented as weakly bound PTG states with upward shifted PTG energies. This is very important because the HFB upper (lower) components of quasiparticle states are likely to have large overlaps with unoccupied (occupied) weakly bound and narrow resonance states.

We note that the GHF states whose width is larger than 1 MeV, as a rule, are not converted to bound PTG states. This is not important, however, because scattering states do not exhibit rapid changes in the energy region of broad resonances. The broad resonance region can indeed be well represented in terms of the continuum basis states.

C. PTG wave functions

As illustrated in Fig. 2 narrow GHF resonant states bear large overlaps with their associated PTG bound states. Hence, the GHF resonant structure present in the HFB quasiparticle wave functions will be sustained by the PTG bound states, thus reducing the coupling to the PTG scattering continuum.

An example indicating the quality of the bound single-particle wave functions resulting from the fitting PTG procedure is shown in Fig. 3 for the bound $0s_{1/2}$, $1s_{1/2}$, and $2s_{1/2}$ neutron states. In this case, nuclear potential has no centrifugal barrier, so that the PTG and the HF potentials possess the same asymptotic behavior. Very good agreement between the PTG (dashed lines) and the GHF (solid lines) wave functions is thus not surprising. The upper panel in Fig. 3 shows the asymptotic region in logarithmic scale where HO wave functions (dotted lines) are also given as a reference. Their Gaussian asymptotics

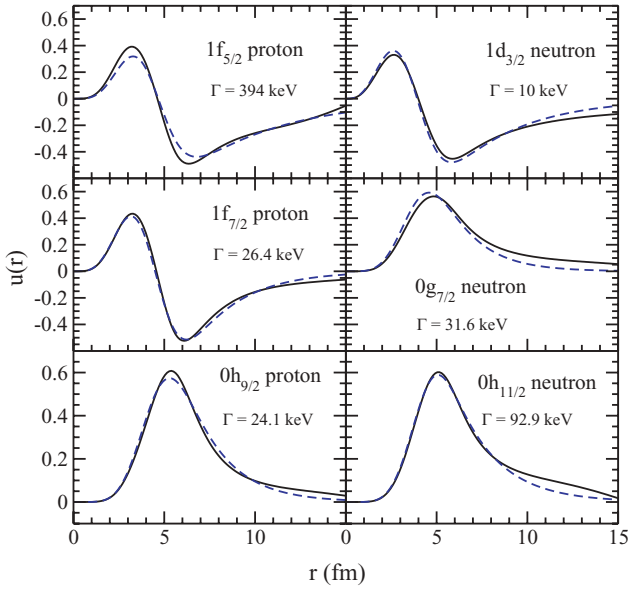

FIG. 2. (Color online) The PTG (dashed lines) and GHF (solid lines) wave functions for various resonance states.

cannot reproduce even approximately the exponential decrease of the PTG and GHF wave functions.

Neutron continuum s-states are illustrated in Fig. 4, which are properly reproduced as well by the scattering states for the PTG potential. In the cases when a centrifugal (and/or Coulomb) barrier exists, as illustrated in Fig. 5 for $d_{3/2}$ states, different phase shifts develop in the PTG and GHF continuum states, as the PTG potential bears no barrier at large distance.

IV. QUASIPARTICLE WAVE FUNCTIONS IN THE ASYMPTOTIC REGION

The necessary truncation of the basis implies that spurious effects will eventually appear at very large radius, where both

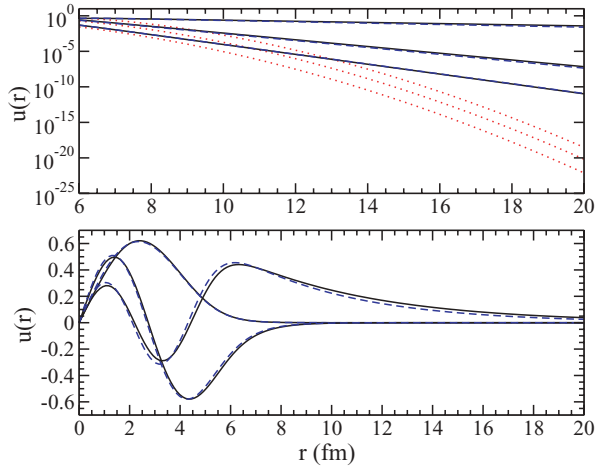

FIG. 3. (Color online) The PTG (dashed lines), GHF (solid lines), and HO (dotted lines) wave functions including the asymptotic region for the bound $0s_{1/2}$, $1s_{1/2}$, and $2s_{1/2}$ neutron states both in normal scale (lower panel) and logarithmic scale (upper panel).

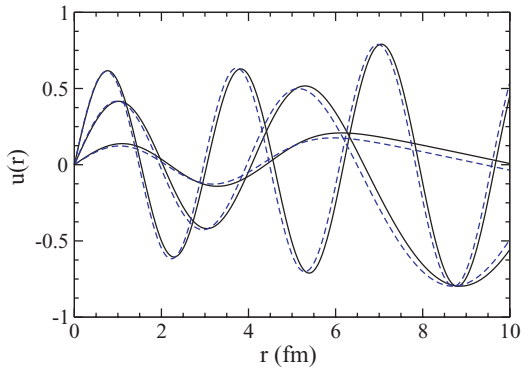

FIG. 4. (Color online) The PTG (dashed lines) and GHF (solid lines) wave functions of the neutron continuum s-states calculated with energies of 0.118 MeV, 9.996 MeV, and 66.119 MeV.

the particle density ρ and the pairing density $\tilde{\rho}$ are very small. Consequently, quasiparticle wave functions have to be matched with their exact asymptotics at moderate distance, where the asymptotic region has been attained and densities are still large enough for basis expansion to be precise. Below we explain how the matching procedure is done for axially deformed nuclei.

In order to deal with the asymptotics of quasiparticle wave functions, we make partial wave decomposition of them:

$$\begin{aligned} U_{km}(\mathbf{r}\sigma) &= \sum_{\alpha} U^{\alpha}_{km}\Psi_{\alpha}(\mathbf{r}) = \sum_{\ell j} U^{(\ell j)}_{km}(r)\,\mathcal{Y}^{\ell j}_{km}(\Omega), \\ V_{km}(\mathbf{r}\sigma) &= \sum_{\alpha} V^{\alpha}_{km}\Psi_{\alpha}(\mathbf{r}) = \sum_{\ell j} V^{(\ell j)}_{km}(r)\,\mathcal{Y}^{\ell j}_{km}(\Omega), \end{aligned} \tag{2}$$

where the subscript k specifies the quasiparticle eigenstates together with the magnetic quantum number m which is always conserved for both spherical and axially symmetric nuclei; $\Psi_{\alpha}(\mathbf{r})$ are the PTG or Bessel/Coulomb wave functions; U^{α}_{km} and V^{α}_{km} are the HFB expansion coefficients; $U^{(\ell j)}_{km}(r)$ and $V^{(\ell j)}_{km}(r)$ are the radial amplitudes with $r = |\mathbf{r}|$ for the (ℓj) partial wave; $\mathcal{Y}^{\ell j}_{m}(\Omega)$ denotes a product wave function where the spherical harmonics with the angular variables Ω and the orbital angular momentum ℓ is coupled with spin to the total angular momentum j.

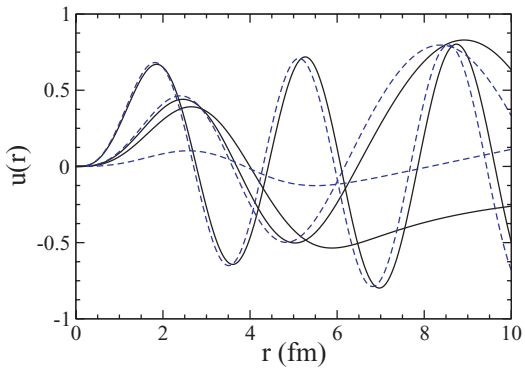

FIG. 5. (Color online) The PTG (dashed lines) and the GHF (solid lines) wave functions for the neutron continuum $d_{3/2}$-states calculated at the same energies as in Fig. 4

The partial wave amplitudes, $U^{(\ell j)}_{km}(r)$ and $V^{(\ell j)}_{km}(r)$, defined above involve a summation over all quantum numbers except the angular momenta ℓ and j. In the spherical case, the sums reduce to a single element as ℓ and j are good quantum numbers. In the asymptotic region, only Coulomb and centrifugal parts remain from the HFB potentials, so that one can continue the quasiparticle wave functions via their partial wave decompositions and decay constants k_u and k_v:

$$\begin{aligned} U^{(\ell j)}_{km}(r) &= C^{(\ell j)+}_{km} H^{+}_{\ell,\eta_u}(k_u r) + C^{(\ell j)-}_{km} H^{-}_{\ell,\eta_u}(k_u r), \\ V^{(\ell j)}_{km}(r) &= D^{(\ell j)+}_{km} H^{+}_{\ell,\eta_v}(k_v r), \\ k_v &= \sqrt{\frac{2m}{\hbar^2}(\lambda - E)}, \quad k_u = \sqrt{\frac{2m}{\hbar^2}(\lambda + E)}, \end{aligned} \tag{3}$$

where E denotes the quasiparticle energy, λ the chemical potential, $H^{\pm}_{\ell,\eta}$ the Hankel (or Coulomb) functions, η being the Sommerfeld parameter, and $C^{(\ell j)+}_{km}$, $C^{(\ell j)-}_{km}$, and $D^{(\ell j)+}_{km}$ are constants to be determined. Matching is performed using Eq. (2) at a radius R_0 in the asymptotic region where the basis expansion is precise, so that $C^{(\ell j)+}_{km}$, $C^{(\ell j)-}_{km}$, and $D^{(\ell j)+}_{km}$ come forward by continuity. The value of R_0 is typically of the order of 10 fm.

V. NUMERICAL EXAMPLES

We have made a feasibility test of the HFB/PTG method for spherical Ni isotopes close to the neutron drip line and for deformed neutron-rich nuclei ^{110}Zr and ^{40}Mg. All calculations were done using the SLy4 density functional [29]. For the pairing interaction, we use the surface-type delta pairing with the strength $t_0' = -519.9$ MeV fm^3 for the density-independent part and $t_3' = -37.5 t_0'$ MeV fm^6 for the density-dependent part with a sharp energy cutoff at 60 MeV in the quasiparticle space. They have been fitted to reproduce the neutron pairing gap of ^{120}Sn. These values are consistent with those given in Ref. [30]; the slight difference is due to different cut-off procedures, sharp cutoff in our case and smooth cutoff in Ref. [30]. Below we discuss the major features of the result of calculation. We also make a detailed comparison between the HFB/PTG and HFB/Box calculations in the spherical case.

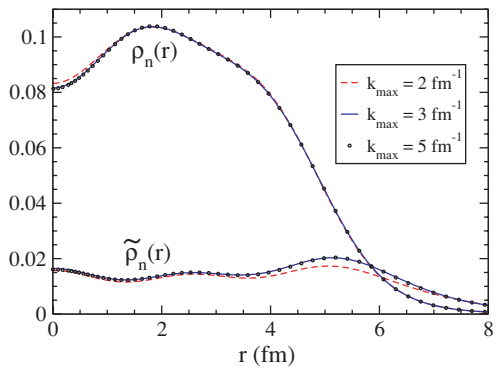

FIG. 6. (Color online) Dependence on $k_{\max}$ of the neutron density ρ_n and the neutron pairing density $\tilde{\rho}_n$ calculated for ^{84}Ni by the HFB/PTG method.

TABLE II. Results of the HFB/PTG calculation for ground state characteristics of Ni isotopes close to the neutron drip line, which are compared with results of the HFB/Box calculation. The SLy4 functional and the surface-type delta pairing [20] are used. The rms radii are in fm and all other quantities are in MeV. Proton chemical potential λ_p is not provided as pairing correlations vanish in the proton space.

	^{84}Ni		^{86}Ni		^{88}Ni		^{90}Ni	
	HFB/Box	HFB/PTG	HFB/Box	HFB/PTG	HFB/Box	HFB/PTG	HFB/Box	HFB/PTG
λ_n	−1.453	−1.429	−1.037	−1.029	−0.671	−0.661	−0.342	−0.329
r_n	4.451	4.450	4.528	4.526	4.603	4.602	4.677	4.674
r_p	3.980	3.981	4.001	4.001	4.021	4.021	4.043	4.043
Δ_n	1.481	1.532	1.667	1.658	1.790	1.780	1.899	1.892
$E_n^{\rm pair}$	−30.70	−30.60	−36.52	−35.92	−41.98	−41.187	−47.158	−46.233
T_n	1084.53	1085.95	1118.65	1118.63	1150.71	1150.64	1182.52	1182.66
T_p	430.47	430.240	425.99	426.01	421.71	421.72	417.38	417.37
$E_n^{\rm so}$	−63.379	−63.177	−61.679	−61.707	−59.558	−59.681	−56.898	−57.889
$E_{\rm dir}^{\rm Coul}$	132.94	132.90	132.26	132.246	131.571	131.578	130.947	130.886
$E_{\rm exc}^{\rm Coul}$	−10.138	−10.136	−10.084	−10.085	−10.033	−10.033	−9.980	−9.980
$E_{\rm tot}$	−654.89	−654.914	−656.933	−656.877	−658.167	−658.084	−658.665	−658.608

A. Spherical nuclei

Let us first examine how the result of calculation depends on the truncation of the basis. Indeed, the basis has to be truncated at a maximal linear momentum $k_{\rm max}$, and discretized with $N_{\ell j}$ continuum states per partial wave in the interval $[0 : k_{\rm max}]$. Figure 6 shows that the use of values larger than $k_{\rm max} = 3$ fm^{-1} does not change the results. Accordingly, in calculations for spherical nuclei, we use $k_{\rm max} = 5$ fm^{-1} and discretize the continuum with $N_{\ell j} = 60$ scattering states per partial wave (see Ref. [22] for its justification).

Results of the HFB/PTG calculation for a set of benchmark Ni isotopes close to the neutron drip line are presented in Table II, Figs. 7 and 8, where results of the HFB/Box calculation are also shown for comparison. The Ni isotopes are spherical with pairing in the neutron channel only. We see immediately a remarkable agreement between the results of the HFB/PTG and HFB/Box calculations. The difference in

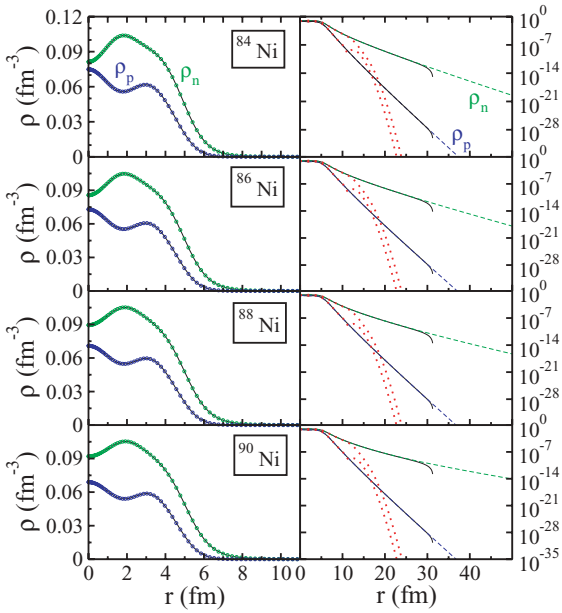

FIG. 7. (Color online) The neutron densities ρ_n and proton densities ρ_p both in normal (left-hand side) and logarithmic (right-hand side) scales. Results of the HFB/Box calculation are displayed by solid lines, while those of the HFB/PTG calculations by open circles and dashed lines. The HFB/HO densities are also indicated by dotted lines in the right panels for comparison.

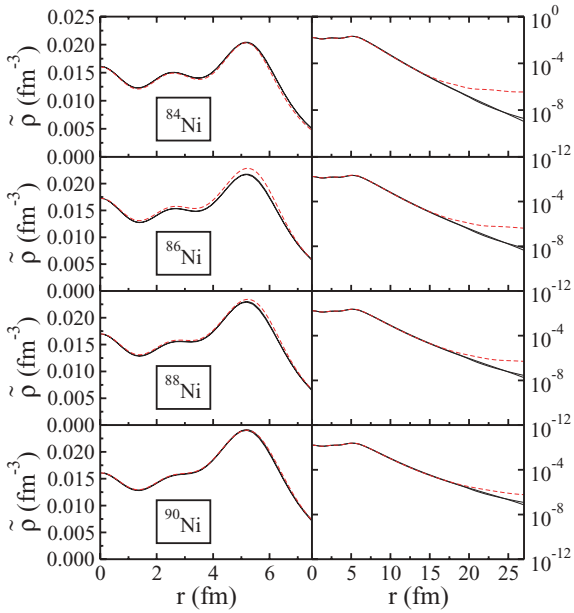

FIG. 8. (Color online) The neutron pairing densities $\tilde{\rho}_n$ in normal (left-hand side) and logarithmic (right-hand side) scales. There are no pairing correlations in the proton channel. Results of the HFB/Box and HFB/PTG calculations are displayed both by solid lines, as they are almost indistinguishable, while HFB/THO pairing densities are represented by dashed lines.

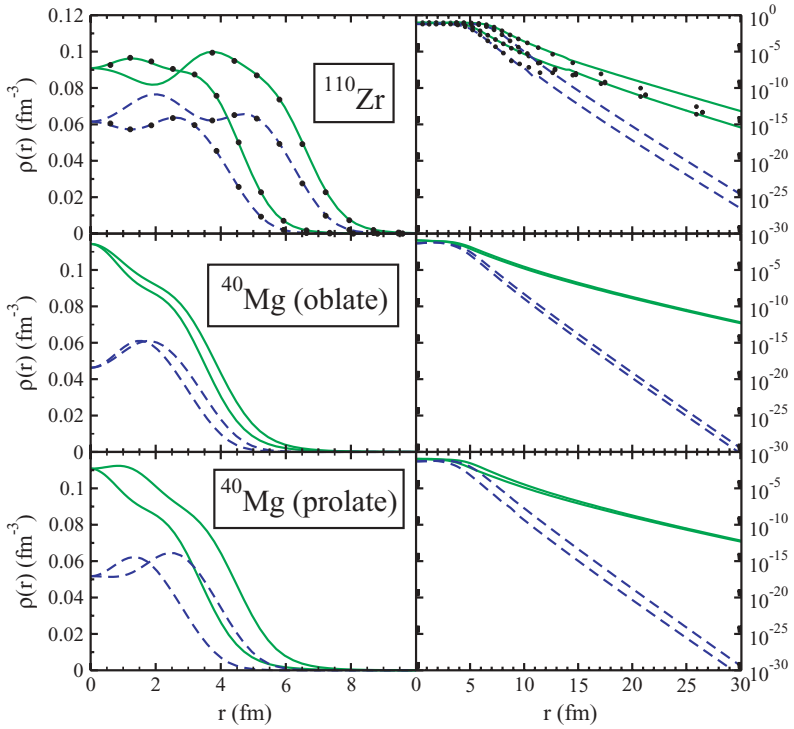

FIG. 9. (Color online) The neutron and proton densities of the prolately deformed nucleus ^{110}Zr ($\beta = 0.40$), respectively calculated by the HFB/PTG (solid and dashed lines, respectively) and HFB/THO (circles) methods in normal (top left) and logarithmic (top right) scale. They are given along the long and short axes of deformation, easily identified from the figure. The neutron and proton densities of ^{40}Mg calculated by the HFB/PTG method for two states with different deformations (oblate $\beta = -0.09$ and prolate $\beta = 0.26$) in normal (middle and bottom left) and logarithmic (middle and bottom right) scale are also provided with the same line convention.

total energies is less than 85 keV and the proton rms radii agree almost perfectly, while the neutron ones are slightly different by less than 0.003 fm. Similarly good agreement is obtained for all other energy counterparts. The good agreement in the ground state characteristics evaluated by the two different approaches is not surprising if one compares the density distributions shown in Figs. 7 and 8. In these figures, the neutron and proton densities, ρ_n and ρ_p, and the neutron pairing density $\tilde{\rho}_n$ are plotted both in normal (left column) and logarithmic (right column) scales. The agreement is almost perfect in the whole range of r except at the box boundary where the HFB/Box densities vanish due to the boundary conditions (however not seen in Fig. 8). This agreement is striking considering the significant impact of the continuum for these nuclei and the fact that the HFB/PTG calculations are nevertheless performed using the basis expansion method.

Special attention has to be paid to the agreement for the pairing quantities. Interestingly, the pairing gap Δ_n increases as one approaches the drip line, indicating the important role of the pairing correlations in the continuum. This result is somehow different from that of Ref. [31] obtained by an alternative HFB calculation in the coordinate space for the same set of nuclei but it is in agreement with the estimates from Ref. [32]. In Fig. 8, the scaling function of the THO basis is calculated with the method described in Ref. [20], for which the quasi-exact density provided by the HFB/PTG calculations is used, and 16 THO shells are taken into account for each partial wave. This implies virtually optimal results, and it has been checked that densities obtained from the HFB/Box and HFB/THO methods are almost identical up to 20 fm. On the other hand, pairing densities given by the THO calculations are not exactly the same with those of the HFB/PTG and HFB/Box calculations, as can be seen from Fig. 8. While pairing densities calculated with both methods for ^{84}Ni and ^{90}Ni are very close, those for ^{86}Ni and ^{88}Ni exhibit visible differences, especially for ^{86}Ni, for which pairing energies differ by about 4 MeV. Asymptotic properties of pairing densities calculated with the THO basis are also not well behaved after 15–20 fm, where they saturate instead of decreasing exponentially. This indicates that THO basis calculations are not always devoid of inaccuracies, even at the spherical HFB level.

B. Axially deformed nuclei

In the case of axially deformed nuclei, few HFB/Box calculations are available to check the HFB/PTG results. We consider the well-deformed nucleus ^{110}Zr (deformation $\beta \approx 0.4$), already studied in Ref. [21] and two states with different deformations for the drip line nucleus ^{40}Mg. We use therein $k_{\max} = 4$ fm^{-1} and $N_{\ell j} = 30$ for all partial waves.

Table III compares the three approaches with respect to ground state properties of ^{110}Zr. In general they yield similar values. The differences seen in Table III are partially due

TABLE III. Comparison of ground state properties of ^{110}Zr calculated with the HFB/Box, HFB/PTG, and HFB/THO approaches. The rms radii are in fm, quadrupole moments are in barn, and all other quantities are in MeV.

	HFB/Box	HFB/PTG	HFB/THO
$Q_{\rm tot}$	12.088	12.53	12.303
Δ_n	0.480	0.626	0.562
$E_n^{\rm pair}$	−1.53	−3.015	−2.05
r_n	4.82	4.836	4.831
r_p	4.55	4.560	4.556
$E_{\rm tot}$	−893.93	−893.952	−893.711

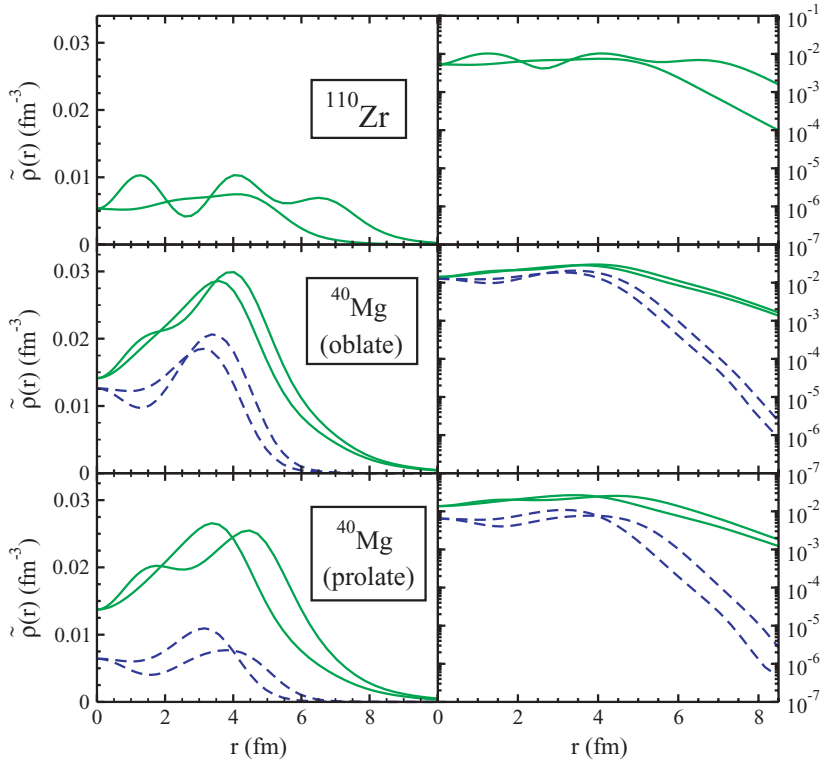

FIG. 10. (Color online) Same as in Fig. 9 but for pairing densities and without HFB/THO results. Proton pairing density is not represented for ^{110}Zr as it is negligible therein.

to different structure of the model spaces adopted and the associated fitting of the pairing strength.

Proton and neutron densities for nuclei ^{110}Zr and ^{40}Mg are displayed in Fig. 9, with comparison with THO results (circles) for ^{110}Zr, in normal scale (left column panels) and logarithmic scale (right column panels). Associated pairing densities are shown in Fig. 10.

While agreement between the PTG and THO densities for ^{110}Zr is good in normal scale, we can notice discrepancies in asymptotic properties, which are visible from the figure in logarithmic scale (see Fig. 9). It is obvious that all densities calculated with the THO basis eventually follow the common asymptote dictated by the scaling function, while they are well reproduced with use of the PTG basis. This comparison also confirms the presence of deformation effects even in the far asymptotic region.

The middle and bottom panels in Figs. 9 and 10 illustrate the HFB/PTG normal and pairing densities for two states with different deformations in the drip line nucleus ^{40}Mg. These states possess pairing correlations in both neutron and proton channels. The prolate and oblate states lead to asymptotic neutron densities which are very close, as seen from the middle and bottom right panels in Fig. 9.

VI. CONCLUSIONS

We have proposed a new method of the CHFB calculation for spherical and axially deformed nuclei, which properly takes the continuum into account. The method combines configuration-space diagonalization of the HFB Hamiltonian in the complete set of analytical PTG and Bessel/Coulomb wave functions with a matching procedure in the coordinate space which restores the correct asymptotic properties of the HFB wave functions. The PTG potential is chosen to fit the nuclear HF potential and effective mass. The resulting PTG wave functions are close to the bound and continuum states of the related HF potential while the resonance states are substituted by the bound PTG states with shifted single-particle energies. Partial waves of high angular momentum are very well represented by Bessel/Coulomb wave functions.

The main results of the present work are twofold:

First, we have obtained a new scheme (HFB/PTG) to solve the CHFB equations as a promising tool for large scale calculation; its performance is comparable, sometimes even better, to that of the HFB/THO code, for example. It properly takes the nuclear continuum into account and therefore could be used for precise density functional calculations for nuclei close to the drip lines. This HFB/PTG method can also be used to provide accurate quasiparticle wave functions for microscopic calculations of dynamics beyond the nuclear mean-field approximation, as for example, the QRPA calculations for deformed nuclei.

Second, the fact that the HFB/PTG calculation reproduces the results of the coordinate-space HFB calculation with the box boundary condition (HFB/Box) even for nuclei up to the neutron drip lines is important. This result indicates the validity of the HFB/Box calculation which is widely used, although its validity is sometimes questioned when it is applied to the drip-line phenomena where continuum effects are crucially important [31].

The inclusion of the resonant structure in the basis is crucial for the success of the HFB/PTG approach. Our test calculations indicate significant disagreement with the HFB/Box result if the PTG bound states representing the resonant GHF states are removed from the basis: in their absence, the pairing densities are overestimated in the surface region, while particle

densities are slightly underestimated in the inner region. This means that the resonance states significantly contribute to the total energy through both the particle-hole and particle-particle channels. Their contributions to the pairing correlation energy are evaluated to be about 2–3 MeV for the case of Ni isotopes close to the neutron drip line.

A more complete investigation of the importance of the HFB resonance states could be made by a detailed comparison with the result of the exact Gamow-HFB calculation. Such an analysis is in progress for spherical nuclei and will be reported in the near future [23].

ACKNOWLEDGMENTS

The authors acknowledge Japan Society for the Promotion of Science for financial support, which make our Collaboration possible. This work was supported by the JSPS Core-to-Core Program "International Research Network for Exotic Femto Systems." This work was carried out as a part of the U.S. Department of Energy under Contract Nos. DE-FG02-96ER40963 (University of Tennessee), DE-AC05-00OR22725 with UT-Battelle, LLC (Oak Ridge National Laboratory), and DE-FG05-87ER40361 (Joint Institute for Heavy Ion Research), the UNEDF SciDAC Collaboration supported by the U.S. Department of Energy under Grant no. DE-FC02-07ER41457.

APPENDIX A: PTG BASIS

A. PTG potential

The one-body Hamiltonian for the exactly solvable PTG model reads

$$H_{\rm PTG} = \frac{\hbar^2}{2m_0}\left(-\frac{d}{dr}\frac{1}{\mu(r)}\frac{d}{dr} + \frac{\ell(\ell+1)}{r^2\mu(r)}\right) + V_{\rm PTG}(r) \tag{A1}$$

with m_0 the particle free mass, r is the radial coordinate (in fm), $\mu(r)$ its dimensionless effective mass [the full effective mass is $m_0\,\mu(r)$], ℓ its orbital angular momentum, and $V_{\rm PTG}$ is the PTG potential. The potential $V_{\rm PTG}(r)$ and the effective mass $\mu(r)$ are written

$$\mu(r) = 1 - a(1-y^2), \tag{A2}$$

$$V_{\rm PTG}(r) = \frac{\hbar^2 s^2}{2\,m_0\,\mu(r)}(V_\mu(r) + V_\ell(r) + V_c(r)), \tag{A3}$$

where s is the scaling parameter, V_μ the potential part issued from the effective mass, V_ℓ its ℓ-dependent part, and V_c its main central part, defined by

$$V_\mu(r) = [1 - a + [a(4-3\Lambda^2) - 3(2-\Lambda^2)]y^2 - (\Lambda^2-1)(5(1-a)+2ay^2)\,y^4] \times \frac{a}{\mu(r)^2}(1-y^2)[1+(\Lambda^2-1)y^2], \tag{A4}$$

$$V_\ell(r) = \ell(\ell+1)\left[\frac{(1-y^2)(1+(\Lambda^2-1)y^2)}{y^2} - \frac{1}{s^2r^2}\right], \quad r>0, \tag{A5}$$

$$V_c(r) = (1-y^2)\left[-\Lambda^2\nu(\nu+1) - \frac{\Lambda^2-1}{4}(2-(7-\Lambda^2)y^2 - 5(\Lambda^2-1)y^4)\right]. \tag{A6}$$

The quantities $V_{\rm PTG}(r)$ and $\mu(r)$ depend on an implicit function $y = y(r)$ defined in the following way:

$$\Lambda^2 s\, r = \operatorname{arctanh}(y) + \sqrt{\Lambda^2-1}\,\arctan\left(\sqrt{\Lambda^2-1}\,y\right) \tag{A7}$$

so that $0 \leqslant y < 1$ for $0 \leqslant r < \infty$.

The numerical solution of Eq. (A7) by way of Newton/bisection methods is stable but one should take special care at large distances when y becomes closely equal to one. For example, this can be done by rewriting Eq. (A7), introducing the new variable $x = \operatorname{arctanh}(y)$:

$$\Lambda^2 s\, r = x + \sqrt{\Lambda^2-1}\,\arctan(\sqrt{\Lambda^2-1}\tanh(x)), \tag{A8}$$

It is solved with respect to x with a fixed-point algorithm. In this region, $1-y^2$ should be calculated in terms of the expression $1-y^2 = 4e^{-2x}/(1+e^{-2x})^2$ to avoid numerical cancellations.

One has to mention that, in the calculation of $V_{\rm PTG}(r)$, $V_\ell(r)$ is finite for all $r \geqslant 0$ but is the difference of two diverging terms for $r \to 0$. Thus, to be precise in this region, Eq. (A7) must be rewritten as a power series in y, so that the main diverging terms of Eq. (A5) cancel analytically.

As seen from the equations above, there are four parameters in the PTG model: the effective mass parameter a, the scaling parameter s, the parameter Λ determining the shape of the potential and the parameter ν associated with the depth of the potential. They can take different values for different angular momenta ℓ. We can use this freedom in order to approximate the nuclear potential for each ℓj-subspace, as described in Sec. II.

B. PTG states

The PTG wave functions and eigenenergies are determined by the Schrödinger equation for the Hamiltonian (A1)

$$H_{\rm PTG}\Phi_k(r) = E\,\Phi_k(r) \tag{A9}$$

with energies

$$E = \frac{\hbar^2 k^2}{2m_0}, \tag{A10}$$

where k stands for the complex linear momentum associated with E.

For bound states, if they exist, the parameter ν determines the maximal value $n_{\rm max}$ of the radial quantum number $n = 0, 1, 2, \ldots, n_{\rm max}$ as the largest integer inferior to

$$\left\{\frac{1}{2}\left(\nu - \ell - \frac{3}{2}\right)\right\}, \tag{A11}$$

and defines the complex momentum

$$k_{nl} = is\frac{-A_{nl} + \sqrt{\Delta_{nl}}}{1-a}, \tag{A12}$$

with

$$A_{nl} = 2n + \ell + \tfrac{3}{2}, \tag{A13}$$

$$\Delta_{nl} = \Lambda^2 \left(\nu + \tfrac{1}{2}\right)^2 (1-a) - [(1-a)\Lambda^2 - 1]A_{nl}^2. \tag{A14}$$

For continuum states, k can take any real positive values from zero to infinity.

C. PTG wave functions

In order to express the PTG wave function $\Phi_k(r)$ in a closed analytical form, let us introduce the following three functions:

$$f_k(r) = F(\nu^-, \nu^+, \ell + \frac{3}{2}, x^-)(x^+)^{\bar\beta/2}, \tag{A15}$$

$$f_k^+(r) = F(\nu^-, \nu^+, \bar\beta + 1, x^+)(x^+)^{\bar\beta/2}, \tag{A16}$$

$$f_k^-(r) = F(\mu^-, \mu^+, -\bar\beta + 1, x^+)(x^+)^{-\bar\beta/2}, \tag{A17}$$

and

$$\chi_k(r) = \sqrt{\frac{x^- + \Lambda^2(1-a)x^+}{\sqrt{x^- + \Lambda^2 x^+}}}(x^-)^{\frac{\ell+\frac{3}{2}}{2}}, \tag{A18}$$

where

$$x = \frac{1-(\Lambda^2+1)y^2}{1+(\Lambda^2-1)y^2}, \quad x^- = \frac{1-x}{2}, \quad x^+ = \frac{1+x}{2}, \tag{A19}$$

$$\nu^+ = \frac{\ell + \frac{3}{2} + \bar\beta + \bar\nu}{2}, \quad \nu^- = \frac{\ell + \frac{3}{2} + \bar\beta - \bar\nu}{2}, \tag{A20}$$

$$\mu^+ = \frac{\ell + \frac{3}{2} - \bar\beta + \bar\nu}{2}, \quad \mu^- = \frac{\ell + \frac{3}{2} - \bar\beta - \bar\nu}{2}, \tag{A21}$$

$$\bar\beta = -\frac{ik}{\Lambda^2 s}, \tag{A22}$$

$$\bar\nu = \sqrt{(\nu + 1/2)^2 + \bar\beta^2(1 - \Lambda^2(1-a))}, \tag{A23}$$

and $F(a, b, c, z)$ is the Gauss hypergeometric function [25].

In the case of bound states, k_{nl} determines the momenta k which are pure imaginary [see Eq. (A12)], while they are real positive numbers in the case of scattering states. This defines all other quantities entering the equations above. For both cases, the PTG wave functions can be written either as

$$\Phi_k(r) = \mathcal{N}\chi_k(r) f_k(r) \tag{A24}$$

or as

$$\Phi_k(r) = \mathcal{N}\chi_k(r)(A^+ f_k^+(r) + A^- f_k^-(r)). \tag{A25}$$

Equation (A24) is suitable for numerical work for small distances since $x^- \to 0$ when $r \to 0$ so that one is away from the pole of the hypergeometric function appearing at $x^- = 1$. Similarly, Eq. (A25) is applicable for large distances since $x^+ \to 0$ when $r \to +\infty$ and the pole $x^+ = 1$ of the hypergeometric function in Eqs. (A16) and (A17) is avoided.

In the case of bound states, the quantum numbers $\{n\ell\}$ are the principal quantum number n and the angular momentum ℓ. The constants $\mathcal{N}$, A^+, A^- entering Eqs. (A24) and (A25) are given by

$$\mathcal{N} = \sqrt{\frac{2\Lambda^2 s\bar\beta\left(\ell + \frac{3}{2} + \bar\beta + 2n\right)}{\left(\ell + \frac{3}{2} + \bar\beta\Lambda^2(1-a) + 2n\right)}} \times \sqrt{\frac{\Gamma\left(\ell + \frac{3}{2} + \bar\beta + n\right)\Gamma\left(\ell + \frac{3}{2} + n\right)}{\Gamma(n+1)\Gamma(\bar\beta + n + 1)\Gamma\left(\ell + \frac{3}{2}\right)^2}}, \tag{A26}$$

$$A^+ = \frac{\Gamma\left(\ell + \frac{3}{2}\right)\Gamma(-\bar\beta)}{\Gamma(\mu^+)\Gamma(\mu^-)}, \quad A^- = 0,$$

where $\Gamma(z)$ is the Gamma function [25].

In the case of scattering states, the quantum numbers $\{k\ell\}$ include the momentum k and the angular momentum ℓ while the associated constants $\mathcal{N}$, A^+, A^- read

$$\mathcal{N} = \sqrt{\frac{\Gamma(\nu^+)\Gamma(\nu^-)\Gamma(\mu^+)\Gamma(\mu^-)}{2\pi\ \Gamma(\bar\beta)\Gamma(-\bar\beta)\Gamma\left(\ell + \frac{3}{2}\right)^2}},$$

$$A^+ = \frac{\Gamma\left(\ell + \frac{3}{2}\right)\Gamma(-\bar\beta)}{\Gamma(\mu^+)\Gamma(\mu^-)}, \tag{A27}$$

$$A^- = \frac{\Gamma\left(\ell + \frac{3}{2}\right)\Gamma(\bar\beta)}{\Gamma(\nu^+)\Gamma(\nu^-)}.$$

The normalization constant $\mathcal{N}$ is determined from the normalization condition

$$\int_0^\infty \Phi_{nl}(r)\Phi_{n'l}(r)dr = \delta_{nn'} \tag{A28}$$

for bound states and from the Dirac delta function normalization for scattering states:

$$\int_0^\infty \Phi_{kl}(r)\Phi_{k'l}(r)dr = \delta(k - k'). \tag{A29}$$

All bound and scattering wave functions are orthogonal to each other

$$\int_0^\infty \Phi_{kl}(r)\Phi_{k'l}(r)dr = 0, \quad k \neq k' \tag{A30}$$

and they form a complete basis

$$\sum_n \Phi_{nl}(r)\Phi_{nl}(r') + \int_0^\infty \Phi_{kl}(r)\Phi_{kl}(r')dk = \delta(r - r'). \tag{A31}$$

One can check that at large distances

$$x \to -1 + 2e^{-2\Lambda^2 s(r - r_1)}, \quad r \to +\infty, \tag{A32}$$

where

$$\Lambda^2 s\, r_1 = \sqrt{\Lambda^2 - 1}\ \arctan\left(\sqrt{\Lambda^2 - 1}\right) - \log\left(\frac{\Lambda}{2}\right). \tag{A33}$$

Substituting this into Eq. (A25) one obtains the asymptotic form of the PTG wave functions

$$\Phi_k(r) \mapsto C^+ e^{ikr} + C^- e^{-ikr}, \tag{A34}$$

where $C^+ = \mathcal{N}A^+ e^{-ikr_1}$ and $C^- = \mathcal{N}A^- e^{ikr_1}$, (see Eqs. (A26), (A27), and (A33)).

The PTG wave functions are numerically stable and accurate when using Eq. (A24) up to $y \leqslant 0.99$ then applying the form (A25). They accurately land onto their asymptotic representation of Eq. (A34) at large distances.

APPENDIX B: MATRIX ELEMENTS

Let us deal with numerical integration in r and k space. The integration in the r space is performed in terms of N_r Gauss-Legendre integration points x_i and weights w_i within the interval $[0, R_{\max}]$,

$$\int_0^{R_{\max}} O(r)\Phi_k(r)\Phi_{k'}(r)dr \simeq \sum_{i=1}^{N_r} O(r_i)\Phi_k(r_i)\Phi_{k'}(r_i)w_i, \quad \text{(B1)}$$

where $O(r)$ is an arbitrary function of r and $R_{\max}$ is a point where nuclear potential disappears. Usually a value $R_{\max} = 15$ fm is used. In the same way, integration in the k space is done in terms of N_k Gauss-Legendre integration points k_i and weights w_{k_i} within the interval $[0, k_{\max}]$,

$$\int_0^{k_{\max}} O(k)\Phi_k(r)\Phi_k(r')dk \simeq \sum_{i=1}^{N_k} O(k_i)\Phi_{k_i}(r)\Phi_{k_i}(r')w_{k_i}, \quad \text{(B2)}$$

where $O(k)$ is an arbitrary function of k.

Radial integrals must be calculated cautiously due to the presence of nonintegrable scattering states in the basis. When the radial operator represents the nuclear potential or explicitly depends on nuclear densities or currents, one can safely integrate the matrix elements to some large but finite distance $R_{\max}$. Beyond $R_{\max}$, the contribution of the integral becomes negligible due to the presence of the densities or currents. However, it is not the case for the kinetic + Coulomb part of the Hamiltonian. This operator is infinite-ranged and induces Dirac delta functions in the matrix elements, which have to be regularized directly. For this, one separates the matrix element in two integrals, defined on the intervals $[0 : R_{\max}]$ and $[R_{\max} : +\infty[$. The first part is finite and treated with standard methods. For the second part, if one deals with Bessel/Coulomb wave functions, one can assume that the nuclear part is negligible after $R_{\max}$ so that they are solutions of the asymptotic HF equations. Hence, one obtains

$$\begin{aligned}
&\int_{R_{\max}}^{+\infty} u_\alpha(r)h(r)u_\beta(r)dr \\
&\quad = k_\alpha^2\left(\delta_{\alpha\beta} - \int_0^{R_{\max}} u_\alpha(r)u_\beta(r)dr\right) \text{ (bound)} \\
&\quad = k_\alpha^2\left(\delta(k_\alpha - k_\beta) - \int_0^{R_{\max}} u_\alpha(r)u_\beta(r)\,dr\right) \text{ (scat)} \\
&\quad = -k_\alpha^2 \int_0^{R_{\max}} u_\alpha(r)u_\beta(r)dr \text{ (mixed)}, \qquad \text{(B3)}
\end{aligned}$$

where $h(r)$ is the HF potential which reduces to the kinetic + Coulomb Hamiltonian asymptotically. Here, "bound" ("scat") means that both α and β states are bound (scattering) and "mixed" means that α is bound and β scattering or *vice versa*. The Dirac delta with a discretized basis becomes $\delta_{\alpha\beta}/w_{k_\alpha}$ with w_{k_α} being the Gauss-Legendre weight associated to the discretized value k_α, so that its implementation is immediate; since all integrals are finite, they pose no problem. When the PTG basis states are used instead of the Bessel/Coulomb wave functions, it turned out that it is numerically precise to disregard the Coulomb/centrifugal part of the Hamiltonian after $R_{\max}$, so that Eq. (B3) is the same for both the PTG and Bessel/Coulomb wave functions. Indeed, Eqs. (A32) and (A34) imply that the PTG wave functions behave asymptotically like neutron waves functions of angular momentum $\ell = 0$. The above seemingly crude approximation can, in fact, be mathematically justified. The HFB matrix evaluated using such a procedure converges weakly to the exact HFB matrix for $R_{\max} \to +\infty$ [33]. This means that the HFB matrix elements depend on $R_{\max}$ asymptotically, some of them even diverging with $R_{\max} \to +\infty$, whereas its eigenvalues and eigenvectors converge to a finite value.

[1] A. Bulgac, preprint FT-194-1980, Central Institute of Physics, Bucharest, 1980; nucl-th/9907088.
[2] J. Dobaczewski, H. Flocard, and J. Treiner, Nucl. Phys. **A422**, 103 (1984).
[3] J. Dobaczewski, W. Nazarewicz, T. R. Werner, J. F. Berger, C. R. Chinn, and J. Dechargé, Phys. Rev. C **53**, 2809 (1996).
[4] B. Gall, P. Bonche, J. Dobaczewski, H. Flocard, and P.-H. Heenen, Z. Phys. A **348**, 183 (1994).
[5] J. Terasaki, H. Flocard, P. H. Heenen, and P. Bonche, Nucl. Phys. **A621**, 706 (1997).
[6] M. Yamagami, K. Matsuyanagi, and M. Matsuo, Nucl. Phys. **A693**, 579 (2001).
[7] P.-G. Reinhard, M. Bender, K. Rut, and J. A. Maruhn, Z. Phys. A **358**, 277 (1997).
[8] N. Tajima, RIKEN Rev. **19**, 29 (1998).
[9] N. Tajima, Phys. Rev. C **69**, 034305 (2004).
[10] E. Terán, V. E. Oberacker, and A. S. Umar, Phys. Rev. C **67**, 064314 (2003).
[11] V. E. Oberacker, A. S. Umar, E. Terán, and A. Blazkiewicz, Phys. Rev. C **68**, 064302 (2003).
[12] D. Gogny, Nucl. Phys. **A237**, 399 (1975).
[13] M. Girod and B. Grammaticos, Phys. Rev. C **27**, 2317 (1983).
[14] J. L. Egido, H.-J. Mang, and P. Ring, Nucl. Phys. **A334**, 1 (1980).
[15] J. L. Egido, J. Lessing, V. Martin, and L. M. Robledo, Nucl. Phys. **A594**, 70 (1995).
[16] J. Dobaczewski and P. Olbratowski, Comput. Phys. Commun. **158**, 158 (2004).
[17] M. V. Stoitsov, J. Dobaczewski, W. Nazarewicz, and P. Ring, Comput. Phys. Commun. **167**, 43 (2005).
[18] P. Ring, Prog. Part. Nucl. Phys. **37**, 193 (1996).
[19] S. Goriely, M. Samyn, P.-H. Heenen, J. M. Pearson, and F. Tondeur, Phys. Rev. C **66**, 024326 (2002).
[20] M. V. Stoitsov, J. Dobaczewski, W. Nazarewicz, S. Pittel, and D. J. Dean, Phys. Rev. C **68**, 054312 (2003).
[21] A. Blazkiewicz, V. E. Oberacker, A. S. Umar, and M. Stoitsov, Phys. Rev. C **71**, 054321 (2005).

[22] N. Michel, W. Nazarewicz, and M. Ploszajczak, Phys. Rev. C **70**, 064313 (2004).
[23] N. Michel, M. Stoitsov, and K. Matsuyanagi (in preparation).
[24] J. Ginocchio, Ann. Phys. (NY) **159**, 467 (1985).
[25] M. Abramowitz and I. A. Stegun, editors, *Handbook of Mathematical Functions*, Applied Mathematics Series, National Bureau of Standards (1972).
[26] N. Michel, Comput. Phys. Commun. **176**, 232 (2007).
[27] I. J. Thomson and A. R. Barnett, Comput. Phys. Commun. **36**, 363 (1986).
[28] S. A. Gurvitz, P. B. Semmes, W. Nazarewicz, and T. Vertse, Phys. Rev. A **69**, 042705 (2004).
[29] E. Chabanat, P. Bonche, P. Haensel, J. Meyer, and F. Schaeffer, Nucl. Phys. **A635**, 231 (1998).
[30] K. Bennaceur and J. Dobaczewski, Comput. Phys. Commun. **168**, 96 (2005).
[31] M. Grasso, N. Sandulescu, Nguen Van Giai, and R. J. Liotta, Phys. Rev. C **64**, 064321 (2001).
[32] M. Yamagami, Phys. Rev. C **72**, 064308 (2005).
[33] *Principles of Functional Analysis*, 2nd ed., M. Schechter (American Mathematical Society, Providence, RI, 2001).

Gamow-Hartree-Fock-Bogoliubov method: Representation of quasiparticles with Berggren sets of wave functions

N. Michel
CEA, Centre de Saclay, IRFU/Service de Physique Nucléaire, F-91191 Gif-sur-Yvette, France

K. Matsuyanagi
Theoretical Nuclear Physics Laboratory, RIKEN Nishina Center, Wako 3510198, Japan

M. Stoitsov
Department of Physics and Astronomy, University of Tennessee, Knoxville, Tennessee 37996, USA
Physics Division, Oak Ridge National Laboratory, P.O. Box 2008, Oak Ridge, Tennessee 37831, USA
Institute of Nuclear Research and Nuclear Energy, Bulgarian Academy of Sciences, Sofia-1784, Bulgaria
(Received 26 June 2008; published 22 October 2008)

Single-particle resonant states, also called Gamow states, as well as bound and scattering states of complex energy form a complete set, the Berggren completeness relation. It is the building block of the recently introduced Gamow shell model, where weakly bound and resonant nuclear wave functions are expanded with a many-body basis of Slater determinants generated by this set of single-particle states. However, Gamow states have never been studied in the context of Hartree-Fock-Bogoliubov theory, except in the Bardeen-Cooper-Schriefer (BCS) approximation, where both the upper and lower components of a quasiparticle wave function are assumed to possess the same radial dependence with that of a Gamow state associated with the Hartree-Fock potential. Hence, an extension of the notion of Gamow state has to be effected in the domain of quasiparticles. It is shown theoretically and numerically that bound, resonant and scattering quasiparticles are well defined and form a complete set, by which bound Hartree-Fock-Bogoliubov ground states can be constructed. It is also shown that the Gamow-Hartree-Fock single-particle basis can be used to solve the Gamow-Hartree-Fock-Bogoliubov problem. As an illustration, the proposed method is applied to neutron-rich nickel isotopes close to the neutron drip-line.

DOI: 10.1103/PhysRevC.78.044319 PACS number(s): 21.10.−k, 21.30.−x, 21.60.Jz

I. INTRODUCTION

One of the current challenges of nuclear theory is the quantitative description of nuclei situated near and beyond drip-lines. Powerful facilities are being built in several countries in order to create these very short-lived states. For a long time, microscopic theories of nuclear structure have been developed for describing ground states of nuclei close to the valley of stability. For describing stable nuclei which are well localized, the harmonic oscillator (HO) bases are useful for both shell model [1] and Hartree-Fock Bogoliubov (HFB) calculations [2–6]; the HO bases converge quickly therein. However, it possesses poor convergence properties for weakly bound nuclei bearing large spatial extensions, which lie very close to neutron drip lines.

A promising approach to this problem has been proposed in Refs. [7–9] within a shell model framework; namely, the Gamow shell model (GSM). The fundamental idea is to replace the HO basis by the Berggren basis consisting of bound states, resonance states and continuum scattering states of complex energy, generated by a single-particle potential. It has been shown numerically that this basis has the ability to expand both halo nuclei and many-body resonant states precisely. The latter indeed belongs to a rigged Hilbert space [10,11], which is an extension of the notion of Hilbert space to non-square integrable wave functions. However, the dimension of the Berggren Slater determinants represented by the GSM basis increase very quickly with increasing number of valence particles; it increases much faster than in standard shell model due to the presence of occupied scattering states. Hence, the GSM is a tool mainly dedicated to the study of light nuclei. For medium and heavy nuclei, a method of choice is the HFB, which can be followed by quasiparticle random phase approximation (QRPA). As pairing correlations are absorbed in the HFB ground state, one-body nature of the HFB framework enables fast evaluations of ground states of medium and heavy nuclei, and it is in fact the only method suitable for systematic calculations; see Ref. [12] for an evaluation of even-even nuclei in the whole nuclear chart with the HFB formalism. In order to properly treat drip-line nuclei within the HFB framework, the real-space coordinate-mesh method has been applied using box boundary conditions [13,14]. Extension of this approach to deformed nuclei is difficult and has been carried out only recently [15,16]. As an alternative more convenient approach, one can adopt basis expansion methods, where direct integration procedure is replaced by matrix diagonalization. A first amelioration of the HO basis had been proposed with the transformed harmonic oscillator (THO) basis [12,17]. Applying unitary transformations to the HO basis, one obtains the THO basis, in which Gaussian fall-off of the HO wave functions is replaced by physical exponential decrease of the THO basis wave functions. However, the THO basis always dictates exponential decrease

in expanding quasiparticle wave functions, for both upper and lower components, even when they are part of scattering states, so that unsatisfactory basis dependence remains. In order to solve this problem, a new basis has been introduced very recently, which consists in using bound and continuum basis states generated by the analytic Pöschl-Teller-Ginocchio (PTG) potential [18]. The PTG basis introduced in this paper [19] possesses a peculiarity to bear no narrow resonance states; those are replaced by bound PTG states. Thus, PTG continuum set of basis states can be discretized very effectively with Gauss-Legendre quadrature, as they contain no resonant structure. It has been shown that they can provide a good description of spatially extended nuclear ground states of both spherical and axially deformed nuclei [19]. On the other hand, the PTG basis formed by bound and real scattering states is not a Berggren complete set of states, so that it would be more convenient to use a Berggren quasiparticle basis set, when we are interested in describing particle-decaying excited states. Up to now, however, resonant quasiparticle states have been studied in the context of Berggren completeness relation only within the BCS approximation [20,21]. The last approach is indeed not satisfactory due to the well-known gas problem arising from the occupation of the continuum: In fact, densities are not localized in the BCS approach, because the lower components of scattering quasiparticle states are of scattering type as well. Contrary to what is stated in Ref. [20], it cannot be regularized using complex scaling because it does not have pure outgoing asymptotic. Use of continuum level density in Ref. [21] is also problematic, even though it suppresses the gas problem. Indeed, it is not part of continuum HFB theory [19], so that its introduction in HFB equations strongly modifies quasiparticle coupling to the continuum. In particular, it suppresses a large part of nonresonant continuum, and thus important physical properties of drip-line nuclei as well. Hence, with this approach, weakly bound systems cannot be studied properly. Only a full application of the HFB framework can unambiguously solve this problem, where densities are localized by construction for bound HFB ground states.

The major purpose of this paper is to develop a new method of solving the continuum HFB equations utilizing the Berggren basis, called Gamow-HFB method, by which bound, resonant and continuum quasiparticle states are provided. It allows expansion of QRPA excited states having escaping widths in terms of the Berggren quasiparticle basis associated with the bound HFB ground state. This is very important because, in weakly bound unstable nuclei, low-lying collective excited states may acquire particle-decay widths.

This paper is organized as follows. Firstly, the standard HFB formalism is briefly summarized. As we use the Skyrme interactions [22], it is effected in the context of density functional theory (DFT). Secondly, we define quasiparticle S-matrix poles and scattering states of complex energy; these are direct extensions of their single-particle counterparts. We then present the quasiparticle Berggren completeness relation generated by those states. Numerical methods to calculate Gamow and complex scattering quasiparticle states are described; they differ significantly from the scattering quasiparticle states discretized by box boundary conditions. We also present another method of solving the continuum HFB equations in which the HFB quasiparticle wave functions are expanded in terms of the Gamow-Hartree-Fock (GHF) basis; this approach may be regarded as an extension of the standard two-basis method [23–25] to complex energy plane. Feasibility of the proposed methods is illustrated for neutron-rich nickel isotopes close to the drip line. Perspectives for unbound HFB theory and QRPA calculations using the Gamow-HFB quasiparticle basis will then be discussed.

II. GENERAL HFB FORMALISM WITH DFT

The HFB equations are expressed in supermatrix form constituted by particle-hole field Hamiltonian h, particle-particle pairing Hamiltonian $\tilde{h}$ and chemical potential λ guaranteeing conservation of particle number in average:

$$\begin{pmatrix} h-\lambda & \tilde{h} \\ \tilde{h} & \lambda-h \end{pmatrix} \begin{pmatrix} u \\ v \end{pmatrix} = E \begin{pmatrix} u \\ v \end{pmatrix}. \tag{1}$$

Using Skyrme and density-dependent contact interactions for the particle-hole and pairing channels, respectively, h and $\tilde{h}$ are expressed in terms of local normal density $\rho(r)$ and pairing density $\tilde{\rho}(r)$. Formulas providing ρ, $\tilde{\rho}$, h, and $\tilde{h}$ can be found in [14,26]. As h and $\tilde{h}$ depend on ρ and $\tilde{\rho}$, determined from quasiparticles eigenvectors of Eq. (1), the HFB equations must be solved in a self-consistent manner [27].

Let us consider the HFB equations with the Skyrme energy density functionals and density-dependent contact pairing interactions assuming spherical symmetry. Fixing orbital and total angular momentum ℓ and j, as well as proton or neutron nature of the wave functions, Eq. (1) becomes a system of radial differential equations [14]:

$$\begin{aligned} &\left(\frac{d}{dr}\frac{\hbar^2}{2m^*(r)}\frac{d}{dr}\right) u(k,r) \\ &\quad = \left[\frac{\hbar^2\ell(\ell+1)}{2m^*(r)r^2} + V(r) - (\lambda + E)\right] u(k,r) + W(r)v(k,r), \\ &\left(\frac{d}{dr}\frac{\hbar^2}{2m^*(r)}\frac{d}{dr}\right) v(k,r) \\ &\quad = \left[\frac{\hbar^2\ell(\ell+1)}{2m^*(r)r^2} + V(r) - (\lambda - E)\right] v(k,r) - W(r)u(k,r), \end{aligned} \tag{2}$$

where

(i) $u(k,r)$ and $v(k,r)$ are respectively the upper and lower components of quasiparticle wave function with energy E, and $k = \sqrt{2mE}/\hbar$ with the nucleon mass m,
(ii) $m^*(r)$, $V(r)$ and $W(r)$ are respectively the effective mass, the particle-hole (field) and particle-particle (pairing) potentials of the HFB Hamiltonian.

Because nuclear interactions are finite range, only Coulomb and centrifugal parts remain for $r \to +\infty$, so that Eq. (2)

becomes asymptotically:

$$\frac{d^2u}{dr^2}(k,r) = \left(\frac{\ell(\ell+1)}{r^2} + \frac{2\eta_u k_u}{r} - k_u^2\right) u(k,r),$$
$$\frac{d^2v}{dr^2}(k,r) = \left(\frac{\ell(\ell+1)}{r^2} + \frac{2\eta_v k_v}{r} - k_v^2\right) v(k,r), \quad (3)$$

where the generalized momenta k_u, k_v and their associated Sommerfeld parameters η_u, η_v are defined by

$$k_u = \sqrt{\frac{2m}{\hbar^2}(\lambda + E)}, \quad k_v = \sqrt{\frac{2m}{\hbar^2}(\lambda - E)}, \quad (4)$$

$$\eta_{u(v)} = \frac{mZC_c}{\hbar^2 k_{u(v)}} \text{ (proton)}, \quad \eta_{u(v)} = 0 \text{ (neutron)} \quad (5)$$

with the number of protons Z and the Coulomb constant C_c. Hence, $u(k,r)$ and $v(k,r)$ are linear combinations of the Hankel or Coulomb wave functions $H^{\pm}_{\ell\eta_{u(v)}}(k_{u(v)}r)$ for $r \to +\infty$. Note that k_v is always imaginary provided the HFB ground state is bound ($\lambda < 0$), while k_u is real (imaginary) for $E > -\lambda$ ($E < -\lambda$).

The chemical potentials λ for neutrons and protons are determined from the requirement of conservation of their number in average:

$$\langle \hat{N} \rangle = \sum_i N_i = N, \quad N_i = \int_0^{+\infty} v_i^2(r)\, dr, \quad (6)$$

(and similar equations for protons). Here the sum runs over all quasiparticle states, N is the number of neutrons and $\langle \hat{N} \rangle$ is the expectation value in the HFB ground state. For a given particle-hole field Hamiltonian h, the chemical potential λ could be calculated in principle exactly at each iteration, recalculating all quasiparticle wave functions from Eq. (1) and updating λ until Eq. (6) is verified. However, in practice, it is much faster to use instead an approximate chemical potential issued from the BCS formulas, which will converge self-consistently to the exact chemical potential along with the HFB Hamiltonian [14]. For that, one defines auxiliary single-particle energies $\bar{e}_i$ and auxiliary pairing gaps $\bar{\Delta}$ by

$$\bar{e}_i = \lambda + E_i(1 - 2N_i), \quad \bar{\Delta}_i = 2E_i\sqrt{N_i(1-N_i)}, \quad (7)$$

which are defined by applying the BCS type formula to the HFB quasiparticle energies E_i, the average particle number N_i defined in Eq. (6) and the chemical potential λ issued from the previous iteration. While $\bar{e}_i$ and $\bar{\Delta}_i$ correspond to the single-particle energy and the pairing gap in the BCS approximation, they are used here as auxiliary variables to solve the HFB equations. The approximate chemical potential λ is obtained by solving its associated BCS equation:

$$\sum_i \left(1 - \frac{\bar{e}_i - \lambda}{\sqrt{(\bar{e}_i - \lambda)^2 + \bar{\Delta}_i^2}}\right) = 2N. \quad (8)$$

III. S-MATRIX POLES AND SCATTERING QUASIPARTICLE STATES

A. Boundary conditions

The upper and lower components, $u(k,r)$ and $v(k,r)$, of the quasiparticle wave function satisfy the following boundary conditions:

$$u(k,r) \sim C_u^0 r^{\ell+1}, \quad v(k,r) \sim C_v^0 r^{\ell+1}, \quad r \to 0, \quad (9)$$
$$u(k,r) \sim C_u^+ H^+_{\ell\eta_u}(k_u r) + C_u^- H^-_{\ell\eta_u}(k_u r), \quad r \to +\infty, \quad (10)$$
$$v(k,r) \sim C_v^+ H^+_{\ell\eta_u}(k_v r), \quad r \to +\infty. \quad (11)$$

Equation (9) is required by regularity of wave functions at $r = 0$. Equations (10) and (11) determine the nature of quasiparticle state, which can be a bound, resonant ($C_u^- = 0$) or scattering ($C_u^- \neq 0$) state, and are generalizations of the boundary conditions defining single-particle states using the Berggren completeness relation. Equation (11) demands outgoing wave function behavior of $v(r)$ for all quasiparticle states. If its energy E is real and positive, as in the standard HFB approach, Eq. (11) is equivalent to the asymptotic condition $v(k,r) \to 0$ for $r \to +\infty$; the condition arising from integrability of nuclear density over all space [14]. Extension to complex energies follows from analyticity of the $v(k,r)$ function in the complex k-plane. Equation (10) with $C_u^- = 0$ then defines quasiparticle S-matrix poles, as it is equivalent to $u(k,r) \to 0$ for $r \to +\infty$ for bound quasiparticle states with $E < |\lambda|$, and provides resonant quasiparticle states if E is complex. Equation (10) with $C_u^- \neq 0$ represents standard scattering quasiparticle states for real and positive E, but they are extended to complex energies by analyticity arguments.

B. Normalization of quasiparticle states

Bound HFB quasiparticle states with energy E_n are normalized by

$$\int_0^{+\infty} [u(k_n,r)^2 + v(k_n,r)^2]\, dr = 1, \quad (12)$$

where $k_n = \sqrt{2mE_n}/\hbar$. For resonant quasiparticle states, the integral in the above equation diverges, so that this normalization condition cannot be used. The complex scaling method has been known as a practical means to normalize single-particle resonance states [28]. Convergence of integrals is obtained therein integrating up to a finite radius R situated in the asymptotic region, after which the interval $[R : +\infty]$ is replaced by a complex contour defined by a rotation angle $\theta > 0$, allowing exponential decrease of the integrand. Owing to Eqs. (10) and (11), the same method can be used to normalize resonant quasiparticle states, so that Eq. (12) becomes

$$\int_0^R [u(k_n,r)^2 + v(k_n,r)^2]\, dr + \int_0^{+\infty} \left[C_u^+ H^+_{\ell\eta_u}(k_u(R + xe^{i\theta_u}))\right]^2 e^{i\theta_u} dx + \int_0^{+\infty} \left[C_v^+ H^+_{\ell\eta_v}(k_v(R + xe^{i\theta_v}))\right]^2 e^{i\theta_v} dx = 1, \quad (13)$$

where $\theta_u > 0$ and $\theta_v > 0$ are chosen such that improper integrals converge. Hence, as in the single-particle case, normalization of quasiparticle S-matrix poles presents no other difficulty. As in Ref. [8], complex-scaled integrals will be denoted $Reg[\int_0^{+\infty} f(r)\,dr]$, i.e., the regularized value of the diverging integral.

Scattering quasiparticle states must be orthonormalized with the Dirac delta distribution:

$$\int_0^{+\infty} [u(k_a,r)u(k_b,r)\,dr + v(k_a,r)v(k_b,r)]\,dr = \delta(k_a - k_b), \tag{14}$$

for those with momenta k_a and k_b. From Eqs. (10) and (11), assuming that Eq. (3) is obtained for $r \geq R$, Eq. (14) becomes

$$\begin{aligned}
&\int_0^R [u(k_a,r)u(k_b,r) + v(k_a,r)v(k_b,r)]\,dr \\
&\quad + C^+_{u_a}C^+_{u_b} Reg\left[\int_R^{+\infty} H^+_{\ell\eta_{u_a}}(k_{u_a}r)H^+_{\ell\eta_{u_b}}(k_{u_b}r)\,dr\right] \\
&\quad + C^-_{u_a}C^-_{u_b} Reg\left[\int_R^{+\infty} H^-_{\ell\eta_{u_a}}(k_{u_a}r)H^-_{\ell\eta_{u_b}}(k_{u_b}r)\,dr\right] \\
&\quad + C^+_{v_a}C^+_{v_b} Reg\left[\int_R^{+\infty} H^+_{\ell\eta_{v_a}}(k_{v_a}r)H^+_{\ell\eta_{v_b}}(k_{v_b}r)\,dr\right] \\
&\quad + C^-_{u_a}C^+_{u_b}\int_R^{+\infty} H^-_{\ell\eta_{u_a}}(k_{u_a}r)H^+_{\ell\eta_{u_b}}(k_{u_b}r)\,dr \\
&\quad + C^+_{u_a}C^-_{u_b}\int_R^{+\infty} H^+_{\ell\eta_{u_a}}(k_{u_a}r)H^-_{\ell\eta_{u_b}}(k_{u_b}r)\,dr \\
&= \delta(k_a - k_b).
\end{aligned} \tag{15}$$

The divergence of the Dirac delta function at $k_a = k_b$ occurs by way of the two last integrals of Eq. (15), as no complex scaling can make them converge if $k_a = k_b$ [8]. The Dirac delta normalization of the Coulomb wave functions implies, as in the single-particle case:

$$\begin{aligned}
&C^-_{u_a}C^+_{u_b}\int_R^{+\infty} H^-_{\ell\eta_{u_a}}(k_{u_a}r)H^+_{\ell\eta_{u_b}}(k_{u_b}r)\,dr \\
&\quad + C^+_{u_a}C^-_{u_b}\int_R^{+\infty} H^+_{\ell\eta_{u_a}}(k_{u_a}r)H^-_{\ell\eta_{u_b}}(k_{u_b}r)\,dr \\
&= 2\pi C^+_{u_a}C^-_{u_a}\delta(k_{u_a} - k_{u_b}) + f(k_{u_a},k_{u_b}),
\end{aligned} \tag{16}$$

where $f(k_{u_a},k_{u_b})$ is finite for all (k_{u_a},k_{u_b}). The relation between $\delta(k_a - k_b)$ and $\delta(k_{u_a} - k_{u_b})$ is easily obtained from Eq. (4):

$$\delta(k_{u_a} - k_{u_b}) = \left[\frac{\partial k_{u_a}}{\partial k_a}(k_a)\right]^{-1}\delta(k_a - k_b) = \frac{k_{u_a}}{k_a}\delta(k_a - k_b). \tag{17}$$

This a direct application of the standard Dirac delta distribution property stating that $\delta(f(k)) = f'(k_0)^{-1}\delta(k - k_0)$ for a given function $f(k)$ bearing a unique simple zero at $k = k_0$ [29]. Note that k_b is fixed while k_a is varied to obtain Eq. (17). Inserting Eqs. (16) and (17) into Eq. (15), one obtains

$$\begin{aligned}
&\int_0^{+\infty} [u(k_a,r)u(k_b,r)\,dr + v(k_a,r)v(k_b,r)]\,dr \\
&\quad = \delta(k_a - k_b) \Leftrightarrow \frac{2\pi k_{u_a}}{k_a}C^+_{u_a}C^-_{u_a}\delta(k_a - k_b) \\
&\quad = \delta(k_a - k_b) + g(k_a,k_b),
\end{aligned} \tag{18}$$

where $g(k_a,k_b)$ bears the same properties as $f(k_{u_a},k_{u_b})$. As quasiparticle scattering states are orthogonal for $k_a \neq k_b$, $g(k_a,k_b) = 0$ therein, so that $\delta(k_a - k_b) + g(k_a,k_b) = \delta(k_a - k_b)$ in all cases.

Dirac delta distribution normalization for scattering states $|k\rangle$ and $|k'\rangle$ immediately follows:

$$\langle k|k'\rangle = \delta(k - k') \Leftrightarrow C^+_u C^-_u = \frac{k}{2\pi k_u}. \tag{19}$$

Hence, besides the additional factor k/k_u, the normalization condition for quasiparticle scattering states is the same as that for single-particle scattering states [8].

C. Completeness of quasiparticle states of real and complex energy

The HFB supermatrix defined in Eq. (1) is Hermitian, so that it possesses a spectral decomposition [30]:

$$\begin{aligned}
&\sum_{n\in b}[u(k_n,r)u(k_n,r') + v(k_n,r)v(k_n,r')] \\
&\qquad + \int_{k_\lambda}^{+\infty}[u(k,r)u(k,r') + v(k,r)v(k,r')]\,dk \\
&\quad = \delta(r - r'),
\end{aligned} \tag{20}$$

where $k_n = \sqrt{2mE_n}/\hbar$ for a bound quasiparticle state with energy E_n, k is a linear momentum for a continuum quasiparticle state, $u(\kappa,r)$, $v(\kappa,r)$ ($\kappa = k_n$ or k) are respectively the upper and lower components of a quasiparticle wave function with quantum numbers ℓ and j (here implicit), and $k_\lambda = \sqrt{-2m\lambda}/\hbar$. All quasiparticle states must be normalized to one (bound) or to a Dirac delta (scattering) (see Sec. III B). Equation (20) can also be demonstrated extending the method of Ref. [31] to quasiparticle states.

In order to obtain Berggren completeness of quasiparticle states, one can proceed as in Ref. [32], deforming the real energy contour in the complex plane. Resonant quasiparticle states appear therein, due to the Cauchy theorem, as S-matrix poles [32]. Hence, Eq. (20) becomes after contour deformation:

$$\begin{aligned}
&\sum_{n\in(b,d)}[u(k_n,r)u(k_n,r') + v(k_n,r)v(k_n,r')] \\
&\qquad + \int_{L^+}^{+\infty}[u(k,r)u(k,r') + v(k,r)v(k,r')]\,dk \\
&\quad = \delta(r - r'),
\end{aligned} \tag{21}$$

where k_n refers now to a bound (b) or resonant (d) (decaying) quasiparticle state and k is complex as it follows the deformed contour in the complex plane, denoted as L^+. Resonant

quasiparticle states are normalized with complex scaling (see Sec. III B).

IV. NUMERICAL DETERMINATION OF QUASIPARTICLE ENERGIES AND WAVE FUNCTIONS WITH DIRECT INTEGRATION

A. Quasiparticle Jost functions

In Eqs. (9), (10), and (11), constants and momenta of S-matrix poles are determined by the requirement of continuity of both the $u(k,r)$ and $v(k,r)$ functions and associated derivatives. These conditions can be expressed in a form of quasiparticle Jost functions, defined as a generalization of the Jost function for single-particle problems, whose zeroes correspond to S-matrix poles [33]. They read

$$\begin{aligned} J_u\left(k,\frac{C_v^0}{C_u^0},\frac{C_v^+}{C_u^+}\right) &= \frac{u'(k,R_0^+)}{u(k,R_0^+)}-\frac{u'(k,R_0^-)}{u(k,R_0^-)},\\ J_v\left(k,\frac{C_v^0}{C_u^0},\frac{C_v^+}{C_u^+}\right) &= \frac{v'(k,R_0^+)}{v(k,R_0^+)}-\frac{v'(k,R_0^-)}{v(k,R_0^-)},\\ J_m\left(k,\frac{C_v^0}{C_u^0},\frac{C_v^+}{C_u^+}\right) &= \frac{u(k,R_0^+)}{u(k,R_0^-)}-\frac{v(k,R_0^+)}{v(k,R_0^-)}, \end{aligned} \tag{22}$$

where R_0 is a radius typically chosen around the nuclear surface and one can demand arbitrarily that $C_u^0 = C_u^+ = 1$ in Eqs. (9) and (10). The functions, $u(k,R_0^+)$, $v(k,R_0^+)$ and their derivatives, are obtained by forward integration of Eq. (2) using Eq. (9) as initial conditions, while $u(k,R_0^-)$, $v(k,R_0^-)$ and their derivatives are calculated by backward integration of Eq. (2) from the initial conditions provided by Eqs. (10) and (11). In Eq. (22), one can clearly see that $u(k,r)$ and $v(k,r)$ will have continuous logarithmic derivatives if $J_u = 0$ and $J_v = 0$, respectively. However, these two equalities are not sufficient to uniquely determine the quasiparticle state. Indeed, they imply that one can choose a set of constants so that either $u(k,r)$, $u'(k,r)$, or $v(k,r)$, $v'(k,r)$ are continuous, but not necessarily both of them. The condition $J_m = 0$ is thus enforced in Eq. (22). The set of three equations, $J_u = 0$, $J_v = 0$ and $J_m = 0$, uniquely determine quasiparticle S-matrix poles.

For quasiparticle scattering states, the linear momentum k is fixed, but constants have to be calculated with a matching procedure. One starts with imposing the condition $C_u^0 = 1$, as for S-matrix poles. As the $u(k,r)$ component is of scattering type, the condition $J_u = 0$ can always be fulfilled with appropriately chosen C_u^+ and C_u^- constants. Thus, it is sufficient to deal only with J_v and J_m:

$$\begin{aligned} J_v\left(\frac{C_v^0}{C_u^0},C_v^+\right) &= \frac{v'(k,R_0^+)}{v(k,R_0^+)}-\frac{v'(k,R_0^-)}{v(k,R_0^-)},\\ J_m\left(\frac{C_v^0}{C_u^0},C_v^+\right) &= \frac{u(k,R_0^+)}{u(k,R_0^-)}-\frac{v(k,R_0^+)}{v(k,R_0^-)}, \end{aligned} \tag{23}$$

the difference with Eq. (22) being that J_v and J_m now depend on two parameters instead of three. As in the S-matrix pole equations, $u(k,R_0^+)$, $v(k,R_0^+)$ and their derivatives are generated by forward integration of Eq. (2). Concerning the implementation of $u(k,R_0^-)$, $v(k,R_0^-)$ and their derivatives, however, one first continues integrating forward in order to obtain $u(k,R)$, $u'(k,R)$, R being in the asymptotic region. At this point R, $u(k,R)$, $u'(k,R)$ provide an initial condition for backward integration, while Eq. (11) is used to initialize $v(k,R)$, $v'(k,R)$. In this way, we obtain $u(k,R_0^-)$, $v(k,R_0^-)$ and their derivatives. Thus, the equations $J_v = 0$ and $J_m = 0$ provide the matching constants rendering $v(k,r)$, $v'(k,r)$ continuous.

The conditions, $J_u = 0$ (for S-matrix poles), $J_v = 0$ and $J_m = 0$, form a system of non-linear equations of two or three dimensions. Consequently, it has to be solved with multi-dimensional Newton method. The only problem therein is to find a good starting point from where one can attain fast convergence to the exact solution in a stable way.

B. Determination of quasiparticle energy and integration constants

Following Ref. [26], it is convenient to introduce linearly independent solutions of Eq. (2) in order to determine the constants defined in Eqs. (9), (10), and (11):

$$\begin{pmatrix} u \\ v \end{pmatrix} = C_u^0 \begin{pmatrix} f_{u_0} \\ g_{u_0} \end{pmatrix} + C_v^0 \begin{pmatrix} f_{v_0} \\ g_{v_0} \end{pmatrix}, \tag{24}$$

$$\begin{pmatrix} u \\ v \end{pmatrix} = C_u^+ \begin{pmatrix} f_{u^+} \\ g_{u^+} \end{pmatrix} + C_u^- \begin{pmatrix} f_{u^-} \\ g_{u^-} \end{pmatrix} + C_v^+ \begin{pmatrix} f_{v^+} \\ g_{v^+} \end{pmatrix}, \tag{25}$$

where the introduced basis functions verify

$$\begin{aligned} &f_{u_0}(r) \sim r^{\ell+1}, \quad g_{v_0}(r) \sim r^{\ell+1}, \quad f_{v_0}(r) \sim D_0 r^{\ell+3},\\ &g_{u_0}(r) \sim -D_0 r^{\ell+3}, \quad r \to 0, \quad f_{u^\pm}(r) \sim H^\pm_{\ell\eta_u}(k_u r),\\ &g_{v^+}(r) \sim H^+_{\ell\eta_v}(k_v r), \quad f_{v^+}(r) \to 0, \quad g_{u^\pm}(r) \to 0,\\ &\quad r \to +\infty, \end{aligned} \tag{26}$$

with

$$D_0 = \frac{m^*(0)W(0)}{(2\ell+3)\hbar^2}. \tag{27}$$

Equation (27) is obtained inserting $u(r) = r^{\ell+1}$ and $v(r) = -D_0 r^{\ell+3}$ in the second equality of Eq. (2) and solving the equation keeping only dominant terms.

As the basis functions of Eqs. (24) and (25) depend only on k of the quasiparticle state, they can be calculated with direct integration, in a forward direction for Eq. (24) and in a backward direction for Eq. (25). Used methods to determine quasiparticle wave function differ according to their characters; S-matrix poles or scattering states, as discussed below.

C. Bound and resonant quasiparticle states

To find S-matrix poles, it is first necessary to start with a good approximation of k, denoted k_{app}. For that, a no-pairing approximation is firstly performed. Neglecting $\tilde{h}$ in Eq. (1), the Gamow-HFB equations reduce to the GHF equations:

$$h|\phi_i\rangle = e_i|\phi_i\rangle, \tag{28}$$

where e_i are complex (real) for resonant (bound) states. Equation (28) provides bound and narrow resonant single-particle

states of interest, which will be in finite number. As pairing potential $\tilde{h}$ is weak compared to h, there will always be unique correspondence between the GHF single-particle S-matrix poles and the HFB quasiparticle S-matrix poles. Unless the quasiparticle S-matrix poles lie close to the Fermi energy, their lower (upper) components will be very close to $\phi_i(r)$ if $|\phi_i\rangle$ are (un)occupied at the HF level, so that the auxiliary energies $\bar{e}_i$, defined in Eq. (7), will be very close to the real parts of e_i. Secondly, the HFB matrix in Eq. (1) is diagonalized. It has been found that the use of a Pöschl-Teller-Ginocchio (PTG) basis provides sufficiently precise results [19]. Therefore, for E_i in Eq. (7) we use the quasiparticle energies obtained by diagonalizing the HFB matrix in the PTG basis. For a given GHF state of energy e_i, the starting quasiparticle energy $E_{\rm app}$ (from which $k_{\rm app}$ is immediately deduced), is then the HFB quasiparticle energy whose $\bar{e}_i$ is closest to the real part of e_i. If the HFB quasiparticle S-matrix pole is far from the Fermi energy, $E_{\rm app}$ is very close to the exact energy. Otherwise, it will still provide a good starting point, as, in practice, one can have only one quasiparticle state close to the Fermi energy for a given (ℓ, j)-partial wave.

Furthermore, one demands $C_u^- = 0$, which translates into a linear eigenvalue problem of dimension equal to four, deduced from Eqs. (24) and (25), which one matches at $r = R_0$:

$$\begin{pmatrix} f_{u_0} & f_{v_0} & -f_{u^+} & -f_{v^+} \\ g_{u_0} & g_{v_0} & -g_{u^+} & -g_{v^+} \\ f'_{u_0} & f'_{v_0} & -f'_{u^+} & -f'_{v^+} \\ g'_{u_0} & g'_{v_0} & -g'_{u^+} & -g'_{v^+} \end{pmatrix} \begin{pmatrix} C_u^0 \\ C_v^0 \\ C_u^+ \\ C_v^+ \end{pmatrix} = 0, \tag{29}$$

where all matrix functions have been evaluated at $r = R_0$ by way of backward or forward integration. As the integration constants are not simultaneously equal to zero, they have to form an eigenvector of the matching matrix of Eq. (29), which we denote M hereafter, of eigenvalue equal to zero. However, the determinant of the 4×4 matrix M is zero uniquely for the exact value of k. Thus, the set of approximate constants to use as a starting point for Newton method is chosen as the eigenvector of ${}^tMM$ whose associated eigenvalue is the smallest in modulus (${}^tMM$ is used instead of M because it is symmetric). The constant ratios C_v^0/C_u^0 and C_v^+/C_u^+ used in Eq. (22) follow, as they are independent of the norm of the considered eigenvector. Exact determination of k, C_v^0/C_u^0 and C_v^+/C_u^+ can then be worked out via three-dimensional Newton method.

D. Scattering quasiparticle state

If one considers a scattering state, it is convenient to define a^+, a^-, b^+, b^- so that $C_u^\pm = a^\pm C_u^0 + b^\pm C_v^0$. Moreover, as all constants are calculated up to a normalization factor, one can impose $C_u^0 = 1$. Upper components of Eqs. (24) and (25) matched at $r = R$ and Eq. (26) provide linear equations for $a^\pm$ and $b^\pm$:

$$\begin{aligned} a^+ f_{u^+}(R) + a^- f_{u^-}(R) &= f_{u_0}(R), \; b^+ f_{u^+}(R) + b^- f_{u^-}(R) \\ &= f_{v_0}(R), \\ a^+ f'_{u^+}(R) + a^- f'_{u^-}(R) &= f'_{u_0}(R), \; b^+ f'_{u^+}(R) + b^- f'_{u^-}(R) \\ &= f'_{v_0}(R). \end{aligned} \tag{30}$$

From the knowledge of $a^\pm$ and $b^\pm$, matching lower components in Eqs. (24) and (25) at $r = R_0$ determines C_v^0 and C_v^+ via linear equations as well:

$$\begin{aligned} &C_v^0[g_{v_0}(R_0) - b^+ g_{u^+}(R_0) - b^- g_{u^-}(R_0)] - C_v^+ g_{v^+}(R_0) \\ &\quad = a^+ g_{u^+}(R_0) + a^- g_{u^-}(R_0) - g_{u_0}(R_0), \\ &C_v^0[g'_{v_0}(R_0) - b^+ g'_{u^+}(R_0) - b^- g'_{u^-}(R_0)] - C_v^+ g'_{v^+}(R_0) \\ &\quad = a^+ g'_{u^+}(R_0) + a^- g'_{u^-}(R_0) - g'_{u_0}(R_0). \end{aligned} \tag{31}$$

As $C_u^\pm = a^\pm + b^\pm C_v^0$, all constants are determined with simple two-dimensional linear systems. Newton method applied to Eq. (23) converges very quickly using the obtained set of constants as a starting point. Note that the use of $H^\pm_{\ell\eta_u}(k_u r)$ functions in Eqs. (25) and (26) can be sometimes unstable, especially for the proton case, where, for low scattering energies, they can be very large and cancel almost exactly in Eq. (10). In this case, it is better to use regular and irregular Coulomb wave functions, $F_{\ell\eta_u}(k_u r)$ and $G_{\ell\eta_u}(k_u r)$, as basis functions.

V. NORMAL AND PAIRING DENSITIES

As quasiparticle states of complex energy form a complete set [see Eq. (21)], one can directly express densities with upper and lower components of quasiparticle states:

$$\begin{aligned} \rho_{\ell j}(r) &= \sum_{n\in(b,d)} v^2(k_n, r) + \int_{L^+} v^2(k, r)\, dk, \\ \rho(r) &= \sum_{\ell j} \rho_{\ell j}(r), \\ \tilde{\rho}_{\ell j}(r) &= -\sum_{n\in(b,d)} u(k_n, r)v(k_n, r) - \int_{L^+} u(k, r)v(k, r)\, dk, \\ \tilde{\rho}(r) &= \sum_{\ell j} \tilde{\rho}_{\ell j}(r), \end{aligned} \tag{32}$$

where $\rho_{\ell j}(r)$ and $\tilde{\rho}_{\ell j}(r)$ are, respectively, partial normal and pairing densities related to a given partial wave with quantum numbers ℓ and j, and $\rho(r)$, $\tilde{\rho}(r)$ are respectively the normal and pairing densities of the HFB ground state. However, due to the zero-range character of Skyrme forces, it is necessary to introduce an energy cut in contour integrals, so that L^+ contour has to stop at finite energy $E_{\rm cut}$ (see Fig. 1). Note that, due to this requirement, it is necessary for L^+ complex contours to come back to the real axis. Even though quasiparticle wave functions are complex in Eq. (32), $\rho_{\ell j}(r)$ and $\tilde{\rho}_{\ell j}(r)$ are real because one is considering a HFB bound ground state, so that, due to Cauchy theorem, complex integration in Eq. (32) is equivalent to real integration in the standard case. As a consequence, the DFT can be applied also to the Gamow HFB formalism, i.e., potentials $V(r)$ and $W(r)$ in Eq. (2) are evaluated using the standard formulas of Ref. [14]. As shown in Fig. 1, the bound HF single-particle states can become resonant states when pairing correlations are added [37]. Thus, physical interpretation of a resonant quasiparticle is somewhat different from that of single-particle resonances: widths of the quasiparticle states associated with the HF

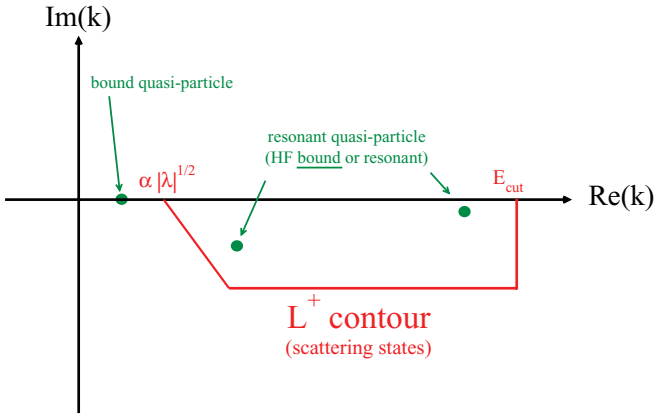

FIG. 1. (Color online) Location of quasiparticle S-matrix poles and deformed complex contour L^+ of scattering quasiparticle states used in the Berggren completeness relation. Here, $\alpha = \sqrt{2m}/\hbar$.

bound single-particle states originates from pairing-induced couplings between the bound and scattering states [34].

In the same way as in the Gamow shell model [7–9], the scattering L^+ contours in Eq. (32) have to be discretized, providing a finite set of linear momenta and weights (k_i, w_i). In practice, the Gauss-Legendre quadrature has been found to be most efficient. Scattering quasiparticle states are also renormalized, multiplying them by $\sqrt{w_i}$ [32], so that the discretized expressions of Eq. (32) are formally identical to the discrete case:

$$\begin{aligned}\rho_{\ell j}(r) &\simeq \sum_{n\in(b,d)} v^2(k_n, r) + \sum_i v^2_{w_i}(k_i, r),\\ \tilde{\rho}_{\ell j}(r) &\simeq -\sum_{n\in(b,d)} u(k_n, r)v(k_n, r) - \sum_i u_{w_i}(k_i, r)v_{w_i}(k_i, r),\end{aligned} \tag{33}$$

where $u_{w_i}(k_i, r) = \sqrt{w_i}u(k_i, r)$ and $v_{w_i}(k_i, r) = \sqrt{w_i}v(k_i, r)$.

VI. ANOTHER METHOD: EXPANSION OF QUASIPARTICLE STATES WITH THE GHF BASIS

Another possibility to solve the HFB equations in complex energy plane is to use the Gamow single-particle states as a basis. The optimal Berggren basis to expand the HFB quasiparticle states is obviously the GHF basis generated by the potential $V(r)$ and the effective mass $m^*(r)$ of Eq. (2). Note that it is not equivalent to the GHF basis issued from the pure HF variational principle in that pairing correlations always give extra contributions to the particle-hole part of the HFB Hamiltonian. Indeed, we noticed in our numerical calculation that other Berggren bases make the HFB self-consistent procedure unstable due to the appearance of very large matrix elements in the HFB Hamiltonian matrix. The use of the optimized Berggren basis mentioned above removes this problem. This approach may be regarded as a generalization of the two-basis method [23–25].

The GHF basis states $\phi(r)$ are defined by the following equation:

$$\left(\frac{d}{dr}\frac{\hbar^2}{2m^*(r)}\frac{d}{dr}\right)\phi(r) = \left[\frac{\hbar^2\ell(\ell+1)}{2m^*(r)r^2} + V(r) - e\right]\phi(r), \tag{34}$$

issued directly from Eqs. (2) and (28), where e is the complex energy of the GHF state. The HFB Hamiltonian matrix represented with this basis becomes

$$\begin{pmatrix} h-\lambda & \tilde{h} \\ \tilde{h} & \lambda - h \end{pmatrix} = \left(\begin{array}{ccc|ccc} e_1-\lambda & & 0 & & & \\ & \ddots & & & \tilde{h} & \\ 0 & & e_N-\lambda & & & \\ \hline & & & \lambda-e_1 & & 0 \\ & \tilde{h} & & & \ddots & \\ & & & 0 & & \lambda-e_N \end{array}\right), \tag{35}$$

where the continuous Berggren basis is discretized with the Gauss-Legendre quadrature (see Sec. V) so that total number of basis states is N. Its particle-hole part is evidently diagonal and matrix elements of $\tilde{h}$ read

$$\langle\phi_a|\tilde{h}|\phi_b\rangle = \int_0^{+\infty} \phi_a(r)W(r)\phi_b(r)\,dr, \tag{36}$$

where $|\phi_b\rangle$ and $|\phi_a\rangle$ are the GHF basis states and $W(r)$ is the HFB pairing potential defined in Eq. (2). For bound HFB ground states, $W(r)$ decreases sufficiently quickly so that no complex scaling is needed to evaluate the integral of Eq. (36). Hence, after discretization of the contours representing scattering basis states, this method takes a formally identical form to the standard matrix diagonalization treatment of the HFB problem.

VII. NUMERICAL APPLICATIONS

The frameworks described above, i.e., the Gamow-HFB approach in the coordinate or the GHF configurational space, are applied to nickel isotopes close to the neutron drip-line, from ^{84}Ni to ^{90}Ni, which possess spherical HFB ground states. In the numerical calculation, the SLy4 Skyrme force [35] is used in combination with the surface-type contact pairing interaction [26] whose pairing strength is fitted to reproduce the pairing gap of ^{120}Sn. Using the standard notation [26], the pairing interaction parameters read $t_0' = -519.9$ MeV fm^3 for the density-independent part and $t_3' = -37.5t_0'$ MeV fm^6 for the density-dependent part. The maximal angular momentum used is $\ell_{\max} = 10$ and a sharp cutoff at $E_{\text{cut}} = 60$ MeV is adopted. Scattering contours of quasiparticle states are discretized with 60, 100, or 300 Gaussian points. Several hundred points are indeed necessary when resonant states lie relatively close to E_{cut} (see Fig. 1), as is the case for the HFB quasiparticle resonance associated with the deeply bound neutron $0s_{1/2}$ HF state for example (see Table I). Scattering contours of single-particle states in the GHF basis are discretized up to $k_{\max} = 4$ fm^{-1} with 100 points, which

TABLE I. Bound and resonant neutron energies and widths for ^{90}Ni, calculated in the GHF approximation and in the GHFB/Coord. formalism. Single-particle energies (e_i) and quasiparticle energies (E_i) are given in MeV and widths (Γ) in keV. Note that the GHF $2s_{1/2}$ state dissolves into continuum quasiparticle states in the Gamow-HFB description.

States	GHF		GHFB/Coord.	
	e	Γ	E	Γ
$0s_{1/2}$	−52.618	0	51.573	$1.099\ 10^{-3}$
$1s_{1/2}$	−24.630	0	24.348	46.006
$2s_{1/2}$	−1.196	0	–	–
$0p_{3/2}$	−41.655	0	40.796	27.282
$1p_{3/2}$	−12.986	0	12.658	490.565
$0p_{1/2}$	−42.881	0	38.870	27.138
$1p_{1/2}$	−11.189	0	10.816	404.299
$0d_{5/2}$	−29.921	0	29.141	0.780
$1d_{5/2}$	−2.592	0	3.181	194.181
$0d_{3/2}$	−30.657	0	25.095	22.567
$1d_{3/2}$	−0.349	0	2.173	560.608
$0f_{7/2}$	−18.177	0	17.654	397.374
$0f_{5/2}$	−11.331	0	11.065	645.638
$0g_{9/2}$	−6.770	0	6.570	0.807
$0g_{7/2}$	1.350	6.410	3.120	63.6131
$0h_{11/2}$	3.852	52.851	5.269	131.776

in this case assures convergence of numerical calculation. This concerns only for the neutron channel, as the pairing gap vanishes in the proton channel.

The result of calculation for normal and pairing densities are presented in Figs. 2 and 3. It is interesting to compare the densities obtained by solving the Gamow-HFB equations in the coordinate or the GHF configurational space to those calculated by the standard coordinate space framework where the continuum is discretized with box boundary conditions. They are denoted GHFB/Coord., GHFB/Config., and HFB/Box., respectively. All results coincide in both normal and logarithmic scales for $r < 30$ fm. It was also checked that spurious imaginary parts of densities, caused by the discretization of the continuum of complex energy, were negligible, of the order of 10^{-6} [fm^{-3}] for GHFB/Coord. and 10^{-12} [fm^{-3}] for GHFB/Config., as the largest error values. In Table I, the bound and resonant single-particle states obtained by the GHF calculation are compared with the corresponding quasiparticle states calculated by the GHFB/Coord. method. It is obvious that bound HF states can give rise to unbound quasiparticle states carrying a sizable width when pairing correlations are switched on.

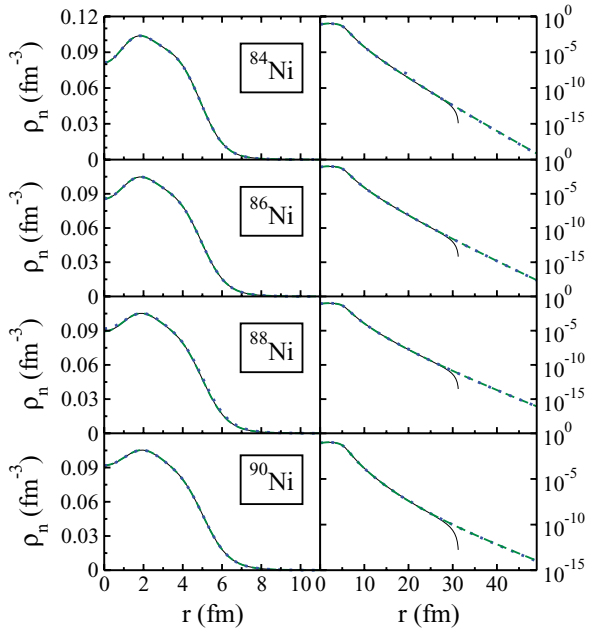

FIG. 2. (Color online) Neutron densities ρ_n both in normal (left-hand side) and logarithmic (right-hand side) scales. Results of the HFB/Box, GHFB/Coord., and GHFB/Config. calculations are displayed by solid, dashed, and dotted lines, respectively.

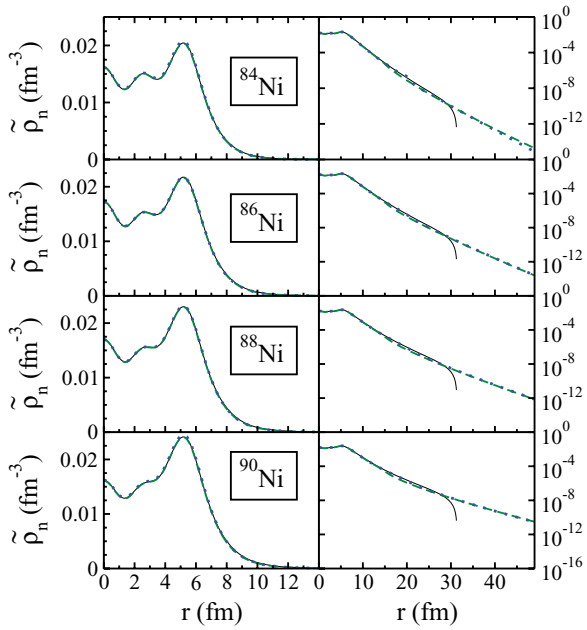

FIG. 3. (Color online) Same as Fig. 2 but for neutron pairing densities.

Physical observables associated with the HFB ground states are provided in Tables II and III. On the one hand, differences occur for neutron pairing energies, which are most sensitive to continuum effects [36]. While those of GHFB/Coord. compared to HFB/Box remain of the order of 500 keV, the difference between GHFB/Config. and HFB/Box pairing energies can be ∼1.5 MeV. On the other hand, the rms radii and total energies are basically the same, with a discrepancy of at most ∼300 keV for the latter. These results indicate that the GHFB/Coord., GHFB/Config., and HFB/Box treatments are all reliable methods to solve the HFB equations taking the continuum effects into account. As resonant states are explicitly treated in the Gamow HFB approach, this implies that the resonant effects can be well accounted for also by means of the HFB/Box method. This point is not necessarily widely accepted [37]. Even though the good agreements among the results of the GHFB/Coord., GHFB/Config., and

TABLE II. Gamow-HFB observables for ^{84}Ni and ^{86}Ni calculated with the GHFB/Coord., GHFB/Config., and HFB/Box methods. The rms radii are given in fm and other quantities in MeV. The proton chemical potential λ_p is not presented as there is no proton pairing gap.

	^{84}Ni			^{86}Ni		
	HFB/Box	GHFB/Coord.	GHFB/Config.	HFB/Box	GHFB/Coord.	GHFB/Config.
λ_n	−1.453	−1.430	−1.440	−1.037	−1.027	−1.029
r_n	4.451	4.450	4.450	4.528	4.526	4.526
r_p	3.980	3.982	3.982	4.001	4.001	4.001
Δ_n	1.481	1.535	1.564	1.667	1.658	1.669
E_n^{pair}	−30.70	−30.72	−31.85	−36.52	−35.85	−36.39
T_n	1084.53	1086.05	1086.46	1118.65	1118.68	1118.78
T_p	430.47	430.23	430.17	425.99	426.01	426.00
E_n^{so}	−63.379	−63.164	−63.01	−61.679	−61.712	−61.631
$E_{\text{dir}}^{\text{Coul}}$	132.94	132.89	132.88	132.26	132.25	132.25
$E_{\text{exc}}^{\text{Coul}}$	−10.138	−10.135	−10.135	−10.084	−10.085	−10.085
E_{tot}	−654.89	−654.89	−655.05	−656.933	−656.836	−656.971

HFB/Box calculations might be surprising, we see no reason to suspect that this is an exceptional case valid only for the Ni isotopes considered here. It will be interesting to examine this point further.

VIII. PERSPECTIVES FOR DESCRIBING DECAYING NUCLEI AND BEYOND-MEAN FIELD APPROACHES

The GHFB/Coord. method directly provides quasiparticle wave functions without using any intermediate basis states. Hence, it may be used also to describe decaying nuclear ground states in the HFB approximation. In fact, no HFB theory capable of describing decaying HFB ground states exists, even though an approximate scheme was proposed in Ref. [38]. The main difficulty is that it is not possible to construct the HFB ground state obeying the outgoing wave condition if one includes the full set of quasiparticle states of positive energy [38]. This arises from the fact that quasiparticles form a degenerate continuum of scattering states for $E < |\lambda|$ if $\lambda > 0$, whereas they can only generate a discrete set of bound states in this region if $\lambda < 0$. It is impossible to remove quasiparticle states with $E < |\lambda|$ with the use of the GHFB/Config. method, because quasiparticle eigenenergies of the HFB matrix are complex. In contrast, the direct integration method (GHFB/Coord.) allows us to select which quasiparticle states are occupied in the HFB ground state. Hence, it may be possible to carefully study properties of decaying HFB states at least for the spherical case.

The GHF configurational approach (GHFB/Config.) may be more appropriate to study excited states in deformed nuclei by means of the QRPA. For deformed nuclei, basis expansion approaches may be easier compared to the calculation of deformed HFB ground states in coordinate space [16]. For calculating bound HFB ground states, we can use the PTG basis, which is more efficient than the GHF basis, considering the numerical cost of recalculating the GHF basis states inherent to the two-basis method (see Sec. VI). Once a HFB ground state is obtained in this way, one can readily calculate the GHF basis wave functions. The QRPA matrix would then

TABLE III. Same as in Table II but for ^{88}Ni and ^{90}Ni.

	^{88}Ni			^{90}Ni		
	HFB/Box	GHFB/Coord.	GHFB/Config.	HFB/Box	GHFB/Coord.	GHFB/Config.
λ_n	−0.671	−0.661	−0.665	−0.342	−0.330	−0.342
r_n	4.603	4.602	4.601	4.677	4.674	4.675
r_p	4.021	4.022	4.022	4.043	4.043	4.043
Δ_n	1.790	1.782	1.800	1.899	1.899	1.935
E_n^{pair}	−41.98	−41.26	−42.17	−47.158	−46.509	−48.449
T_n	1150.71	1150.74	1151.02	1182.52	1182.91	1183.79
T_p	421.71	421.71	421.70	417.38	417.35	417.31
E_n^{so}	−59.558	−59.559	−59.470	−56.898	−56.887	−56.822
$E_{\text{dir}}^{\text{Coul}}$	131.571	131.576	131.576	130.947	130.883	130.878
$E_{\text{exc}}^{\text{Coul}}$	−10.033	−10.033	−10.033	−9.980	−9.980	−9.980
E_{tot}	−658.167	−658.082	−658.272	−658.665	−658.635	−658.936

be represented afterward with respect to the quasiparticles wave functions expanded in the GHF basis, thus allowing the description of unbound QRPA excited states.

IX. CONCLUSION

The Berggren completeness relation, originally developed in the context of standard Schrödinger equation, has been extended to quasiparticles in the HFB formalism. It was shown that, as in the standard single-particle potential problem, bound, resonant and scattering quasiparticles are well defined and form a complete set, by which bound HFB ground states can be constructed. Both situations are very similar and can be treated by contour deformation of continuous real sets of states, even though physical interpretation of resonant quasiparticles is different from that of resonant single-particles. Numerical applications have been effected with neutron-rich nickel isotopes close to the drip line, for which continuum coupling is important. It was shown that the Gamow-HFB approach, both in coordinate and configurational space representations, properly describe densities and physical observables. Thus, it provides us with an efficient tool to study ground states of medium and heavy nuclei close to the drip line. With these approaches, QRPA calculation fully taking into account continuum coupling may be efficiently carried out.

ACKNOWLEDGMENTS

The authors acknowledge the Japan Society for the Promotion of Science (JSPS) for support via an invitation for long-term research in Japan to M.S. and for postdoctoral support via a grant for foreign researchers to N.M., which make the collaboration with our colleagues at Kyoto University possible. This work was supported by the JSPS Core-to-Core Program "International Research Network for Exotic Femto Systems," and carried out as a part of the U.S. Department of Energy under Contract Nos. DE-FG02-96ER40963 (University of Tennessee), DE-AC05-00OR22725 with UT-Battelle, LLC (Oak Ridge National Laboratory), and DE-FG05-87ER40361 (Joint Institute for Heavy Ion Research), the UNEDF SciDAC Collaboration supported by the U.S. Department of Energy under grant No. DE-FC02-07ER41457.

[1] E. Caurier, G. Martinez-Pinedo, F. Nowacki, A. Poves, and A. P. Zuker, Rev. Mod. Phys. **77**, 427 (2005).
[2] D. Gogny, Nucl. Phys. **A237**, 399 (1975).
[3] M. Girod and B. Grammaticos, Phys. Rev. C **27**, 2317 (1983).
[4] J. L. Egido, H.-J. Mang, and P. Ring, Nucl. Phys. **A334**, 1 (1980).
[5] J. L. Egido, J. Lessing, V. Martin, and L. M. Robledo, Nucl. Phys. **A594**, 70 (1995).
[6] J. Dobaczewski and P. Olbratowski, Comput. Phys. Commun. **158**, 158 (2004).
[7] N. Michel, W. Nazarewicz, M. Płoszajczak, and K. Bennaceur, Phys. Rev. Lett. **89**, 042502 (2002).
[8] N. Michel, W. Nazarewicz, M. Płoszajczak, and J. Okolowicz, Phys. Rev. C **67**, 054311 (2003).
[9] N. Michel, W. Nazarewicz, and M. Płoszajczak, Phys. Rev. C **70**, 064313 (2004).
[10] R. de la Madrid, A. Bohm, and M. Gadella, Fortschr. Phys. **50**, 185 (2002).
[11] R. de la Madrid, J. Phys. A: Math. Theor. **35**, 319 (2002); J. Phys. A: Math. Gen. **37**, 8129 (2004).
[12] M. V. Stoitsov, J. Dobaczewski, W. Nazarewicz, S. Pittel, and D. J. Dean, Phys. Rev. C **68**, 054312 (2003).
[13] A. Bulgac, Preprint FT-194-1980, Central Institute of Physics, Bucharest, 1980; nucl-th/9907088.
[14] J. Dobaczewski, H. Flocard, and J. Treiner, Nucl. Phys. **A422**, 103 (1984).
[15] E. Terán, V. E. Oberacker, and A. S. Umar, Phys. Rev. C **67**, 064314 (2003).
[16] V. E. Oberacker, A. S. Umar, E. Terán, and A. Blazkiewicz, Phys. Rev. C **68**, 064302 (2003).
[17] M. V. Stoitsov, J. Dobaczewski, W. Nazarewicz, and P. Ring, Comput. Phys. Commun. **167**, 43 (2005).
[18] J. N. Ginocchio, Ann. Phys. **152**, 203 (1984); **159**, 467 (1985).
[19] M. Stoitsov, N. Michel, and K. Matsuyanagi, Phys. Rev. C **77**, 054301 (2008).
[20] R. Id Betan, N. Sandulescu, and T. Vertse, Nucl. Phys. **A771**, 93 (2006).
[21] G. G. Dussel, R. Id Betan, R. J. Liotta, and T. Vertse, Nucl. Phys. **A789**, 182 (2007).
[22] D. Vautherin and D. M. Brink, Phys. Rev. C **5**, 626 (1972); D. Vautherin, *ibid*. **7**, 296 (1973).
[23] B. Gall, P. Bonche, J. Dobaczewski, H. Flocard, and P. H. Heenen, Z. Phys. A **348**, 183 (1994).
[24] J. Terasaki, H. Flocard, P. H. Heenen, and P. Bonche, Nucl. Phys. **A621**, 706 (1997).
[25] M. Yamagami, K. Matsuyanagi, and M. Matsuo, Nucl. Phys. **A693**, 579 (2001).
[26] K. Bennaceur and J. Dobaczewski, Comput. Phys. Commun. **168**, 96 (2005).
[27] P. Ring and P. Schuck, *The Nuclear Many-Body Problem* (Springer, New York, 1980).
[28] B. Gyarmati and T. Vertse, Nucl. Phys. **A160**, 523 (1971).
[29] A. Messiah, *Quantum Mechanics* (Courier Dover, New York, 1999).
[30] N. Dunford and J. T. Schwartz, *Linear Operators* (Wiley Classics Library, New York, 1988).
[31] N. Michel, J. Math. Phys. **49**, 022109 (2008).
[32] P. Lind, Phys. Rev. C **47**, 1903 (1993).
[33] R. G. Newton, *Scattering Theory of Waves and Particles*, 2nd ed. (Courier Dover, New York, 2002).
[34] S. T. Belyaev, A. V. Smirnov, S. V. Tolokonnikov, and S. A. Fayans, Sov. J. Nucl. Phys. **45**, 783 (1987).
[35] E. Chabanat, P. Bonche, P. Haensel, J. Meyer, and F. Schaeffer, Nucl. Phys. **A635**, 231 (1998).
[36] A. Blazkiewicz, V. E. Oberacker, A. S. Umar, and M. Stoitsov, Phys. Rev. C **71**, 054321 (2005).
[37] M. Grasso, N. Sandulescu, Nguyen Van Giai, and R. J. Liotta, Phys. Rev. C **64**, 064321 (2001).
[38] N. Michel, W. Nazarewicz, and M. Płoszajczak, Proceedings of New Developments in Nuclear Self-Consistent Mean-Field Theories, YITP, Kyoto, Japan, YITP-W-05-01, B32 (2005).

Progress of Theoretical Physics, Vol. 120, No. 6, December 2008

Triaxiality Dependence of Octupole Excitations on Superdeformed States in ^{44}Ti

Hiromichi Ogasawara,[1] Kenichi Yoshida,[2] Masayuki Yamagami,[2]
Shoujirou Mizutori[3] and Kenichi Matsuyanagi[2]

[1]*Department of Physics, Graduate School of Science, Kyoto University, Kyoto 606-8502, Japan*
[2]*Theoretical Nuclear Physics Laboratory, RIKEN Nishina Center, Wako 351-0198, Japan*
[3]*Department of Human Science, Kansai Women's College, Osaka 582-0026, Japan*

(Received September 1, 2008)

By random phase approximation (RPA) calculation based on triaxially deformed Woods-Saxon potential, we investigate how axial-symmetry breaking in the mean field affects the properties of octupole vibrational excitations built on superdeformed states in ^{44}Ti. We find a remarkable dependence of their properties on signature quantum number with respect to rotation about an axis perpendicular to the longest axis by the angle of π. Detailed numerical analysis of the signature dependence is made by considering the magnitude of the triaxial deformation γ as a parameter.

§1. Introduction

In the last two decades, more than two hundred superdeformed (SD) bands have been found in various mass regions.[1)–5)] The SD shell structure is significantly different from that of normal deformation; each major shell at the SD shape consists of about equal numbers of positive- and negative-parity levels. This is a favourable situation for the appearance of negative-parity collective modes. In fact, various mean-field calculations[6)–9)] and random phase approximation (RPA) calculations[10),11)] based on the rotating mean field (cranked shell model) indicated that SD nuclei are very soft against both the axial and nonaxial octupole deformations. Thus, low-frequency soft octupole vibrations were predicted to appear near the SD yrast lines,[12),13)] and identified in experiments for SD states in the Hg-Pb region,[14),15)] and in ^{152}Dy.[16)]

In recent years, the SD bands have been discovered also in the ^{40}Ca region: the rotational band built on the excited 0^+ state at about 5.2 MeV in ^{40}Ca was found to be superdeformed.[17),18)] The rotational band built on the excited 0^+ state at about 1.9 MeV in ^{44}Ti may also be regarded as belonging to a family of the SD band.[19)] In view of the fact that the low-angular-momentum portions of the SD bands in heavy nuclei are unknown in almost all cases (except the fission isomers), the observation of rotational bands starting from the 0^+ states is a unique feature characterizing the SD states in the ^{40}Ca region. It was then confirmed that symmetry-unrestricted Skyrme-Hartree-Fock (SHF) calculation indeed yields the SD local minima corresponding to these experimental data.[20)] Thus, it has become clear nowadays that even the doubly magic nucleus in the spherical shell model, like ^{40}Ca, can easily take a strongly

deformed shape if it is given excitation energy of only about 5 MeV. One of the significances of this type of phenomenon is that it exhibits the ability of the nucleus to take quite different microscopic structures with almost the same binding energy, and these different structures can coexist while retaining their identities.

The investigation of low-frequency octupole vibrations built on the SD states in the $A = 30$–50 region showed some new features that are absent in the study of heavy SD nuclei. For the $N = Z$ nuclei in the ^{40}Ca region, it may be possible to observe in experiment such collective modes built on the known SD 0^+ states. Moreover, because the proton and neutron shell structures are essentially the same, we can expect that strong coherence takes place between the proton and neutron excitations and brings about an enhanced collectivity of these modes. Thus, Inakura et al.[21] theoretically explored such a possibility by means of the mixed-representation RPA[22),23)] based on the SHF mean field, and suggested the appearance of low-frequency negative-parity collective modes possessing strongly enhanced isoscalar octupole transition strengths. In this region of nuclear chart, the number of particle-hole configurations is smaller than those in heavier nuclei. This might be an unfavorable situation to generate vibrational collectivity by coherent superposition of a large number of particle-hole excitations. On the other hand, it provides a unique situation to make a detailed microscopic analysis of how collective modes emerge out of a relatively small number of particle-hole configurations. Thus we can learn the similarity and difference of octupole vibrations built on SD states in various mass regions. The mixed-representation RPA calculation in Ref. 21) is fully self-consistent in the sense that the same effective interaction is used in both the mean-field and RPA calculations. On the other hand, it is not easy in this approach to identify microscopic particle-hole configurations generating individual RPA modes. Therefore, with the use of deformed Woods-Saxon potential and the conventional matrix formulation of the RPA, Yoshida et al.[24] carried out a detailed analysis of the microscopic structure of octupole excitation modes built on the SD states in ^{40}Ca and other nuclei. In that work, however, the single-particle Hamiltonian was solved in terms of the two-dimensional mesh representation with cylindrical coordinate system. Thus, the mean field was restricted to axially symmetric shapes.

In this paper, we extend the previous work[24] so as to allow for the breaking of axial symmetry in the mean field. For this purpose, we construct a new computer code to solve the triaxially deformed Woods-Saxon potential in terms of the three-dimensional Cartesian coordinate system. On the single-particle basis thus obtained, we carry out RPA calculation diagonalizing the RPA matrix. Our major purpose is to investigate the effects of the triaxial deformation of the mean field on the properties of octupole vibrations built on SD states. As a typical example, we take up the case of ^{44}Ti where experimental data is available for a candidate of the SD yrast state[19)] and a sizable triaxial deformation is predicted in SHF calculations.[20),21)] The magnitude of the calculated triaxial deformation parameter γ depends on the version of the Skyrme interaction and takes the values in the range $7°$–$18°$. In the present paper, we consider γ as a parameter and make a detailed analysis of how axial-symmetry breaking in the mean field affects the properties of octupole vibrational excitations built on the SD state in ^{44}Ti. We find a remarkable dependence of their properties

on signature quantum number with respect to rotation about the intermediate axis by the angle of π.

This paper is organized as follows. In §2, the properties of single-particle wave functions in triaxially deformed potential are recapitulated. In §3, the RPA scheme for octupole vibrational excitations on the triaxially deformed mean field is summarized, with special attention on their symmetry properties with respect to reflections about the (x, y)-, (y, z)-, and (z, x)-planes. In §4, results of numerical analysis of octupole excitations built on the SD state in ^{44}Ti are presented. In §5, concluding remarks are given.

§2. Triaxially deformed mean field

2.1. *Single-particle Hamiltonian*

We write nucleon creation and annihilation operators in a single-particle state k as $\hat{c}_k^\dagger$ and $\hat{c}_k$. With the use of the two-component single-particle wave function $\varphi_k(\vec{r})$ consisting of spin-up and spin-down components with respect to the z-axis, nucleon creation and annihilation operators at a spatial position $\vec{r}$ are then represented as

$$\hat{\psi}^\dagger(\vec{r}) = \sum_k \varphi_k^\dagger(\vec{r})\hat{c}_k^\dagger = \sum_k \left(\varphi_{k\uparrow}^*(\vec{r}),\ \varphi_{k\downarrow}^*(\vec{r})\right)\hat{c}_k^\dagger, \tag{2·1}$$

$$\hat{\psi}(\vec{r}) = \sum_k \varphi_k(\vec{r})\hat{c}_k = \sum_k \begin{pmatrix}\varphi_{k\uparrow}(\vec{r})\\ \varphi_{k\downarrow}(\vec{r})\end{pmatrix}\hat{c}_k. \tag{2·2}$$

We use a mean-field potential consisting of an axially asymmetric Woods-Saxon potential $V_{\rm WS}(\vec{r})$ and a spin-orbit potential $V_{\rm so}(\vec{r}, \vec{\nabla})$. In terms of the field operators defined above, the single-particle Hamiltonian is then written as

$$\hat{h} = \int \hat{\psi}^\dagger(\vec{r})h(\vec{r}, \vec{\nabla})\hat{\psi}(\vec{r})d^3\vec{r}, \tag{2·3}$$

$$h(\vec{r}, \vec{\nabla}) = \left[-\frac{\hbar^2}{2m}\Delta + V_{\rm WS}(\vec{r})\right]\mathbf{1} + V_{\rm so}(\vec{r}, \vec{\nabla}), \tag{2·4}$$

where $\mathbf{1}$ denotes the unit matrix in the 2×2 spin space. Explicit expressions of the Woods-Saxon and spin-orbit potentials are

$$V_{\rm WS}(\vec{r}) = -V_0\left[1 + \exp((r - R(\theta, \phi))/a)\right]^{-1}, \tag{2·5}$$

$$V_{\rm so}(\vec{r}, \vec{\nabla}) = \frac{i\hbar^2 q}{2}\left[\frac{\partial V_{\rm WS}(\vec{r})}{\partial \vec{r}} \times \vec{\sigma}\right]\cdot\vec{\nabla}, \tag{2·6}$$

where a is the diffuseness parameter and

$$R(\theta, \phi) = R_0(\beta, \gamma)\Bigg(1 + \beta\cos\gamma\ Y_{2,0}(\theta, \phi) + \frac{1}{\sqrt{2}}\beta\sin\gamma\ \left(Y_{2,+2}(\theta, \phi) + Y_{2,-2}(\theta, \phi)\right)\Bigg). \tag{2·7}$$

The deformation parameters, β and γ, indicate the magnitude of quadrupole deformation and its triaxiality, respectively. In this parametrization of nuclear surface,

when $\beta > 0$, at $\gamma = 0°$, the potential is symmetric about the z-axis, which is the longest principal axis (prolate shape). With increasing value of γ, the potential extends in the direction of the x-axis, and becomes at $\gamma = 60°$ symmetric about the y-axis, which is the shortest principal axis (oblate shape). Although an angle-dependent diffuseness parameter $a(\theta, \phi)$ is better for accurate calculation,[25] we use a constant a for simplicity.

The effective spherical radius $R_0(\beta, \gamma)$ is fixed under the condition that the volume enclosed by $R(\theta, \phi)$ takes the constant value $\frac{4}{3}\pi r_0^3 A$, A being the mass number. Its explicit expression is

$$R_0(\beta,\gamma) = r_0 A^{1/3}\left(1 + \frac{3}{4\pi}\beta^2 + \frac{\sqrt{5}}{28\pi\sqrt{\pi}}\beta^3\cos 3\gamma\right)^{-1/3}. \tag{2·8}$$

In the numerical calculation, we use the parameters shown in Ref. 28) for the $N = Z$ case, i.e., $V_0 = 51\,\mathrm{MeV}$, $\hbar^2 q = -0.44 r_0^2$, $r_0 = 1.27\,\mathrm{fm}$, and $a = 0.67\,\mathrm{fm}$.

2.2. *Symmetry properties of single-particle wave functions*

The single-particle Hamiltonian $h(\vec{r}, \vec{\nabla})$, the parity transformation $\mathcal{P}$, and the rotation about the z-axis by the angle of π, $\mathcal{R}_z = e^{i\pi j_z/\hbar}$, commutes with each other: i.e., $[h(\vec{r}, \vec{\nabla}), \mathcal{P}] = 0$, $[h(\vec{r}, \vec{\nabla}), \mathcal{R}_z] = 0$, and $[\mathcal{P}, \mathcal{R}_z] = 0$. Accordingly, we can adopt single-particle wave functions $\varphi_k(\vec{r})$ that are simultaneous eigenvectors of these operators:

$$h(\vec{r}, \vec{\nabla})\varphi_k(\vec{r}) = \varepsilon_k \varphi_k(\vec{r}), \tag{2·9}$$

$$\mathcal{P}\varphi_k(\vec{r}) = p_k \varphi_k(\vec{r}), \tag{2·10}$$

$$\mathcal{R}_z\varphi_k(\vec{r}) = \alpha_k \varphi_k(\vec{r}). \tag{2·11}$$

The quantum number α_k is called z-signature and takes values $\alpha_k = \pm i$. Thus, the single-particle wave functions $\varphi_k(\vec{r})$ are specified by parity p_k and z-signature as well as single-particle energy ε_k. In fact, the single-particle Hamiltonian $h(\vec{r}, \vec{\nabla})$ commutes with $\mathcal{R}_x = e^{i\pi j_x/\hbar}$ and also with $\mathcal{R}_y = e^{i\pi j_y/\hbar}$, as well as $\mathcal{R}_z$. Therefore, we can adopt x-signature or y-signature in place of z-signature to specify single-particle wave functions. It is, however, convenient to use the z-signature when we adopt the z-axis as a quantization axis of spin. In this case, the spin-up and spin-down components of the wave function in Eq. (2·2) satisfy the following symmetry properties with respect to reflections about the (y, z)-, $(z.x)$-, and (x, y)-planes (see Appendix A):[26),27]

$$\varphi_{k\sigma}(-x, y, z) = -i\alpha_k \sigma \varphi^*_{k\sigma}(x, y, z), \tag{2·12}$$

$$\varphi_{k\sigma}(x, -y, z) = \varphi^*_{k\sigma}(x, y, z), \tag{2·13}$$

$$\varphi_{k\sigma}(x, y, -z) = -ip_k \alpha_k \sigma \varphi_{k\sigma}(x, y, z), \tag{2·14}$$

where $\sigma = +1$ and -1 for spin-up $\uparrow$ and spin-down $\downarrow$, respectively. The single-particle Hamiltonian $h(\vec{r}, \vec{\nabla})$ is also invariant with respect to time reversal $\mathcal{T} = i\sigma_y \mathcal{K}$, where $\mathcal{K}$ denotes operation of taking the complex conjugate of all c-numbers, and

the phase convention of Bohr-Mottelson[28] is adopted. Operating $\mathcal{T}$ on both sides of the Schrödinger equation (2·9), we readily see that the time-reversal partner $\mathcal{T}\varphi_k(\vec{r})$ possesses the z-signature quantum number $\alpha_k^* = -\alpha_k$. Thus, there is a one-to-one correspondence between a time-reversal partner and a z-signature partner. Thanks to this property, we need to diagonalize the single-particle Hamiltonian only for the $\alpha = +i$ sector or the $\alpha = -i$ sector. Single-particle wave functions having opposite z-signatures are then immediately obtained as time-reversal partners of these eigenfunctions.

In diagonalizing the single-particle Hamiltonian, we use, instead of the well-known harmonic-oscillator basis, three-dimensional Cartesian coordinate mesh representation with box boundary condition.[26),27)] As discussed in Refs. 26) and 27), we need to explicitly consider only the octant region in space with $x \geq 0$, $y \geq 0$, and $z \geq 0$, owing to the reflection symmetries (2·12)–(2·14).

The major reason why we use the coordinate mesh representation is that we intend to apply, in due course, the present approach to neutron-rich unstable nuclei close to the drip line where the continuum plays an essential role and the coordinate mesh representation is better suited for this aim. We also intend to replace, in the future, the Woods-Saxon potential with the SHF potential. The computer program constructed in this work will serve as a first step toward such self-consistent mean-field approach.

In the numerical calculation, we take the box size extending about 2.5 times of the radius $R(\theta, \phi)$ in each direction and the space is discretized with the mesh spacing 0.6 fm. Numerical reliability with respect to the box size and the mesh spacing was carefully checked by Inakura et al.[21)] and shown that this choice gives fairy accurate results. Specifically, we take 17, 17, and 25 lattice points in the x-, y-, and z-direction, respectively, for the region of the triaxiality parameter $0^\circ \leq \gamma \leq 4^\circ$. These numbers are 17, 15, and 25 (19, 15, and 25) for $6^\circ \leq \gamma \leq 16^\circ$ ($18^\circ \leq \gamma \leq 30^\circ$). For the nucleus ^{44}Ti with $N = Z$, we use the same single-particle wave functions for protons and neutrons ignoring the Coulomb potential.

§3. RPA for octupole vibrations in triaxially deformed nuclei

3.1. *Eigenvalue equations*

Introducing a residual interaction $\hat{v}$, we solve the RPA eigenvalue equation for the total Hamiltonian $\hat{H} = \hat{h} + \hat{v}$ with

$$\hat{v} = \frac{1}{2} \sum_{\substack{k_1, k_2 \\ k_1', k_2'}} v_{k_1' k_2' k_1 k_2} \hat{c}_{k_2'}^\dagger \hat{c}_{k_1'}^\dagger \hat{c}_{k_1} \hat{c}_{k_2}, \tag{3·1}$$

$$v_{k_1' k_2' k_1 k_2} = \sum_{\substack{\sigma_1, \sigma_2 \\ \sigma_1', \sigma_2'}} \iint \varphi_{k_1' \sigma_1'}^*(\vec{r}_1) \varphi_{k_2' \sigma_2'}^*(\vec{r}_2) v_{\sigma_1' \sigma_1 \sigma_2' \sigma_2}(\vec{r}_1, \vec{r}_2) \varphi_{k_1 \sigma_1}(\vec{r}_1) \varphi_{k_2 \sigma_2}(\vec{r}_2) d^3\vec{r}_1 d^3\vec{r}_2. \tag{3·2}$$

Specifically, we use a density-dependent contact interaction of the following form:[29)]

$$v_{\sigma_1' \sigma_1 \sigma_2' \sigma_2}(\vec{r}_1, \vec{r}_2) = \left\{ \left[t_0 + \frac{1}{6} t_3 \rho(\vec{r}_1) \right] \delta_{\sigma_1 \sigma_1'} \delta_{\sigma_2 \sigma_2'} \right.$$

$$+\left[t_0x_0+\frac{1}{6}t_3x_3\rho(\vec{r}_1)\right]\delta_{\sigma_1\sigma_2'}\delta_{\sigma_2\sigma_1'}\Bigg\}\delta^3(\vec{r}_1-\vec{r}_2). \tag{3·3}$$

Here, $\rho(\vec{r})$ is the nucleon density. For the interaction parameters t_0, t_3, x_0, and x_3, we use the same values as in Shlomo-Bertsch:[29] $t_0 = -1100$ MeV·fm^3, $t_3 = 16000$ MeV·fm^6, $x_0 = 0.5$, and $x_3 = 1.0$.

We now introduce the particle-hole concept. The single-particle states above the Fermi energy $\varepsilon_{\rm F}$ is called *particle states* and those below $\varepsilon_{\rm F}$ is called *hole states*. The *particle* creation and annihilation operators $(\hat{a}_k^\dagger, \hat{a}_k)$ and the *hole* creation and annihilation operators $(\hat{b}_k^\dagger, \hat{b}_k)$ are defined as

$$\hat{c}_k^\dagger = (1-\theta_k)\hat{a}_k^\dagger + \theta_k\hat{b}_k, \tag{3·4}$$

$$\hat{c}_k = (1-\theta_k)\hat{a}_k + \theta_k\hat{b}_k^\dagger, \tag{3·5}$$

where θ_k is the occupation number defined as

$$\theta_k = \begin{cases} 1 & \text{for} \quad \varepsilon_k \le \varepsilon_{\rm F}, \\ 0 & \text{for} \quad \varepsilon_k > \varepsilon_{\rm F}. \end{cases} \tag{3·6}$$

The creation operators of the RPA eigenmodes are written as

$$\hat{X}_n^\dagger = \sum_{p,h}(f_{ph}^n\hat{a}_p^\dagger\hat{b}_h^\dagger - g_{ph}^n\hat{b}_h\hat{a}_p). \tag{3·7}$$

From now on, we use the index p (h) to specify the particle (hole) states and keep the index k for general cases. As usual, from the linearized equation of motion,

$$[\hat{H}, \hat{X}_n^\dagger] = \hbar\omega_n\hat{X}_n^\dagger, \tag{3·8}$$

we obtain eigenvalue equations in matrix form

$$\sum_{p'h'}\begin{pmatrix} A_{php'h'} & B_{php'h'} \\ -B^*_{php'h'} & -A^*_{php'h'} \end{pmatrix}\begin{pmatrix} f^n_{p'h'} \\ g^n_{p'h'} \end{pmatrix} = \hbar\omega_n\begin{pmatrix} f^n_{ph} \\ g^n_{ph} \end{pmatrix} \tag{3·9}$$

for each sector specified by parity p and z-signature α. The matrix elements $A_{php'h'}$ and $B_{php'h'}$ are given as

$$A_{php'h'} = (\varepsilon_p-\varepsilon_h)\delta_{pp'}\delta_{hh'} + \bar{v}_{ph'hp'}, \quad B_{php'h'} = \bar{v}_{pp'hh'}, \tag{3·10}$$

where $\bar{v}_{k_1'k_2'k_1k_2} = v_{k_1'k_2'k_1k_2}$ when (k_1, k_2) are between a proton and a neutron (vice versa) while $\bar{v}_{k_1'k_2'k_1k_2} = v_{k_1'k_2'k_1k_2} - v_{k_2'k_1'k_1k_2}$ taking both combinations (k_1, k_1') and (k_2, k_2') when (k_1, k_2) are identical nucleons. In the numerical calculation, we take into account all the particle-hole pairs with $\varepsilon_p - \varepsilon_h \le 30$ MeV.

3.2. *Octupole transition amplitudes*

For any one-body operator

$$\hat{O} = \sum_{k,k'}O_{k'k}\hat{c}_{k'}^\dagger\hat{c}_k \quad \text{with} \quad O_{k'k} = \int\varphi_{k'}^\dagger(\vec{r})O(\vec{r})\varphi_k(\vec{r})d^3\vec{r}, \tag{3·11}$$

Table I. Octupole operators classified according to z-component K and x-signature ξ.

	$\xi = +1$	$\xi = -1$
$K = 0$		$\sqrt{\frac{7}{16\pi}}\left\{2z^2 - 3(x^2+y^2)\right\} z$
$K = 1$	$\sqrt{\frac{21}{32\pi}}\left\{4z^2 - (x^2+y^2)\right\} x$	$\sqrt{\frac{21}{32\pi}}\left\{4z^2 - (x^2+y^2)\right\} y$
$K = 2$	$\sqrt{\frac{105}{4\pi}} xyz$	$\sqrt{\frac{105}{16\pi}}(x^2 - y^2) z$
$K = 3$	$\sqrt{\frac{35}{32\pi}}(x^2 - 3y^2) x$	$\sqrt{\frac{35}{32\pi}}(3x^2 - y^2) y$

transition amplitudes between the RPA ground state $|0\rangle$ and excited states $|n\rangle = \hat{X}_n^\dagger|0\rangle$ are evaluated as

$$\langle 0|\hat{O}|n\rangle = \langle 0|[\hat{O}, \hat{X}_n^\dagger]|0\rangle = \sum_{p,h}(O_{hp} f_{ph}^n + O_{ph} g_{ph}^n). \tag{3·12}$$

In this paper, we focus our attention on octupole transition strengths. It is then convenient to classify the octupole operators according to z-component K of its angular momentum and x-signature ξ representing symmetry property for rotation π about the x-axis:

$$\mathcal{R}_x O^{(K,\xi)}(\vec{r}) \mathcal{R}_x^{-1} = \xi O^{(K,\xi)}(\vec{r}) \quad \text{for} \quad \mathcal{R}_x = e^{i\pi j_x/\hbar}. \tag{3·13}$$

In terms of the spherical coordinates (r, θ, ϕ), they are given as

$$O^{(0,-)}(\vec{r}) = r^3 Y_{3,0}(\theta, \phi) \qquad \text{for} \quad K = 0, \tag{3·14}$$

$$O^{(K,+)}(\vec{r}) = \frac{i}{\sqrt{2}} r^3 \left[Y_{3,-K}(\theta,\phi) - (-1)^K Y_{3,+K}(\theta,\phi)\right] \qquad \text{for} \quad K \neq 0, \tag{3·15}$$

$$O^{(K,-)}(\vec{r}) = \frac{1}{\sqrt{2}} r^3 \left[Y_{3,-K}(\theta,\phi) + (-1)^K Y_{3,+K}(\theta,\phi)\right] \qquad \text{for} \quad K \neq 0. \tag{3·16}$$

In this classification, $O^{(K,\xi)}(\vec{r})$ are real functions; their explicit expressions in terms of the Cartesian coordinates are listed in Table I. We note that the octupole operators with odd-K (even-K) values have z-signature $\alpha = -1$ $(+1)$, which follows from the transformation property for rotation about the z-axis by the angle of π:

$$\mathcal{R}_z O^{(K,\xi)}(\vec{r}) \mathcal{R}_z^{-1} = (-1)^K O^{(K,\xi)}(\vec{r}). \tag{3·17}$$

3.3. *Symmetry for rotation about the x-axis by angle of π (x-signature)*

The single-particle Hamiltonian $h(\vec{r}, \vec{\nabla})$ commutes with $\mathcal{R}_x$ and $\mathcal{R}_z$ individually but the commutator between $\mathcal{R}_x$ and $\mathcal{R}_z$ is nonzero, so that it is impossible to construct a single-particle basis spanned by simultaneous eigenstates of x- and z-signatures. In contrast, creation and annihilation operators of the RPA eigenmodes $\hat{X}_n^\dagger$ and $\hat{X}_n$, carry definite x- and z-signatures simultaneously. We can examine this fact in the following manner. First, we can prove that the A and B matrix elements associated with z-signature partners are identical; $A_{\bar{p}\bar{h}\bar{p}'\bar{h}'} = A_{php'h'}$ and $B_{\bar{p}\bar{h}\bar{p}'\bar{h}'} = B_{php'h'}$ (see Appendix B). It immediately follows that the RPA particle-hole amplitudes of z-signature partners differ at most by sign, i.e., $(f_{\bar{p}\bar{h}}^n, g_{\bar{p}\bar{h}}^n) = \pm(f_{ph}^n, g_{ph}^n)$.

Next, let us evaluate transition matrix elements of the octupole operators with definite x- and z-signatures $\hat{O}^{(K,\xi)}$ between RPA excited states and the ground state (recall that z-signature $\alpha = (-1)^K$). They are calculated as

$$\begin{aligned}\langle 0|\hat{O}^{(K,\xi)}|n\rangle &= \sum_{p,h}(O_{ph}^{(K,\xi)*} f_{ph}^n + O_{ph}^{(K,\xi)} g_{ph}^n) \\ &= \sum_{p,h}{}'(O_{ph}^{(K,\xi)*} f_{ph}^n + O_{\bar{p}\bar{h}}^{(K,\xi)*} f_{\bar{p}\bar{h}}^n + O_{ph}^{(K,\xi)} g_{ph}^n + O_{\bar{p}\bar{h}} g^{(K,\xi)} g_{\bar{p}\bar{h}}^n) \\ &= \sum_{p,h}{}' \left[O_{ph}^{(K,\xi)*}(f_{ph}^n - \xi f_{\bar{p}\bar{h}}^n) + O_{ph}^{(K,\xi)}(g_{ph}^n - \xi g_{\bar{p}\bar{h}}^n) \right]. \end{aligned} \tag{3·18}$$

In the second equality above, the sum over the particle and hole states is divided into two parts consisting of z-signature partners; $\sum'_{p,h}$ denotes a summation over such signature pairs. Then, in the third equality, the relation, $O_{\bar{p}\bar{h}}^{(K,\xi)} = -\xi O_{ph}^{(K,\xi)}$, is utilized (see Appendix B). Assuming that the x-signature of the RPA ground state $|0\rangle$ is $+1$, the above expression indicates that the RPA excited states $|n\rangle$ created by $\hat{X}_n^\dagger$ possess definite ξ values. In other words, the RPA eigenmodes whose amplitudes possess such properties as $(f_{\bar{p}\bar{h}}^n, g_{\bar{p}\bar{h}}^n) = (f_{ph}^n, g_{ph}^n)$ create excited states with $\xi = -1$, while those with $(f_{\bar{p}\bar{h}}^n, g_{\bar{p}\bar{h}}^n) = -(f_{ph}^n, g_{ph}^n)$ create excited $\xi = +1$ states.

It should be noted here that, owing to the identity $\mathcal{R}_x\mathcal{R}_y\mathcal{R}_z = \mathbf{1}$ (see Appendix B), essentially the same argument as above holds when we adopt the y-signature associated with $\mathcal{R}_y$ (rotation about the y-axis by the angle of π) in place of the x-signature.

By taking into account the relation $O_{hp}^{(K,\xi)} = -(-1)^K \xi O_{ph}^{(K,\xi)}$ (see Appendix B) and that the proton and neutron contributions are the same for nuclei with $N = Z$ under the present approximation, the transition amplitudes for the isoscalar octupole operators with definite (K, ξ) are calculated as

$$\langle 0|\hat{O}^{(K,\xi)}|n\rangle = 4\sum_{p,h}{}'' O_{ph}^{(K,\xi)}(-(-1)^K \xi f_{ph}^n + g_{ph}^n) \equiv \sum_{p,h}{}'' M_{ph}^{(K,\xi)}, \tag{3·19}$$

where $\sum''_{p,h}$ denotes a summation over z-signature partners of protons (or neutrons).

We call the quantities $S_{3K} \equiv |\langle 0|\hat{O}^{(K,\xi)}|n\rangle|^2$ "isoscalar octupole transition strengths" often omitting the adjective "isoscalar". Note that these are quantities defined in the intrinsic coordinate frame and we cannot directly compare these quantities with experimental data. For this, it is necessary to construct wave functions in the laboratory frame by means of the Bohr-Mottelson approach[30] or the angular momentum projection method.[31] This subject is left for a future work, however.

3.4. *Elimination of spurious components*

Owing to the rotational symmetry breaking associated with the deformed mean field, dipole excitation modes can mix with the octupole excitation modes. As is well known, in the self-consistent RPA scheme where the same microscopic Hamiltonian is used in constructing the mean field and RPA excitation modes, the lowest isoscalar

modes corresponding to the center of mass motions appear at zero energy and they are separated from other excitation modes. In our present nonself-consistent calculation, such components associated with center of mass motion may mix in the RPA solutions representing octupole vibrations of interest. It is therefore necessary to adopt some recipe to eliminate such spurious coupling effects. For this purpose, we adopt the recipe that is widely used (see, e.g., Ref. 32)). First, we multiply a common factor λ to the interaction matrix elements $v_{k_1'k_2'k_1k_2}$ and determine its value so that the lowest eigenvalue of the RPA matrix becomes zero. There are three center of mass modes representing displacements in the x, y, and z directions. It is easily seen that they carry quantum numbers $(K,\xi) = (1,+1)$, $(1,-1)$, and $(0,-1)$, respectively. Therefore, we determine λ separately for the $(\alpha,\xi) = (-1,+1)$, $(-1,-1)$, and $(+1,-1)$ sectors. Note that the z-signature $\alpha = (-1)^K$ is conserved under the K-mixing owing to the triaxial deformation and that there is no spurious mode in the $(\alpha,\xi) = (+1,+1)$ sector. We can easily identify these spurious modes among the solutions of the RPA eigenvalue problem by evaluating isoscalar dipole transition amplitudes, since they have extremely large values.

If the separation of the spurious modes is perfectly carried out, the transition amplitudes of the isoscalar dipole operators $\hat{D}^{(K,\xi)}$, which are proportional to x, y, and z individually, should vanish for the octupole excited states of interest:

$$\langle 0|\hat{D}^{(K,\xi)}|n\rangle = 0. \tag{3·20}$$

In practice, it is difficult to meet this condition owing to the small but nonnegligible mixture of the spurious component. Thus, in the next step, we remove such a mixture from the octupole excited states obtained in the RPA calculation "by hand". Namely, we subtract the dipole component corresponding to the center of mass excitation, $\hat{D}^{(K,\xi)}|0\rangle$, from every RPA excited state $|n\rangle$ in each (α,ξ) sector (there is a connection between (K,ξ) and (α,ξ) as mentioned above):

$$|n\rangle \longrightarrow \mathcal{N}(|n\rangle - \chi\hat{D}|0\rangle) \quad \text{with} \quad \chi = \frac{\langle 0|\hat{D}|n\rangle}{\langle 0|\hat{D}^2|0\rangle}, \tag{3·21}$$

where $\mathcal{N} = (1 - |\chi|^2\langle 0|\hat{D}^2|0\rangle)^{-1/2}$. It is easily seen that this is equivalent to the replacement of the RPA forward and backward amplitudes, (f^n_{ph}, g^n_{ph}), in the following manner:
For the $\alpha = -1$ sector,

$$f^n_{ph} + g^n_{ph} \longrightarrow f^n_{ph} + g^n_{ph} - \frac{\sum_{p',h'} x_{p'h'}(f^n_{p'h'} + g^n_{p'h'})}{\sum_{p',h'} |x_{p'h'}|^2} x^*_{ph}, \quad (\xi = +1) \tag{3·22}$$

$$f^n_{ph} - g^n_{ph} \longrightarrow f^n_{ph} - g^n_{ph} - \frac{\sum_{p',h'} y_{p'h'}(f^n_{p'h'} - g^n_{p'h'})}{\sum_{p',h'} |y_{p'h'}|^2} y^*_{ph}. \quad (\xi = -1) \tag{3·23}$$

For the $\alpha = +1$ sector,

$$f^n_{ph} + g^n_{ph} \longrightarrow f^n_{ph} + g^n_{ph} - \frac{\sum_{p',h'} z_{p'h'}(f^n_{p'h'} + g^n_{p'h'})}{\sum_{p',h'} |z_{p'h'}|^2} z^*_{ph}, \quad (\xi = -1) \tag{3·24}$$

$$f^n_{ph} - g^n_{ph} \longrightarrow f^n_{ph} - g^n_{ph}. \quad (\xi = +1) \tag{3·25}$$

Here x_{ph}, y_{ph}, and z_{ph} represent $\langle 0|\hat{x}|ph\rangle$, $\langle 0|\hat{y}|ph\rangle$, and $\langle 0|\hat{z}|ph\rangle$, respectively. After the above replacements, we renormalize them such that new amplitudes satisfy the normalization condition $\sum_{p,h}(|f^n_{ph}|^2 - |g^n_{ph}|^2) = 1$.

§4. Numerical analysis and discussion

4.1. *Dependence of single-particle energies on β and γ*

Figure 1 shows the single-particle energies as functions of the deformation parameter β. We can clearly see that the shell gap at $N = Z = 20$ at the superdeformed shape with $\beta \simeq 0.6$–0.7 is responsible for the superdeformed excited state in ^{40}Ca. For ^{44}Ti with $N = Z = 22$, the superdeformed minimum obtained in the SHF calculation[20),21)] corresponds to the relatively small shell gap at $\beta \simeq 0.5$.

In Fig. 2, single-particle energies are plotted as functions of the triaxiality parameter γ fixing β at 0.5. It is seen that the shell gap at $N = Z = 22$ slightly increases with increasing γ indicating that the triaxial deformation is favoured but the effect is not very strong. This property of the single-particle diagram suggests the triaxial minimum of the mean field is rather soft with respect to the γ degree of

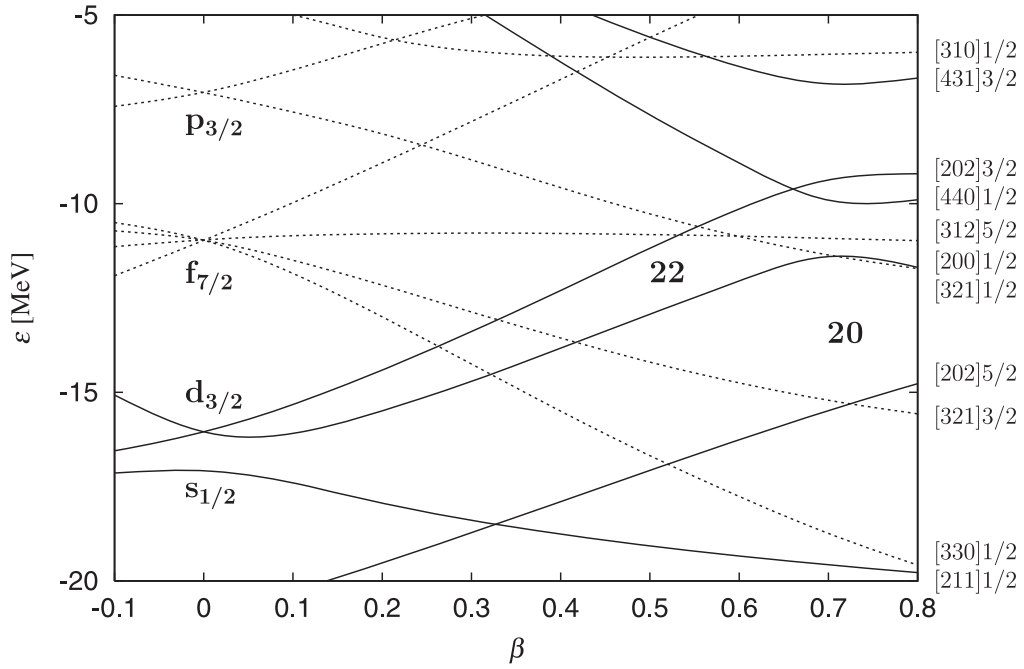

Fig. 1. Single-particle energies ε in the $N = Z$ nucleus ^{44}Ti for the Woods-Saxon plus spin-orbit potentials of Eq. (2·4) plotted as functions of the deformation parameter β. Positive and negative parity levels are indecated by solid and dotted lines, respectively. For convenience, they are labelled in the region of large β by asymptotic quantum numbers indicating the largest components at $\beta \simeq 0.5$ and connected adiabatically through the level crossing region. These single-particle energies are used for both protons and neutron.

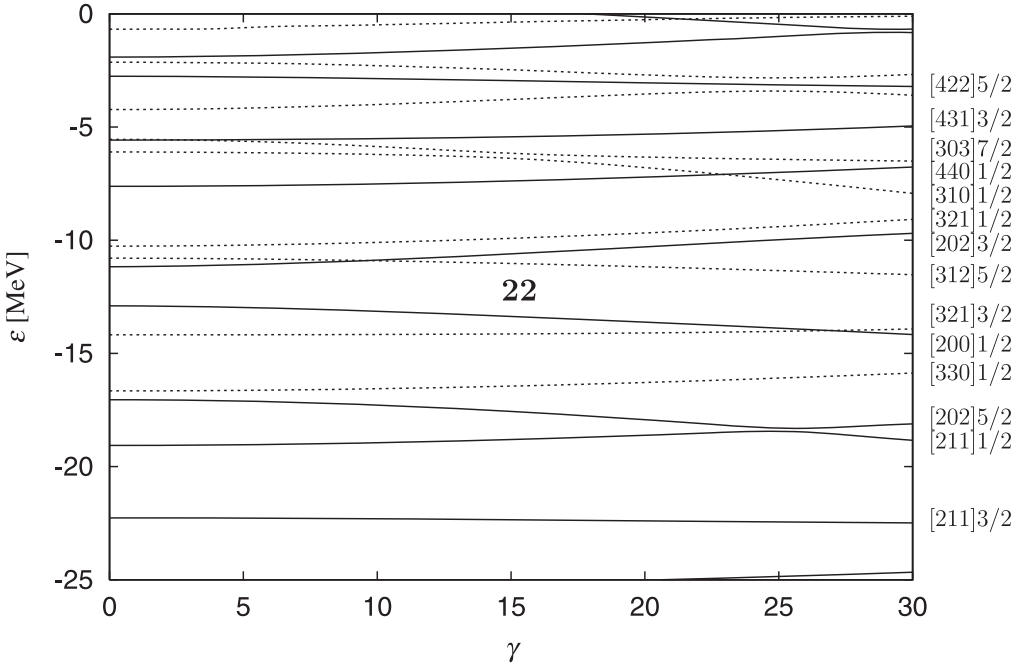

Fig. 2. Dependence of single-particle energies ε on the triaxiality parameter γ. The β is fixed at 0.5. Positive and negative parity levels are indicated by solid and dotted lines, respectively. For convenience, they are labelled with asymptotic quantum numbers indicating the largest components at the prolate limit ($\gamma = 0^\circ$) and connected adiabatically for variation of γ.

freedom. In such a situation, large-amplitude vibrational motions in this direction may take place, and it would be necessary to consider γ as a dynamical variable. This challenging subject is beyond the scope of the present paper, however. Below, we investigate the properties of octupole excitation modes built on the SD state in ^{44}Ti considering γ as a parameter. We discuss the $\alpha = \pm 1$ sectors separately.

4.2. *Interplay of $K = 1$ and 3 components in the $\alpha = -1$ sector*

In Fig. 3, we show the excitation energies and transition strengths S_{31} ($K = 1$) of low-lying RPA octupole excitation modes with negative z-signature ($\alpha = -1$) built on a superdeformed state in ^{44}Ti as functions of the triaxiality parameter γ. In the prolate limit ($\gamma = 0^\circ$), the z-component of angular momentum K (= 1 or 3) is a good quantum number and the x-signature pairs ($\xi = \pm 1$) are degenerate in energy. In this figure, the first and second excited states have $K = 3$. Their S_{33} values are small indicating their noncollective character. In contrast, the third excited state has $K = 1$ and fairly large value of S_{31}, indicating its collective character. With increasing γ, the mixing between the $K = 1$ and $K = 3$ modes takes place, the doublets split in energy, and transition strengths become different between the x-signature partners. Let us call these properties "x-signature splitting" and "x-signature dependence". In Fig. 3, we see that the first and third $\xi = +1$ modes have larger S_{31} values than their signature partners $\xi = -1$. In particular, we see a

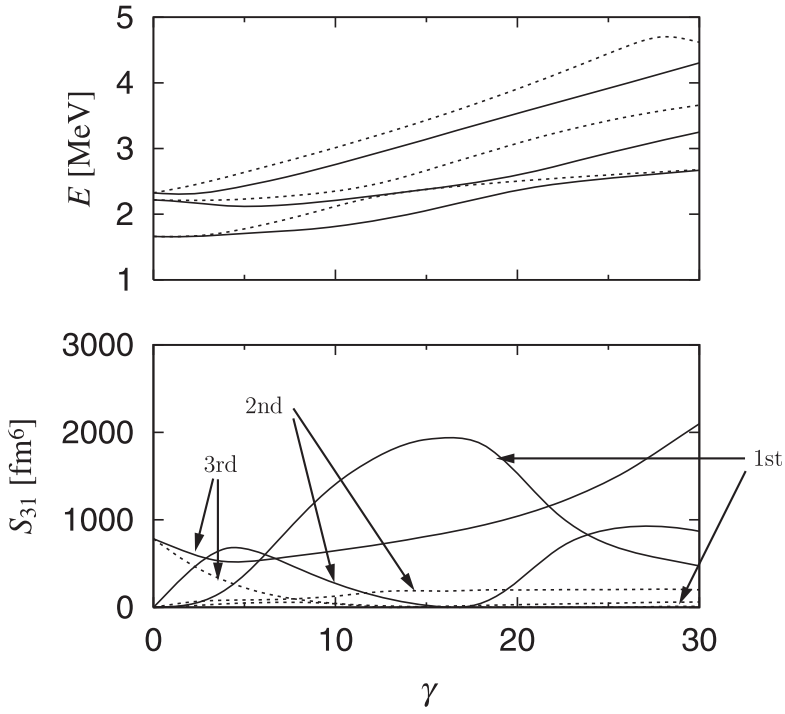

Fig. 3. Dependence on the triaxiality parameter γ of the RPA excitation energies (upper panel) and octupole transition strengths S_{31} ($K = 1$) (lower panel), calculated for octupole excitation modes with negative z-signature ($\alpha = -1$) built on a superdeformed state in ^{44}Ti. The β is fixed at 0.5. Modes with positive x-signature ($\xi = +1$) are indicated by solid lines, while those with negative x-signature ($\xi = -1$) by dotted lines. Only the lowest three x-signature pairs are presented. Octupole transition strengths S_{33} ($K = 3$) are not shown because they are very small.

remarkable increase in the $K = 1$ strength, S_{31}, of the first $\xi = +1$ mode starting from zero at $\gamma = 0°$. Let us examine the microscopic origin of this trend in more detail.

In Figs. 5 and 6, various quantities characterizing the lowest octupole modes with negative z-signature ($\alpha = -1$) at $\gamma = 4°$ and $\gamma = 16°$ are shown, respectively. These include the RPA forward and backward amplitudes, f_{ph} and g_{ph}, unperturbed particle-hole matrix elements of the octupole operator with $K = 1$, $O_{ph}^{(K=1,\xi)}$, and individual contributions to the RPA octupole transition amplitude, $M_{ph}^{(K=1,\xi)}$. Note that, although signs of f_{ph}, g_{ph}, and $O_{ph}^{(K=1,\xi)}$ depend on the chosen relative signs of single-particle wave functions, those of $M_{ph}^{(K=1,\xi)}$ are uniquely determined, because they are products of the former quantities. Thus, the relative signs of $M_{ph}^{(K=1,\xi)}$ between different particle-hole configurations serve as a good indicator of the coherence among them, and we can learn from their properties about the collectivity of the RPA mode under consideration. Therefore, in this figure, values of $M_{ph}^{(K=1,\xi)}$ are

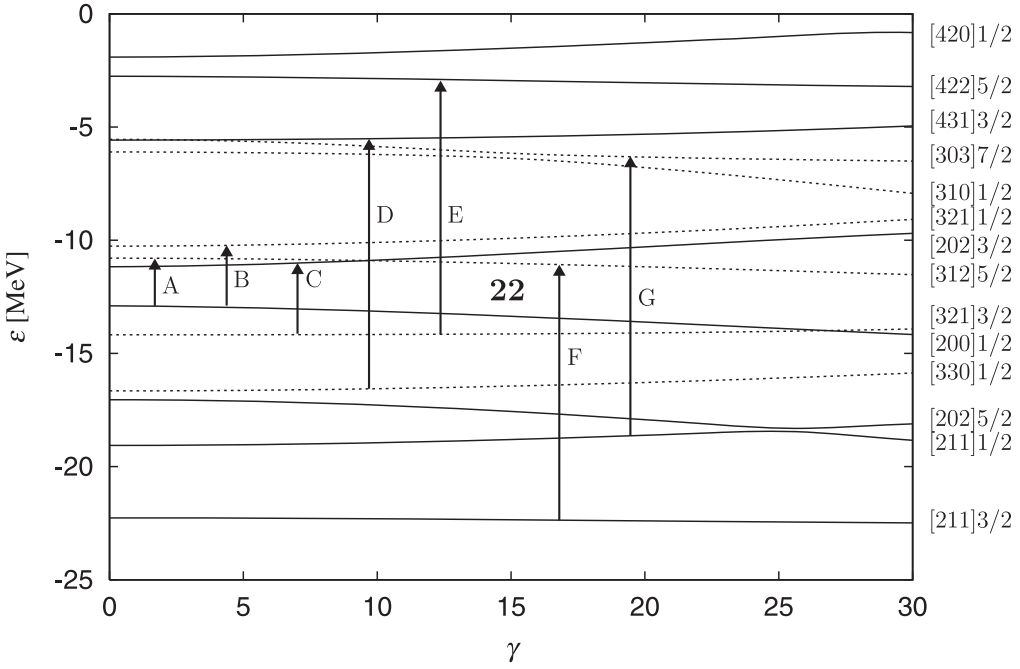

Fig. 4. Particle-hole configurations playing major roles in building up the lowest octupole vibrations with negative z-signature ($\alpha = -1$) (for both $\xi = \pm 1$). They are indicated by transition arrows with labels A, B, C, D, E, F, and G. The single-particle energies are plotted as functions of γ for a fixed value of $\beta = 0.5$. For convenience, they are labelled with asymptotic quantum numbers indicating the largest components at the prolate limit ($\gamma = 0^\circ$) and connected adiabatically for variation of γ. The arrows are drawn at arbitrary positions in γ. Positive and negative parity levels are indicated by solid and dotted lines, respectively. Note that only levels playing major roles in building up the lowest $\alpha = -1$ mode are explicitly drawn here; see Fig. 2 for a more complete single-particle diagram.

presented with their signs, while absolute values are shown for the other quanties. The $\gamma = 4^\circ$ case is chosen to examine the effect of incipient triaxial deformation on the octupole mode of interest and the $\gamma = 16^\circ$ case to represent typical triaxial deformation obtained in the SHF calculations.[20),21)]

According to the bottom panel of Fig. 5, the particle-hole configurations, [200]1/2 $\rightarrow$ [321]1/2 and [321]3/2 $\rightarrow$ [202]3/2, labelled B and C, respectively (illustrated in Fig. 4), give the major contributions to the strength S_{31} of the lowest mode at $\gamma = 4^\circ$ for both modes with x-signature $\xi = \pm 1$. It should be noted that Fig. 5 applies to both protons and neutrons: in the $N = Z$ nucleus under consideration, proton and neutron excitations act coherently and markedly enhance the transition strengths. Thus, the proton and neutron contributions are summed up in the transition amplitude $M_{ph}^{(K=1,\xi)}$ (see their definition (3·19)).

We can notice some different properties between signature partners already at such a small triaxiality. The difference significantly develops at $\gamma = 16^\circ$ shown in Fig. 6. In fact, the octupole transition amplitude $M_{ph}^{(K=1,\xi)}$ associated with the

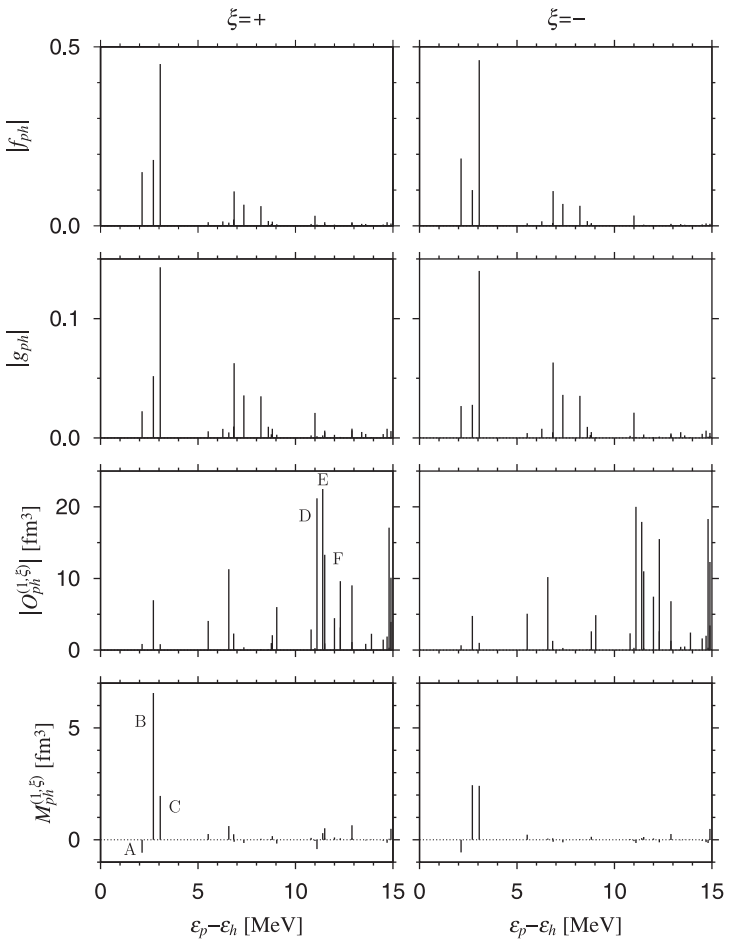

Fig. 5. Properties of the lowest octupole modes with negative z-signature ($\alpha = -1$) at the triaxiality parameter $\gamma = 4^\circ$. The result of calculation for the positive x-signature ($\xi = +1$) mode is displayed on the left-hand side, while that for the negative x-signature ($\xi = -1$) on the right-hand side. From the top to the bottom panels, RPA forward and backward amplitudes, f_{ph} and g_{ph}, unperturbed particle-hole matrix elements of the octupole operator with $K = 1$, $O_{ph}^{(K=1,\xi)}$, and individual contributions to the RPA octupole transition amplitude, $M_{ph}^{(K=1,\xi)}$, are displayed at positions of the abscissa axis representing unperturbed excitation energies, $\varepsilon_p - \varepsilon_h$, of individual particle-hole configurations composing the lowest RPA mode. Labels A, B, C, D, E, and F indicate some important configurations displayed in Fig. 4. Note that absolute values are shown except for $M_{ph}^{(K=1,\xi)}$. Note also that different scales are used for f_{ph} and g_{ph}.

configuration B, markedly increases for the positive x-signature mode ($\xi = +1$) but decreases for the negative x-signature mode ($\xi = -1$). Furthermore, higher-lying configurations, [330]1/2 → [431]3/2, [321]3/2 → [422]5/2, [211]3/2 → [312]5/2, and [211]1/2 → [303]7/2, respectively labelled D, E, F, and G (see Fig. 4), contribute appreciably only for the $\xi = +1$ mode. Note that they all contribute in the phase indicating that the collective character of the $\xi = +1$ mode is developed remarkably. In contrast, these contributions are much smaller for the $\xi = -1$ mode. This is the

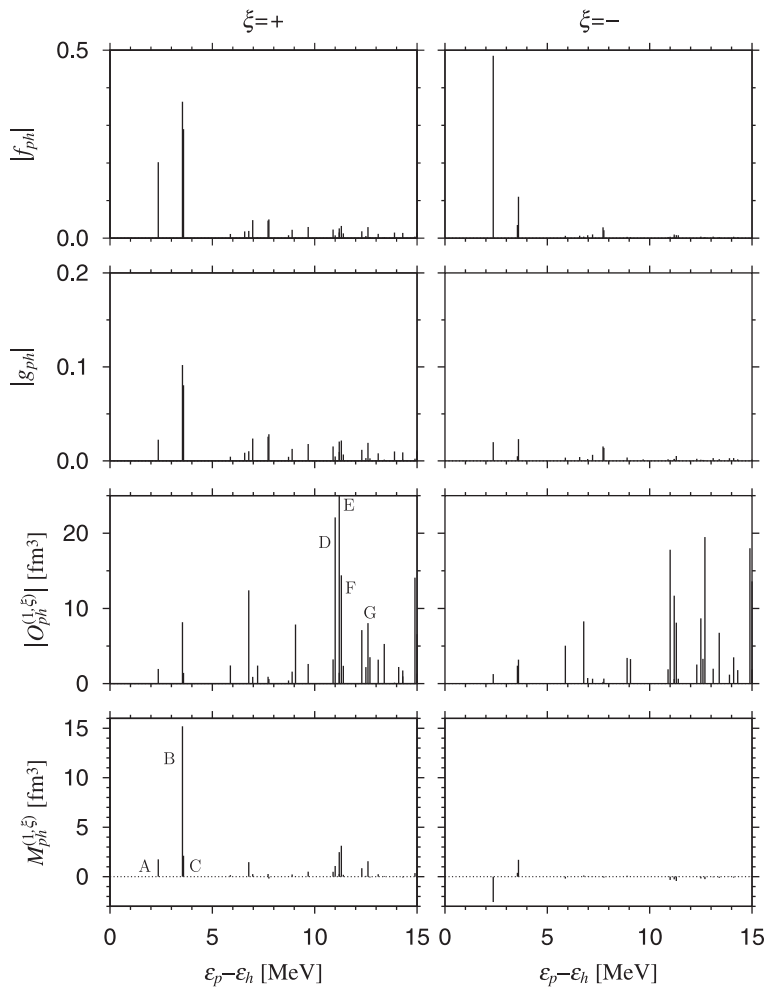

Fig. 6. Same as Fig. 5 but at the triaxiality parameter $\gamma = 16^\circ$. Note that different scales are used for g_{ph} and $M_{ph}^{(K=1,\xi)}$. The particle-hole excitation energy of configuration B is approximately the same with that of C.

microscopic origin of the striking difference of the octupole transition strength S_{31} between the lowest signature partners exhibited in Fig. 3.

4.3. *Interplay of $K = 0$ and 2 components in the $\alpha = +1$ sector*

In Fig. 7, we present the RPA excitation energies, octupole transition strengths with $K = 0$ and 2 (S_{30} and S_{32}) calculated for low-lying octupole excitation modes with positive z-signature ($\alpha = +1$) built on the SD state in ^{44}Ti as functions of triaxiality parameter γ. The lowest pair of excitation modes with $\xi = \pm 1$ has $K = 2$ in the prolate limit ($\gamma = 0^\circ$) and corresponds to the $K = 2$ doublet discussed in Ref. 21). As pointed out in that paper, appearance of this type of doublet pattern in excitation spectra may serve as a good indicator of triaxial deformation in the mean field. This signature-doublet possesses a large octupole strength S_{32} indicating

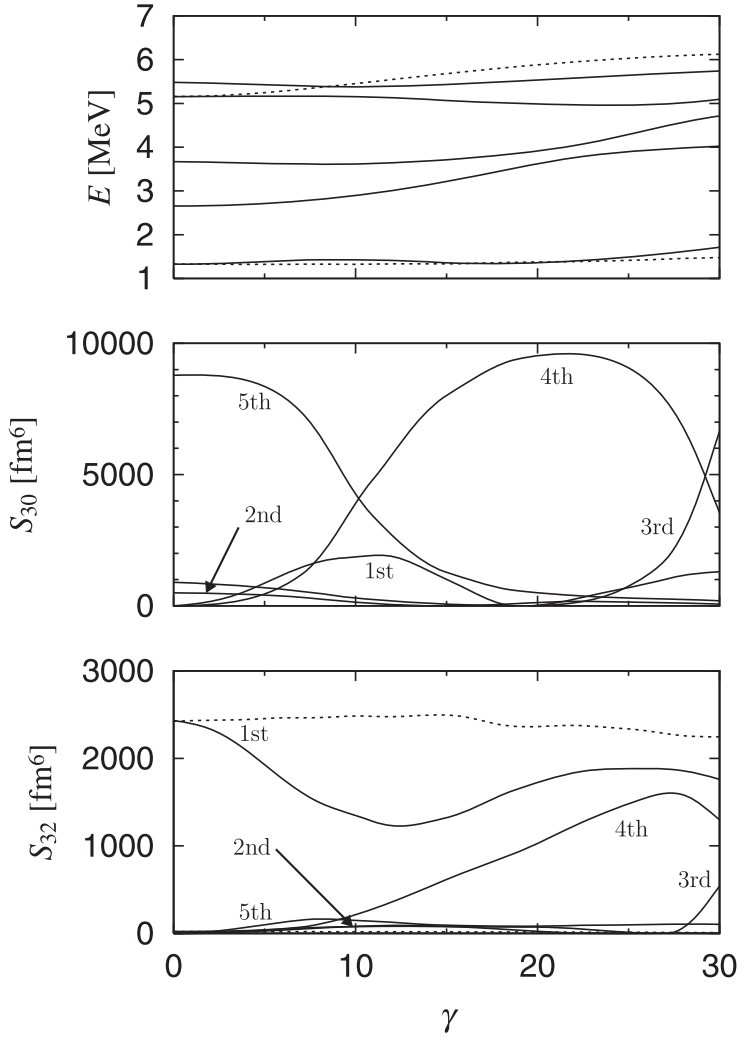

Fig. 7. Dependence on the triaxiality parameter γ of the RPA excitation energies (top panel), octupole transition strengths S_{30} ($K = 0$) (middle panel), and S_{32} ($K = 2$) (bottom panel), calculated for octupole excitation modes with positive z-signature ($\alpha = +1$) built on a superdeformed state in ^{44}Ti. The β is fixed at 0.5. Modes with negative x-signature ($\xi = -1$) are indecated by solid lines, while those with positive x-signature ($\xi = +1$) by dotted lines. Only the lowest five $\xi = -1$ modes are presented. Note that their signature partners with $\xi = +1$ exist only for the first and fourth modes which have $K = 2$ in the prolate limit.

their collective character. The main components of this doublet are the particle-hole excitations of protons and neutrons from the [200]1/2 level to the [312]5/2 level as illustrated with label H in Fig. 8, but coherent contributions of a large number of high-lying particle-hole excitations also play an indispensable role in generating collectivity of these lowest excitation modes.

The fourth pair of excitation modes, which exhibits a doublet pattern with

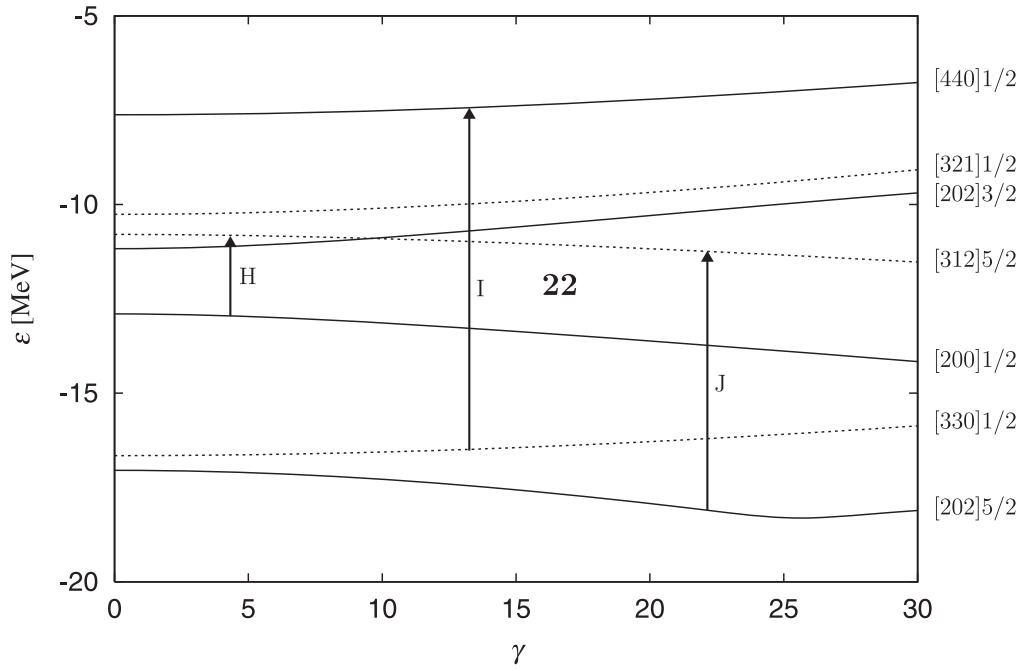

Fig. 8. Same as Fig. 4 but for the octupole vibrations with $(\alpha, \xi) = (+1, -1)$. Major particle-hole configurations are indicated by transition arrows with labels H, I, and J. Note that only levels playing major roles in building up the lowest $(\alpha, \xi) = (+1, -1)$ mode are explicitly drawn here; see Fig. 2 for a more complete single-particle diagram.

$\xi = \pm 1$ near the prolate limit, also has $K = 2$ there, but its S_{32} strength is very small indicating its noncollective character.

The second, third, and fifth excitation modes with $\xi = -1$ have $K = 0$ in the prolate limit, so that they have no x-signature partners. The $K = 0$ octupole strength S_{30} of the fifth mode is extremely large, indicating a strong collective character of this mode. On the other hand, the S_{30} strengths of the second and third modes are moderate. When the axial symmetry is broken, K-mixing takes place in the single-particle wave functions. Furthermore, the RPA modes that have different K quantum numbers (0 or 2) in the prolate limit start to interact with each other. Accordingly, x-signature splitting and K-mixing in the RPA modes develop with increasing γ. Thus, the $\xi = -1$ branch of the lowest excitation mode acquires an appreciable amount of the $K = 0$ octupole strength S_{30} in the region of $\gamma \simeq 5°$–$15°$. Correspondingly, its S_{32} strength decreases in this region. In contrast, the S_{32} strength of its $\xi = +1$ partner stays almost constant because, as mentioned above, there is no $\xi = +1$ mode of $K = 0$ to mix with.

It is interesting to observe that a level crossing between the fourth and fifth modes slowly takes place in the region of $\gamma \simeq 10°$. More precisely, because of the no crossing rule between the modes having the same quantum numbers, the two modes repel each other and exchange their characters when going through this region. This point is clearly seen in the plot of their S_{30} values. We note that this kind of interplay

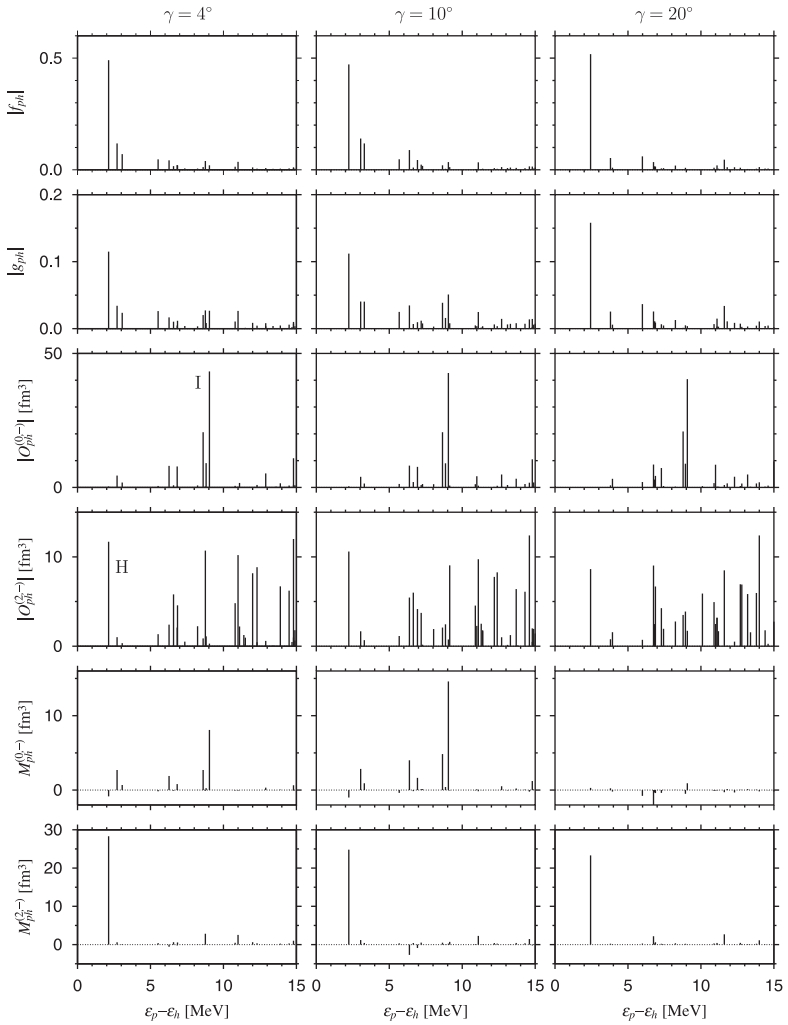

Fig. 9. Properties of the lowest octupole modes with $(\alpha, \xi) = (+1, -1)$. The results of calculation at the triaxiality parameter $\gamma = 4°$, $10°$, and $20°$ are presented on the left, middle, and right panels, respectively. From the top to the bottom panels, RPA forward and backward amplitudes, f_{ph} and g_{ph}, unperturbed particle-hole matrix elements of the octupole operators with $K = 0$ and $K = 2$, $O_{ph}^{(K=0,-)}$ and $O_{ph}^{(K=2,-)}$, and individual contributions to the RPA octupole transition amplitudes, $M_{ph}^{(K=0,-)}$ and $M_{ph}^{(K=2,-)}$, are displayed at positions of the abscissa axis representing unperturbed excitation energies, $\varepsilon_p - \varepsilon_h$, of individual particle-hole configurations composing the lowest RPA mode. Labels H and I indicate some important configurations displayed in Fig. 8. Note that absolute values are shown except for $M_{ph}^{(K=0,\xi)}$ and $M_{ph}^{(K=2,\xi)}$. Note aslso that different scales are used for f_{ph} and g_{ph}.

among a few $\xi = -1$ modes was not seen in the previous calculation.[21] The main cause of this difference is that, owing to slightly different single-particle energies, the lowest $K = 0$ mode and the other $K = 0$ modes are approximately separated in the latter calculation. This suggests that such detailed properties associated with

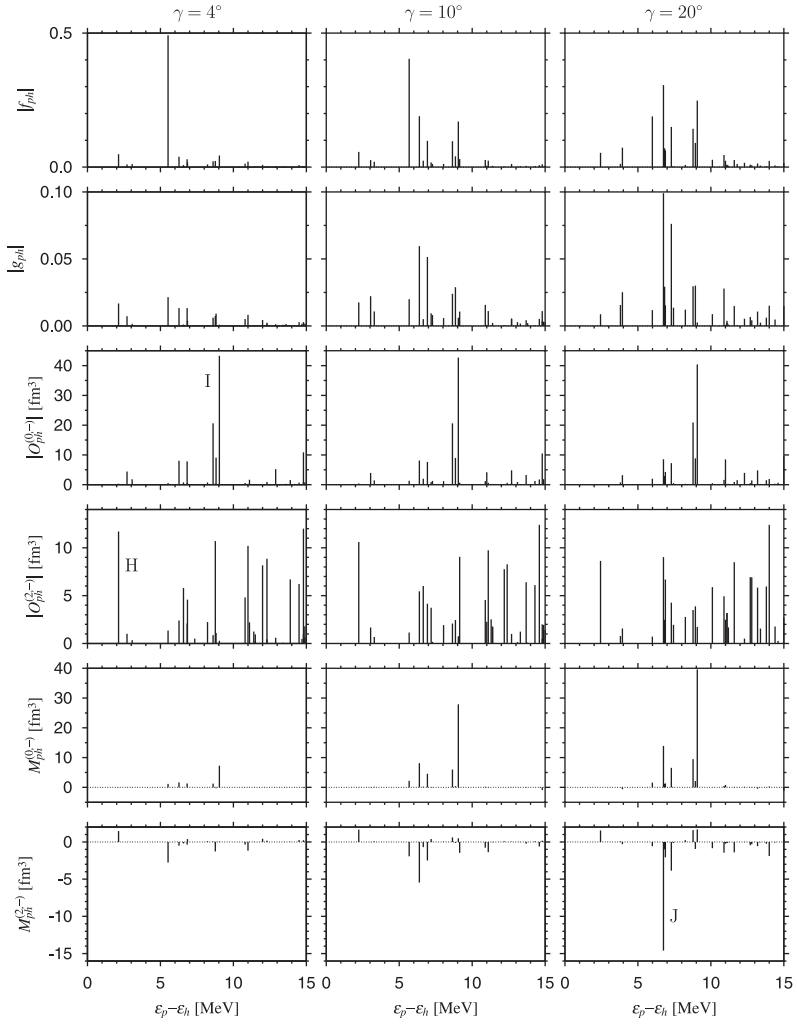

Fig. 10. Same as Fig. 9 but for the fourth excitation mode with $(\alpha, \xi) = (+1, -1)$.

interference among a few excitation modes are quite sensitive to the detailed shell structure of the mean field used in the RPA calculation.

We can investigate the microscopic origins of the γ dependence in the properties of excitation modes, exhibited in Fig. 7, by examining in detail the calculated RPA forward and backward amplitudes, f_{ph} and g_{ph}, unperturbed particle-hole matrix elements $O_{ph}^{(K,\xi)}$ of the octupole operators, and individual contributions $M_{ph}^{(K,\xi)}$ to the RPA octupole transition strengths. These quantities are displayed in Figs. 9 and 10 for the lowest and the fourth $\xi = -1$ modes, respectively. We again note that these figures apply to both protons and neutrons and their contributions are summed up in the transition amplitude $M_{ph}^{(K,\xi)}$. From Fig. 9, we learn that the increase in the S_{30} strength seen in Fig. 7 around $\gamma \simeq 10^\circ$ is associated with the mixture of the relatively high-lying particle-hole configuration, $[330]1/2 \rightarrow [440]1/2$ labelled I,

into this low-lying mode. This high-lying configuration corresponds to the excitation from the $f_{7/2}$ shell to the $g_{9/2}$ shell in the spherical limit and possesses an extremely large octupole matrix element $O_{ph}^{(0,-)}$. Therefore, its contribution to the transition amplitude $M_{ph}^{(0,-)}$ is large in spite of the fact that the RPA amplitudes, f_{ph} and g_{ph}, of this configuration are less than 0.1. In this manner, the low-lying collective RPA modes are generated by coherent superpositions of not only low-lying configurations but also many particle-hole configurations lying in the higher energy region.

In a similar manner, we can understand the reason why the S_{32} strength of the fourth mode increases in the region around $\gamma = 20^\circ$ by looking at Fig. 10. We see that the contribution to the transition amplitude $M_{ph}^{(2,-)}$ from the high-lying configuration, $[202]5/2 \rightarrow [312]5/2$, labelled J (see Fig. 8) markedly increases there. Note that, although these asymptotic quantum numbers are used for convenience to label the single-particle states, the z-component of angular momentum like $5/2$ is no longer a good quantum number under the triaxial deformation. In fact, the $[202]5/2$ level contains an appreciable amount of the $[200]1/2$ component so that the particle-hole configuration J possesses rather large $K = 2$ octupole matrix elements $O_{ph}^{(2,-)}$.

Finally, we point out another interesting trend seen in Fig. 7. The S_{30} strength of the lowest excitation modes is maximum in the region around $\gamma \simeq 10^\circ$ where the level crossing between the fourth and fifth excitation modes takes place, one of which carries an extremely large transition strength. Obviously, the mixing among these three modes is enhanced in this region. A similar trend is seen also near $\gamma = 30^\circ$ where the third and fourth excitation modes cross. Although we have not yet understood the deeper meaning of this result of calculation, it certainly indicates that the interplay of high-lying and low-lying particle-hole excitations plays an important role in generating collectivity of the low-lying octupole modes of excitation of interest.

§5. Concluding remarks

By means of the RPA calculation based on the triaxially deformed Woods-Saxon potential, we have investigated how axial-symmetry breaking in the mean field affects properties of the octupole vibrational excitations built on SD states in ^{44}Ti. By considering the magnitude of triaxial deformation γ as a parameter, detailed numerical analysis has been carried out with special attention to their dependence on signature quantum number with respect to rotation about an axis perpendicular to the longest axis by the angle of π. We have found a marked dependence of their properties on the signature quantum number.

Acknowledgements

We thank T. Inakura for giving us the result of the Skyrme-Hartree-Fock calculation to compare with our calculation result. The numerical calculations were carried out on supercomputers, NEC SX8 at the Yukawa Institute for Theoretical Physics in Kyoto University and NEC SX8R at the Research Center for Nuclear

Physics in Osaka University.

Appendix A
Symmetry Properties of Single-Particle Wave Functions

A.1. *Reflection symmetries*

The symmetry properties (2·12)–(2·14) are known[26),27)] but we here summarize their proof because the ideas used here are further developed in the succeeding sections.

The relation (2·14) for reflection about the (x, y)-plane is obtained through the following manipulation:

$$\varphi_k(x, y, -z) = \mathcal{P} e^{i\pi\ell_z/\hbar}\varphi_k(x, y, z) \tag{A·1}$$
$$= e^{-i\frac{\pi}{2}\sigma_z}\mathcal{P}\mathcal{R}_z\varphi_k(x, y, z) \tag{A·2}$$
$$= -ip_k\alpha_k\sigma_z\varphi_k(x, y, z), \tag{A·3}$$

where the z-component of orbital angular momentum operator, ℓ_z, is replaced with $j_z - \frac{\hbar}{2}\sigma_z$.

The relation (2·13) for reflection about the (z, x)-plane is obtained through the following consideration. The eigenvalue equations (2·9)–(2·11) are invariant against the transformation $\mathcal{I} = \mathcal{K}\mathcal{P}e^{i\pi\ell_y/\hbar}$. As the eigenvalue for $\mathcal{I}$ is ± 1 and the two equations, $\mathcal{I}\varphi_k(x, y, z) = \varphi_k(x, y, z)$ and $\mathcal{I}\{i\varphi_k(x, y, z)\} = -\{i\varphi_k(x, y, z)\}$ are apparently equivalent, we can choose the phase of our single-particle wave function satisfying the former relation without loss of generality. Since $\mathcal{I}\varphi_k(x, y, z) = \varphi_k^*(x, -y, z)$, Eq. (2·13) follows immediately.

With this phase convention, Eq. (2·9) for reflection about the (y, z)-plane is derived in the following manner:

$$\varphi_k(-x, y, z) = \mathcal{P} e^{i\pi\ell_y/\hbar}e^{i\pi\ell_z/\hbar}\varphi_k(x, y, z) \tag{A·4}$$
$$= e^{-i\frac{\pi}{2}\sigma_z}\mathcal{K}\mathcal{I}\mathcal{R}_z\varphi_k(x, y, z) \tag{A·5}$$
$$= -i\alpha_k\sigma_z\varphi_k^*(x, y, z). \tag{A·6}$$

A.2. *Axially symmetric limit*

In the prolate limit with $\gamma = 0^\circ$, the single-particle Hamiltonian $h(\vec{r}, \vec{\nabla})$ is symmetric about the z-axis, so that the single-particle wave functions $\varphi_k(\vec{r})$ can be written

$$\varphi_k(\vec{r}) = \begin{pmatrix} f_k(r, \theta)e^{i(m-\frac{1}{2})\phi} \\ g_k(r, \theta)e^{i(m+\frac{1}{2})\phi} \end{pmatrix}, \tag{A·7}$$

where $m\hbar$ is the angular momentum about the z-axis, and $f_k(r, \theta)$ and $g_k(r, \theta)$ possess the following symmetry properties for reflection about the (x, y)-plane: $f_k(r, \pi-\theta) = -ip_k\alpha_k f_k(r, \theta)$ and $g_k(r, \pi - \theta) = ip_k\alpha_k g_k(r, \theta)$.

Appendix B
—— Symmetries of the A, B, and O Matrix Elements ——

As we adopt the phase convention that the single-particle wave functions $\varphi_k(\vec{r})$ satisfy $\mathcal{I}\varphi_k(x,y,z) = \varphi_k(x,y,z)$, complex conjugation of these wave functions is equivalent to reflection about the (z,x)-plane ($\mathcal{K} = \mathcal{P}e^{i\pi\ell_y/\hbar}$), and time reversal is equivalent to symplex transformation about the (z,x)-plane ($\mathcal{T} = \mathcal{P}\mathcal{R}_y$). Also, there is a simple relation between the z-signature partner $\varphi_{\bar{k}}(\vec{r})$ and time-reversal partner $\mathcal{T}\varphi_k(\vec{r})$:

$$\varphi_{\bar{k}}(\vec{r}) = -i\alpha_k \mathcal{T}\varphi_k(\vec{r}). \tag{B·1}$$

Using the above properties, we can prove that the RPA matrix elements possess the symmetries $A_{\bar{p}\bar{h}\bar{p}'\bar{h}'} = A_{php'h'}$ and $B_{\bar{p}\bar{h}\bar{p}'\bar{h}'} = B_{php'h'}$ through the following manner. These symmetries immediately follow from the corresponding symmetries of the matrix elements of the residual interaction $v_{\bar{k}'_1\bar{k}'_2\bar{k}_1\bar{k}_2}$, which are examined through the following manipulation:

$$\begin{aligned}
v_{\bar{k}'_1\bar{k}'_2\bar{k}_1\bar{k}_2} &= \int \left[t_0 + \frac{1}{6}t_3\rho(\vec{r})\right] \Big\{\left[\mathcal{T}\varphi_{k'_1}(\vec{r})\right]^\dagger \left[\mathcal{T}\varphi_{k_1}(\vec{r})\right]\Big\} \Big\{\left[\mathcal{T}\varphi_{k'_2}(\vec{r})\right]^\dagger \left[\mathcal{T}\varphi_{k_2}(\vec{r})\right]\Big\} d^3\vec{r} \\
&\quad + \int \left[t_0x_0 + \frac{1}{6}t_3x_3\rho(\vec{r})\right] \Big\{\left[\mathcal{T}\varphi_{k'_1}(\vec{r})\right]^\dagger \left[\mathcal{T}\varphi_{k_2}(\vec{r})\right]\Big\} \Big\{\left[\mathcal{T}\varphi_{k'_2}(\vec{r})\right]^\dagger \left[\mathcal{T}\varphi_{k_1}(\vec{r})\right]\Big\} d^3\vec{r} \\
&= \int \left[t_0 + \frac{1}{6}t_3\rho(x,-y,z)\right] \\
&\qquad \times \left[\varphi^\dagger_{k'_1}(x,-y,z)\varphi_{k_1}(x,-y,z)\right] \left[\varphi^\dagger_{k'_2}(x,-y,z)\varphi_{k_2}(x,-y,z)\right] d^3\vec{r} \\
&\quad + \int \left[t_0x_0 + \frac{1}{6}t_3x_3\rho(x,-y,z)\right] \\
&\qquad \times \left[\varphi^\dagger_{k'_1}(x,-y,z)\varphi_{k_2}(x,-y,z)\right] \left[\varphi^\dagger_{k'_2}(x,-y,z)\varphi_{k_1}(x,-y,z)\right] d^3\vec{r} \\
&= v_{k'_1k'_2k_1k_2}.
\end{aligned} \tag{B·2}$$

In the first equality above, the relation $\varphi_{\bar{k}}(\vec{r}) = -i\alpha_k\mathcal{T}\varphi_k(\vec{r})$ is used. Note that $\alpha^*_{k'_1}\alpha_{k_1}\alpha^*_{k'_2}\alpha_{k_2} = +1$, because these are matrix elements between particle-hole pairs that carry a definite z-signature. In the second equality, the symmetry of the density, $\rho(x,-y,z) = \rho(x,y,z)$, and the relation, $\mathcal{T} = \mathcal{P}\mathcal{R}_y$, are used as

$$\begin{aligned}
[\mathcal{T}\varphi_{k'}(\vec{r})]^\dagger[\mathcal{T}\varphi_k(\vec{r})] &= [\mathcal{P}\mathcal{R}_y\varphi_{k'}(x,y,z)]^\dagger[\mathcal{P}\mathcal{R}_y\varphi_k(x,y,z)] \\
&= \varphi^\dagger_{k'}(x,-y,z)\varphi_k(x,-y,z).
\end{aligned} \tag{B·3}$$

In a similar fashion, we can prove the relations,

$$O^{(K,\xi)}_{hp} = -(-1)^K\xi O^{(K,\xi)}_{ph} \quad \text{and} \quad O^{(K,\xi)}_{\bar{p}\bar{h}} = -\xi O^{(K,\xi)}_{ph}, \tag{B·4}$$

between particle-hole matrix elements of the Hermitian octupole operators $O^{(K,\xi)}(\vec{r})$ through the following steps:

$$O^{(K,\xi)}_{hp} = O^{(K,\xi)*}_{ph}$$

$$
\begin{aligned}
&= \int [\mathcal{K}\varphi_p(\vec{r})]^\dagger O^{(K,\xi)}(\vec{r})[\mathcal{K}\varphi_h(\vec{r})]d^3\vec{r} \\
&= \int [\mathcal{P}e^{-i\pi\ell_x/\hbar}e^{-i\pi\ell_z/\hbar}\varphi_p(\vec{r})]^\dagger O^{(K,\xi)}(\vec{r})[\mathcal{P}e^{-i\pi\ell_x/\hbar}e^{-i\pi\ell_z/\hbar}\varphi_h(\vec{r})]d^3\vec{r} \\
&= \int \varphi_p^\dagger(\vec{r})e^{i\pi\ell_z/\hbar}e^{i\pi\ell_x/\hbar}\mathcal{P}^{-1}O^{(K,\xi)}(\vec{r})\mathcal{P}e^{-i\pi\ell_x/\hbar}e^{-i\pi\ell_z/\hbar}\varphi_h(\vec{r})d^3\vec{r} \\
&= -\int \varphi_p^\dagger(\vec{r})e^{i\pi\ell_z/\hbar}e^{i\pi\ell_x/\hbar}O^{(K,\xi)}(\vec{r})e^{-i\pi\ell_x/\hbar}e^{-i\pi\ell_z/\hbar}\varphi_h(\vec{r})d^3\vec{r} \\
&= -\xi\int \varphi_p^\dagger(\vec{r})e^{i\pi\ell_z/\hbar}O^{(K,\xi)}(\vec{r})e^{-i\pi\ell_z/\hbar}\varphi_h(\vec{r})d^3\vec{r} \\
&= -(-1)^K\xi\int \varphi_p^\dagger(\vec{r})O^{(K,\xi)}(\vec{r})\varphi_h(\vec{r})d^3\vec{r} \\
&= -(-1)^K\xi O_{ph}^{(K,\xi)}, \qquad \text{(B·5)}
\end{aligned}
$$

$$
\begin{aligned}
O_{\bar{p}\bar{h}}^{(K,\xi)} &= \int \varphi_{\bar{p}}^\dagger(\vec{r})O^{(K,\xi)}(\vec{r})\varphi_{\bar{h}}(\vec{r})d^3\vec{r} \\
&= (-1)^K\int [\mathcal{T}\varphi_p(\vec{r})]^\dagger O^{(K,\xi)}(\vec{r})[\mathcal{T}\varphi_h(\vec{r})]d^3\vec{r} \\
&= (-1)^K\int [\mathcal{P}\mathcal{R}_x^{-1}\mathcal{R}_z^{-1}\varphi_p(\vec{r})]^\dagger O^{(K,\xi)}(\vec{r})[\mathcal{P}\mathcal{R}_x^{-1}\mathcal{R}_z^{-1}\varphi_h(\vec{r})]d^3\vec{r} \\
&= (-1)^K\int \varphi_p^\dagger(\vec{r})\mathcal{R}_z\mathcal{R}_x\mathcal{P}^{-1}O^{(K,\xi)}(\vec{r})\mathcal{P}\mathcal{R}_x^{-1}\mathcal{R}_z^{-1}\varphi_h(\vec{r})d^3\vec{r} \\
&= -(-1)^K\int \varphi_p^\dagger(\vec{r})\mathcal{R}_z\mathcal{R}_xO^{(K,\xi)}(\vec{r})\mathcal{R}_x^{-1}\mathcal{R}_z^{-1}\varphi_h(\vec{r})d^3\vec{r} \\
&= -(-1)^K\xi\int \varphi_p^\dagger(\vec{r})\mathcal{R}_zO^{(K,\xi)}(\vec{r})\mathcal{R}_z^{-1}\varphi_h(\vec{r})d^3\vec{r} \\
&= -\xi\int \varphi_p^\dagger(\vec{r})O^{(K,\xi)}(\vec{r})\varphi_h(\vec{r})d^3\vec{r} \\
&= -\xi O_{ph}^{(K,\xi)}. \qquad \text{(B·6)}
\end{aligned}
$$

In the above manipulation, use is made of the relations, $\mathcal{T} = \mathcal{P}\mathcal{R}_y$, $\varphi_{\bar{k}}(\vec{r}) = -i\alpha_k\mathcal{T}\varphi_k(\vec{r})$, $\alpha_p^*\alpha_h = (-1)^K$, $\mathcal{P}O^{(K,\xi)}(\vec{r})\mathcal{P}^{-1} = -O^{(K,\xi)}(\vec{r})$, $\mathcal{R}_zO^{(K,\xi)}(\vec{r})\mathcal{R}_z^{-1} = (-1)^KO^{(K,\xi)}(\vec{r})$ and $\mathcal{R}_xO^{(K,\xi)}(\vec{r})\mathcal{R}_x^{-1} = \xi O^{(K,\xi)}(\vec{r})$, together with identities,

$$
e^{i\pi\ell_x/\hbar}e^{i\pi\ell_y/\hbar}e^{i\pi\ell_z/\hbar} = 1 \quad \text{and} \quad \mathcal{R}_x\mathcal{R}_y\mathcal{R}_z = \mathbf{1}. \qquad \text{(B·7)}
$$

References

1) P. J. Nolan and P. J. Twin, Annu. Rev. Nucl. Part. Sci. **38** (1988), 533.
2) S. Åberg, H. Flocard and W. Nazarewicz, Annu. Rev. Nucl. Part. Sci. **40** (1990), 439.
3) R. V. F. Janssens and T. L. Khoo, Annu. Rev. Nucl. Part. Sci. **41** (1991), 321.
4) C. Baktash, B. Haas and W. Nazaerewicz, Annu. Rev. Nucl. Part. Sci. **45** (1995), 485.
5) C. Baktash, Prog. Part. Nucl. Phys. **38** (1997), 291.
6) J. Dudek, T. R. Werner and Z. Szymanski, Phys. Lett. B **248** (1990), 235.
7) J. Skalski, Phys. Lett. B **274** (1992), 1.
8) P. A. Butler and W. Nazarewicz, Rev. Mod. Phys. **68** (1996), 349.

9) M. Bender, P.-H. Heenen and P.-G. Reinhard, Rev. Mod. Phys. **75** (2003), 121.
10) S. Mizutori, Y. R. Shimizu and K. Matsuyanagi, Prog. Theor. Phys. **85** (1991), 559; Prog. Theor. Phys. **86** (1991), 131.
11) S. Mizutori, T. Nakatsukasa, K. Arita, Y. R. Shimizu and K. Matsuyanagi, Nucl. Phys. A **557** (1993), 125.
12) T. Nakatsukasa, K. Matsuyanagi, S. Mizutori and W. Nazarewicz, Phys. Lett. B **343** (1995), 19.
13) T. Nakatsukasa, K. Matsuyanagi, S. Mizutori and Y. R. Shimizu, Phys. Rev. C **53** (1996), 2213.
14) A. Korichi et al., Phys. Rev. Lett. **86** (2001), 2746.
15) D. Rossbach et al., Phys. Lett. B **513** (2001), 9.
16) T. Lauritsen et al., Phys. Rev. Lett. **89** (2002), 282501.
17) E. Ideguchi et al., Phys. Rev. Lett. **87** (2001), 222501.
18) C. J. Chiara et al., Phys. Rev. C **67** (2003), 041303.
19) C. D. O'Leary, M. A. Bentley, B. A. Brown, D. E. Appelbe, R. A. Bark, D. M. Cullen, S. Ertürk, A. Maj and A. C. Merchant, Phys. Rev. C **61** (2000), 064314.
20) T. Inakura, S. Mizutori, M. Yamagami and K. Matsuyanagi, Nucl. Phys. A **710** (2002), 261.
21) T. Inakura, H. Imagawa, Y. Hashimoto, S. Mizutori, M. Yamagami and K. Matsuyanagi, Nucl. Phys. A **768** (2006), 61.
22) A. Muta, J.-I. Iwata, Y. Hashimoto and K. Yabana, Prog. Theor. Phys. **108** (2002), 1065.
23) H. Imagawa and Y. Hashimoto, Phys. Rev. C **67** (2003), 037302.
24) K. Yoshida, M. Yamagami and K. Matsuyanagi, Prog. Theor. Phys. **113** (2005), 1251.
25) H. C. Pauli, Phys. Rep. **7** (1973), 35.
26) P. Bonche, H. Focard, P. H. Heenen, S. J. Kriger and M. S. Weiss, Nucl. Phys. A **443** (1985), 39.
27) P. Bonche, H. Focard and P. H. Heenen, Nucl. Phys. A **467** (1987), 115.
28) A. Bohr and B. R. Motteleson, *Nuclear Structure*, Vol. I (W. A. Benjamin Inc., 1969; World Scientific, 1998).
29) S. Shlomo and G. F. Bertsch, Nucl. Phys. A **243** (1975), 507.
30) A. Bohr and B. R. Motteleson, *Nuclear Structure*, Vol. II (W. A. Benjamin Inc., 1975; World Scientific, 1998).
31) P. Ring and P. Schuck, *The Nuclear Many-Body Problem* (Springer, 1980).
32) G. Colò, N. Van Giai, P. F. Bortignon and M. R. Quaglia, Phys. Lett. B **485** (2000), 362.

Progress of Theoretical Physics, Vol. 121, No. 2, February 2009

Rotational Frequency Dependence of Octupole Vibrations on Superdeformed States in ^{40}Ca

Hiromichi Ogasawara,[1] Kenichi Yoshida,[2] Masayuki Yamagami,[2]
Shoujirou Mizutori[3] and Kenichi Matsuyanagi[2]

[1]*Department of Physics, Graduate School of Science, Kyoto University, Kyoto 606-8502, Japan*
[2]*Theoretical Nuclear Physics Laboratory, RIKEN Nishina Center, Wako 351-0198, Japan*
[3]*Department of Human Science, Kansai Women's College, Osaka 582-0026, Japan*

(Received October 26, 2008)

By means of the random phase approximation (RPA) calculation based on cranked deformed Woods-Saxon potential, we investigate how rotational motion affects the properties of octupole vibrations built on superdeformed states in ^{40}Ca. A major structure change of the superdeformed yrast states toward a reflection-asymmetric shape is suggested to take place in the region of angular momentum a little higher than the observed maximum value $16\hbar$, owing to a cooperative effect of octupole vibrational correlation and the rotation-aligned particle-hole excitations from the $f_{7/2}$ to the $g_{9/2}$ shell.

Subject Index: 213

§1. Introduction

In medium and heavy mass regions of nuclei, the effects of rotational motion on octupole vibrations in deformed nuclei have been investigated extensively.[1)–3)] As reviewed by Butler and Nazarewicz,[1)] how the octupole instability of the mean field develops as a function of angular momentum is one of the central questions underlying these investigations. An early work on this subject by Neergård and Vogel[4)] demonstrated the importance of Coriolis force already at low-spin band head states of octupole vibrational bands. In that work, using the particle-rotor model Hamiltonian,[5)] the Coriolis coupling effects were evaluated between octupole vibrational modes with $K = 0$, 1, 2, and 3, determined at the ground state by means of the random phase approximation (RPA), K being the component of angular momentum along the symmetry axis of the prolately deformed nuclei. In a succeeding paper,[6)] the importance of accurately evaluating the competition between the rotational alignment of angular momenta of octupole vibrations and that of noncollective two quasiparticle excitations was pointed out. In those works,[4),6)] the possible change of internal structure of the octupole vibrations with increasing rotational angular momentum was ignored.

The limitation mentioned above was removed in the eighties: It became possible to carry out RPA calculation on the basis of rotating (cranked) shell model;[7)] it is called "RPA in the rotating frame" or more shortly "cranked RPA".[8)–12)] In this approach, single-particle basis is constructed taking into account the rotational motion

of deformed mean field, so that microscopic structure change of RPA eigenmodes as a function of the rotational frequency can be investigated. Thus, for negative-parity modes near the yrast line, the importance of competition between octupole correlation energies and energy gain due to alignment of specific single-particle angular momentum associated with high-j orbits like $\mathrm{i}_{13/2}$ and $\mathrm{j}_{15/2}$ was pointed out.[13)–15)] This is so because such high-j single-particle states are usually involved, as a microscopic ingredient, in octupole vibrations described by RPA.

A breakthrough of the study on the nature of negative-parity excitations near the yrast states was brought about by the discovery of superdeformed rotational bands.[16)–20)] In such strongly deformed nuclei exhibiting beautiful rotational spectra, one can investigate the competitions mentioned above in a much clean way. Thus, on the basis of the RPA calculation in the rotating frame, Mizutori et al.[21),22)] and Nakatsukasa et al.[23),24)] suggested several interesting possibilities of how the rotational alignments of individual single-particle motions and octupole correlations compete in a new situation of superdeformed shell structure. Some of the theoretical predictions were already confirmed by later experiments[25)–27)] and some await further experiments.

In comparison with medium and heavy mass regions of nuclei discussed above, the properties of octupole vibration in deformed nuclei in lighter mass region are less understood: Collective octupole vibrations are well known also in light nuclei, but they are restricted mainly for spherical nuclei. Instead, the possibility of intrinsic reflection asymmetry has been discussed largely in connection with cluster and molecular structure of $N = Z$ nuclei from ^{12}C to ^{44}Ti (see references cited in Ref. 1)).

Several years ago, a superdeformed (SD) band built on the excited 0^+ state lying at approximately 5.2 MeV in ^{40}Ca was found by Ideguchi et al.[28),29)] It is characterized by a strongly deformed prolate shape with axis ratio of approximately 2:1 and exhibits a beautiful rotational spectrum from $J^\pi = 0^+$ to 16^+. In view of the fact that the low-angular-momentum portions of the SD bands in heavy nuclei are unknown in almost all cases (except the fission isomers), the observation of rotational band starting from the 0^+ states provides a unique opportunity to study low-frequency collective vibrations built on SD states as a function of angular momentum. It may be possible to observe experimentally such collective modes. For theoretical investigation, the study of ^{40}Ca has additional advantages. First, because the proton and neutron shell structures are essentially the same for such an $N = Z$ nucleus, we can expect that strong coherence takes place between the proton and neutron excitations and brings about an enhanced collectivity of these modes. Second, because the number of particle-hole configurations is smaller than those in heavier nuclei, it may be easier to analyze the competition between the rotational alignment effects of collective octupole and single-particle modes of excitation.

In this paper, we study the possible octupole excitations on the SD states in ^{40}Ca and change of their properties as a function of rotational frequency ω_{rot} by extending the previous RPA calculations[30)] to include the cranking term associated with the rotating deformed mean field. For this purpose, we construct a new computer code to solve the single-particle states in rotating deformed Woods-Saxon potential in terms

of the three-dimensional Cartesian coordinate system. On the single-particle basis thus obtained, we carry out RPA calculation diagonalizing the RPA matrix. The result of calculation suggests that a major structure change of the SD yrast states may take place in the region of angular momentum a little higher than the highest angular momentum $16\hbar$ identified in experiments to date, owing to an interplay between octupole vibrational modes and a rotation-aligned particle-hole excitation from the $f_{7/2}$ to the $g_{9/2}$ shell.

In the next section, we briefly summarize the calculational scheme of the RPA in the rotating frame. Because the method itself is well known, we describe only those necessary for discussion on octupole vibrations of present interest. In §3, results of numerical analysis of octupole excitations built on the SD state in ^{40}Ca are presented and discussed.

§2. RPA in the rotating frame

2.1. *Single-particle motion in a rotating deformed Woods-Saxon potential*

Let $\hat{c}_k^\dagger$ and $\hat{c}_k$ denote nucleon creation and annihilation operators in a single-particle state k. By using single-particle wave functions $\varphi_k(\vec{r})$ consisting of two components, $\varphi_{k\sigma}(\vec{r})$ ($\sigma = \pm 1$), with spin x-components $\frac{\hbar}{2}\sigma$, nucleon creation and annihilation operators at a spatial position $\vec{r}$ are written as

$$\hat{\psi}^\dagger(\vec{r}) = \sum_k \varphi_k^\dagger(\vec{r})\hat{c}_k^\dagger = \sum_k \left(\varphi_{k,+1}^*(\vec{r}),\ \varphi_{k,-1}^*(\vec{r})\right)\hat{c}_k^\dagger, \tag{2·1}$$

$$\hat{\psi}(\vec{r}) = \sum_k \varphi_k(\vec{r})\hat{c}_k = \sum_k \begin{pmatrix}\varphi_{k,+1}(\vec{r})\\ \varphi_{k,-1}(\vec{r})\end{pmatrix}\hat{c}_k. \tag{2·2}$$

We consider the following single-particle Hamiltonian describing independent-particle motion in the axially deformed Woods-Saxon potential that is uniformly rotating with rotational frequency $\omega_{\rm rot}$ about the x-axis perpendicular to the symmetry axis (z-axis):

$$\hat{h} = \int \hat{\psi}^\dagger(\vec{r})h(\vec{r},\vec{\nabla})\hat{\psi}(\vec{r})d^3\vec{r} = \sum_{k,k'}\left[\sum_{\sigma,\sigma'}\int \varphi_{k'\sigma'}^\dagger(\vec{r})h_{\sigma'\sigma}(\vec{r},\vec{\nabla})\varphi_{k\sigma}(\vec{r})d^3\vec{r}\right]\hat{c}_{k'}^\dagger\hat{c}_k \tag{2·3}$$

with

$$h(\vec{r},\vec{\nabla}) = \left[-\frac{\hbar^2}{2m}\Delta + V_{\rm WS}(\vec{r})\right]\mathbf{1} + V_{\rm so}(\vec{r},\vec{\nabla}) - \omega_{\rm rot}j_x, \tag{2·4}$$

where $\mathbf{1}$ denotes the unit matrix in the 2×2 spin space, and $V_{\rm WS}(\vec{r})$ and $V_{\rm so}(\vec{r},\vec{\nabla})$ represent the axially deformed Woods-Saxon potential and the spin-orbit potential, respectively;

$$V_{\rm WS}(\vec{r}) = -V_0\left[1+\exp((r-R(\theta))/a)\right]^{-1}, \tag{2·5}$$

$$V_{\rm so}(\vec{r},\vec{\nabla}) = \frac{i}{2}\hbar^2 q\left(\frac{\partial V_{\rm WS}(\vec{r})}{\partial\vec{r}}\times\vec{\sigma}\right)\cdot\vec{\nabla}, \tag{2·6}$$

with

$$R(\theta) = R_0(\beta)\left(1 + \sqrt{\frac{5}{4\pi}}\beta P_2(\cos\theta)\right), \tag{2·7}$$

where β is the quadrupole deformation parameter, $P_2(\cos\theta)$ is the second-order Legendre polynomial of $\cos\theta$, and $R_0(\beta)$ is fixed under the condition that the volume enclosed by $R(\theta)$ takes the constant value $\frac{4}{3}\pi r_0^3 A$, A being the mass number. We use the parameters of Ref. 31): $V_0 = 51$ MeV, $r_0 = 1.27$ fm, $a = 0.67$ fm, and $\hbar^2 q = -0.44 r_0^2$.

Because the single-particle Hamiltonian $h(\vec{r}, \vec{\nabla})$ is commutable with the parity transformation $\mathcal{P}$ and the rotation about the x-axis by the angle of π, $\mathcal{R}_x = e^{i\pi j_x/\hbar}$, we can construct simultaneous eigenfunctions of these operators:

$$h(\vec{r}, \vec{\nabla})\varphi_k(\vec{r}) = \varepsilon_k \varphi_k(\vec{r}), \tag{2·8}$$

$$\mathcal{P}\varphi_k(\vec{r}) = \wp_k \varphi_k(\vec{r}), \tag{2·9}$$

$$\mathcal{R}_x\varphi_k(\vec{r}) = \alpha_k \varphi_k(\vec{r}). \tag{2·10}$$

The eigenvalues $\wp_k$ $(= \pm 1)$ and α_k $(= \pm i)$ are called parity and x-signature, respectively. Hereafter, we simply call the latter "signature". Because we choose the quantization axis of intrinsic spin to coincide with the rotation axis (x-axis), we can determine single-particle wave functions such that they satisfy the following reflection symmetries (see Appendix A):[32),33)]

$$\varphi_{k\sigma}(-x, y, z) = -i\alpha_k \wp_k \sigma \varphi_{k\sigma}(x, y, z), \tag{2·11}$$

$$\varphi_{k\sigma}(x, -y, z) = -i\alpha_k \sigma \varphi^*_{k\sigma}(x, y, z), \tag{2·12}$$

$$\varphi_{k\sigma}(x, y, -z) = \varphi^*_{k\sigma}(x, y, z). \tag{2·13}$$

In diagonalizing the single-particle Hamiltonian, we use three-dimensional Cartesian coordinate mesh representation with box boundary condition.[32),33)] Owing to the reflection symmetries (2·11)–(2·13), we need to explicitly consider only the octant region in space with $x \geq 0$, $y \geq 0$, and $z \geq 0$. The major reason why we use the coordinate mesh representation is that we intend to apply, in due course, the present approach to neutron-rich unstable nuclei close to the drip line where the continuum plays an essential role. For this aim, the coordinate mesh representation may be better suited in comparison with that in terms of the harmonic-oscillator basis. We also intend to replace, in the future, the Woods-Saxon potential with the Skyrme-Hartree-Fock (SHF) potential.[34)] The computer program constructed in this work will serve as a first step toward such a self-consistent mean-field approach. In numerical calculation, we take the box size extending approximately 2.5 times of the radius $R(\theta)$ in each direction and the space is discretized with the mesh spacing of 0.6 fm. Numerical reliability with respect to the box size and the mesh spacing was carefully checked by Inakura et al.[35)] and shown that this choice gives fairly accurate results. Specifically, we take 15 lattice points in the x- and y-directions and 25 lattice points in the z-direction. We use the deformation parameter $\beta = 0.6$ and the same single-particle wave functions for protons and neutrons ignoring the Coulomb potential.

2.2. *Octupole vibrations on rotating superdeformed states*

As a residual interaction for the RPA calculation, we use a density-dependent contact interaction $\hat{v}$ whose matrix elements are given by Ref. 36):

$$v_{k'_1k'_2k_1k_2} = \sum_{\substack{\sigma_1,\sigma_2\\ \sigma'_1,\sigma'_2}} \iint \varphi^*_{k'_1\sigma'_1}(\vec{r}_1)\varphi^*_{k'_2\sigma'_2}(\vec{r}_2) v_{\sigma'_1\sigma_1\sigma'_2\sigma_2}(\vec{r}_1,\vec{r}_2)\varphi_{k_1\sigma_1}(\vec{r}_1)\varphi_{k_2\sigma_2}(\vec{r}_2) d^3\vec{r}_1 d^3\vec{r}_2 \quad (2\cdot14)$$

with

$$v_{\sigma'_1\sigma_1\sigma'_2\sigma_2}(\vec{r}_1,\vec{r}_2) = \Bigg\{ \left[t_0 + \frac{1}{6}t_3\rho(\vec{r}_1)\right]\delta_{\sigma_1\sigma'_1}\delta_{\sigma_2\sigma'_2} + \left[t_0x_0 + \frac{1}{6}t_3x_3\rho(\vec{r}_1)\right]\delta_{\sigma_1\sigma'_2}\delta_{\sigma_2\sigma'_1}\Bigg\}\delta^3(\vec{r}_1-\vec{r}_2), \quad (2\cdot15)$$

where $\rho(\vec{r})$ denotes the nucleon density and $t_0 = -1100\,\mathrm{MeV\cdot fm^3}$, $t_3 = 16000\,\mathrm{MeV\cdot fm^6}$, $x_0 = 0.5$, and $x_3 = 1.0$.[36)]

We now introduce creation and annihilation operators of *particle*, $(\hat{a}^\dagger_k, \hat{a}_k)$ and *hole*, $(\hat{b}^\dagger_k, \hat{b}_k)$, defined as

$$\hat{c}^\dagger_k = (1-\theta_k)\hat{a}^\dagger_k + \theta_k\hat{b}_k, \quad (2\cdot16)$$

$$\hat{c}_k = (1-\theta_k)\hat{a}_k + \theta_k\hat{b}^\dagger_k, \quad (2\cdot17)$$

where $\theta_k = 1$ when $\varepsilon_k \le \varepsilon_\mathrm{F}$ (Fermi energy) and 0 otherwise. In terms of these particle and hole operators, the RPA eigenmode creation operators are written as

$$\hat{X}^\dagger_n = \sum_{p,h}(f^n_{ph}\hat{a}^\dagger_p\hat{b}^\dagger_h - g^n_{ph}\hat{b}_h\hat{a}_p), \quad (2\cdot18)$$

where $\sum_{p,h}$ indicates a summation over particle-hole configurations of both protons and neutrons. We use the index p (h) to specify the particle (hole) states, while the index k is used for general cases. From the linearized equation of motion,

$$[\hat{H},\ \hat{X}^\dagger_n] = \hbar\omega_n\hat{X}^\dagger_n, \quad (2\cdot19)$$

we obtain eigenvalue equations in matrix form

$$\sum_{p',h'}\begin{pmatrix} A_{php'h'} & B_{php'h'} \\ -B^*_{php'h'} & -A^*_{php'h'}\end{pmatrix}\begin{pmatrix} f^n_{p'h'} \\ g^n_{p'h'}\end{pmatrix} = \hbar\omega_n\begin{pmatrix} f^n_{ph} \\ g^n_{ph}\end{pmatrix} \quad (2\cdot20)$$

for each sector specified by parity $\wp$ and signature α. In Eq. (2·19), $\hat{H} = \hat{h} + :\hat{v}:$ with $:\hat{v}:$ denoting the normal product of $\hat{v}$ with respect to the particle and hole operators. The matrix elements $A_{php'h'}$ and $B_{php'h'}$ are given as

$$A_{php'h'} = (\varepsilon_p - \varepsilon_h)\delta_{pp'}\delta_{hh'} + \bar{v}_{ph'hp'}, \quad B_{php'h'} = \bar{v}_{pp'hh'}, \quad (2\cdot21)$$

where $\bar{v}_{k'_1k'_2k_1k_2} = v_{k'_1k'_2k_1k_2}$ when (k_1,k_2) represents a pair of a proton and a neutron while $\bar{v}_{k'_1k'_2k_1k_2} = v_{k'_1k'_2k_1k_2} - v_{k'_2k'_1k_1k_2}$ when (k_1,k_2) corresponds to a pair of identical

nucleons. We diagonalize the RPA eigenvalue equation (2·20) treating the rotational frequency $\omega_{\rm rot}$ as a parameter and taking into account all particle-hole configurations with $\varepsilon_p - \varepsilon_h \leq 30$ MeV. It is certainly desirable to check the convergence of numerical results by comparing with calculation using a larger cutoff energy. Because it is computationally demanding, this task is deferred to a future work, however.

We evaluate isoscalar transition amplitudes for octupole operators between the yrast state $|0\rangle$ and the RPA excited states $|n\rangle = \hat{X}_n^\dagger|0\rangle$ as functions of $\omega_{\rm rot}$. The octupole operators are classified in terms of their K values (z-component of angular momentum) and signature α, and denoted as $O^{(K,\alpha)}(\vec{r})$. The signature α is defined as $\mathcal{R}_x O^{(K,\alpha)}(\vec{r})\mathcal{R}_x^{-1} = \alpha O^{(K,\alpha)}(\vec{r})$. Explicitly, they are given as

$$O^{(0,-)}(\vec{r}) = r^3 Y_{3,0}(\theta,\phi), \tag{2·22}$$

$$O^{(K,+)}(\vec{r}) = \frac{i}{\sqrt{2}} r^3 \big[Y_{3,-K}(\theta,\phi) - (-1)^K Y_{3,+K}(\theta,\phi)\big], \quad (K \neq 0) \tag{2·23}$$

$$O^{(K,-)}(\vec{r}) = \frac{1}{\sqrt{2}} r^3 \big[Y_{3,-K}(\theta,\phi) + (-1)^K Y_{3,+K}(\theta,\phi)\big], \quad (K \neq 0) \tag{2·24}$$

where the index $\pm$ stands for ± 1. The isoscalar transition amplitudes are calculated as

$$\langle 0|\hat{O}^{(K,\alpha)}|n\rangle = \langle 0|[\hat{O}^{(K,\alpha)},\ \hat{X}_n^\dagger]|0\rangle \tag{2·25}$$

$$= \sum_{p,h} (O_{hp}^{(K,\alpha)} f_{ph}^n + O_{ph}^{(K,\alpha)} g_{ph}^n) \tag{2·26}$$

$$\equiv \sum_{p,h} M_{ph}^{(K,\alpha)}, \tag{2·27}$$

where the sum is taken over particle-hole configurations of protons and neutrons, and

$$\hat{O}^{(K,\alpha)} = \sum_{k,k'} O_{k'k}^{(K,\alpha)} \hat{c}_{k'}^\dagger \hat{c}_k \quad \text{with} \quad O_{k'k}^{(K,\alpha)} = \int \varphi_{k'}^\dagger(\vec{r}) O^{(K,\alpha)}(\vec{r}) \varphi_k(\vec{r}) d^3\vec{r}. \tag{2·28}$$

The signs of f_{ph}, g_{ph}, and $O_{ph}^{(K,\alpha)}$ depend on the chosen signs of single-particle wave functions. On the other hand, the relative signs of $M_{ph}^{(K,\alpha)}$ defined above as products of these quantities are uniquely determined. Therefore, relative signs of $M_{ph}^{(K,\alpha)}$ between different particle-hole configurations serve as a good indicator of the coherence among them, and thus we can learn about the collectivity of individual RPA eigenmodes from their properties.

We call the quantities $S_{3K\alpha} \equiv |\langle 0|\hat{O}^{(K,\alpha)}|n\rangle|^2$ "transition strengths", although these are defined in the rotating coordinate frame so that we cannot directly compare these quantities with experimental data. For this, it is necessary to construct wave functions in the laboratory frame by the Bohr-Mottelson approach[5] or the angular momentum projection method.[37] This subject is left for a future work, however.

2.3. *Elimination of spurious center of mass modes*

It is well known that, provided the same Hamiltonian is consistently used in the mean-field and the RPA calculations, the spurious center of mass modes appear at

zero energy and they are decoupled from other eigenmodes of RPA. This is no longer true for the RPA calculation in the rotating frame, because the cranking term $-\omega_{\rm rot} j_x$ in the Hamiltonian $\hat{H}$ does not commute with the y- and z-components of linear momentum operators. Thus, some recipe to decouple such spurious modes from octupole vibrational modes in deformed nuclei has been proposed.[38] Fortunately, the numerical calculation of Ref. 13) indicates that the center of mass corrections is unimportant for excitation energies and B(E3) values of heavy nuclei (see also Ref. 1)). Thus, instead of trying to achieve exact decoupling of the center of mass modes, we adopt a procedure to eliminate the spurious mixing components from the RPA eigenmodes in the following two steps. First, we note that here are three center of mass modes representing the displacements in the x-, y-, and z-directions and they carry quantum numbers $(K, \alpha) = (1, +1)$, $(1, -1)$, and $(0, -1)$, respectively. Among them, only the $(K, \alpha) = (1, +1)$ mode commutes with the cranking term $-\omega_{\rm rot} j_x$, so that it should appear as a zero-frequency mode even in a rotating frame if a self-consistent mean-field plus RPA calculation is carried out. Because we are using a phenomenological Woods-Saxon potential in place of the self-consistent mean field, this merit of the RPA theory is lost, unfortunately. To remedy this shortcoming, we multiply a common factor λ to the interaction matrix elements $v_{k_1' k_2' k_1 k_2}$ and determine its value for each $\omega_{\rm rot}$ such that the lowest eigenvalue of the RPA matrix in the $\alpha = +1$ sector becomes zero. We can easily identify the spurious modes among solutions of the RPA eigenvalue problem by evaluating the isoscalar dipole transition strength, since it has an extremely large value.

If separation of the spurious modes is perfectly done, the transition amplitudes for the $\hat{x}$-, $\hat{y}$-, and $\hat{z}$-operators should vanish for the octupole excited states of interest:

$$\langle 0|\hat{x}|n\rangle = \langle 0|\hat{y}|n\rangle = \langle 0|\hat{z}|n\rangle = 0. \tag{2·29}$$

In practice, it is difficult to satisfy this condition owing to the small but nonnegligible mixture of the spurious components. Thus, in the next step, we remove such a mixture from the octupole excited states obtained in the RPA calculation "by hand", as for example, in Ref. 39). Namely, we subtract the center of mass components from every RPA excited states $|n\rangle$ in each sector:

$$|n\rangle \longrightarrow \begin{cases} \mathcal{N}_x(|n\rangle - \chi_x \hat{x}|0\rangle) & \text{for} \quad \alpha = +1, \\ \mathcal{N}_{yz}(|n\rangle - \chi_y \hat{y}|0\rangle - \chi_z \hat{z}|0\rangle) & \text{for} \quad \alpha = -1, \end{cases} \tag{2·30}$$

where

$$\mathcal{N}_x = \left[1 - |\chi_x|^2 \langle 0|\hat{x}^2|0\rangle\right]^{-1/2}, \tag{2·31}$$

$$\mathcal{N}_{yz} = \left[1 - |\chi_y|^2 \langle 0|\hat{y}^2|0\rangle - |\chi_z|^2 \langle 0|\hat{z}^2|0\rangle\right]^{-1/2}, \tag{2·32}$$

$$\chi_x = \frac{\langle 0|\hat{x}|n\rangle}{\langle 0|\hat{x}^2|0\rangle}, \quad \chi_y = \frac{\langle 0|\hat{y}|n\rangle}{\langle 0|\hat{y}^2|0\rangle}, \quad \text{and} \quad \chi_z = \frac{\langle 0|\hat{z}|n\rangle}{\langle 0|\hat{z}^2|0\rangle}. \tag{2·33}$$

It is easily seen that this is equivalent to the replacement of the RPA forward and backward amplitudes, (f^n_{ph}, g^n_{ph}), in the following manner:

- For modes with $\alpha = +1$,

$$f^n_{ph} + g^n_{ph} \longrightarrow f^n_{ph} + g^n_{ph} - \frac{\sum_{p'h'} x_{p'h'}(f^n_{p'h'} + g^n_{p'h'})}{\sum_{p'h'} |x_{p'h'}|^2} x^*_{ph}, \tag{2·34}$$

$$f^n_{ph} - g^n_{ph} \longrightarrow f^n_{ph} - g^n_{ph}. \tag{2·35}$$

- For modes with $\alpha = -1$,

$$f^n_{ph} + g^n_{ph} \longrightarrow f^n_{ph} + g^n_{ph} - \frac{\sum_{p'h'} y_{p'h'}(f^n_{p'h'} + g^n_{p'h'})}{\sum_{p'h'} |y_{p'h'}|^2} y^*_{ph}, \tag{2·36}$$

$$f^n_{ph} - g^n_{ph} \longrightarrow f^n_{ph} - g^n_{ph} - \frac{\sum_{p'h'} z_{p'h'}(f^n_{p'h'} - g^n_{p'h'})}{\sum_{p'h'} |z_{p'h'}|^2} z^*_{ph}. \tag{2·37}$$

Here, x_{ph}, y_{ph}, and z_{ph} represent $\langle 0|\hat{x}|ph\rangle$, $\langle 0|\hat{y}|ph\rangle$, and $\langle 0|\hat{z}|ph\rangle$, respectively. After the above replacements, we renormalize them such that new amplitudes satisfy the normalization condition $\sum_{p,h}(|f^n_{ph}|^2 - |g^n_{ph}|^2) = 1$.

§3. Numerical analysis and discussions

3.1. *Dependence of single-particle energies on rotational frequency*

Let us first examine the single-particle energy diagram in the uniformly rotating frame. Figure 1 shows the single-particle energies as functions of the rotational frequency $\omega_{\rm rot}$. We can clearly see the shell gap at $N = Z = 20$ associated with the superdeformed state in ^{40}Ca. An interesting feature seen in this figure is that the single-particle energy of the level labelled [440]1/2 at $\omega_{\rm rot} = 0$ gradually decreases with increasing $\omega_{\rm rot}$ and crosses the Fermi surface at approximately $\omega_{\rm rot} = 2$ MeV/$\hbar$. This indicates that a major structure change of the SD yrast states will occur in the vicinity of the angular momentum corresponding to this rotational frequency. This level originates from the $g_{9/2}$ shell. In the spherical shell model, its energy is much higher but, owing to the superdeformation, it comes down to this position. Its energy further decreases owing to the Coriolis effect. At $\omega_{\rm rot} = 0$, this level is situated at approximately 6 MeV above the Fermi level, so that its aligned angular momentum is estimated to be approximately $6\,[\mathrm{MeV}]\,/\,2\,[\mathrm{MeV}/\hbar] = 3\hbar$. In analyzing numerical results of the RPA calculation, we shall focus our attention on the role this level plays.

3.2. *Properties of octupole excitations on SD states in ^{40}Ca*

The results of the RPA calculation for negative-parity excitation modes on the SD yrast states in ^{40}Ca are presented in Fig. 2. In this figure, the RPA excitation

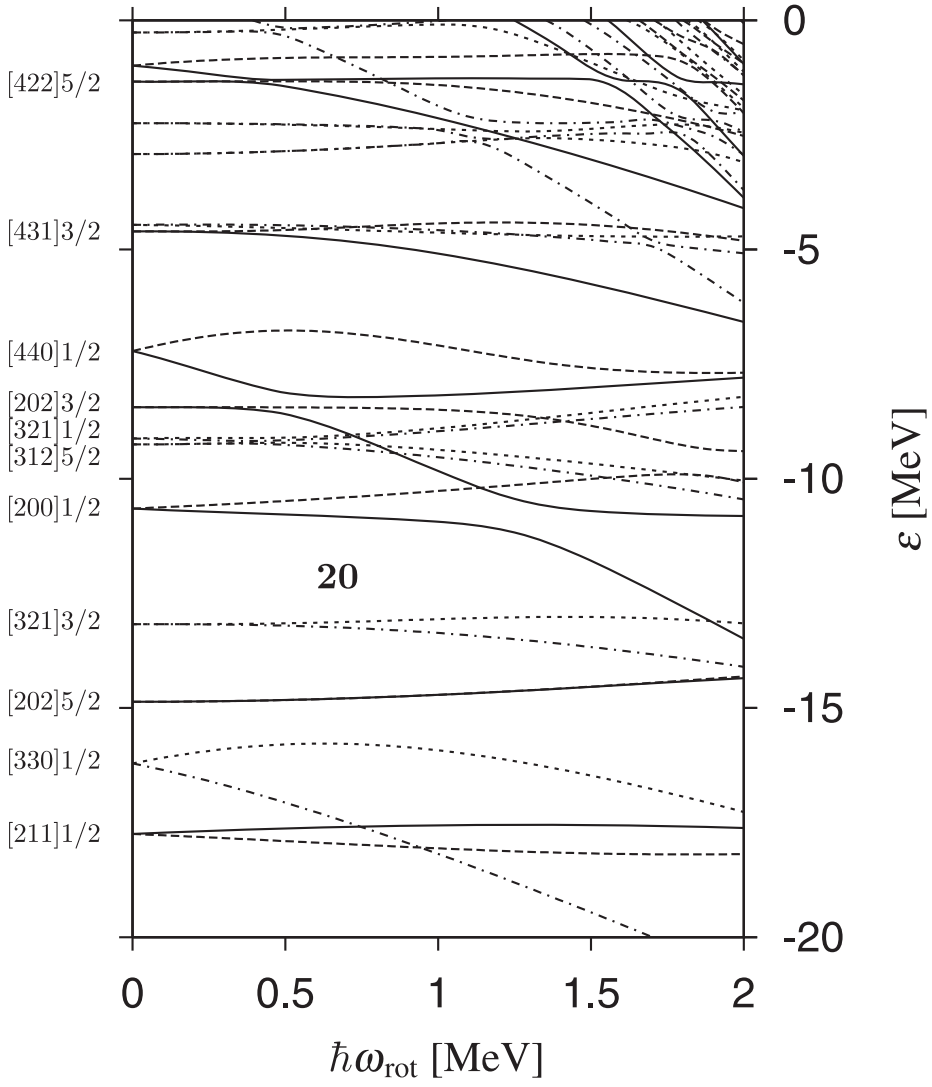

Fig. 1. Single-particle energies ε in the $N = Z$ nucleus ^{40}Ca for the rotating deformed Woods-Saxon plus spin-orbit potentials of Eq. (2·4), plotted as functions of rotational frequency $\omega_{\rm rot}$. The deformation parameter β is fixed at 0.6. Single-particle levels are classified according to the parity ($\wp$) and signature (α) quantum numbers; solid lines for $(\wp, \alpha) = (+1, +i)$, broken lines for $(\wp, \alpha) = (+1, -i)$, dotted lines for $(\wp, \alpha) = (-1, +i)$, and dot-dashed lines for $(\wp, \alpha) = (-1, -i)$. For convenience, they are labelled at $\omega_{\rm rot} = 0$ with asymptotic quantum numbers indicating the largest components of their wave functions. These single-particle energies are used for both protons and neutrons.

energies, the octupole transition strengths S_{30-} ($K = 0$) and $S_{31\pm}$ ($K = 1$) for individual RPA modes, and the sum, denoted as $S_{3K\alpha}^{(\rm sum)}$, of individual $S_{3K\alpha}$ values (over the RPA modes with excitation energies less than 5.5 MeV) are plotted as functions of rotational frequency $\omega_{\rm rot}$. Note that there is no positive-signature mode

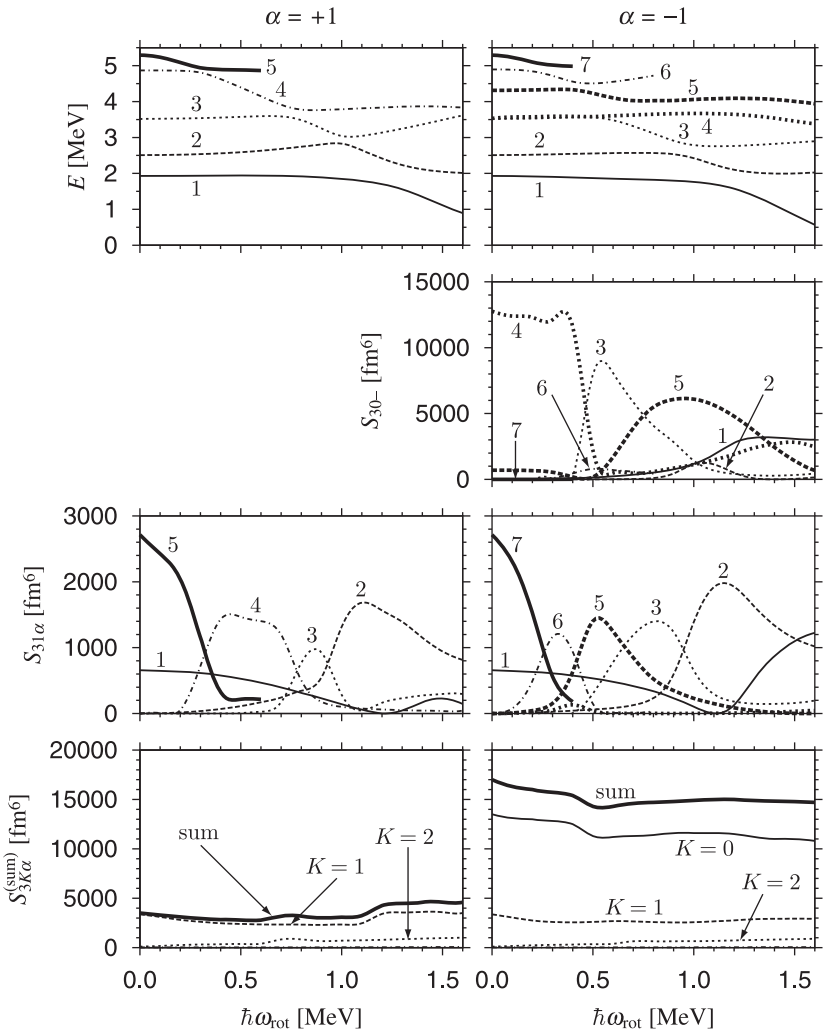

Fig. 2. Results of the RPA calculation for negative-parity excitation modes on the SD yrast states in ^{40}Ca, plotted as functions of the rotational frequency $\omega_{\rm rot}$. Positive-signature excitations are displayed on the left-hand side, while negative-signature excitations on the right-hand side. From the top to the bottom, the RPA excitation energies, the octupole transition strengths S_{30-} ($K = 0$) and $S_{31\pm}$ ($K = 1$) for individual RPA modes, and the sum $S^{(\rm sum)}_{3K\pm}$ of individual $S_{3K\pm}$ values (over the RPA modes with excitation energies less than 5.5 MeV) are plotted as functions of $\omega_{\rm rot}$. The numbers adjacent to individual lines indicate their sequential order according to excitation energy. (On each side, except the bottom panel, line types correspond to individual excitation modes.) The deformation parameter β is fixed at 0.6. Note that there is no positive-signature mode for $K = 0$. Note also that other RPA solutions in the region approximately 5 MeV are not displayed in order to avoid complicating the figure. Continuations of some of the RPA modes of interest are also not shown when they strongly mix with other RPA modes and lose their identities. The S_{31-} strength of the fourth excitation mode is very small so that it is hardly seen in this figure. In the bottom panel, the solid, broken, dotted, and dash-dotted lines indicate the sum $S^{(\rm sum)}_{3K\pm}$ for $K = 0$, 1, 2, and 3, respectively, while the bold-solid line shows the sum of these, $\sum_K S^{(\rm sum)}_{3K\pm}$. The sum $S^{(\rm sum)}_{33\pm}$ is very small so that it is hardly seen in this figure.

for $K = 0$. Because we find no octupole modes with $K = 2$ or 3 possessing a large strength below 5.5 MeV, the transition strengths of individual RPA eigenmodes are shown only for $K = 0$ and 1. This point is reflected in the $S^{(\mathrm{sum})}_{3K\pm}$ values shown in the bottom panels; it is seen that these values for $K = 2$ and 3 are much smaller than those for $K = 0$ and 1.

Let us start the discussion from the case of $\omega_{\mathrm{rot}} = 0$. In this case, signature partners ($\alpha = \pm 1$) with $K \neq 0$ are degenerate in energy. Counting these signature partners as units, we find seven eigenmodes below 5.5 MeV. Among them, the most collective mode is the fourth excitation mode at approximately 3.5 MeV. This mode has $K = 0$ and an extremely large value of octupole transition strength S_{30-}. Note that the Weisskopf unit (W.u.) is approximately 95 fm^6 for ^{40}Ca. Its major microscopic components are the particle-hole excitations [202]5/2 $\rightarrow$ [312]5/2, [321]3/2 $\rightarrow$ [431]3/2, and [330]1/2 $\rightarrow$ [440]1/2 for both protons and neutrons. Another interesting mode is the seventh excitation mode at approximately 5.3 MeV. This mode has $K = 1$ and a large value of $S_{31\alpha}$. It is characterized, in a very good approximation, as particle-hole excitations of protons and neutrons from the single-particle level [321]3/2 to [440]1/2. In comparison to these modes, the octupole transition strength of the first excitation mode at approximately 1.9 MeV is not very large, although it has strength several times of W.u. for $K = 1$. Its major component is the particle-hole excitation from [321]3/2 to [200]1/2. The second excitation mode with $K = 2$ at approximately 2.5 MeV is an almost pure particle-hole excitation from [321]3/2 to [200]1/2. The third excitation mode at approximately 3.5 MeV (which is almost degenerate, in energy, by chance, with the fourth mode discussed above) has $K = 3$. Although it consists of several particle-hole configurations like [321]3/2 $\rightarrow$ [202]3/2, [202]5/2 $\rightarrow$ [321]1/2, and [211]1/2 $\rightarrow$ [312]5/2, its transition strength $S_{33\alpha}$ is very small, because, for each configuration, either the octupole matrix element $O^{(3,\pm)}_{ph}$ or the RPA amplitude f_{ph} is small so that their product $M^{(3,-)}_{ph}$ is small.

It is interesting to note that the particle-hole excitations, like [321]3/2 $\rightarrow$ [431]3/2, [330]1/2 $\rightarrow$ [440]1/2, and [321]3/2 $\rightarrow$ [440]1/2, are the major sources of the large octupole transition strengths of the fourth and seventh eigenmodes. They correspond to the excitation from the $\mathrm{f}_{7/2}$ shell to the $\mathrm{g}_{9/2}$ shell in the spherical j-j coupling shell model. At the spherical shape, the $\mathrm{f}_{7/2}$ shell is unoccupied and the $\mathrm{g}_{9/2}$ shell is situated far above the Fermi surface. The energies of low-Ω single-particle states originating from such high-j orbits markedly decrease owing to the superdeformation, Ω being the component of angular momentum along the symmetry axis of the mean field. It is well known that such high-j shells play an important role in generating low-lying octupole vibrations in both spherical and normal deformed nuclei. However, the particle-hole excitation from the lower high-j shell to the higher high-j shell is a new feature unique to superdeformed states. It is also well known that the response of such high-j orbits to rotational motion is very strong because their Coriolis matrix elements are large. Thus it is interesting to examine how the microscopic structures and properties of the collective octupole vibrational modes change when the rotational frequency ω_{rot} increases, focusing our attention to the fourth and seventh excitation modes.

3.3. *Rotational frequency dependence of the octupole vibrations*

We are particularly interested in the strongly collective $K = 0$ mode that belongs to the negative-signature sector and its interaction with other eigenmodes. By comparing the positive- and negative-signature sectors in Fig. 2, we can imagine that the properties of the $\alpha = +1$ and $\alpha = -1$ octupole excitations with $K \neq 0$ would be similar to each other if the $K = 0$ collective mode and its interactions with other modes were absent. Thus, we focus our attention on the negative-signature sector in the discussion below.

It is immediately seen in Fig. 2 that strong mixings among the RPA modes take place following the variation of $\omega_{\rm rot}$. The most conspicuous trend is that the seventh excitation mode (bold-solid line) quickly comes down in energy and strongly interacts with other modes. The origin of this trend is the rotational alignment of the [440]1/2 ($\alpha = +i$) single-particle state, which is the major ingredient of the seventh mode; owing to the Coriolis coupling effect, its energy quickly decreases as $\omega_{\rm rot}$ increases (see Fig. 1). In the region approximately $\omega_{\rm rot} = 0.5$ MeV/$\hbar$, we see a strong interaction of the collective mode possessing a large $K = 0$ strength S_{30-} with other modes. Note that K is no longer a good quantum number, even approximately, already in this region of $\omega_{\rm rot}$. Namely, these modes contain both the $K = 0$ and 1 components, owing to the Coriolis K-mixing effects. Thus, they exhibit avoided crossing phenomena and exchange their main characters when going through the adiabatic crossing region. Similar avoided crossings successively take place. Accordingly, the octupole transition strengths S_{30-} and S_{31-} are redistributed among these modes, keeping the sum of their strengths for each K approximately constant, as shown in the bottom panel of Fig. 2.

Details of numerical data useful for understanding microscopic structures and properties of collective octupole excitation modes of interest are presented in Figs. 3–6 for some representative cases.

In Fig. 3, the RPA forward and backward amplitudes, f_{ph} and g_{ph}, the unperturbed particle-hole matrix elements of the octupole operator with $K = 0$ and $\alpha = -1$, $O_{ph}^{(0,-)}$ and individual contributions to the RPA octupole transition amplitude, $M_{ph}^{(0,-)}$, are displayed for the fourth excitation mode with $(\wp, \alpha) = (-1, -1)$ at $\omega_{\rm rot} = 0$. Some important particle-hole configurations constituting this mode are also illustrated. Because of the reason mentioned below Eq. (2·28), values of $M_{ph}^{(0,-)}$ are presented with their signs, while absolute values are shown for the other quantities. It is seen that the signs of $M_{ph}^{(0,-)}$ associated with the major configurations denoted A, B, and C are in phase, indicating the collective character of this mode. It is also seen that the particle-hole excitation C, [330]1/2 $\rightarrow$ [440]1/2, possesses an extremely large octupole matrix element $O_{ph}^{(0,-)}$ (in absolute magnitude). This excitation mode corresponds to the collective $K = 0$ mode obtained in the mixed representation RPA calculation by Inakura et al.,[35] but its detailed microscopic structure was not clarified in that previous work.

In Fig. 4, the quantities f_{ph}, g_{ph}, $O_{ph}^{(0,-)}$, $O_{ph}^{(1,-)}$, $M_{ph}^{(0,-)}$, and $M_{ph}^{(1,-)}$ are displayed for the sixth excitation mode (dash-dotted line in Fig. 2) with $(\wp, \alpha) = (-1, -1)$ at

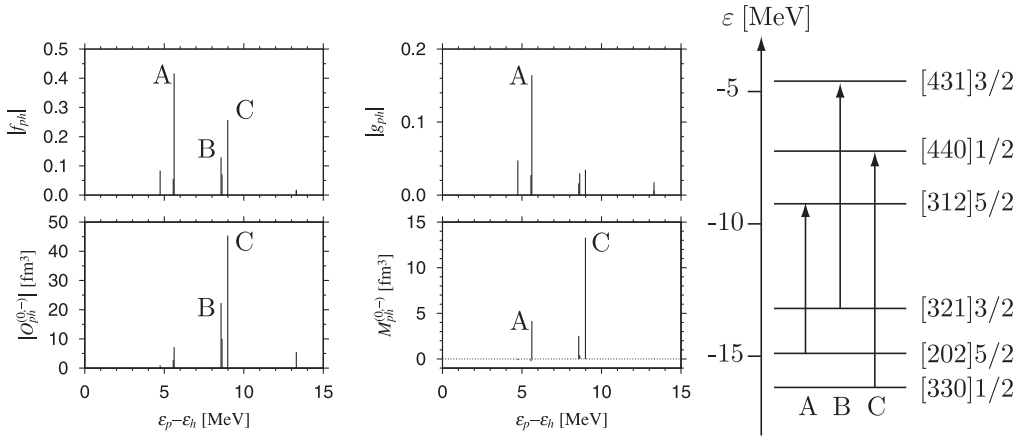

Fig. 3. Microscopic structure of the fourth excitation mode with $(\wp, \alpha) = (-1, -1)$ at $\omega_{\rm rot} = 0$. The RPA forward and backward amplitudes, f_{ph} and g_{ph}, are shown in the upper-left and upper-middle panels, respectively, while the unperturbed particle-hole matrix elements of the octupole operator with $K = 0$ and $\alpha = -1$, $O_{ph}^{(0,-)}$ and individual contributions to the RPA octupole transition amplitude, $M_{ph}^{(0,-)}$, are displayed in the lower-left and lower-middle panels, respectively, at positions of the abscissa axis representing unperturbed excitation energies, $\varepsilon_p - \varepsilon_h$, of individual particle-hole configurations. Labels A, B, and C indicate some important particle-hole configurations illustrated on the right-hand side. Here, the asymptotic quantum numbers $[N_{\rm osc}, n_z, \Lambda]\Omega$ are used to label the single-particle levels for convenience. Note that absolute values are shown except for $M_{ph}^{(0,-)}$. Note also that different scales are used for f_{ph} and g_{ph}.

$\omega_{\rm rot} = 0.4$ MeV/$\hbar$. It is clearly seen that the particle-hole excitation D_1, [321]3/2 $(\alpha = -i) \rightarrow$ [440]1/2 $(\alpha = +i)$, is mainly responsible for the large $K = 1$ octupole strength S_{31-} of this mode. This indicates that the sixth excitation mode at $\omega_{\rm rot} = 0.4$ MeV/$\hbar$ inherits the major component of the seventh excitation mode at $\omega_{\rm rot} = 0$. At the same time, it is seen that this same configuration carries also the $K = 0$ strength indicating that the Coriolis K-mixing effect is important already at this rotational frequency.

The same quantities are shown in Fig. 5 for the third excitation mode (dotted line in Fig. 2) with $(\wp, \alpha) = (-1, -1)$ at $\omega_{\rm rot} = 0.8$ MeV/$\hbar$. It is clearly seen that this mode takes over the main characteristics of the sixth excitation mode discussed above at $\omega_{\rm rot} = 0.4$ MeV/$\hbar$. A remarkable new feature realized at this value of $\omega_{\rm rot}$ is a beautiful coherence over many particle-hole configurations. The coherence takes place among almost all $K = 0$ and $K = 1$ transition amplitudes associated with individual particle-hole excitations. Namely, almost all individual contributions, $M_{ph}^{(0,-)}$ and $M_{ph}^{(1,-)}$, exhibited in the bottom panels of this figure take the same sign. This result suggests an interesting possibility that the rotation-aligned high-j particle and the octupole vibrations collaborate to produce a new type of correlation at high angular momentum. It would be interesting to examine this conjecture in a more systematic calculation in the future.

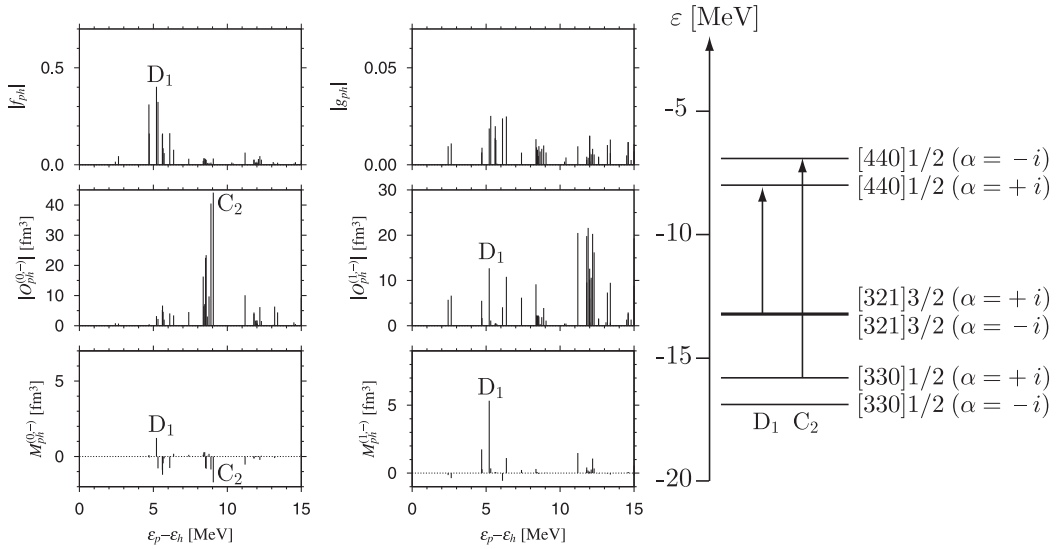

Fig. 4. Microscopic structure of the sixth excitation mode with $(\wp, \alpha) = (-1, -1)$ at $\omega_{\rm rot} = 0.4$ MeV/$\hbar$. In the left part, the RPA forward amplitude f_{ph}, the unperturbed particle-hole matrix elements of the octupole operator with $(K, \alpha) = (0, -1)$, $O_{ph}^{(0,-)}$, and individual contributions to the RPA octupole transition amplitude, $M_{ph}^{(0,-)}$, are displayed in the top, middle, and bottom panels, respectively, at positions of the abscissa axis representing unperturbed excitation energies, $\varepsilon_p - \varepsilon_h$, of individual particle-hole configurations. In the middle part, the RPA backward amplitudes g_{ph}, the matrix elements $O_{ph}^{(1,-)}$, and $M_{ph}^{(1,-)}$ for $(K, \alpha) = (1, -1)$ are shown in a similar fashion. Labels C_2 and D_1 indicate important particle-hole configurations illustrated on the right-hand side. Here, the asymptotic quantum numbers $[N_{\rm osc}, n_z, \Lambda]\Omega$ are used to label the single-particle levels for convenience. Note that signature partners with $\alpha = \pm i$ (degenerated at $\omega_{\rm rot} = 0$) are split at finite $\omega_{\rm rot}$ (signature splitting). Since the signature splitting of the [321]3/2 level is small, it is hard to see but the configuration D_1 involves a hole in the $\alpha = -i$ level. Note also that absolute values are shown except for $M_{ph}^{(K,-)}$ and different scales are used for f_{ph} and g_{ph}.

At $\omega_{\rm rot} = 1.2$ MeV/$\hbar$, as exhibited in Fig. 6, the first excitation mode (solid line in Fig. 2) takes over the major characteristics of the third excitation mode discussed above at $\omega_{\rm rot} = 0.8$ MeV/$\hbar$. We again see the beautiful coherence among many particle-hole configurations indicating the collective character of this mode. Recall that the collectivity of the first excitation mode at $\omega_{\rm rot} = 0$ is much weaker. Namely, the microscopic structure and properties of the first excitation mode are essentially changed in this region of rotational frequency owing to the avoided crossing. Note that, as seen in Fig. 1, the down-sloping [440]1/2 ($\alpha = +i$) level strongly interacts with the [200]1/2 ($\alpha = +i$) level just above the Fermi surface so that the two single-particle wave functions are strongly mixed with each other in this region of rotational frequency. Accordingly, the particle state in the configuration labelled E_1 contains an appreciable fraction of the [440]1/2 ($\alpha = +i$) wave function. As seen in Fig. 2, the $K = 0$ octupole transition strength S_{30-} of the first excitation mode gradually increases when $\omega_{\rm rot}$ exceeds 1.0 MeV/$\hbar$, and this mode acquires a sizable fraction of the $K = 0$ strength, which originally resides in the fourth excitation mode at

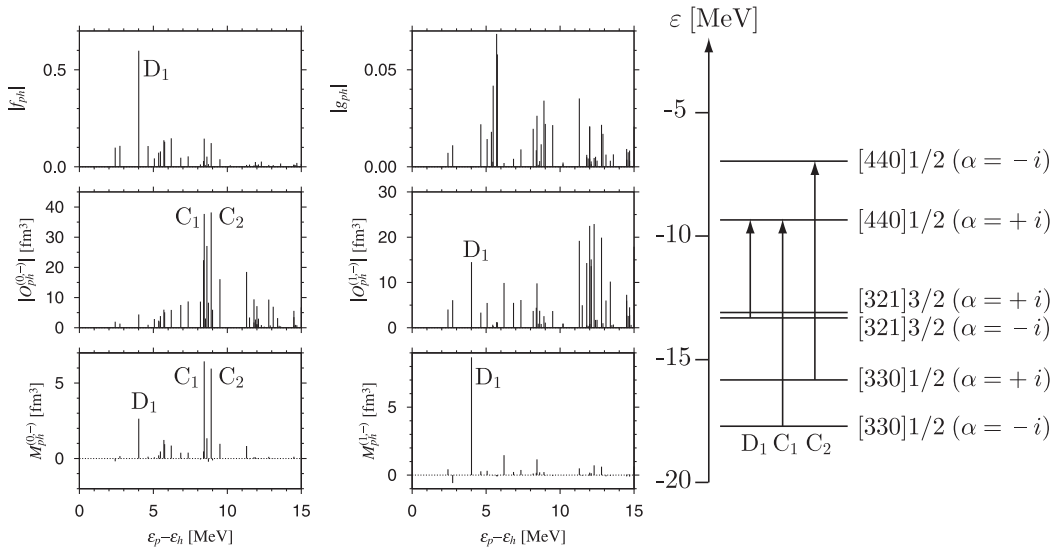

Fig. 5. Same as Fig. 4 but for the third excitation mode with $(\wp, \alpha) = (-1, -1)$ at $\omega_{\rm rot} = 0.8$ MeV/$\hbar$. Labels C_1, C_2, and D_1 indicate some important particle-hole configurations illustrated on the right-hand side.

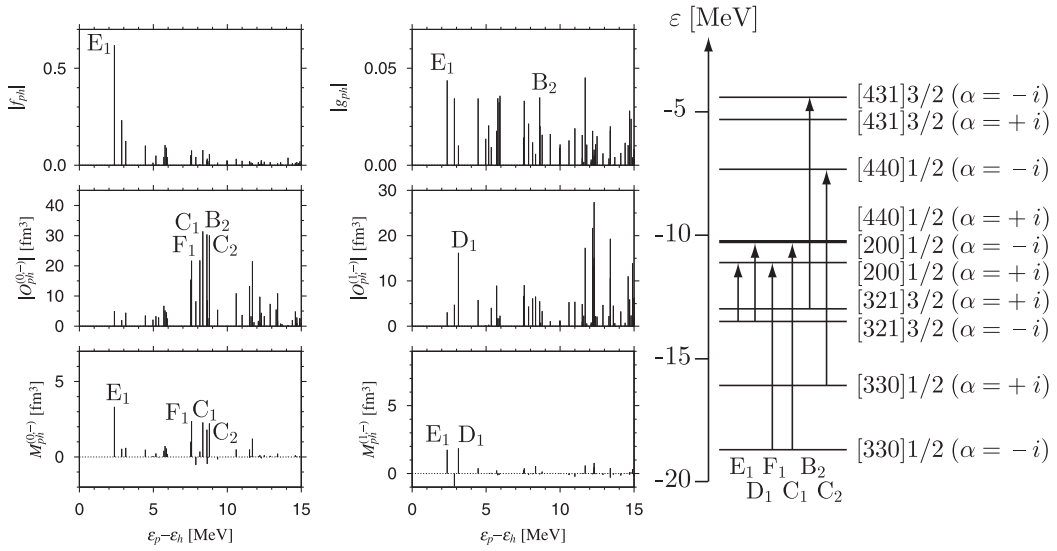

Fig. 6. Same as Fig. 4 but for the first excitation mode with $(\wp, \alpha) = (-1, -1)$ at $\omega_{\rm rot} = 1.2$ MeV/$\hbar$. Labels B_2, C_1, C_2, D_1, E_1, and F_1 indicate some important particle-hole configurations illustrated on the right-hand side. The C_1 and D_1 configurations both involve a particle in the single-particle level labelled [440]1/2 ($\alpha = +i$).

$\omega_{\rm rot} = 0$.

It is quite interesting to ask what will happen if the rotational frequency is increased further. Unfortunately, we encountered a difficulty in our RPA calculation when the RPA vibrational frequency becomes very small. In such a situation, aside

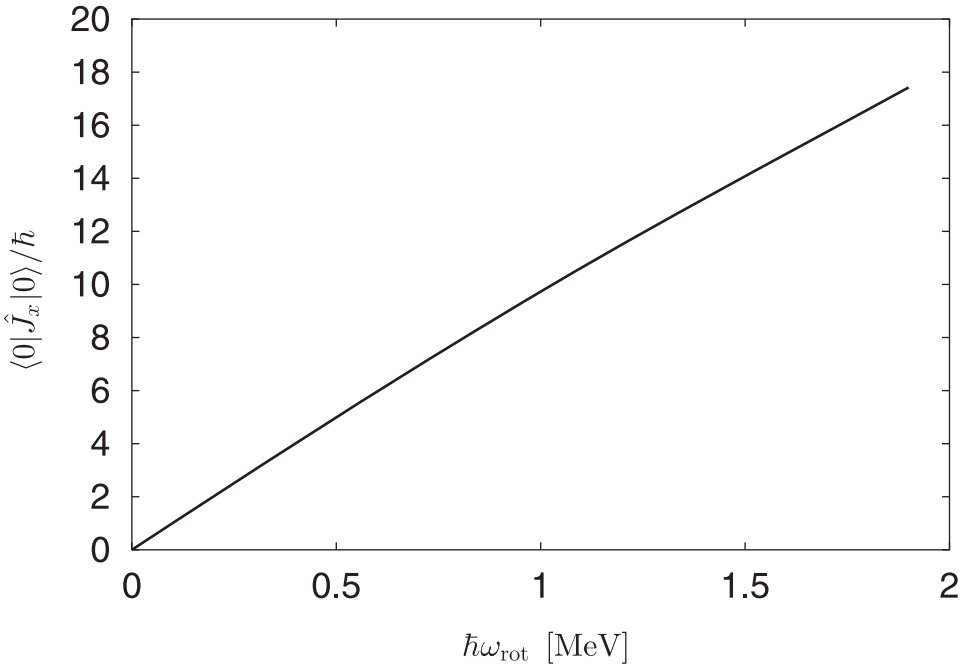

Fig. 7. Expectation value of the angular momentum with respect to the SD yrast states, $\langle 0|\hat{J}_x|0\rangle$, in ^{40}Ca plotted as a function of rotational frequency $\omega_{\rm rot}$. An instability of the axially symmetric SD shape with respect to the octupole vibrational mode is expected to occur beyond $\hbar\omega_{\rm rot} \simeq$ 1.7 MeV, which corresponds to angular momentum approximately $16\hbar$.

from the well-known limitation of the RPA, our recipe (described in §2.3) of approximately eliminating the spurious center of mass mode gradually loses its accuracy and we finally failed to obtain a reliable numerical result for $\omega_{\rm rot} \geq 1.6$ MeV/$\hbar$. A better method of eliminating the spurious components is badly needed, but this task is deferred to a future work. Nevertheless, it seems reasonable to assume that the trend discussed above, which is induced by the rotation-aligned particle (originating from the $g_{9/2}$ shell), will continue. Namely, the energy of the first excitation mode will further decrease and cross the yrast line. This may indicate the occurrence of an instability of the SD shape against the octupole vibration. Then, we would expect that a major structure change of the SD yrast states, like the breaking of reflection symmetry of the mean field, may take place. As shown in Fig. 7, this region of rotational frequency corresponds to angular momentum slightly higher than the maximum value $16\hbar$ so far observed in experiments.[28),29)] The suggested value of the critical angular momentum is a little lower than $24\hbar$ obtained in the symmetry-unrestricted cranked SHF calculation by Inakura et al.[40)] In that work, the nature of the instability occurring at this angular momentum was not clarified.

§4. Concluding remarks

By means of the RPA calculation based on the cranked deformed Woods-Saxon potential, we have investigated how rotational motion affects the properties of octupole vibrations built on SD states in ^{40}Ca. A major structure change of the

SD yrast states toward a reflection-asymmetric shape is suggested to take place in the region of angular momentum a little higher than the observed maximum value $16\hbar$, owing to a cooperative effect of octupole vibrational correlation and the rotation-aligned particle-hole excitations from the $f_{7/2}$ to the $g_{9/2}$ shell.

Acknowledgements

We thank T. Inakura for providing us with the result of their SHF and RPA calculation to compare with our calculation result. One of the authors (H. O.) is supported by the Grant-in-Aid for the Global COE Program "The Next Generation of Physics, Spun from Universality and Emergence" from the Ministry of Education, Culture, Sports, Science and Technology (MEXT) of Japan. Another author (K. Y.) is supported by the Special Postdoctoral Researcher Program of RIKEN. The numerical calculations were carried out on supercomputers, NEC SX8 at the Yukawa Institute for Theoretical Physics in Kyoto University and NEC SX8R at the Research Center for Nuclear Physics in Osaka University.

Appendix A

— *Derivation of Eqs. (2·11)–(2·13)* —

Equation (2·11) is derived through the following steps:

$$\varphi_k(-x,y,z) = \mathcal{P}e^{i\pi\ell_x/\hbar}\varphi_k(x,y,z) \tag{A·1}$$

$$= e^{-i\frac{\pi}{2}\sigma_x}\mathcal{P}\mathcal{R}_x\varphi_k(x,y,z) \tag{A·2}$$

$$= -i\alpha_k\wp_k\sigma_x\varphi_k(x,y,z). \tag{A·3}$$

To derive Eq. (2·13), we note that the eigenvalue equations (2·8)–(2·10) are invariant against the transformation $\mathcal{I} = \mathcal{K}\mathcal{P}e^{i\pi\ell_z/\hbar}$, where $\mathcal{K}$ denotes complex conjugation. The eigenvalues for the transformation $\mathcal{I}$ can take ± 1. We then notice that

$$\mathcal{I}\varphi_k(x,y,z) = \varphi_k(x,y,z) \tag{A·4}$$

and

$$\mathcal{I}\{i\varphi_k(x,y,z)\} = -\{i\varphi_k(x,y,z)\} \tag{A·5}$$

are equivalent. Therefore, we can choose the eigenvalue $+1$ without loss of generality. It is easily seen that the left-hand side of Eq. (A·4) is equal to $\varphi_k^*(x,y,-z)$. Thus, Eq. (2·13) follows.

Equation (2·12) is derived in a similar manner:

$$\varphi_k(x,-y,z) = \mathcal{P}e^{i\pi\ell_z/\hbar}e^{i\pi\ell_x/\hbar}\varphi_k(x,y,z) \tag{A·6}$$

$$= e^{-i\frac{\pi}{2}\sigma_x}\mathcal{K}\mathcal{I}\mathcal{R}_x\varphi_k(x,y,z) \tag{A·7}$$

$$= -i\alpha_k\sigma_x\varphi_k^*(x,y,z). \tag{A·8}$$

The above derivations are essentially the same, albeit slightly more detailed, as in Refs. 32) and 33).

References

1) P. A. Butler and W. Nazarewicz, Rev. Mod. Phys. **68** (1996), 349.
2) S. Frauendorf, Rev. Mod. Phys. **73** (2001), 463.
3) W. Satuła and R. A. Wyss, Rep. Prog. Phys. **68** (2005), 131.
4) K. Neergård and P. Vogel, Nucl. Phys. A **145** (1970), 33; Nucl. Phys. A **149** (1970), 209; Nucl. Phys. A **149** (1970), 217.
5) A. Bohr and B. R. Mottelson, *Nuclear Structure*, Vol. II (W. A. Benjamin Inc., 1975; World Scientific, 1998).
6) P. Vogel, Phys. Lett. B **60** (1976), 431.
7) R. Bengtsson and S. Frauendorf, Nucl. Phys. A **314** (1979), 27; Nucl. Phys. A **327** (1979), 139.
8) E. R. Marshalek, Nucl. Phys. A **266** (1976), 317; Nucl. Phys. A **331** (1979), 429.
9) D. Janssen and I. N. Mikhailov, Nucl. Phys. A **318** (1979), 390.
10) J. L. Egido, H. J. Mang and P. Ring, Nucl. Phys. A **341** (1980), 229; Nucl. Phys. A **339** (1980), 390.
11) V. G. Zelevinsky, Nucl. Phys. A **344** (1980), 109.
12) Y. R. Shimizu and K. Matsuyanagi, Prog. Theor. Phys. **70** (1983), 144; Prog. Theor. Phys. **72** (1984), 799.
13) L. M. Robledo, J. L. Egido and P. Ring, Nucl. Phys. A **449** (1986), 201.
14) R. G. Nazmitdinov, I. N. Mikhailov and Ch. Briancon, Phys. Lett. B **188** (1987), 171.
15) R. G. Nazmitdinov, Sov. J. Nucl. Phys. **46** (1987), 412.
16) P. J. Nolan and P. J. Twin, Annu. Rev. Nucl. Part. Sci. **38** (1988), 533.
17) S. Åberg, H. Flocard and W. Nazarewicz, Annu. Rev. Nucl. Part. Sci. **40** (1990), 439.
18) R. V. F. Janssens and T. L. Khoo, Annu. Rev. Nucl. Part. Sci. **41** (1991), 321.
19) C. Baktash, B. Haas and W. Nazaerewicz, Annu. Rev. Nucl. Part. Sci. **45** (1995), 485.
20) C. Baktash, Prog. Part. Nucl. Phys. **38** (1997), 291.
21) S. Mizutori, Y. R. Shimizu and K. Matsuyanagi, Prog. Theor. Phys. **85** (1991), 559; Prog. Theor. Phys. **86** (1991), 131.
22) S. Mizutori, T. Nakatsukasa, K. Arita, Y. R. Shimizu and K. Matsuyanagi, Nucl. Phys. A **557** (1993), 125.
23) T. Nakatsukasa, K. Matsuyanagi, S. Mizutori and W. Nazarewicz, Phys. Lett. B **343** (1995), 19.
24) T. Nakatsukasa, K. Matsuyanagi, S. Mizutori and Y. R. Shimizu, Phys. Rev. C **53** (1996), 2213.
25) A. Korichi et al., Phys. Rev. Lett. **86** (2001), 2746.
26) D. Rossbach et al., Phys. Lett. B **513** (2001), 9.
27) T. Lauritsen et al., Phys. Rev. Lett. **89** (2002), 282501.
28) E. Ideguchi et al., Phys. Rev. Lett. **87** (2001), 222501.
29) C. J. Chiara et al., Phys. Rev. C **67** (2003), 041303.
30) K. Yoshida, M. Yamagami and K. Matsuyanagi, Prog. Theor. Phys. **113** (2005), 1251.
31) A. Bohr and B. R. Motteleson, *Nuclear Structure*, Vol. I (W. A. Benjamin Inc., 1969; World Scientific, 1998).
32) P. Bonche, H. Focard, P. H. Heenen, S. J. Kriger and M. S. Weiss, Nucl. Phys. A **443** (1985), 39.
33) P. Bonche, H. Focard and P. H. Heenen, Nucl. Phys. A **467** (1987), 115.
34) M. Bender, P.-H. Heenen and P.-G. Reinhard, Rev. Mod. Phys. **75** (2003), 121.
35) T. Inakura, H. Imagawa, Y. Hashimoto, S. Mizutori, M. Yamagami and K. Matsuyanagi, Nucl. Phys. A **768** (2006), 61.
36) S. Shlomo and G. F. Bertsch, Nucl. Phys. A **243** (1975), 507.
37) P. Ring and P. Schuck, *The Nuclear Many-Body Problem* (Springer, 1980).
38) S. Cwiok, J. Kvasil and B. Choriev, J. of Phys. G **10** (1984), 903.
39) G. Colò, N. Van Giai, P. F. Bortignon and M. R. Quaglia, Phys. Lett. B **485** (2000), 362.
40) T. Inakura, S. Mizutori, M. Yamagami and K. Matsuyanagi, Nucl. Phys. A **710** (2002), 261.

Microscopic description of oblate-prolate shape mixing in proton-rich Se isotopes

Nobuo Hinohara,[1,*] Takashi Nakatsukasa,[2] Masayuki Matsuo,[3] and Kenichi Matsuyanagi[1,2]
[1]*Yukawa Institute for Theoretical Physics, Kyoto University, Kyoto 606-8502, Japan*
[2]*Theoretical Nuclear Physics Laboratory, RIKEN Nishina Center, Wako 351-0198, Japan*
[3]*Department of Physics, Faculty of Science, Niigata University, Niigata 950-2181, Japan*
(Received 18 February 2009; published 7 July 2009)

The oblate-prolate shape coexisting/mixing phenomena in proton-rich ^{68,70,72}Se are investigated by means of the adiabatic self-consistent collective coordinate (ASCC) method. The one-dimensional collective path and the collective Hamiltonian describing the large-amplitude shape vibration are derived in a fully microscopic way. The excitation spectra, $B(E2)$ and spectroscopic quadrupole moments are calculated by requantizing the collective Hamiltonian and solving the collective Schrödinger equation. The basic properties of the coexisting two rotational bands in low-lying states of these nuclei are well reproduced. It is found that the oblate-prolate shape mixing becomes weak as the rotational angular momentum increases. We point out that the rotational energy plays a crucial role in causing the localization of the collective wave function in the (β, γ) deformation space.

DOI: 10.1103/PhysRevC.80.014305 PACS number(s): 21.60.Ev, 21.10.Re, 27.50.+e

I. INTRODUCTION

Atomic nuclei exhibit various intrinsic shapes in their ground and excited states. Coexistence of different shapes in one nucleus is widely observed all over the nuclear chart [1]. Among varieties of such phenomena, much attention has been paid on proton-rich $N = Z$ nuclei in the $A \sim 70$ region where very rich shape coexistence phenomena are seen. In this region, dramatic competition of different shapes occurs due to shell-structure effects: the oblately deformed shell gaps at N or $Z = 34$ and 36, the prolately deformed shell gaps at 34 and 38, and the spherical shell gap at 40 [2].

The $N = Z$ nucleus ^{68}Se is a particularly interesting nucleus, because it has deformed shell gaps both at the oblate and prolate shapes. For this nucleus, mean-field calculations predict the oblate-prolate shape coexistence [3–5]. In experiment, two rotational bands were observed in low-energy excitations, and the ground and excited bands were interpreted to have the oblate and prolate deformations, respectively [6,7]. For ^{70}Se and ^{72}Se, $B(E2)$ values for the 2_1^+, 4_1^+, 6_1^+ states in the ground bands were obtained by a recent lifetime measurement [8]. These data indicate gradual change of their characters from oblate to prolate with increasing angular momentum; it occurs in lower angular momentum in ^{72}Se compared to ^{70}Se. The data also suggest considerable mixing of the oblate and prolate shapes in these low-lying states. We also note that candidates for the excited 0_2^+ states have been known for a long time at 2011 keV in ^{70}Se [9] and at 937 keV in ^{72}Se [10].

Because shape mixing is caused by large-amplitude collective motion connecting different shapes, its theoretical description is beyond the static mean-field approximation or the small-amplitude fluctuation about equilibrium shapes. A difficulty in theoretical description of the shape coexisting/mixing phenomena is that various kinds of microscopic configurations associated with different shapes participate in them and thus quite a large number of particle-hole degrees of freedom are involved in the large-amplitude collective dynamics. Therefore, microscopic description of shape mixing is a challenging subject in nuclear structure theory.

Theoretical investigations on the shape coexisting/mixing phenomena may be divided into two categories: i.e., time-independent and time-dependent approaches. For the former, we can refer, e.g., the projected shell model [11], the large-scale shell model [12,13], the interacting boson model [14] calculations for ^{68}Se, and the excited-vampir variational calculation for ^{68,70}Se [15,16]. For neighboring isotopes $^{72-78}$Kr, a detailed study based on the number and angular-momentum-projected generator-coordinate method was recently reported [17].

A well-known approach belonging to the latter is the adiabatic time-dependent Hartree-Fock-Bogoliubov (ATDHFB) theory started in late 1970s for the description of slow collective motions like low-frequency quadrupole vibrations and fissions, which exhibit strong nonlinearity [18]. Various versions of the ATDHFB theory have been proposed, e.g., by Baranger-Véneroni [19], Villars [20], and Goeke-Reinhard [21]. However, the ATDHFB approaches encountered some difficulties, e.g., in uniquely determining the collective path (see Ref. [22] for a review), so application of the theory without introducing some additional approximations to the real nuclear structure has not yet been attained.

Still, the challenge to develop a workable microscopic method of describing large-amplitude collective motions based on the ATDHF theory has been pursued. Libert *et al.* [23] developed a practical approach assuming the quadruple operators as collective coordinates and using the cranking mass. Quite recently, this approach was used in the discussion on low-lying states of ^{68,70,72}Se [8]. Using the generalized valley equation and the local random-phase approximation (RPA) equation, which are based on the ATDHFB theory, the shape mixing in ^{68}Se was studied by Almehed and Walet [24,25]. It is not clear, however, how the number-fluctuation degrees of freedom are decoupled from the large-amplitude shape vibrations in their work.

*Present address: Theoretical Nuclear Physics Laboratory, RIKEN Nishina Center, Wako 351-0198, Japan.

On the basis of the time-dependent Hartree-Fock-Bogoliubov (TDHFB) theory, the self-consistent collective coordinate (SCC) method was proposed to describe the large-amplitude collective motions in superconducting nuclei [26,27]. A new scheme of solving the SCC equations using an expansion in terms of the collective momentum, called the adiabatic SCC (ASCC) method, was formulated for describing shape coexistence dynamics in superconducting nuclei [28,29]. It was firstly applied to the solvable multi-$O(4)$ model to demonstrate that it provides an efficient scheme to determine the collective path [30].

In the previous series of our works, the ASCC method was applied to the oblate-prolate shape coexisting/mixing phenomena in ^{68}Se and ^{72}Kr, and the one-dimensional collective path was successfully determined [31,32]. It was shown that the triaxial deformation plays a crucial role in the shape mixing dynamics of these nuclei. Furthermore, we constructed a four-dimensional collective Hamiltonian that can describe the coupled motion of one-dimensional collective vibration and the three-dimensional rotational motion of a triaxial shape. By requantizing the collective Hamiltonian, excitation spectra and quadrupole transition properties were evaluated [33].

The advantage of using the ASCC method for the description of shape coexistence dynamics is that a few collective degrees of freedom relevant to the collective motion of interest can be extracted self-consistently from the TDHFB phase space. Because the collective dynamics is described in terms of single or a few collective variables, it yields a clear physical interpretation of the collective dynamics. From the collective path determined by the ASCC method, the direction of the collective motion can be visualized by projecting the collective path onto the (β, γ) quadrupole deformation plane. It is also easy to evaluate the collective inertial functions (collective mass) with respect to the (β, γ) deformation coordinates. The obtained collective mass includes both contributions from the time-even and time-odd components of the moving mean field [18]. The time-odd contribution from the moving mean field is ignored in the Inglis-Belyaev cranking formula for the collective mass, which is widely used for the description of large-amplitude collective motions. In the previous article [34], we have shown that the quadrupole pairing interaction enhances the collective mass through the time-odd component of the moving mean field.

The major purpose of this article is to give a microscopic description, on the basis of the ASCC method, of the oblate-prolate shape mixing dynamics in proton-rich Se isotopes. We show that the deformation degree of freedom breaking axial symmetry plays a crucial role in the shape mixing. Taking into account the coupling of the large-amplitude shape vibrations connecting the oblate and prolate shapes and three-dimensional rotations of the triaxial shape, we show that the shape mixing gradually becomes weak as the rotational angular momentum increases. Dynamical reason of this trend will be clarified.

This article is organized as follows. In Sec. II, the basic equations of the ASCC method are summarized. In Sec. III, the theoretical scheme of deriving the quantum collective Hamiltonian and solving the collective Schrödinger equation is described. In Sec. IV, results of the calculation for proton-rich ^{68,70,72}Se isotopes are presented and discussed. Conclusions are given in Sec. V.

II. THE ASCC METHOD

In this section the basic equations of the ASCC method are summarized. Details of their derivations are given in Ref. [28].

The starting point is the time-dependent variational principle for a TDHFB Slater determinant representing the collective state $|\phi(t)\rangle$

$$\delta \langle \phi(t)| \, i\frac{\partial}{\partial t} - \hat{H} \, |\phi(t)\rangle = 0, \tag{1}$$

where $\hat{H}$ denotes the microscopic Hamiltonian. In the SCC method, it is assumed that the collective motion could be described by a few canonical sets of collective variables. In the present application to the shape coexistence phenomena, we assume that the shape dynamics can be described by a single collective coordinate q and its canonically conjugate momentum p. Because the system is superconducting, we also introduce the gauge angles $\boldsymbol{\varphi} = [\varphi^{(n)}, \varphi^{(p)}]$ conjugate to the number variables $\boldsymbol{n} = [n^{(n)}, n^{(p)}]$ of neutrons and protons. Thus the TDHFB state $|\phi(t)\rangle$ is written in terms of these collective variables as follows.

$$|\phi(t)\rangle = |\phi(q, p, \boldsymbol{\varphi}, \boldsymbol{n})\rangle = e^{-i\sum_\tau \varphi^{(\tau)}\tilde{N}^{(\tau)}} |\phi(q, p, \boldsymbol{n})\rangle, \tag{2}$$

where τ denotes n or p. Note that the number operators $\tilde{N}^{(\tau)}$ and the number variables $n^{(\tau)}$ are measured from the expectation values $N_0^{(\tau)}$ with respect to the moving-frame HFB state $|\phi(q)\rangle$, i.e., $\tilde{N}^{(\tau)} \equiv \hat{N}^{(\tau)} - N_0^{(\tau)}$ and $n^{(\tau)} \equiv N^{(\tau)} - N_0^{(\tau)}$.

Using the generalized Thouless theorem, the intrinsic state for the pairing rotation, $|\phi(q, p, \boldsymbol{n})\rangle$, can be written in terms of the moving-frame HFB state $|\phi(q)\rangle$ as

$$|\phi(q, p, \boldsymbol{n})\rangle = e^{i\hat{G}(q,p,\boldsymbol{n})} \, |\phi(q)\rangle, \tag{3}$$

where $\hat{G}(q, p, \boldsymbol{n})$ is a one-body operator. Note that this state reduces to $|\phi(q)\rangle$ for $p = 0$ and $\boldsymbol{n} = \boldsymbol{0}$; namely $|\phi(q, p = 0, \boldsymbol{n} = \boldsymbol{0})\rangle = |\phi(q)\rangle$. Assuming the adiabaticity of the large-amplitude collective motion, the operator $\hat{G}(q, p, \boldsymbol{n})$ is expanded up to first order with respect to p and $n^{(\tau)}$,

$$\hat{G}(q, p, \boldsymbol{n}) = p\hat{Q}(q) + \sum_\tau n^{(\tau)}\hat{\Theta}^{(\tau)}(q), \tag{4}$$

$$\begin{aligned}\hat{Q}(q) &= \hat{Q}^A(q) + \hat{Q}^B(q) \\ &= \sum_{\alpha\beta}\left[Q^A_{\alpha\beta}(q)a^\dagger_\alpha a^\dagger_\beta + Q^{A*}_{\alpha\beta}(q)a_\beta a_\alpha \right. \\ &\quad \left. + Q^B_{\alpha\beta}(q)a^\dagger_\alpha a_\beta\right],\end{aligned} \tag{5}$$

$$\hat{\Theta}^{(\tau)}(q) = \sum_{\alpha\beta}\left[\Theta^{(\tau)A}_{\alpha\beta}(q)a^\dagger_\alpha a^\dagger_\beta + \Theta^{(\tau)A*}_{\alpha\beta}(q)a_\beta a_\alpha\right], \tag{6}$$

where the quasiparticle creation and annihilation operators, $a^\dagger_\alpha$ and a_α, are defined with respect to the moving-frame HFB state $|\phi(q)\rangle$ that satisfies the vacuum conditions $a_\alpha \, |\phi(q)\rangle = 0$ for them. Therefore these quasiparticle operators are also functions of the collective coordinate q. Note that the operator $\hat{Q}(q)$ contains, in addition to the A part [the first and the second terms of Eq. (5)], the B part (the third term) to satisfy the

gauge invariance of the ASCC equations. They are uniquely determined by imposing the condition $[\tilde{N}^{(\tau)}, \hat{Q}(q)] = 0$ [29].

The collective Hamiltonian is given by

$$\mathcal{H}(q, p, \boldsymbol{n}, \vec{I}) = \langle \phi(q, p, \boldsymbol{n})| \hat{H} |\phi(q, p, \boldsymbol{n})\rangle + \sum_{i=1}^{3} \frac{1}{2\mathcal{J}_i(q)} I_i^2$$
$$= V(q) + \frac{1}{2}B(q)p^2 + \sum_{\tau} \lambda^{(\tau)}(q) n^{(\tau)}$$
$$+ \sum_{i=1}^{3} \frac{1}{2\mathcal{J}_i(q)} I_i^2, \tag{7}$$

where

$$V(q) = \mathcal{H}(q, p, \boldsymbol{n}, \vec{I})|_{p=0, \boldsymbol{n}=\boldsymbol{0}, \vec{I}=\vec{0}}, \tag{8}$$

$$B(q) = \left. \frac{\partial^2 \mathcal{H}}{\partial p^2} \right|_{p=0, \boldsymbol{n}=\boldsymbol{0}, \vec{I}=\vec{0}}, \tag{9}$$

$$\lambda^{(\tau)}(q) = \left. \frac{\partial \mathcal{H}}{\partial n^{(\tau)}} \right|_{p=0, \boldsymbol{n}=\boldsymbol{0}, \vec{I}=\vec{0}}, \tag{10}$$

are the collective potential, inverse of the collective inertial function, and the chemical potentials. The rotational energy term is introduced to treat the large-amplitude shape vibration and the three-dimensional rotation of triaxially deformed mean field in a unified manner.

The moving-frame HFB equations

$$\delta \langle \phi(q)| \hat{H}_M(q) |\phi(q)\rangle = 0, \tag{11}$$

and the moving-frame QRPA equations

$$\delta \langle \phi(q)| [\hat{H}_M(q), \hat{Q}(q)] - \frac{1}{i} B(q) \hat{P}(q) |\phi(q)\rangle = 0, \tag{12}$$

$$\delta \langle \phi(q)| \left[\hat{H}_M(q), \frac{1}{i} \hat{P}(q) \right] - C(q) \hat{Q}(q)$$
$$- \frac{1}{2B(q)} \left[\left[\hat{H}_M(q), \frac{\partial V}{\partial q} \hat{Q}(q) \right], \hat{Q}(q) \right]$$
$$- \sum_{\tau} \frac{\partial \lambda^{(\tau)}}{\partial q} \tilde{N}^{(\tau)} |\phi(q)\rangle = 0, \tag{13}$$

are the basic equations that determine the collective path in the TDHFB phase space. They are derived by expanding the TDHFB equation of motion (1) up to second order with respect to p. Here $\hat{H}_M(q)$ denotes the moving-frame Hamiltonian

$$\hat{H}_M(q) = \hat{H} - \sum_{\tau} \lambda^{(\tau)}(q) \tilde{N}^{(\tau)} - \frac{\partial V}{\partial q} \hat{Q}(q). \tag{14}$$

The operator $\hat{P}(q)$ is defined by

$$\hat{P}(q) |\phi(q)\rangle = i \frac{\partial}{\partial q} |\phi(q)\rangle . \tag{15}$$

The stiffness parameter $C(q)$ is given by

$$C(q) = \frac{\partial^2 V}{\partial q^2} + \frac{1}{2B(q)} \frac{\partial B}{\partial q} \frac{\partial V}{\partial q}, \tag{16}$$

and connected to the moving-frame QRPA frequency as $\omega^2(q) = B(q)C(q)$.

The basic equations of the ASCC method are scale invariant, in other words, the arbitrary scale for the collective coordinate can be chosen [28]. We fix the scale by the condition $B(q) = 1$. Note also that the method is formulated in a gauge-invariant way; that is, the basic equations are invariant under the following transformations [29].

$$\hat{Q}(q) \to \hat{Q}(q) + \alpha^{(\tau)} \tilde{N}^{(\tau)}, \tag{17}$$

$$\lambda^{(\tau)}(q) \to \lambda^{(\tau)}(q) - \alpha^{(\tau)} \frac{\partial V}{\partial q}(q), \tag{18}$$

$$\frac{\partial \lambda^{(\tau)}}{\partial q}(q) \to \frac{\partial \lambda^{(\tau)}}{\partial q}(q) - \alpha^{(\tau)} C(q). \tag{19}$$

Therefore, it is necessary to fix the gauge when we solve the ASCC equations. We adopt the same gauge fixing condition as in Ref. [29], which is convenient to describing shape coexisting/mixing phenomena.

In the following, we summarize the procedure of solving the ASCC equations starting from one of the solutions of the static HFB equations, which corresponds to a local minimum of the collective potential. The lowest frequency QRPA eigenmode at the starting HFB state $|\phi(q = 0)\rangle$ determines the operators $\hat{Q}(q = 0)$ and $\hat{P}(q = 0)$. We solve the moving-frame HFB equation (11) and the moving-frame QRPA equations, (12) and (13), off the equilibrium to obtain the solution at q. At nonequilibrium HFB states, these ASCC equations are coupled with each other, so that the self-consistency between the moving-frame HFB state $|\phi(q)\rangle$ and the moving-frame QRPA mode $\hat{Q}(q)$ is required. Let us assume that the solution of the ASCC equations at $q - \delta q$ is already known. We find the solution at q by starting from solving the moving-frame HFB equation with the initial guess for the collective coordinate operator $\hat{Q}(q)$

$$\hat{Q}(q)^{(0)} = (1 - \varepsilon)\hat{Q}_1(q - \delta q) + \varepsilon \hat{Q}_2(q - \delta q), \tag{20}$$

where ε is a small number that mixes the lowest and the second-lowest solutions of the moving-frame QRPA equations at $q - \delta q$. These two solutions usually possess different K-quantum numbers when the HFB mean field is axially symmetric. Therefore this choice for the initial guess is crucial to find a symmetry-breaking solution if the previous moving-frame QRPA mode $\hat{Q}_1(q - \delta q)$ possesses the axial symmetry [32]. In this article, we set $\varepsilon = 0.1$ in numerical calculation.

After constructing the collective path, we evaluate the three rotational moments of inertia $\mathcal{J}_i(q)$. For this purpose, we solve the following Thouless-Valatin equations at every point q on the collective path using the moving-frame HFB state $|\phi(q)\rangle$

$$\delta \langle \phi(q)| [\hat{H}_M(q), \hat{\Psi}_i(q)] - \frac{1}{i} \mathcal{J}_i^{-1}(q) \hat{I}_i |\phi(q)\rangle = 0, \tag{21}$$

$$\langle \phi(q)| [\Psi_i(q), \hat{I}_i] |\phi(q)\rangle = i. \tag{22}$$

In this way, we derive the collective Hamiltonian (7) from the microscopic Hamiltonian $\hat{H}$, which simultaneously describes the large-amplitude shape vibration and the three-dimensional rotation.

III. REQUANTIZATION OF THE COLLECTIVE HAMILTONIAN

Because the collective Hamiltonian (7) derived by the ASCC method is a classical one, it is necessary to requantize it to obtain collective wave functions describing shape mixing and discuss experimental observables such as excitation spectra and electromagnetic transition probabilities.

The total kinetic energy of the coupled motion of the one-dimensional large-amplitude shape vibration and the three-dimensional rotation is given by

$$T = \frac{1}{2}B^{-1}(q)\dot{q}^2 + \sum_{i=1}^{3}\frac{1}{2}\mathcal{J}_i(q)\omega_i^2 = \frac{1}{2}\sum_{m,n}G_{mn}(q)\dot{a}_m\dot{a}_n, \tag{23}$$

where ω_i are angular velocities, $\dot{\boldsymbol{a}} \equiv (\dot{q}, \omega_1, \omega_2, \omega_3)$, and the metric $G_{mn}(q) = \delta_{mn}[B^{-1}(q), \mathcal{J}_1(q), \mathcal{J}_2(q), \mathcal{J}_3(q)]$. The kinetic energy term is requantized by means of the Pauli prescription:

$$\begin{aligned}\hat{T} &= -\frac{1}{2}\sum_{mn}|G(q)|^{-\frac{1}{2}}\frac{\partial}{\partial a_m}|G(q)|^{\frac{1}{2}}[G^{-1}(q)]^{mn}\frac{\partial}{\partial a_n}\\ &= -\frac{1}{2}\frac{\partial}{\partial q}B(q)\frac{\partial}{\partial q} - \frac{1}{4}\frac{\partial|G|}{\partial q}\frac{B(q)}{|G(q)|}\frac{\partial}{\partial q} + \sum_{i=1}^{3}\frac{\hat{I}_i^2}{2\mathcal{J}_i(q)},\end{aligned} \tag{24}$$

where $|G(q)| = B^{-1}(q)\mathcal{J}_1(q)\mathcal{J}_2(q)\mathcal{J}_3(q)$ is the determinant of $G_{mn}(q)$. In this article, we take into account the second term containing the derivative of $|G(q)|$, which was ignored in our previous work [33]. Concerning the collective mass $B^{-1}(q)$, we can set it to unity without loss of generality, because it merely defines the scale for measuring the length of the collective path [28]. The three components $\hat{I}_i$ of the angular momentum operator are defined with respect to the principal axes $(1, 2, 3) \equiv (x', y', z')$ associated with the moving-frame HFB state $|\phi(q)\rangle$. Care is needed when the collective path partially runs with axially symmetric shape where the moment of inertia about the symmetry axis vanishes. We discuss this problem in subsection IV C with the concrete examples of the collective path for ^{70}Se and ^{72}Se.

The collective Schrödinger equation is thus given

$$[\hat{T} + V(q)]\Psi_{IMk}(q, \Omega) = E_{I,k}\Psi_{IMk}(q, \Omega), \tag{25}$$

where $\Psi_{IMk}(q, \Omega)$ represents the collective wave function in the laboratory frame. It is a function of the collective coordinate q and the three Euler angles Ω and specified by the total angular momentum I, its projection M on the laboratory z axis, and the index k distinguishing different quantum states having the same I and M.

Using the rotational wave functions $\mathcal{D}^I_{MK}(\Omega)$, the collective wave functions in the laboratory frame is written as

$$\Psi_{IMk}(q, \Omega) = \sum_{K=0}^{I}\Phi_{IKk}(q)\langle\Omega|IMK\rangle, \tag{26}$$

$$\langle\Omega|IMK\rangle = \sqrt{\frac{2I+1}{16\pi^2(1+\delta_{K0})}}\left[\mathcal{D}^I_{MK}(\Omega) + (-)^I\mathcal{D}^I_{M-K}(\Omega)\right], \tag{27}$$

where $\Phi_{IKk}(q)$ represents the large-amplitude vibrational motion, and the sum in Eq. (26) is restricted to even K. Needless to say, this is a particular form in the general framework of the Bohr and Mottelson [35].

Normalization of the vibrational part of the collective wave functions is given by

$$\int d\tau' \sum_{K=0}^{I}\Phi^*_{IKk}(q)\Phi_{IKk'}(q) = \delta_{kk'}, \tag{28}$$

where the volume element is

$$d\tau = d\tau' d\Omega = \sqrt{|G(q)|}dq d\Omega. \tag{29}$$

The boundary conditions for the collective Schrödinger equation (25) can be specified by projecting the collective path obtained by the ASCC method onto the (β, γ) plane and by using the well-known symmetry properties of the Bohr-Mottelson collective Hamiltonian [33,35,36].

IV. SHAPE MIXING IN PROTON-RICH Se ISOTOPES

A. Model Hamiltonian and parameters

For the microscopic Hamiltonian, we use a version of the pairing-plus-quadrupole (P+Q) force model [37,38] that includes the quadrupole-pairing in addition to the monopole-pairing interaction. Two major shells ($N_{\rm sh} = 3, 4$) are considered as the active model space for neutrons and protons. The single-particle energies are calculated using the modified oscillator potential [39]. As in Ref. [32], the monopole-pairing strength $G_0^{(\tau)}$ and the quadrupole-particle-hole interaction strength χ' for ^{68}Se are determined such that the magnitudes of quadrupole deformations and pairing gaps at the oblate and prolate local minima approximately reproduce those obtained in the Skyrme-HFB calculation by Yamagami *et al.* [4]. The interaction strengths for ^{70,72}Se are then determined from those of ^{68}Se, assuming a simple mass number dependence $G^{(\tau)} \sim A^{-1}$ and $\chi' \sim A^{-\frac{5}{3}}$ [38]. For the quadrupole-pairing interaction strengths $G_2^{(\tau)}$, the self-consistent values proposed by Sakamoto and Kishimoto [40] are evaluated from the monopole pairing interaction (see Ref. [33] for details). These values of the interaction strengths are listed in Table I.

Following the conventional treatment of the P+Q model, we ignore the Fock term, so that, in the following, we use the abbreviation HB (Hartree-Bogoliubov) in place of HFB.

TABLE I. Strengths of the monopole-pairing, the quadrupole particle-hole, and the quadrupole-pairing interactions adopted in the numerical calculation. The same monopole-pairing strength is used for neutrons and protons, i.e., we set $G_0 \equiv G_0^{(n)} = G_0^{(p)}$. For the quadrupole-pairing interactions, the strengths multiplied by the oscillator length biquadrate, $G_2'^{(\tau)} \equiv G_2^{(\tau)}b^4$, are shown.

	G_0 (MeV)	χ' (MeV)	$G_2'^{(n)}$ (MeV)	$G_2'^{(p)}$ (MeV)
^{68}Se	0.320	0.248	0.185	0.185
^{70}Se	0.311	0.236	0.174	0.184
^{72}Se	0.302	0.225	0.161	0.183

TABLE II. Calculated values for the quadrupole deformations (β, γ), the monopole pairing gaps for neutrons and protons $[\Delta_0^{(n)}, \Delta_0^{(p)}]$, the potential energy V measured from the lowest minimum of the HB equilibrium states, the frequencies $(\omega_\gamma, \omega_\beta)$ of the lowest two QRPA modes at the HB equilibrium states, the collective mass M for the lowest QRPA mode. The QRPA modes with $K = 0$ and $K = 2$ are denoted β and γ, respectively, where K is the symmetry axis component of the vibrational angular momentum. The rotational moments of inertia $\mathcal{J}$ about the axis perpendicular to the symmetry axis are also shown.

	β	γ	$\Delta_0^{(n)}$ (MeV)	$\Delta_0^{(p)}$ (MeV)	V (MeV)	ω_γ (MeV)	ω_β (MeV)	M (MeV^{-1})	$\mathcal{J}$ (MeV^{-1})
^{68}Se (ob)	0.296	60°	1.17	1.26	0	1.373	2.131	50.96	6.38
^{68}Se (pro)	0.260	0°	1.34	1.40	0.41	0.886	1.367	34.29	4.60
^{70}Se (ob)	0.313	60°	1.21	1.16	0	1.617	1.421	83.07	7.52
^{70}Se (pro)	0.325	0°	1.34	1.30	0.55	1.161	1.120	47.51	6.89
^{72}Se (ob)	0.268	60°	1.42	1.16	0	1.294	1.482	52.90	6.18
^{72}Se (pro)	0.381	0°	1.08	1.23	0.32	1.411	1.042	72.28	10.25

The effective charges $(e_n, e_p) = (0.4e, 1.4e)$ are used in the calculation of $E2$ transition matrix elements. In numerical calculation of solving the ASCC equations, we use $\delta q = 0.01$.

B. Properties of the HB states and the QRPA vibrations

The static HB solution and the QRPA calculation based on it provide the ASCC solution at $q = 0$. Properties of the HB mean field and of the QRPA modes are summarized in Table II. In all the three isotopes, we obtain two HB solutions possessing the oblate and prolate shapes. While the magnitude of the quadrupole deformation of the oblate HB state depends on the neutron number rather weakly, that of the prolate HB state significantly increases from ^{68}Se to ^{72}Se. This trend of equilibrium deformation is consistent with what we expect from the deformed shell gap in the Nilsson diagram. The oblate HB solutions are always the lowest in energy, but the energy difference between the oblate and prolate HB local minima are only $0.3 \sim 0.6$ MeV.

Concerning the QRPA vibrations in ^{68}Se, the γ vibration is the lowest frequency mode, and the β vibration is the second-lowest mode both at the oblate and prolate minima. The situation is different in ^{70}Se, where the β vibration is the lowest mode both at the oblate and prolate minima. In the case of ^{72}Se, the γ vibration is the lowest mode at the oblate minimum, while the β vibration is the lowest mode at the prolate minimum.

It is also seen in Table II that the rotational moments of inertia at the prolate minimum significantly increases from ^{68}Se to ^{72}Se following the increase of the quadrupole deformation β. The calculated values for ^{68}Se and ^{70}Se seem a little too small, however, compared to the values experimental data suggest. We plan to make a more detailed analysis about this problem in the future.

C. Collective path

We have solved the ASCC equations and determined the collective path choosing one of the HB solutions in Table II in each nucleus and setting it as $|\phi(q = 0)\rangle$. The results are displayed in Fig. 1 where the obtained collective paths are drawn in the (β, γ) deformation plane.

1. ^{68}Se

In this nucleus, the potential barrier height is about 0.5 and 0.07 MeV measured from the oblate and prolate local minima, respectively. The oblate HB state is chosen as a starting state for solving the ASCC equations. Though the collective path for ^{68}Se is already reported in the previous work [33],

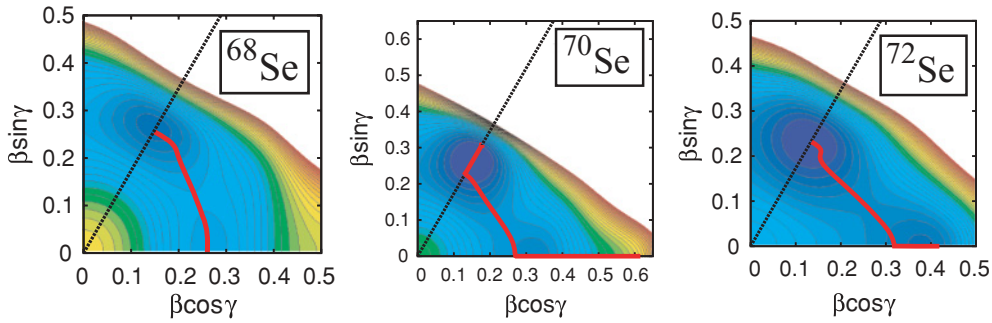

FIG. 1. (Color online) The collective paths for $^{68-72}$Se obtaind by the ASCC method. The collective path projected onto the (β, γ) deformation plane are drawn by solid lines on the potential energy surface. The equipotential lines are drawn every 100 keV. Note that the collective path is symmetric with respect to the reflections about the prolate ($\gamma = 0°$) and the oblate ($\gamma = 60°$) axes. The collective path going along the symmetry axis eventually terminates at large β when the neutron pairing gap collapses (see the text).

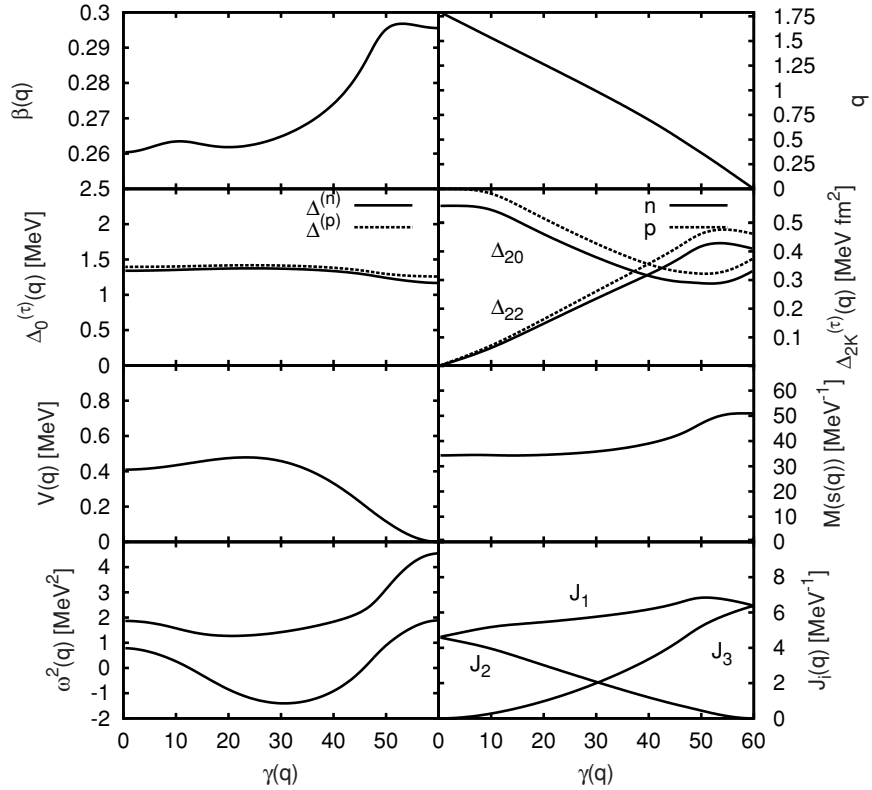

FIG. 2. Results of the ASCC calculation for ^{68}Se. The monopole pairing gaps $\Delta_0^{(\tau)}(q)$, the quadrupole pairing gaps $\Delta_{20}^{(\tau)}(q)$ and $\Delta_{22}^{(\tau)}(q)$, the collective potential $V(q)$, the collective mass $M[s(q)]$, the rotational moments of inertia $\mathcal{J}_i(q)$, the lowest two moving-frame QRPA frequencies squared $\omega^2(q)$, the axial quadrupole deformation $\beta(q)$, and the canonical collective coordinate q are plotted as functions of $\gamma(q)$.

we summarize the character of the solution of the ASCC equations for later convenience. The collective path starting from the oblate HB states almost follows the triaxial potential valley.

In Fig. 2, we see that the deformation β almost stays constant during when the triaxial deformation γ changes from 60° to 0° along the collective path. This clearly indicates that the triaxial degree of freedom plays much more important role than the axial degree of freedom in ^{68}Se. The γ dependence of the calculated moments of inertia exhibits a behavior similar to the irrotational moments of inertia; two of them coincide at the axially symmetric limit while the largest moment of inertia is about the intermediate axis.

In Fig. 2, the collective mass defined as a function of the geometrical length $ds = \sqrt{d\beta^2 + \beta^2 d\gamma^2}$ in the (β, γ) plane,

$$M[s(q)] = B^{-1}(q)\left[\left(\frac{d\beta}{dq}\right)^2 + \beta^2(q)\left(\frac{d\gamma}{dq}\right)^2\right], \qquad (30)$$

is also presented. As mentioned in Sec. III, we can set $M(q) = B(q)^{-1} = 1$ MeV^{-1} using the units where $\hbar = 1$ and the collective variables (q, p) are nondimensional.

2. ^{70}Se

In this nucleus, the potential barrier height is about 0.7 and 0.1 MeV measured from the oblate and prolate local minima, respectively. The collective path is obtained starting from the prolate HB state. The two HB local minima are connected by the one-dimensional path. Because the QRPA mode with the lowest frequency at the prolate shape has β-vibrational character with $K = 0$, the collective path starting from the prolate HB state goes along the axial symmetry axis in the beginning. As seen in Figs. 1 and 3, at $q \simeq 0.4\,(\beta \simeq 0.27)$, the collective path deviates from the $\gamma = 0°$ line due to the character change of the lowest mode from $K = 0$ to $K = 2$. To describe such a dynamical breaking of the axial symmetry taking place along the collective path, it is crucial to use Eq. (20) as an initial trial for self-consistently determining the collective coordinate operator $\hat{Q}(q)$. The collective path encounters a similar avoided crossing of the moving-frame QRPA modes at $q \simeq 1.8$ (the oblate side with $\beta \simeq 0.27$). Then, the triaxial path again changes its direction and go along the $\gamma = 60°$ line. This kind of dynamical breaking of the axial symmetry was previously reported in the analysis of the collective path for ^{72}Kr [32,33]. At the oblate side of the collective path, the β-vibrational degrees of freedom strongly couples with the pairing-vibrational degree of freedom of neutrons, and it ends at a large β point where the neutron pairing gap collapses. When approaching this point, the collective mass diverges.

As the rotation about the symmetry axis disappear, the moments of inertia $\mathcal{J}_3(q)$ and $\mathcal{J}_2(q)$ should be dropped in the determinant $|G(q)|$ of the metric $G_{mn}(q)$ when the collective path runs along the $\gamma = 0°$ and $\gamma = 60°$ lines, respectively. To avoid discontinuity at the point where the collective path starts to deviate from the symmetry axis, we use $|G(q)| = B^{-1}(q)\mathcal{J}_1(q)$ for the whole region of the collective path of this nucleus.

In the region of prolate shape with $\beta > 0.34$, the lowest two QRPA modes with β and γ characters approximately degenerate in energy and compete (see Fig. 3). In such a situation, it may be appropriate to introduce two collective

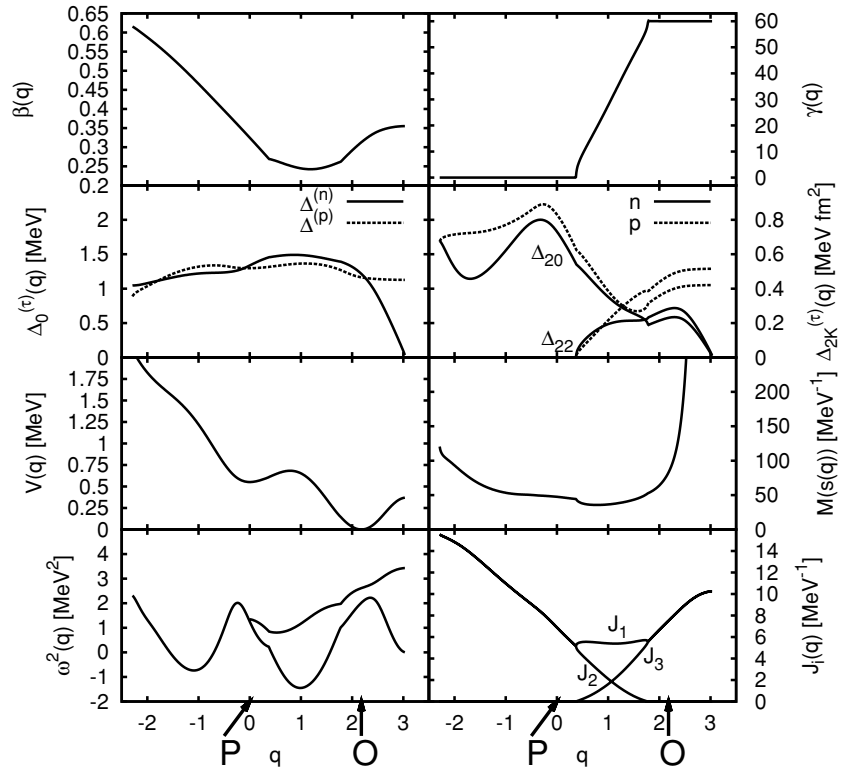

FIG. 3. The same as described in the caption to Fig. 2 but for ^{70}Se plotted as functions of q along the collective path. The point $q = 0$ corresponds to the prolate local minimum, while the oblate minimum is located at $q = 2.18$. These positions are indicated by arrows with P or O.

coordinates. In the present calculation, however, we have solved the ASCC equations in this region assuming that the collective path continues to go along the $\gamma = 0^\circ$ axis. We shall attempt to introduce two collective coordinates in the same framework of the ASCC method in the future.

3. ^{72}Se

In this nucleus, the potential barrier height is about 0.5 and 0.3 MeV measured from the oblate and prolate local minima, respectively. The collective path is determined starting from the oblate HB state. As seen in Figs. 1 and 4, the collective

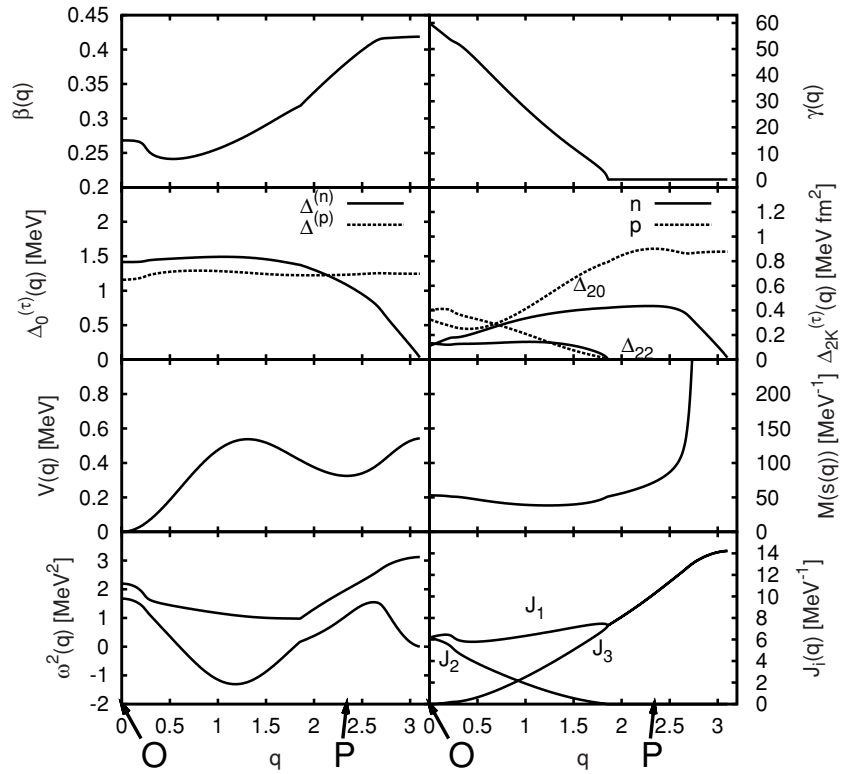

FIG. 4. The same as described in the caption to Fig. 2 but for ^{72}Se plotted as functions of q along the collective path. The point $q = 0$ corresponds to the oblate minimum, while the prolate local minimum is located at $q = 2.34$. These positions are indicated by arrows with O or P.

path directs to the triaxial region because the character of the lowest QRPA mode at the oblate minimum is γ vibrational. At $q \simeq 0.2$ in the triaxial region, the collective path curves due to an interplay of the lowest two moving-frame QRPA modes. The collective path reaches the prolate side at $q \simeq 1.6\,(\beta \simeq 0.32)$. Then the path changes its direction to the $\gamma = 0^\circ$ line. Thus, the oblate and prolate local minima are connected by a single collective coordinate. After passing through the prolate minimum at $q \simeq 2.1(\beta \simeq 0.38)$, it continues to go along the $\gamma = 0^\circ$ line and finally terminates at $\beta \simeq 0.42$, where the neutron pairing gap collapses. Correspondingly, the collective mass increases with increasing β and finally diverges.

As discussed above for ^{70}Se, the moment of inertia $\mathcal{J}_3(q)$ should be dropped in the determinant $|G(q)|$ when the collective path runs along the $\gamma = 0^\circ$ line. Because the collective path for ^{72}Se does not run along the $\gamma = 60^\circ$ line at all, we use $|G(q)| = B^{-1}(q)\mathcal{J}_1(q)\mathcal{J}_2(q)$ for the whole region of the collective path of this nucleus.

D. Shape mixing, excitation spectra, quadrupole transitions, and moments

We have calculated collective wave functions solving the collective Schrödinger equation (25) and evaluated excitation spectra, quadrupole transition probabilities, and spectroscopic quadrupole moments. Below we discuss these results denoting the eigenstates belonging to the ground and excited bands as $0_1^+, 2_1^+, 4_1^+, 6_1^+$ and $0_2^+, 2_2^+, 4_2^+, 6_2^+$, respectively.

1. ^{68}Se

In Fig. 5, excitation spectrum and $B(E2)$ values calculated for ^{68}Se are displayed together with experimental data. It is seen that the calculation yields two bands that exhibit significant deviations from the regular rotational pattern. We note, in particular, that the calculated 0_2^+ state is located above the 2_2^+ state. This is consistent with the available experimental data where the 0_2^+ state has not yet been found. We see in Fig. 6 that the vibrational wave functions of the $0_1^+, 0_2^+, 2_1^+,$

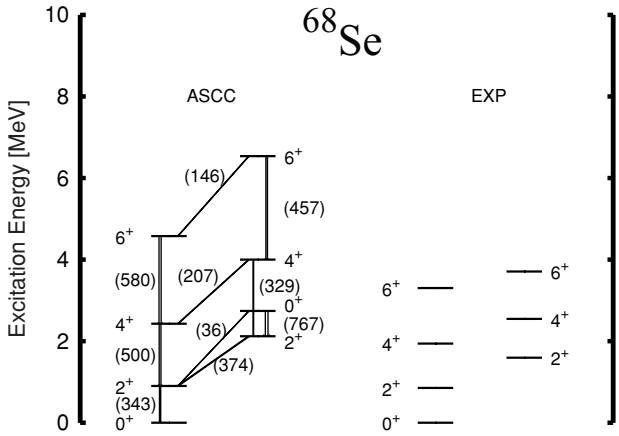

FIG. 5. Theoretical (left) and experimental (right) excitation spectra and $B(E2)$ values for low-lying states in ^{68}Se. Only $B(E2)$'s larger than 1 Weisskopf unit are shown in units of e^2 fm^4. Experimental data are taken from Refs. [6,7].

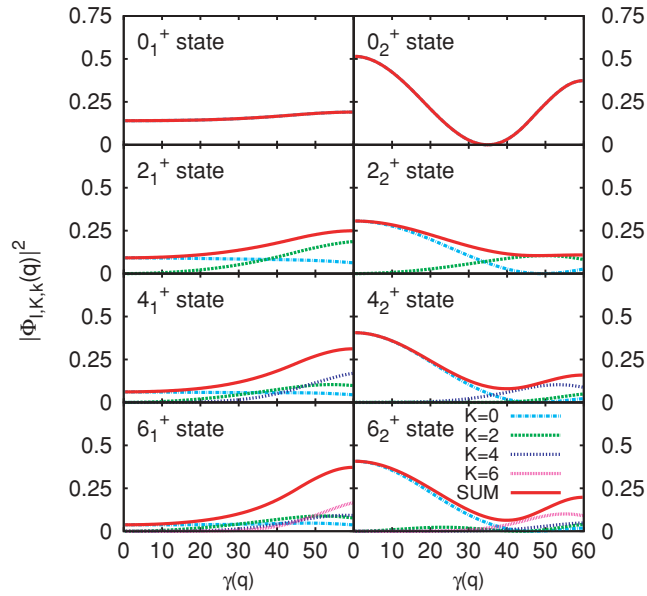

FIG. 6. (Color online) Vibrational wave functions $\Phi_{IKk}(q)$ squared of the lowest (left) and the second-lowest states (right) for each angular momentum in ^{68}Se. In each panel, different K components of the vibrational wave function and the sum of them are plotted as functions of $\gamma(q)$.

and 2_2^+ states spread over the whole extent of γ from the oblate to the prolate shapes. This result of calculation is reasonable considering the very low potential barrier along the triaxial collective path, as we have already seen in Fig. 2. The unusual behavior of the excited 0^+ state noted above suggests that the low-lying states in ^{68}Se are in an intermediate situation between the oblate-prolate shape coexistence and the Wilets-Jean γ-unstable model [41]. In fact, we can find a pattern in the calculated $E2$-transition probabilities, which is characteristic to the γ-unstable situation; for instance, $B(E2; 6_2^+ \to 6_1^+)$, $B(E2; 4_2^+ \to 4_1^+)$, and $B(E2; 2_2^+ \to 2_1^+)$ are much larger than $B(E2; 6_2^+ \to 4_1^+)$, $B(E2; 4_2^+ \to 2_1^+)$, and $B(E2; 2_2^+ \to 0_1^+)$. This point will be discussed with a more general perspective in a future publication [42]. It is quite interesting to notice that the shape mixing becomes weak as the angular momentum increases, and the collective wave functions of the 4^+ and 6^+ states tend to localize in the region near either the oblate or the prolate shape; namely it becomes possible to characterize the 4^+ and 6^+ states as oblatelike or prolatelike.

2. ^{70}Se

Calculated and experimental excitation spectra and $B(E2)$ values for ^{70}Se are displayed in Fig. 7. The excitation energies of the ground band is well reproduced. The calculated $B(E2; 2_1^+ \to 0_1^+)$ value 390 e^2 fm^4 is also in reasonable agreement with the experimental data 342 e^2 fm^4. The calculated $E2$-transition probabilities exhibit a pattern somewhat different from that of ^{68}Se; for instance, we see significant cross talks among the $2_1^+, 2_2^+, 4_1^+$, and 4_2^+ states. The vibrational wave functions of the $0_1^+, 0_2^+, 2_1^+$, and 2_2^+ states displayed in Fig. 8 show strong oblate-prolate shape mixings. In contrast,

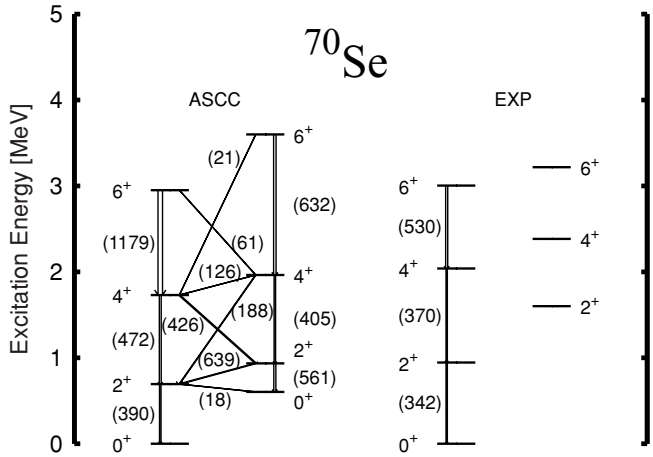

FIG. 7. The same as described in the caption to Fig. 5 but for ^{70}Se. Experimental data are taken from Refs. [8,43]. A candidate of the 0_2^+ state is suggested in experiment [9] at about 2 MeV, although it is not drawn.

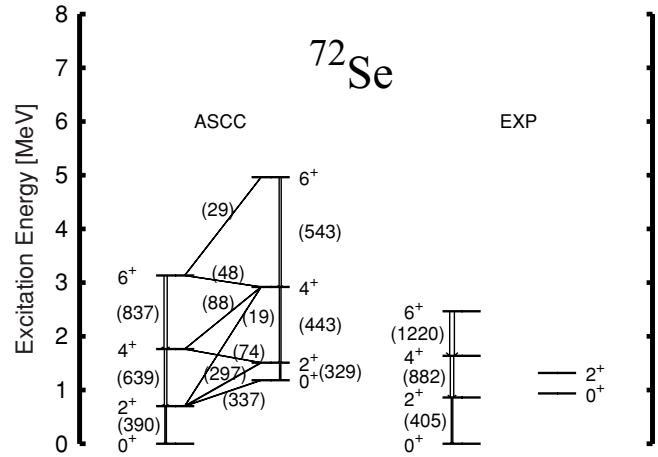

FIG. 9. The same as described in the caption to Fig. 5 but for ^{72}Se. Experimental data are taken from Refs. [8,44].

the 4_1^+ and 6_1^+ (4_2^+ and 6_2^+) states are rather well localized around the prolate (oblate) shape. Thus, the characteristic cross-talk of the $E2$ transition strengths mentioned above is associated with the significant change in localization properties of the vibrational wave functions between angular momenta 2 and 4. Experimental data for such inter- and intraband $B(E2)$ values will certainly serve as a very good indicator of the shape mixing.

3. ^{72}Se

Calculated excitation spectrum and $B(E2)$ values for ^{72}Se are shown in Fig. 9 together with experimental data. It is seen that the experimental spectrum is reproduced fairly well. The calculated $B(E2; 2_1^+ \to 0_1^+)$ value 390 e^2 fm^4 is also in good agreement with the experimental data 405 e^2 fm^4. We see that the calculated interband $E2$ transitions, $B(E2; 4_2^+ \to 4_1^+)$, $B(E2; 4_2^+ \to 2_1^+)$, $B(E2; 2_2^+ \to 2_1^+)$, and $B(E2; 4_1^+ \to 2_2^+)$, are reduced from those in ^{70}Se, except for $B(E2; 0_2^+ \to 2_1^+)$.

The vibrational wave functions are displayed in Fig. 10. Similarly to ^{70}Se, the 0_1^+ wave function widely spreads over the triaxial region. It takes the maximum at the oblate shape but extends to the prolate region. The 2_1^+ wave function also extends the whole region of γ. In the ground band, the prolate character develops with increasing angular momentum, as clearly seen in the wave functions of the 4_1^+ and 6_1^+ states.

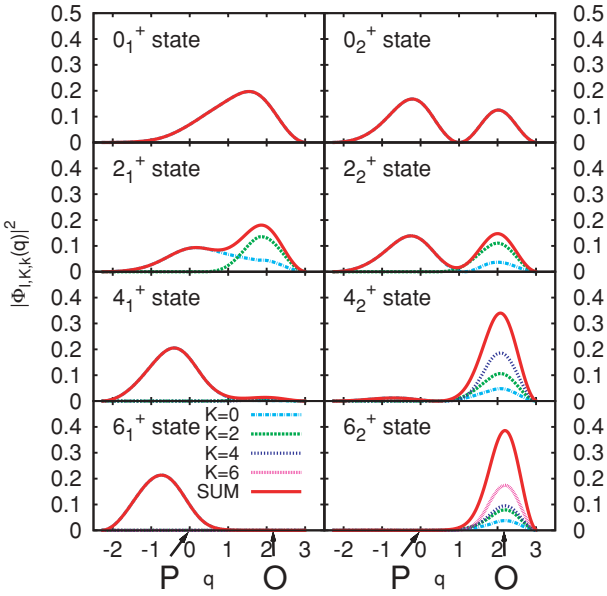

FIG. 8. (Color online) Same as described in the caption to Fig. 6 but for ^{70}Se. The vibrational collective wave functions squared are plotted as functions of q. The arrows indicate the positions of the oblate (O) and the prolate (P) minima.

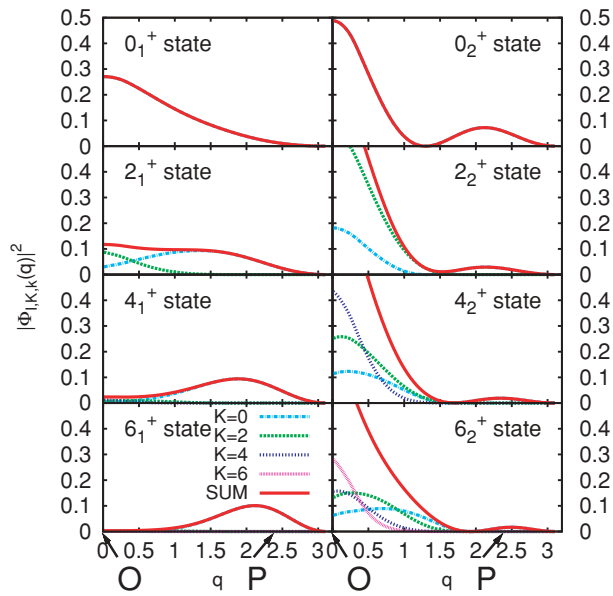

FIG. 10. (Color online) Same as described in the caption to Fig. 6 but for ^{72}Se. The vibrational wave functions squared are plotted as functions of q. The arrows indicate the positions of the oblate (O) and the prolate (P) minima.

Dynamical reason why the prolate character of the ground band develop with increasing angular momentum may be understood in terms of the competition between the potential and kinetic energies as function of the collective coordinate q. We find that the rotational energy term plays a particularly important role. Because the quadrupole deformation $\beta \simeq 0.38$ at the prolate local minimum is much larger than that ($\beta \simeq 0.27$) at the oblate minimum, the moment of inertia $\mathcal{J} \simeq 10.3\ \mathrm{MeV}^{-1}$ at the former is appreciably larger than $\mathcal{J} \simeq 6.2\ \mathrm{MeV}^{-1}$ at the latter. The difference between the rotational energies at the prolate and oblate minima is easily evaluated to be about 0.19, 0.64, 1.35 MeV for the $2^+, 4^+, 6^+$ states, respectively. Therefore, the prolate shape is favored to reduce the rotational energy. As the rotational angular momentum increases, this rotational effect becomes more important and overcomes the small disadvantage in the potential energy. In contrast, for the 0^+ ground state where the rotational effect is absent, the vibrational wave function takes the maximum at the oblate minimum. For the 2_1^+ state, the difference of the rotational energies, about 0.19 MeV, is slightly smaller than that of the potential energies, about 0.32 MeV, so its collective wave function exhibits a transitional character from oblatelike to prolatelike. For the excited states, the vibrational wave functions possess the dominant bumps around the oblate shape, exhibiting at the same time the second bumps around the prolate shape.

4. Quadrupole moments

The spectroscopic quadrupole moments calculated for ^{68,70,72}Se are displayed in Fig. 11. For ^{68}Se, the 4_1^+ and 6_1^+ states possess positive signs indicating dominance of the oblate character, while the 4_2^+ and 6_2^+ states have negative signs indicating dominance of the prolate character. In contrast to the ^{68}Se case, the 4_1^+ and 6_1^+ states in ^{70}Se and ^{72}Se have negative signs, indicating the growth of prolate character of these states with increasing rotational angular momentum. These results are in qualitative agreement with the HFB-based configuration-mixing calculation reported by Ljungvall *et al.* [8]. Both calculations indicate the oblate (prolate) dominance for the ground (excited) band in ^{68}Se while the prolate character develops with increasing angular momentum for the ground bands in ^{70}Se and ^{72}Se. For the excited bands of ^{70}Se and ^{72}Se, results of the configuration-mixing calculation are not reported in Ref. [8]. Our calculation indicates the growth of oblate character for the 4_2^+ and 6_2^+ states in these isotopes.

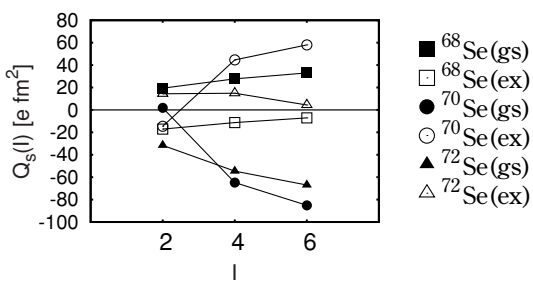

FIG. 11. Spectroscopic quadrupole moments calculated for the low-lying states in ^{68,70,72}Se. The square, circle, and triangular symbols represents those for ^{68}Se, ^{70}Se, and ^{72}Se, respectively. The filled (open) symbols denotes the ground (excited) band.

Careful interpretation is necessary when absolute values of the calculated spectroscopic quadrupole moment are small. In our results of calculation, small values have nothing to do with spherical character of the states of interest; it is a particular consequence of large-amplitude shape vibration. We find a number of situations where the contributions from the components of the vibrational wave function with $\gamma > 30^\circ$ are largely canceled with those from $\gamma < 30^\circ$. Such a cancellation is the main reason why the calculated quadrupole moments are rather small for all the 2_1^+ and 2_2^+ states of interest.

5. Discussion

Before concluding, we remark on a few questions to be examined in a future publication.

In this article, we have taken into account the function $G(q)$ in the volume element (29) while it was put unity in the previous calculation [33]. Thus, we have obtained, for instance, different ordering between the 0_2^+ and 2_2^+ states for ^{68}Se from that in Ref. [33]. This indicates importance of proper treatment of the volume element. In numerical calculations for ^{70}Se and ^{72}Se, however, the volume element was treated in an approximate way. We plan to examine the validity of this approximation by deriving a five-dimensional quadrupole collective Hamiltonian on the basis of the ASCC method and make a detailed comparison of the present results with those of the five-dimensional calculation [42].

Another question is the validity of evaluating the rotational moment of inertia after determining the collective path. Obviously, the assumption that the collective path does not change due to the rotational motion will be eventually violated with increasing angular momentum. Namely, the present approach may be valid only for low-spin states. We have therefore restricted our calculation to low-spin states with angular momentum $I \leqslant 6$. By comparing with the five-dimensional calculation mentioned above, we shall be able to examine also the range of applicability of the present approach. Alternatively, one can use the rotating mean field when determining the collective path. Such an approach was once tried in Refs. [25] and [45].

V. CONCLUSIONS

Using the ASCC method we have investigated the oblate-prolate shape coexisting/mixing phenomena in proton-rich selenium isotopes, ^{68,70,72}Se. The collective paths connecting the oblate and prolate HB local minima were successfully determined. Requantizing the collective Hamiltonian obtained by means of the ASCC method, we have derived the quantum collective Hamiltonian that describes the large-amplitude shape vibration along the collective path and the three-dimensional rotational motion in a unified manner. Solving the collective Schrödinger equation, we have calculated excitation spectra, $E2$ transition probabilities and spectroscopic quadrupole moments. It has been shown that the basic properties of the

coexisting two rotational bands in low-lying states of these nuclei are well reproduced.

The result of calculation clearly shows that the oblate-prolate shape mixing becomes weak as the rotational angular momentum increases. We have analyzed dynamical origin of this trend and found that the rotational energy plays a crucial role in determining the degree of localization of the collective wave function in the (β, γ) deformation space. The rotational effect causing the localization of the collective wave function may be called "rotational hindrance of shape mixing." To our knowledge, importance of such a dynamical effect has not been received enough attention in connection with the oblate-prolate shape coexistence phenomena of interest. The rotational hindrance effect will be discussed with a more general perspective in a future publication [42].

ACKNOWLEDGMENTS

One of the authors (N.H.) thanks Professor Y. Kanada-En'yo for valuable discussions. The numerical calculations were carried out on Altix3700 BX2 at Yukawa Institute for Theoretical Physics in Kyoto University. This work is supported by Grants-in-Aid for Scientific Research (No. 20540259) from the Japan Society for the Promotion of Science and the JSPS Core-to-Core Program "International Research Network for Exotic Femto Systems."

[1] J. L. Wood, K. Heyde, W. Nazarewicz, M. Huyse, and P. van Duppen, Phys. Rep. **215**, 101 (1992).
[2] W. Nazarewicz, J. Dudek, R. Bengtsson, T. Bengtsson, and I. Ragnarsson, Nucl. Phys. **A435**, 397 (1985).
[3] S. Takami, K. Yabana, and M. Matsuo, Phys. Lett. **B431**, 242 (1998).
[4] M. Yamagami, K. Matsuyanagi, and M. Matsuo, Nucl. Phys. **A693**, 579 (2001).
[5] S. Skoda, B. Fiedler, F. Becker, J. Eberth, S. Freund, T. Steinhardt, O. Stuch, O. Thelen, H. G. Thomas, L. Käubler *et al.*, Phys. Rev. C **58**, R5 (1998).
[6] S. M. Fischer, D. P. Balamuth, P. A. Hausladen, C. J. Lister, M. P. Carpenter, D. Seweryniak, and J. Schwartz, Phys. Rev. Lett. **84**, 4064 (2000).
[7] S. M. Fischer, C. J. Lister, and D. P. Balamuth, Phys. Rev. C **67**, 064318 (2003).
[8] J. Ljungvall, A. Görgen, M. Girod, J.-P. Delaroche, A. Dewald, C. Dossat, E. Farnea, W. Korten, B. Melon, R. Menegazzo *et al.*, Phys. Rev. Lett. **100**, 102502 (2008).
[9] A. Ahmed, A. V. Ramayya, D. L. Sastry, J. H. Hamilton, R. B. Piercey, H. Kawakami, A. P. de Lima, C. F. Maguire, R. L. Robinson, H. J. Kim *et al.*, Phys. Rev. C **24**, 1486 (1981).
[10] J. H. Hamilton, A. V. Ramayya, W. T. Pinkston, R. M. Ronningen, G. Garcia-Bermudez, H. K. Carter, R. L. Robinson, H. J. Kim, and R. O. Sayer, Phys. Rev. Lett. **32**, 239 (1974).
[11] Y. Sun, Eur. Phys. J. A **20**, 133 (2004).
[12] K. Kaneko, M. Hasegawa, and T. Mizusaki, Phys. Rev. C **70**, 051301(R) (2004).
[13] M. Hasegawa, K. Kaneko, T. Mizusaki, and Y. Sun, Phys. Lett. **B656**, 51 (2007).
[14] F. H. Al-Khudair, Y. S. Li, and G. L. Long, Phys. Rev. C **75**, 054316 (2007).
[15] A. Petrovici, K. W. Schmid, and A. Faessler, Nucl. Phys. **A710**, 246 (2002).
[16] A. Petrovici, K. W. Schmid, and A. Faessler, Nucl. Phys. **A728**, 396 (2003).
[17] M. Bender, P. Bonche, and P.-H. Heenen, Phys. Rev. C **74**, 024312 (2006).
[18] P. Ring and P. Schuck, *The Nuclear Many-Body Problem* (Springer-Verlag, New York, 1980).
[19] M. Baranger and M. Véneroni, Ann. Phys. **114**, 123 (1978).
[20] F. Villars, Nucl. Phys. **A285**, 269 (1977).
[21] K. Goeke and P.-G. Reinhard, Ann. Phys. **112**, 328 (1978).
[22] G. D. Dang, A. Klein, and N. R. Walet, Phys. Rep. **335**, 93 (2000).
[23] J. Libert, M. Girod, and J.-P. Delaroche, Phys. Rev. C **60**, 054301 (1999).
[24] D. Almehed and N. R. Walet, J. Phys. G **31**, S1523 (2005).
[25] D. Almehed and N. R. Walet, nucl-th/0509079 (unpublished).
[26] T. Marumori, T. Maskawa, F. Sakata, and A. Kuriyama, Prog. Theor. Phys. **64**, 1294 (1980).
[27] M. Matsuo, Prog. Theor. Phys. **76**, 372 (1986).
[28] M. Matsuo, T. Nakatsukasa, and K. Matsuyanagi, Prog. Theor. Phys. **103**, 959 (2000).
[29] N. Hinohara, T. Nakatsukasa, M. Matsuo, and K. Matsuyanagi, Prog. Theor. Phys. **117**, 451 (2007).
[30] M. Kobayasi, T. Nakatsukasa, M. Matsuo, and K. Matsuyanagi, Prog. Theor. Phys. **110**, 65 (2003).
[31] M. Kobayasi, T. Nakatsukasa, M. Matsuo, and K. Matsuyanagi, Prog. Theor. Phys. **112**, 363 (2004).
[32] M. Kobayasi, T. Nakatsukasa, M. Matsuo, and K. Matsuyanagi, Prog. Theor. Phys. **113**, 129 (2005).
[33] N. Hinohara, T. Nakatsukasa, M. Matsuo, and K. Matsuyanagi, Prog. Theor. Phys. **119**, 59 (2008).
[34] N. Hinohara, T. Nakatsukasa, M. Matsuo, and K. Matsuyanagi, Prog. Theor. Phys. **115**, 567 (2006).
[35] A. Bohr and B. R. Mottelson, *Nuclear Structure* (World Scientific, Singapore, 1998), Vol. II.
[36] K. Kumar and M. Baranger, Nucl. Phys. **A92**, 608 (1967).
[37] D. R. Bes and R. A. Sorensen, *Advances in Nuclear Physics* (Plenum Press, New York, 1969), Vol. 2.
[38] M. Baranger and K. Kumar, Nucl. Phys. **A110**, 490 (1968).
[39] S. G. Nilsson and I. Ragnarsson, *Shapes and Shells in Nuclear Structure* (Cambridge University Press, Cambridge, 1995).
[40] H. Sakamoto and T. Kishimoto, Phys. Lett. **B245**, 321 (1990).
[41] L. Wilets and M. Jean, Phys. Rev. **102**, 788 (1956).
[42] K. Sato, N. Hinohara, T. Nakatsukasa, M. Matsuo, and K. Matsuyanagi (in preparation).
[43] G. Rainovski, H. Schnare, R. Schwengner, C. Plettner, L. Käubler, F. Dönau, I. Ragnarsson, J. Eberth, T. Steinhardt, O. Thelen *et al.*, J. Phys. G **28**, 2617 (2002).
[44] R. Palit, H. C. Jain, P. K. Joshi, J. A. Sheikh, and Y. Sun, Phys. Rev. C **63**, 024313 (2001).
[45] D. Almehed and N. R. Walet, Phys. Lett. **B604**, 163 (2004).

Progress of Theoretical Physics, Vol. 123, No. 1, January 2010

A Model Analysis of Triaxial Deformation Dynamics in Oblate-Prolate Shape Coexistence Phenomena

Koichi Sato,[1,2] Nobuo Hinohara,[2] Takashi Nakatsukasa,[2]
Masayuki Matsuo[3] and Kenichi Matsuyanagi[2,4]

[1]*Department of Physics, Graduate School of Science, Kyoto University, Kyoto 606-8502, Japan*
[2]*Theoretical Nuclear Physics Laboratory, RIKEN Nishina Center, Wako 351-0198, Japan*
[3]*Department of Physics, Niigata University, Niigata 950-2181, Japan*
[4]*Yukawa Institute for Theoretical Physics, Kyoto University, Kyoto 606-8502, Japan*

(Received September 8, 2009; Revised November 18, 2009)

From the viewpoint of oblate-prolate symmetry and its breaking, we adopt the quadrupole collective Hamiltonian to study the dynamics of triaxial deformation in shape coexistence phenomena. It accommodates the axially symmetric rotor model, the γ-unstable model, the rigid triaxial rotor model, and an ideal situation for the oblate-prolate shape coexistence as particular cases. Numerical solutions of this model yield a number of interesting suggestions. (1) The relative energy of the excited 0^+ state can be a signature of the potential shape along the γ direction. (2) Specific $E2$ transition probabilities are sensitive to the breaking of the oblate-prolate symmetry. (3) Nuclear rotation may induce the localization of collective wave functions in the (β, γ) deformation space.

Subject Index: 211

§1. Introduction

In recent years, experimental data suggesting the coexistence of the ground-state rotational band with the oblate shape and the excited band with the prolate shape have been obtained in proton-rich unstable nuclei.[1)–3)] Together with a variety of shape coexistence phenomena observed in various regions of a nuclear chart,[4)–7)] some of which also involve the spherical shape, these discoveries stimulate the development of nuclear structure theory capable of describing this new class of phenomena.[8)–13)] Recently, Hinohara et al.[14),15)] have carried out detailed microscopic calculations for the oblate-prolate shape mixing by the adiabatic self-consistent collective coordinate (ASCC) method.[8)] They suggest that the excitation spectrum of ^{68}Se may be regarded as a case corresponding to an intermediate situation between the well-developed oblate-prolate shape coexistence limit, where the shapes of the two coexisting rotational bands are well localized in the (β, γ) deformation space, and the γ-unstable limit, where a large-amplitude shape fluctuation takes place in the γ degree of freedom. Here, β and γ are well-known dynamical variables denoting the magnitude of the quadrupole deformation and the degree of axial symmetry breaking, respectively. These calculations indicate the importance of the coupled motion of the large-amplitude shape fluctuation in the γ degree of freedom and the

three-dimensional rotation associated with the triaxial shape.

To discuss the oblate-prolate shape coexistence phenomena in a wider perspective including their relations to other classes of low-energy spectra of nuclei, we introduce in this paper a simple phenomenological model capable of describing the coupled motion of the large-amplitude γ-vibrational motions and the three-dimensional rotational motions. We call it *(1+3)D model* to explicitly indicate the numbers of vibrational (γ) and rotational (three Euler angles) degrees of freedom. This model can be used to describe several interesting limits in a unified perspective. It includes the axially symmetric rotor model, the γ-unstable model,[16] the triaxial rigid rotor model,[17] and an ideal situation of the oblate-prolate shape coexistence. It also enables us to describe intermediate situations between these different limits by varying a few parameters. This investigation will provide a new insight concerning connections between microscopic descriptions of oblate-prolate shape mixing and various macroscopic pictures on low-energy spectra in terms of phenomenological models. It is intended to be complementary to the microscopic approach we are developing on the basis of the ASCC method.

The (1+3)D model is introduced on the basis of the well-known five-dimensional (5D) quadrupole collective Hamiltonian[18] by fixing the axial deformation parameter β. Simple functional forms are assumed for the collective potential and the collective mass (inertial function) with respect to the triaxial deformation γ. We analyze the properties of excitation spectra, quadrupole moments, and transition probabilities from the viewpoint of *oblate-prolate symmetry and its breaking*, varying a few parameters characterizing the collective potential and collective mass. Specifically, we investigate the sensitivity of these properties to 1) the barrier height between the oblate and prolate local minima in the collective potential, 2) the asymmetry parameter that controls the degree of oblate-prolate symmetry breaking in the collective potential, and 3) the mass-asymmetry parameter introducing the oblate-prolate asymmetry in the vibrational and rotational collective mass functions. The dynamical mechanism determining the localization and delocalization of collective wave functions in the deformation space is investigated. We find a number of interesting features that have received little attention to date: 1) the unique behavior of the excited 0^+ state as a function of the barrier-height parameter, 2) specific $E2$ transition probabilities sensitive to the degree of oblate-prolate symmetry breaking, and 3) the rotation-assisted localization of collective wave functions in the deformation space. We also examine the validity of the (1+3)D model by taking into account the β degree of freedom, i.e., by solving the collective Schrödinger equation for a 5D quadrupole collective Hamiltonian that simulates the situation under consideration.

In this paper, therefore, we intend to clarify the role of the β-γ dependence of the collective mass. Since the original papers by Bohr and Mottelson,[19,20] the collective Schrödinger equation with the 5D quadrupole collective Hamiltonian[18] has been widely used as the basic framework to investigate low-frequency quadrupole modes of excitation in nuclei. The collective potential and collective masses appearing in the Hamiltonian have been introduced either phenomenologically[21–24] or through microscopic calculations.[25–29,31–35] In recent years, powerful algebraic methods of solving the collective Schrödinger equation have been developed[36,37] and analytical

solutions have been found[38)–42)] for some special forms of the collective potential (see the recent review[43)] for an extensive list of references). However, all collective masses are assumed to be equal and a constant in these papers.[38)–42)] It should be emphasized that this approximation is justified only for harmonic vibrations about the spherical shape. The collective masses express inertia of vibrational and rotational motions, so that they play crucial roles in determining the collective dynamics. In general, they are coordinate-dependent, i.e., functions of β and γ. In fact, various microscopic calculations for the collective masses indicate their significant variations as functions of β and γ.[28),29),31)–35),44)–48)] In phenomenological analysis of experimental data, for instance, Jolos and Brentano[49)] have shown that it is necessary to use different collective masses for the rotational and β- and γ-vibrational modes to describe interband $E2$ transitions in prolately deformed nuclei.

This paper is organized as follows. After recapitulating the 5D quadrupole collective Hamiltonian and the collective Schrödinger equation in §2, we introduce in §3 the (1+3)D model of triaxial deformation dynamics. In §4, using the (1+3)D model, we first discuss the properties of excitation spectra for the collective potentials possessing oblate-prolate symmetry. We then investigate how they change when this symmetry is broken in the collective potential and/or in the collective mass. In §5, we examine the validity of the (1+3)D model by introducing β-γ coupling effects on the basis of the 5D quadrupole collective Hamiltonian. Concluding remarks are given in §6.

§2. Five-dimensional quadrupole collective Hamiltonian

We start with the 5D quadrupole collective Hamiltonian involving five collective coordinates, i.e., two deformation variables (β, γ) and three Euler angles:

$$H = T_{\rm vib} + T_{\rm rot} + V(\beta, \gamma), \tag{2·1}$$

$$T_{\rm vib} = \frac{1}{2} D_{\beta\beta}(\beta, \gamma)\dot{\beta}^2 + D_{\beta\gamma}(\beta, \gamma)\dot{\beta}\dot{\gamma} + \frac{1}{2} D_{\gamma\gamma}(\beta, \gamma)\dot{\gamma}^2, \tag{2·2}$$

$$T_{\rm rot} = \sum_{k=1}^{3} \frac{1}{2} \mathcal{J}_k(\beta, \gamma)\omega_k^2. \tag{2·3}$$

Here, the collective potential $V(\beta, \gamma)$ is a function of two deformation coordinates, β and γ, which represent the magnitudes of quadrupole deformation and triaxiality, respectively. It must be a scalar under rotation, so that it can be written as a function of β^2 and $\beta^3 \cos 3\gamma$.[18)] As is well known, one can restrict the range of γ to be $0^\circ \leq \gamma \leq 60^\circ$ by virtue of the transformation properties between different choices of the principal axes. The first term $T_{\rm vib}$ in Eq. (2·1) represents the kinetic energies of shape vibrations; it is a function of β and γ as well as their time derivatives $\dot{\beta}$ and $\dot{\gamma}$. The second term $T_{\rm rot}$ represents the rotational energy written in terms of three angular velocities ω_k, which are related to the time derivatives of the Euler angles. The three moments of inertia can be written as

$$\mathcal{J}_k(\beta, \gamma) = 4\beta^2 D_k(\beta, \gamma) \sin^2 \gamma_k, \tag{2·4}$$

with respect to the principal axes ($k = 1-3$), where $\gamma_k = \gamma - (2\pi k)/3$. In this paper, we adopt Bohr and Mottelson's notation[18] for the six collective mass functions, $D_{\beta\beta}, D_{\beta\gamma}, D_{\gamma\gamma}, D_1, D_2$, and D_3. They must fulfill the following conditions,

$$D_1(\beta, \gamma = 0^\circ) = D_2(\beta, \gamma = 0^\circ), \tag{2·5}$$

$$D_3(\beta, \gamma = 0^\circ) = D_{\gamma\gamma}(\beta, \gamma = 0^\circ)\beta^{-2}, \tag{2·6}$$

$$D_1(\beta, \gamma = 60^\circ) = D_3(\beta, \gamma = 60^\circ), \tag{2·7}$$

$$D_2(\beta, \gamma = 60^\circ) = D_{\gamma\gamma}(\beta, \gamma = 60^\circ)\beta^{-2}, \tag{2·8}$$

in the prolate ($\gamma = 0^\circ$) and oblate ($\gamma = 60^\circ$) axially symmetric limits.[27]

The classical collective Hamiltonian (2·1) is quantized according to the Pauli prescription. Then, the explicit expressions for the vibrational and rotational kinetic energies are given by[26]

$$\hat{T}_{\rm vib} = \frac{-\hbar^2}{2\sqrt{WR}} \left\{ \frac{1}{\beta^4} \left[\partial_\beta \left(\beta^2 \sqrt{\frac{R}{W}} D_{\gamma\gamma} \partial_\beta \right) - \partial_\beta \left(\beta^2 \sqrt{\frac{R}{W}} D_{\beta\gamma} \partial_\gamma \right) \right] \right.$$
$$\left. + \frac{1}{\beta^2 \sin 3\gamma} \left[-\partial_\gamma \left(\sqrt{\frac{R}{W}} \sin 3\gamma D_{\beta\gamma} \partial_\beta \right) + \partial_\gamma \left(\sqrt{\frac{R}{W}} \sin 3\gamma D_{\beta\beta} \partial_\gamma \right) \right] \right\} \tag{2·9}$$

and

$$\hat{T}_{\rm rot} = \sum_{k=1}^{3} \frac{\hat{I}_k^2}{2\mathcal{J}_k(\beta, \gamma)}, \tag{2·10}$$

respectively, where W and R are the abbreviations of

$$W(\beta, \gamma) = \beta^{-2} \left[D_{\beta\beta}(\beta, \gamma) D_{\gamma\gamma}(\beta, \gamma) - D_{\beta\gamma}^2(\beta, \gamma) \right], \tag{2·11}$$

$$R(\beta, \gamma) = D_1(\beta, \gamma) D_2(\beta, \gamma) D_3(\beta, \gamma), \tag{2·12}$$

and $\hat{I}_k$ denotes the angular momentum operators with respect to the principal-axis frame associated with a rotating deformed nucleus (the body-fixed PA frame).

The collective Schrödinger equation is written as

$$[\hat{T}_{\rm vib} + \hat{T}_{\rm rot} + V(\beta, \gamma)] \Psi_{IM\alpha}(\beta, \gamma, \Omega) = E_{I,\alpha} \Psi_{IM\alpha}(\beta, \gamma, \Omega), \tag{2·13}$$

where the collective wave function $\Psi_{IM\alpha}(\beta, \gamma, \Omega)$ is specified by the total angular momentum I, its projection M onto the z-axis in the laboratory frame, and α distinguishing eigenstates possessing the same values of I and M. In Eq. (2·13), Ω denotes a set of the three Euler angles, which are here dynamical variables describing the directions of the body-fixed PA frame with respect to the laboratory frame. By using the rotational wave functions $\mathcal{D}^I_{MK}(\Omega)$, the orthonormalized collective wave functions in the laboratory frame can be written as

$$\Psi_{IM\alpha}(\beta, \gamma, \Omega) = \sum_K \Phi_{IK\alpha}(\beta, \gamma) \langle \Omega | IMK \rangle, \tag{2·14}$$

where

$$\langle \Omega | IMK \rangle = \sqrt{\frac{2I+1}{16\pi^2(1+\delta_{K0})}} \left(\mathcal{D}^I_{MK}(\Omega) + (-)^I \mathcal{D}^I_{M-K}(\Omega) \right). \tag{2·15}$$

The functions $\Phi_{IK\alpha}(\beta,\gamma)$ are vibrational wave functions orthonormalized by

$$\int d\tau' \sum_K \Phi^*_{IK\alpha}(\beta,\gamma)\Phi_{IK\alpha'}(\beta,\gamma) = \delta_{\alpha\alpha'} \tag{2·16}$$

with the intrinsic volume element

$$d\tau' = 2\beta^4 \sqrt{W(\beta,\gamma)R(\beta,\gamma)} \sin 3\gamma d\beta d\gamma. \tag{2·17}$$

In Eqs. (2·14) and (2·16), the sum is taken over even values of K from 0 to I for even I (from 2 to $I-1$ for odd I). Detailed discussions on the symmetries and boundary conditions in the vibrational wave functions $\Phi_{IK\alpha}(\beta,\gamma)$ are given, e.g., in Ref. 27).

§3. Reduction to the (1+3)-dimensional collective Hamiltonian

For the reason mentioned in §1, we are particularly interested in triaxial deformation dynamics. To concentrate on the γ degree of freedom, we introduce a simple (1+3)D model involving only one vibrational coordinate γ and three rotational coordinates. This is done by freezing the β degree of freedom in the 5D quadrupole collective Hamiltonian (2·1) as explained below.

The collective potential of this model takes a very simple form:

$$V(\gamma) = V_0 \sin^2 3\gamma + V_1 \cos 3\gamma. \tag{3·1}$$

This form is readily obtained by retaining up to the second order with respect to $\beta^3 \cos 3\gamma$ and fixing β at a constant value in an expansion of $V(\beta,\gamma)$ in powers of β^2 and $\beta^3 \cos 3\gamma$.[50] When $V_1 = 0$, the collective potential is symmetric about $\gamma = 30^\circ$ with respect to the transformation $\gamma \to 60^\circ - \gamma$. For brevity, let us call this symmetry and transformation *OP (oblate-prolate) symmetry* and *OP inversion*, respectively. For positive V_0, two degenerate minima appear at the oblate ($\gamma = 60^\circ$) and prolate ($\gamma = 0^\circ$) shapes, and they are separated by a barrier that takes the maximum at $\gamma = 30^\circ$. We therefore call V_0 *the barrier-height parameter*. On the other hand, the maximally triaxial shape at $\gamma = 30^\circ$ becomes the minimum for negative V_0, and it becomes deeper as $|V_0|$ increases. When $V_1 \neq 0$, the OP symmetry is broken, and the oblate (prolate) shape becomes the minimum for a combination of positive V_0 and positive (negative) V_1. We call V_1 *the asymmetry parameter* after its controlling the magnitude of the OP symmetry breaking. Thus, by varying the two parameters V_0 and V_1, we can see how the excitation spectrum depends on the barrier height and symmetry breaking between the two local minima in the collective potential.

We present in Fig. 1 some examples of the collective potential $V(\gamma)$ that seem to be relevant to a variety of oblate-prolate shape coexistence phenomena. In this figure, we can clearly see how the asymmetry between the oblate and prolate minima grows

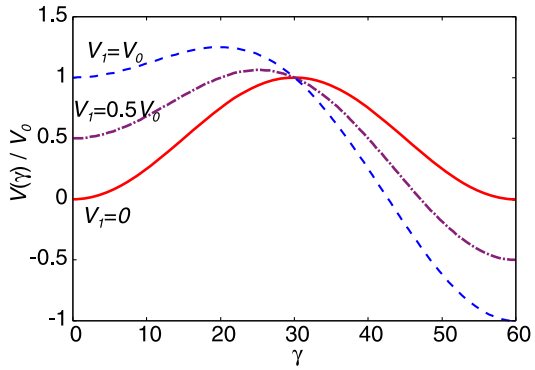

Fig. 1. The collective potentials $V(\gamma)$ defined by Eq. (2·4) are plotted for the $V_0 > 0$ case with solid, dash-dotted, and dashed lines as functions of γ for $V_1/V_0 = 0.0, 0.5$, and 1.0, respectively.

as a function of V_1 and how the barrier height measured from the second minimum sensitively depends on the ratio of V_1 to V_0.

The vibrational kinetic energy term reduces, in the (1+3)D model Hamiltonian, to the following form:

$$\hat{T}_{\rm vib} = \frac{-\hbar^2}{2\sqrt{D_{\gamma\gamma}(\beta_0,\gamma)R(\beta_0,\gamma)}}\frac{1}{\sin 3\gamma}\partial_\gamma\left(\sqrt{\frac{R(\beta_0,\gamma)}{D_{\gamma\gamma}(\beta_0,\gamma)}}\sin 3\gamma\partial_\gamma\right). \tag{3·2}$$

We parametrize the collective mass functions as

$$D_{\gamma\gamma}(\gamma) \equiv D_{\gamma\gamma}(\beta_0,\gamma) = D\beta_0^2(1+\epsilon\cos 3\gamma), \tag{3·3}$$
$$D_k(\gamma) \equiv D_k(\beta_0,\gamma) \ = D(1+\epsilon\cos\gamma_k). \tag{3·4}$$

These are the most simple forms involving only one parameter ϵ that controls the degree of OP symmetry breaking in these four mass functions under the requirement that they should fulfill the conditions (2·5)–(2·8). We call ϵ *the mass-asymmetry parameter*. These functional forms are obtainable also by taking the lowest-order term that brings about the OP symmetry breaking in the expressions of the collective mass functions microscopically derived by Yamada[48] by the SCC method.[51] In this paper, we use $\beta_0^2 = 0.1$ and $D = 50$ MeV^{-1}, which roughly simulate the values obtained in the microscopic ASCC calculation.[14),15)]

We solve the collective Schrödinger equation (2·13) replacing $V(\beta,\gamma)$, $\hat{T}_{\rm vib}$, and $\mathcal{J}_k(\beta,\gamma)$ in $\hat{T}_{\rm rot}$ by Eqs. (3·1), (3·2), and $\mathcal{J}_k(\beta_0,\gamma)$, respectively, with Eqs. (3·3), and (3·4). Accordingly, the collective wave function is denoted $\Psi_{IM\alpha}(\gamma,\Omega)$. Note that the sign change $V_1 \to -V_1$ corresponds to the OP inversion. One can then easily confirm that the OP inversion is equivalent to the simultaneous sign change of the parameters, $(\epsilon, \pm V_1) \to (-\epsilon, \mp V_1)$, in the (1+3)D model Hamiltonian. Therefore, it is enough to study only the case of positive ϵ.

Figure 2(a) shows, for an example of $\epsilon = 0.5$, how the collective mass functions $D_{\gamma\gamma}$ and D_k behave as functions of γ. Figure 2(b) indicates the degree of oblate-prolate asymmetry in the moments of inertia $\mathcal{J}_k(\gamma)$ brought about by the terms

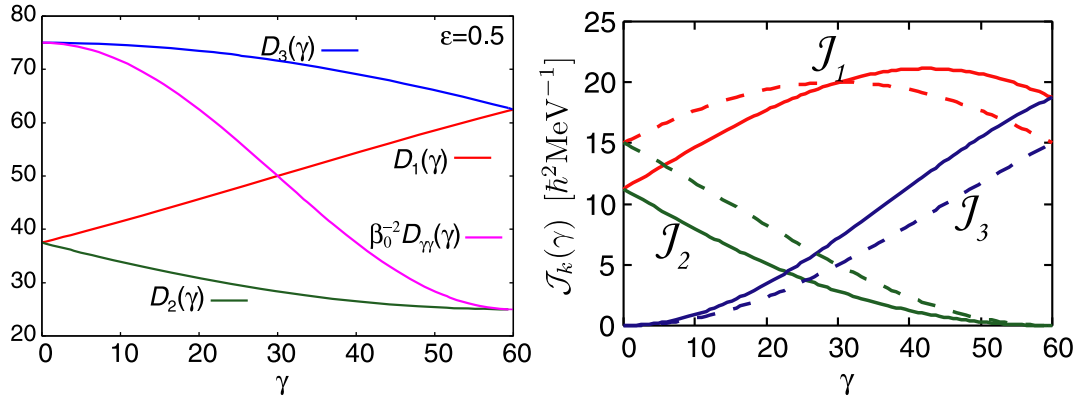

(a) Mass Parameters (b) Moments of Inertia

Fig. 2. (a) The vibrational and rotational collective mass functions $D_{\gamma\gamma}(\gamma)$ and $D_k(\gamma)$, defined by Eqs. (2·2) and (2·3), are plotted as functions of γ for the mass-asymmetry parameter $\epsilon = 0.5$. (b) Three rotational moments of inertia $\mathcal{J}_k(\beta, \gamma)$ with k =1, 2, and 3, defined by Eqs. (2·4) and (3·4), are plotted with solid lines as functions of γ for the mass-asymmetry parameter $\epsilon = 0.5$. The magnitude of the quadrupole deformation β is fixed at $\beta^2 = 0.1$. For comparison, the moments of inertia for the $\epsilon = 0$ case are also plotted with dashed lines.

involving ϵ. From these figures we can anticipate that, for positive (negative) ϵ and under the parameterizations of Eqs. (3·3) and (3·4), the rotational energy favors the oblate (prolate) shape, whereas the vibrational energy prefers the prolate (oblate) shape.

§4. Triaxial deformation dynamics

We have built a new computer code to solve the collective Schrödinger equation (2·13) for general 5D quadrupole collective Hamiltonian as well as its reduced version for the (1+3)D model. A numerical algorithm similar to that of Kumar and Baranger[27] is adopted in this code, except that we discretize the (β, γ) plane using meshes in the β and γ directions in place of their triangular mesh. Numerical accuracy and convergence were checked by comparing our numerical results with analytical solutions in the spherical harmonic vibration limit, in the so-called square-well-type β dependence limit and in the γ-unstable model.[16] In the following, we discuss how the solutions of the collective Schrödinger equation depend on the barrier-height parameter V_0, the asymmetry parameter V_1, and the mass-asymmetry parameter ϵ. We use the adjectives *yrast* and *yrare* for the lowest and second-lowest states for a given angular momentum I, respectively, and distinguish the two by suffix as I_1 and I_2.

4.1. *Excitation spectra in the presence of OP symmetry*

Let us first discuss the situation where $V_1 = 0$ and $\epsilon = 0$. In this case, both the collective potential and collective mass functions are symmetric about $\gamma = 30°$, so that the (1+3)D model Hamiltonian possesses OP symmetry. Furthermore, the collective mass parameter D and β_0 enter the collective Schrödinger equation only in the form of the overall factor $(2D\beta_0^2)^{-1}$ in the kinetic energy terms. Hence, only the ratio of the barrier-height parameter V_0 to this factor is important to determine the collective dynamics. In the particular case of $V_0 = 0$, i.e., $V(\gamma) = 0$, which is well known as the Wilets-Jean γ-unstable model,[16] the excitation spectra are completely scaled by this factor.

In Fig. 3, we show the excitation spectra for the case of $V_1 = 0$ and $\epsilon = 0$ as functions of V_0. Here, the excitation energies are normalized by the excitation energy of the first excited 0^+ state (denoted 0_2^+) at $V_0 = 0$, $E(0_2^+)$ (which is 1.8 MeV for

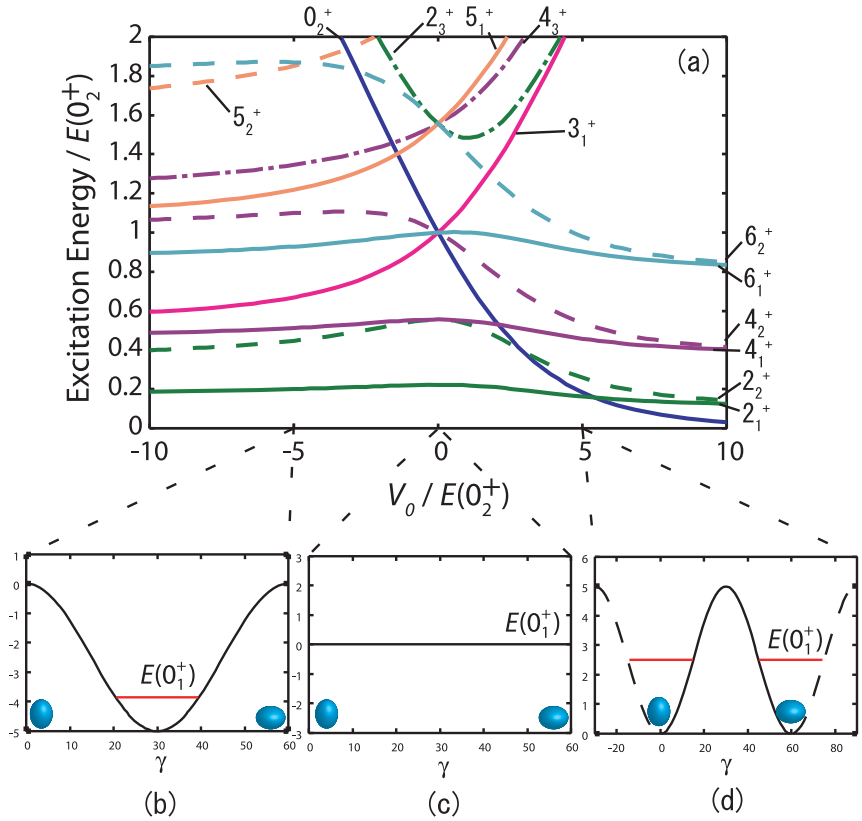

Fig. 3. In the upper panel (a), the dependence of excitation spectrum on the parameter V_0 is displayed. Excitation energies as well as V_0 values are normalized by the excitation energy $E(0_2^+)$ of the second (the first excited) 0^+ state for $V(\gamma) = 0$. In the lower panels (b), (c), and (d), the potentials $V(\gamma)$ and the ground 0^+ state energies $E(0_1^+)$ are illustrated for three different values of $V_0/E(0_2^+) = -5.0, 0.0$, and 5.0, respectively. Note that $E(0_1^+) = 0$ for $V_0 = 0$. Because the collective potential $V(\gamma)$ is a periodic function of 60° in γ, only the region $0° \leq \gamma \leq 60°$ is drawn with a solid line in (d).

$\beta_0^2 = 0.1$ and $D = 50$ MeV^{-1} adopted in this calculation). Accordingly, this figure is valid for any value of $(2D\beta_0^2)^{-1}$ by virtue of the scaling property mentioned above. In the lower panels of this figure, the collective potentials $V(\gamma)$ and the ground 0^+ state energies $E(0_1^+)$ are illustrated for three typical situations: 1) a triaxially deformed case where a deep minimum appears at the triaxial shape with $\gamma = 30°$, 2) the γ-unstable case, where the collective potential is flat with respect to γ, and 3) an extreme case of shape coexistence where the oblate and prolate minima are exactly degenerate in energy. (Strictly, shape coexistence does not appear in a case where the two minima are *exactly* degenerate as we shall see in Fig. 9.) Note that the collective potential $V(\gamma)$ is a periodic function of 60° in γ. Therefore, it is indicated by the solid line only in the region $0° \leq \gamma \leq 60°$.

In the positive-V_0 side of this figure, it is clearly seen that a doublet structure emerges when the barrier-height parameter V_0 becomes very large. In other words, approximately degenerate pairs of eigenstates appear for every angular momentum when $V_0/E(0_2^+) \gg 1$. This is nothing but the doublet pattern known well in the problems of double-well potential.[52] In the present case, this doublet structure is associated with the OP symmetry. Furthermore, one immediately notices a very unique behavior of the 0_2^+ state. When the barrier-height parameter V_0 decreases (from the limiting situation mentioned above), its energy rises more rapidly than those of the yrare 2_2^+, 4_2^+, and 6_2^+ states. Thus, a level crossing of the 0_2^+ and 2_2^+ states takes place at $V_0/E(0_2^+) \simeq 3$. When V_0 further decreases and approaches zero, the excitation energy of the 0_2^+ state approaches those of the 4_2^+ and 6_1^+ states. In the γ-unstable limit of $V_0 = 0$, they are degenerate.

In the negative-V_0 side, the excitation energies of the 3_1^+ and 5_1^+ states markedly decrease as V_0 decreases, and the excitation spectrum characteristic of the Davydov-Filippov rigid triaxial rotor model[17] appears when the triaxial minimum becomes very deep, i.e., when $V_0/E(0_2^+) \ll -1$.

4.2. *Breaking of the OP symmetry in the collective potential*

Next, let us investigate effects of the OP-symmetry-breaking term $V_1 \cos 3\gamma$ in the collective potential $V(\gamma)$. The effects are manifestly seen for the case of $\epsilon = 0$ and $V_0 = 0$. We present in Fig. 4 the excitation spectrum for this case as a function of the asymmetry parameter V_1. For $V_1 = 0$, the spectrum exhibits the degeneracy characteristic of the γ-unstable model:[16] e.g., the $0_2^+, 3_1^+, 4_2^+$, and 6_1^+ states are degenerate. With increasing magnitude of V_1, such degeneracies are lifted and the yrare $0_2^+, 2_2^+, 4_2^+$, and 6_2^+ states as well as the odd angular momentum 3_1^+ and 5_1^+ states increase in energy. As a consequence, the well-known ground-state rotational band spectrum appears for sufficiently large values of $|V_1|$. For instance, we can see in Fig. 4 that, as V_1 increases, the ratio of the yrast 2_1^+ and 4_1^+ energies, $E(4_1^+)/E(2_1^+)$, increases from 2.5 at $V_1 = 0$, which is the value peculiar to the γ-unstable model, to 3.3 for sufficiently large V_1. This figure perfectly demonstrates the fact that the breaking of spherical symmetry is insufficient for the appearance of regular rotational spectra even if the magnitude of quadrupole deformation is considerably large: we also need an appreciable amount of the OP symmetry breaking. We also note that the spectrum does not depend on the sign of V_1. This is because, for $\epsilon = 0$, both the

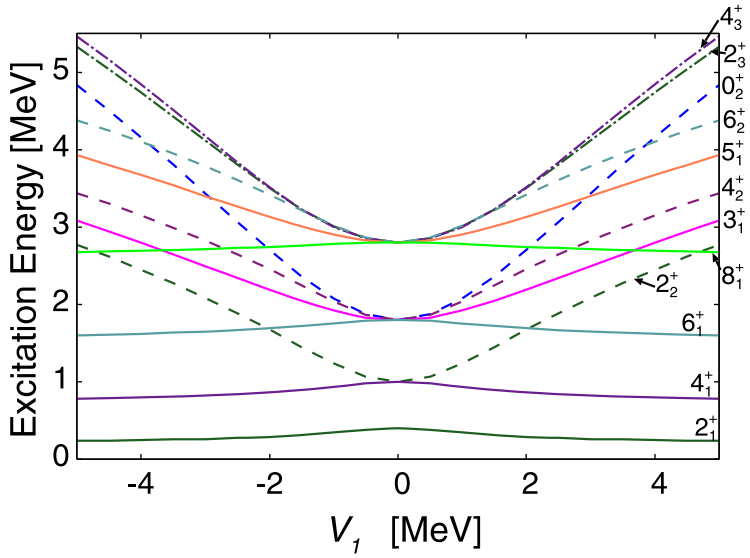

Fig. 4. Dependence of excitation spectrum on the asymmetry parameter V_1 is displayed for the case of $V_0 = 0$.

vibrational and rotational kinetic energy terms in the (1+3)D collective Hamiltonian possess the symmetry under the OP inversion. In short, the inversion $V_1 \to -V_1$ merely interchanges the roles of the oblate and prolate shapes.

Let us proceed to more general situations where $\epsilon = 0$ but both V_0 and V_1 are nonzero. Three typical situations are illustrated in Fig. 5. In this figure, the collective potentials and energy spectra are drawn for three different sets of parameters, $(V_0, V_1) = (-2, 1), (1, 0.5)$, and (10, 1) MeV. Panel (a) simulates a situation where the minimum of the collective potential occurs at a triaxial shape but it is rather shallow, so that the potential pocket accommodates only the ground 0^+ state and the first excited 2^+ state. Panel (b) simulates the situation encountered in the microscopic ASCC calculation,[14),15)] where two local minima appear both at the oblate and prolate shapes but the barrier between them is so low that strong shape mixing may take place. Panel (c) illustrates an ideal situation for shape coexistence, where the barrier between the oblate and prolate minima is so high that two rotational bands associated with them retain their identities.

For three typical situations illustrated in Fig. 5, we examine the sensitivity of excitation spectra to the asymmetry parameter V_1. This is done in Fig. 6. (Panels (a), (b), and (c) show the excitation spectra as functions of V_1 for $V_0 = -2, 1$, and 10 MeV, respectively.) We see that the dependence on V_1 is rather weak in cases (a) and (b). In contrast, the effect of the V_1 term is extremely strong in case (c): the approximate doublet structure at $V_0 = 0$ is quickly broken as soon as the V_1 term is switched on, and the excitation energies of the yrare partners $(0_2^+, 2_2^+, 4_2^+, 6_2^+)$ markedly increase as V_1 increases. Quantitatively, the energy splittings between the yrast and yrare states with the same angular momenta are proportional to V_1^2 for $V_1 \lesssim 0.2$ MeV and then increase almost linearly in the region of $V_1 \gtrsim 0.2$ MeV.

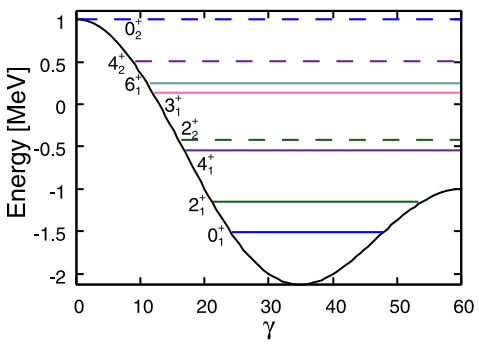

(a) $V_0 = -2.0$ MeV, $V_1 = 1.0$ MeV

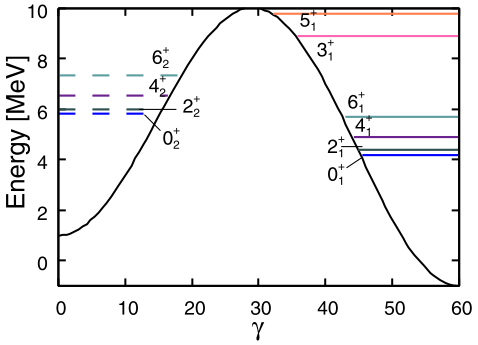

(c) $V_0 = 10.0$ MeV, $V_1 = 1.0$ MeV

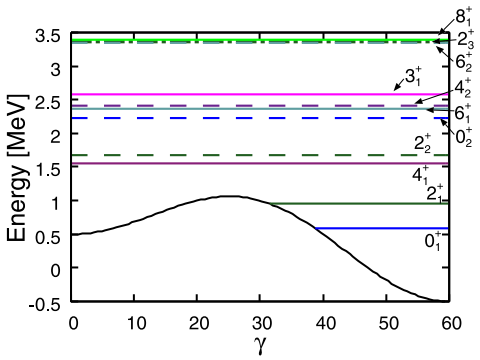

(b) $V_0 = 1.0$ MeV, $V_1 = 0.5$ MeV

Fig. 5. The collective potentials $V(\gamma)$ and eigenenergies are displayed in panels (a), (b), and (c) for $(V_0, V_1) = (-2.0, -1.0)$, $(1.0, 0.5)$, and (10.0, 1.0) MeV, respectively.

The quadratic dependence on V_1 in the small-V_1 region can be understood as the second-order perturbation effects in the double-well problem. In this case, what is important is not the absolute magnitude of V_1 but its ratio to the energy splitting due to the quantum tunneling through the potential barrier between the two minima. The structure of the collective wave functions is markedly changed by the small perturbation. Indeed, for $V_1 \gtrsim 0.2$ MeV, they are already well localized in one of the potential pockets, as we shall discuss below in connection with Fig. 9. Once the collective wave functions are well localized, the energy shifts are mainly determined by the diagonal matrix elements of the V_1 term (with respect to the localized wave functions), leading to the almost linear dependence on V_1.

The effects of the V_1 term are observed more clearly in the collective wave functions. Figures 7, 8, and 9 show the collective wave functions squared $\sum_K |\Phi_{IK\alpha}(\gamma)|^2$ of the yrast and yrare states for $V_0 = -2, 1$, and 10 MeV, which respectively correspond to the potentials in panels (a), (b), and (c) of Fig. 5. In Figs. 7 and 8, one sees that the localization (with respect to the γ coordinate) of the collective wave functions of the yrast states grows as V_1 increases, while that of the yrare states

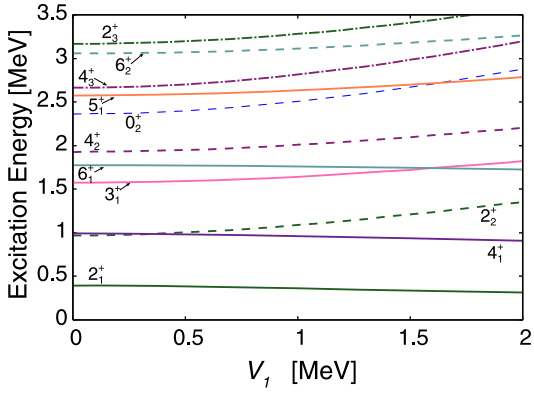

(a) $V_0 = -2.0$ MeV

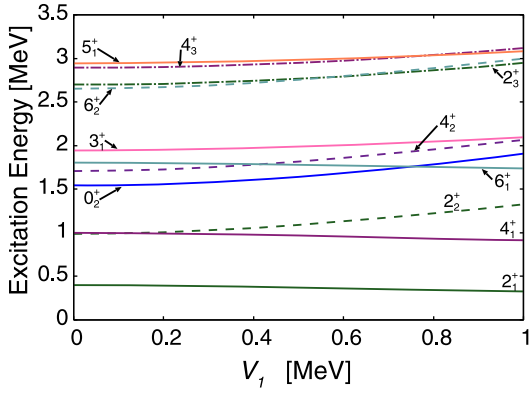

(c) $V_0 = 10.0$ MeV

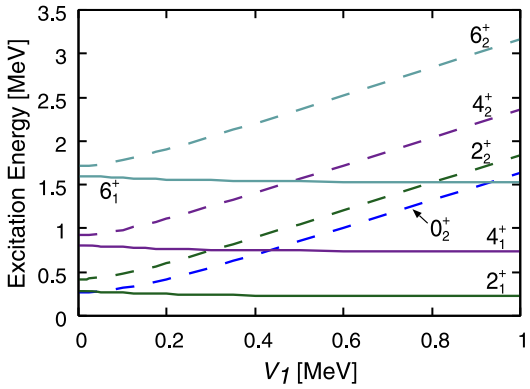

(b) $V_0 = 1.0$ MeV

Fig. 6. Dependence of excitation spectrum on the asymmetry parameter V_1 is displayed for $V_0 = -2.0$ (panel a), 1.0 (panel b), and 10.0 MeV (panel c).

are insensitive to V_1. This can be easily understood by considering that the kinetic-energy effects tend to dominate over the potential-energy effects with the increase in the excitation energies. It is interesting to note that in Fig. 8, although the yrast 4^+_1 state is situated above the potential barrier, its wave function is well localized around the oblate minimum. Concerning the yrare 4^+_2 state, although its wave function has the maximum at the prolate shape due to the orthogonality to the 4^+_1 state, it is considerably extended over the entire region of γ. For the reason mentioned above, the effects of the V_1 term on the localization properties of the yrare states are much weaker than those of the yrast states.

In Fig. 9, we see considerable effects of the V_1 term. At $V_1 = 0$, the wave functions squared are symmetric about $\gamma = 30°$. This symmetry is immediately broken after the V_1 term is switched on: the wave functions of the yrast states rapidly localize around the potential minimum even if the energy difference between the two local

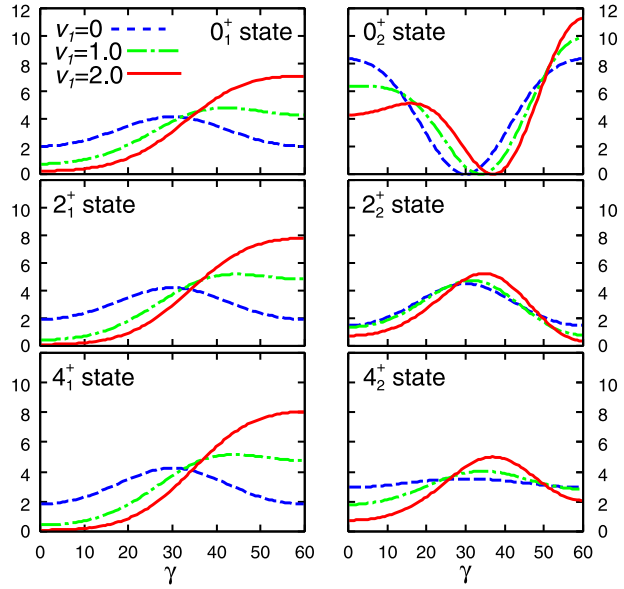

Fig. 7. Collective wave functions squared $\sum_K |\Phi_{IK\alpha}(\gamma)|^2$ of the yrast and yrare states for the collective potentials $V(\gamma)$ with $V_1 = 0.0, 1.0$, and 2.0 MeV. The barrier-height parameter V_0 is fixed at -2.0 MeV.

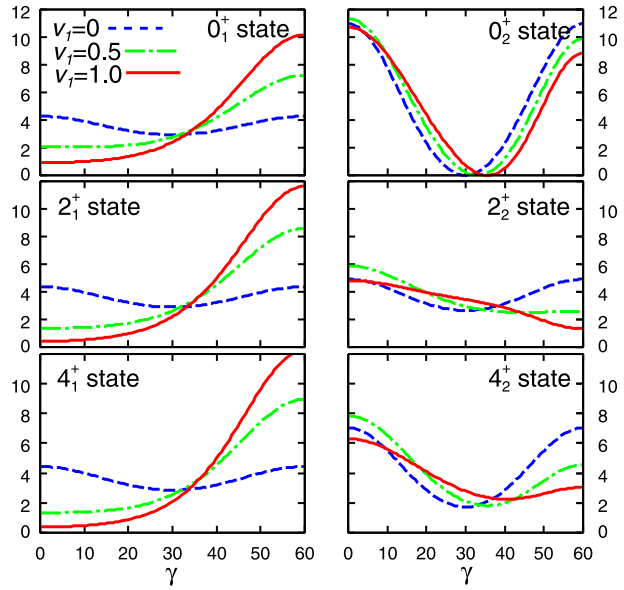

Fig. 8. The same as Fig. 7 but for $V_0 = 1.0$ and V_1 =0.0, 0.5, and 1.0 MeV.

minima is very small. In striking contrast to the situation presented in Fig. 8, the wave functions of the yrare states also localize about the second minimum of the potential. We confirmed that V_1 of 0.2 MeV is sufficient to bring about such strong localization. As pointed out above in connection with the double-well problem, this

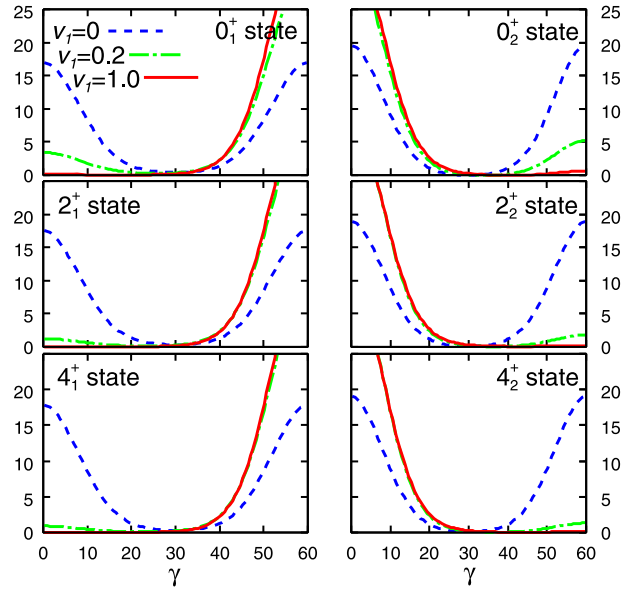

Fig. 9. The same as Fig. 7 but for $V_0 = 10.0$ and V_1 =0.0, 0.2, and 1.0 MeV.

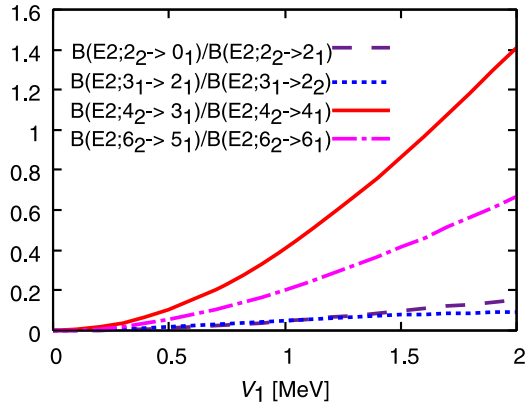

Fig. 10. Dependence on the asymmetry parameter V_1 of selected $E2$ branching ratios that vanish in the oblate-prolate symmetric limit $V_1 = 0$. The barrier-height parameter V_0 is fixed at -2.0 MeV.

value of V_1 is small but comparable to the energy splittings. Thus, one can regard Fig. 9 as a very good example demonstrating that even a small symmetry breaking in the collective potential can cause a marked change in the properties of the collective wave function, provided that the barrier is sufficiently high.

In the remaining part of this subsection, we discuss how the V_1 term affects the properties of electric quadrupole ($E2$) transitions and moments. In Fig. 10, the $B(E2)$ ratios that vanish in the $V_1 = 0$ limit are plotted as functions of V_1 for the $V_0 = -2.0$ MeV case corresponding to Figs. 5(a), 6(a), and 7. The vanishing of these ratios is well known as one of the signatures of the triaxial shape with $\gamma = 30^\circ$ in

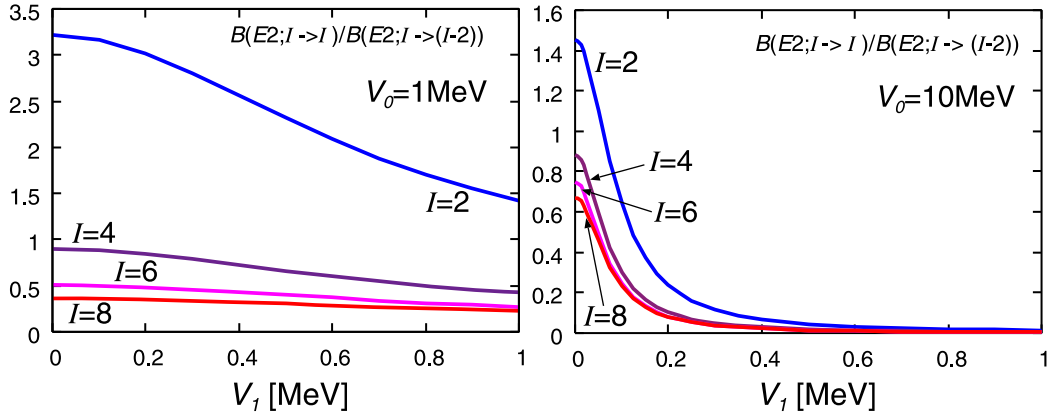

(a) $V_0 = 1.0$ MeV (b) $V_0 = 10.0$ MeV

Fig. 11. Dependence on the asymmetry parameter V_1 of the branching ratios $B(E2; I_{\rm yrare} \to I_{\rm yrast})/B(E2; I_{\rm yrare} \to (I-2)_{\rm yrare})$. Here, $I_{\rm yrast}$ and $I_{\rm yrare}$ denote the yrast and yrare states having the same values of angular momenta I, while $(I-2)_{\rm yrare}$ denotes the yrare states with angular momentum $I-2$. The left and right panels show the results of calculation for $V_0 = 1.0$ and 10.0 MeV, respectively.

the rigid triaxial rotor model.[17] It should be emphasized, however, that this is in fact a consequence of OP symmetry: these $E2$ transitions vanish owing to the exact cancellation between the contribution from the prolate side ($0^\circ \le \gamma < 30^\circ$) and that from the oblate side ($30^\circ < \gamma \le 60^\circ$). Therefore, the localization around $\gamma = 30^\circ$ is not a necessary condition. In fact, these ratios vanish also in the γ-unstable model.[16] As anticipated, we see in Fig. 10 that these ratios increase as the collective potential becomes more asymmetric with respect to the oblate and prolate shapes. In particular, the significant increases in the ratios, $B(E2; 4_2^+ \to 3_1^+)/B(E2; 4_2^+ \to 4_1^+)$ and $B(E2; 6_2^+ \to 5_1^+)/B(E2; 6_2^+ \to 6_1^+)$, are remarkable. This may be interpreted as an incipient trend that the sequence of states $(2_2^+, 3_1^+, 4_2^+, 5_1^+,$ and $6_2^+)$ forms a γ-vibrational bandlike structure about the axially symmetric shape (oblate in this case) when V_1 becomes very large.

In Fig. 11, the ratios $B(E2; I_{\rm yrare} \to I_{\rm yrast})/\ B(E2; I_{\rm yrare} \to (I-2)_{\rm yrare})$ are plotted as functions of V_1 for the two cases of $V_0 = 1.0$ and 10.0 MeV. The $V_0 = 1.0$ case corresponds to Figs. 5(b), 6(b), and 8, while the $V_0 = 10.0$ case corresponds to Figs. 5(c), 6(c), and 9. Here, the numerator denotes $B(E2)$ values for $\Delta I = 0$, $E2$ transitions from the yrare to the yrast states with the same angular momenta I, while the denominator indicates $\Delta I = -2$, $E2$ transitions between the yrare states. One immediately notices a sharp contrast between the two cases: when the barrier between the oblate and prolate local minima is very low ($V_0 = 1.0$ MeV), these values are sizable even at $V_1 = 1.0$ MeV, although they gradually decrease with increasing V_1. In contrast, when the barrier is very high ($V_0 = 10.0$ MeV), they quickly decrease once the OP-symmetry-breaking term is turned on. The reason why the interband

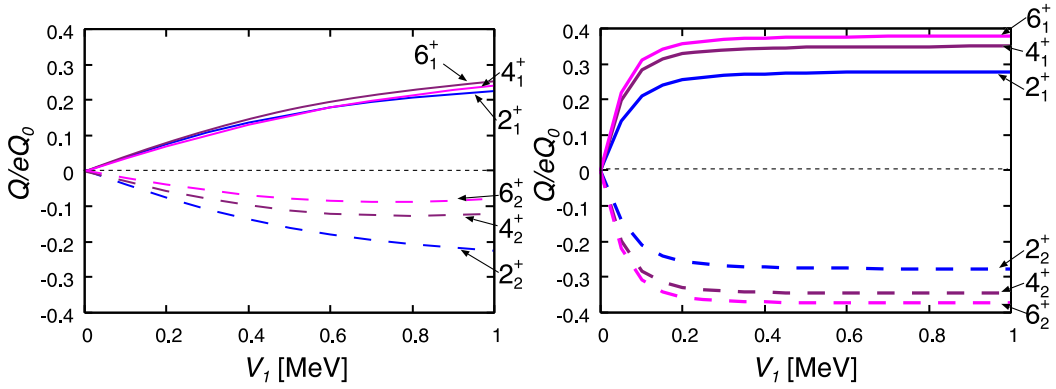

(a) $V_0 = 1.0$ MeV (b) $V_0 = 10.0$ MeV

Fig. 12. Dependence of the spectroscopic quadrupole moments on the asymmetry parameter V_1, calculated for $V_0 = 1.0$ MeV (left panel) and $V_0 = 10.0$ MeV (right panel). Their values are plotted in units of the intrinsic quadrupole moment, $eQ_0 = 3e/\sqrt{5\pi}ZR_0^2\beta_0$.

$E2$ transitions almost vanish is apparent from Fig. 9; the collective wave functions of the yrast and yrare states are well localized around the oblate and prolate shapes, respectively.

One can further confirm the same point by looking at the spectroscopic quadrupole moments displayed in Fig. 12 in a way parallel to Fig. 11. They vanish in the presence of the OP symmetry owing to the exact cancellation between the contributions from the oblate and prolate sides. In Fig. 12(a) for the low barrier case ($V_0 = 1.0$ MeV), the quadrupole moments of both the yrast and yrare states first increase after the V_1 term is switched on, but those for the yrare states eventually saturate. This trend is obvious especially for the 4_2^+ and 6_2^+ states. These results are easily understandable from the properties of their wave functions displayed in Fig. 8. That is, while the localization in the yrast states develops with increasing V_1, the wave functions of the yrare states widely extend over the entire region of γ, and the effects of the V_1 term are rather weak. In contrast, Fig. 12(b) for the high barrier case ($V_0 = 10.0$ MeV) demonstrates that both the yrast and yrare states quickly acquire quadrupole moments as soon as the V_1 term is switched on. This is a direct consequence of the wave function localization displayed in Fig. 9. Note again that the sign change, $V_1 \leftrightarrow -V_1$, corresponds to the OP inversion.

When V_0 is large and V_1 is small, just as in the above case, the yrast and yrare states can be grouped, in a very good approximation, into two rotational bands: one associated with the oblate shape and the other with the prolate shape. This is an ideal situation for the emergence of an oblate-prolate shape coexistence phenomenon. According to the realistic HFB calculations for the collective potential,[53] however, it seems hard to obtain such a large value of V_0. Therefore, for the shape coexistence phenomena we need to take into account dynamical effects going beyond the consideration on the collective potential energies. We shall discuss this point in

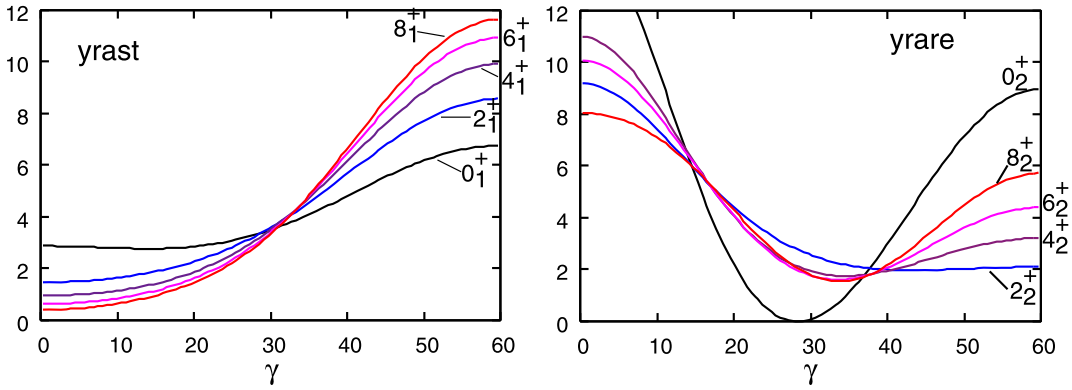

Fig. 13. Dependence on angular momentum of the collective wave functions calculated for the mass-asymmetry parameter $\epsilon = 0.5$ and the collective potential $V(\gamma)$ with $V_0 = 1.0$ and $V_1 = 0.5$ MeV. The left and right panels show the results of calculation for the yrast and yrare states, respectively.

the succeeding subsection.

4.3. *Breaking of OP symmetry in the collective mass*

We examine dynamical effects on the localization properties of the collective wave functions. As mentioned in §1, we are particularly interested in understanding the nature of the shape coexistence phenomena observed in nuclei for which approximately degenerate oblate and prolate local minima and a rather low barrier between them are suggested from the microscopic potential energy calculations.[14),15),53)] In the following, we therefore focus our discussion on the case of the collective potential with a low barrier ($V_0 = 1.0$) and weak OP asymmetry ($V_1 = 0.5$) represented in Fig. 5(b). We shall investigate how the results discussed in the previous subsections for the $\epsilon = 0$ case, where the collective mass $D_{\gamma\gamma}(\gamma), D_k(\gamma)$ and the rotational moments of inertia $\mathcal{J}_k(\gamma)$ are symmetric functions about $\gamma = 30°$, are modified when the mass-asymmetry parameter ϵ becomes nonzero.

In Fig. 13, the collective wave functions squared $\sum_K |\Phi_{IK\alpha}(\gamma)|^2$ calculated for $\epsilon = 0.5$ are displayed. It is clearly seen that, for the yrast states, the localization around the oblate shape ($\gamma = 60°$) develops with the increase in the angular momentum. The reason is easily understood: for positive ϵ, the rotational moments of inertia perpendicular to the oblate symmetry axis (2nd axis), $\mathcal{J}_1(\gamma = 60°)$ and $\mathcal{J}_3(\gamma = 60°)$, are larger than those perpendicular to the prolate symmetry axis (3rd axis), $\mathcal{J}_1(\gamma = 0°)$ and $\mathcal{J}_2(\gamma = 0°)$, as shown in Fig. 2(b). Therefore, the rotational energy for a given angular momentum decreases by increasing the probability of existence around the oblate shape. Since the rotational energy dominates over the vibrational and potential energies, the localization is enhanced for higher angular momentum states. We call this type of dynamical effect *rotation-assisted localization.* On the other hand, the wave functions of the yrare states exhibit a two-peak structure: the first peak at the prolate shape ($\gamma = 0°$) and the second at the oblate shape($\gamma = 60°$) except in the 2_2^+ state. One might naively expect that the yrare

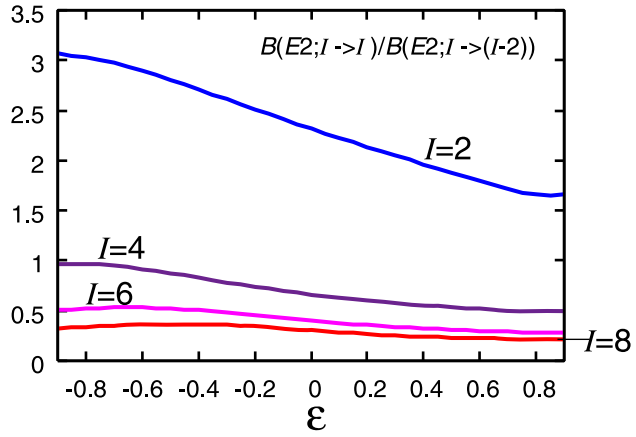

Fig. 14. Dependence on the mass-asymmetry parameter ϵ of the ratios $B(E2; I_{\rm yrare} \to I_{\rm yrast})/B(E2; I_{\rm yrare} \to (I-2)_{\rm yrare})$, calculated for $V_0 = 1.0$ and $V_1 = 0.5$ MeV. Here, $I_{\rm yrast}$ and $I_{\rm yrare}$ denote the yrast and yrare states having the same values of angular momenta I, while $(I-2)_{\rm yrare}$ denotes the yrare states with angular momentum $I-2$.

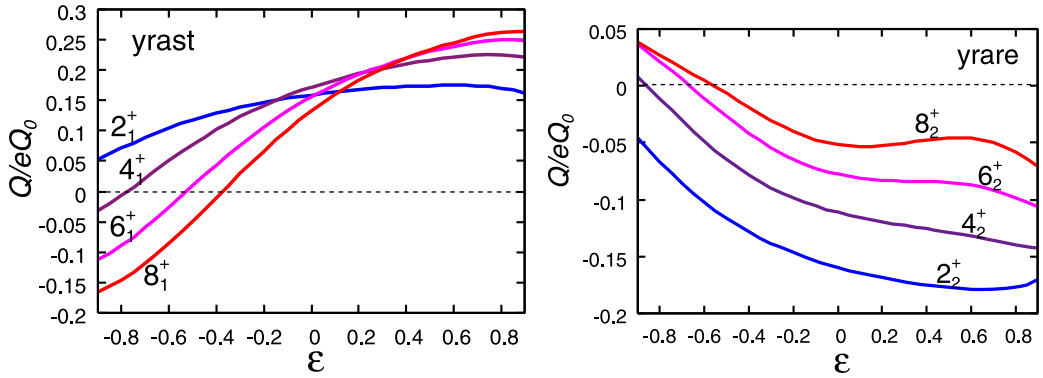

Fig. 15. Dependence of the quadrupole moments on the mass-asymmetry parameter ϵ, calculated for $V_0 = 1.0$ and $V_0 = 0.5$ MeV. The left and right panels show the results of calculation for the yrast and yrare states, respectively.

states would localize about the prolate shape because of the orthogonality requirement to the yrast states. However, the second peak is formed around the oblate shape to save the rotational energy while keeping the orthogonality condition.

Owing to the two-peak structure of the yrare wave functions mentioned above, the ratios of $B(E2)$ values from an yrare state to an yrast state to those between the yrare states remain rather large for a wide region of the mass-asymmetry parameter ϵ. This is shown in Fig. 14.

Despite the two-peak structure of the yrare wave functions, we can find a feature of shape coexistence in the spectroscopic quadrupole moments Q, which are shown in Fig. 15 as functions of ϵ. Let us first concentrate on the $\epsilon > 0$ part of this figure. We see that the Q values of the yrast states are positive, indicating their oblatelike

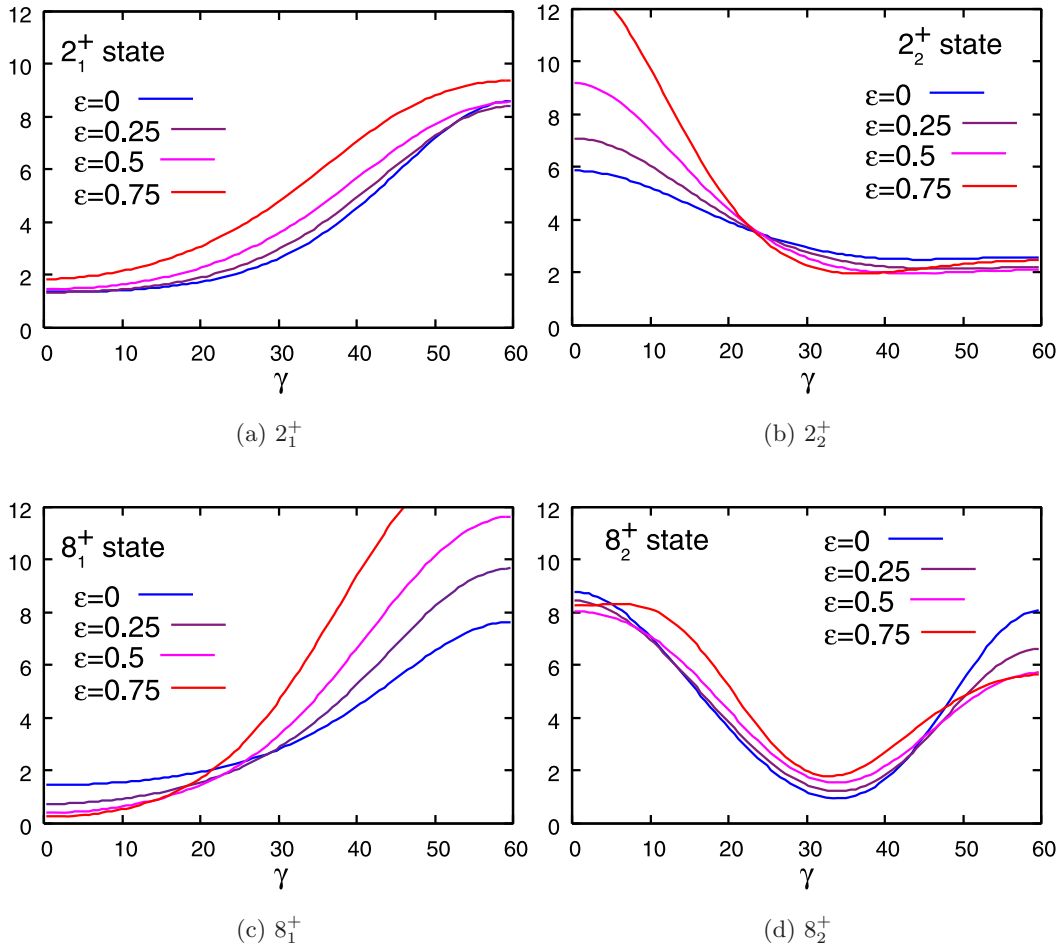

(a) 2_1^+ (b) 2_2^+

(c) 8_1^+ (d) 8_2^+

Fig. 16. Dependence of the collective wave functions on the mass-asymmetry parameter ϵ, calculated for $V_0 = 1.0$ and $V_1 = 0.5$ MeV. The upper-left and upper-right panels show the results of calculation for the yrast and yrare states with $I^\pi = 2^+$, while the lower-left and lower-right panels show those for the yrast and yrare states with $I^\pi = 8^+$.

character, while the yrare states have negative Q, indicating their prolatelike character. This can be regarded as a feature of the shape coexistence. Furthermore, it is seen that the absolute magnitude of Q increases as ϵ increases, except the 8_2^+ state. As discussed above in connection with Fig. 13, for positive ϵ, the oblate shape is favored to lower the rotational energy. Consequently, with ϵ increasing, the collective wave functions in the yrast band tend to localize around the oblate shape more and more and those of the yrare states localize around the prolate shape because of the orthogonality if the angular momentum is not so high.

It is also noticeable that the absolute magnitude of Q in the yrare band decreases with increasing angular momentum. This is because the cancellation mechanism between the contributions from the oblatelike and prolatelike regions of the collective

Table I. Expectation values of the vibrational and rotational energies in units of MeV for the $2_1^+, 2_2^+, 8_1^+$, and 8_2^+ states. The results for $\epsilon = 0.0$ and 0.5 are shown.

		2_1^+	2_2^+	8_1^+	8_2^+
$\epsilon = 0.0$	$\langle \hat{T}_{\rm vib} \rangle$	0.23	0.42	0.35	1.09
	$\langle \hat{T}_{\rm rot} \rangle$	0.29	0.55	2.56	2.87
$\epsilon = 0.5$	$\langle \hat{T}_{\rm vib} \rangle$	0.20	0.51	0.49	1.03
	$\langle \hat{T}_{\rm rot} \rangle$	0.24	0.60	2.40	3.18

wave function works more strongly as the two-peak structure grows.

Next, let us discuss the $\epsilon < 0$ part of Fig. 15. For negative ϵ, the prolate shape is favored to lower the rotational energy. On the other hand, the collective potential under consideration ($V_1 = 0.5$ MeV) is lower for the oblate shape. Hence, the rotational energy and potential energy compete to localize the collective wave function into the opposite directions. It is seen in Fig. 15 that the spectroscopic quadrupole moments of the yrast states decrease with ϵ decreasing and that this trend is stronger for higher angular momentum states. As a consequence, the Q values of the 6_1^+ and 8_1^+ states become negative for large negative ϵ, which implies that the rotational effect dominates there.

Finally, we show in Fig. 16 how the localization properties of the collective wave functions depend on the mass-asymmetry parameter ϵ, taking the 2^+ and 8^+ states as representatives of low- and high-angular-momentum states. It is clearly seen that, for the yrast states, while the localization of the 2_1^+ state around the oblate shape is rather insensitive to ϵ, that of the 8_1^+ state markedly develops with increasing ϵ. For the yrare states, the localization of the 2_2^+ state around the prolate shape grows with increasing ϵ, while the 8_2^+ state retains the two-peak structure discussed above for every value of ϵ. The different effects of the mass-asymmetry parameter ϵ on the 2^+ and 8^+ states are comprehensible from the consideration of the relative importance of the rotational and vibrational energies shown in Table I. We see that the rotational energies dominate in the 8^+ states, while the vibrational energies are comparable in magnitude to the rotational energies in the 2^+ states. Thus, the effect of the mass-asymmetry parameter ϵ on the localization properties of the 8^+ states can be easily accounted by the rotational energy. On the other hand, in the situation characterized by the parameters $V_0 = 1.0$ and $V_1 = 0.5$ MeV, the properties of the 2^+ states are determined by a delicate competition between the rotational and vibrational kinetic energies as well as the potential energy. The growth of the prolate peak with increasing ϵ in the 2_2^+ state occurs mainly because of the increase in the vibrational mass $D_{\gamma\gamma}$ at the prolate shape.

Summarizing this subsection, we have found that the OP symmetry breaking in the collective mass plays an important role in developing the localization of the collective wave functions of the yrast states. On the other hand, the asymmetry of the collective mass tends to enhance the two-peak structure of the yrare states.

§5. Role of β-γ couplings

In this section, we examine whether the results obtained in the previous section using the (1+3)D model remain valid when we take into account the β degree of freedom. Because this is a vast subject, we concentrate here on the situation in which we are most interested: namely, the case with $V_0 = 1.0, V_1 = 0.5$ MeV, and $\epsilon = 0.5$.

5.1. *A simple (2+3)-dimensional model*

We come back to the collective Schrödinger equation (2·13) for the general 5D quadrupole collective Hamiltonian and set up the collective potential in the following form:

$$V(\beta,\gamma) = \frac{1}{2}C(\beta^2-\beta_0^2)^2 - v_0\beta^6\cos^2 3\gamma + v_1\beta^3\cos 3\gamma + C_6\beta^6, \tag{5·1}$$

where $v_0 = V_0/\beta_0^6$ and $v_1 = V_1/\beta_0^3$. The first term ensures that the collective wave functions localize around $\beta \simeq \beta_0$. The second and third terms are reduced to the collective potential $V(\gamma)$ in the (1+3)D model when the collective coordinate β is frozen at $\beta = \beta_0$. The fourth term guarantees that the potential satisfies the boundary condition, $V(\beta,\gamma) \to \infty$ as $\beta \to \infty$. Obviously, the collective potential (5·1) fulfills the requirement that it should be a function of β^2 and $\beta^3\cos 3\gamma$. We note that various parameterizations of the collective potential similar to Eq. (5·1) have been used by many authors.[27),37),40)] It is certainly interesting and possible to derive the coefficients C, v_0, v_1, C_6, and β_0 using microscopic theories of nuclear collective motion. In this paper, however, we simply treat these coefficients as phenomenological parameters and determine these values so that the resulting collective potential $V(\beta,\gamma)$ qualitatively simulates that obtained using the microscopic HFB calculation[53)] for ^{68}Se . They are $C = 800$, $V_0 = 1.0$, $V_1 = 0.5$, $C_6 = 1000$ MeV, and $\beta_0^2 = 0.1$. In Fig. 17, the collective potential with these coefficients is drawn in the (β,γ) plane. One may immediately note the following characteristic features of this collective potential. 1) There are two local minima, one at the oblate shape and the other at the prolate shape. They are approximately degenerate in energy but the oblate minimum is slightly lower. 2) There is a valley along the $\beta = \beta_0$ line connecting the two local minima. 3) The spherical shape is a local maximum, which is approximately 4 MeV higher than the oblate minimum.

We set up the collective mass functions appearing in the collective kinetic energy terms as

$$D_{\beta\beta}(\beta,\gamma) = D(1-\epsilon'\beta\cos 3\gamma), \tag{5·2}$$

$$D_{\gamma\gamma}(\beta,\gamma) = D\beta^2(1+\epsilon'\beta\cos 3\gamma), \tag{5·3}$$

$$D_{\beta\gamma}(\beta,\gamma) = D\epsilon'\beta\sin 3\gamma, \tag{5·4}$$

$$D_k(\beta,\gamma) = D(1+\epsilon'\beta\cos\gamma_k), \tag{5·5}$$

where $\epsilon' = \epsilon/\beta_0$. These expressions are adopted to take into account the lowest-order (β,γ) dependence of the collective mass functions derived by Yamada[48)] by the SCC method.[51)] We use the same values for D and ϵ as in Fig. 13, namely, $D = 50$ MeV^{-1} and $\epsilon = 0.5$.

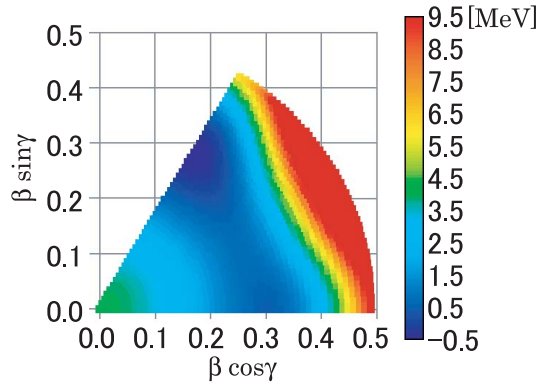

Fig. 17. Map of the two-dimensional collective potential $V(\beta,\gamma)$ defined by Eq. (5·1) for $C = 800.0$, $V_0 = 1.0$, $V_1 = 0.5$, $C_6 = 1000.0$ MeV, and $\beta_0^2 = 0.1$.

5.2. *Comparison of the (1+3)D and (2+3)D model calculations*

We have solved the collective Schrödinger equation (2·13) using the collective potential (5·1) and the collective masses (5·2)–(5·5). Below, the results of the numerical calculation are presented and compared with those of the (1+3)D model.

Figures 18 and 19 show on the (β,γ) plane the two-dimensional collective wave functions squared, $\sum_K |\Phi_{IK\alpha}(\beta,\gamma)|^2$, and the β^4-weighted ones, $\beta^4 \sum_K |\Phi_{IK\alpha}(\beta,\gamma)|^2$, respectively, of the yrast and yrare states with even angular momenta $I = 0-8$. The β^4 factor carries the major β dependence of the intrinsic volume element $d\tau'$ given by Eq. (2·17). We see in Fig. 18 that, except for the 0^+ states, the yrast (yrare) wave functions are well localized around the oblate (prolate) shape. While the localization of the yrast wave functions grows as the angular momentum increases, the yrare wave functions gradually develop the second peaks around the oblate shape. These behaviors are qualitatively the same as those we have seen for the collective wave functions in the (1+3)D model in Fig. 13. For the 0^+ states, the wave functions squared in Fig. 18 appear to be spread over a rather wide region around the spherical shape, but the β^4-weighted ones in Fig. 19 take the maxima (as functions of β) near the constant-β line with $\beta = \beta_0$. Thus, we can see in Fig. 19 a very good correspondence with the (1+3)D wave functions including the 0^+ states also. That is, the behaviors along the constant-β line of the collective wave functions in the (2+3)D model exhibit qualitatively the same features as those of the (1+3)D model. (A minor difference is seen only in the relative heights of the oblate and prolate peaks of the 0_2^+ wave function.) We note that the localization properties of the collective wave function are seen better in the β^4-weighted wave functions squared than those multiplied by the total intrinsic volume element, $d\tau' \sum_K |\Phi_{IK\alpha}(\beta,\gamma)|^2$, which always vanish at the oblate and prolate shapes owing to the $\sin 3\gamma$ factor contained in $d\tau'$.

Finally, we compare in Fig. 20 the excitation spectrum obtained in the (2+3)D model with that in the (1+3)D model. It is evident that they agree very well. Aside from the quantitative difference that the excitation energies are slightly higher and the $B(E2)$ values increase more rapidly with increasing angular momentum in the (2+3)D model than in the (1+3)D model, the essential features of the excitation

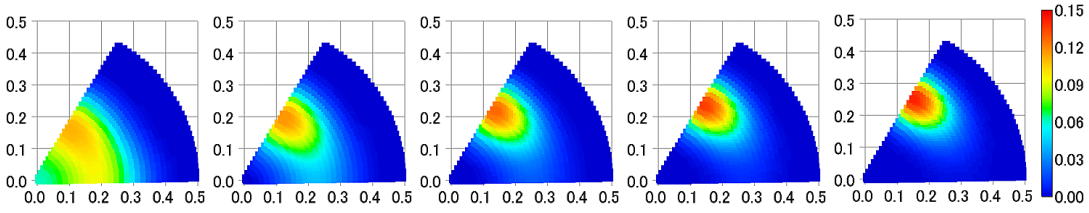

(a) 0_1 state (b) 2_1 state (c) 4_1 state (d) 6_1 state (e) 8_1 state

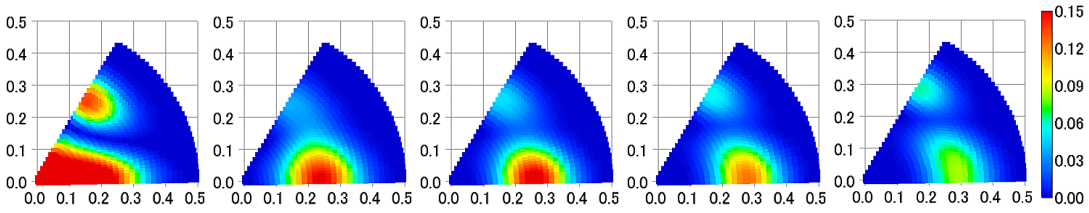

(f) 0_2 state (g) 2_2 state (h) 4_2 state (i) 6_2 state (j) 8_2 state

Fig. 18. Collective wave functions squared $\sum_K |\Phi_{IK\alpha}(\beta,\gamma)|^2$ calculated for the mass-asymmetry parameter $\epsilon = 0.5$ and the two-dimensional collective potential $V(\beta,\gamma)$ with $C = 800.0, V_0 = 1.0$, $V_1 = 0.5$, $C_6 = 1000.0$ MeV, and $\beta_0^2 = 0.1$. The upper and lower panels show the results for the yrast and yrare states, respectively.

spectrum are the same. In particular, we find a perfect agreement in the level sequences: the energy ordering of these eigenstates are exactly the same between the two calculations. This agreement implies that the β-γ coupling plays only a secondary role here, and the major feature of the excitation spectrum is determined by triaxial deformation dynamics. In this dynamics, the γ dependence of the collective mass functions plays an important role as well as that of the collective potential.

The excitation spectra of Fig. 20 are quite different from any of the patterns known well in axially symmetric deformed nuclei, in the rigid triaxial rotor model, and in the γ-unstable model. It also deviates considerably from the spectrum expected in an ideal situation of the oblate-prolate shape coexistence where two rotational bands keep their identities without strong mixing between them. Among a number of interesting features, we first notice the unique character of the 0_2^+ state. It is significantly shifted up in energy from its expected position when the yrare $0_2^+, 2_2^+, 4_2^+, 6_2^+$, and 8_2^+ states form a regular rotational band. As we have discussed in connection with Fig. 3, the position of the 0_2^+ state relative to the 2_2^+ state serves as a sensitive measure indicating where the system locates between the γ-unstable situation ($V_0 = V_1 = 0$) and the ideal oblate-prolate shape coexistence (large V_0 and small V_1). Thus, the results of our calculation suggest that experimental data for the excitation energy of the 0_2^+ state provide very valuable information on the barrier height between the oblate and prolate local minima. In this connection, we also note that the 3_1^+ (5_1^+) state is situated slightly higher in energy than the 6_1^+ and 4_2^+ (8_1^+

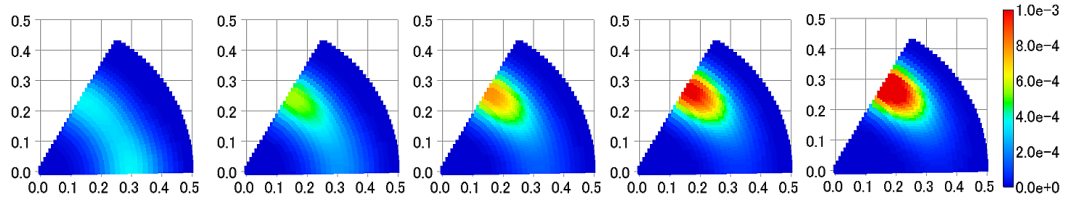

(a) 0_1 state (b) 2_1 state (c) 4_1 state (d) 6_1 state (e) 8_1 state

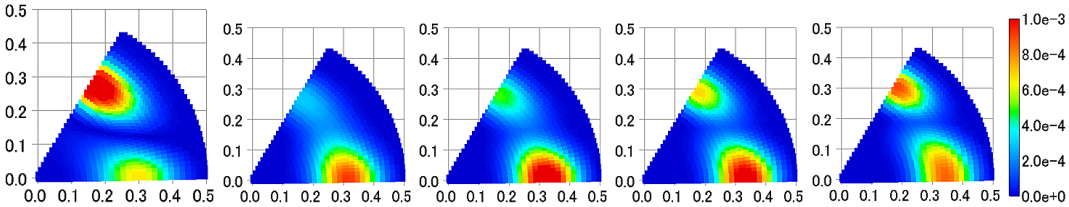

(f) 0_2 state (g) 2_2 state (h) 4_2 state (i) 6_2 state (j) 8_2 state

Fig. 19. The same as Fig. 18 but for weighted collective wave functions squared $\beta^4 \sum_K |\Phi_{IK\alpha}(\beta,\gamma)|^2$.

and 6_2^+) states. These are other indicators suggesting that the system is located in an intermediate situation between the two limits mentioned above.

In Fig. 20, we further notice interesting properties of the $E2$ transitions from the yrare to the yrast states: for instance, the $E2$ transitions with $\Delta I = -2$, or $B(E2; I_{\rm yrare} \to (I-2)_{\rm yrast})$, and those with $\Delta I = +2$, or $B(E2; I_{\rm yrare} \to (I+2)_{\rm yrast})$, are much smaller than other yrare-to-yrast $E2$ transitions. These transitions are forbidden in the γ-unstable model[16] because they transfer the boson seniority v by $\Delta v = 2$ and $\Delta v = 0$, respectively. Thus, some features characteristic of the γ-unstable situation persist here. On the other hand, although $B(E2; 3_1 \to 4_2)$ and $B(E2; 5_1 \to 6_2)$ are also forbidden transitions with $\Delta v = 0$ in the γ-unstable limit, they are not very small in Fig. 20 and indicate a significant deviation from the γ-unstable limit.

The spectroscopic quadrupole moments Q calculated in the (1+3)D and (2+3)D models are compared in Fig. 21. It is seen again that the two calculations show the same qualitative features: both calculations yield the positive (negative) sign for the spectroscopic quadrupole moments of the yrast (yrare) states to indicate an oblatelike (prolatelike) character. Quantitatively, in the (2+3)D model, the yrast Q value increases with angular momentum more significantly and the absolute values of the yrare Q moments are slightly smaller than those of the (1+3)D model. As we discussed above, in both calculations, the Q value of the yrare states approaches zero with increasing angular momentum owing to the cancellation mechanism associated with the growth of the two-peak structure in the collective wave functions. Despite such deviations from a simple picture, we can see in Fig. 21 some qualitative features

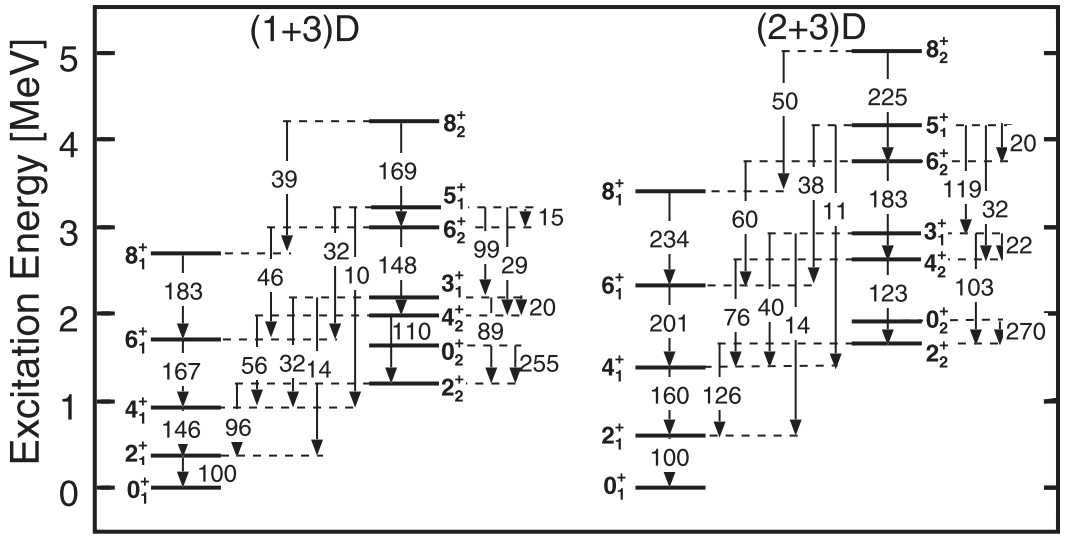

Fig. 20. Comparison of the excitation spectra and $E2$-transition properties in the (1+3)D model (left side) and those in the (2+3)D model (right side), calculated for the potential parameters $V_0 = 1.0, V_1 = 0.5$ MeV, and the mass-asymmetry parameter $\epsilon = 0.5$. Additional parameters for the two-dimensional potential $V(\beta, \gamma)$ in the (2+3)D model are $C = 800.0$ and $C_6 = 1000.0$ MeV. The $B(E2)$ values are written on the transition arrows normalizing $B(E2; 2_1 \to 0_1)$ as 100. Weak $E2$ transitions whose $B(E2)$ values smaller than 10 are not shown.

characteristic of the oblate-prolate shape coexistence.

We conclude that the excitation spectrum and the properties of the quadrupole transitions and moments exhibited in Figs. 20 and 21 can be regarded as those characteristic of an intermediate situation between the well-developed oblate-prolate shape coexistence and the γ-unstable limit.

§6. Concluding remarks

From the viewpoint of the oblate-prolate symmetry and its breaking, we have proposed a simple (1+3)D model capable of describing the coupled motion of the large-amplitude shape fluctuation in the γ-degree of freedom and the three-dimensional rotation. Using this model, we have carried out a systematic investigation of the oblate-prolate shape coexistence phenomena and their relationships to other classes of low-frequency quadrupole modes of excitation, including particular cases described using the γ-unstable model and rigid triaxial rotor model. We have also adopted the (2+3)D model to check the validity of freezing the β degree of freedom in the (1+3)D model. We have obtained a number of interesting suggestions for the properties of low-lying states that are characteristic of an intermediate situation between the well-developed oblate-prolate shape-coexistence and γ-unstable limits. In particular, 1) the relative energies of the excited 0^+ states can be indicators of the barrier height of the collective potential. 2) Specific $E2$ transition probabilities are sensitive to the oblate-prolate symmetry breaking. 3) Nuclear rotation can as-

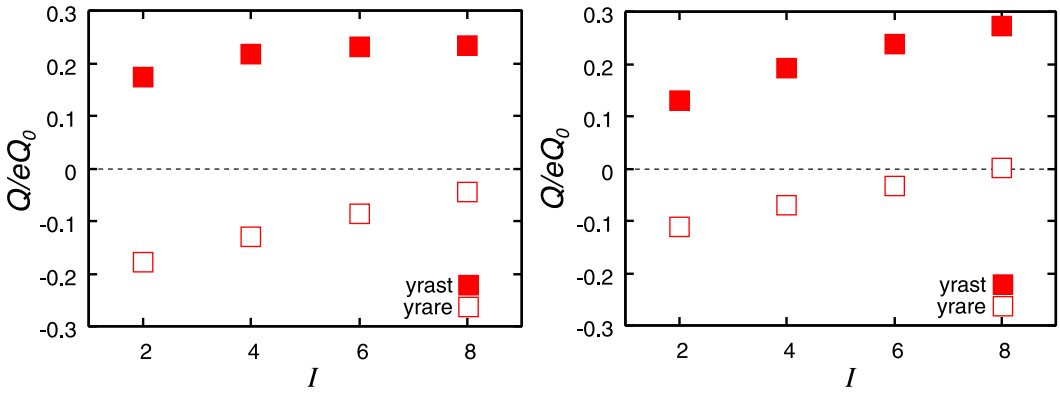

(a) (1+3)D (b) (2+3)D

Fig. 21. The same as Fig. 20 but for the spectroscopic quadrupole moments in units of the intrinsic quadrupole moment, $eQ_0 = 3e/\sqrt{5\pi}ZR_0^2\beta_0$. The results of calculation in the (1+3)D model and (2+3)D model are displayed as functions of angular momentum I in the left and right panels, respectively. The values for the yrast (yrare) states are indicated by filled (open) squares.

sist the localization of the collective wave functions in the (β, γ) deformation space. However, even if the rotation-assisted localization is realized in the yrast band, it is not necessarily in the yrare band: the two-peak structure may develop in the yrare band.

Acknowledgements

One of the authors (N. H.) is supported by the Special Postdoctoral Researcher Program of RIKEN. This work is supported by Grants-in-Aid for Scientific Research (Nos. 20540259, 21340073) from the Japan Society for the Promotion of Science and the JSPS Core-to-Core Program "International Research Network for Exotic Femto Systems".

References

1) S. M. Fischer et al., Phys. Rev. Lett. **84** (2000), 4064.
2) S. M. Fischer et al., Phys. Rev. C **67** (2003), 064318.
3) J. Ljungvall et al., Phys. Rev. Lett. **100** (2008), 102502.
4) J. L. Wood, K. Heyde, W. Nazarewicz, M. Huyse and P. van Duppen, Phys. Rep. **215** (1992), 101.
5) A. N. Andreyev et al., Nature **405** (2000), 430.
6) T. Duguet, M. Bender, P. Bonche and P.-H. Heenen, Phys. Lett. B **559** (2003), 201.
7) R. R. Rodríguez-Guzmán, J. L. Egido and L. M. Robledo, Phys. Rev. C **69** (2004), 054319.
8) M. Matsuo, T. Nakatsukasa and K. Matsuyanagi, Prog. Theor. Phys. **103** (2000), 959.
9) M. Kobayasi, T. Nakatsukasa, M. Matsuo and K. Matsuyanagi, Prog. Theor. Phys. **113** (2005), 129.
10) T. Nikšić, Z. P. Li, D. Vretenar, L. Próchniak, J. Meng and P. Ring, Phys. Rev. C **79** (2009), 034303.
11) Z. P. Li, T. Nikšić, D. Vretenar, J. Meng, G. A. Lalazissis and P. Ring, Phys. Rev. C **79**

(2009), 054301.
12) M. Bender and P.-H. Heenen, Phys. Rev. C **78** (2008), 024309.
13) M. Girod, J.-P. Delaroche, A. Görgen and A. Obertelli, Phys. Lett. B **676** (2009), 39.
14) N. Hinohara, T. Nakatsukasa, M. Matsuo and K. Matsuyanagi, Prog. Theor. Phys. **119** (2008), 59; Prog. Theor. Phys. **117** (2007), 451.
15) N. Hinohara, T. Nakatsukasa, M. Matsuo and K. Matsuyanagi, Phys. Rev. C **80** (2009), 014305.
16) L. Wilets and M. Jean, Phys. Rev. **102** (1956), 788.
17) A. S. Davydov and G. F. Filippov, Nucl. Phys. **8** (1958), 237.
18) A. Bohr and B. R. Mottelson, *Nuclear Structure*, Vol. II (W. A. Benjamin Inc., 1975; World Scientific, 1998).
19) A. Bohr, Mat. Fys. Medd. Dan. Vid. Selsk. **26**, No. 14 (1952).
20) A. Bohr and B. R. Mottelson, Mat. Fys. Medd. Dan. Vid. Selsk. **27**, No. 16 (1953).
21) G. Gneuss and W. Greiner, Nucl. Phys. A **171** (1971), 449.
22) P. O. Hess, M. Seiwert, J. Maruhn and W. Greiner, Z. Phys. A **296** (1980), 147.
23) J. Libert and P. Quentin, Z. Phys. A **306** (1982), 315.
24) D. Troltenier, J. Maruhn, W. Greiner and P. O. Hess, Z. Phys. A **343** (1992), 25.
25) T. Marumori, M. Yamamura and H. Bando, Prog. Theor. Phys. **28** (1962), 87.
26) S. T. Belyaev, Nucl. Phys. **64** (1965), 17.
27) K. Kumar and M. Baranger, Nucl. Phys. A **92** (1967), 608.
28) K. Kumar, Nucl. Phys. A **92** (1967), 653; Nucl. Phys. A **231** (1974), 189.
29) M. Baranger and K. Kumar, Nucl. Phys. **62** (1965), 113; Nucl. Phys. A **110** (1968), 490; Nucl. Phys. A **110** (1968), 529; Nucl. Phys. A **122** (1968), 241; Nucl. Phys. A **122** (1968), 273.
30) I. Deloncle, J. Libert, L. Bennour and P. Quentin, Phys. Lett. B **233** (1989), 16.
31) S. G. Rohoziński, J. Dobaczewski, B. Nerlo-Pomorska, K. Pomorski and J. Srebrny, Nucl. Phys. A **292** (1977), 66.
32) L. Próchniak, K. Zajac, K. Pomorski, S. G. Rohoziński and J. Srebrny, Nucl. Phys. A **648** (1999), 181.
33) J. Libert, M. Girod and J.-P. Delaroche, Phys. Rev. C **60** (1999), 054301.
34) L. Próchniak, P. Quentin, D. Samsoen and J. Libert, Nucl. Phys. A **730** (2004), 59.
35) J. Srebrny et al., Nucl. Phys. A **766** (2006), 25.
36) D. J. Rowe, Nucl. Phys. A **735** (2004), 372.
37) D. J. Rowe, T. A. Welsh and M. A. Caprio, Phys. Rev. C **79** (2009), 054304.
38) F. Iachello, Phys. Rev. Lett. **85** (2000), 3580; Phys. Rev. Lett. **87** (2001), 052502; Phys. Rev. Lett. **91** (2003), 132502.
39) M. A. Caprio and F. Iachello, Nucl. Phys. A **781** (2007), 26.
40) M. A. Caprio, arXiv:0902.0022.
41) S. De Baerdemacker, L. Fortunato, V. Hellemans and K. Heyde, Nucl. Phys. A **769** (2006), 16.
42) D. Bonatsos et al., Phys. Rev. C **76** (2007), 064312.
43) L. Fortunato, Eur. Phys. J. A **26** Suppl. 1 (2005), 1.
44) S. G. Lie and G. Holzwarth, Z. Phys. **249** (1972), 332; Phys. Rev. C **12** (1975), 1035.
45) T. Tamura, K. Weeks and T. Kishimoto, Phys. Rev. C **20** (1979), 307.
46) K. Weeks and T. Tamura, Phys. Rev. C **22** (1980), 888; Phys. Rev. C **22** (1980), 1323.
47) H. Sakamoto, Phys. Rev. C **52** (1995), 177; Phys. Rev. C **64** (2001), 024303.
48) K. Yamada, Prog. Theor. Phys. **89** (1993), 995.
49) R. V. Jolos and P. von Brentano, Phys. Rev. C **79** (2009), 044310; Phys. Rev. C **78** (2008), 064309; Phys. Rev. C **77** (2008), 064317; Phys. Rev. C **76** (2007), 024309; Phys. Rev. C **74** (2006), 064307.
50) N. Onishi, I. Hamamoto, S. Åberg and A. Ikeda, Nucl. Phys. A **452** (1986), 71.
51) T. Marumori, T. Maskawa, F. Sakata and A. Kuriyama, Prog. Theor. Phys. **64** (1980), 1294.
52) L. D. Landau and E. M. Lifschitz, *Quantum Mechanics (Non-relativistic Theory)* (Pergamon Press, 1958).
53) M. Yamagami, K. Matsuyanagi and M. Matsuo, Nucl. Phys. A **693** (2001), 579.